Looking for hot Jupiters around young stars

Louise Yu

▶ **To cite this version:**

Louise Yu. Looking for hot Jupiters around young stars. Solar and Stellar Astrophysics [astro-ph.SR]. Université Paul Sabatier - Toulouse III, 2019. English. NNT : 2019TOU30240 . tel-02799114v2

HAL Id: tel-02799114
https://hal.science/tel-02799114v2

Submitted on 2 Oct 2020

HAL is a multi-disciplinary open access archive for the deposit and dissemination of scientific research documents, whether they are published or not. The documents may come from teaching and research institutions in France or abroad, or from public or private research centers.

L'archive ouverte pluridisciplinaire **HAL**, est destinée au dépôt et à la diffusion de documents scientifiques de niveau recherche, publiés ou non, émanant des établissements d'enseignement et de recherche français ou étrangers, des laboratoires publics ou privés.

THÈSE

En vue de l'obtention du

DOCTORAT DE L'UNIVERSITÉ DE TOULOUSE

Délivré par : *l'Université Toulouse 3 Paul Sabatier (UT3 Paul Sabatier)*

Présentée et soutenue le *06/12/2019* **par :**

Louise Yu

Recherche de Jupiters chauds autour d'étoiles jeunes

JURY

RIEUTORD	Michel	Président du Jury
DELEUIL	Magali	Rapportrice
DOUGADOS	Catherine	Rapportrice
BARUTEAU	Clément	Examinateur
BOUVIER	Jérôme	Examinateur
COLLIER CAMERON	Andrew	Examinateur
MOUTOU	Claire	Co-Encadrante

École doctorale et spécialité :
SDU2E : Astrophysique, Sciences de l'Espace, Planétologie
Unité de Recherche :
Institut de Recherche en Astrophysique en Planétologie (IRAP, UMR 5277)
Directeur de Thèse :
Jean-François DONATI
Rapporteurs :
Magali DELEUIL et *Catherine DOUGADOS*

Abstract

The past 25 years have seen the detection of about 400 hot Jupiters (hJs), giant exoplanets similar to Jupiter but orbiting their star a hundred times closer than Jupiter does the Sun. These puzzling planets are believed to have formed far from their star before migrating inwards, however the physical processes that drive this orbital transfer are still poorly constrained by observations. This question, essential to our understanding of planetary system formation, has profound implications for the architecture of these systems, and in particular for the probability of forming planets like the Earth in the habitable zone of stars.

In order to better constrain the early orbital evolution of planetary systems, we analyze data collected within the frame of the MaTYSSE programme to search for hJs around weak-line T Tauri stars (wTTSs), i.e. very young Sun-like stars that stopped accreting. The main goal of MaTYSSE is to characterize the high magnetic activity of wTTSs. This activity makes hJ detection difficult, indeed, we look for hJs with the velocimetry technique, but the strong presence of magnetic dark spots and bright plages on the surface of wTTSs adds a jitter in the radial velocities (RVs), of much greater amplitude than that expected of a hJ signature.

In this thesis, we model the magnetic activity of wTTSs TAP 26 and V410 Tau and filter the activity jitter out of their RVs. We also present the MaTYSSE results for star V830 Tau, for comparison. Using Zeeman-Doppler Imaging on spectropolarimetric data sets to reconstruct surface brightness distributions and magnetic topologies, we derive spot-and-plage coverages of 10 – 18 % and field strengths of 300 – 600 G. All three stars exhibit intrinsic variability not explained by differential rotation.

The activity jitter is modelled with two independent methods: deriving it from our ZDI maps, or applying Gaussian Process Regression to the raw RVs. Both methods concur on the detection of a hJ around V830 Tau and another around TAP 26. The $\sim$2 Myr V830 Tau b has a $M \sin i$ of $0.57 \pm 0.10\,\mathrm{M_{Jup}}$ and orbits at 0.057 ± 0.001 au from its star (orbital period $\sim$4.93 d). Due to the observing window, the orbital period of TAP 26 b cannot be uniquely determined; the case with highest likelihood is a hJ with $M \sin i = 1.66 \pm 0.31\,\mathrm{M_{Jup}}$ on an orbit of semi-major axis 0.0968 ± 0.0032 au (orbital period 10.79 ± 0.14 d). These detections suggest that type II disc migration is efficient at generating newborn hJs, and that hJs may be more frequent around young stars than around mature stars, or the MaTYSSE sample is biased towards hJ-hosting stars.

Our V410 Tau RVs exclude the presence of a Jupiter-mass companion below $\sim$0.1 au, which is suggestive that hJ formation may be inhibited by the early depletion of the circumstellar disc, which for V410 Tau may have been caused by the M dwarf stellar companion orbiting a few tens of au away.

Resumé

Les 25 dernières années ont vu la détection d'environ 400 Jupiters chauds (hJs), exoplanètes géantes semblables à Jupiter mais sur des orbites cent fois plus resserrées. Ces planètes étonnantes se seraient formées loin de leur étoile avant de migrer vers elle, cependant les processus physiques à l'origine de ce transfert orbital sont encore peu contraints par les observations. Cette question, essentielle à notre compréhension de la formation des systèmes planétaires, a de profondes répercussions sur l'architecture de ces systèmes, et en particulier sur la probabilité de former des planètes telles que la Terre dans la zone habitable des étoiles.

Afin de mieux contraindre l'évolution orbitale précoce des systèmes planétaires, nous analysons des données recueillies dans le cadre du programme MaTYSSE pour rechercher des hJs autour d'étoiles T Tauri à raies faibles (wTTSs), c'est-à-dire de très jeunes étoiles de type solaire qui n'accrètent plus. L'objectif principal de MaTYSSE est de caractériser l'importante activité magnétique des wTTSs. Cette activité rend la détection de hJs difficile, en effet, nous recherchons des hJs par la technique de vélocimétrie, mais la forte présence de taches sombres et de plages brillantes magnétiques à la surface des wTTSs ajoute une perturbation dans les vitesses radiales (RVs), d'amplitude bien supérieure à celle attendue d'une signature de hJ.

Dans cette thèse, nous modélisons l'activité magnétique des wTTSs TAP 26 et V410 Tau et filtrons la perturbation des RVs due à l'activité. Nous présentons également les résultats MaTYSSE sur l'étoile V830 Tau pour comparaison. En utilisant l'imagerie Zeeman-Doppler sur des jeux de données spectropolarimétriques pour reconstruire les distributions surfaciques de brillance et les topologies magnétiques, nous obtenons des couvertures en taches et plages de $10 - 18\,\%$ et des champs de $300 - 600\,\mathrm{G}$. Les trois étoiles présentent une variabilité intrinsèque non expliquée par la rotation différentielle.

La perturbation RV due à l'activité est modélisée à l'aide de deux méthodes indépendantes : nous la dérivons à partir de nos cartes ZDI, ou nous appliquons la régression par processus gaussiens aux RVs brutes. Les deux méthodes s'accordent sur la détection d'un hJ autour de V830 Tau et d'un autre autour de TAP 26. V830 Tau b, âgé de $\sim 2\,\mathrm{Myr}$, a un $M \sin i$ de $0.57 \pm 0.10\,\mathrm{M_{Jup}}$ et orbite à $0.057 \pm 0.001\,\mathrm{au}$ de son étoile (période orbitale $\sim 4.93\,\mathrm{d}$). La période orbitale de TAP 26 b ne peut être déterminée de façon unique à cause de la fenêtre d'observation ; le cas le plus probable est un hJ avec $M \sin i = 1.66 \pm 0.31\,\mathrm{M_{Jup}}$ sur une orbite de demi-grand axe $0.0968 \pm 0.0032\,\mathrm{au}$ (période orbitale $10.79 \pm 0.14\,\mathrm{d}$). Ces détections suggèrent que la migration de type II dans le disque est efficace pour générer des hJs nouveau-nés, et que les hJs sont peut-être plus fréquents autour des étoiles jeunes qu'autour des étoiles matures, ou que l'échantillon MaTYSSE est biaisé vers les étoiles hôtes de hJs.

Nos RVs de V410 Tau excluent la présence d'un compagnon de masse Jovienne en-deçà de $\sim 0.1\,\mathrm{au}$, ce qui suggère que la formation de hJs est peut-être inhibée par l'épuisement précoce du disque circumstellaire, qui pour V410 Tau aurait été causé par le compagnon stellaire, une naine M orbitant à quelques dizaines de au de l'étoile.

Contents

Remerciements

Tout d'abord, un énorme merci à Magali et Catherine pour avoir bien voulu lire et évaluer mon manuscrit en un intervalle de temps restreint. Merci bien sûr à Jean-François, sans qui cette thèse n'aurait pas eu lieu, pour ton accompagnement durant presque quatre ans, pour ta patience, le temps que tu as toujours pu me consacrer, et pour tout ce que tu m'as appris. Merci beaucoup à Claire et Clément pour des discussions toujours enrichissantes et pour votre bonne humeur constante. Enfin, merci à Michel, Andrew et Jérôme d'avoir bien voulu être examinateurs de ma soutenance et pour des discussions intéressantes pendant ma thèse.

Ces trois ans et demi ont été l'occasion de former de belles amitiés, qui ont agrémenté ce passage de vie particulier de précieux moments de bonheur. Un merci plein de tendresse donc aux Bras Cassés : Adrien, Mathilde, Edo, Pauline, Geoffroy, pour les jeux, les soirées, les rires. Et un grand merci à Babak, pour tous les fous rires, la musique, ton soutien, ton aide, ta bonne humeur et ta joie de partager inépuisables.

Je remercie l'équipe du PS2E pour leur accueil, pour les discussions, les Journal Clubs, les workshops : les sus-mentionnés Clément et Michel, mais aussi Pascal, Arturo, Laurène (merci pour l'école SunStars à Banyuls !), Sébastien. Merci également à tous ceux, au sein de l'IRAP, qui m'ont aidée à diverses occasions : Geneviève, Émilie, Carole, Patricia, Isabelle, Loïc.

A special thank you to those who welcomed me in St Andrews in October 2017 : Andrew and Moira, and the students Josh, Chris, Dom, Laith, Kirsten, Meng and Fran for the Friday meals and game nights. Finally, thanks to Paloma for your company and to Maries for hosting me.

Merci également à toute l'équipe d'UniverSCiel, pour d'inoubliables moments lors des festivals astrojeunes et autres sorties : Marina, Gab, Wilou, Turpin, Jason, Ppeille, Tata, Lulu, Neuha, Heussaff, Edo, Didi, Jeff, Babak, Ines, Damien, Sacha, Gabi, Simon, Mika, PM, Momo, Hadrien, Mehdi, Abe.

Je remercie tous les doctorants et post-doctorants qui sont passés à l'IRAP avant, en même temps et après moi, pour les conseils, les discussions, les parties de tarot et, pour certains, leur amitié : CHill, Colin F, Andres, Logithan, Elodie, Giovanni, Cyril, Damien, Ppeille, Wrappin, Fitouss, Kevin, Nicolas, Jessie, David, Najda, Annick, Armelle, Étienne, Damien, Gaylor, Paul, Abe, Anthony, Bonnie, Tianqi, Benjamin, Nu, Grégoire, Paul, Benjamin, Florian, Ludivine, Mélina, Léo, Mégane.

Merci aux amis d'horizons divers, pour certains loin de Toulouse, mais toujours là dans ma vie : Antoine, Audrey, Florian, Marine, Raphaël, Élise, Ao, Julien, Luana, Marion, Ambroise, Momo, Fred, Lina, HS, Jenn, Lilly, Claire et Lætitia.

Et enfin, le plus grand des mercis à ma famille, Maman, Papa, Raph, qui ont toujours été là pour moi, merci pour votre soutien et votre amour inconditionnels, j'ai beaucoup de chance de vous avoir.

Foreword

The search for exoplanets has yielded around 4000 confirmed detections in the past 30 years, in around 3000 planetary systems. Those extrasolar systems are of very diverse configurations, with many tightly-packed systems of terrestrial planets all on orbits smaller than the orbit of Mercury, some systems with one or several gas giants as massive as Jupiter or Saturn, a few systems orbiting two stars (Winn & Fabrycky, 2015)... A few candidate Solar system analogs, with a gas giant on a low-eccentricity orbit of several astronomical units around a Sun-like star, were detected as well (Barbato et al., 2018). Simultaneously to observational efforts of establishing exoplanetary population statistics, theories on the formation and evolution of planetary systems were developed to explain the current diversity of orbital configurations, and eventually assess how much of an exception the Solar system is (e.g. Mordasini, 2018).

In particular, the origins of hot Jupiters (hJs), i.e. giant planets on close-in orbits, estimated to occur around $\sim$1 % of Sun-like stars (Wright et al., 2012), are mysterious. In-situ formation in the protoplanetary disc, the primordial dust and gas planet-forming matrix around the forming star, has long been considered implausible, because the high keplerian velocities and the limited quantity of material close to the star make it difficult to build up sufficiently massive cores. Some recent studies have argued in favor of it (e.g. Batygin et al., 2016), but its feasibility is still debated (Dawson & Johnson, 2018). Two theories suggesting that giant planets form far from the star and then migrate inwards have been proposed. Such massive planets have a large gravitational influence impacting their whole planetary systems, constraining their migration would therefore be an essential first step to model the evolution of planetary systems. Shortly after the first confirmed detection of a planet around a Sun-like star (Mayor & Queloz, 1995), a circular hJ in fact, Lin et al. (1996) showed that a scenario where the giant planet migrated within its protoplanetary disc through interactions with the surrounding dust and gas, on a time scale shorter than the lifetime of the disc ($\sim$1 Myr), could explain the observations. As more giant planets got detected, their distributions of orbital eccentricities and of obliquities, depending on the distance separating them to their host star, led to another scenario where gravitational interactions between planets and with their star caused instabilities, sending them on eccentric and inclined orbits. Those which were sent on orbits crossing the influence area of stellar tidal forces would then lose orbital energy and see their orbit become circular again, over time scales of 10^2 – 10^3 Myr (Dawson & Johnson, 2018). The study of hJs aged a few Myr, around stars whose protoplanetary discs have dissipated, can therefore be a key element to investigate which migration processes dominate.

However, Sun-like stars of a few Myr that have lost their discs, called weak-line T Tauri stars (wTTSs), have an important magnetic activity that causes large-amplitude modulations of their measured luminosity and radial velocity (RV; Grankin et al., 2008; Crockett et al., 2012). As a result, potential hints of a planetary presence, either a dip in the light curve betraying a transiting planet, or a wobble in the RV curve indicating the star's reflex motion from the planet's gravitational pull, are drowned in variations an order of magnitude larger than the expected planetary signature amplitudes. Astronomers have studied the variability and activity of wTTSs since the mid-20th century, but the research for hJs around them had to wait for the advent of spectropolarimetry,

combined with magnetic imaging techniques, and its application to wTTS targets. This thesis is part of one of the pioneering programmes in the search for young hJs: MaTYSSE (Donati et al., 2014).

More precisely, MaTYSSE, which stands for Magnetic Topologies of Young Stars and the Survival of close-in massive Exoplanets, aims at characterizing the magnetic activity of wTTSs, comparing it to the magnetic activity of Sun-like stars at earlier and later evolution stages, and searching for hJs around them. It is based upon the spectropolarimetric monitoring of 35 wTTSs, with observations collected between 2013 and 2016 with the twin echelle spectropolarimeters ESPaDOnS (Donati, 2003), installed at the Canada-France-Hawaii Telescope (CFHT), Hawaii since 2004, and NARVAL, installed at the Télescope Bernard Lyot (TBL), France since 2006. From the spectra provided by these instruments, both unpolarized and circularly polarized, we use the Zeeman-Doppler Imaging (ZDI) technique, first developed in the 90s (Semel, 1989) and having undergone successive updates until 2014 (Donati et al., 2014), to reconstruct the surface distribution of brightness and of magnetic field for our wTTSs. Because RVs are measured from the spectral lines in the unpolarized spectra, the activity RV jitter originates from distorsions of the spectral lines mainly due to surface brightness inhomogeneities; therefore our ZDI brightness maps are used to model the activity RV jitter and filter it out, in order to investigate the potential presence of hJ signatures in the filtered RV curves. ZDI has proven an efficient filtering technique for wTTSs prior to this thesis, with the first two MaTYSSE papers on stars LkCa 4 (Donati et al., 2014), V819 Tau and V830 Tau (Donati et al., 2015).

This thesis presents the investigation of the activity and RVs of two more MaTYSSE stars, $\sim$17 Myr, $\sim$1 $M_\odot$ TAP 26 and $\sim$0.8 Myr, $\sim$1.4 $M_\odot$ V410 Tau, as well as V830 Tau, on which more recent data sets were collected. On top of using ZDI, another numerical technique is applied, called Gaussian Process Regression (GPR) and first proposed to the application of exoplanet hunting by velocimetry in Haywood et al. (2014). Applied directly to the raw RVs, GPR is a technique independent from ZDI, that does not rely on a physical model but assumes a given statistical behaviour of the RV curve, with the RV activity jitter being described as a correlated noise. The modelling process thus consists in finding the main parameters characterizing this statistical behaviour, providing at the same time information on the stellar activity.

The first chapter outlines the context of the whole study and presents the broad lines of what constitutes the current theories of star and planet formation and early evolution; in a second chapter, we detail the problem of modelling wTTS activity and describe the various complementary modelling techniques used for this work; chapter three then presents the results of applying our activity modelling techniques to TAP 26, V410 Tau and V830 Tau, and chapter four presents the investigation of the RV curves of these stars. Finally, we draw some conclusions that this thesis brought to the field of star and planet formation, and give some future perspectives.

Avant-propos

La recherche d'exoplanètes a donné lieu à environ 4000 détections confirmées au cours des 30 dernières années, dans environ 3000 systèmes planétaires. Ces systèmes extrasolaires sont de configurations très diverses, avec de nombreux systèmes de planètes telluriques très resserrés, sur des orbites plus petites que celle de Mercure, certains systèmes avec une ou plusieurs géantes gazeuses aussi massives que Jupiter ou Saturne, quelques systèmes en orbite autour de deux étoiles (Winn & Fabrycky, 2015)... Quelques systèmes potentiellement analogues du système solaire, avec une géante gazeuse sur une orbite à faible excentricité de plusieurs unités astronomiques autour d'une étoile semblable au Soleil, ont également été détectés (Barbato et al., 2018). Parallèlement aux efforts d'observation visant à établir des statistiques sur les populations exoplanétaires, des théories sur la formation et l'évolution des systèmes planétaires ont été élaborées pour expliquer la diversité actuelle des configurations orbitales, et finalement évaluer dans quelle mesure le système solaire fait exception (voir par exemple Mordasini, 2018).

En particulier, les origines des Jupiters chauds (hJ), planètes géantes placées sur des orbites resserrées, dont la fréquence autour des étoiles semblables au Soleil est estimée à $\sim$1 % (Wright et al., 2012), sont mystérieuses. La formation in-situ dans le disque protoplanétaire, la matrice de poussière et de gaz autour de l'étoile et des planètes en formation, a longtemps été considérée comme improbable, car les vitesses képlériennes élevées et la quantité limitée de matière à proximité de l'étoile rendent difficile la constitution de noyaux suffisamment massifs. Certaines études récentes ont plaidé en sa faveur (par exemple Batygin et al., 2016), mais sa faisabilité est encore débattue (Dawson & Johnson, 2018). Deux théories suggérant que les planètes géantes se forment loin de l'étoile et migrent ensuite vers l'intérieur ont été proposées. De telles planètes massives ont une grande influence gravitationnelle qui a un impact sur l'ensemble de leur système planétaire, comprendre leur migration serait donc une première étape essentielle pour modéliser l'évolution des systèmes planétaires. Peu après la première détection confirmée d'une planète autour d'une étoile semblable au Soleil (Mayor & Queloz, 1995), qui était d'ailleurs un hJ sur orbite circulaire, Lin et al. (1996) a montré qu'un scénario où la planète géante migrait à l'intérieur de son disque protoplanétaire par des interactions avec la poussière et le gaz environnant, sur une échelle de temps plus courte que la durée de vie du disque ($\sim$1 Myr), pourrait expliquer les observations. Au fur et à mesure que des planètes géantes furent détectées, la distribution de leurs excentricités et de leurs obliquités orbitales, en fonction de la distance qui les sépare de leur étoile hôte, a conduit à un autre scénario où les interactions gravitationnelles entre les planètes et avec leur étoile provoquent des instabilités, les envoyant sur des orbites excentriques et inclinées. Celles qui étaient envoyées sur des orbites traversant la zone d'influence des forces de marée stellaires perdraient alors de l'énergie orbitale et verraient leur orbite redevenir circulaire, sur des échelles de temps de 10^2 – 10^3 Myr (Dawson & Johnson, 2018). L'étude des hJs âgés de quelques Myr, autour d'étoiles dont les disques protoplanétaires se sont dissipés, peut donc être un élément clé pour étudier les processus de migration.

Cependant, les étoiles de quelques Myr, semblables au Soleil, qui ont perdu leurs disques, appelées étoiles T Tauri à raies faibles (wTTS), ont une activité magnétique importante qui provoque

des modulations de grande amplitude dans leurs courbes de luminosité et de vitesse radiale (RV ; Grankin et al., 2008; Crockett et al., 2012). Par conséquent, les indices potentiels d'une présence planétaire, soit une baisse de la courbe de lumière trahissant une planète en transit, soit une oscillation de la courbe RV indiquant le mouvement réflexe de l'étoile causé par l'attraction gravitationnelle de la planète, sont noyés dans des variations d'un ordre de grandeur supérieur aux amplitudes attendues des signatures planétaires. Les astronomes ont étudié la variabilité et l'activité des wTTSs depuis le milieu du 20e siècle, mais la recherche des hJs autour d'elles a dû attendre l'avènement de la spectropolarimétrie, combinée aux techniques d'imagerie magnétique, et leur application aux wTTSs. Cette thèse fait partie d'un des programmes pionniers dans la recherche de jeunes hJs : MaTYSSE (Donati et al., 2014).

Plus précisément, MaTYSSE, qui signifie Magnetic Topologies of Young Stars and the Survival of close-in massive Exoplanets, vise à caractériser l'activité magnétique des wTTSs, à la comparer à celle des étoiles semblables au Soleil à des stades d'évolution antérieurs et postérieurs, et à rechercher des hJs autour de ces wTTSs. Le programme se base sur le suivi spectropolarimétrique de 35 wTTSs, avec des observations collectées entre 2013 et 2016 avec le spectropolarimètre à échelle ESPaDOnS (Donati, 2003), installé au Télescope Canada-France-Hawaï (CFHT), Hawaï depuis 2004, ainsi que son jumeau NARVAL, installé au Télescope Bernard Lyot (TBL), France depuis 2006. À partir des spectres, non polarisés et polarisés circulairement, fournis par ces instruments, nous utilisons la technique d'imagerie Zeeman-Doppler (ZDI), développée pour la première fois dans les années 90 (Semel, 1989) et ayant subi des mises à jour successives jusqu'en 2014 (Donati et al., 2014), pour reconstruire la distribution surfacique de brillance et de champ magnétique de nos wTTSs. Les RVs étant mesurées à partir des raies spectrales des spectres non polarisés, la perturbation d'activité des RVs provient des distorsions des raies spectrales essentiellement dues aux inhomogénéités de brillance surfacique ; par conséquent, nos cartes de brillance ZDI sont utilisées pour modéliser la perturbation d'activité des RVs et la soustraire de notre signal, afin d'explorer la présence potentielle de signatures de hJs dans les courbes de RVs filtrées. ZDI a prouvé son efficacité en tant que technique de filtrage pour les wTTSs avant cette thèse, avec les deux premiers articles MaTYSSE sur les étoiles LkCa 4 (Donati et al., 2014), V819 Tau et V830 Tau (Donati et al., 2015).

Cette thèse présente l'étude de l'activité et des RVs de deux autres étoiles MaTYSSE : TAP 26, âgée de $\sim$17 Myr et de masse $\sim$1 $M_\odot$, et V410 Tau, âgée de $\sim$0.8 Myr et de masse $\sim$1.4 $M_\odot$. Des résultats sur des jeux de données plus récents de la wTTS V830 Tau sont également présentés. En plus de l'utilisation de ZDI, une autre technique numérique est utilisée, appelée Régression par Processus Gaussiens (GPR) et appliquée pour la première fois à la recherche d'exoplanètes par vélocimétrie dans Haywood et al. (2014). Appliquée directement aux RVs brutes, GPR est une technique indépendante de ZDI, qui ne repose pas sur un modèle physique mais qui suppose un comportement statistique donné de la courbe des RVs, la perturbation d'activité des RVs étant décrite comme un bruit corrélé. Le processus de modélisation consiste donc à trouver les principaux paramètres caractérisant ce comportement statistique, en fournissant en même temps des informations sur l'activité stellaire.

Le premier chapitre décrit le contexte d'ensemble de l'étude et brosse un portrait grossier des théories actuelles sur la formation et de l'évolution précoce des étoiles et des planètes ; dans un deuxième chapitre, nous détaillons le problème de la modélisation de l'activité des wTTSs et décrivons les différentes techniques de modélisation complémentaires utilisées pour ce travail ; le chapitre trois présente ensuite les résultats de l'application de nos techniques de modélisation de l'activité à TAP 26, V410 Tau et V830 Tau, et le chapitre quatre présente l'étude des courbes RV de ces étoiles. Enfin, nous tirons quelques conclusions que cette thèse a apportées au domaine de la formation des étoiles et des planètes, et donnons quelques perspectives d'avenir.

1 | Introduction: the formation of stars and their planets

Contents

1.1 A few notions on the diversity of stars and exoplanets

1.1.1 Stages of stellar evolution

Stars form in clouds of dust and gas, accreting plasma until they reach a stable mass. This mass, which varies between ∼0.1 – 100 solar masses ($M_\odot$), is the predominant factor that determines a star's evolution. In particular, one can follow the path of a star along its life on a temperature-luminosity plot, or Hertzsprung-Russell (HR) diagram (see figure 1.1). The main sequence (MS) is a region of the HR diagram where stars spend most of their life: it corresponds to the stage during which they burn hydrogen through nuclear fusion in their cores. In general, the more massive a star is, the hotter and brighter it is on the MS, and the faster it evolves through the various evolutionary stages described in the following paragraphs.

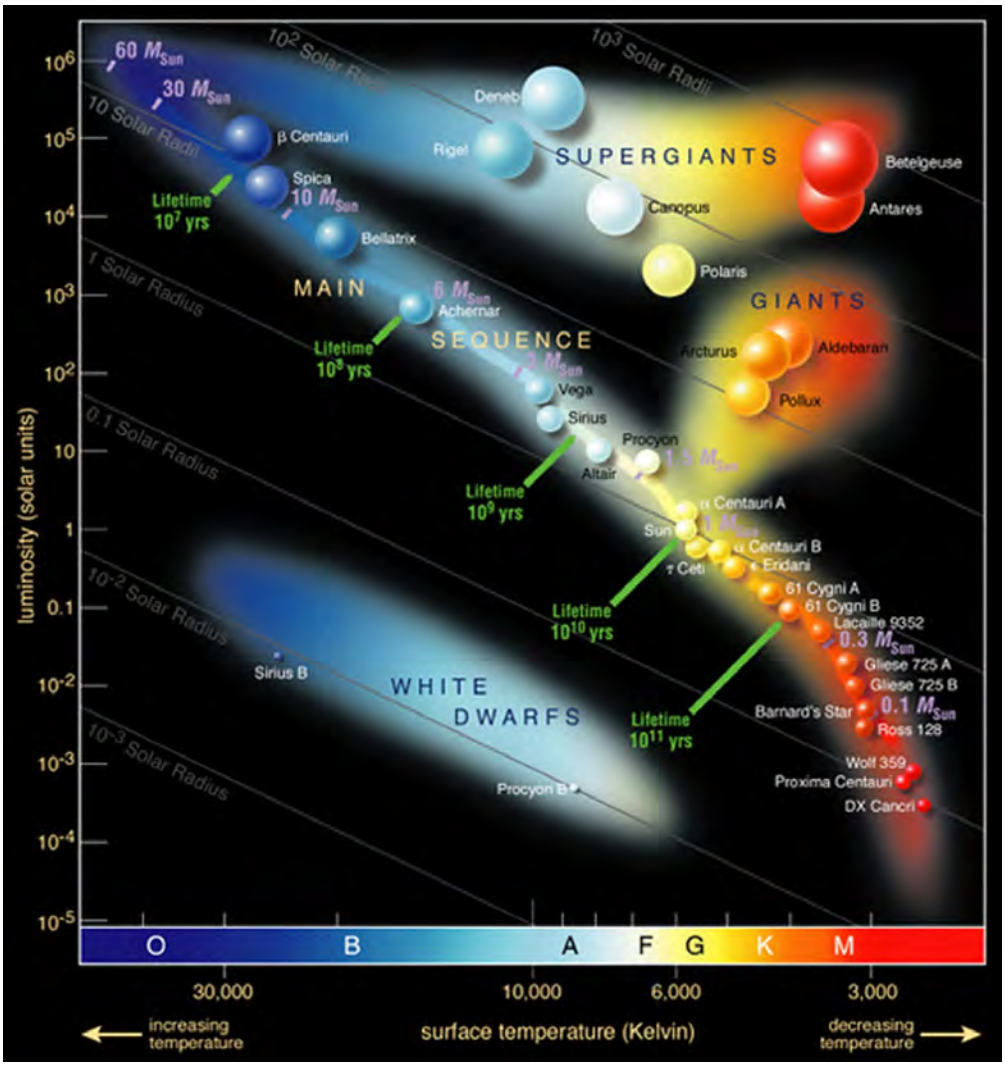

Figure 1.1 – Some famous stars on the Hertzsprung-Russell diagram. Masses and lifetimes are noted along the main sequence. Source: `https://www.eso.org/public/images/eso0728c/` through `https://commons.wikimedia.org/wiki/File:Hertzsprung-Russel_StarData.png`.

- The most massive stars ($M_\star \gtrsim 8\,M_\odot$) reach the MS at ages 0.02 – 0.2 Myr. They initiate hydrogen nuclear fusion in their cores before they have finished accreting their mass, then stay on the MS until ages 3 – 100 Myr (Maeder, 2009, chapter 18). When they have exhausted the

hydrogen reserves in their cores, they leave the MS and enter an inflated state as supergiants for 0.5 – 5 Myr, during which they fuse progressively heavier elements in their cores, until developping an iron core, at which point they explode into supernovae and their cores collapse into neutron stars or black holes (Maeder, 2009).

- Stars of masses $\sim$0.5 – 8 $M_\odot$ reach the MS at ages 0.2 – 100 Myr and stay on the MS until ages 0.1 – 10 Gyr. When they exhaust their core hydrogen fuel, they inflate into red giants, fusing helium at their core for 0.5 – 10^3 Myr. After running out of nuclear fuel (they are not massive enough to initiate full-scale carbon fusion), these stars contract, expelling their outer layers into planetary nebulae through superwinds. Their cores then cool down to become white dwarfs.
- Low-mass stars ($M_\star \lesssim 0.5\,M_\odot$) have a lifetime longer than the age of the Universe, and what happens to them after leaving the MS is yet unobserved.

At the beginning of their life, stars of masses $\lesssim 8\,M_\odot$ go through a protostar phase, during which they accrete most of their mass, and a pre-main sequence (PMS) phase, during which they contract towards the MS. For stars of masses $\sim$0.5 – 2 $M_\odot$, the PMS track on the HR diagram is composed of a phase of luminosity decrease at roughly constant temperature (Hayashi track) and a phase of temperature increase at roughly constant luminosity (Henyey track). These stars follow the Hayashi track for 2 – 20 Myr, during which their interiors are fully convective, and they bifurcate on the Henyey track when a radiative core starts developing. Stars of lower masses stay fully convective, so they follow the Hayashi track up to the MS, and stars of higher masses spend their PMS phase following the Henyey track (e.g. Bodenheimer, 2011, chapter 8).

Protostars and some PMS stars are embedded in circumstellar dust and gas, from which they grow; a protostar/PMS star and its circumstellar environment is referred to as a young stellar object (YSO). YSOs are extensively studied to constrain the theories of stellar formation, for example to explain observed distributions of masses (see studies about the Initial Mass Function, e.g. Offner et al., 2014) and of multiplicity (e.g. solar-type MS stars have on average ~ 0.6 stellar companion gravitationally bound to them, Duchêne & Kraus, 2013) among MS stars. Moreover, planets can form from the circumstellar matter around PMS stars; therefore, investigating YSOs is also important to understand the initial conditions of the evolution of planetary systems.

1.1.2 The diversity of exoplanetary systems

The search for exoplanets, i.e. planets orbiting around stars other than the Sun, has yielded about 4000 confirmed detections as of 2019 October. Traditionally, a substellar object orbiting a star was classified as a planet if its mass was below 13 Jovian masses ($M_{\rm Jup}$), and as a brown dwarf otherwise, that criterion roughly corresponding to the start of the thermonuclear fusion of deuterium in the core (Boss et al., 2007). However the distinction between giant planets and brown dwarfs is still debated as of today (e.g. Schneider, 2018).

Various observation/detection techniques exist, complementing each other (see e.g. Perryman, 2018, for a comprehensive review). Velocimetry (see section 2.4.1) yields orbital periods, lower boundaries on planet masses and orbital eccentricities. Photometry enables to detect transiting planets (planets passing between their host star and the observer), giving access to their radii and orbital periods, potentially to their eccentricities and planetary albedos, as well as an estimate of their masses in multiplanetary systems (from transit time variations, see e.g. Holman et al., 2010). Spectroscopy of transiting planets' host stars unveils their sky-projected obliquities, i.e. the inclinations between planets' orbital axes and their hosts' rotation axes (Rossiter-McLaughlin effect, see e.g. Fabrycky & Winn, 2009), as well as, potentially, some atmospheric characteristics (Madhusudhan, 2019). Other observation/detection techniques include direct imaging and gravitational lensing, which enable the detection of planets located far from their host stars.

Figure 1.2 shows a mass/period diagram of confirmed exoplanets. Three populations stand out: the super-Earths (planets of masses $\sim$1 – 10 Earth masses), the hot giants (massive planets on close-in orbits) and the warm giants (massive planets on intermediate orbits). Many observed systems have architectures that are strikingly different from that of the Solar system (Winn & Fabrycky, 2015): for example, accounting for observational biases, it is estimated that $\sim$30 – 50 % of Sun-like stars have a super-Earth on an orbit closer-in than Mercury's, while $\sim$10 % host a giant planet, usually on either a close-in orbit or a larger one but significantly eccentric (Raymond et al., 2018). The occurrence rate of hot Jupiters, the most massive of hot giants, was estimated at $\sim$1 % around Sun-like stars (Wright et al., 2012).

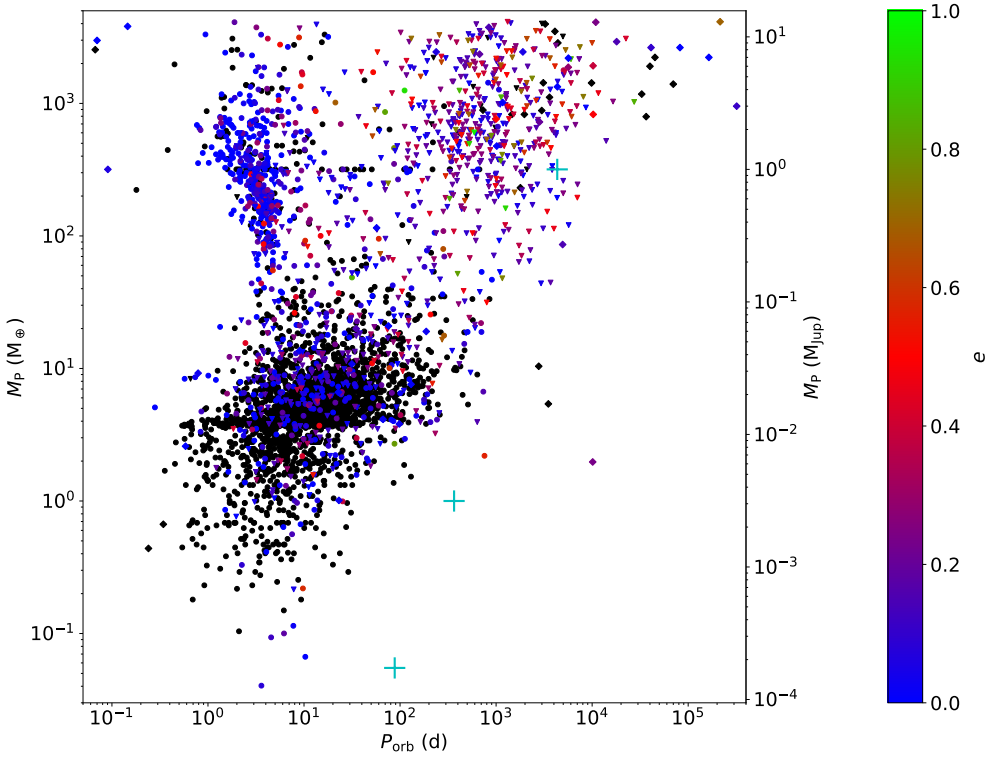

Figure 1.2 – Exoplanets mass-period plot, with the color scale representing the orbit eccentricity, when known. Cyan crosses represent, from left to right, Mercury, the Earth and Jupiter. The data was downloaded from `http://exoplanet.eu` (Schneider et al., 2011) on 2019 October 28, totalling 3725 exoplanets. The masses of 851 among them were known (diamond symbols), those of 768 others were assimilated to their known lower boundaries (triangular symbols), and those of the 2106 remaining planets were derived from their radii (circular dots), following the method described in Han et al. (2014).

Because planets form together with their star, investigating the processes at play early in the life of stars and of their stellar/planetary systems is a primordial first step to understand the evolution of planetary systems, to explain their observed statistics (e.g. Mordasini, 2018), to assess how much of an exception the Solar system is and to estimate the likelihood of finding Solar-System analogs in the galaxy (e.g. Agnew et al., 2018; Barbato et al., 2018). In the next section, we present the broad lines of the current paradigm of stellar formation.

1.2 The formation of stars

YSOs are often seen in groups, whether in gravitationally bound clusters or in associations, within which age and proper motion are roughly homogeneous. These groups bathe in giant clouds of

gas and dust and are called star-forming regions (SFRs). Famous examples of SFRs are: the Taurus-Auriga molecular cloud, located ∼140 pc away from Earth (Galli et al., 2018), the Orion cloud (∼390 pc, Kounkel et al., 2017), the Scorpius-Centaurus association (∼140 pc, de Zeeuw et al., 1999), the ρ Ophiuchi nebula (∼140 pc, Ortiz-León et al., 2017)... It is noted that many SFRs are located in a particular region of the galaxy, the Gould Belt: an elliptic ring of semi-major and semi-minor axes ∼350 pc and ∼230 pc respectively, whose center lies ∼100 pc away from the Sun in the direction opposite to the galactic center (e.g. Perrot & Grenier, 2003), but the physical origin of the Gould Belt is debated (see e.g. Bobylev, 2014; Bouy & Alves, 2015).

The current understanding is that stars are born from the gravitational collapse of dense cores within these clouds, first appearing at the center of the collapsing core and then growing by matter accretion. Best seen in infrared wavelengths, YSOs are categorized into four classes (0, I, II and III) depending on their spectral energy distribution (SED), each class corresponding to an evolutionary stage as illustrated in figure 1.3 (Adams et al., 1987; André, 2015).

1.2.1 From molecular clouds to protostars

Dark regions have been observed in the sky, with low densities of apparent stars. We now know that they are clouds of gas and dust that dim the light coming from background stars. These clouds are composed in large majority of molecular Hydrogen (H_2), with small amounts of interstellar dust and traces of other molecular gases: CO, NH_3, HCN, etc (see e.g. Wilson et al., 1970). Lada (1992) among others showed that molecular clouds are major sites of stellar formation. André et al. (2014) observed that molecular clouds have a filamentary structure, with filaments always roughly 0.1 pc thick and preferentially in the direction of the cloud elongation. At the crossing of filaments, or at various places along these filaments, we can observe denser clumps, called pre-stellar cores, which are defined as the immediate vicinity of local minima of the gravitational potential within the cloud.

Magnetism and turbulence are thought to be the main factors that drive star formation (Bodenheimer, 2011; Crutcher, 2012). In magnetically-controlled star formation scenarios, magnetic fields maintain the core against gravitational collapse but see their influence decrease as the core contracts and acquires mass (ambipolar diffusion), until the core reaches a critical mass and collapses. In turbulence-controlled star formation scenarios, supersonic turbulence within the cloud leads to complicated shock patterns that randomly generate highly-compressed regions that can collapse. Both magnetic fields and turbulence generally coexist at comparable levels in molecular clouds, so formation models including them together are favored (see Crutcher, 2012, for a review). Moreover, star formation can be triggered by factors external to the cloud, like supernovae shocks or cloud-cloud collisions, which create high-density regions that can collapse. YSOs clusters or associations are assumedly a result of either simultaneous collapse, where an external factor (such as galactic density waves) increases the density in the cloud on a global scale, or contagious star formation, where core collapses generate shockwaves that locally increase the density, resulting in more neighboring collapses (Maeder, 2009, Part V); turbulence can also lead to the simultaneous formation of several cores within a molecular cloud (Bodenheimer, 2011, Chapter 2).

Simulations of simplified cases (plasma ball with solid rotation and uniform magnetic field, e.g. Machida & Matsumoto, 2011; Machida & Basu, 2019) show that the birth of a protostar happens after two successive collapses (Masunaga & Inutsuka, 2000):

First collapse - When the density at the center of the pre-stellar core reaches $\sim 10^{10}\,\mathrm{cm}^{-3}$, the pressure at the center becomes high enough to create a shock, which defines the contour of what is called the first core. The first core accretes mass from the rest of the pre-stellar core, supported by thermal pressure and rotation against self-gravity (e.g. Wurster et al., 2018). The higher the

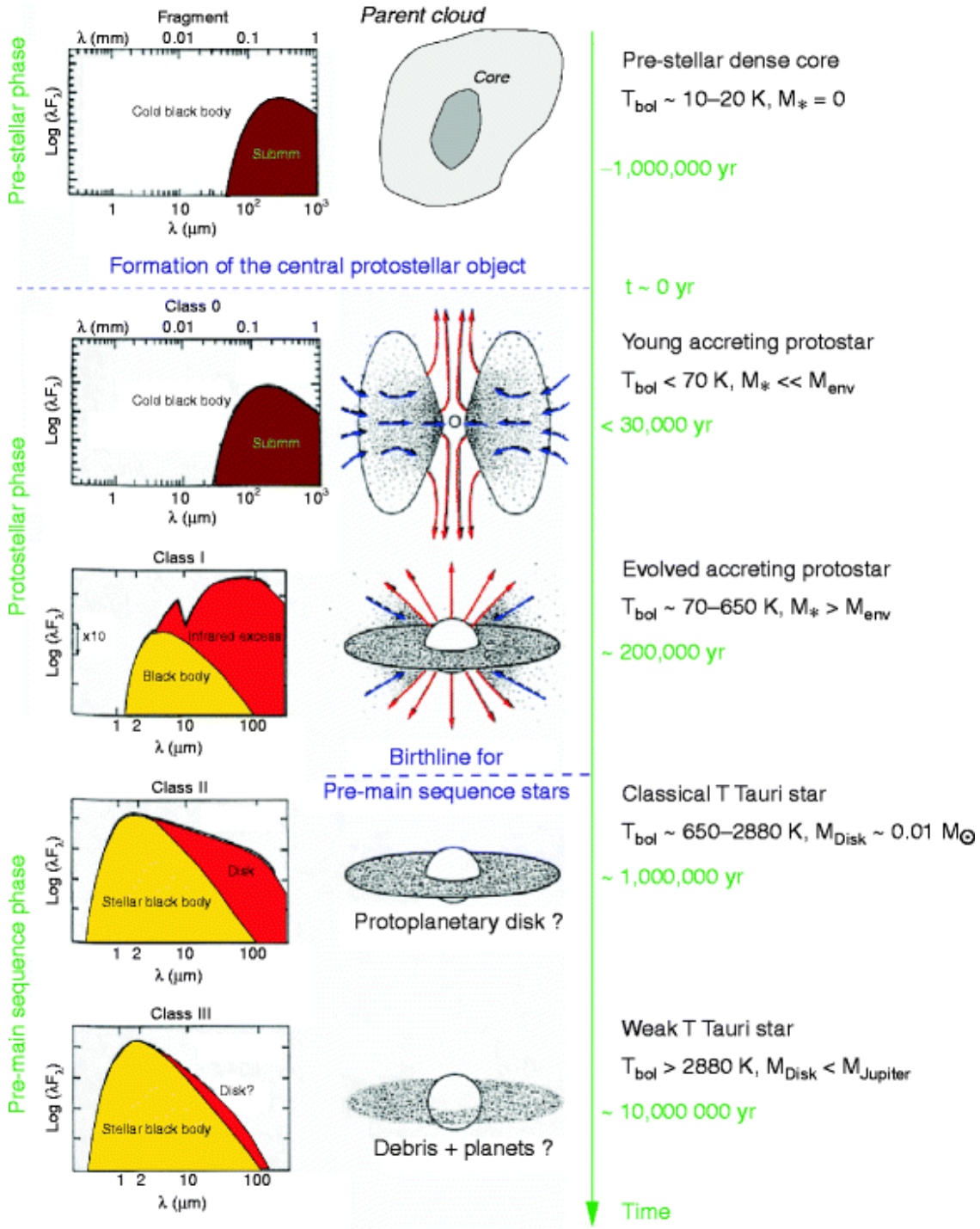

Figure 1.3 – Empirical sequence for the formation and circumstellar evolution of a single star from a prestellar cloud core to a class-III YSO, based on the shape of the SED (*left*), the bolometric temperature, and the mass of circumstellar (envelope + disc) material (*right*). The lifetime of a cTTS can in fact be as long as 10 Myr, making class-II and class-III phases hardly distinguishable in terms of age sample-wise. Source: André (2002).

initial angular momentum, the longer the first core lives before the second collapse, as centrifugal forces play against self-gravity to slow down the increase of density at its center. If given enough time, the first core takes a flattened shape before the second collapse, and the initial magnetic field

inside the first core gets dissipated by Ohmic and ambipolar diffusion, leading to a suppression of the magnetic braking (the magnetic field is no longer well-coupled to the neutral gas). Under some conditions, e.g. on the angle between the magnetic field and the angular momentum axis, the disc can become a Keplerian disc early on (see Hennebelle & Ciardi, 2009; Maury et al., 2019, for precise studies). During the accretion of the outer envelope by the first core, low-velocity outflows are driven from the outer boundary of the first core by magnetic forces, because magnetic field lines are twisted horizontally by the rotation (toroidal magnetic field). A very high angular momentum can lead to a fragmentation of the first core (Goodwin et al., 2007; Boss, 2009), which is one of the potential processes for generating multiple star systems (others being disc fragmentation post-protostar formation or gravitational capture; this question still constitutes an active field of research; see e.g. Goodwin et al., 2007; Maury et al., 2010).

Second collapse - When the temperature at the center of the first core reaches $\gtrsim 2000\,\mathrm{K}$, the dissociation of H_2 at the center changes the thermodynamics and triggers the second collapse. This second collapse can be as fast as a few years, until the density at the center reaches $\sim 10^{18} - 10^{20}\,\mathrm{cm}^{-3}$, at which point we consider that the protostar is born. The rest of the first core surrounds the newborn class-0 protostar. If the angular momentum of the first core is very low, the first core remnant quickly falls onto the protostar. Otherwise, a Keplerian circumstellar disc appears (Machida & Matsumoto, 2011). Far from the star, in the outer envelope, the magnetic field is well coupled with the neutral gas, then in the area $10^{11}\,\mathrm{cm}^{-3} \lesssim n \lesssim 10^{15}\,\mathrm{cm}^{-3}$, the dust absorbs the ions and the magnetic field is efficiently dissipated by Ohmic dissipation and ambipolar diffusion, letting the disc adopt a quasi-Keplerian rotation profile, then close to the star again, the degree of ionization increases and the magnetic field becomes coupled with the neutral gas again (Machida & Basu, 2019).

Main accretion phase - The main accretion phase starts, where the disc accretes mass from the primordial envelope which has not collapsed into the first core, while the protostar accretes mass from the surrounding disc. On top of the low-velocity outflows driven by the disc, high-velocity collimated jets appear near the protostar, fueled by disc material approaching the star at Keplerian velocities and being redirected outwards by toroidal magnetic fields. The accretion and jets are episodic, triggered by gravitational instabilities where clumps of material fall from the disc to the protostar, where a portion is evacuated as jets. The disc and the outer envelope are coupled by magnetic forces and exchange angular momentum, leading to a braking of the disc that prevents it from growing in size. The class-0 stage is characterized by a high mass ratio between the circumstellar environment and the protostar ($M_{\mathrm{env}} \gg M_\star$) and lasts for a few $10^4\,\mathrm{yr}$ (e.g. Andre et al., 2000; Masunaga & Inutsuka, 2000). During that phase, the protostar grows at an accretion rate of $10^{-6} - 10^{-5}\,\mathrm{M}_\odot/\mathrm{yr}$ (André, 2015). From an observational point of view, its SED is almost the same as that of a prestellar core, but the presence of the protostar is betrayed by signatures of powerful highly-collimated jets (Bontemps et al., 1996; Bachiller, 1996). Eventually, the outer envelope depletes, allowing the disc to grow. A YSO enters class-I when the protostar becomes more massive than its circumstellar environment. Jets and outflows then broaden and weaken, and the accretion rate decreases to $10^{-7} - 10^{-6}\,\mathrm{M}_\odot/\mathrm{yr}$ (André, 2015). The envelope is still present but the protostar signature appears in the SED at infrared wavelengths. The class I stage lasts for a few $10^5\,\mathrm{yr}$ (Evans et al., 2009).

1.2.2 Classical T Tauri stars

Eventually, the protostar has accumulated the majority of its mass and becomes a PMS star. It is at first a class-II source; a distinction is made between class-II YSOs of less than $2\,\mathrm{M}_\odot$, called

classical T Tauri stars (cTTSs), and those of more than $2\,M_\odot$, called Herbig Ae/Be stars (we do not discuss the latters). Having emerged from their now depleted envelope, cTTSs become visible at near-infrared and optical wavelengths, surrounded by an optically thick disc that causes an infrared excess in the SED (see figure 1.3). Material is channeled onto the star at a rate of 10^{-9} – $10^{-7}\,M_\odot$/yr (André, 2015).

CTTSs were observed to have strong magnetic fields (several kG), amplified from the remnants of the primordial field by the dynamo of the star (Johns-Krull et al., 1999; Johns-Krull, 2007). These fields open a cavity around the star in the region where magnetic forces dominate over rotation, called the magnetospheric gap. At the edge of this gap, a magnetic coupling exists between the surface of the protostar and the disc (Collier Cameron & Li, 1994; Bessolaz et al., 2008), and accretion happens by funneling disc material along the magnetic field lines. This magnetic coupling induces a rotational braking of the star (Bouvier, 2007; Bouvier et al., 2014), especially in the propeller regime early on, when high-velocity jets are driven from the protostar (e.g. Romanova et al., 2004; Zanni & Ferreira, 2013).

Even though cTTSs are still contracting under their own gravity and gain angular momentum from the accretion, their rotation rates are observed to be much lower than expected (Rebull et al., 2004). Bouvier et al. (2014) provides a review of the sources of angular momentum gain/loss for cTTSs (star-disc interactions, stellar winds...), revising the widely used paradigm of disc-locking proposed by Ghosh & Lamb (1979), where the star would co-rotate with the inner edge of its disc because of magnetic locking between the stellar surface and the disc plasma. Though models have to be refined, it is still apparent that both the disc and the magnetic field play a major role in braking the star rotation. As the star evolves, its structure becomes more complex and so does its magnetic field, meaning the dipole weakens and the field strength quickly decreases with distance to the star. Thus the disc-braking is less and less efficient, eventually leading to a liberation of the star, which starts to spin up.

During this phase, dust grains can agglomerate within the disc, which can eventually lead to the formation of planetesimals and planets (see section 1.3.2).

1.2.3 Weak-line T Tauri stars

As the inner disc depletes due to its material being either accreted or ejected, accretion gets progressively weaker, then intermittent (cTTSs then become transitional T Tauri stars), before the inner disc is finally exhausted, and the star becomes a weak-line T Tauri star (wTTS, class-III YSO, see e.g. White et al., 2007). The age at which this transition occurs varies widely from star to star, being generally between 1 – 10 Myr (e.g. Richert et al., 2018), which implies that the population of $\lesssim 10$ Myr T Tauri stars is composed of both cTTSs and wTTSs, undistinguishable by age alone.

The liberation from disc-locking can be triggered either by the dipole weakening as mentioned above, or by the dissipation of the disc. Free from disc-braking and still contracting, wTTSs spin up until age $\sim$10 – 100 Myr (depending on the mass). On the Hayashi track, the star shrinks at roughly constant temperature (4000 – 4500 K), then, around 1 – 3 Myr, it starts developing a radiative core and bifurcates on the Henyey track: the star keeps contracting, but at roughly constant luminosity and with a temperature rising with time, until reaching 4500 – 6500 K. For a $0.8\,M_\odot$ star, the contraction phase lasts for $\sim$25 Myr and for a $1.35\,M_\odot$ star, it lasts for $\sim$10 Myr; stars shrink by a radius factor of $\sim$20 – 60 (Amard et al., 2019).

After the contraction slows down, WTTSs spin down because of stellar winds until they reach the main sequence (see e.g. figure 1.4 for $1\,M_\odot$ stars; for a more complete study, see Gallet & Bouvier, 2015). The rotation periods of wTTSs reach down to $\sim$0.5 – 5 d when they spin the fastest (figure 1.4); their fast rotation induce a strong magnetic activity (see section 2.1.2).

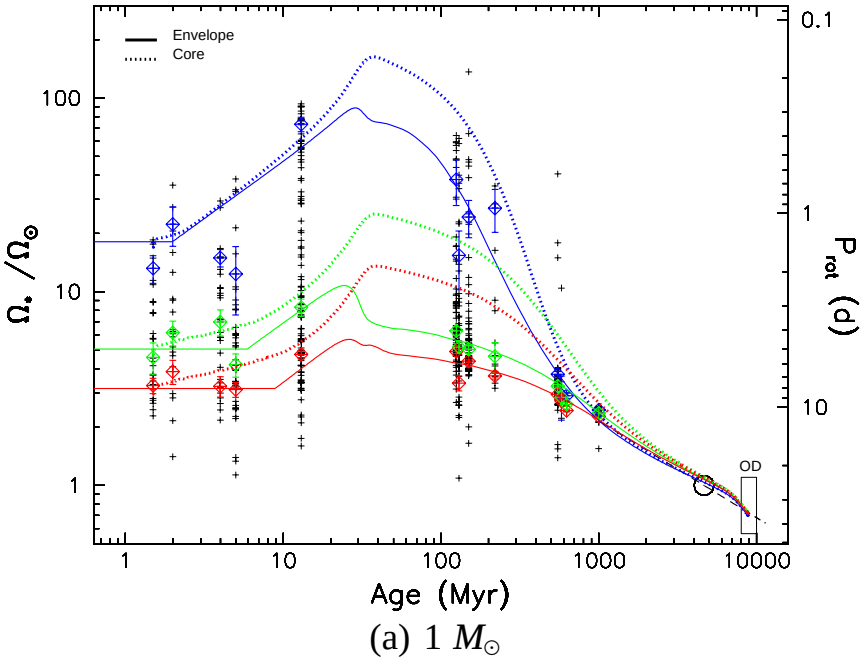

Figure 1.4 – Figure extracted from Gallet & Bouvier (2015, figure 5). Angular velocity of the convective envelope (solid lines) and of the radiative core (dashed lines) shown as a function of time between 1 Myr and 10 Gyr for slow (red), median (green), and fast (blue) rotator models in a mass bin centered on 1 $M_\odot$. The left vertical axis is labelled with angular velocity normalised to the Sun's, while the right vertical axis is labelled with rotational periods (days). The black crosses represent the observed angular velocities of stars in a selection of star-forming clusters of various ages. The red, green and blue tilted squares and associated error bars represent the 25th, 50th and 90th percentiles of the observed rotational distributions at each sampled age. The black rectangle labelled OD (lower right corner) shows the angular velocity dispersion of old disc field stars. The open circle is the angular velocity of the present Sun shown for reference, and the dashed black line illustrates Skumanich's relationship (Skumanich, 1972), $\Omega \propto t^{-1/2}$.

1.3 Protoplanetary discs

We now focus on planetary formation within discs, called protoplanetary discs in this context. The content of this section is largely inspired from the review Armitage (2018).

1.3.1 Structure

We consider the disc around a cTTS (see figure 1.5). Discs around cTTSs have been observed to extend up to ∼100 astronomical units (au; e.g. TW Hya, Nomura et al., 2016). Their masses are estimated to be $\sim 10^{-3}$ – 10^{-2} times the mass of the star ($M_\star$; see Andrews et al., 2013; Williams & Best, 2014). The surface density (volumic density integrated over the thickness of the disc) is expected to follow a law $\Sigma \propto r^{-1}$. Moreover, axisymmetric rings and non-axisymmetric structures in discs have been observed (e.g. ALMA Partnership et al., 2015; Dong et al., 2018), the origins of which are uncertain but are hypothesized to be tied to planetary formation (Baruteau et al., 2019).

The disc is heated through various sources. Irradiation from the star leads to a global temperature profile $T \propto r^{-1/2}$ (Kenyon & Hartmann, 1987). Close to the star, accretion heating increases the temperature in the mid-plane, leading to a vertical gradient of temperature (Armitage, 2018). Further away from the star, the thickness of the disc divides it into several regions: an isothermal inner region centered around the mid-plane, where $T_{\rm dust} = T_{\rm gas}$, then a warm layer of dust directly heated by stellar radiation, and a hot gas atmosphere. The temperature profile defines various "ice

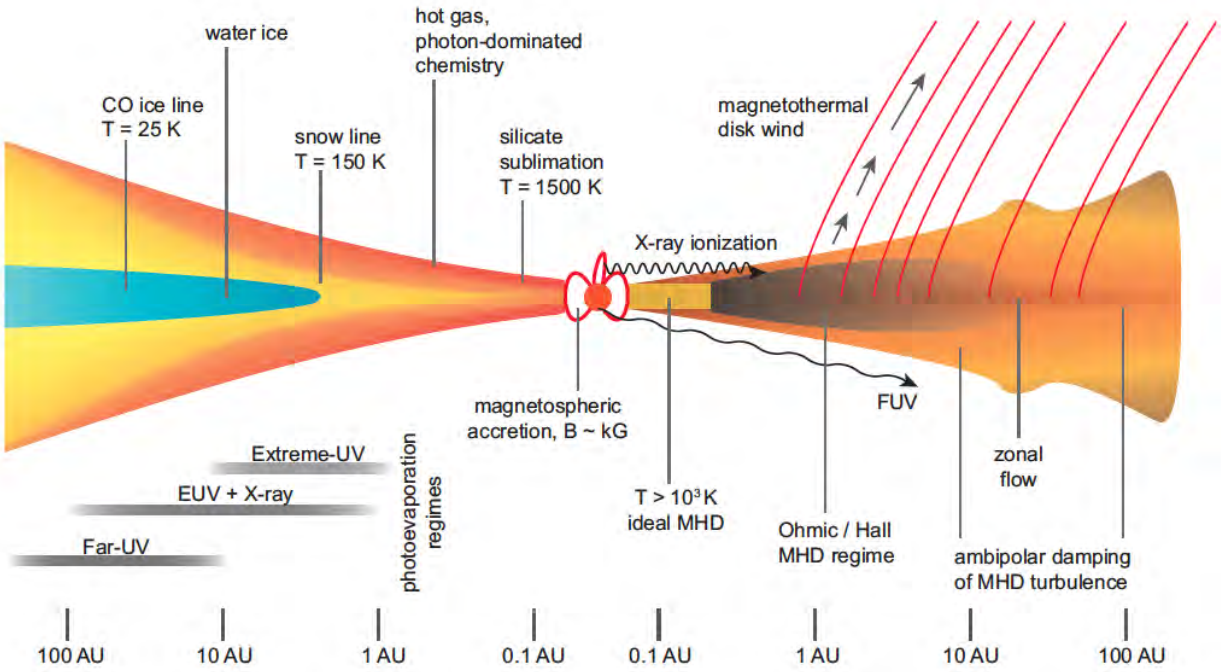

Figure 1.5 – Cartoon of a protoplanetary disc viewed from the side (source: Armitage, 2018). The left part shows the thermal structure of the disc while the right part shows the magnetohydrodynamic regimes in various regions of the disc.

lines", which are the limits between areas where given chemicals are under solid or gaseous form. For example, the water snow line is located where $T \simeq 150\,\mathrm{K}$. Since the accretion heating wanes with time and the radius and temperature of the protostar evolve, the locations of the ice lines also evolve with time.

An important factor in the structure of the disc is the magnetic field. Close to the star ($T > 3000\,\mathrm{K}$), the disc is thermally ionized and the magnetic field is thus efficiently coupled with the gas. Further away, sources of non-thermal ionization (X-rays, UV photons or cosmic rays) are weak enough to let non-ideal MHD effects take place: the Ohmic diffusion and Hall effect decrease the influence of the magnetic field on the charged and neutral species, and beyond $\sim 30\,\mathrm{au}$, the low density opens the way to ambipolar diffusion, where neutral species drift independently of the magnetic field, because the rate of collision with magnetically-tied electrons and ions is low. Magnetic fields also generate winds that participate to depleting the disc.

The phenomenon of photoevaporation, where gas heated by X-rays or UV photons escapes the disc, taking away matter and angular momentum, is most efficient at $2 - 3\,\mathrm{au}$ and can create a dip of density withing the disc, potentially even a gap, and eventually blow the disc away on long time scales.

1.3.2 From dust particles to planets

Not all mechanisms of planet formation within protoplanetary discs are understood as of today, especially as direct observation of disc-embedded planet formation is difficult. The paradigm of planetary formation is that of a bottom-up growth: dust grains (length scale: micrometer) aggregate into pebbles (cm), which themselves aggregate into planetesimals (km), some of which eventually grow into planets (Baruteau et al., 2016).

At first, when the dust grains are very small, aerodynamic forces dominate over gravitational forces, and dust grains grow from µm sized to mm sized thanks to 2-body collisions. Interactions

between the dust grains and their surrounding gas plays a role in the collision velocities and subsequent trajectory of the dust grains. These collisions, at first, can happen anywhere in the disc but as the solid grows, it is submitted to gas drag and tends to join the mid-plane and to drift radially towards the star. Bouncing and fragmentation are barriers to the growth of solids, and the critical relative velocities at which they happen depend on the solid composition (for example water ice is more resistant to fragmentation than silicates, Armitage, 2018). Eventually, these processes reach an equilibrium and the dust solids, now pebbles, can generally reach sizes of mm-cm, with pebble traps at the snow line and at the inner edge of the disc.

How pebbles grow into planetesimals is not well-constrained by observations, especially as meter-sized solids typically fall into the star in $\sim$100 yr from an original distance of 1 au, implying that planetesimal formation has to happen faster than solid infall into the star. Ideas proposed by the theory include porous growth, where pebbles stick to each other with little compression, giving birth to porous aggregates with increased cross sections, or streaming instability (Youdin & Goodman, 2005) where the disc gets fragmented and clumps of dust get trapped together, ending up aggregating.

As the planetesimals grow, gravitational forces become dominant and *runaway growth* starts. The heavier a planetesimal becomes, the faster its cross section grows thanks to its gravitational potential, and the more chances it has to collide with its neighbors. This phase leads to a size distribution of solids where a small number of very large planetesimals stand out. Pebble accretion can occur during this phase, where planetesimals absorb radially-drifting pebbles that arrive on their orbit.

Eventually, the biggest planetesimals, or oligarchs (10^3 km), grow so massive that their interaction with their neighbours scatters them, thus slowing down their growth. During this *oligarchic growth* phase, the oligarchs dominate the gravitational choreography: each of them settles into its own area of gravitational domination, and eventually "eats" the smaller planetesimals in this feeding zone, to grow into a planet embryo. Oligarchs can interact with each other, impacting their respective orbits and the general architecture of the system.

Finally, giant planets are formed from solid cores that have reached at least 10 – 15 Earth masses ($M_\oplus$), massive enough to trigger runaway accretion of a gaseous atmosphere from the surrounding gas (Pollack et al., 1996). The time scale for forming such massive cores can be shorter than the lifetime of the disc, thanks to the enhancement of surface density beyond the snow line (e.g. Kennedy & Kenyon, 2008), and type I migration trapping solids near the snow line (see section 1.4.1).

1.4 The mystery of hot Jupiters

In 1995, the first confirmed detection of an exoplanet around a Sun-like star is published: 51 Peg b is a > 0.5 M_{Jup} planet orbiting at 0.05 au from its host (Mayor & Queloz, 1995). With only the Solar System to compare at that time, finding a giant planet this close to the star was surprising. Furthermore, such close-in orbits are not expected to provide favorable conditions for giant planet formation, since the high Keplerian velocities favor fragmentation during large planetesimal encounters, and the accretion of a massive gaseous envelope is difficult in the limited area around the orbit.

1.4.1 Two theories of giant planet migration

Disc migration - To explain the orbit of 51 Peg b, Lin et al. (1996) showed that giant planets can migrate within their protoplanetary disc from original distances of a few au to the inner edge of the disc, within the lifetime of the disc. In general, interactions between a forming planet and the

surrounding material in the protoplanetary disc impact the orbit of the planet, causing an orbital migration. The nature of the migration, caused by a wake torque and a corotation torque (Baruteau et al., 2016), depends on the mass of the planet and on properties of the disc. Planets below $\sim 10\,M_\oplus$ undergo type I migration, which generally drives them inwards (towards the star), except around the silicate evaporation line and the water ice line. Outward migration around those lines and inward migration elsewhere create "planet traps" behind the silicate evaporation and water ice lines. Massive planets that open deep gaps in the disc around their orbits (masses typically $\gtrsim M_{Jup}$) undergo type II migration, which also drives them inwards on time scales $\gtrsim 10^4 - 10^5$ yr. Planets massive enough to open partial gaps in low- to moderate-density discs follow a migration regime intermediate between type I and type II, but in massive discs, they undergo type III migration which drives them outwards (Baruteau et al., 2016). Type II migration would enable to form hJs, generally keeping their orbit quasi-circular and coplanar. The planet still grows by accreting gas as it migrates, and the migration is slowed down when the planet mass becomes larger than the mass outside the planet gap. The migration stops when the planet reaches the inner edge of the disc.

Eccentricity excitation and tidal circularization - Since 1995, ∼400 hot Jupiters have been detected (estimated masses between $0.5 - 13\,M_{Jup}$ and orbital periods lower than 10 day, see figure 1.2 and its caption). Figure 1.6 shows the distribution of orbital eccentricities and sky-projected obliquities of giant planets. The eccentricities of hJs are generally low, whereas they are more dispersed for warm Jupiters. Few obliquities were measured for warm Jupiters, but we observe a large dispersion for hJs. A large eccentricity and/or a large obliquity are interpreted to result from gravitational interactions between oligarchs and/or fully-formed planets, which induce orbital instabilities (e.g. planet-planet scattering, Kozai-Lidov cycles, Dawson & Johnson 2018), changing their orbital angular momentums, eccentricities, semi-major axes and even potentially the planes of their orbits. For a cold giant planet to become a hJ, it would need to be placed on a highly eccentric orbit, with a periastron in the close-in region and an apoastron in the region where the planet originally was. The low eccentricities of hJs are believed to be the result of tidal circularization by the star: tidal forces work on the planet every time it goes through its periastron (close enough to be within reach of the stellar tidal influence), and the orbit circularizes within a few 10^2 Myr. In the latter case, the obliquity does not get dampened as fast as the eccentricity (Dawson & Johnson, 2018).

1.4.2 In-situ formation?

Recent studies have argued in favor of in-situ formation of hot Jupiters, motivated by the difference of mass distribution between hot and cold Jupiters, and the detection of many $10 - 15\,M_\oplus$ exoplanets on very close-in orbits (Batygin et al., 2016). Batygin et al. (2016) ran simulations showing runaway accretion of a gaseous atmosphere onto $15\,M_\oplus$ cores at 0.05 au, however, simulations by Coleman et al. (2017) taking different hypotheses showed no runaway atmosphere accretion on orbits below 0.1 au. The in-situ formation theory is still quite new and its feasibility not yet well established.

1.4.3 Further orbital migration

In the close vicinity of the host star, tidal and magnetic interactions between the star and the planet are strong enough to impact the orbit of the planet; in particular, these interactions transfer angular momentum between the star and the planet, by tending to synchronize the rotation of the star with the revolution of the planet. Thus, once a Jupiter-size planet reaches this region, depending on the geometry of the system, the hot Jupiter can either migrate slightly outwards or fall into the star (Bolmont & Mathis, 2016).

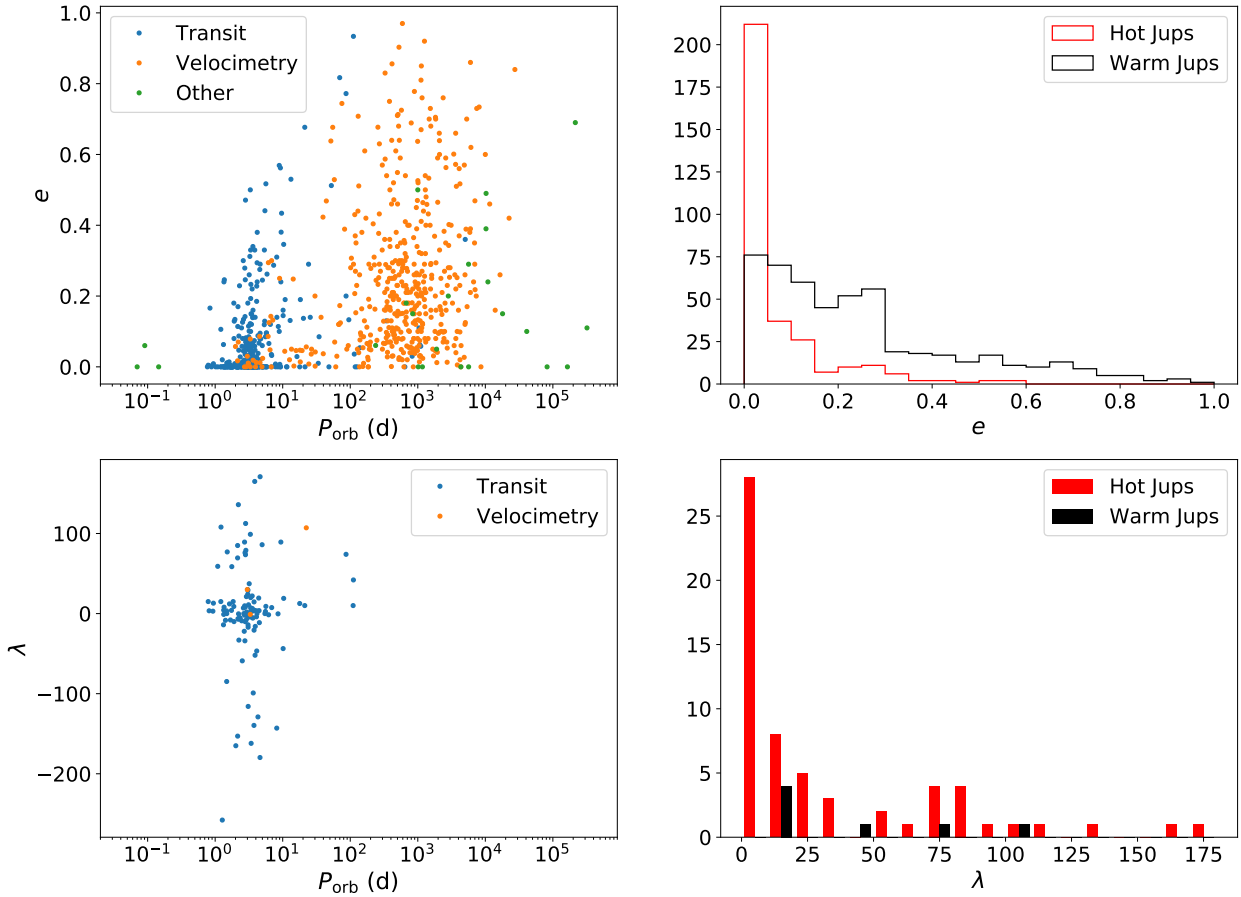

Figure 1.6 – Eccentricities (noted e) and obliquities (noted λ) of giant planets against their orbital periods (*left*) and as distributions (*right*). Data downloaded from `http://exoplanet.eu` on 2019 Oct 28 and from TEPCat (Southworth, 2011).

1.5 Summary

Stars are born at the center of collapsing dense cores within molecular clouds. After a rapid accretion phase during which the protostar is deeply embedded in its envelope, the protostar becomes a pre-main sequence star, emerging from its cocoon. T Tauri stars, PMS stars under $2\,M_\odot$, are still surrounded by an accretion disc at first (classical TTSs), in which planets can form. After the disc dissipates, they become weak-line TTSs surrounded by their planetary systems.

The estimated occurrence of hot Jupiters around $\sim$1 % of mature stars, combined with current planet formation theories, indicate that giant planets likely migrate after/while forming. Giant planets have an enormous gravitational influence on the rest of their planetary systems, it is therefore essential to understand their migration well, so as to accurately predict the architecture and orbital evolution of planetary systems. To distinguish which scenario dominates between type II migration within the protoplanetary disc and eccentricity excitation followed by tidal circularization, they have been confronted to observations of mature hJs, in particular to their statistics, orbital characteristics and potential presence of moons (see Dawson & Johnson, 2018, for a review). But detecting and characterizing actually young hJs, for example when tidal circularization has not had the time to happen yet, is necessary to make the distinction with better certainty; this is why this thesis focuses on the search for hJs around wTTSs, as detailed in the next chapter.

2 | Observing wTTSs

Contents

2.1 Interests

To investigate the mechanisms of formation of hot Jupiters, we propose to search them around stars as young as possible, i.e. around cTTSs and/or wTTSs (1 – 15 Myr), and to characterize their orbital parameters. Because of the large dispersion of disc dissipation ages, wTTSs occupy roughly the same age domain as cTTSs, and because they no longer accrete, wTTSs make ideal targets to search for young hJs, without needing to model the accretion that adds variability in light curves and RV curves .

2.1.1 Hot Jupiters

The very young age of wTTSs makes them ideal targets to differenciate between the two main hypotheses for hJ formation. At their age, a planet that migrated through planet-disc type II migration should have a quasi-circular orbit (Baruteau et al., 2014), while one that got scattered through planet-planet interactions has not yet had the time to circularize to align and circularize its orbit via star-planet tidal interactions, so its orbit should be highly eccentric and perhaps tilted with respect to the stellar equator (see section 1.4). Moreover, comparing the statistics of young hJs to those of mature hJs would enable to better constrain their evolution as a function of their intrinsic and orbital parameters.

In this thesis, we use the velocimetry detection technique to look for hJs around wTTSs, which gives us access to their orbital periods, eccentricities and minimal masses (see section 2.4.1). This technique uses measurements of the radial velocity (RV) of the targetted stars, i.e. their velocity projected onto the line of sight (direction linking the observer and the targetted star).

However, the RVs of wTTSs present a strong variability which makes the detection of hJs around them difficult: the RV modulation of wTTSs typically reach semi-amplitudes of a few $\mathrm{km\,s^{-1}}$, drowning potential RV signals from hot Jupiters whose expected semi-amplitudes are of the order of $0.1\,\mathrm{km\,s^{-1}}$ (Mahmud et al., 2011; Crockett et al., 2012). This RV modulation can be explained by the stellar magnetic activity, which for example manifests itself with dark and bright features covering large fractions of the stellar surface (several tens of percent of the surface, see e.g. Grankin et al., 2008; Gully-Santiago et al., 2017). It is thus necessary to understand and model the stellar activity well enough to be able to filter it out of the data without removing potential planet signatures. Modelling the magnetic field of wTTSs can also inform about potential star-planet magnetic interactions.

2.1.2 Stellar activity

WTTSs have been shown to trigger strong magnetic fields, from a few 100 G to several kG (Skelly et al., 2010; Donati et al., 2014, 2015). The processes driving exchanges between the cinetic energy of the plasma and the magnetic energy, involving the stellar rotation and the convection, are described by the dynamo theory (see e.g. Charbonneau, 2013, for a comprehensive explanation). More precisely, we can describe the magnetic field as the sum of its poloidal and its toroidal components (Chandrasekhar, 1961). The dynamo theory describes how the field is amplified and in particular how both poloidal and toroidal fields are regenerated from each other. For instance, from the field lines of an aligned dipole (poloidal), azimuthal field lines (toroidal) can appear if some latitudinal differential rotation twists the dipole lines (Ω effect). Conversely, poloidal field can be generated from toroidal field thanks to cyclonic convection, which also twists the field lines (α effect, see Parker, 1955). This process is called an α-Ω dynamo, but other types of dynamo are equally possible (Brun & Browning, 2017).

The Rossby number Ro, which is the ratio between the stellar rotation period and the convective turnover time scale, quantifies the capacity of the stellar rotation to generate cyclonic convection,

i.e. orientate the convective cells in a privileged direction. The shorter the rotation, the lower the Rossby number, the more active the star is. For Ro < 0.1 however, the dynamo is saturated, which means that the magnetic field is strong enough to retroact on the velocity field and prevent any further amplification of the field. The convective turnover time scale is of the order of a few hundred days for fully-convective wTTSs, and their rotation periods are well under ten days, which means that most of them have saturated dynamos. They are thus extremely active (Preibisch et al., 2005).

The stellar magnetic activity manifests itself all the way from the stellar interior to the the outer stellar amosphere, through phenomena of various time and space scales. In particular, the magnetic fields of stars with an external convective layer - a fortiori of wTTSs - generate a heated extended stellar atmosphere, composed, just above the photosphere, of a chromosphere and a corona (see e.g. Narain & Ulmschneider, 1996). The following is a list of the main activity-related phenomena relevant to this thesis.

Flares - Flares are impulsive releases of magnetic energy during explosive field line reconnections. They can be accompanied by coronal mass ejections, if clumps of plasma were attached to the field lines that reconnected. They manifest through sudden increases of the luminosity over time scales of a few minutes, followed by a decay and return to the regular luminosity over a few hours (see e.g. Benz, 2017). Flares on the Sun typically release energies of 10^{27} – 10^{32} erg, while on wTTSs, large flares can release energies of the order of 10^{35} erg. Flares happen relatively often on wTTSs: for example Stelzer et al. (2007) measured a frequency of 1 large flare per star every $\sim$9 d in the Taurus molecular region.

Spots and plages - Magnetic fields generate dark and bright features at the surface of low-mass stars. The dark features, called spots, are regions where the magnetic field emerges from (or plunges into) deeper convective layers, and is strong enough to suppress the convective motion, so that the plasma in the spot is darker and cooler than the surrounding photosphere. The bright features, either faculae on the photosphere or plages on the chromosphere, are regions of brighter and hotter plasma. As the star rotates, the distribution of brightness over the visible disc changes, from the point of view of an Earthly observer, causing modulations in the light curve and in the spectral line profiles of the star. Long-term photometric monitorings of wTTSs have shown that they generally exhibit light curves with quasi-periodic high-amplitude modulations (up to 0.6 mag), indicating that dark and/or bright areas cover an important fraction of the surface of wTTSs and have long lifetimes compared to the stellar rotation periods (Grankin et al., 2008). Spot maps reconstructed through Doppler Imaging (DI, see section 2.2) tend to show large dark spots on the surfaces of wTTSs (see e.g. Strassmeier 2009 for a list up to 2009). These high-contrast brightness inhomogeneities cause spectral line distortions, and thus RV changes of the order of a few km s^{-1} over time scales of the order of 1 d (Huerta et al., 2008; Mahmud et al., 2011).

Moreover, latitudinal differential rotation can shear the surface and spots have a limited lifetime, eventually leading to a loss of periodic coherence in the rotational modulations. Differential rotation has been investigated on a few wTTSs, from both light curves and DI techniques: in some cases it did not fit data significantly better than solid-body rotation (Skelly et al., 2010; Donati et al., 2014), whereas in others it was found to present an equator rotating faster than the poles, like on the Sun, but with a somewhat weaker shear (Donati et al., 2015).

Secular evolution and magnetic cycles - Finally, even though wTTSs light curves generally exhibit strong periodicity, astronomers have observed changes in the shape, amplitude and sometimes period of their light curves over the years (Sokoloff et al., 2008; Hambálek et al., 2019). They are attributed to changes in the distribution of brightness features on the surface; in particular,

amplitude changes are associated to longitudinal redistributions of spots while period changes, combined with the presence of latitudinal differential rotation, are associated with latitudinal redistributions of spots. There has been no confirmed detection of a Sun-like magnetic cycle (with total spot coverage variation, mean spot latitude variation and reversal of the magnetic dipole) on a wTTS yet, but an analysis of the light curve of the wTTS V410 Tau over $\sim$50 yr revealed complex variations where several time scales appear (4 – 5 yr spot configuration lifetime, brightness minima every 11 – 13 yr, see Sokoloff et al., 2008).

Other phenomena not related to the magnetic activity, namely acoustic oscillations and granulation, can cause modulations of the brightness and RV. The characteristic time scale of oscillations is a few minutes (Gilliland et al., 2010) so their impact is averaged out for sufficiently long observations. Granulation, i.e. partial coverage of the photosphere by the top of convective cells, adds a negative contribution to the RVs, called the convective blueshift (negative RV balance over the visible disc of hot bright rising plasma and cold dark sinking plasma), estimated at $-100 \pm 50\,\mathrm{m\,s^{-1}}$ for stars of 4500 – 5000 K (Meunier et al., 2017). Because the magnetic field suppresses convection, changes in the magnetic topology lead to granulation-related RV modulations over a few years.

2.2 The MaTYSSE observation programme

2.2.1 Scientific goals

To characterize the magnetic activity of wTTSs and look for their hot Jupiters, the MaTYSSE (Magnetic Topologies of Young Stars and the Survival of massive close-in Exoplanets) observation programme (Donati et al., 2014) carried out the observation between 2013a and 2016b of 35 wTTSs in some of the most well-known SFRs: the Taurus-Auriga SFR, the closest to Earth at a distance of $\sim$140 pc, ρ Ophiuchius, Lupus, the TWA stellar association, etc... More specifically, its aims are:

- to better understand the evolution of magnetic fields in forming stars, by mapping the brightness distribution and magnetic topologies of wTTSs and comparing them to those reconstructed for cTTSs within the sister programme MaPP (Magnetic Protostars and Planets, see Donati et al. 2010b to Donati et al. 2013),
- to bring observational constraints to the formation and/or migration processes of hot Jupiters, by searching for potential close-in giant planets around wTTSs and, if found, by characterizing their orbits.

2.2.2 Instruments and data

The collected data are mainly high-resolution spectra from the intrument ESPaDOnS (Echelle SpectroPolarimetric Device for the Observation of Stars, Donati, 2003) at CFHT (Canada-France-Hawaii Telescope), Mauna Kea, Hawaii, and from its twin NARVAL at TBL (Télescope Bernard Lyot), Pic du Midi, France, complemented with contemporaneous photometric observations from the CrAO (Crimean Astrophysical Observatory).

The raw frames from ESPaDOnS and NARVAL (see figure 2.1) are processed with the nominal reduction package Libre ESpRIT as described in e.g. Donati et al. (2010b), to output them under the form of continuum-normalized 1D spectra. All spectra are automatically corrected for Doppler shifts resulting from instrumental effects (e.g. mechanical flexures, temperature or pressure variations) by using telluric lines as a reference (absorption lines in the spectra that come from the Earth's atmosphere). Though not perfect, this procedure provides spectra with a relative RV precision of better than $30\,\mathrm{m\,s^{-1}}$ (e.g. Moutou et al., 2007; Donati et al., 2008b). The collected stellar spectra span the entire optical domain (370 – 1000 nm) at a resolving power of 65k (i.e. a resolved velocity element of 4.6 $\mathrm{km\,s^{-1}}$).

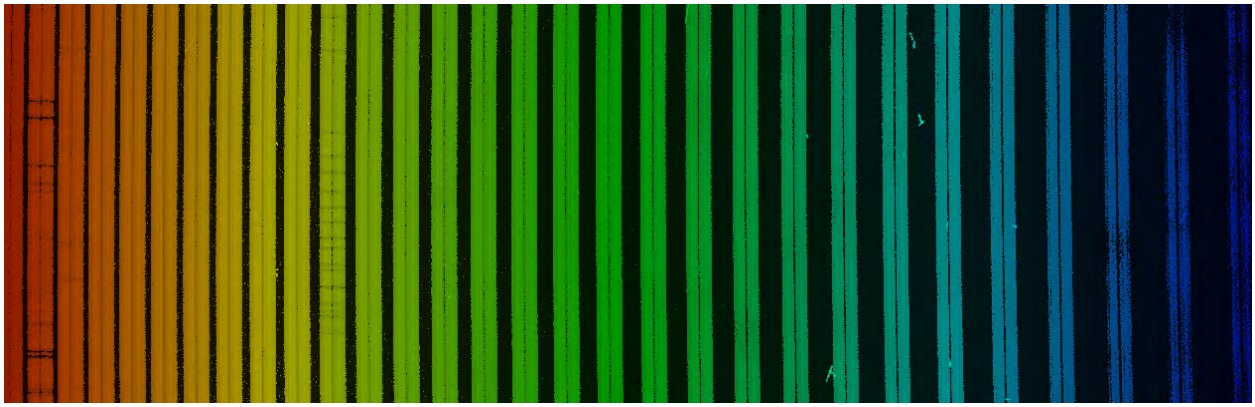

Figure 2.1 – Portion of an ESPaDOnS data frame (TAP 26 in the night of 2015 Nov 18 to 19). The colors were artificially added to show wavelength evolution along the frame. The grating orders separated through prism cross dispersion are roughly vertical, each divided into two polarization channels. Some spectral lines are visible.

ESPaDOnS and NARVAL can provide unpolarized, linearly polarized and circularly polarized spectra. The next section describes the techniques we use to retrieve brightness and magnetic topologies from these data: spectropolarimetry, velocimetry and time-frequency analysis.

2.3 Spectropolarimetry of wTTSs

2.3.1 Spectroscopy and Doppler Imaging

First we consider unpolarized spectra, i.e. intensity spectra, and in particular their spectral lines. Let us consider an element of surface on the visible disc of an observed star. The spectra we receive from it are Doppler-shifted according to its local RV (impacted by stellar rotation, convection, pulsations...) and the shape of the spectral lines depends on local physical parameters (e.g. chemical composition, temperature, turbulence, magnetic field) and geometric parameters (projected area, limb darkening). This shape is called the intrinsic profile and is not well-constrained for most stars, since very few stars are spatially resolved.

Stellar rotation induces a RV dispersion between -$v \sin i$ and $v \sin i$ over the visible disc, where v is the rotation velocity at the equator of the star, and i is the inclination of its rotation axis to the line of sight (see e.g. figure 2.5 for solid-body rotation). WTTSs generally have a $v \sin i$ of several $10\,\mathrm{km\,s^{-1}}$ (e.g. Bouvier et al., 1997; Strassmeier, 2009), unless i is very low. For these stars, rotation dominates over other effects as far as surface RV is concerned, so the RV distribution over the visible disc is well-approximated by the rotation-induced RV distribution. The spectral lines in the collected spectrum, integrated over the visible disc, are thus subjected to a Doppler broadening $v \sin i$, as the spectral contributions of the elemental surface regions undergo various Doppler shifts, and a strong correlation between surface rotational RV and position within the spectral lines appears. For instance, the presence of a spot/plage on the photosphere respectively lessens/enhances the contribution of the corresponding area to the integrated spectrum, causing distorsions in the integrated line profiles at positions corresponding to the rotational RV of the spot/plage. Therefore, a distorsion in the spectral lines indicates the presence of brightness features in the area whose rotational RV corresponds to the position of the distorsion. The effect of spots on the spectral lines of fast rotators is illustrated in figure 2.2).

Doppler imaging (DI) of starspots, a technique first described by Vogt & Penrod (1983b) and further elaborated by Vogt et al. (1987), takes advantage of this correlation on high-$v \sin i$ stars to

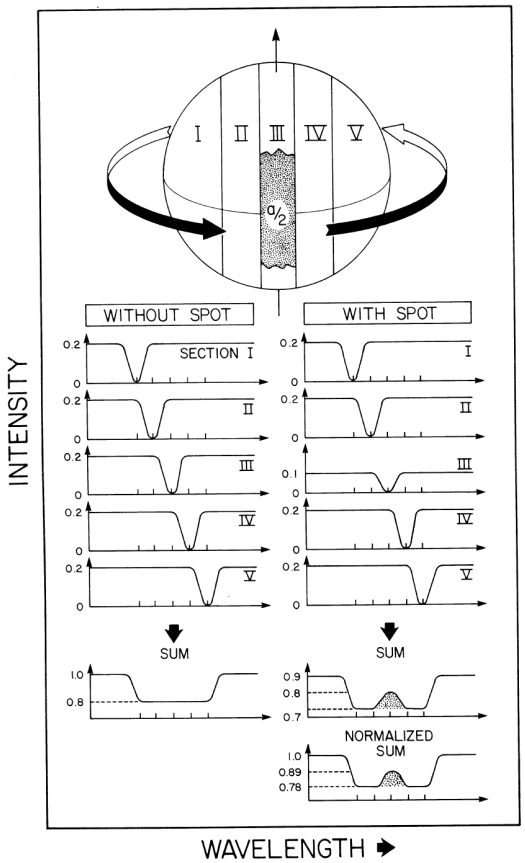

Figure 2.2 – Effet of a dark spot on a spectral absorption line of a fast rotator: the visible disc of the star is partitioned into areas of different local surfacic RVs, and the contribution of each individual area is shown. Note how, after rescaling the profile, the spot-related distorsion appears as a bump in the line profile in the wavelength band corresponding to the RVs affected by the spot, but also an enhancement of the line profile on both sides of that wavelength band. Illustration taken from Vogt & Penrod (1983a).

derive the spot distribution at their surfaces. Akin to medical tomography techniques, DI derives the two-dimensional brightness distribution on the photosphere from a series of one-dimensional spectra, observed at various phases of the stellar rotation (figure 2.3 illustrates the different effects of low-latitude and high-latitude spots on time-series of spectra). However, the number of solutions that can fit the data down to noise level is usually inifinite. The degeneracy of the inversion problem is lifted by choosing the solution with maximum entropy (minimal amount of information; unicity demonstrated in Skilling & Bryan, 1984), thus ensuring that the retrieved model, bearing an amount of information as low as possible while still fitting the data, is reliable.

DI can be applied to many spectral absorption lines that originate from photospheric chemical elements. As a matter of fact, building "average" line profiles to increase the signal-to-noise ratio (S/N), by applying least-squares deconvolution (LSD, see appendix A.2) to thousands of spectral absorption lines across the spectra, has proven an efficient way to extract the information repeated in all those lines under a compact form (Donati et al., 1997).

2.3.2 Polarimetry and Zeeman-Doppler Imaging

Light, as an electromagnetic wave, can be polarized. Polarization characterizes the way a vectorial wave vibrates as it propagates. In isotropic media, it describes the vibration of the electric field

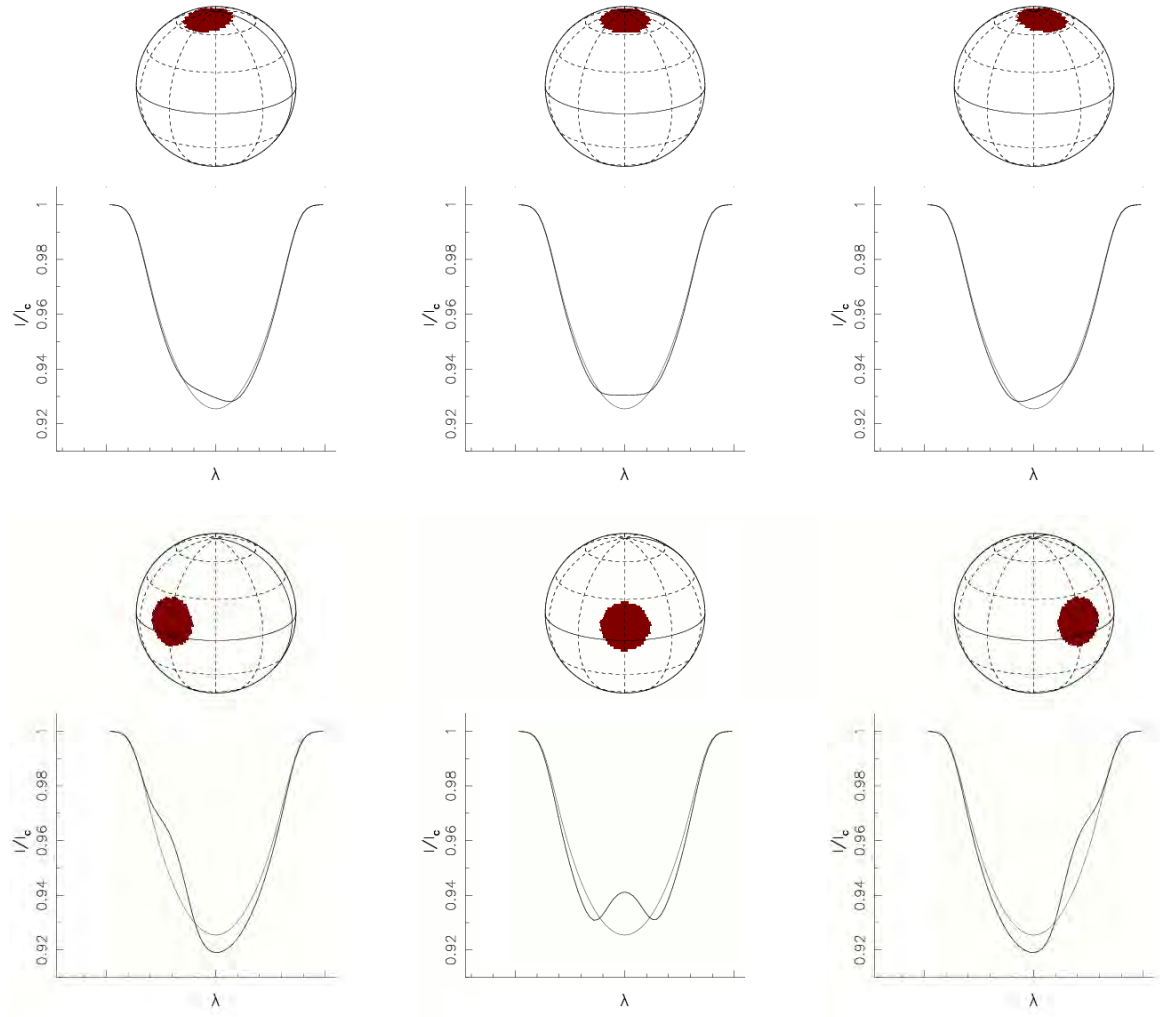

Figure 2.3 – Effect of a dark spot on intensity line profiles as the star rotates, depending on its latitude. *Top row*: high-latitude spot and corresponding spectral absorption line at different rotation phases. *Bottom row*: low-latitude spot and corresponding spectral absorption line at different rotation phases. The spotless line profile is displayed in gray for each case. Credit: Dr. Jean-François Donati. Extracted from: `http://www.ast.obs-mip.fr/article.php3?id_article=457`.

component of light in the plane perpendicular to the propagation direction: polarisation can be linear if it vibrates only in one other direction than the propagation direction, circular if the vector describes circles in the plane perpendicular to the propagation, or a combination of both (elliptic). The polarization of light can be described with the Stokes parameters I, Q, U and V, with I corresponding to the intensity, Q and U characterizing linear polarization and V circular polarization (see Appendix A.1).

The presence of a magnetic field introduces polarization in a beam of light by virtue of the Zeeman effect. For a detailed explanation and rigorous demonstrations about the Zeeman effect, the reader is invited to refer to Landi degl'Innocenti & Landolfi (2004). In short, magnetic fields such as those encountered in wTTSs split the excitation energy levels $(E_J)_{J=0,1,2...}$ of an element into:

$$(E_{J,M})_M = E_J + \mu_0 g B M,$$

where $M = -J, -J+1, ..., J-1, J$, and μ_0 and g are respectively the Bohr magneton and a property

of energy level E_J called the Landé factor.

Transitions between levels E_J and $E_{J'}$ can then occur between $E_{J,M}$ and $E_{J',M'}$ for any M, M' such that $|M - M'| \leq 1$. Among these transitions, those where $M' = M - 1, M, M + 1$ are called π, σ_b, σ_r transitions respectively. This therefore creates a splitting of the spectral lines: when summing over the transitions for all values of M, the π group adds up to a spectral line centered around the line wavelength without magnetic field λ_0, but the $\sigma_{b,r}$ groups have shorter/longer mean wavelengths respectively, the distance to λ_0 being proportional to B.

Because these three types of transitions have different vibration modes, this results in a net balance of polarization in the Q, U and V spectra (see appendix A.1 for more details).

In the case of wTTSs, the Doppler broadening of Stokes I spectral lines is already so large that the Zeeman effect is barely noticeable in Stokes I. But the Stokes V profiles, null in the absence of magnetic fields, present clear signatures in their presence, as illustrated on figure 2.4.

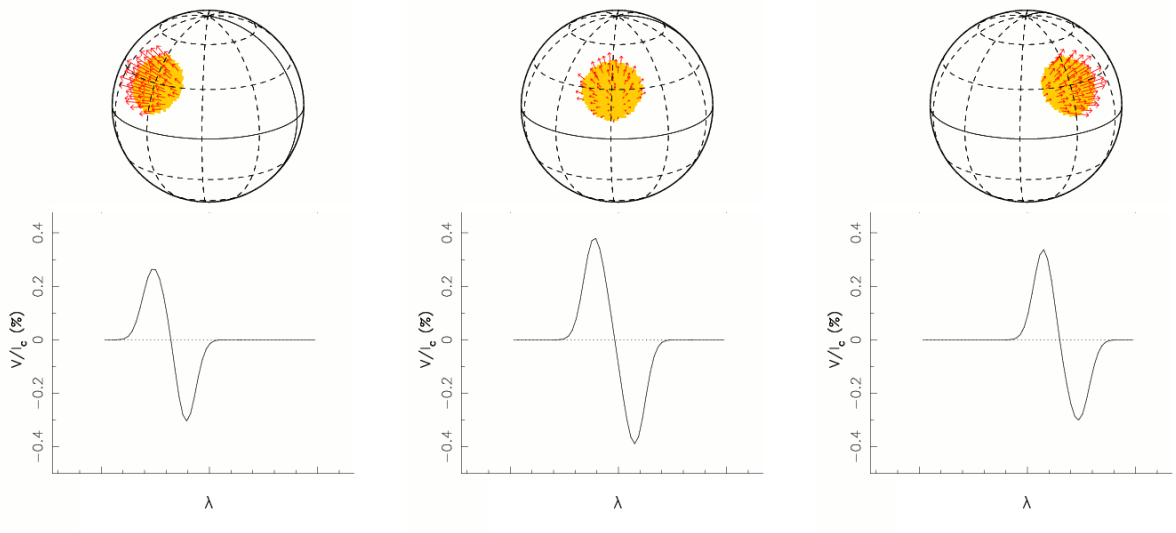

Figure 2.4 – Effect of a radial field spot on Stokes V line profiles as the star rotates. Credit: Dr. Jean-François Donati. Extracted from: `http://www.ast.obs-mip.fr/article.php3?id_article=457`

Zeeman-Doppler Imaging (ZDI) of active stars, described in a series of papers from Semel (1989) to Donati & Brown (1997) and with major updates detailed in Donati et al. (2006, 2014), is a tomography technique inspired from DI which inverts simultaneous series of Stokes I and Stokes V profiles into surface maps of brightness and magnetic field. The next three paragraphs give a short summary of how ZDI works; further explanation is provided in appendix A.3.

ZDI is an inversion problem which looks for the maps that will give the best fit to the spectral data. For the direct problem, ZDI builds a spherical mesh where each cell has a given brightness value and magnetic field vector (radial, meridional and azimuthal components), and the local line profiles of each cell, in Stokes I and Stokes V, are derived using Unno-Rachkovsky's analytical solution to the polarised radiative transfer equations in a Milne-Eddington model atmosphere (Landi degl'Innocenti & Landolfi, 2004). Then, at each observation date, the local profiles are Doppler-shifted and weighted according to the geometry of the system (inclination, current rotation phase, rotation velocity, see figure 2.5), before being added up into the integrated line profile.

Like for DI, the inversion problem is ill-posed and the degeneracy is lifted by looking for the maximum entropy solution. The inversion algorithm, inspired from Skilling & Bryan (1984), is thus an iterative conjugate gradient algorithm, where the model line profiles are to approach the data until noise level is reached (χ^2_r decreases towards 1) and the entropy of the surface maps is to

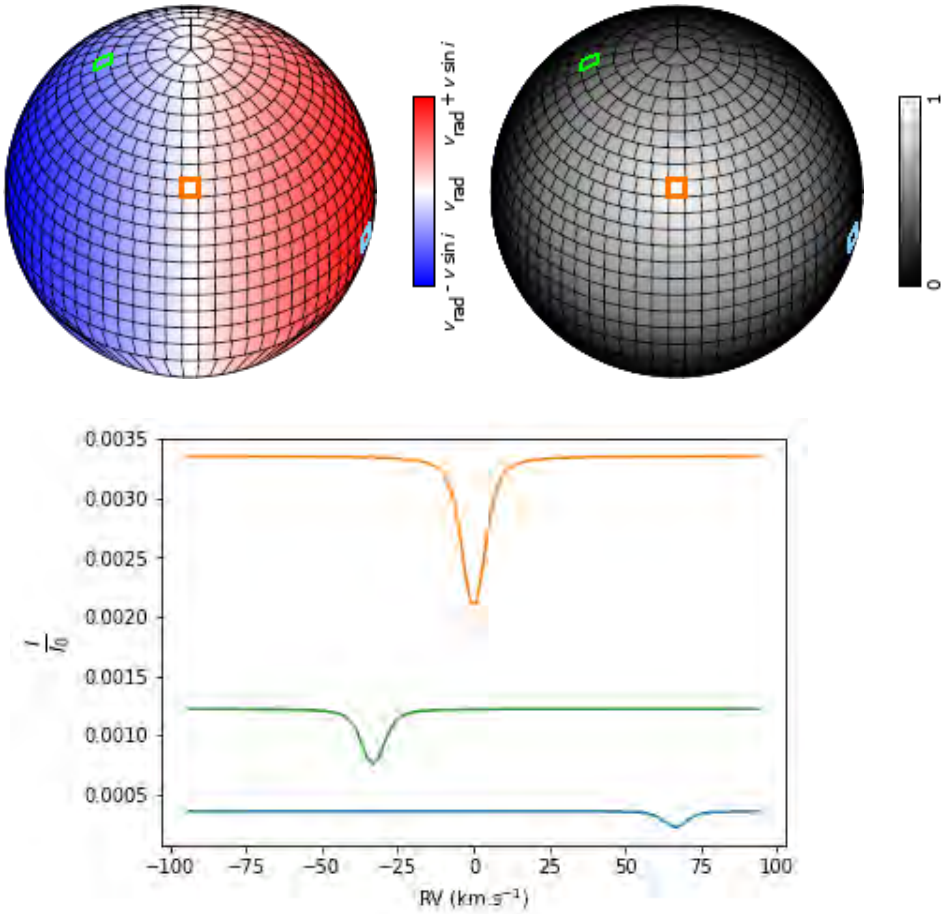

Figure 2.5 – **Top**: ZDI mesh with $i = 50°$ and 1000 cells, at phase 0. There are 20 rings of 5 to 70 cells. Three cells are colored in green, orange and blue respectively, to show their relation with the curves in the bottom plot. *Left*: Local radial velocity at the surface of the star. *Right*: Limb darkening factor. **Bottom**: Individual contributions of the highlighted cells to the synthetic Stokes I line profile, with $v \sin i = 70\,\mathrm{km\,s^{-1}}$ and $v_{\mathrm{rad}} = 0\,\mathrm{km\,s^{-1}}$, and assuming uniform brightness and no magnetic field.

increase as high as possible. The inclination of the rotation axis i, the $v \sin i$ and the bulk RV of the star v_{rad} are all quantities that intervene in the direct problem of ZDI; it is therefore possible to measure them by applying ZDI with different values of these parameters and looking for the maximal entropy reached at convergence.

Since Donati et al. (2000), differential rotation was added to the model of ZDI, by allowing the mesh cells to rotate at different rates depending on their latitude, following a two-parameter sine-square law (see equation A.1). Thus, the equatorial rotation rate, Ω_{eq}, and the difference between the equatorial and polar rotation rates, $d\Omega$, are also parameters that we can optimize using ZDI.

Chapter 3 shows the study of the stellar activity of three wTTSs using ZDI.

2.3.3 Activity proxies

Some particular spectral lines are interesting to study individually (Donati et al., 2010a).

For example, the emission detected in the Hα Stokes I line (located at 656 nm) comes from the magnetically heated high atmosphere and its equivalent width (EW, the integral of the continuum-subtracted line) can undergo periodic modulations due to the stellar rotation. It can also trace the presence of prominences in the chromosphere, which are tied to the stellar surface by magnetic

field lines and rotate together with the star, absorbing some of the Hα emission when passing in front of the visible disc (Collier Cameron & Robinson, 1989).

We use averaged profiles of the Ca II infrared triplet (IRT) in Stokes I, located at 850 nm, 854 nm and 866 nm, whose emission component reflect the heated material in the corona. The emission core EW also presents quasi-periodical modulations of period $P_{\rm rot}$.

The last particular line we use is the He I D_3 line at 588 nm. This line, thought to be produced during accretion shocks when the accreted matter hits the chromosphere, is a good marker of accretion and, for wTTSs, its EW and modulations are expected to be low. This line is also a good indicator for flares, during which its EW greatly increases.

2.4 Velocimetry of wTTSs

2.4.1 Searching for planetary signatures

The general idea of the velocimetry detection method for exoplanets is that, if there is an exoplanet around the star, then its gravitational pull will cause the star to follow a small orbit around the star-planet barycenter. This reflex motion of the star should be detectable in its RVs as a periodic signal (unless the orbit is in the plane perpendicular to the line of sight, in which case the planet is undetectable with this method), the period corresponding to the revolution period of the planet. Using Newton's laws of motion and Kepler's laws of planetary motion, one can derive the RV variation in the general case of an elliptic orbit (see appendix A.4). For example, in the case of a unique planet on a circular orbit, the RV modulation is expected to be:

$$V_r(t) = K\cos\left(2\pi\left(\frac{t}{P_{\rm orb}} - \phi\right)\right) + V_{r,\rm B}, \tag{2.1}$$

$$K \simeq M_{\rm J}\sin i_{\rm J}\sqrt{\frac{\mathcal{G}}{dM_\star}} \quad \text{for } M_{\rm J} \ll M_\star,$$

$$P_{\rm orb} \simeq \frac{2\pi d^{3/2}}{\sqrt{\mathcal{G}M_\star}} \quad \text{for } M_{\rm J} \ll M_\star.$$

where $P_{\rm orb}$ is the orbital period, ϕ depends on the chosen origin of time, $V_{r,\rm B}$ is the constant RV of the star-planet barycenter, $i_{\rm J}$ is the inclination of the orbital axis to the line of sight, $\mathcal{G}$ is the gravitational constant, d is the star-planet separation and $M_\star$ and $M_{\rm J}$ are the masses of the star and of the planet respectively. The amplitude K is higher the more massive and the closer to the star the planet is, which is why hJs are the easiest planets to detect with this method.

For a Jupiter-size planet around a solar-size star, $M_J/M_\star \simeq 10^{-3}$ so we consider that $M_J \ll M_\star$ and derive information on M_J and d as follows:

$$M_J\sin i_{\rm J} \simeq K\left(\frac{P_{\rm orb}M_\star^2}{2\pi\mathcal{G}}\right)^{1/3}$$

$$d \simeq \left(\frac{P_{\rm orb}\sqrt{\mathcal{G}M_\star}}{2\pi}\right)^{2/3}.$$

We note that, with V_r alone, it is not possible to derive M_J and $i_{\rm J}$ individually. To pinpoint the value of M_J, it is therefore necessary to constrain $i_{\rm J}$, for example by using ZDI to find the inclination of the stellar rotation axis i, and assuming that the planet has a null obliquity with respect to the stellar equatorial plane. We can also find $i_{\rm J}$ if the planet transits, or by studying atmospheric signatures (Brogi et al., 2012). We also underline the importance of knowing stellar parameters, in particular the mass of the star, to be able to characterize the planet precisely.

2.4.2 RV activity jitter for wTTSs

Measuring the Doppler shift in Stokes I LSD profiles of wTTSs is far from trivial, because the profiles are highly broadened and distorted. In the context of this thesis, we derive the RVs as the first-order moment of the continuum-subtracted Stokes I LSD profiles. This method is close to computing a weighted average of the local surfacic RV over the visible disc.

$$\mathrm{RV} = \alpha \int_{-\infty}^{+\infty} (I_c - I(v)) v \, \mathrm{d}v,$$

where $\alpha = \left(\int_{-\infty}^{+\infty} (I_c - I(v)) \, \mathrm{d}v \right)^{-1}$ is the normalization constant and the inverse of the line equivalent width (in units of velocity).

To link it to the actual bulk RV of the star V_r, we represent the Doppler effect as: $I(v) = I_0(v - Vr)$, where I_0 is the Stokes I LSD profile of a star identical to ours except with no bulk RV. Thus:

$$\begin{aligned}
\mathrm{RV} &= \alpha \int_{-\infty}^{+\infty} (I_c - I_0(v - Vr)) v \, \mathrm{d}v \\
&= \alpha \int_{-\infty}^{+\infty} (I_c - I_0(v')) (v' + V_r) \, \mathrm{d}v' \\
&= \alpha \int_{-\infty}^{+\infty} (I_c - I_0(v')) v' \, \mathrm{d}v' + V_r \alpha \int_{-\infty}^{+\infty} (I_c - I_0(v')) \, \mathrm{d}v' \\
&= \mathrm{RV}_{\mathrm{jitter}} + V_r
\end{aligned}$$

because $\int_{-\infty}^{+\infty} (I_c - I_0(v')) \, \mathrm{d}v' = \int_{-\infty}^{+\infty} (I_c - I(v)) \, \mathrm{d}v = \alpha^{-1}$.

The measured RV is therefore the sum of a quantity called the activity jitter and of the bulk RV of the star. For a star with no activity, the activity jitter is zero and $\mathrm{RV} = V_r$. Figure 2.6 sums up the contributions of activity and of a planet to observed RVs.

2.4.3 Time-frequency analysis tools

To study the periodicity in our activity proxies, RVs and photometric data, we use Lomb-Scargle periodograms (see appendix A.5.1). In particular, the activity jitter can be modelled from ZDI brightness maps, as the first-order moment of the continuum-subtracted Stokes I synthetic profiles. Once the activity jitter is subtracted from the RVs, we compute Lomb-Scargle periodograms of the filtered RVs to look for any periodicity standing out, which could betray the presence of a hJ. Basically, this method looks for a periodic signature in the Stokes I LSD profiles which ZDI does not manage to model with spots and plages, because its period is not commensurable with the stellar rotation period. However this method does not account for intrinsic variability, whether in the ZDI-modelling of activity jitter or when investigating activity proxies.

This is why we also used another numerical tool, called Gaussian Process Regression (GPR, see appendix A.5.2), to model our activity proxies, RVs and photometric data. GPR does not use a physical model, but a priori knowledge on the statistical behaviour of the data, given under the form of a covariance function. The covariance function informs how correlated any two measurements should be, depending on the time at which they are taken. For example, for the RV activity jitter of a wTTS, we use a pseudo-periodic covariance function:

$$k(t, t') = \theta_1^2 \ \exp\left(-\frac{(t - t')^2}{\theta_3^2} - \frac{\sin^2\left(\frac{\pi(t - t')}{\theta_2}\right)}{\theta_4^2} \right), \tag{2.2}$$

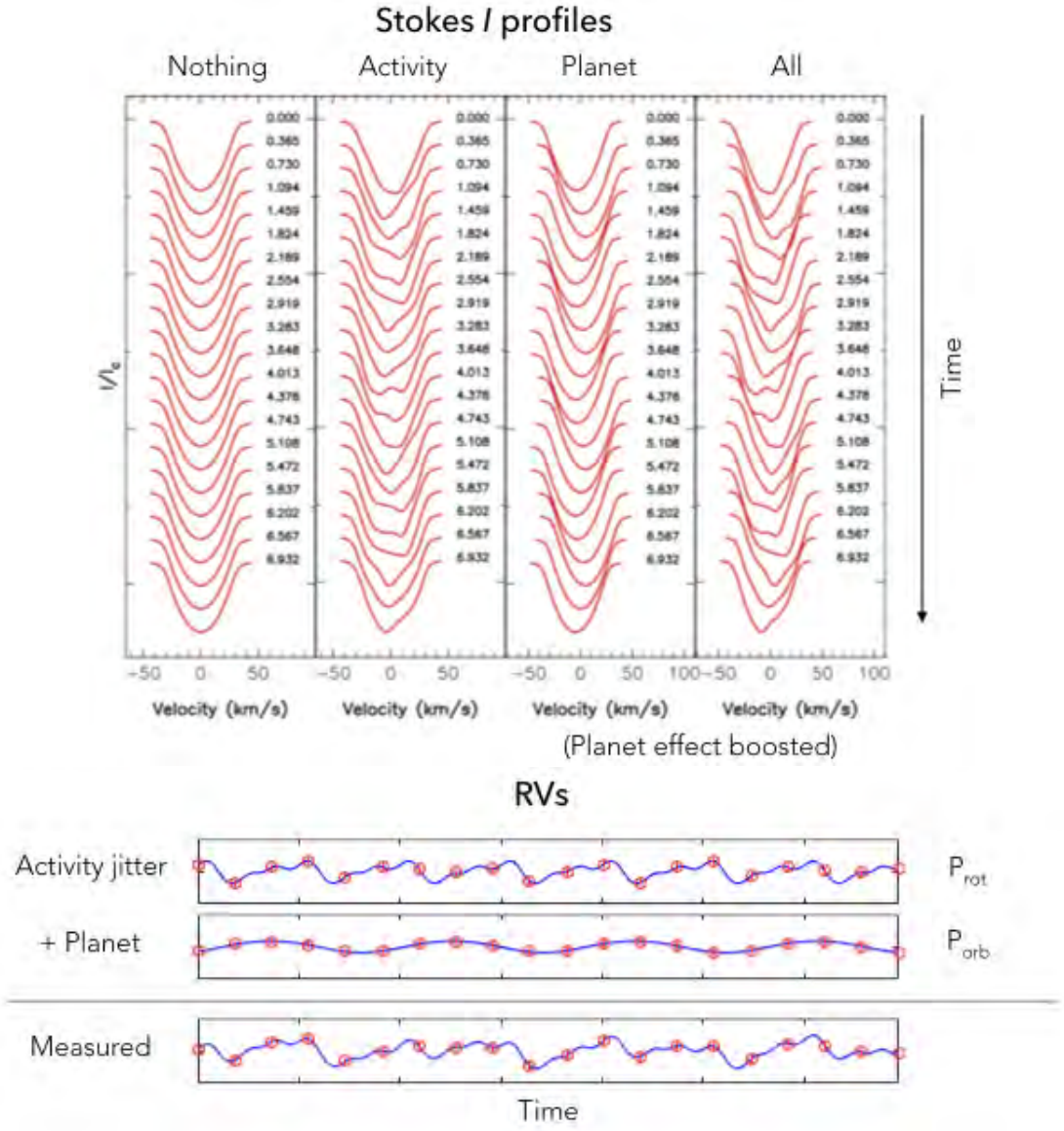

Figure 2.6 – *Top*: Time series of Stokes I LSD profiles for various cases. Activity distorts the profiles while the presence of a planet shifts them without distorting them. The effect of the planet is artificially boosted here for visualization purposes. *Bottom*: corresponding RVs. The activity jitter presents modulations of period $P_{\rm rot}$, the rotation period of the star, while the reflex motion caused by the presence of a planet is a sine curve of period $P_{\rm orb}$.

where the amplitude $\theta_1 > 0$, the cycle $\theta_2 > 0$, the decay time $\theta_3 > \theta_2$ and the smoothing parameter $\theta_4 \in [0; 1[$ are called the hyperparameters of the model (Aigrain et al., 2012; Haywood et al., 2014). GPR then uses the data to predict RV jitter values at all times, according to the covariance function. The output is actually a probability distribution over the space of time functions, as illustrated in figure 2.7.

We note that it is possible to add a mean function $m(t)$ to the prior knowledge that GPR uses, which in our case would be the expected planetary signature (a sine wave for a circular orbit, or a keplerian curve for an elliptic orbit). The likelihood $\mathcal{L}$ of the resulting model is given by (Rasmussen

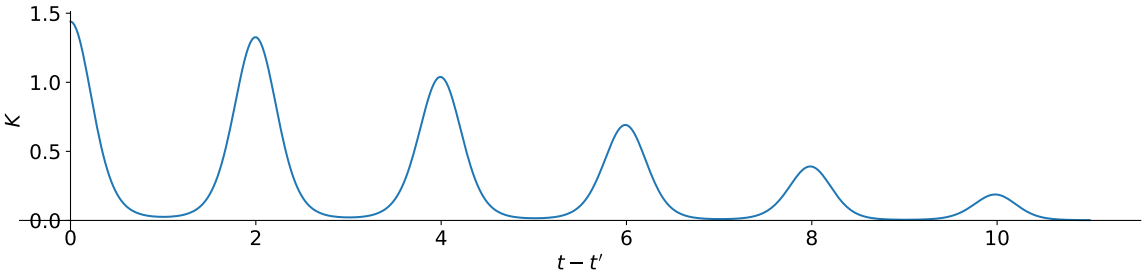

(a) Covariance function

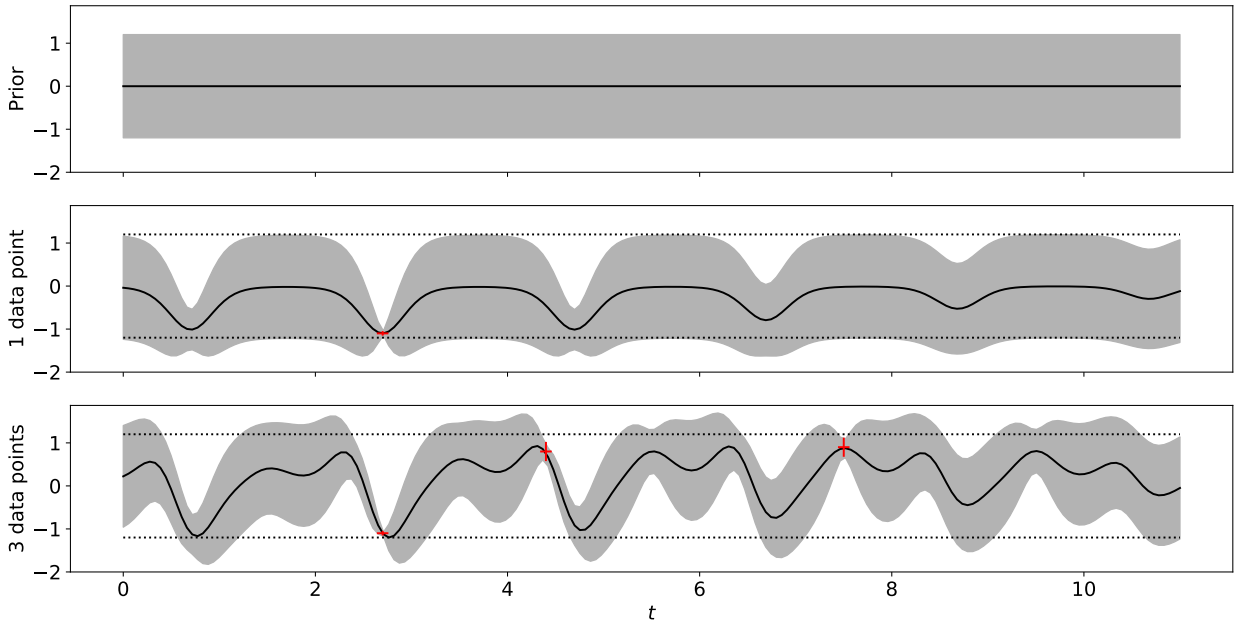

(b) Gaussian process regression with 0, 1 or 3 data points

Figure 2.7 – Example of GPR with a pseudo-periodic covariance function. *Top:* covariance function for a pseudo-periodic GPR model, as defined in equation 2.2 with $\theta_1 = 1.2$, $\theta_2 = 2$, $\theta_3 = 7$, $\theta_4 = 0.5$ (arbitrary units). *Bottom:* result of the GPR depending on the number of data points. When no data point exist, the probability distribution at t is the prior $\mathcal{N}(0, \theta_1^2)$. The black line represents the mean of the point-wise probability distribution while the grey area represents the standard deviation of the point-wise probability distribution. The prior is also reproduced on the second and third graph as dotted black lines. The data points (2.7, -1.1, 0.03), (4.4, 0.8, 0.2), (7.5, 0.9, 0.2) are represented as red crosses whose vertical extension indicates the error bar. Note how measurements constrain the point-wise probability distribution, especially how the sizes of the standard deviations are decreased.

& Williams, 2006):

$$\log \mathcal{L}(m,k) = -\frac{1}{2}\Big(N\log(2\pi) + \log(\det C) + (\mathbf{y}-\mathbf{m})^T C^{-1}(\mathbf{y}-\mathbf{m})\Big), \tag{2.3}$$

where C is the covariance matrix between all the times of observations, $\mathbf{y}$ is the vector of observed RV values and $\mathbf{m}$ is the vector of planetary signature values at all observed times. In general, m and k are not well-constrained a priori, so modelling the RV curve actually consists of looking for the likelihood distribution over the space of hyperparameters of m and k, namely: K, P_{orb}, ϕ for the planetary signature (see equation A.3), potentially with two additional parameters for eccentric orbits (see appendix A.4), and $\theta_1, \theta_2, \theta_3$ and θ_4 for the activity jitter.

GPR comes in handy when data sets span more than a month, as ZDI cannot model intrinsic variability of the brightness distribution (spots/plages fading or intensifying over time), and therefore loses accuracy in the jitter modelling over time, or requires the data set to be split into short subsets. With the pseudo-periodic covariance function, in particular hyperparameter θ_3, GPR allows the signal to lose coherence after a certain amount of time, which can account for, and even inform on, the photospheric intrinsic variability.

Chapter 4 details the analysis of the RVs of three wTTSs carried through within this thesis.

3 | Modelling stellar activity - imaging brightness inhomogeneities and magnetic topologies

Contents

3.1 Chosen targets within the MaTYSSE programme

During this thesis, I analyzed MaTYSSE data on two wTTSs, TAP 26 and V410 Tau, and I closely followed the analysis of the V830 Tau observations, which I partially describe here as well for comparison purposes. These three stars, whose location and physical parameters are displayed in figure 3.1 and table 3.1, are all of particular interest in their own respect. Prior to my thesis, V830 Tau was discovered to host a hJ, and became the youngest star around which a hJ detection was confirmed (other hJs around TTSs are candidates CVSO 30 b, van Eyken et al. 2012 and CI Tau b, Johns-Krull et al. 2016; ∼5 Myr K2-33 has a confirmed hot Neptune Mann et al. 2016; David et al. 2016 and ∼23 Myr V1298 Tau has four confirmed hot giants, David et al. 2019b).

V410 Tau and V830 Tau are evidence that disc dissipation for PMS stars in Taurus may occur on time-scales as short as 1 – 2 Myr (Williams & Cieza, 2011; Ingleby et al., 2012), even though 80 – 90 % of single stars in this star formation region still host discs at similar ages (Kraus et al., 2012). This makes them atypical in this respect, and thus of obvious interest for MaTYSSE. Looking back to figure 1.4, we focus on the rotation rates during the disc-locking phase (see section 1.2.2). Observations of cTTSs (e.g. Affer et al., 2013) seem to suggest that, somehow, cTTSs tend to rotate with a period of 5 – 10 d rather than with arbitrary rotation rates. Supposing that the angular momentum has not changed significantly since the liberation from disc-locking, we could roughly estimate, from the current angular momentum of our stars, the age at which they freed themselves from their discs. Using the moments of inertia from the evolutionary models by Siess et al. (2000), we over-plotted rough iso-angular-momentum tendencies (orange dashed lines) passing through our target stars, as well as the rotation rate of AA Tau (black dashed line at $\Omega/\Omega_\odot \simeq 3.1$) in figure 3.2. Assuming that all disc-locked stars rotate with periods of ∼8 d, the intersection between those dashed lines should indicate the age at which our stars got freed from disc-locking. Of course this is a very rough estimation, but the main conclusion is that our target stars most likely got liberated from disc-locking at very young ages (< 1 Myr). Since their magnetic dipoles are expected to be strong at such young ages, it is then plausible that TAP 26, V410 Tau and V830 Tau dissipated their inner discs, stopped accreting and became wTTSs at those young ages.

In particular, TAP 26 closely resembles an evolved version of V830 Tau, with the same mass and angular momentum, that would have contracted and spun up by four times towards the zero-age main sequence. The increase in rotation rate matches quite well the predicted decrease in the moment of inertia between both epochs according to evolutionary models of Siess et al. (2000). Given the prominent role of the disc in braking the rotation of the star and thus decreasing its angular momentum (Gallet & Bouvier, 2015; Davies et al., 2014), this suggests that TAP 26 dissipated its accretion disc very early, typically as early as, or earlier than V830 Tau.

Finally, V410 Tau, as one of the brightest wTTSs, has been the subject of numerous studies, is one of the youngest observed wTTSs, and is part of a binary star of sky-projected separation ∼17 au (see section 3.1.2).

3.1.1 TAP 26

TAP 26 is a well-studied single wTTSs (Feigelson et al., 1987; Grankin et al., 2008; Grankin, 2013) located in the Taurus star-forming region. TAP 26 was observed in late 2015 and early 2016 with both the ESPaDOnS spectropolarimeter and the 1.25 m telescope at the Crimean Astrophysical Observatory (CrAO). The full journal of observations is available at Yu et al. (2017).

TAP 26 was observed in November 2015 and January 2016 using the high-resolution spectropolarimeter ESPaDOnS at the 3.6-m CFHT at Mauna Kea (Hawaii). A total of 29 Stokes I and Stokes V spectra were collected over a timespan of 72 d, 16 spectra over 16 nights in 2015 Nov, and 13 spectra over 13 nights in 2016 Jan. The frequency of visits was one per night, except at the beginning of the 2015 Nov session where a three-day gap following the first observation was

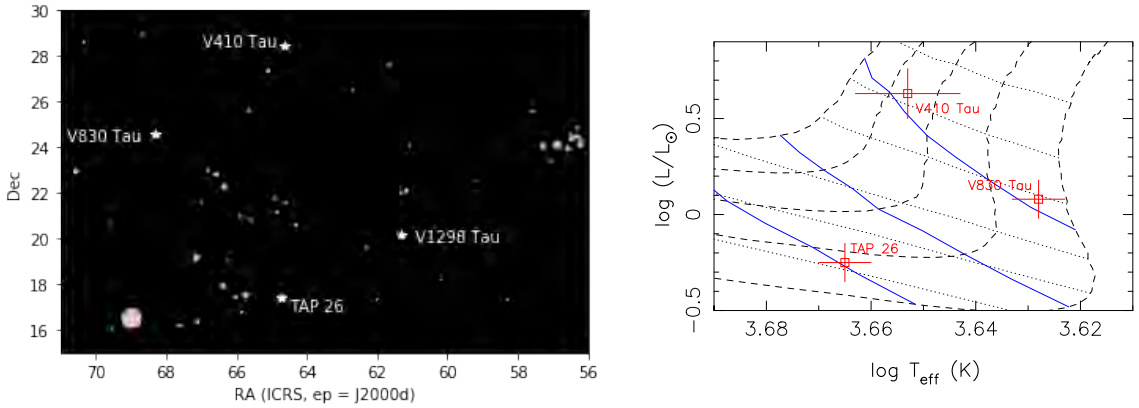

Figure 3.1 – *Left*: positions of TAP 26, V410 Tau and V830 Tau in the sky. Astronomical coordinates are given in the J2000 reference system and surrounding stars are represented with size proportional to their luminosity in the V band according to the Simbad database (Wenger et al., 2000), colored red if their B-V is positive and blue otherwise. The luminous red star in the bottom left corner is α Tau a.k.a. Aldebaran, and the blue cluster in the middle right is the Pleiades cluster. *Right*: observed location of TAP 26, V410 Tau and V830 Tau in the HR diagram. The PMS evolutionary tracks are displayed in dashed lines, for 1.7 $M_\odot$, 1.5 $M_\odot$, 1.3 $M_\odot$, 1.1 $M_\odot$ and 0.9 $M_\odot$ from top to bottom. Isochrones are displayed in dotted lines, for 0.5 Myr, 1 Myr, 2 Myr, 5 Myr, 10 Myr and 20 Myr from top to bottom. The thresholds where the radiative core starts developping and where it reaches 50% and 60% of the stellar radius are marked in blue (from top to bottom). These models (Siess et al., 2000) assume solar metallicity and include convective overshooting.

compensated by pairs of observations on Nov 25, Nov 29 and Dec 01. However, given the 0.71 d rotation period of TAP 26, phase coverage is not optimal and the 2015 Nov data set presents gaps of 0.15 – 0.25 rotation cycle.

Rotational cycles (noted E in the following equation) are computed from Barycentric Julian Dates (BJDs) according to the ephemeris:

$$\text{BJD (d)} = 2,457,344.8 + P_{\text{rot}} E \tag{3.1}$$

in which the photometrically-determined rotation period P_{rot} (equal to 0.7135 d, Grankin, 2013) is taken from the literature and the initial Julian date (2,457,344.8 d) is chosen arbitrarily. The stellar rotational phase is defined as the decimal part of the cycle E.

Applying the automatic spectral classification tool especially developed in the context of MaPP (Magnetic Protostars and Planets) and MaTYSSE, following that of Valenti & Fischer (2005) and discussed in Donati et al. (2012), we find that the photospheric temperature and logarithmic surface gravity of TAP 26 are respectively equal to $T_{\text{eff}} = 4620 \pm 50$ K and $\log g = 4.5 \pm 0.2$ (base-10 logarithm with g in cgs units).

To derive the mass and age of TAP 26, we use the evolutionary models for PMS stars by Siess et al. (2000), assuming solar metallicity and including convective overshooting, for compatibility purposes with MaPP and previous MaTYSSE studies. These models provide $\log g$ as a function of mass and age, so one way to proceed would be to derive the mass and age of TAP 26 from the measured T_{eff} and $\log g$ above. However we prefer to infer them from an HR diagram, with the absolute bolometric luminosity of TAP 26 being derived from photometric measurements and from T_{eff}, as well as results of our imaging code ZDI (see section 3.2), deemed more reliable. Using ZDI, we derived from the spectra that the inclination of the star rotation axis is $i = 55 \pm 10\,^\circ$ and its $v \sin i$ is $68.2 \pm 0.5\,\text{km}\,\text{s}^{-1}$. Since the star rotation period is $P_{\text{rot}} = 0.7135\,\text{d}$, we derive $R_\star \sin i = 0.962 \pm 0.007\,R_\odot$ and $R_\star = 1.17 \pm 0.15\,R_\odot$, which corresponds to a logarithmic luminos-

Table 3.1 – Physical parameters of TAP 26, V410 Tau and V830 Tau. From top to bottom: distance from Earth, mass, radius, minimum stellar radius, effective temperature, base-10 logarithm of surface gravity, logarithmic luminosity, age, rotation period, inclination of the rotation axis to the line of sight, line-of-sight-projected equatorial rotation velocity, equatorial rotation rate, difference between equatorial and polar rotation rates, mean RV in the Solar System barycentric rest frame. References: most values for V830 Tau are taken from Donati et al. (2015), for the rest, *a* is Gaia Collaboration et al. (2018), *b* Grankin (2013), *c* Galli et al. (2018), *d* Stelzer et al. (2003), *e* Donati et al. (2016). The rest are derived in sections 3.1.1, 3.1.2 or 3.2.1.

Parameter	TAP 26	V410 Tau	V830 Tau
d (pc)	121.8 ± 0.6^a	129.0 ± 0.5^c	130.6 ± 0.7^a
$M_\star$ ($\mathrm{M}_\odot$)	1.04 ± 0.10	1.42 ± 0.15	1.00 ± 0.05
$R_\star$ ($\mathrm{R}_\odot$)	1.17 ± 0.15	3.4 ± 0.5	2.0 ± 0.2
$R_\star \sin i$ ($\mathrm{R}_\odot$)	0.962 ± 0.007	2.708 ± 0.007	1.65 ± 0.03
T_{eff} (K)	$4{,}620 \pm 50$	4500 ± 100	4250 ± 50
$\log g$	4.5 ± 0.2	3.8 ± 0.2	3.9 ± 0.2
$\log_{10}(L_\star/\mathrm{L}_\odot)$	-0.25 ± 0.11	0.63 ± 0.13	0.08 ± 0.10
Age (Myr)	$\sim$17	0.84 ± 0.20	$\sim$2.2
P_{rot} (d)	0.7135^b	$1.871\,97 \pm 0.000\,10^d$	2.741^b
i (°)	55 ± 10	50 ± 10	55 ± 10
$v \sin i$ ($\mathrm{km\,s^{-1}}$)	68.2 ± 0.5	73.2 ± 0.2	30.5 ± 0.5
Ω_{eq} ($\mathrm{mrad\,d^{-1}}$)	8819.9 ± 0.3	3359.57 ± 0.06	2295.25 ± 0.20^e
$d\Omega$ ($\mathrm{mrad\,d^{-1}}$)	49.2 ± 1.0	9.7 ± 0.3	17.2 ± 1.4^e
v_{rad} ($\mathrm{km\,s^{-1}}$)	16.25 ± 0.20	$\sim$16.45 (see Chap. 3)	17.5 ± 0.1

ity $\log_{10}(L_\star/\mathrm{L}_\odot) = -0.25 \pm 0.11$ and a bolometric absolute magnitude of 5.36 ± 0.28. To compare this value to the minimum apparent V magnitude of TAP 26 (12.16, see Grankin et al., 2008), we have to account for the following effects:

- A spot coverage of r % adds $-2.5 \log_{10}(1 - r/100)$ to the magnitude (r % of the light is suppressed because of spots). The spot coverage of a wTTS at its brightest varies from star to star (Grankin, 1998; Gully-Santiago et al., 2017, note that, in those papers, the derived quantity is not the fraction of suppressed luminosity, but the fractional area of cool spots of a given temperature).
- The visual extinction caused by the interstellar medium is equal to $A_{\mathrm{V}} = 3.1\ E_{\mathrm{B-V}}(T_{\mathrm{eff}})$. The $\mathrm{B} - \mathrm{V}$ index expected at T_{eff} =4620 K being 0.99 ± 0.02 (Pecaut & Mamajek, 2013, Table 6), and the averaged value measured for TAP 26 being 1.13 ± 0.05 (Kenyon & Hartmann, 1995; Grankin et al., 2008), and given the very weak impact of starspot on $\mathrm{B} - \mathrm{V}$ (Grankin et al., 2008), we derive that the amount of visual extinction that TAP 26 suffers is A_{V} =0.43 ± 0.17 (within 1.5σ of the value of Herczeg & Hillenbrand, 2014, despite the very different methods used to estimate this parameter).
- The bolometric correction to subtract from the bolometric magnitude in order to obtain the apparent magnitude is -0.55 ± 0.05 for $T_{\mathrm{eff}} = 4620$ K (Pecaut & Mamajek, 2013, Table 6).
- The distance d between the star and Earth adds a distance modulus of $-5\ \log_{10}(d/(10\,\mathrm{pc}))$. TAP 26 is at a distance $d = 121.8 \pm 0.6$ pc (Gaia Collaboration et al., 2018), so the distance modulus is 5.84 ± 0.04.

We obtain that $\mathrm{Mag}_{\mathrm{abs},\star} + 2.5 \log_{10}(1 - r/100) = 11.77 \pm 0.33$, and that the minimum V magnitude measured by Grankin et al. (2008) is compatible with a spot coverage of 30 ± 20 %.

Using the Siess et al. (2000) evolutionary models, we obtained that TAP 26 is a $\sim$17 Myr star (in good agreement with the estimate of Grankin, 2013, 18.6 ± 4.0 Myr) and that its mass is $M_\star = 1.04 \pm 0.10\,\mathrm{M}_\odot$ (see figure 3.1). This leads to a $\log g$ of 4.32 ± 0.17, which is consistent

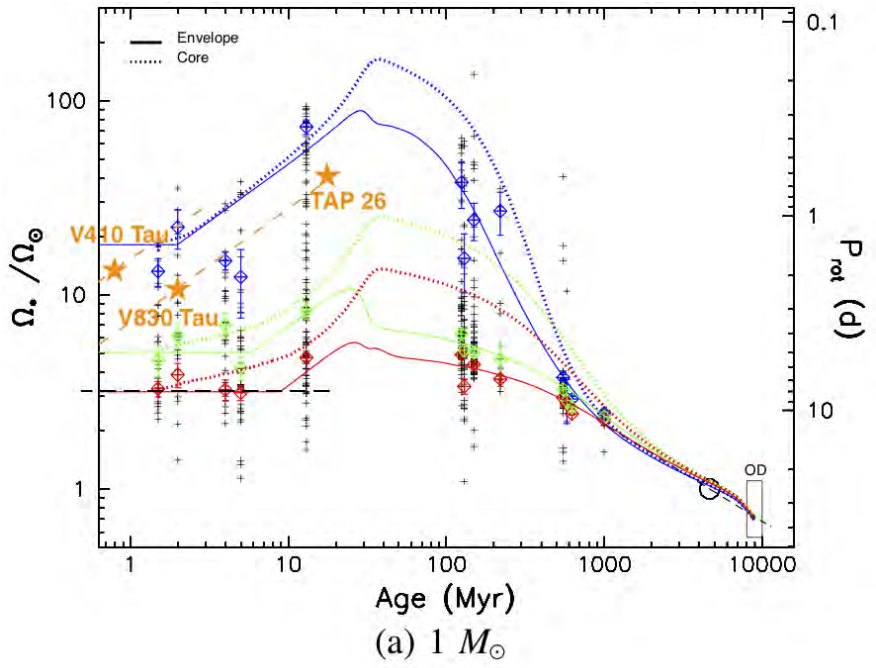

Figure 3.2 – Position of V830 Tau, TAP 26 and V410 Tau on the plot of figure 1.4. The rotation rate of AA Tau (∼8 d, Bouvier et al., 2007) is shown as a horizontal black dashed line. Following the evolution models for the rotation of cores (solid lines) and envelopes (dotted lines), a rough trend for an evolution track passing through V830 Tau and TAP 26 was plotted as an orange dashed line. One can speculate that cTTSs in disc-locked configuration like AA Tau rotate approximately at the same rate, and extrapolate from these black and orange dashed lines that V830 Tau and TAP 26 might have lost their discs before the age of 1 Myr. The same treatment was applied to V410 Tau even though its stellar mass is larger, so its position should not be compared to the percentiles, but similar speculations about its age at disc dissipation can be drawn.

with the value derived from our spectra. The average EW of the 670.7 nm Li line is equal to 0.045 nm, in good agreement with that measured for solar-mass PMS stars in the 10 – 15 Myr Sco-Cen association at the corresponding temperature (Pecaut & Mamajek, 2016), which further confirms our age estimate and thus the evolutionary status of TAP 26. We also note that our target is located past the theoretical threshold at which stars start to be more than half radiative in radius, suggesting that the magnetic field of TAP 26 already started to evolve into a complex topology, if the magnetic topologies of wTTSs follow the same trends as those of cTTSs (Gregory et al., 2012).

The emission core of the Ca II IRT lines exhibits an average EW of $\sim$10 km s^{-1}, corresponding to the amount expected from chromospheric emission for such a wTTS. The He I D_3 line is relatively faint (average EW of $\sim$5 km s^{-1}), demonstrating that accretion is no longer taking place at its surface, in agreement with previous studies (Donati et al., 2014, 2015). The Hα line is also relatively weak by wTTS standards (Kenyon & Hartmann, 1995), with an average EW of 40 km s^{-1}, thereby confirming that TAP 26 is a bona fide wTTS.

Least-Squares Deconvolution (LSD, Donati et al., 1997) was applied to all spectra. The Stokes I and Stokes V LSD profiles can be seen in figure 3.3. Significant distortions are visible in all Stokes I LSD profiles, indicating the presence of brightness inhomogeneities covering a large fraction of the surface of TAP 26 at the time of our observations. Among the 29 profiles we used, 11 were contaminated by solar light reflected off the Moon (5 in 2015 Nov, the Moon being at 9.5° from TAP 26 and at 99% illumination on 2015 Nov 26, and 6 in 2016 Jan, the Moon being at 12° from

TAP 26 and at 85% illumination on 2016 Jan 19); we filtered out this contamination from our Stokes I LSD profiles.

The contemporaneous VR_J photometric observations indicate a brightness modulation with a period of 0.7138 ± 0.0001 d of full amplitude 0.116 mag in V. By analogy with other wTTSs, these photometric variations can be safely attributed to the presence of brightness features at the surface of TAP 26 modulated by rotation. The small difference with the value found in Grankin (2013) suggests the presence of differential rotation in TAP 26 (see section 3.2.2).

3.1.2 V410 Tau

V410 Tau is a three-star system located in the Taurus constellation, composed of an inner binary (V410 Tau A-B Ghez et al., 1995) around which orbits the third component (C, Ghez et al., 1997). V410 Tau B was estimated to have a mass 0.2 ± 0.1 times that of V410 Tau A, and V410 Tau C to have a mass $0.08^{+0.10}_{-0.08}$ times that of V410 Tau AB (Kraus et al., 2011). The sky-projected separation between V410 Tau A and V410 Tau B was measured at $0.13 \pm 0.01''$ for a distance of 16.8 ± 1.4 au, and that between V410 Tau AB and V410 Tau C was measured at $0.28 \pm 0.01''$ for a distance of 36 ± 3 au. Given that V410 Tau A is much brighter than V410 Tau B and V410 Tau C in the optical bandwidth (Ghez et al., 1997), we consider that the spectra analysed in this study characterize the light of V410 Tau A predominantly.

V410 Tau is a very well-observed ∼1 Myr disc-less wTTS (Skelly et al., 2010; Luhman et al., 2010) with a well-constrained rotation period of $1.871\,97 \pm 0.000\,10$ d (Stelzer et al., 2003). One of the most observed wTTSs, it has been the target of both photometric and spectropolarimetric observation campaigns. High variability detected in its light curve (Bouvier & Bertout, 1989; Sokoloff et al., 2008; Grankin et al., 2008) indicates a high level of activity, confirmed with Doppler maps (Skelly et al., 2010; Rice et al., 2011; Carroll et al., 2012) showing that the photosphere features large polar and equatorial cool spots, responsible for the observed temporal modulation as the star rotates. Magnetic maps made by Skelly et al. (2010) and Carroll et al. (2012) have shown a largely toroidal and non-axisymmetric large-scale field despite the mostly convective structure of the star.

Our spectropolarimetric data set spanned 2008 Oct to 2016 Jan, totalling 144 high-resolution optical spectra, both in Stokes I and Stokes V, collected by ESPaDOnS and NARVAL. It is composed of 8 runs, most of which cover around 15 days, taken during 4 different seasons: 2008b-2009a and 2011a prior to MaTYSSE, and 2013b and 2015b-2016a within the frame of MaTYSSE. The full journal of observations is available in the online appendix of Yu et al. (2019). Phase coverage is of different quality depending on the observation epoch. The 2008b data set, with only 6 points, covers only half the surface of the star (phases -0.20 – 0.30). The 2009a data set, although the densest with 48 points in 16 days and including data from both instruments, lacks observations between phases 0.05 and 0.20. The 2011a data set presents a large gap between phases -0.05 and 0.15, and a smaller one between phases 0.65 and 0.80. The 2013b and 2015b data sets are well sampled at the expense of no continuous observations throughout the night like in early 2009, and the 2016a data set, with only 9 points, lacks observations between phases 0.25 – 0.45 and -0.15 – 0.05.

Contemporaneous BVR_JI_J photometric measurements were taken from the Crimean Astrophysical Observatory 1.25 m and 0.60 m telescopes between August 2008 and March 2017, counting 420 observations distributed over 9 runs at a rate of one run per year, each run covering 3 – 7 months. We also used 2703 data points of visible magnitude from the Wide Angle Search for Planets (WASP, Pollacco et al., 2006) photometric campaign covering semesters 2010b-2011a.

Rotational cycles (noted E in the following equation) are computed from Barycentric Julian Dates (BJDs) according to the ephemeris:

$$\mathrm{BJD\ (d)} = 2,454,832.58033 + P_{\mathrm{rot}}E, \tag{3.2}$$

where the reference date and rotation period are chosen to be the same as in Skelly et al. (2010), in particular $P_{\rm rot} = 1.871\,970 \pm 0.000\,010$ d (Stelzer et al., 2003).

Applying the automatic spectral classification tool, we constrain the temperature and logarithmic gravity of V410 Tau to, respectively, $T_{\rm eff} = 4500 \pm 100$ K and $\log g = 3.8 \pm 0.2$. V410 Tau is at $d = 129.0 \pm 0.5$ pc from Earth (Galli et al., 2018, we chose this value over the Gaia result, 130.4 ± 0.9 pc, because it is both in agreement with it and more precise). We find a minimum measured magnitude of 10.52 ± 0.02 and a mean B − V index of 1.17 ± 0.02, from which we derive an absolute bolometric magnitude of 3.93 ± 0.11.

Assuming a spot coverage at maximum brightness of 50 ± 15 %, we derive an absolute unspotted magnitude of 3.17 ± 0.33, a logarithmic luminosity $\log_{10}(L_\star/{\rm L}_\odot) = 0.63 \pm 0.13$, and a stellar radius $R_\star = 3.4 \pm 0.5\,{\rm R}_\odot$. Since our ZDI optimization yields $v \sin i = 73.2 \pm 0.2\,{\rm km\,s^{-1}}$, this implies an inclination of $53 \pm 11\,^\circ$, which is in agreement with the value derived from the imaging code: $i = 50 \pm 10\,^\circ$.

The position of V410 Tau on the Hertzsprung-Russell diagram is displayed in figure 3.1. According to Siess et al. (2000) PMS stellar evolution models, V410 Tau is a $1.42 \pm 0.15\,{\rm M}_\odot$ star, aged 0.84 ± 0.20 Myr and fully convective. Our values are in good agreement with Welty & Ramsey (1995) and Skelly et al. (2010), who had previously derived masses of $\sim$1.5 $\rm M_\odot$ and $1.4 \pm 0.2\,{\rm M}_\odot$, radii of $\sim$2.64 $\rm R_\odot$ and $\sim$3.0 $\rm R_\odot$, and ages of $1 - 2$ Myr 1.2 ± 0.3 Myr respectively. Moreover, Skelly et al. (2010) had deduced that V410 Tau could have a radiative core of radius between $0.0\,R_\star$ and $0.28\,R_\star$. Table 3.1 sums up the stellar parameters of V410 Tau found in this study.

The emission core of the Ca II IRT presents an average EW of $\sim$13 $\rm km\,s^{-1}$ (0.37 Å). The He I D_3 line is relatively weak with an average EW of 13 $\rm km\,s^{-1}$ as well (0.25 Å), in agreement with the non-accreting status of V410 Tau. The Hα line has an average EW of 14 $\rm km\,s^{-1}$ (0.33 Å) and a rms EW of 27 $\rm km\,s^{-1}$.

We detected three small flares from the He I D_3 line, which affected 5 spectra, and one big flare that was visible in He I D_3, Ca II and Hα (EW in Hα: $\sim$ 230 $\rm km\,s^{-1}$). We removed the 6 flare-subjected observations from our data sets for the rest of the analysis.

Least-squares deconvolution (LSD, see Donati et al., 1997) was applied to all our spectra, moonlight pollution affected 15 of our Stokes I LSD profiles and was filtered out. Some of the Stokes I and Stokes V LSD profiles are visible in figure 3.3.

In each run, the visible magnitude presents modulations of a period $\sim$1.87 d and amplitude varying from 0.04 – 0.24 mag.

3.1.3 V830 Tau

V830 Tau is another wTTS within the MaTYSSE sample, it is $\sim$2.2 Myr, has a mass of $1.00 \pm 0.05\,{\rm M}_\odot$, a radius of $2.0 \pm 0.2\,{\rm R}_\odot$ and a rotation period of 2.741 d. As such, it has the same mass and same angular momentum as TAP 26 so it could be a 2 Myr version of TAP 26. I did not personally analyze the data on that star but comparing the results on V830 Tau to the results on TAP 26 and V410 Tau is of very high interest. The text below is partially extracted from Donati et al. (2015) and Donati et al. (2017).

V830 Tau is a well-studied single wTTS (from direct imaging and spectroscopic monitoring; e.g. Kraus et al., 2011; Nguyen et al., 2012) and bona fide member of the Taurus L1495 dark cloud (Xiao et al., 2012), showing clear photometric variations of large amplitudes (Grankin et al., 2008; Xiao et al., 2012).

It was observed in 2014 December and 2015 January using ESPaDOnS at the CFHT. A total of 15 Stokes V and Stokes I spectra were collected over a time-span of 28 nights, corresponding to 10 rotation cycles (Donati et al., 2015). In late 2015, 48 high-resolution spectra were collected (Donati et al., 2016). V830 Tau was re-observed from 2016 Jan 14 to Feb 10 (Donati et al., 2017),

using again ESPaDOnS at the CFHT, its clone Narval at the TBL, and ESPaDOnS coupled to Gemini-North through the GRACES fibre link (Chene et al., 2014). A total of 15, 6, and 6 spectra were, respectively, collected with ESPaDOnS, Narval, and ESPaDOnS/GRACES, at a daily rate from Jan 14 – 30 and more sparsely afterwards. For the 2016a run, contemporaneous BVR_JI_J photometric observations were also collected from the CrAO 1.25 metre telescope.

We note that our target is located close to the theoretical threshold at which $1\,M_\odot$ stars cease to be fully convective (see Fig. 3.1). This may suggest that V830 Tau is still fully convective; our error bars on the location of the star in the HR diagram is, however, still too large to reach a firm conclusion. V830 Tau shows no traces of leftover dust from the original disc (e.g. Cieza et al., 2013).

The next two sections give a detailed account of the application of ZDI to TAP 26 and V410 Tau, as well as an overview of the results of ZDI on V830 Tau. The ZDI model we used constitutes a good approximation for wTTSs unless they are undergoing flares, which is why observations taken during flares were removed.

3.2 Zeeman-Doppler imaging of TAP 26 and V410 Tau

With ZDI, we reconstructed brightness and magnetic surface maps at all observation epochs for both TAP 26 and V410 Tau. Thanks to our data sets spanning more than two months, we were also able to measure the surfacic latitudinal differential rotation of our targets. Finally, with the 8 years worth of data we have on V410 Tau, we investigated the mid-term variability of that wTTS.

3.2.1 Brightness and magnetic reconstruction

Applying ZDI to our data sets, we derived the surface brightness and magnetic maps of TAP 26 and V410 Tau. For numerical computation, the default brightness value given to the quiet photosphere here was 1, meaning that cells with brightness $0 < Q < 1$ had dark spots and cells with brightness $Q > 1$ had bright plages (Donati et al., 2014).

Parameter optimization was done with $n_{\rm cell} = 1000$ cells for the stellar surface mesh, and spherical harmonics for the magnetic reconstruction up to order $\ell_{\rm max} = 15$ (see appendix A.3), for both stars. We produced our final figures with $n_{\rm cell} = 10000$ for aesthetic purposes, the differences in model optimization induced by the change in $n_{\rm cell}$ are negligible.

The local profile used for TAP 26 is described by a central wavelength, a Doppler width and a Landé factor of typical values 670 nm, $1.8\,{\rm km\,s^{-1}}$ and 1.2 respectively, and an EW of $4.6\,{\rm km\,s^{-1}}$. To fit the LSD profiles of V410 Tau, we chose a spectral line of mean wavelength, Doppler width, Landé factor and EW of respective values 640 nm, $1.8\,{\rm km\,s^{-1}}$, 1.2 and $3.8\,{\rm km\,s^{-1}}$.

In a first pass, we set a null differential rotation ($\beta = \gamma = 0$, see appendix A.1) and we tried a grid of values for i, $v \sin i$ and $v_{\rm rad}$. Because ZDI does not reconstruct intrinsic temporal variability except for differential rotation, there is a limit to the duration a fittable data set can span. For that reason, ZDI was applied separately to observation runs that spanned at most one month.

The stellar parameters that yield the maps with highest entropy are, for TAP 26, $i = 55 \pm 10\,^\circ$, $v \sin i = 68.2 \pm 0.5\,{\rm km\,s^{-1}}$ and $v_{\rm rad} = 17.0 \pm 0.2\,{\rm km\,s^{-1}}$, and, for V410 Tau, $i = 50 \pm 10\,^\circ$ and $v \sin i = 73.2 \pm 0.5\,{\rm km\,s^{-1}}$ for all observation epochs, while $v_{\rm rad}$ was found to vary over the years for V410 Tau (see table 3.2).

In a second pass, we optimized differential rotation parameters at fixed values of i, $v \sin i$ and $v_{\rm rad}$ for extended data sets that each spanned at most six months. The models shown next are the final models after this second optimization and the results concerning the differential rotation are discussed in section 3.2.2.

Stokes I and V LSD profiles are displayed in figures 3.3 and 3.4, together with the corresponding synthetic spectra from ZDI. For both stars, the synthetic profiles presented in the figure match the observed ones at $\chi^2_{\rm r} = 1$, whereas unspotted magnetic maps corresponded to much higher $\chi^2_{\rm r}$ values, for example $\chi^2_{\rm r} = 13$ and 9 for the 2015 Nov and 2016 Jan data sets on TAP 26. This shows that the iterative algorithm of ZDI successfully manages to reproduce the data at noise level.

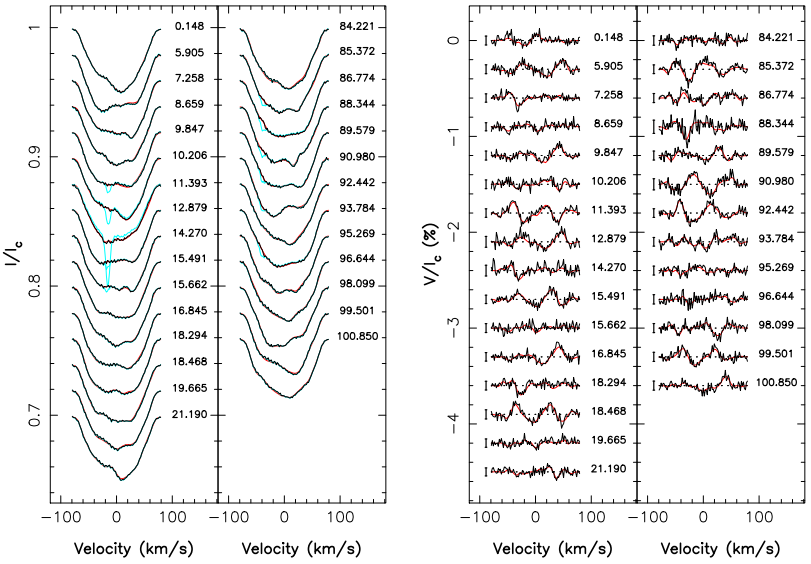

Figure 3.3 – Maximum entropy fit (thin red lines) to the observed (thick black lines) Stokes I (*left*) and V (*right*) LSD profiles of TAP 26. The 2015 Nov data set is represented in the 1st and 3rd panels and the 2016 Jan data set in the 2nd and 4th panels. The Stokes I LSD profiles before the removal of lunar pollution are coloured in cyan, and 3σ-error bars are displayed for the Stokes V profiles. The rotational cycles are written beside their corresponding profiles.

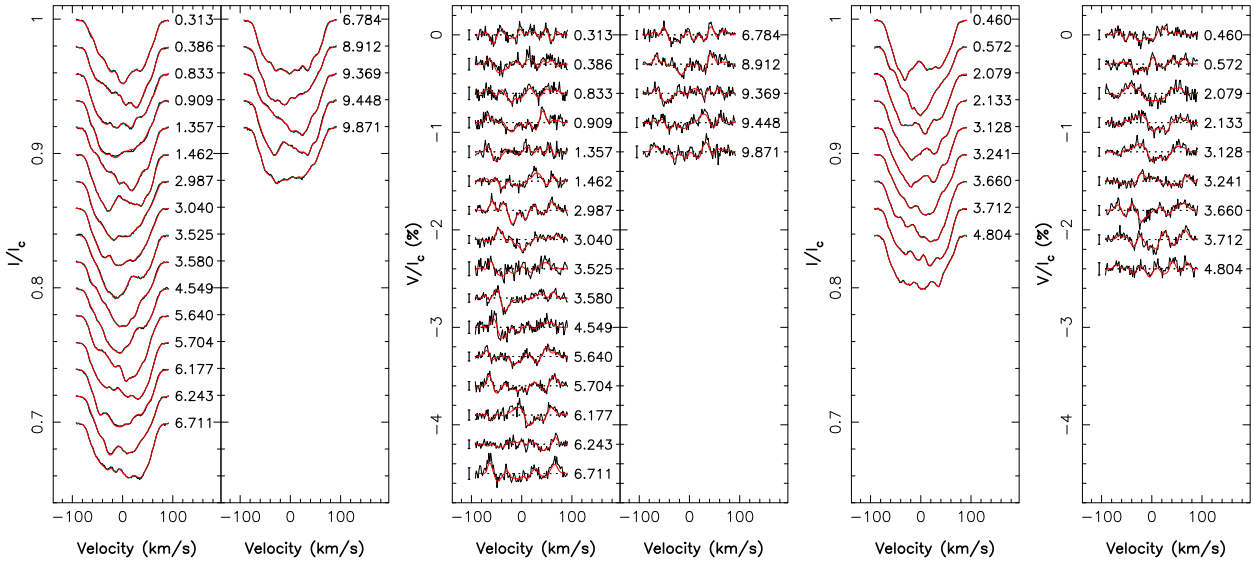

Figure 3.4 – Stokes I (1st and 3rd panels) and Stokes V (2nd and 4th panels) LSD profiles of V410 Tau for observation epochs 2015 Dec (*left*) and 2016 Jan (*right*). The black and red lines represent respectively the oberved profiles and the maximum-entropy fit obtained with Zeeman Doppler Imaging.

The reconstructed brightness and magnetic maps are shown in figures 3.5 and 3.6. Properties of these reconstructed maps are listed in table 3.2.

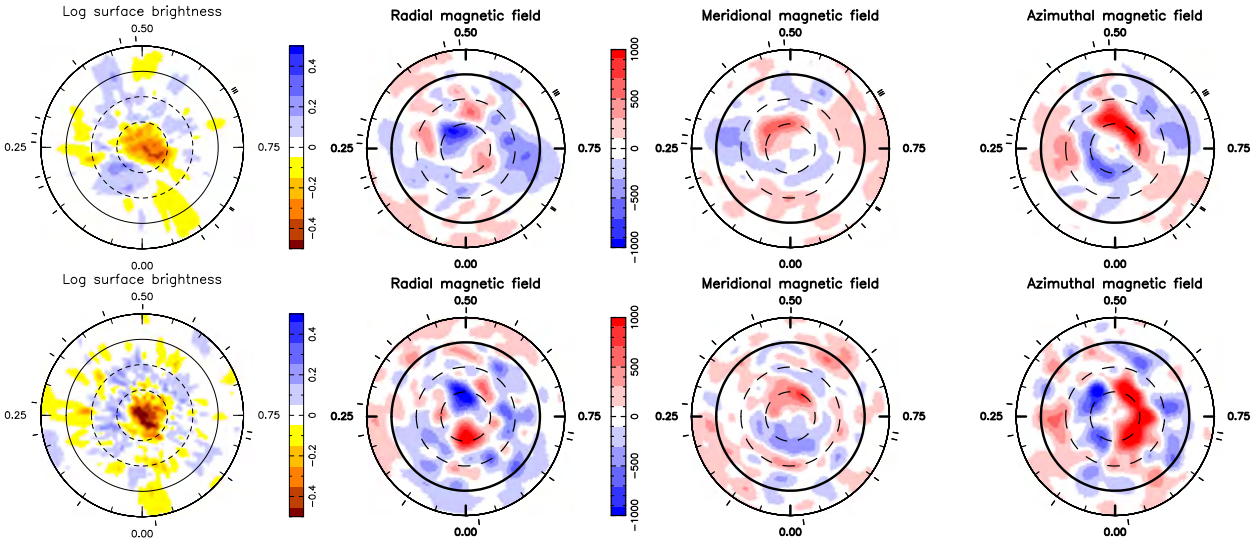

Figure 3.5 – Flattened polar view of the surface brightness (1st column) and magnetic (2nd to 4th columns) maps for the TAP 26 2015 Nov (top) and 2016 Jan (bottom) data sets. The equator and the 60°, 30° and -30° latitude parallels are depicted as solid and dashed black lines respectively. In brightness maps, the colour scale indicates the logarithm of the relative brightness, with brown/blue areas representing cool spots/bright plages. In the magnetic maps, the radial, meridional and azimuthal components are displayed from left to right, using a colour scale in G, with red representing outwards and anti-clockwise field on the radial and azimuthal field maps respectively, and the direction pointing towards the visible pole on the meridional field maps. Finally, the outer ticks mark the phases of observation.

Table 3.2 – Characteristics of the ZDI models for TAP 26 (first subset or rows) and V410 Tau (second subset or rows) at each observation epoch. *Column 1*: observation epoch. *Column 2*: number of spectropolarimetric observations used for ZDI. *Column 3*: contribution of cool ("spots") and hot ("plages") areas on the brightness map. *Column 4*: average magnetic strength, defined as the square root of the average squared magnetic field over the surface of the star. *Columns 5 to 7*: normalized contribution of the poloidal field, part of the poloidal field that is dipolar and part of the poloidal field that is symmetric. *Columns 8-9*: part of the toroidal field that is dipolar and part of the toroidal field that is symmetric. *Column 10*: dipole characteristics: field strength, tilt with respect to the rotation axis and phase of the pole. *Column 11*: systemic RV of the star as measured with ZDI, the error bar on those values is $0.20\,\mathrm{km\,s^{-1}}$. Error bars on the magnetic field ratios are typically of 0.1.

Run	N_{sp}	Sp.+pl. cov. (%)	$\langle B \rangle$ (G)	r_{pol}	Poloidal		Toroidal		Dip. str. (G), tilt, phase	v_{rad} ($\mathrm{km\,s^{-1}}$)
					r_{dip}	r_{sym}	r_{dip}	r_{sym}		
2015 Nov	16	5+5	328	0.69	0.15	0.51	0.14	0.73	171, 25°, 0.73	17.0
2016 Jan	13	7+5	428	0.65	0.07	0.42	0.02	0.90	141, 36°, 0.85	17.0
2008 Dec	6	5.8+4.4	486	0.32	0.13	0.37	0.89	0.96	129, 23°, 0.71	16.30
2009 Jan	48	9.6+7.1	556	0.55	0.26	0.09	0.54	0.79	165, 54°, 0.54	16.30
2011 Jan	20	8.1+6.6	560	0.40	0.24	0.23	0.72	0.85	239, 44°, 0.62	16.40
2013 Dec	25	11.0+7.5	568	0.49	0.23	0.34	0.66	0.81	254, 18°, 0.56	16.50
2015 Dec	21	8.9+6.7	600	0.68	0.37	0.45	0.62	0.78	458, 30°, 0.54	16.65
2016 Jan	9	7.9+6.5	480	0.77	0.38	0.30	0.68	0.87	400, 44°, 0.51	16.65

The 2008 Dec data set on V410 Tau has a phase coverage of only half the star, so the derived parameters at this epoch are no more than weakly meaningful and are not further discussed.

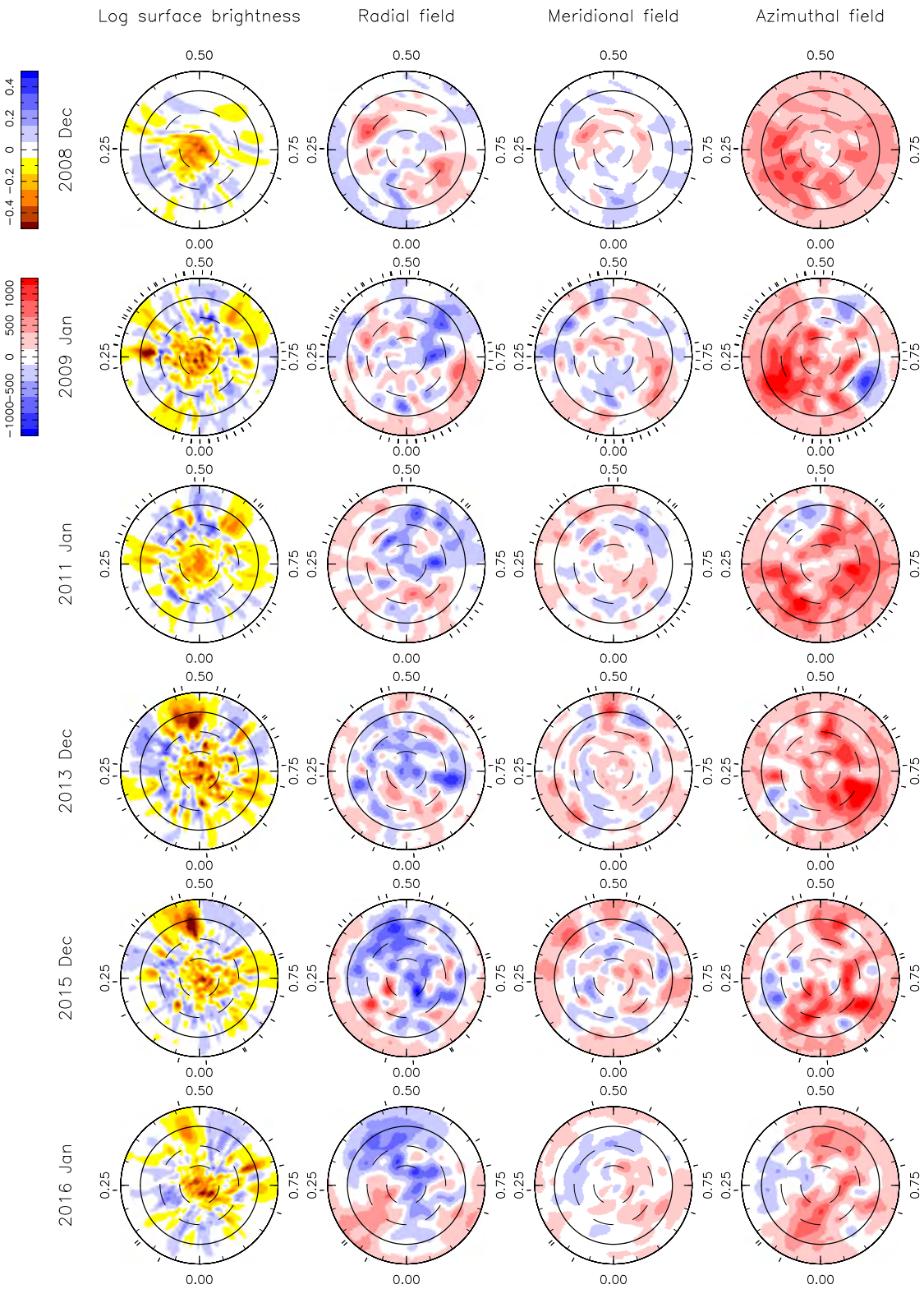

Figure 3.6 – ZDI maps of the logarithmic relative surface brightness (first column), and the radial, meridional and azimuthal magnetic field (second to fourth columns) of V410 Tau, reconstructed from data collected in 2008 Dec, 2009 Jan, 2011 Jan, 2013 Dec, 2015 Dec and 2016 Jan (top to bottom rows). Refer to the caption of figure 3.5 for more details.

Brightness maps

The ZDI models suggest that V410 Tau is significantly more spotted than TAP 26, with 15 – 18 % versus 10 – 12 % spot coverage respectively. This is consistent with the spottedness assumptions in sections 3.1.1 and 3.1.2, considering that ZDI is only sensitive to mid- to large-scale surface features, and thus underestimates the total spot coverage.

For both stars, the brightness maps exhibit a number of small-scale features, with a large cool polar cap at all epochs, like in the previous V410 Tau maps published in Skelly et al. (2010); Rice et al. (2011); Carroll et al. (2012), and those reconstructed on other rapidly rotating wTTSs (e.g. LkCa 4, Donati et al., 2014).

For TAP 26, both reconstructed maps share two equatorial spots, located at phases 0.22 and 0.92 in 2015 Nov, and 0.27 and 0.97 in 2016 Jan, interleaved with bright plages. We observe a number of differences between both images potentially attributable to differential rotation and / or intrinsic variability (see sections 3.2.2 and 3.2.4); however, the limited phase coverage at both epochs makes the direct comparison of individual surface features between maps ambiguous and hazardous.

For V410 Tau, brightness maps display a high contrast. In 2009 Jan, 2013 Dec and 2015 Dec, the brightness map exhibits a strong equatorial spot, respectively at phases 0.27, 0.48 and 0.48. The equatorial spot at phase 0.27, and another equatorial spot at phase 0.60 from the 2009 Jan map are also visible in both Skelly et al. (2010) and Rice et al. (2011) (figure 8), albeit less contrasted compared to other features than they are on our map. A remnant of the 2015 Dec equatorial spot is observed on the 2016 Jan map, where its intensity seems to have decreased, but this has to be taken with caution since ZDI maps are somewhat dependent on phase coverage.

To get a rough estimate of the temperature in the spotted regions of V410 Tau, we computed B − V (V) models from the Kurucz models for colors of main sequence stars with $\log g = 3.5$, $T_{\rm eff} = 4500\,{\rm K}$ and $\mathrm{E(B-V)} = 0.10\,{\rm mag}$ (Kurucz, 1993): we fit a two-temperature model with a photospheric temperature of 4500 K and different values for the spot temperature. Then, for each tested spot temperature, for all values of spot coverage from 0 – 100 %, we computed the resulting B and the resulting V using the following formulas, from which we derived the B − V.

$$\mathrm{V}(r) = -2.5\log_{10}(r\ 10^{-\frac{\mathrm{V_{spot}}}{2.5}} + (1-r)10^{-\frac{\mathrm{V_{star}}}{2.5}})$$
$$\mathrm{B}(r) = -2.5\log_{10}(r\ 10^{-\frac{\mathrm{B_{spot}}}{2.5}} + (1-r)10^{-\frac{\mathrm{B_{star}}}{2.5}})$$

The resulting models are plotted in figure 3.7. We find that a spot temperature of 3750 K fits our B − V measurements well, from which we deduce that the spot coverage on V410 Tau varies between 50 – 75 %, in agreement with the assumption in section 3.1.2. This implies a contrast of ∼750 K between dark spots and the photosphere. This contrast is slightly lower than the one retrieved for the 2 Myr wTTS LkCa 4 in Gully-Santiago et al. (2017).

Photometry curves from the ZDI brightness maps were synthesized and a comparison to contemporary CrAO data, and WASP data in the case of the V410 Tau 2011 Jan set, is shown in figures 3.8 and 3.9. Despite a slightly underestimated amplitude at some phases, ZDI manages to retrieve the measured photometric variations rather satisfyingly. The most obvious evidence of mid-term variability is the small temporal evolution in the 2010b-2011a WASP data of V410 Tau, where the regions around phases 0.20 and 0.70 globally darken by 0.02 – 0.03 mag ($\sim 4\sigma$) over the 4 months that the data set spans.

Magnetic maps

The large-scale field reconstructed for TAP 26 features a rms magnetic flux of 330 and 430 G in 2015 Nov and 2016 Jan respectively. The field is found to be mainly poloidal (70 % of the reconstructed

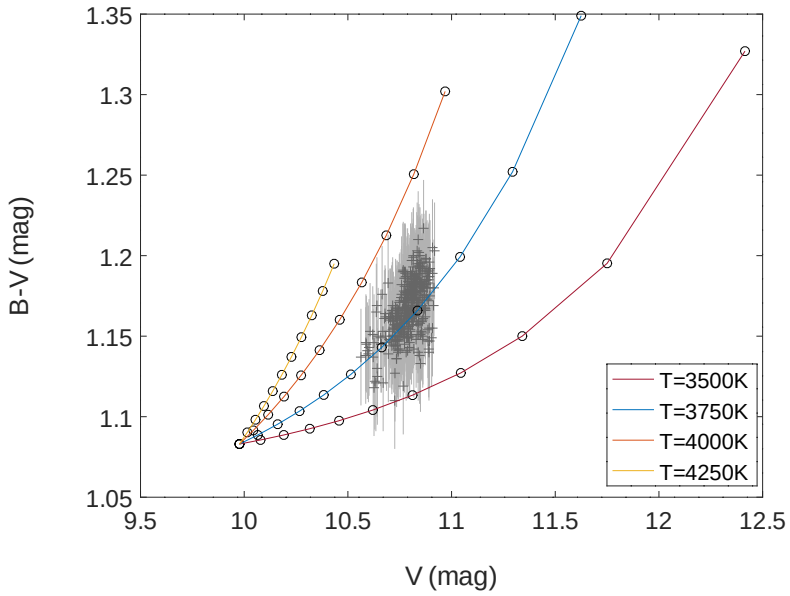

Figure 3.7 – Fit of the B − V (V) curve with Kurucz models, with a photosphere temperature of 4500 K, $\log g$ of 3.5, E(B − V) of 0.10. Each full line corresponds to a particular value of the spot temperature, and dots mark the spot coverage with steps of 10 % (the dot at V = 10.0 and B − V = 1.08 corresponding to a 0 % spot coverage). The extension of our data correspond to a spot coverage constantly between 50 – 75 %.

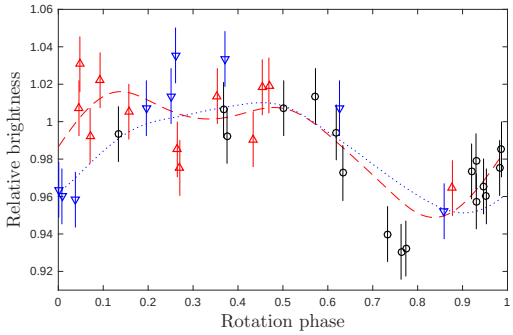

Figure 3.8 – Photometry curves of the relative brightness as function of the rotation phase for TAP 26. The light curves synthesised from the reconstructed brightness maps for 2015 Nov and 2016 Jan are represented by a dashed red line and a dotted blue line respectively. The CrAO measurements are represented as dots with 1σ error bars, with the observations from 2015 Aug to 2015 Oct in black circles, the observations from 2015 Oct to 2015 Dec in red upward-pointing triangles and the observations from 2015 Dec to 2016 Mar in blue downward-pointing triangles.

magnetic energy), though with a significant toroidal component (30 % of the reconstructed magnetic energy). It is also largely axisymmetric (50 % and 80 % of the poloidal and toroidal field energy respectively). The dipolar component of the large-scale field has a strength of 140 ± 10 G at both epochs, corresponding to about 10 % of the reconstructed poloidal field energy, and is tilted at $40 \pm 5°$ to the line of sight, i.e., midway to the equator, towards phase 0.73 ± 0.03 and 0.85 ± 0.03 in 2015 Nov and 2016 Jan respectively. The increase in the phase towards which the dipole is tilted suggests that intermediate to high latitudes (at which the dipole poles are anchored) are rotating more slowly than average by 0.19 %, i.e., with a period of ∼0.7148 d; this is confirmed by the fact

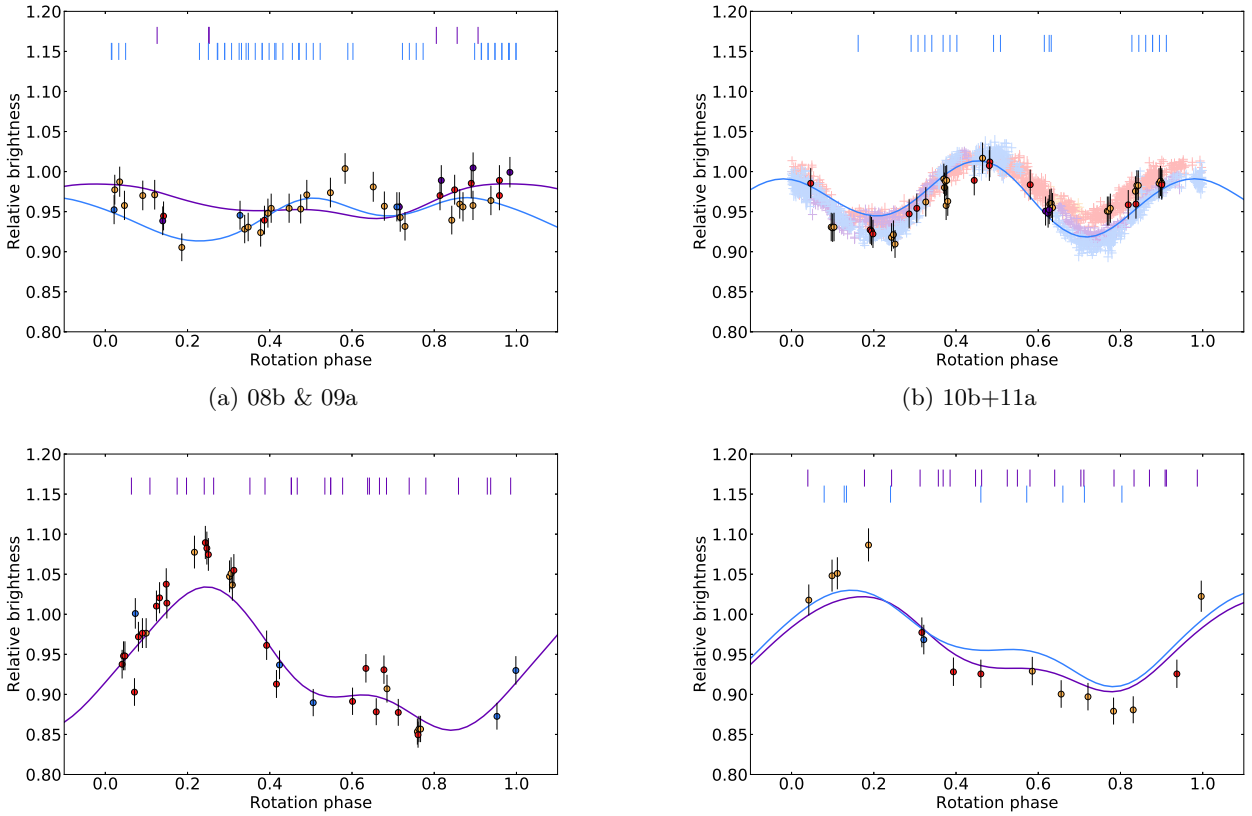

(a) 08b & 09a

(b) 10b+11a

(c) 13b+14a

(d) 15b & 16a

Figure 3.9 – Phase-folded photometry data (dots with 1σ error bars) and ZDI models (lines) for V410 Tau in our four observation epochs. In the case of 08b & 09a and 15b & 16a, two ZDI curves are plotted for the two ZDI maps reconstructed within each epoch. Red, pink, purple and blue colors each indicate a quarter of the total time span of the observations (photometric and spectropolarimetric together), in chronological order. Spectropolarimetric observations are marked by ticks above the light curves. In figure b, WASP data were added as desaturated crosses, with the size of the cross branches indicating their 1σ error bars.

that the longitudinal magnetic field B_ℓ (proportional to the first moment of the Stokes V profiles, e.g., Donati et al., 1997, and most sensitive to the low-order components of the large-scale field) exhibits a recurrence timescale of $1.0014 \pm 0.0003\,P_{\rm rot}$ (see section 3.1.1), i.e., slightly longer than $P_{\rm rot}$ by a similar amount. Higher order terms in the spherical harmonics expansion describing the field (in particular the quadrupolar and octupolar modes) get stronger between 2015 Nov and 2016 Dec, with total magnetic energies increasing from 85 % to 93 % of the poloidal field. Similarly to the brightness maps, the magnetic maps seem to point to a variation of the surface topology between late 2015 and early 2016, which is not explained by differential rotation alone, though the limited phase coverage calls for caution when comparing features between those maps.

V410 Tau has a relatively strong large-scale magnetic field, with an average surface intensity that is roughly constant over the years at 550 ± 50 G. Its radial field reaches local values beyond -1 kG and 1 kG in several epochs. The brightness and magnetic surface maps both present some variability from epoch to epoch (figure 3.6, table 3.2), which points to a dynamo-generated magnetic field rather than a fossil one. The magnetic energy is, at all epochs, equally distributed between the poloidal and toroidal components of the field, with the poloidal component being rather non-dipolar and non-axisymmetric, whereas the toroidal component is mostly dipolar and axisymmetric. The poloidal dipole, tilted towards a phase that stays within 0.6 ± 0.1 during the whole survey,

but at an angle varying between 20° and 55° depending on the epoch, sees its intensity increase almost monotonously from 165 G to 458 G over 8 years, and the dipolar contribution to the poloidal field also increases from ∼25 % to ∼40 % (see table 3.2). We note that the maximum emission of Hα corresponds to the phase at which the dipole is tilted (figure 3.19). The toroidal component of V410 Tau, which displays a constant orientation throughout our data set, is unusually strong compared to other fully convective rapidly-rotating stars (e.g. V830 Tau is 90 percent poloidal, see Donati et al., 2017). This is further discussed in section 3.4.

At ∼0.8 Myr, V410 Tau is one of the youngest observed wTTSs (Kraus et al., 2012, figure 3). Assuming that, when the disc was present, V410 Tau was magnetically locked to it at a rotation period of ∼8 d with a cavity of ∼0.085 au (similarly to cTTSs BP Tau, AA Tau and GQ Lup, see Donati et al., 2008a, 2010a, 2012, resp.), then V410 Tau should have had a radius of ∼7 $R_\odot$ when the disc dissipated, to match the angular momentum that we measure today (Bouvier, 2007). According to the Siess models (Siess et al., 2000), this corresponds to an age of ∼0.2 Myr. With a radius of ∼7 $R_\odot$, V410 Tau would have needed a magnetic dipole barely above 100 G to maintain the assumed magnetospheric cavity, even with an accretion rate of $\sim 1 \times 10^{-8}$ $M_\odot$/yr just before disc dissipation. That value is compatible with the ∼400 G dipole we measure on the ∼3.5 $R_\odot$ star today and assuming magnetic flux conservation between both epochs. Kraus et al. 2012 shows a correlation between the presence of a close companion and the early depletion of the accretion disc, which indicates that V410 Tau B, observed at a projected separation of 16.8 ± 1.4 au (Ghez et al., 1995), could have been responsible for the early depletion of the disc.

We do not observe a particular correlation between our brightness and our magnetic maps, which shows that there is also medium to strong magnetic fields outside spots, according to the ZDI reconstruction. The spots probably host strong magnetic fields, but we are most likely missing them due to the low level of emitted light in those areas.

For visualisation purposes, 3-dimensional potential fields were extrapolated from the radial components of the magnetic maps, and displayed in Figure 3.10.

3.2.2 Differential rotation

Whether for the TAP 26 or the V410 Tau data sets, when applying ZDI without differential rotation to subsets spanning more than a month, it is impossible to reach χ^2_r =1. In fact, even when taking into account differential rotation, the χ^2_r reaches lower values but still not 1. This indicates that intrinsic variability occurs over ∼40 – 50 d.

Despite this variability, we attempted to retrieve differential rotation from longer data sets. The search for differential rotation parameters is done by minimising the value of χ^2_r at a fixed amount of information, in this present case using the Stokes I profiles and brightness map reconstruction only. From the curvature of the χ^2_r paraboloid around the minimum, one can infer error bars on differential rotation parameters (Donati et al., 2003).

For TAP 26, the whole 2015 Dec-2016 Jan data set was modeled together, and the spot coverage was fixed at 13 % (chosen to be slightly higher than the values found in each reconstruction). The values we found are Ω_{eq} =8.8199 ± 0.0003 rad/d and $d\Omega$ =0.0492 ± 0.0010 rad/d, with a minimum χ^2_r of 1.4116. A map of $\Delta\chi^2$ is shown in figure 3.11, which presents a very clear paraboloid around the minimum we found, even if, due to our phase coverage, these precise values ask for further confirmation with the help of future data. This value of $d\Omega$ is close to the solar differential rotation (0.055 rad/d). To assess the false-alarm probability (i.e. the probability that differential rotation was detected in the noise, whereas it has no physical existence), we found that the case with no differential rotation yields χ^2_r = 2.6907. Normalising $\Delta\chi^2$ by the minimum χ^2 achieved over the map (to scale up error bars as a way to account for the contribution from the reported intrinsic variability) still yields a value in excess of 3300 and a negligible false alarm probability (FAP),

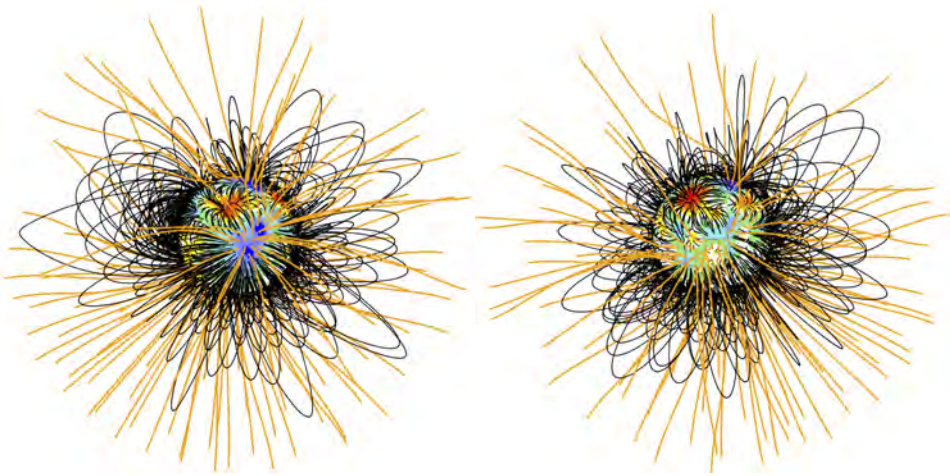

(a) TAP 26 2015 Nov (b) TAP 26 2016 Jan

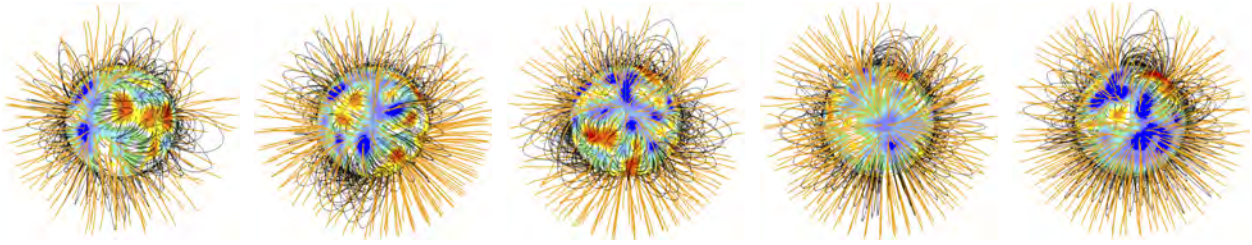

(c) V410 Tau 2009 Jan (d) V410 Tau 2011 Jan (e) V410 Tau 2013 Dec (f) V410 Tau 2015 Dec (g) V410 Tau 2016 Jan

Figure 3.10 – Potential field extrapolations of the ZDI-reconstructed surface radial fields, as seen by an Earth-based observer, at phase 0.8 for TAP 26 and 0.5 for V410 Tau. Open/closed field lines are shown in orange/black respectively, and colours on the stellar surface depict the local value of the radial field (in G, as shown in the left-hand panels of figures 3.5 and 3.6). The source surface at which the field becomes radial is set to 4 $R_\star$ for TAP 26 and 2.1 $R_\star$ for V410 Tau, corresponding to the corotation radius (at which the Keplerian period equals the stellar rotation period) and beyond which field lines are expected to quickly open under centrifugal forces.

unambiguously demonstrating that the star is not rotating as a solid body.

The differential rotation parameters we obtain imply a lap time of 128 ± 3 d, with rotation periods of $0.712\,39 \pm 0.000\,03$ d and $0.716\,38 \pm 0.000\,08$ d for the equator and pole respectively, in good agreement with the range of rotation periods derived from photometry (ranging from 0.7135 – 0.7138 , Grankin, 2013). The 0.7132 d period found for the EW of the Hα line and the 0.7145 d period found for the longitudinal magnetic field B_ℓ (see figures 3.12 and 3.13) are also consistent. We note that the rotation periods found with photometry, the longitudinal magnetic field and Hα line correspond to latitudes between 30 – 50 °, indicating that an important amount of activity is concentrated at these mid-latitudes, with the dipole pole located in the upper part of this range, in good agreement with the ZDI reconstruction (see section 3.2.1).

For V410 Tau, we obtained six values for $\Omega_{\rm eq}$ and for $d\Omega$, by using separately our Stokes I and Stokes V LSD profiles from each of the three data sets 2008b+2009a, 2013b and 2015b+2016a hereafter shortened to 08b+09a, 13b and 15b+16a resp.). From the resulting $\chi^2_{\rm r}$ maps over the $\{\Omega_{\rm eq}$,$d\Omega$ $\}$ space, one can plot the contours of the 1σ- (68.3 %) and 3σ- (99.7 %) areas of confidence for each observation epoch. Figure 3.11, which shows such contours, highlights clear minima surrounded by almost elliptic areas of confidence at each epoch, and shows that each 3σ-confidence area overlaps at least two other 3σ-confidence areas. Numerical results for each epoch are given

in table 3.3. We chose to use a unique set of parameters to reconstruct all images shown in Chapter 3: the weighted means of the six seasonal minima, $\Omega_{\rm eq} = 3.359\,57 \pm 0.000\,06$ rad/d and $d\Omega = 0.0097 \pm 0.0003$ rad/d. The differential rotation of V410 Tau is thus relatively weak, with a pole-to-equator rotation rate difference 5.6 times smaller than that of the Sun, and a lap time of 648 ± 73 d.

The differential rotation of V410 Tau is similar to that of V830 Tau (see section 3.3) but much smaller than that of TAP 26, which is almost of solar level, consistent with the fact that TAP 26 is no longer fully convective and has developped a radiative core.

Table 3.3 – Summary of differential rotation parameters obtained for V410 Tau on each season. All rotation rates are given in mrad d^{-1}. Column 2 gives the total number of data points used in the imaging process, then columns 3 to 7 correspond to Stokes I data while column 8 to 12 correspond to Stokes V data. Columns 3 and 8 list the derived equatorial rotation rate $\Omega_{\rm eq}$, with its 68% (i.e. 1σ) confidence interval, columns 4 and 9 the difference in rotation rate $d\Omega$ between the equator and pole, with its 68% confidence interval, columns 5 and 10 give the reduced chi square of the ZDI model compared to the data, columns 6 and 11 give the inverse slope of the ellipsoid in the $\Omega_{\rm eq}$-$d\Omega$ plane (also equal to $\cos^2\,\theta_s$, where θ_s denotes the colatitude of the gravity centre of the spot distribution, see Donati et al. 2000), and columns 7 and 12 give the rotation rate Ω_s at colatitude θ_s.

	Stokes I data / brightness reconstruction					
Epoch	n	$\Omega_{\rm eq}$	$d\Omega$	$\chi^2_{\rm r}$	$\cos^2\,\theta_s$	Ω_s
08b+09a	5562	3360.0 ± 0.1	11.1 ± 0.6	1.276	0.12 ± 0.03	3358.7 ± 0.4
13b	2781	3360.0 ± 0.1	8.1 ± 0.7	1.341	0.11 ± 0.03	3359.1 ± 0.3
15b+16a	3090	3358.6 ± 0.1	8.8 ± 0.5	2.583	0.18 ± 0.03	3357.0 ± 0.4
	Stokes V data / magnetic field reconstruction					
Epoch	n	$\Omega_{\rm eq}$	$d\Omega$	$\chi^2_{\rm r}$	$\cos^2\,\theta_s$	Ω_s
08b+09a	5562	3358.7 ± 0.3	8.1 ± 1.8	1.127	0.11 ± 0.03	3357.9 ± 0.5
13b	2781	3361.8 ± 1.3	19.0 ± 4.3	1.038	0.23 ± 0.03	3354.6 ± 2.1
15b+16a	3090	3361.3 ± 0.4	13.7 ± 1.0	1.046	0.32 ± 0.03	3352.7 ± 0.8

Following the method described in Donati et al. (2003), we computed, for each epoch, the colatitude at which the rotation rate is constant along the confidence ellipse major axis. This value corresponds to the colatitude where the barycenter of the brightness/magnetic features imposing a correlation between $\Omega_{\rm eq}$ and $d\Omega$ are located. For both Stokes I and Stokes V, we note a slight increase with time of the cosine of this colatitude (table 3.3), i.e. an increase in the barycentric latitude of the dominant features of $5 \pm 2\,^\circ$ and $15 \pm 5\,^\circ$ respectively.

Our ZDI reconstructions exclude solid-body rotation at a level of 3.6 to 22σ depending on the epoch. Again, we note that, even with differential rotation, ZDI cannot fit the data of 08b+09a and of 15b+16a down to $\chi^2_{\rm r} = 1$, no matter the amount of information allowed. This indicates that surface features are also altered by a significant level of intrinsic variability within the 2-month span of our data sets. This issue is further discussed in the next section.

3.2.3 Activity proxies

In this section we investigate the spectral line Hα and the integrated longitudinal (i.e. line-of-sight projected) magnetic field B_ℓ. The latter can be derived from the Stokes V LSD profiles (Donati et al., 1997) as:

$$B_\ell = \frac{-2.14 \times 10^{11}}{\lambda_0 g_{\rm eff} c} \frac{\int v V(v) {\rm d}v}{\int (I_c - I(v)) {\rm d}v}.$$

The Hα emission EW and the longitudinal magnetic field B_ℓ of TAP 26 feature modulations of periodicities 0.7145 ± 0.0002 d and 0.7132 ± 0.0002 d respectively. Periodograms for Hα and B_ℓ are

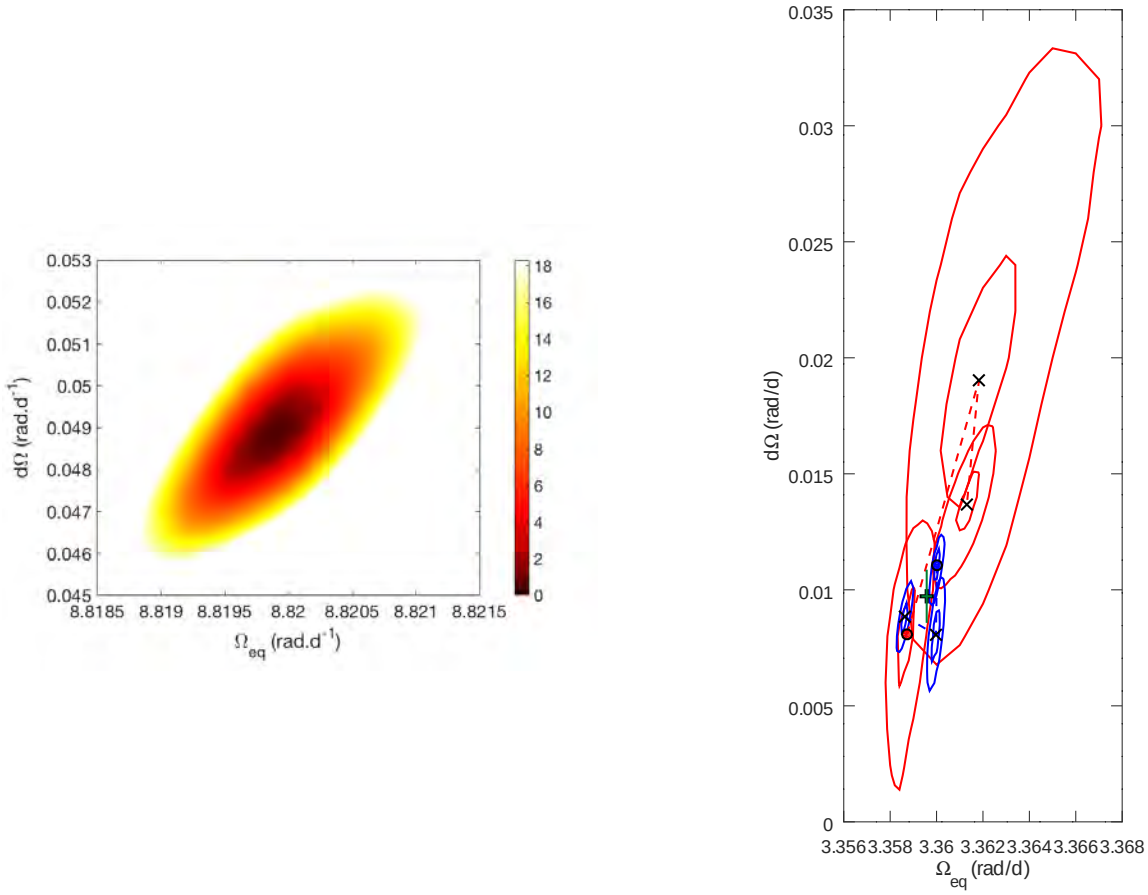

Figure 3.11 – *Left*: map of $\Delta\chi^2$ as a function of $\Omega_{\rm eq}$ and $d\Omega$, derived from the modelling of our Stokes I LSD profiles of TAP 26 at constant information content. A well-defined paraboloid is observed with the outer colour contour corresponding to the 99.99 % confidence level area (i.e., a χ^2 increase of 18.4 for the 2581 Stokes I data points). The minimum value of $\chi^2_{\rm r}$ is 1.4116. The minimum $\chi^2_{\rm r}$ achieved is above unity due to intrinsic variability affecting the LSD profiles but not being taken into account within ZDI. The derived differential rotation parameters are $\Omega_{\rm eq} = 8.8199 \pm 0.0003$ rad/d and $d\Omega = 0.0492 \pm 0.0010$ rad/d. *Right*: evolution of the differential rotation of V410 Tau as measured from Stokes I (blue) and Stokes V (red) profiles. The points corresponding to observation epoch 2008b-2009a are marked with o symbols, then the dashed lines link the epochs in chronological order (2013b-2014a and 2015b-2016a are marked with x symbols). 68.3 % and 99.7 % contours of confidence are displayed for each observation epoch. The weighted average of the six measurements, chosen to produce the maps shown in chapter 3, is represented as a black +, with overlayed error bars in green.

shown in figures 3.12 and 3.13 respectively: peak frequencies and their aliases are clearly outlined. Corresponding phase-folded plots are shown in figure 3.14.

Plotting phase-folded curves of B_ℓ and the Hα emission EW for TAP 26 (where the x-axis indicates the rotation phase as defined in Eq. 3.1), in figure 3.14, we observe a decrease in B_ℓ around phase 0.77 in 2015 Nov and phase 0.97 in 2016 Jan, which correspond approximately to the phases where the dipole pole points towards the Earth (0.73 ± 0.03 and 0.85 ± 0.03 respectively), causing B_ℓ to have strong negative values and showing the correlation between the dipole and B_ℓ. Similarly, the increase in emission EW of the Hα line between phases 0.6 and 0.9 illustrates the correlation between the lower harmonics of the magnetic field of TAP 26 and this activity proxy.

For V410 Tau, applying GPR with MCMC parameter exploration to the Hα EWs and to B_ℓ, we found rotation periods of 1.8720 ± 0.0009 d and 1.8700 ± 0.0007 d respectively. It is worth mentioning that we also find long decay times for these two activity proxies: 589^{+774}_{-335} d and 604^{+553}_{-289} d

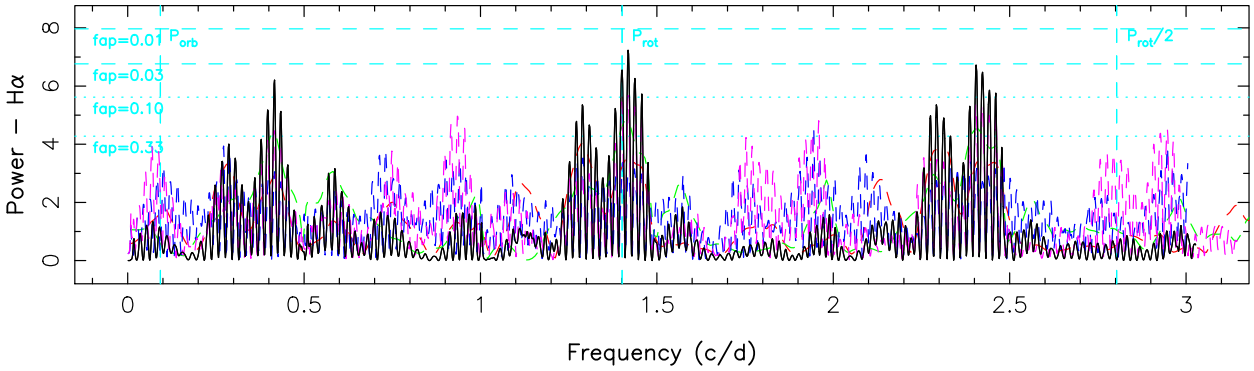

Figure 3.12 – Periodogram of the Hα line EW. The rotation period at 0.7135 d is represented by a dashed vertical cyan line.

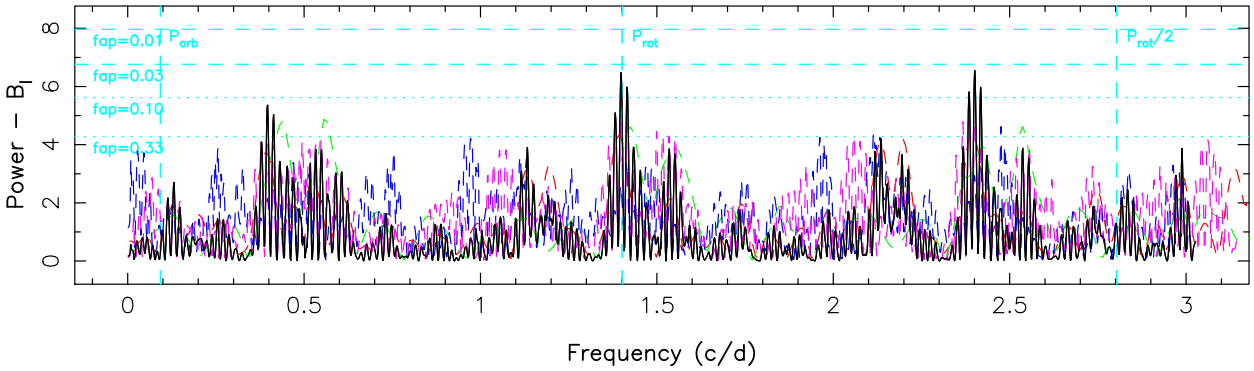

Figure 3.13 – Periodogram of the longitudinal magnetic field. The rotation period at 0.7135 d is represented by a dashed vertical cyan line.

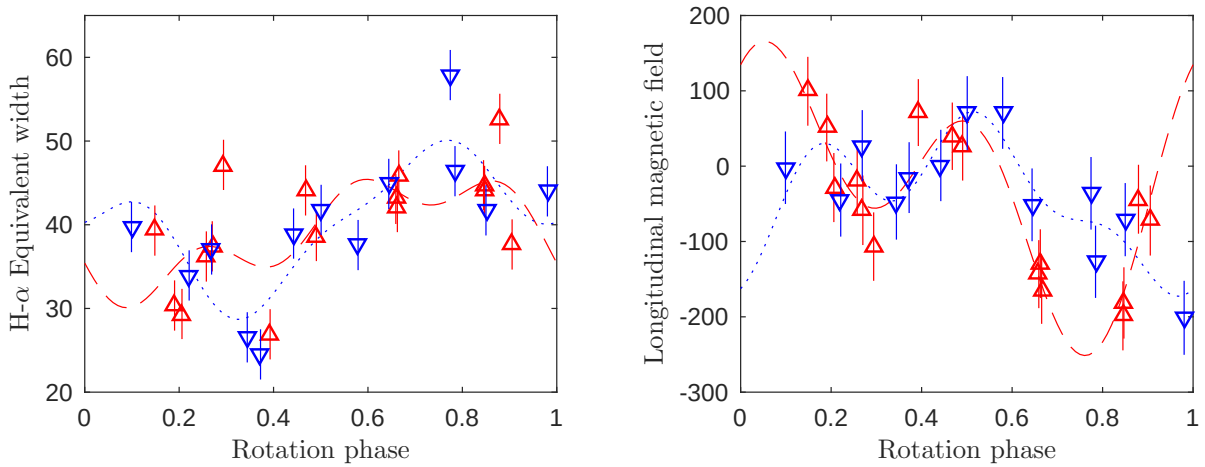

Figure 3.14 – *Left*: folded curve of the EW of Hα against the rotation phase. 2015 Nov (red upward-pointing triangles) and 2016 Jan (in blue) data are fitted with the sum of a sine curve and 2 harmonics (red dashed line and blue dotted line respectively). *Right*: folded curve of the longitudinal magnetic field against the rotation phase. 2015 Nov (red upward-pointing triangles) data are fitted with the sum of a sine curve and 1 harmonic (red dashed line) and 2016 Jan (blue downward-pointing triangles) data are fitted with the sum of a sine curve and 2 harmonics (blue dotted line).

respectively, which suggests, with the caution needed with such high error bars, that the Hα and B_ℓ modulations are particularly sensitive to large, long-lasting features. The MCMC phase plots are displayed in figure 3.15.

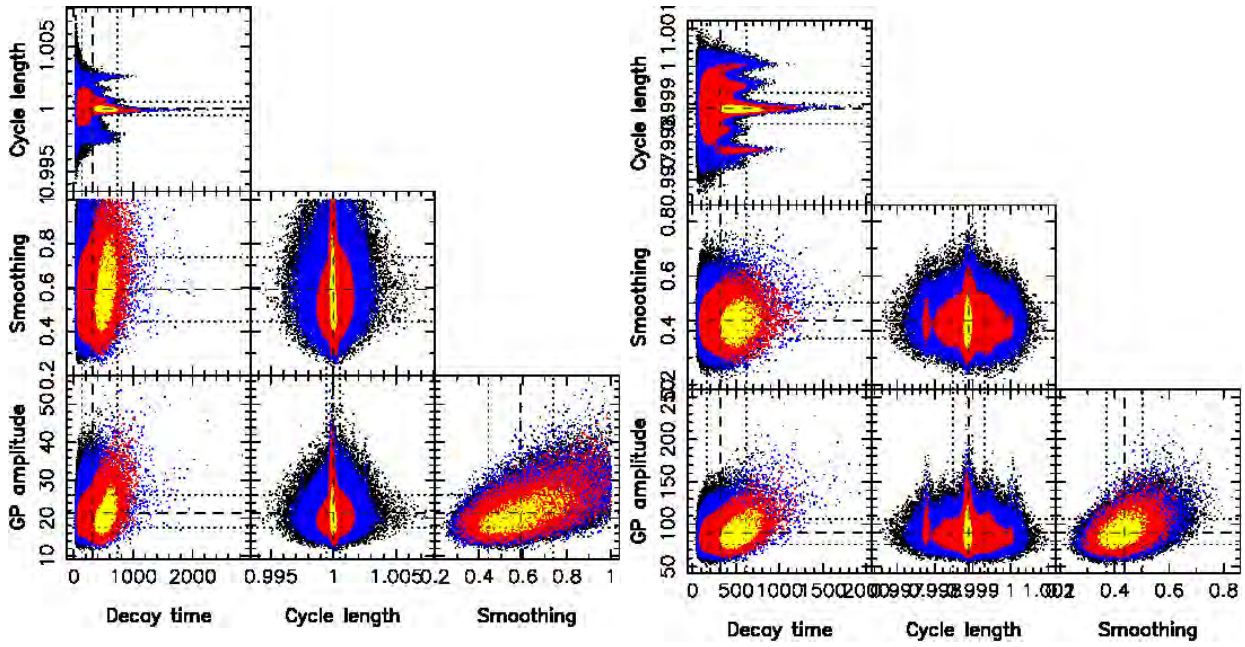

Figure 3.15 – *Left:* GPR-MCMC phase plot for V410 Tau Hα EW data. Amplitude $\theta_1 = 21.4^{+4.7}_{-3.9}$ km s^{-1}, decay time $\theta_3 = 315^{+414}_{-179}$ $P_{\rm rot}$, Cycle length $\theta_2 = 1.0000 \pm 0.0005$ $P_{\rm rot}$, Smoothing $\theta_4 = 0.59 \pm 0.15$ $P_{\rm rot}$. *Right:* GPR-MCMC phase plot for V410 Tau B_ℓ. GP amplitude $\theta_1 = 90^{+16}_{-14}$ G, cycle length $\theta_2 = 0.9989 \pm 0.0004$ $P_{\rm rot}$, decay time $\theta_3 = 322^{+295}_{-154}$ $P_{\rm rot}$, smoothing $\theta_4 = 0.436 \pm 0.066$ $P_{\rm rot}$.

We derived mean latitudes of features constraining the modulations of Hα EWs and B_ℓ from our measurement of their rotation periods (figure 3.16). The period found from Hα, equal within error bars to the one derived in Stelzer et al. 2003 from photometry, corresponds to latitudes around 35°, whereas the period found from B_ℓ seems tied to equatorial features.

3.2.4 Mid-term variability

Even with differential rotation, it is impossible for our current version of ZDI to model data sets spanning a few months down to noise level, which shows that the surfaces of TAP 26 and V410 Tau undergo significant instrinsic variability.

For the rest of this section, we focus on V410 Tau for which we have data over several years. The dipole doubles in strength throughout our observation run (see table 3.3). However measures of $d\Omega$ on individual yearly data sets do not show an increase, which, if we are to assume a cyclic dynamo, would imply a phase shift between the magnetic field and the differential rotation.

We looked for long-term variability in our photometric data. We retrieved the stellar rotation period at each epoch to see how this period evolves along the years. To retrieve the stellar rotation period, we applied two types of models to our V magnitude curves: a periodic fit involving the fundamental frequency and the first two harmonics to each of the 9 data sets individually (as well as a periodic fit involving the fundamental frequency and the first four harmonics to the whole data set), and GPR (see section 2.4.3). Since the data sets 15b+16a and the 16b+17a are particularly small (15 and 13 points respectively) and consecutive, we grouped them together for the GPR.

Placing the periods found from the photometric data on a period-latitude diagram representing the modeled differential rotation (figure 3.17), we observe that the latitudes corresponding to the

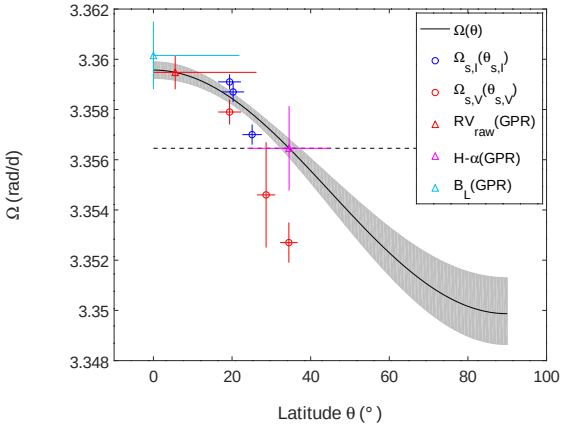

Figure 3.16 – Differential rotation curve of V410 Tau (black full line) with 1σ uncertainty in gray, with $\Omega_{\rm eq} = 3.359\,57 \pm 0.000\,06$ rad/d and $d\Omega = 0.0097 \pm 0.0003$ rad/d. The stellar rotation rate chosen to phase our data is represented as a dashed horizontal line. The rotation rates derived from the RVs (red), from the Hα equivalent widths (magenta) and from the longitudinal field measurements (cyan) are positioned on the differential rotation curve as triangles with 1σ error bars, thus yielding the barycentric latitude of the features determining the period. The dots represent couples $\{90 - \theta_s, \Omega_s\}$ derived in our epoch-wise differential rotation measurements, those coming from Stokes I/ Stokes V data being plotted in blue / red respectively.

successive periods tend to increase from 0 in 2008 to $\sim$50° in 2016. We note that this trend is observed with both the periods derived from sine fits to the photometric data and those derived from GPR. This implies that the largest features, i.e. those with the biggest impact on the photometric curve, underwent a poleward migration, reminiscent of the Solar butterfly diagram, albeit reversed. This would suggest that the dynamo wave, if cyclic, has a period of at least 8 yr and likely much longer (16 yr if our data covers only one half of a full cycle). Previous studies using different data have suggested the existence of an activity cycle on V410 Tau, with periods of 5.4 yr and 15 yr respectively (Stelzer et al., 2003; Hambálek et al., 2019). Photometric data over the past 60 yr show a complex evolution of the light curve of V410 Tau with time scales of 4 – 5 yr and $\sim$11 yr appearing (Sokoloff et al., 2008). We also observe a decrease in the amplitude of the V magnitude modulations in the 1970s (Sokoloff et al., 2008) and around 2008 (figure 3.18), which could be attributed to either a lower level of activity or a more axisymmetric distribution of surface brightness features. We further note that our differential rotation measurements confirm that the barycenter of surface features migrates to higher latitudes over time (see Fig 3.11).

All derived rotation periods, from sine fits and GPR, are plotted against their corresponding latitude using the ZDI-retrieved differential rotation, and the thus-derived latitudes are plotted against time in figure 3.17, showing a global increasing trend of that latitude, regardless of the period retrieval method.

We summarize the long-term variation time scales of V410 Tau, found from applying GPR-MCMC to various activity proxies, as well as the differential rotation lap time, in table 3.4.

On another hand, the bulk RV of V410 Tau exhibits a drift throughout our 8-year campaign, from $16.30 \pm 0.05\,{\rm km\,s^{-1}}$ in 2008b-2009a to $16.65 \pm 0.05\,{\rm km\,s^{-1}}$ in 2015b-2016a. This drift could reflect the binary motion with V410 Tau B (see section 4.2.2). An alternative interpretation could be a variation in the suppression of convective blueshift in regions of strong magnetic field (Haywood et al., 2016; Meunier et al., 2010), which could further support a secular evolution of the magnetic topology.

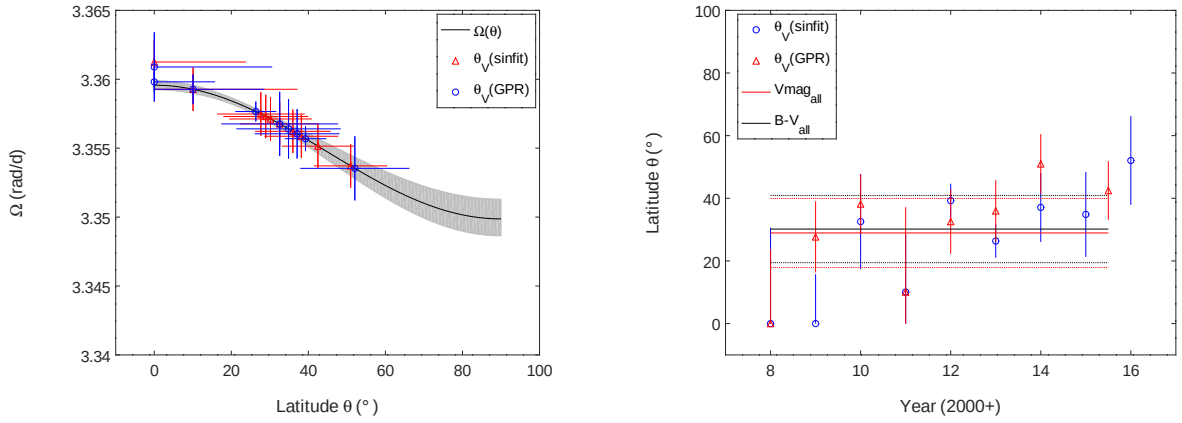

Figure 3.17 – *Left*: Differential rotation curve of V410 Tau in blue. Red: Hα rotation rates, green: B_ℓ rotation rates, circles: derived from 2013 Dec data set, triangles: derived from 2015 Dec data set, x symbols: derived from the whole data set (143 points for Hα and 135 for B_ℓ). Photometry rotation rates are displayed, derived with sine fits in green and with GPR in magenta. *Right*: Colatitude found for the V magnitude, for each epoch and for the whole data set.

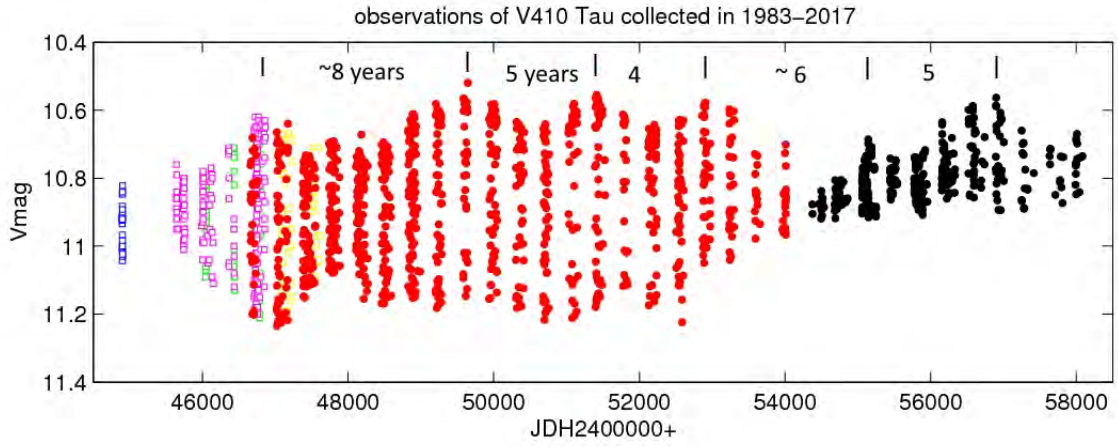

Figure 3.18 – V410 Tau light curve between 1983 and 2017. BJD 2400000+46000, 50000, 54000 and 58000 correspond to years 1984, 1995, 2006 and 2017 respectively. Yellow dots are data from Herbst (1989), pink dots from Vrba et al. (1988), green dots from Bouvier et al. (1988), blue dots from Rydgren & Vrba (1983), red dots are Maidanak observations collected by K. Grankin and the black dots are CrAO observations collected by K. Grankin. We thank Pr. Konstantin Grankin for communicating this figure to us.

3.2.5 Prominences

In our Hα dynamic spectra (figure 3.19), we observe a conspicuous absorption feature in the second part of the 2009 Jan run, crossing the spectral line from blue to red between phases 0.9 and 1, that could be the signature of a prominence (see e.g. Collier Cameron & Robinson, 1989). We also

Table 3.4 – Various evolution time scales of V410 Tau.

Quantity	Time scale (d)
RV decay time (see section 4.2.1)	160^{+45}_{-35}
V magnitude decay time	314^{+31}_{-29}
Hα decay time	589^{+774}_{-335}
B_ℓ decay time	604^{+553}_{-289}
Differential rotation lap time	648 ± 73

observe similar absorption features in 2009 Jan around phase 0.8 and in 2011 Jan around phase 0.35, but they are less well-covered by our observations. Fitting a sine curve in the absorption features yields amplitudes of $\sim 2\, v \sin i$ for all three, corresponding to prominences $\sim 2\, R_\star$ away from the center of V410 Tau, i.e. close to the corotation radius.

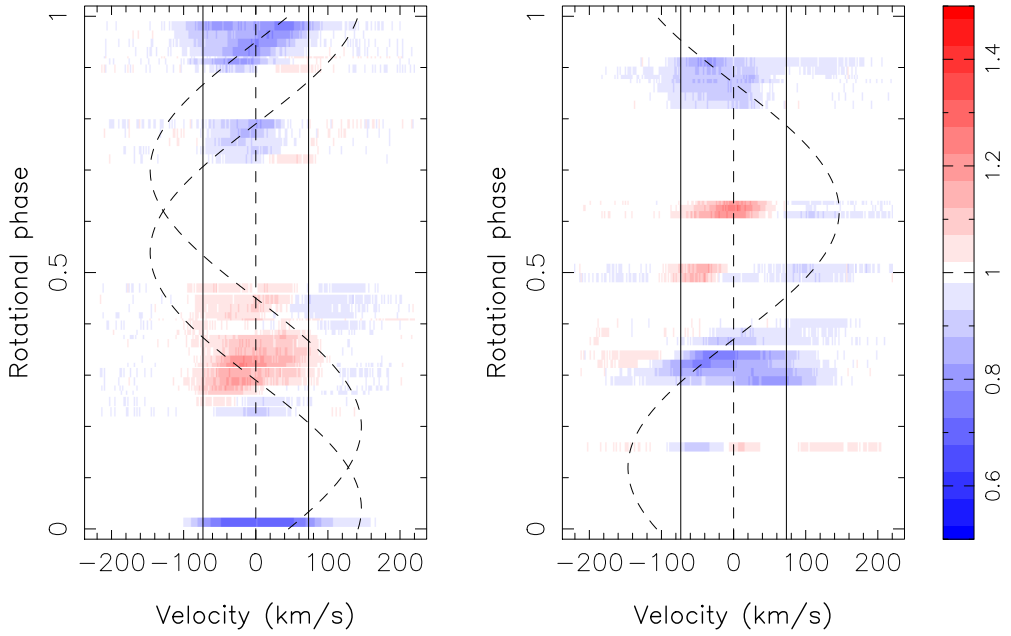

Figure 3.19 – Hα dynamical spectra for epochs 2009 Jan cycles 5 to 8 (left) and 2011 Jan (right).

Plotting the 3D potential field extrapolation of the reconstructed surface radial field for 2009 Jan and 2011 Jan, we observe the presence of closed field lines reaching $\sim 2\, R_\star$ at phases 0.95 and 0.8 in 2009 Jan, and at phase 0.35 in 2011 Jan, which may be able to support the observed prominences (figure 3.20).

3.3 Application to V830 Tau

In Donati et al. (2015), V830 Tau is found to have an inclination $i = 55 \pm 10\,^\circ$, a $v \sin i$ of $30.5 \pm 0.5\,\mathrm{km\,s^{-1}}$ and a $v_{\rm rad}$ of $17.5 \pm 0.1\,\mathrm{km\,s^{-1}}$. ZDI maps yield a 12 % spot and plage coverage and a 300 G field that is 90 % poloidal, and where the poloidal component is mainly dipolar. The dipole is tilted at an angle of $\sim 30°$ towards phase 0.65. The differential rotation parameters are found to be $\Omega_{\rm eq}$ $=2.2950 \pm 0.0005\,\mathrm{rad/d}$ and $d\Omega$ $=0.0124 \pm 0.0029\,\mathrm{rad/d}$. The results from the 15b-16a data do not differ much (Donati et al., 2017), though the dipole pole moves slightly

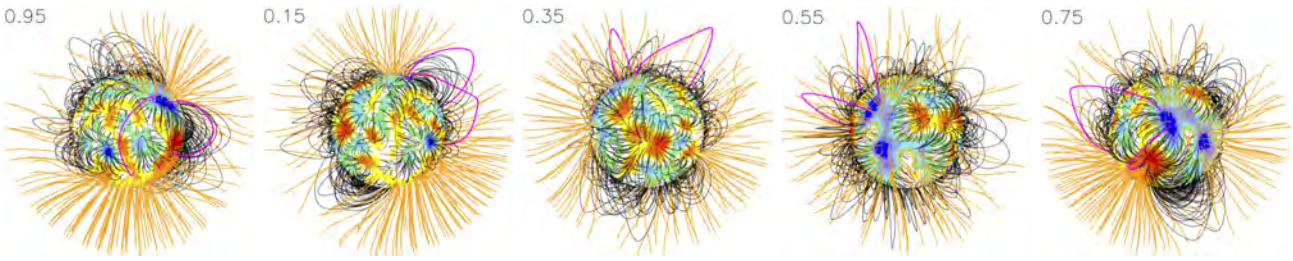

(a) V410 Tau 2009 Jan

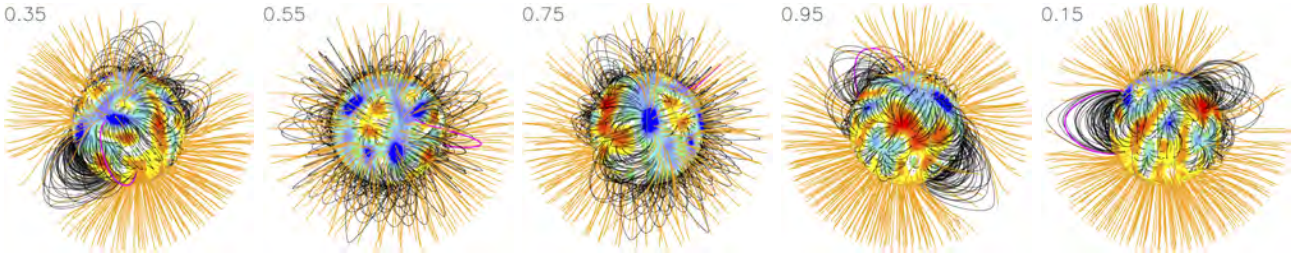

(b) V410 Tau 2011 Jan

Figure 3.20 – Potential field extrapolations of the ZDI-reconstructed surface radial field, as seen by an Earth-based observer, for observation epochs 2009 Jan (top) and 2011 Jan (bottom) at different phases. Open/closed field lines are shown in orange/black respectively, and colours at the stellar surface depict the local value of the radial field (in G, as shown in the left-hand panels of Fig. 3.6). The source surface at which field lines open is set to $2.18\,R_\star$. The field lines that would carry the potential observed prominences (phase 0.95 and 0.8 in 2009, phase 0.35 in 2011) are colored in magenta. Animated versions with the star rotating are available at `http://userpages.irap.omp.eu/~lyu/jan09a.gif` and `http://userpages.irap.omp.eu/~lyu/jan11n.gif`.

(tilted at an angle $22 \pm 5\,^\circ$ towards phases 0.79 ± 0.03 and 0.88 ± 0.03 in 2015 Dec and 2016 Jan respectively).

3.4 Contribution of our ZDI reconstructions to the MaTYSSE programme

Some main characteristics of magnetic topologies of wTTSs found within MaTYSSE so far can be summarized in a plot, commonly known as "confusogram", which is an HR diagram where the size, shape and color of each pictogram give information on the magnetic topology of the star it represents (figure 3.21). Given the variety of stars in the sample (in terms of mass, age, and evolutionary status), it is still too early to draw general conclusions on the magnetic topologies of wTTSs. We stress that the pattern seen on cTTSs, i.e. with fields that are strong and poloidal when the star is largely convective and getting weaker and more complex when the star gets radiative (see e.g. Hill et al., 2019), does not really show up clearly here.

V830 Tau, at $\sim$2 Myr, has a mainly axisymmetric magnetic topology where the dipole contributes a major part of the energy. Such topologies, with strong dipoles, are expected for fully convective stars. TAP 26, on the other hand, is one of the most evolved stars within the MaTYSSE sample, and we found that it has a rather complex magnetic topology, where the poloidal dipole only constitutes 10 % of the magnetic energy. Its toroidal component, contributing to 30 % of the total magnetic energy, is relatively high compared to other wTTSs (see figure 3.21). This level of complexity in the field topology is somewhat expected from a star that has a substantial radiative core, such as TAP 26.

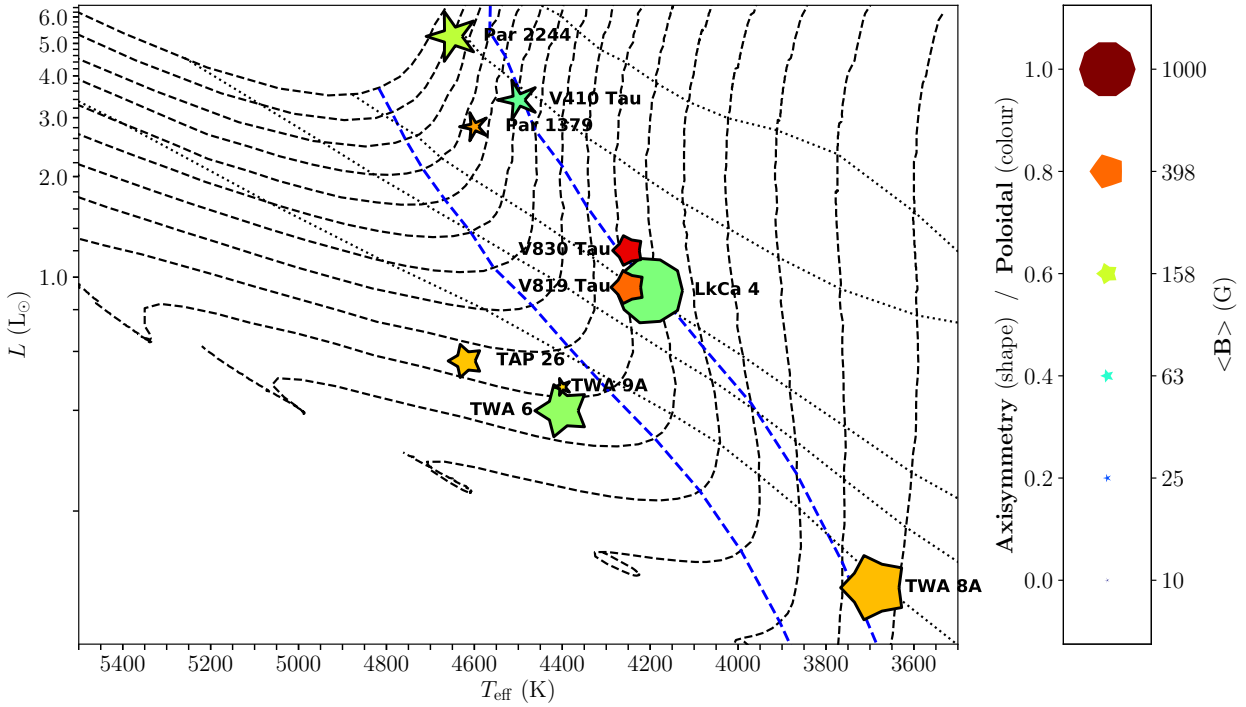

Figure 3.21 – MaTYSSE stars on the HR diagram, with the size, shape and colour of the pictograms representing respectively the strength, degree of axisymmetry and contribution of the poloidal component of their magnetic topologies, as derived with ZDI. Siess et al. (2000) evolution tracks from 0.1 – 0.9 $M_\odot$ are plotted in dashed lines and isochrones for 0.5, 1, 3, 5 and 10 Myr in dotted lines, while locations of radiative core formation start and half-radius-reaching-point are also represented as dotted lines.

The magnetic topology of V410 Tau displays a stronger toroidal component (half of the magnetic energy), that keeps a constant orientation throughout the span of our data, and a non-axisymmetric poloidal field, both not typical to fully convective stars. Only three other stars within the MaTYSSE sample (out of eleven) have exhibited similarly important toroidal components, among which only one is still fully convective like V410 Tau, the ∼2 Myr, $0.79 \pm 0.05\,M_\odot$ LkCa 4 (Donati et al., 2014). The only two other fully convective wTTSs for which magnetic topologies were reconstructed within MaTYSSE so far have mainly poloidal magnetic topologies (V830 Tau and TWA 8A, resp. Donati et al., 2015; Hill et al., 2019), and none is as massive as V410 Tau (1.00 ± 0.05 and $0.45 \pm 0.10\,M_\odot$ resp.). The origin of this strong toroidal component is unclear: in terms of rotation rate, both V410 Tau and LkCa 4 find themselves around the middle of the spectrum within the MaTYSSE sample, so standard dynamo processes due to their fast rotation would not be sufficient to explain the phenomenon, not to mention that dynamos are expected to be saturated in these stars. Maybe it is generated through an α^2 dynamo (like in the simulations of low-Rossby fully convective stars by Yadav et al., 2015), or maybe it is he remnants of a subsurfacic radial shear between internal layers accelerating due to contraction, and disc-braked outer layers. If it is the remnant of the original toroidal field from when the star formed (as found in the simulations of Vaytet et al., 2018), we lack an explanation on how this field escaped dissipation until now, and why it does not show up in cTTSs. Would the early dissipation of the disc, a common factor between LkCa 4 and V410 Tau, have something to do with this?

Completing the analysis of the MaTYSSE sample is therefore necessary to hope for a better overview on this phenomenon and its possible roots. More data, e.g. collected with SPIRou, are also needed to clarify the magnetic panorama of wTTSs.

3.5 Towards a new version of ZDI

Because ZDI does not reconstruct intrinsic temporal variability, its use is limited to short data sets. We explored two ways to implement some degree of variability in the ZDI model, beyond differential rotation, but this work is far from finished.

3.5.1 First approach

We try to improve our ZDI filtering process by implementing a new feature: instead of only having one brightness value in each cell, we give it a brightness value and an evolution parameter, so that ZDI brightness maps are allowed to evolve with time to better fit time-series of LSD profiles with variability. Thus we reconstruct two maps for the brightness: the brightness at time 0 and the map of the evolution parameter. We choose, for now, a simple model where the logarithmic relative brightness of each cell k is allowed to evolve linearily with time:

$$\log Q_k(t) = \log Q_k(0) + m_k t, \tag{3.3}$$

where $Q_k(t)$ is the local surface brightness and m_k is the evolution parameter.

Applying this new method to the V410 Tau 2015-2016 extended data set, we manage to fit the whole data set down to a χ^2_r of 1 where classical ZDI, even with differential rotation, could not reach lower than $\chi^2_r = 2.5$ (see Section 3.2.2). Maps associated to this reconstruction are shown in figure 3.22. We observe for instance that, in the reconstruction, the dark equatorial spot at phase 0.45 gets weaker with time since it coincides with a blue patch in the brightness evolution map, while the polar spot itself does not evolve much.

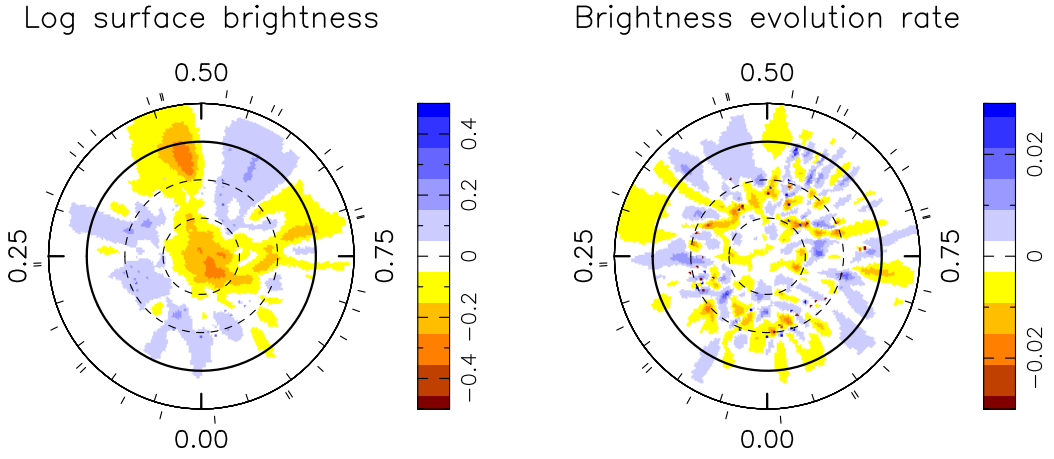

Figure 3.22 – Brightness map and evolution rate reconstructed by ZDI on data set Dec 2015-Jan 2016. Pole-on view with the equator being represented as a full line, and 60°, 30°, and −30° latitude parallels as dashed lines. Cool spots are colored in brown and bright plages in blue, and ticks around the star mark the spectropolarimetric observations.

3.5.2 Next objective

The approach above increases the amount of intrinsic variability that ZDI can model, but it is still restrictive, as the brightness of a cell can only evolve monotonously. We are thus incapable of modeling the successive appearance and disappearance of a spot at the same location. To remedy this, we wish to model the brightness variability with GPs, however, with thousands of cells in the ZDI mesh, this would amount to a huge number of parameters in the ensuing GPR-MCMC exploration, which would end up in very time-consuming computations.

The next idea is thus to express the brightness map no longer as independent cells, but as a weighted sum of a limited number of base maps, such as spherical harmonics (akin to the magnetic topology), and to model the evolving brightness map by using GPR on the spherical harmonics coefficients. We use spherical harmonics in a preliminary attempt, but other bases can be investigated in future developments. Figure 3.23 shows example of spherical harmonics modes and their corresponding spectra.

So far, only a code to decompose a classical ZDI map into a sum of spherical harmonics was written, to show that there is little difference in the corresponding spectra when only the lowest orders of spherical harmonics are kept (see figure 3.24, with $\ell_{\max} = 15$).

A main challenge of the remaining work is to reconcile the fact that the data are in the spectral space, yet the quantities to be modelled with GPR are in the image space.

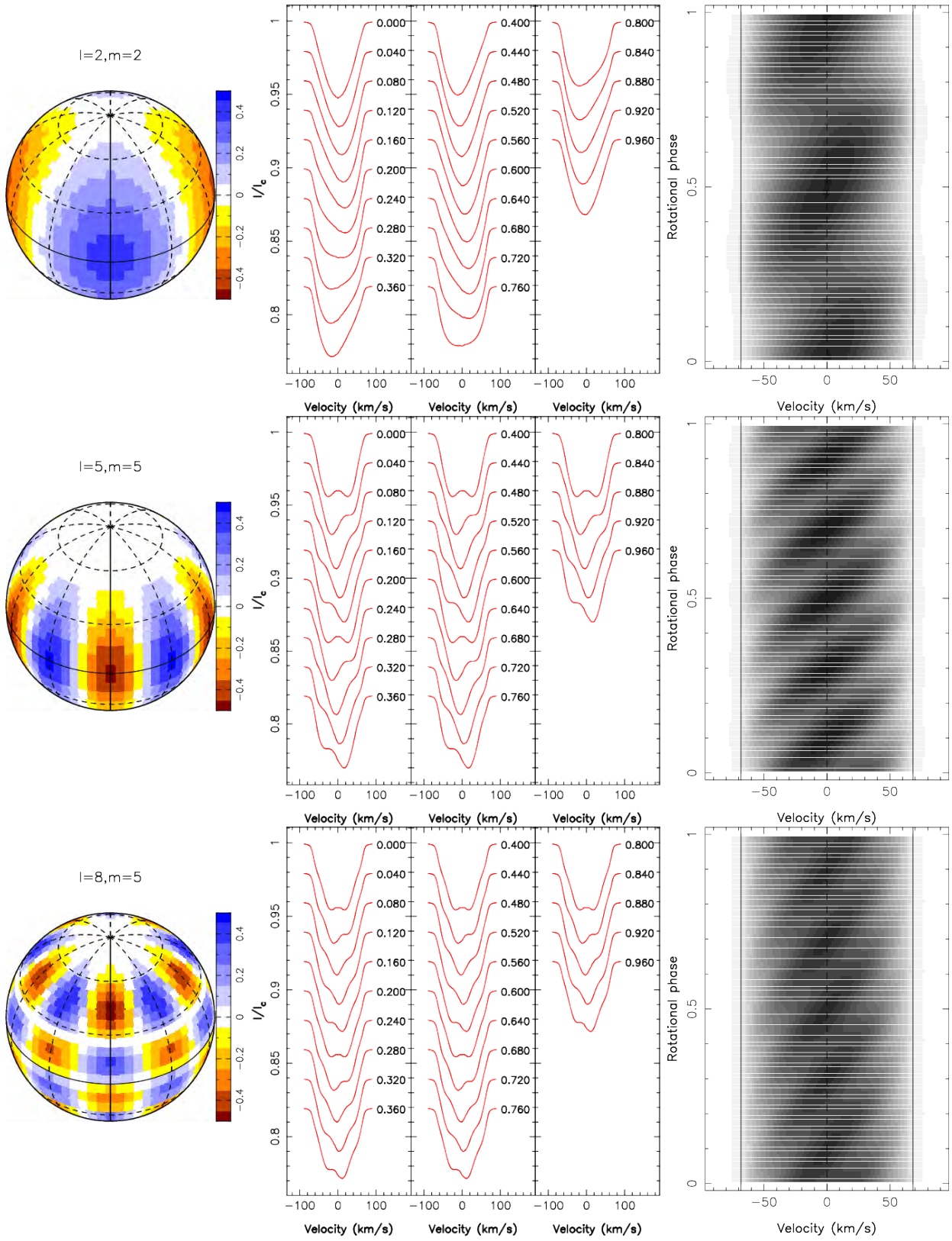

Figure 3.23 – Examples of spherical harmonics modes for the brightness map and corresponding spectra. *Top:* $\ell = 2, m = 2$, *Middle:* $\ell = 5, m = 5$, *Bottom:* $\ell = 8, m = 5$.

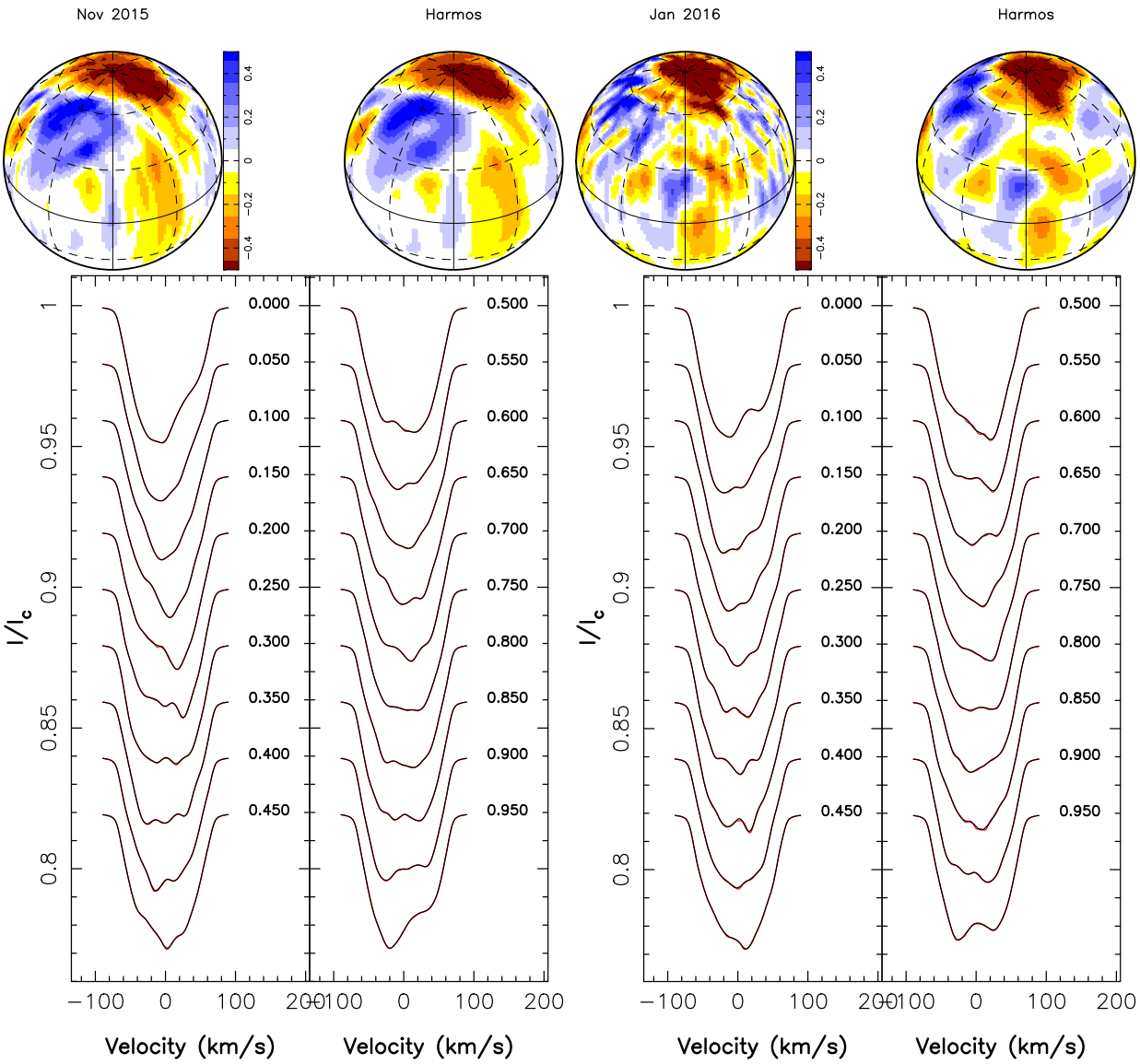

Figure 3.24 – *Top:* Classical ZDI maps, shown at phase 0, which are the ZDI-reconstructed maps for TAP 26 at observation epochs 2015 Nov (1st map) and 2016 Jan (3rd map). Their spherical harmonics approximations, up to order $\ell = 15$, are displayed beside them (2nd and 4th maps). *Bottom:* Stokes I LSD profiles synthesized over one rotation cycle from the classical ZDI maps (red) and the spherical harmonics approximations (black), with 2015 Nov spectra in the left panels and 2016 Jan spectra in the right panels.

4 | RV analyses

Contents

After having modelled the activity of our stars, we aim at filtering out the activity jitter from the RV curves to investigate the potential presence of hot Jupiters around our targets.

4.1 The hot Jupiter of TAP 26

We describe below three different techniques aimed at characterising the RV curve of TAP 26. The first two are those used in Donati et al. (2016): filtering out the activity modelled with the help of ZDI, and the simultaneous fit of the planet parameters and the stellar activity in the Stokes I LSD profiles. The third method uses GPR-MCMC (section 2.4.3) to model the activity directly from the raw RVs. The results obtained from these three methods are outlined and discussed in the following sections.

4.1.1 Filtering out the ZDI-modelled jitter

The first technique consists of using the previously reconstructed maps to predict the pollution to the RV curve caused by activity (the activity jitter) and subtract it from the raw RVs. From the observed Stokes I LSD profiles, we compute, at both epochs, the raw RVs $\mathrm{RV_{raw}}$, as the first-order moment of the continuum-subtracted corresponding profiles (Donati et al., 2017). Likewise, the synthesised Stokes I LSD profiles yield the synthesised activity jitter of the star (RV signal caused by the brightness distribution and stellar rotation). By subtracting the activity jitter from the raw RVs, we obtain filtered RVs $\mathrm{RV_{filt}}$. We observe that the jitter has a mean semi-amplitude of $1.81\,\mathrm{km\,s^{-1}}$ in 2015 Nov and $1.21\,\mathrm{km\,s^{-1}}$ in 2016 Jan, whereas the filtered RV curve features a signal with a semi-amplitude of $\simeq 0.15\,\mathrm{km\,s^{-1}}$ (figure 4.1), i.e., 8 to 12 times smaller than the activity signal we filtered out. We note the very significant evolution in the activity curve between 2015 Nov and 2016 Jan, demonstrating that the brightness distribution has evolved at the surface of TAP 26, through differential rotation and intrinsic variability (see chapter 3).

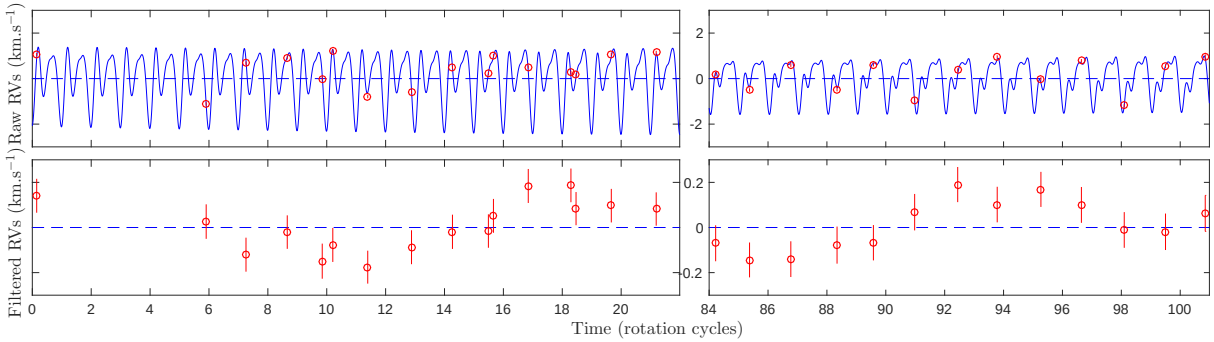

Figure 4.1 – *Top:* RV (in the stellar rest frame) of TAP 26 as a function of rotation phase, as measured from our observations (open circles) and predicted by the tomographic maps (blue line). The synthesised raw RV curves exhibit only low-level temporal evolution resulting from differential rotation. *Bottom:* filtered RVs derived by subtracting the modelled activity jitter from the raw RVs, with a 10x zoom-in on the vertical axis.

With a rms dispersion of 109 $\mathrm{m\,s^{-1}}$, the filtered RVs clearly show the presence of a signal. Looking for a planet signature, we want to fit a sine curve (of semi-amplitude K, period P_{orb}, phase of inferior conjunction ϕ, and offset $\mathrm{RV_0}$) to these filtered RVs, which corresponds to a circular orbit (see figure 4.2). The phase of inferior conjunction ϕ, i.e., corresponding to the epoch at which the planet is closest to us, is defined relatively to the reference date $\mathrm{BJD_{c\,0}}$=2,457,352.6485 (rotation cycle 11.0, approximately at the centre of the 2015 Nov observation run), such that the inferior conjunction occurs at $\mathrm{BJD_c} = \mathrm{BJD_{c\,0}} + (\phi\text{-}1)P_{\mathrm{orb}}$. Due to the gap between both observing

runs, several sine fits with different frequencies match the RV_{filt} as local minima of χ^2_r. This demonstrates the need for observations that are as continuous as possible to avoid such aliases in the determination of the orbital period. The four best fits are shown in figure 4.2 and their characteristics are given in table 4.1, with the value of the log likelihood as computed from the $\Delta\chi^2$ over these 29 RV data points. The residual RVs, derived from subtracting the best sine fit to the filtered RVs (shown in figure 4.2), feature a rms value of 51 $m\,s^{-1}$.

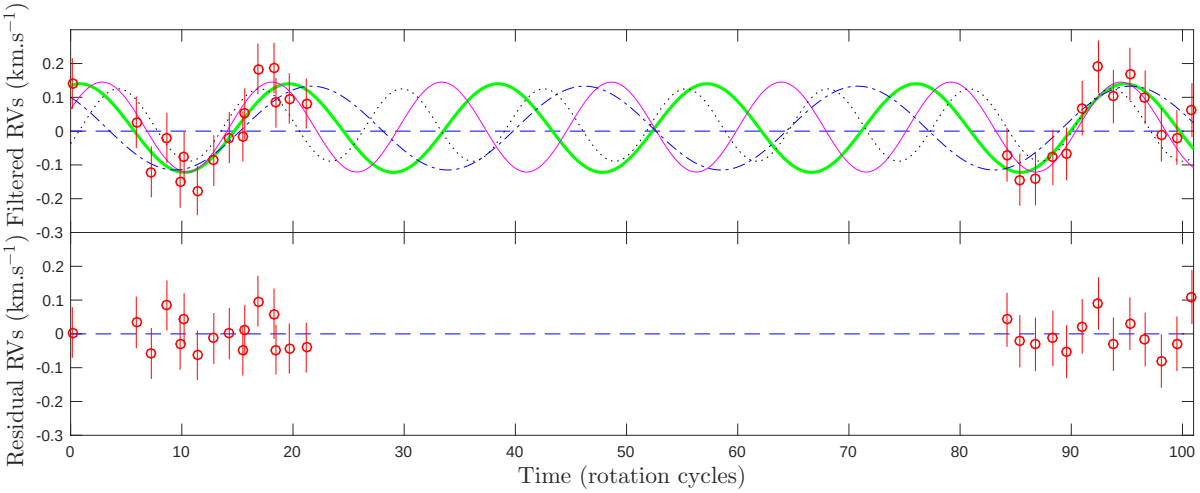

Figure 4.2 – *Top:* filtered RVs of TAP 26 and four sine curves representing the best fits. The thick green curve represents the case P_{orb}/P_{rot} =18.80, the thin magenta one P_{orb}/P_{rot} =15.27, the dash-and-dotted blue one P_{orb}/P_{rot} =24.56 and the dotted black one P_{orb}/P_{rot} =12.76. *Bottom:* residual RVs resulting from the subtraction of the best fit (green curve) from the filtered RVs. The residual RVs feature a rms value of 51 $m\,s^{-1}$.

Table 4.1 – Characteristics of the four best sine curve fits to the filtered RVs, and the case without planet. Respectively: semi-amplitude K, orbital period P_{orb} in units of P_{rot}, orbital period P_{orb} in days, phase of inferior conjunction ϕ relative to cycle 11.0 (see ephemeris in Eq. 3.1), BJD of inferior conjunction (reference BJD: 2,457,340), mean RV, corresponding χ^2_r, difference in χ^2 with the best fit ($\Delta\chi^2$, summed on the 29 data points), and natural logarithm ($\log_e$) of the likelihood $\mathcal{L}_{r1}$ relative to the best fit. ϕ relates to the epoch of inferior conjuntion BJD_c through BJD_c =2,457,352.6485+ϕP_{orb}, the reference date being chosen so as to minimise the variation of ϕ between the four cases.

K ($km\,s^{-1}$)	P_{orb} (P_{rot})	P_{orb} (d)	ϕ	BJD_c	RV_0 ($km\,s^{-1}$)	χ^2_r	$\Delta\chi^2$	$\log\mathcal{L}_{r1}$	style in fig. 4.2
0.131 ±0.020	18.80 ±0.23	13.41 ±0.16	0.709 ±0.026	8.75 ±0.35	0.009 ±0.014	0.445	0	0.00	thick green
0.133 ±0.021	15.27 ±0.14	10.90 ±0.10	0.715 ±0.024	9.54 ±0.26	0.012 ±0.014	0.542	2.80	-0.53	thin magenta
0.124 ±0.020	24.56 ±0.41	17.52 ±0.30	0.684 ±0.028	7.11 ±0.50	0.009 ±0.016	0.673	6.61	-1.85	dashed blue
0.107 ±0.021	12.76 ±0.14	9.11 ±0.10	0.724 ±0.031	10.14 ±0.28	0.018 ±0.015	1.079	18.38	-6.87	dotted black
0					0.013 ±0.014	2.025	45.82	-19.73	

Plotting Lomb-Scargle periodograms for the raw RVs, filtered RVs and residual RVs further demonstrates the presence of a periodic signal in the filtered RVs (figure 4.3). The above-mentioned

dominant periods are seen as peaks in the periodogram; periodograms of partial data (only the 2015 Nov dataset, only the 2016 Jan dataset, odd points and even points) are also shown, yielding peaks at the same frequencies albeit with a lower power. We highlight the fact that the highest peaks in the raw RVs correspond to the activity jitter and are located at $P_{\rm rot}/2$ and its aliases, whereas little power concentrates at $P_{\rm rot}$ itself. A zoom-in of the filtered RV periodogram is also shown in figure 4.3 (bottom panel). The FAP is 0.06% for the highest peak ($P_{\rm orb}$ = 13.41 d = 18.80 $P_{\rm rot}$), and no significant period stands out in the residual RVs after filtering out both the activity jitter and the planet signal corresponding to the highest peak. We carried out simulations to ensure that the detected peaks are not generated by the filtering process, see details in Yu et al. (2017). Study of other activity proxies shows that the detected orbital periods are not present in the activity signal either (Yu et al., 2017).

By fitting the filtered RVs with a Keplerian orbit rather than a circular orbit, we obtain an eccentricity of 0.16 ± 0.15, indicating that there is no evidence for an eccentric orbit (following the precepts of Lucy & Sweeney, 1971). We can thus conclude that the orbit of TAP 26 b is likely close to circular, or no more than moderately eccentric.

4.1.2 Deriving the planetary parameters from the LSD profiles

A second technique, following the method of Petit et al. (2015), consists of taking into account the presence of a planet into the ZDI model. Rather than fitting the measured Stokes I LSD profiles with a synthetic activity jitter directly, we first apply a translation in velocity to each of them, to remove the reflex motion caused by a planet of given parameters, and then apply ZDI to the corrected data set. Practically speaking, we repeat the experiment for a range of values for the orbital parameters (K, $P_{\rm orb}$, ϕ) at the vicinity of the minima previously identified, and look for the set of values that yields the best result. The same way as for differential rotation, we derive the error bars on all parameters from the curvature of the 3D $\chi^2_{\rm r}$ paraboloid around the minimum.

In the present case, since we have two datasets separated by a 45 d gap and we know that intrinsic variability occurred (see chapter 3 and section 4.1.1), a modification to the method described above was implemented: after correcting the global dataset from the reflex motion, ZDI is applied separately on each dataset, reconstructing two different brightness maps (one for late 2015 and one for early 2016) in order to obtain a more precise reconstruction. The quantity used to measure the likelihood of each set of parameters is therefore a global $\chi^2_{\rm r}$, computed as a weighted average of both individual $\chi^2_{\rm r}$, with respective weights proportional to the number of data points in each set (1424 for 2015 Nov and 1157 for 2016 Jan).

As in the previous section, several minima are found, which are listed in table 4.2. We also computed the relative likelihood of each case compared to the best one from the corresponding difference in $\chi^2_{\rm r}$. We note that the case with no planet yields $\Delta\chi^2_{\rm r} = 0.0181$, which leads to a relative probability lower than 10^{-9} compared to the case with a 10.91 d period planet.

Figure 4.4 displays a $\Delta\chi^2$ map around the local minimum $P_{\rm orb}/P_{\rm rot}$ =15.29, at ϕ=0.67, showing the 99.99% confidence area.

4.1.3 Applying GPR-MCMC

The third method consists in applying GPR-MCMC, as described in sections 2.4.3 and A.5.2, on the raw RVs, with the following GP prior:

$$m(t) = K\sin(2\pi t/P_{\rm orb} + \phi) \quad \text{or} \quad m(t) = K\big(e\cos(\omega) + \cos(\omega + \nu(t, e, \phi, P_{\rm orb}))\big)$$

$$k(t,t') = \theta_1^2 \ \exp\left(-\frac{(t-t')^2}{\theta_3^2} - \frac{\sin^2\left(\frac{\pi(t-t')}{\theta_2}\right)}{\theta_4^2}\right),$$

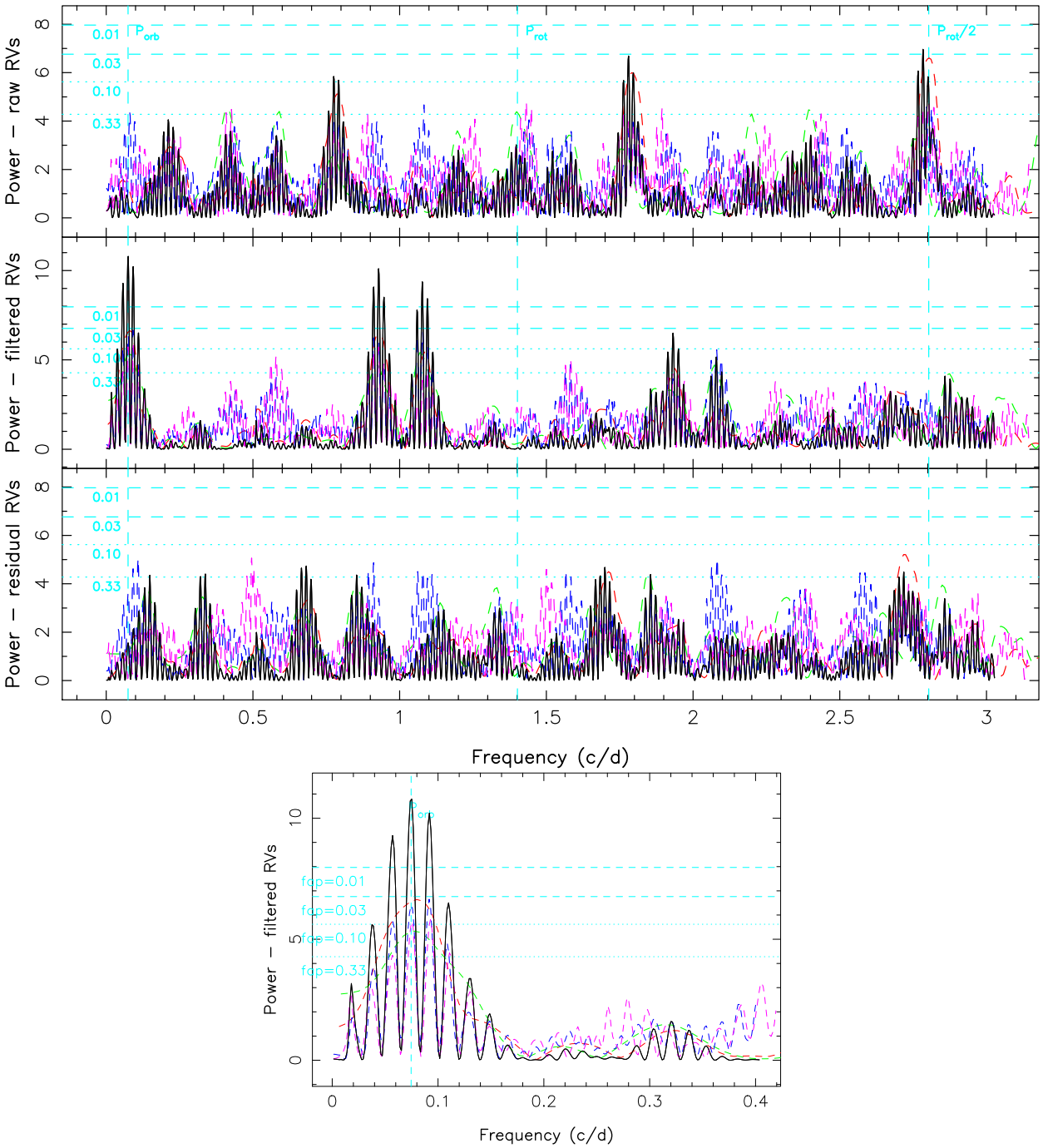

Figure 4.3 – *Top:* Periodograms of the raw (top), filtered (middle) and residual (bottom) RV curves over the TAP 26 15b-16a dataset (black line). The red line represents the 2015 Nov dataset, the green line the 2016 Jan dataset, the blue line the odd data points and the magenta line the even data points. FAP levels of 0.33, 0.10, 0.03 and 0.01 are displayed as horizontal dashed cyan lines. The rotation frequency (1.402 cycles per day) is marked by a cyan dashed line, as well as its first harmonic (2.803 cycles per day) and the frequency that has the smallest FAP (0.06% at 0.075 cycles per day, corresponding to $P_{\rm orb}$ =13.41 d). Aliases of the highest peaks, related to the observation window, appear as lower peaks separated by one cycle per day. *Bottom:* Zoom in the periodogram of filtered RVs.

where θ_1 is the amplitude (in km s^{-1}) of the GP, θ_2 the recurrence timescale (in units of $P_{\rm rot}$), θ_3 the decay timescale (i.e., the typical spot lifetime in the present case, in units of $P_{\rm rot}$) and

Table 4.2 – Optimal orbital parameters derived with the method described in section4.1.2, respectively: semi-amplitude K, orbital period $P_{\rm orb}$ in units of $P_{\rm rot}$, orbital period $P_{\rm orb}$ in days, phase of inferior conjunction ϕ relative to cycle 11.0, BJD of inferior conjunction, $\chi^2_{\rm r}$, $\Delta\chi^2$ summed on 2581 data points, and natural logarithm of the likelihood $\mathcal{L}_{r2}$ relative to the best fit. The case where no planet is taken into account in the model is given for comparison.

K ($\mathrm{km\,s^{-1}}$)	$P_{\rm orb}$ ($P_{\rm rot}$)	$P_{\rm orb}$ (d)	ϕ	BJD$_{\rm c}$ (2,457,340+)	$\chi^2_{\rm r}$	$\Delta\chi^2$	$\log\mathcal{L}_{r2}$
0.154 ±0.022	15.29 ±0.15	10.91 ±0.11	0.671 ±0.035	9.06 ±0.38	0.9682	0.00	0.00
0.144 ±0.023	18.78 ±0.25	13.40 ±0.18	0.685 ±0.041	8.43 ±0.55	0.9698	4.00	-1.34
0.148 ±0.025	12.83 ±0.12	9.16 ±0.09	0.677 ±0.038	9.69 ±0.35	0.9718	9.17	-3.61
0					0.9863	46.62	-21.60

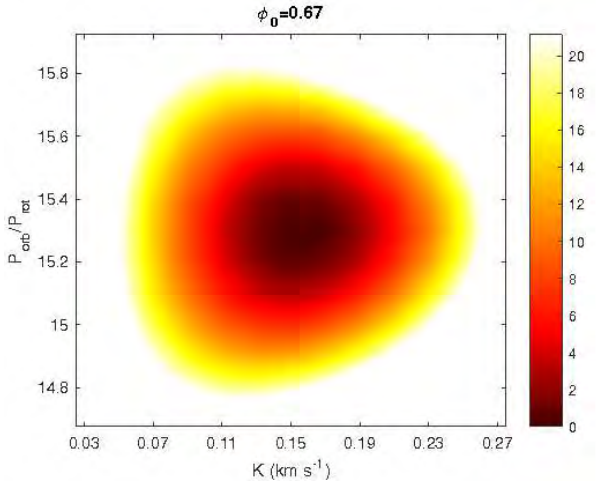

Figure 4.4 – $\Delta\chi^2$ map as a function of K and $P_{\rm orb}/P_{\rm rot}$, derived with ZDI from corrected Stokes I LSD profiles at constant information content. Here the phase is fixed at 0.67, i.e., the value of ϕ at which the 3D paraboloid is minimum. The outer colour delimits the 99.99% confidence level area (corresponding to a χ^2 increase of 21.10 for 2581 data points in our Stokes I LSD profiles). The minimum value of $\chi^2_{\rm r}$ is 0.96824.

θ_4 a smoothing parameter (within [0,1]) setting the amount of high frequency structures that we allow the fit to include. The two possibilities for m correspond to circular and keplerian orbits respectively (see section 2.4.1), where $\nu = \theta - \omega$ in equation A.9. In practice in the Keplerian case, e and ω themselves are not directly hyperparameters, but instead $C = \sqrt{e}\cos\omega$ and $S = \sqrt{e}\sin\omega$ for computational reasons, following the prescription in Haywood et al. (2014).

After an initial run where all the parameters are free to vary, we fix θ_4 and θ_3 to their respective best values (0.50 ± 0.09 and $180 \pm 60\,P_{\rm rot}$=128 ± 43 d) before carrying out the main MCMC run to find the best estimates of the 5 remaining parameters. We note that the best value found for the decay time is exactly equal to the differential rotation lap time within error bars, and to twice the total span of our data. This decay time corresponds to both the differential rotation lap time and the starspot coherence time, since these are the most influent phenomena on the periodicity of the activity jitter. Such a starspot coherence time is consistent with previous studies (Grankin et al., 2008; Bradshaw & Hartigan, 2014; Lanza, 2006).

As shown in figure 4.5, this method succesfully recovers the different minima previously found with the first two techniques, with little correlation between the various parameters thus minimum

bias in the derived values. Applying the method of Chib & Jeliazkov (2001) to the MCMC posterior samples, we obtain that the marginal likelihood of the case $P_{\rm orb}$ =12.61 $P_{\rm rot}$ is larger than that of the case $P_{\rm orb}$ =15.12 $P_{\rm rot}$ by a Bayes factor of only 1.28, which implies that there is as yet no clear evidence in favor of either of them. The third most likely case, $P_{\rm orb}$ =18.74 $P_{\rm rot}$, has a marginal likelihood which is inferior to the first one by a Bayes' factor of > 8, and the case with no planet has a marginal likelihood which is smaller than that of the first case by a Bayes factor of 2 10^5. The three most likely sets of parameters are summarised in table 4.3.

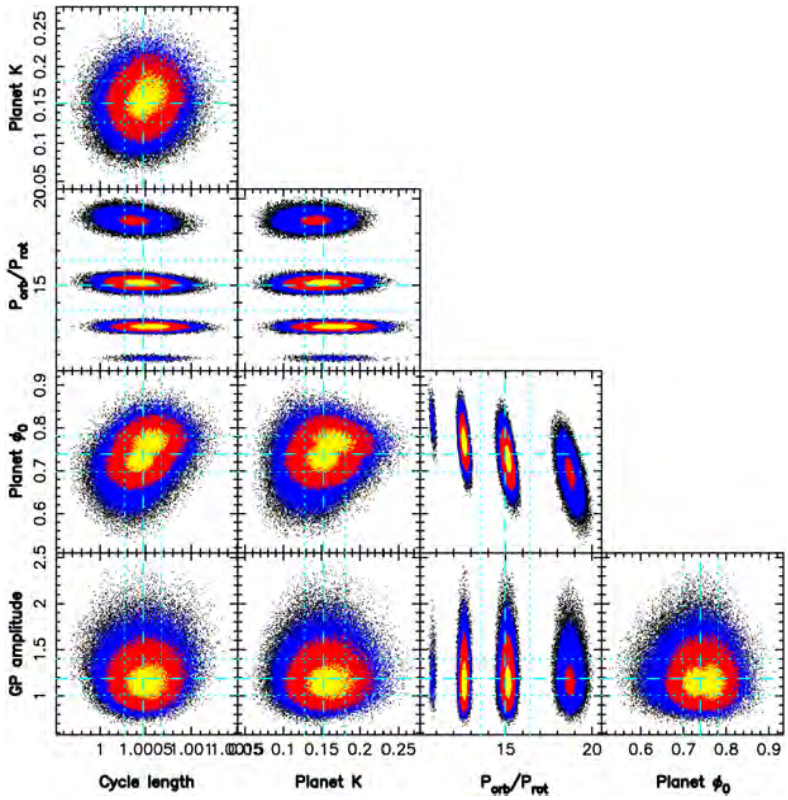

Figure 4.5 – Phase plots of our 5-parameter MCMC run with yellow, red and blue points marking respectively the 1σ, 2σ and 3σ confidence regions. The optimal values found for each parameters are: θ_1=1.19 $\pm$ 0.21 km s^{-1}, θ_2=1.0005 $\pm$ 0.0002 $P_{\rm rot}$, K=0.152 $\pm$ 0.029 km s^{-1}. Several optima are detected for $P_{\rm orb}$: 12.61 $\pm$ 0.13 $P_{\rm rot}$, 15.12 $\pm$ 0.20 $P_{\rm rot}$ and 18.74 $\pm$ 0.34 $P_{\rm rot}$, ordered by decreasing likelihood. The corresponding phases ϕ are: 0.766 $\pm$ 0.030, 0.728 $\pm$ 0.033 and 0.694 $\pm$ 0.042 respectively.

Trying to fit a non-circular Keplerian orbit to our data, i.e. adding the periapsis argument and the eccentricity e to the parameters in our MCMC run, we obtain e=0.05 $\pm$ 0.18, with a marginal likelihood slightly smaller than that of the case of a circular orbit. This further supports that the planet eccentricity is low if non-zero.

The best fit with our third method is shown in figure 4.6, where we see the raw RVs and the modelled RV curve predicted with this method, i.e., the sum of the GPR-fitted activity jitter and of the planet signal. Zooming in shows that this curve presents similarities with the RV jitter curve derived by ZDI (figure 4.1), indicating that, although working only with the RV data points, GPR successfully retrieves a convincing model for the activity. We also note the ability of the GP to model the activity jitter not only during our observing runs, but also during the 45 d gap between them, emphasising the variability of the RV signal with time. The residual RVs in the case presented here have a rms value of 29 m s^{-1} (close to the instrument RV precision 20-30 m s^{-1}) whereas the residual RVs derived with the 1st method yield a rms value of 51 m s^{-1}. Though the rms value is 2.5 times smaller than the error bar, GPR only fits 2 parameters, which illustrates its

Table 4.3 – Sets of orbital parameters that allow to fit the corrected RV curve best, using a GP with a covariance function given in Eq. 2.2, derived from the MCMC run. Respectively: reflex motion RV semi-amplitude K, orbital period $P_{\rm orb}$ in units of $P_{\rm rot}$, orbital period $P_{\rm orb}$ in days, phase of inferior conjunction ϕ relative to rotation cycle 11.00 (ephemeris defined in Eq. 3.1), BJD of inferior conjunction, natural logarithm of the marginal likelihood $\mathcal{L}$ and natural logarithm of the relative marginal likelihood $\mathcal{L}_{r3}$ as compared to the best case. The case where no planet is taken into account in the model is given for comparison.

K ($\rm km\,s^{-1}$)	$P_{\rm orb}$ ($P_{\rm rot}$)	$P_{\rm orb}$ (d)	ϕ	$\rm BJD_c$ (2,457,340+)	$\log\mathcal{L}$	$\log\mathcal{L}_{r3}$
0.163	12.61	8.99	0.766	10.54	-3.48	0.00
±0.028	±0.13	±0.09	±0.030	±0.27		
0.149	15.12	10.79	0.728	9.71	-3.73	-0.25
±0.026	±0.20	±0.14	±0.033	±0.36		
0.139	18.74	13.37	0.694	8.56	-5.60	-2.12
±0.026	±0.34	±0.24	±0.042	±0.57		
0					-15.80	-12.52

flexibility without decreasing its reliability, since the results are consistent with those found using independent methods (sections 4.1.1, 4.1.2). This demonstrates that GPR does a better job at modelling the activity jitter and its temporal evolution than the 2 previous methods, in agreement with the conclusions of Donati et al. (2017) in the case of the wTTS V830 Tau. As a result, we consider the optimal planet parameters derived with GPR as the most reliable ones, and therefore conclude that the orbital periods of 10.8 and 9.0 d are more or less equally likely.

4.1.4 Conclusions about TAP 26 b

Table 4.4 summarises the likelihood of the different periods found with each method.

We find that GPR succeeds best at modelling the intrinsic variability occurring at the surface of TAP 26, and is able to fit raw RVs at a rms precision of 29 $\rm m\,s^{-1}$, i.e., close to the instrumental precision of ESPaDOnS (20-30 $\rm m\,s^{-1}$, Moutou et al., 2007; Donati et al., 2008b) and 30% better than with our first method (yielding a rms precision of 51 $\rm m\,s^{-1}$).

For Hα and B_ℓ, no signal is detected at the planet periods found with any of those three methods.

All three methods demonstrate the clear presence of a planet signature in the data, although the gap between both data sets generates aliasing problems, causing multiple nearby peaks to stand out in the periodogram. Of the dominant periods, the 10.8 d one emerges strongly for all three methods. It is the most likely with the second method, and equally likely as other periods when using the first and third methods (13.4 d and 9.0 d respectively). Although the 9.0 d orbital period ranks low (and in particular lower than the 13.4 d period) with our first and second methods, we nonetheless consider it as the second most likely given its first rank with GPR; the most probable explanation for this apparent discrepancy lies in the higher ability of GPR at modelling intrinsic variability of the activity jitter plaguing the RV curve. Allowing ZDI to model temporal evolution of spot distributions and magnetic topologies should bring all methods on an equal footing; this upgrade is planned for a forthcoming study.

Assuming the 10.79 ± 0.14 d period is the true orbital period, and using the values yielded by GPR for K and ϕ, we find a circular orbit of semi-major axis $a = 0.0968 \pm 0.0032$ au $= 17.8 \pm 2.7\,R_\star$, epoch of inferior conjunction $\rm BJD_c$ =2,457,349.71 ± 0.36 and $M \sin i$ =1.66 ± 0.31 $\rm M_{Jup}$. If the orbital plane is aligned with the equatorial plane of TAP 26, with an assumed inclination of 55°, we obtain a mass M=2.03 ± 0.46 $\rm M_{Jup}$ for TAP 26 b. The 8.99 ± 0.09 d period leads to a=0.086 ± 0.003 au, $\rm BJD_c$ =2,457,350.54 ± 0.27 and $M \sin i$ =1.71 ± 0.31 $\rm M_{Jup}$.

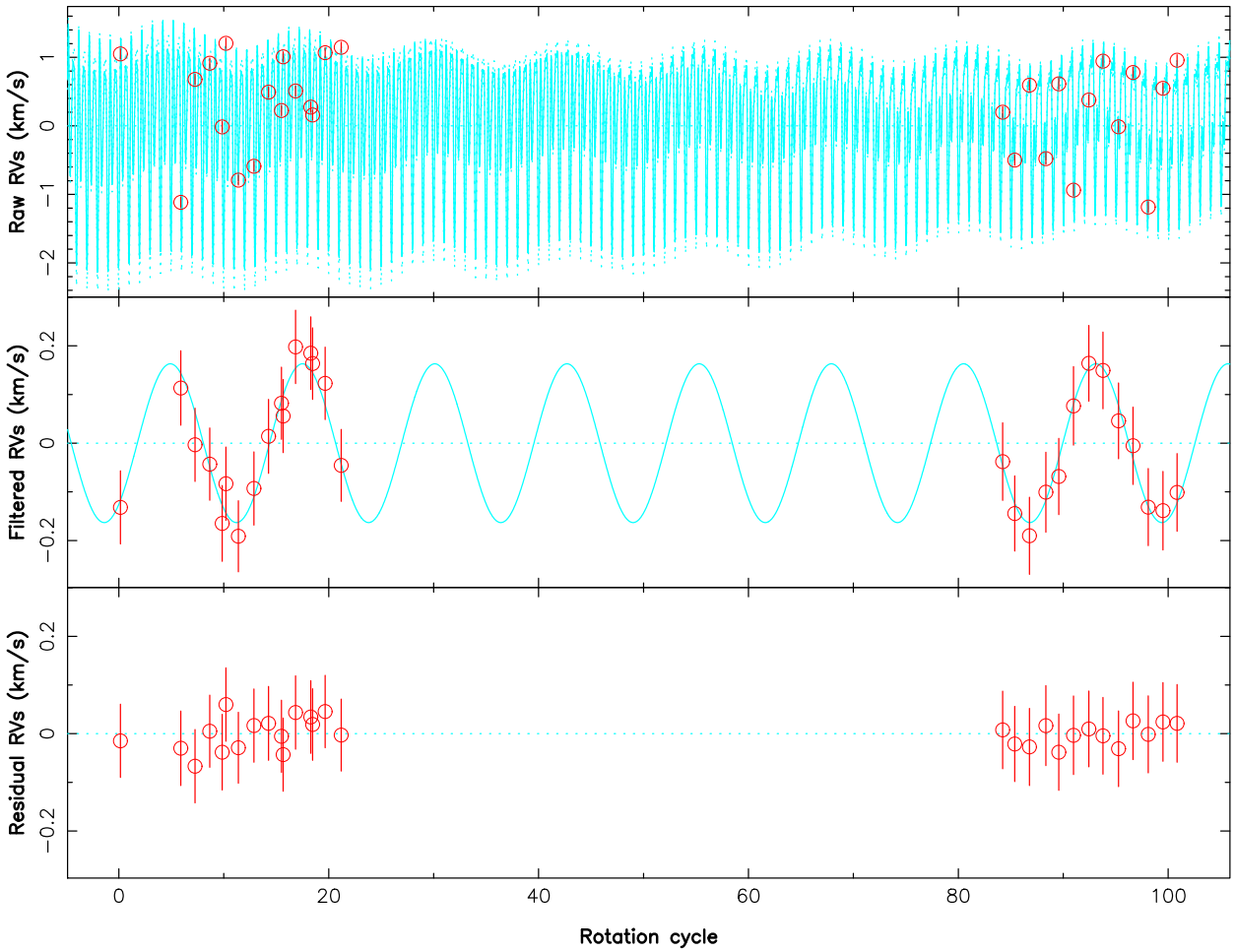

Figure 4.6 – RV curves for a GPR fit of the activity jitter, with parameters K=0.163 km s^{-1}, $P_{\rm orb}$ =12.61 $P_{\rm rot}$, ϕ=0.766, θ_1=1.19 km s^{-1}, θ_2=1.0005 $P_{\rm rot}$, θ_3=180 $P_{\rm rot}$, θ_4=0.50 $P_{\rm rot}$. *Top:* raw RVs and their error bars are shown in red, the solid cyan curve is the sum of the activity jitter predicted by GPR and the planet signal, and the dashed cyan lines show the 68.3% confidence intervals about the prediction around this model. Middle panel: filtered RVs and their error bars, resulting from the subtraction of the GP-fitted activity jitter from the raw RVs (in red), and the sine curve corresponding to the assumed planet signal (in cyan). *Bottom:* residual RVs resulting from the subtraction of the planet signal from the filtered RVs, and their error bars. The residual RVs feature a rms value of 29 m s^{-1}, i.e. the GP fits the RVs down to $\chi^2_{\rm r}$ =0.151.

With an age of $\simeq$17 Myr, TAP 26 is already an aging T Tauri star and on the verge of becoming a post T Tauri star, as demonstrated by its complex geometry and weaker dipole field component (consistent with TAP 26 having a mostly radiative interior). The hJ in a nearly circular orbit that we have discovered in the young system TAP 26 is better explained by type II disc migration than by planet-planet scattering coupled to tidal circularisation.

More observations of TAP 26, featuring in particular a more regular temporal sampling, are currently under analysis to better determine the characteristics of the newborn hJ we detected.

Table 4.4 – Results yielded by the methods ZDI #1, ZDI #2 and GPR, for the two periods ≃15 $P_{\rm rot}$ and ≃13 $P_{\rm rot}$. From top to bottom: reflex motion semi-amplitude K, phase of inferior conjunction ϕ relative to cycle 11.0, orbital period $P_{\rm orb}$ in units of $P_{\rm rot}$, orbital period $P_{\rm orb}$ in days, semi-major axis a, $M \sin i$, BJD of inferior conjunction $\mathrm{BJD_c}$, natural logarithm of relative likelihood as compared to the best case $\mathcal{L}_r$, GP amplitude θ_1 and GP recurrence timescale θ_2. Results are displayed in bold font when the period is found with the highest likelihood using the corresponding method.

	ZDI #1	ZDI #2	GPR
K ($\mathrm{km\,s^{-1}}$)	0.133 ± 0.021	$\mathbf{0.154 \pm 0.022}$	0.149 ± 0.026
ϕ	0.715 ± 0.024	$\mathbf{0.671 \pm 0.035}$	0.728 ± 0.033
$P_{\rm orb}$ ($P_{\rm rot}$)	15.27 ± 0.14	$\mathbf{15.29 \pm 0.15}$	15.12 ± 0.20
$P_{\rm orb}$ (d)	10.90 ± 0.10	$\mathbf{10.91 \pm 0.11}$	10.79 ± 0.14
a (au)	0.0974 ± 0.0032	$\mathbf{0.0975 \pm 0.0032}$	0.0968 ± 0.0032
$M \sin i$ ($\mathrm{M_{Jup}}$)	1.49 ± 0.25	$\mathbf{1.73 \pm 0.27}$	1.66 ± 0.31
$\mathrm{BJD_c}$ (2,457,340+)	9.54 ± 0.26	$\mathbf{9.06 \pm 0.38}$	9.71 ± 0.36
$\log \mathcal{L}_r$	-0.53	**0.00**	-0.25
θ_1 ($\mathrm{km\,s^{-1}}$)			1.19 ± 0.21
θ_2 ($P_{\rm rot}$)			1.0004 ± 0.0002
K ($\mathrm{km\,s^{-1}}$)	0.107 ± 0.021	0.148 ± 0.025	$\mathbf{0.163 \pm 0.028}$
ϕ	0.724 ± 0.031	0.677 ± 0.038	$\mathbf{0.766 \pm 0.030}$
$P_{\rm orb}$ ($P_{\rm rot}$)	12.76 ± 0.14	12.83 ± 0.12	$\mathbf{12.61 \pm 0.13}$
$P_{\rm orb}$ (d)	9.11 ± 0.10	9.16 ± 0.09	$\mathbf{8.99 \pm 0.09}$
a (au)	0.0864 ± 0.0028	0.0868 ± 0.0028	$\mathbf{0.0858 \pm 0.0028}$
$M \sin i$ ($\mathrm{M_{Jup}}$)	1.13 ± 0.23	1.56 ± 0.28	$\mathbf{1.71 \pm 0.31}$
$\mathrm{BJD_c}$ (2,457,340+)	10.14 ± 0.28	9.69 ± 0.35	$\mathbf{10.54 \pm 0.27}$
$\log \mathcal{L}_r$	-6.87	-3.61	**0.00**
θ_1 ($\mathrm{km\,s^{-1}}$)			$\mathbf{1.19 \pm 0.21}$
θ_2 ($P_{\rm rot}$)			$\mathbf{1.0005 \pm 0.0002}$

4.2 Results on V410 Tau

4.2.1 Jitter filtering

Radial velocity values were derived for all spectra except the 3 with low S/N and the 6 in which we identified flares (see section 3.1.2). The raw RVs present modulations whose amplitude vary between 4 – 8.5 $\mathrm{km\,s^{-1}}$, with a global rms of 1.8 $\mathrm{km\,s^{-1}}$. Like with the photometric data, the RV variations are the lowest in 2009 Jan and the strongest in 2013 Dec.

The activity jitter is modelled with two different techniques, ZDI and GPR. Raw RVs and jitter models are plotted in figure 4.7 and listed in Yu et al. (2017). The phase plot of the MCMC is displayed in figure 4.8 and the best fit is shown in figure 4.7, together with the ZDI fits. We note that, contrary to ZDI, GPR, being capable of describing intrinsic variability in a consistent way, is able to fit our whole 8-year-long data set with one model. We obtain $\theta_1 = 1.8^{+0.2}_{-0.2}$ $\mathrm{km\,s^{-1}}$, $\theta_2 = 0.9991 \pm 0.0002$ $P_{\rm rot}$, $\theta_3 = 86^{+24}_{-19}$ $P_{\rm rot}$ and $\theta_4 = 0.35 \pm 0.03$ $P_{\rm rot}$.

The rms of the filtered RVs for each epoch and each method are summarized in table 4.5. The RV curve filtered from the ZDI model presents a global rms of 0.167 $\mathrm{km\,s^{-1}}$, i.e. $\sim 2\langle\sigma_{\rm RV}\rangle$. The epoch where the filtering is most efficient is 2009 Jan, although the rms of the filtered RVs is only at $1.5\langle\sigma_{\rm RV}\rangle$, and it goes up to $3\langle\sigma_{\rm RV}\rangle$ in 2011 Jan and 2013 Dec. On the other hand, the GPR model filters the RV out down to $0.076\,\mathrm{km\,s^{-1}} = 0.94\langle\sigma_{\rm RV}\rangle$.

Lomb-Scargle periodograms for both raw and filtered RVs, for both methods (figure 4.9 for each individual epoch, 4.10 for the whole data set), show that the stellar rotation period or its

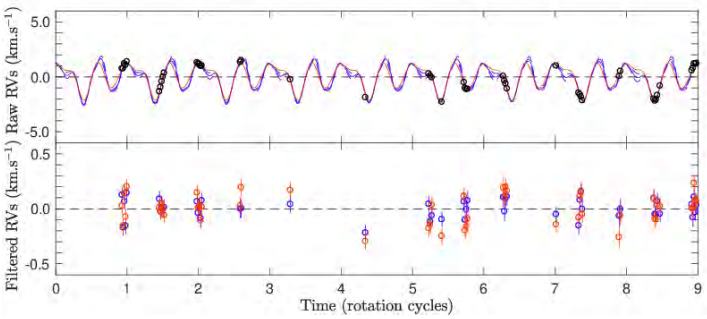

(a) 2009 Jan. Respective rms: 1.20, 0.13, 0.08 km s^{-1}

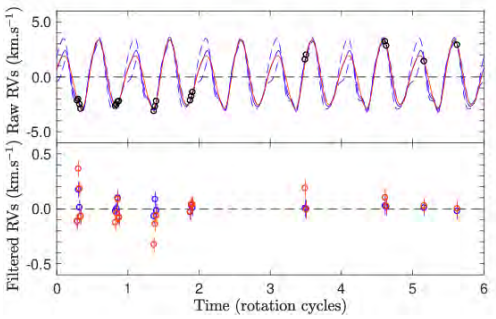

(b) 2011 Jan. Respective rms: 2.40, 0.14, 0.06 km s^{-1}

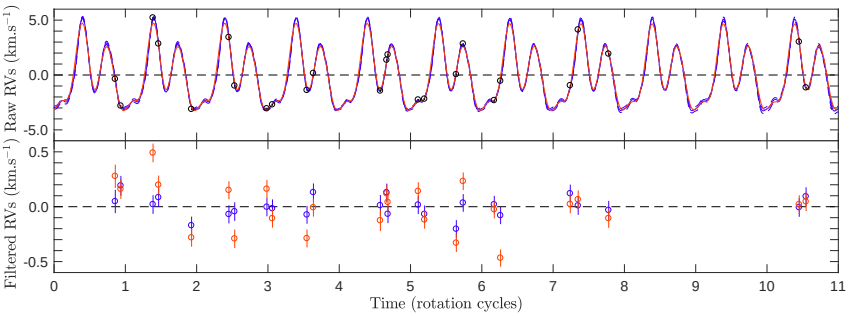

(c) 2013 Dec. Respective rms: 2.43, 0.22, 0.09 km s^{-1}

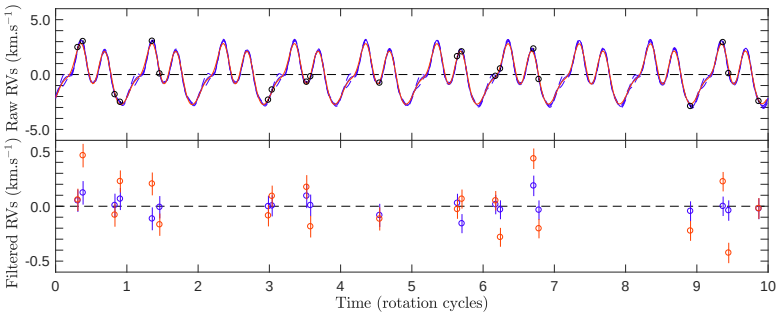

(d) 2015 Dec. Respective rms: 1.93, 0.22, 0.08 km s^{-1}

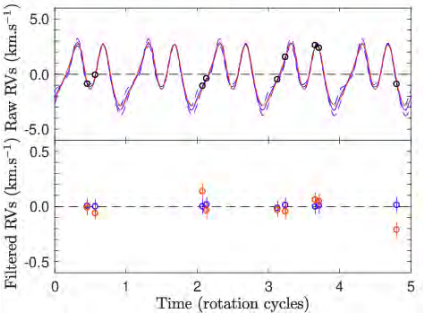

(e) 2016 Jan. Respective rms: 1.41, 0.09, 0.01 km s^{-1}

Figure 4.7 – Raw and filtered RVs of V410 Tau for each observation epoch. On each figure, the top plot depicts the raw RVs (red dots), the ZDI reconstruction (red full line) and the GP fit (blue full line with 1-σ area of confidence marked as blue dashed lines). The bottom plot depicts the RVs filtered from the ZDI-modelled activity (red dots) and the RVs filtered from the GP-modelled activity (blue dots). Note the different scales on the y-axis between the filtered and raw RVs. The subcaptions indicate the rms of the raw RVs, the ZDI-filtered RVs and the GPR-filtered RVs respectively. All rotational cycles are displayed as in table A1 of Yu et al. (2019).

first harmonic are clearly present in 2009 Jan and 2011 Jan, but not well retrieved in 2013 Dec, 2015 Dec and 2016 Jan. However the periodogram for the whole $\mathrm{RV_{raw}}$ data set presents neat peaks at P_{rot} and its first two harmonics. P_{rot} and its first harmonic are well filtered out by both modelling methods, and the second harmonic is well filtered out in the GP residuals. A weak signal remains at $P_{\mathrm{rot}}/3$ in the ZDI residuals but looking at a phase-folded plot does not reveal any particularly obvious tendency, leading us to suspect that it mostly reflects the contribution of a few stray points. No other period stands out with a false-alarm-probability lower than 5%, which

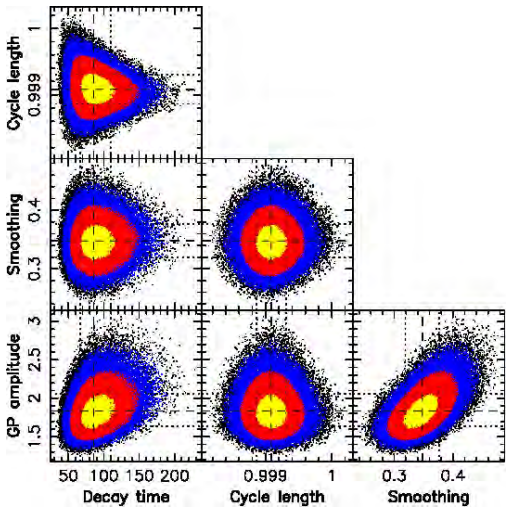

Figure 4.8 – Phase plot of the MCMC-GPR run on the raw RVs of V410 Tau, model without planet. The yellow, red and blue colors indicate respectively the 1σ-, 2σ- and 3σ-areas of confidence, and the optimal values for the hyperparameters are marked with black dashed lines, with 1σ-intervals marked with black dotted lines. GP amplitude (θ_1): $1.8^{+0.2}_{-0.2}$ km s^{-1}, Cycle length (θ_2): $0.9991 \pm 0.0002\, P_{\rm rot}$, Decay time ($\theta_3$): 86^{+24}_{-19} $P_{\rm rot}$, Smoothing (θ_4): 0.35 ± 0.03.

Table 4.5 – Rms of V410 Tau raw and filtered RVs, using either ZDI or GPR-MCMC. All rms RVs are given in km s^{-1}.

Epoch	2009	2011	2013	2015	2016	All
Raw	1.200	2.392	2.429	1.932	1.411	1.8
ZDI filt.	0.131	0.141	0.215	0.222	0.094	0.167
GP filt.	0.084	0.064	0.087	0.075	0.009	0.076

allows us to conclude that no planet signature is found in this data set with our filtering methods.

For the 2015-2016 points, the ability of the new version of ZDI (presented in section 3.5.1) to filter the jitter out was tested. RVs derived from the maps shown in figure 3.22 are plotted in figure 4.11 and 4.12, to be compared with RVs derived from classical ZDI maps. The rms of the filtered RVs here, 0.194 km s^{-1}, does not decrease compared to when using classical ZDI, despite the significant better fit to the profile (see section 3.5), which means our model is still too simple and cannot fully account for the observed variability. However, figure 4.12 shows that global trends in the temporal evolution of the RV curve are well-reproduced by this new ZDI model, such as the jitter maximum moving from phase 0.37 to 0.32, or the local minimum at phase 0.54 in 2015 Dec moving to 0.50 in 2016 Jan.

The period derived from the GPR on our raw RVs is shorter than the period we used to phase our data, and corresponds to a latitude of 5.5°. This period is much closer to the period derived with GPR from B_ℓ than to the period derived from Hα, showing that in this case, B_ℓ is a better activity proxy than Hα (for a more systematic study of the correlation of B_ℓ with stellar activity, see Hébrard et al., 2016). The decay time associated to RVs is much shorter than the differential rotation lap time and the decay times of the V magnitude, Hα and B_ℓ (see Table 3.4), which suggests that RVs are more sensitive to small-scale short-lived features while the photometry, Hα and B_ℓ are more sensitive to large-scale long-lasting features.

Through both processes, the residual RVs present no significant periodicity which would betray the presence of a potential planet. To estimate the planet mass detection threshold, GPR-MCMC was run on simulated data sets, composed of a base activity jitter (our GP model), and a circular

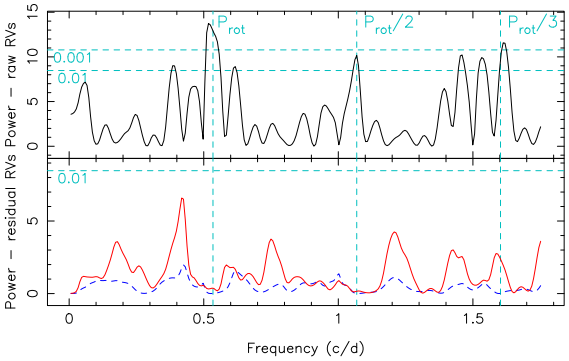

(a) 2009 Jan

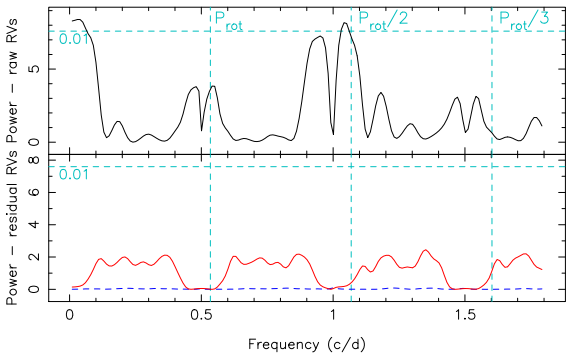

(b) 2011 Jan

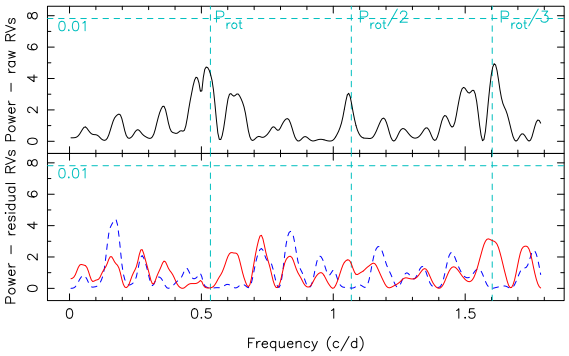

(c) 2013 Dec

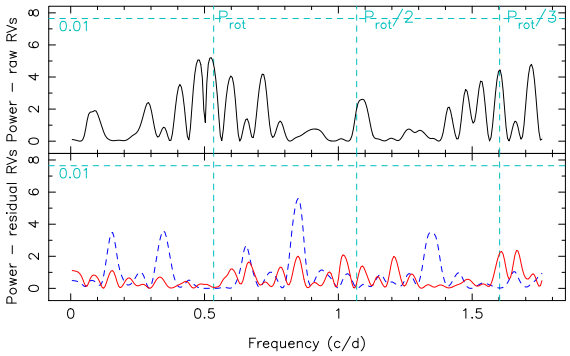

(d) 2015 Dec

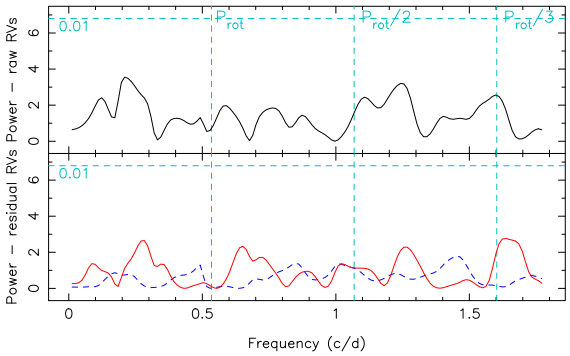

(e) 2016 Jan

Figure 4.9 – Periodograms of the raw RVs (top), of the ZDI-filtered RVs (bottom, red full line) and of the GP-filtered RVs (bottom, blue dashed line), for observation epochs 2009 Jan (a), 2011 Jan (b), 2013 Dec (c), 2015 Dec (d) and 2016 Jan (e). False-alarm probability levels of 1% and 0.1% are represented as horizontal cyan dashed lines, and $P_{\rm rot}$ and its first two harmonics as vertical cyan dashed lines.

planet signature, plus a white noise of level $0.081\,\mathrm{km\,s^{-1}}$. Various planet separations and masses were tested, and for each case, GPR-MCMC was run several times with different randomization seeds, to mitigate statistical bias. For every randomization seed, GPR-MCMC was run with a model including a planet and a model including no planet, and the difference of logarithmic marginal likelihood between them (hereafter $\Delta\mathcal{L}$) was computed. Finally, the detection threshold was set at $\Delta\mathcal{L} = 10$ (4.5σ) and the minimum detectable mass at each separation was interpolated from the mass/$\Delta\mathcal{L}$ curve. Figure 4.13 shows the planet mass detection threshold as a function of planet-star separation: we thus obtained a detectability threshold of $\sim$1 $\mathrm{M_{Jup}}$ for $a < 0.09$ au and $\sim$4.6 $\mathrm{M_{Jup}}$ for $a = 0.15$ au. The figure also shows the parameters of V830 Tau b and TAP 26 b, showing that

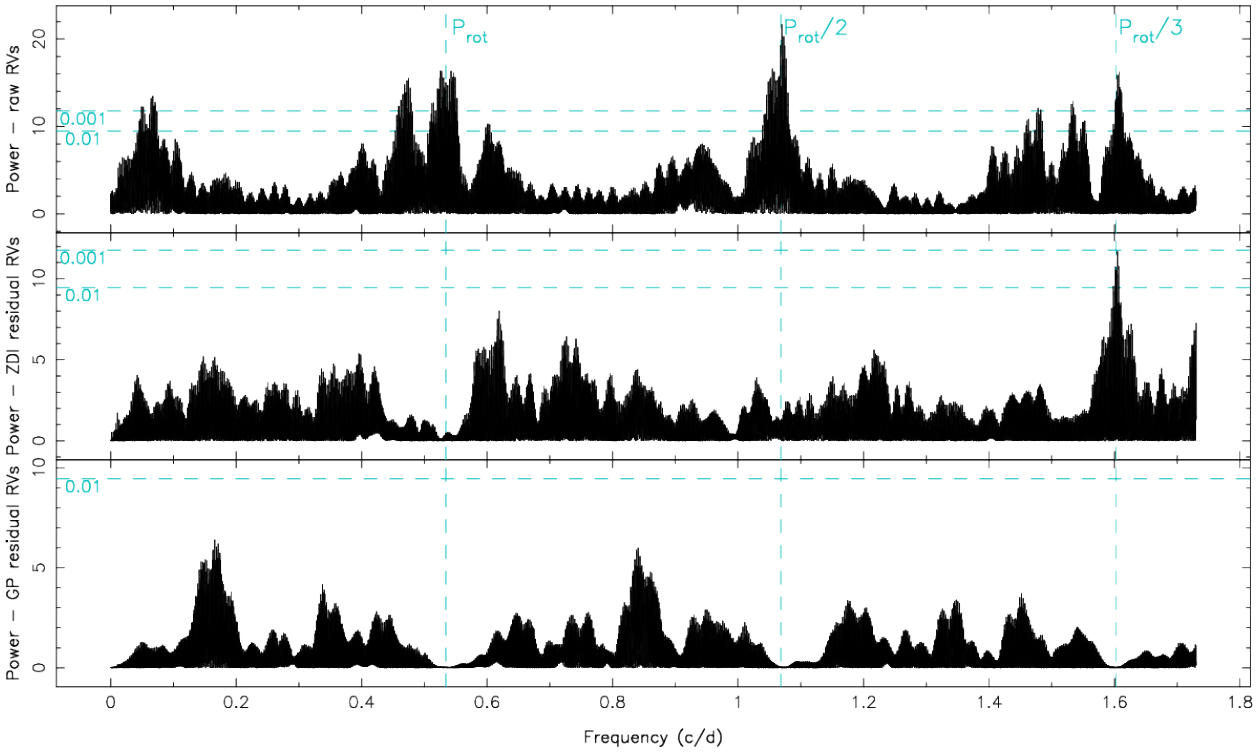

Figure 4.10 – Periodograms of the raw RVs (top), of the RVs filtered from ZDI-modelled activity (middle) and of the RVs filtered from GP-modelled activity (bottom, blue dashed line), for observation epochs 2009 Jan (a), 2011 Jan (b), 2013 Dec (c), 2015 Dec (d) and 2016 Jan (e). Periodograms of the whole data set raw RVs (top), RVs filtered from ZDI-modelled activity (middle) and RVs filtered from GP-modelled activity (bottom). False-alarm probability levels of 1% and 0.1% are represented as horizontal cyan dashed lines, and $P_{\rm rot}$ and its first two harmonics as vertical cyan dashed lines.

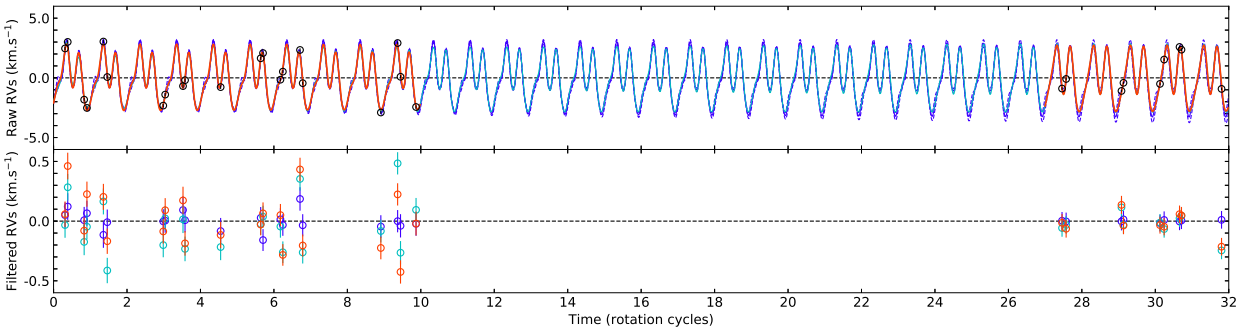

Figure 4.11 – Comparison between the GP model, the new ZDI model and the classical ZDI models for V410 Tau RVs in season 2015b-2016a. Rotation cycles are offset to concur with table A1 of Yu et al. (2019). *Top:* raw RVs (black dots) with 1σ-error bars, GP model (purple full line), new ZDI model (cyan full line) and classical ZDI models for both observation epochs 2015 Dec and 2016 Jan (red full lines). *Bottom:* RVs filtered from the GP model (purple dots), from the new ZDI model (cyan dots) or from the classical ZDI models (red dots). The rms of the filtered RVs with GP, new ZDI and classical ZDI are respectively 0.065, 0.194 and 0.193 km s^{-1}.

we would likely have detected a planet like TAP 26 b but not one like V830 Tau b. Planets beyond $a = 0.15$ au are difficult to detect due to the temporal coverage of our data, that never exceeds 19 d at any given epoch. The early depletion of the disc may have prevented the formation and/or the migration of giant exoplanets.

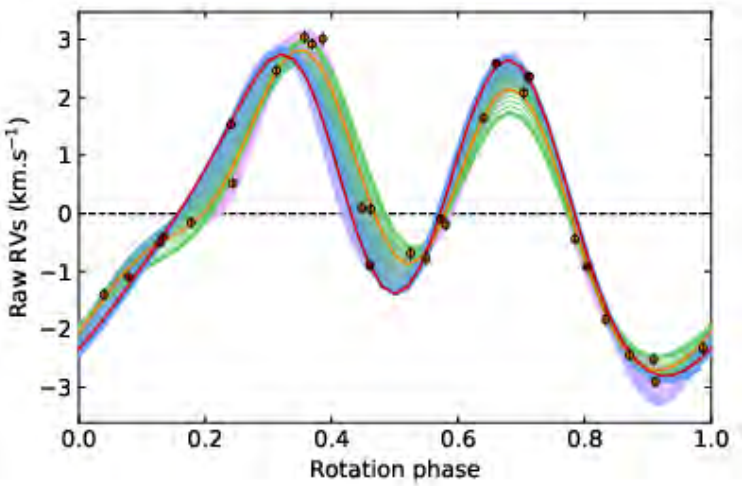

Figure 4.12 – Raw RVs of V410 Tau in the 2015b-2016a season, between cycles 1349 and 1381 as referenced in table A1 of Yu et al. (2019), plotted against stellar rotation phase. The GPR and new ZDI models are represented by full lines colored in gradients, from earliest to latest cycle, respectively pink to purple and green to blue, while the classical ZDI models for 2015 Dec and 2016 Jan are plotted in orange and red respectively. Observations are plotted as dots with 1σ-error bars, orange for 2015 Dec and 2016 Jan.

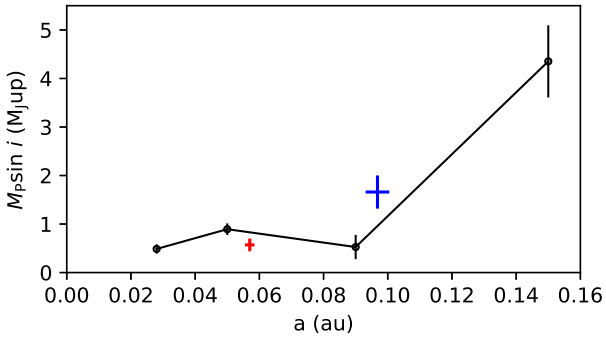

Figure 4.13 – Detectability threshold (associated to $\Delta(L) = 10$, or equivalently 4.5σ) in terms of $M \sin i$ for planets at various a, with the RV filtering technique involving GPR. V830 Tau b is plotted in red (parameters from Donati et al., 2017) and TAP 26 b in blue (parameters from Yu et al., 2017).

4.2.2 Long-term RV drift

As mentioned in section 3.2.4, the bulk RV of V410 Tau exhibits a drift throughout our 8-year campaign, from $16.30 \pm 0.05\,\mathrm{km\,s^{-1}}$ in 2008b-2009a to $16.65 \pm 0.05\,\mathrm{km\,s^{-1}}$ in 2015b-2016a. It could be a manifestation of the binary motion of V410 Tau A-B. The central binary of V410 Tau was observed twice, with a sky-projected separation of $16.8 \pm 1.4\,\mathrm{au}$ in 1991 Oct and $9.5 \pm 0.3\,\mathrm{au}$ in 1994 Oct (0.13 ± 0.01 arcsec and 0.074 ± 0.002 arcsec resp. in Ghez et al., 1995), and a mass ratio of 0.20 ± 0.10 (Kraus et al., 2011). Assuming a mass ratio of 0.2 and an edge-on circular orbit, we find that an orbit of the primary star of radius 6.0 au, i.e. binary separation 36.0 au and period 166 yr, fits our bulk RVs and the sky-projected separations at a level of 2σ (see figure 4.14). No binary motion was detected in the 2013 to 2017 astrometry measurements of Galli et al. (2018), which is consistent with our model where the sky-projected velocity varies by only $0.13\,\mathrm{m''\,yr^{-1}}$ over these 3.5 years (roughly a 50th of the orbital period). More measurements would enable to estimate the eccentricity and potentially fit the sky-projected separations to a better level, as well as to decide whether the binary motion can explain the RV drift observed in this study.

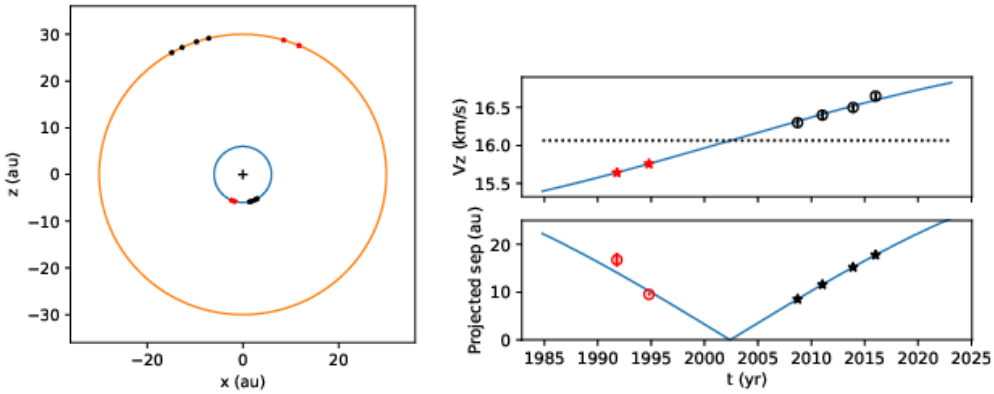

Figure 4.14 – Circular model for the binary motion of V410 Tau A and V410 Tau B: edge-on orbit, separation 36.0 au, period 166 yr and systemic radial velocity 16.06 km s^{-1}. **Left:** top-view of the model orbit, with the z-axis parallel to the line-of-sight, where the positions of V410 Tau A and B according to the model are marked by red and black stars at the times of the separation measurements and of our spectropolarimetric seasons (2008b-2009a, 2011a, 2013b and 2015b-2016a) respectively. **Right:** *Top:* RV_{bulk} of V410 Tau A with time, as measured by us in black dots with 1σ error bars and as derived from the model orbit in blue. The predicted RV_{bulk} at the times of the separation measurements are represented by red stars. *Bottom:* Sky-projected binary separation as a function of time, as measured by Ghez et al. 1995 in red dots with 1σ error bars, and as derived from the model orbit in blue. The predicted sky-projected separations at the dates of our observing seasons are marked in black stars.

Kraus et al. 2016 outlines a correlation between the presence of a companion under 50 au and a lack of planets, in a sample of binary stars with mass ratios $q > 0.4$, which could support the hypothesis that V410 Tau B, although having a slightly lower mass ratio ($q = 0.2 \pm 0.1$, Kraus et al., 2011), played a role in the early disc dissipation, which in turn prevented the formation of a hJ.

4.3 Results on V830 Tau

Raw RVs were computed for V830 Tau at all observation epochs: 2014b-2015a, 2015b, 2016a (Donati et al., 2015, 2016, 2017). After applying GPR-MCMC on them, we find that those RVs present modulations of semi-amplitude 0.878 ± 0.135 km s^{-1}, period 2.737 ± 0.002 d, decay time 120 ± 30 d and smoothing parameter 0.6 ± 0.1. All three methods described in 4.1 enable to detect a planetary signature of orbital period $\sim$4.93 d (4.927 ± 0.008 d with GPR-MCMC on the whole data set, compatible within error bars with the values yielded by other methods, see Donati et al., 2017) and amplitude $\sim$70 m s^{-1} (68 ± 11 m s^{-1} with GPR-MCMC on the whole data set). With GPR-MCMC, the likelihood of the model including a planet is found to be higher than that of the model without planet by a Bayes factor of 10^9. Absence of a peak at the derived orbital frequency in the periodograms of activity proxies (Hα and B_ℓ) further cements the confirmed status of this detection. V830 Tau b is a planet orbiting at 0.057 ± 0.001 au from its host star, with a mass that verifies $M_p \sin i = 0.57 \pm 0.10\,M_{Jup}$. If modelled with an eccentric orbit, the filtered RVs yield an eccentricity of 0.21 ± 0.15, not significantly high enough to say that the hJ is on an eccentric orbit. Like TAP 26 b, this detection thus suggests that V830 Tau b underwent type II migration across the protoplanetary disc.

4.4 Synthesis on MaTYSSE hot Jupiters

Regarding the hJs we detected around the ∼17 Myr TAP 26 and the ∼2 Myr V830 Tau and despite their differences (in mass in particular), it is intesting to investigate whether the evolutionary link noted between the host stars (see section 3.1) also applies to their hJs. This would actually imply that TAP 26 b migrated outwards under tidal forces from a distance of ∼0.057 au (where V830 Tau b is located) to its current orbital distance of 0.094 au, as a result of the spin period of TAP 26 being ∼15x shorter than the orbital period of TAP 26 b. This option seems however unlikely given the latest predictions of tidal interactions between a young TTS and its close-in hJ (Bolmont & Mathis, 2016), indicating that tidal forces can only have a significant impact on a hJ within 0.06 au of a solar-mass host star (for a typical TTS with a radius of $\sim 2\,R_\odot$). The most likely explanation we see is thus that TAP 26 b:

- ended up its type-II migration in the accretion disc at the current orbital distance, when TAP 26 was still young, fully convective and hosting a large-scale dipole field of a few kG similar to that of AA Tau (Donati et al., 2010a), i.e., strong enough to disrupt the disc up to a distance of 0.09 au,
- was left over once the disc has dissipated at an age significantly smaller than 2 Myr, i.e., before the large-scale field had time to evolve into a weaker and more complex topology, and the inner accretion disc to creep in as a result of the decreasing large-scale field and the subsequent chaotic accretion (e.g., Blinova et al., 2016).

Admittedly, this scenario requires favorable conditions to operate; in particular, it needs the accretion disc to vanish in less than 2 Myr, which happens to occur in no more than 10 % of single TTSs in Taurus (Kraus et al., 2012). In fact, since both TAP 26 and V830 Tau have the same angular momentum content, it is quite likely that TAP 26 indeed dissipated its disc very early as otherwise the disc would have dissipated a larger amount of angular momentum of the host star through disc coupling (see Sec. 3.5). Quantitatively speaking, assuming (i) that the hJ we detected tracks the location of the inner disc when the disc dissipated, (ii) that the spin period at this time was locked on the Keplerian period of the inner disc (equal to the orbital period of the detected hJ) and (iii) that stellar angular momentum was conserved since then, we derive that the disc would have dissipated when TAP 26 was about three times larger in radius, at an age of less than 1 Myr (according to Siess et al., 2000). Generating a magnetospheric cavity of the adequate size (0.085 – 0.097 au depending on the orbital period) would have required TAP 26 to host at this time a large scale dipole field of 0.3 – 1.0 kG for mass accretion rates in the range $\sim 10^{-9}$ – $10^{-8}\,M_\odot$/yr, compatible with the large-scale fields found in cTTSs of similar masses (e.g., GQ Lup, Donati et al., 2012).

Along with other recent reports of close-in giant planets (or planet candidates) detected (or claimed) around young stars (van Eyken et al., 2012; Donati et al., 2016; David et al., 2016; Mann et al., 2016; Johns-Krull et al., 2016; David et al., 2019b), our result may suggest a higher frequency of hJs around young solar-type stars than around more evolved stars ($\simeq$1%, Wright et al., 2012). However, this may actually reflect no more than a selection bias in the observation samples (as for their mature equivalents in the early times of velocimetric planet detections). Planets are obviously much easier to detect around non-accreting TTSs as a result of their lower level of intrinsic variability; observation samples (like that of MaTYSSE) are thus naturally driven towards young TTSs whose accretion discs vanished early, i.e., at a time when their large-scale fields were still strong and their magnetospheric gaps large, and thus for which hJs had more chances to survive type-II migration. A more definite conclusion must wait for a complete analysis of the full MaTYSSE sample. Ultimately, only a full-scale planet survey of young TTSs such as that currently carried out with SPIRou, the new generation spectropolarimeter installed at CFHT since 2018, will be able to bring a consistent picture of how young close-in planets form and migrate, how their

population relates to that of mature hJs, and more generally how young hJs impact the formation and early architecture of planetary systems like our Solar System.

5 | Conclusion and future prospects

This thesis was focused on bringing observational constraints to the theoretical scenarii of formation and migration of hot Jupiters, by searching for hJs around weak-line T Tauri stars and by characterizing their orbital properties. In order to be able to detect potential signatures of hJs in the radial velocities of such active stars, an accurate understanding of their activity is mandatory so as to filter out the RV jitter introduced by the stellar activity that contributes to RV variations at a typical level of $1\,\mathrm{km\,s^{-1}}$. Our observations also help constraining theories of stellar dynamos, as well as theories of star / planet formation. Constraining both hJ formation and stellar formation theories in parallel is crucial as the planet-star interactionsplay a major role in the evolution of both bodies and of the whole system.

5.1 Activity and magnetic fields of wTTSs

5.1.1 Surface brightness and magnetic fields of WTTSs

Our results enable to see and compare the surface brightness and magnetic topologies of three wTTSs of different masses and ages. The brightness maps of TAP 26,V410 Tau and V830 Tau all exhibit a cool polar cap, like other MaTYSSE stars LkCa 4 (Donati et al., 2014), Par 1379 (Hill et al., 2017) and V1095 Sco (Nicholson et al., 2018). However, unlike the low-complexity maps of LkCa 4, Par 1379 and V1095 Sco, our stars display a relatively spread-out distribution of spots and plages over the surface, similarly to MaTYSSE stars Par 2244 (Hill et al., 2017) and TWA 6 (Hill et al., 2019). While both TAP 26 and V830 Tau have brightness maps with 10 – 12 % spot+plage coverage, the V410 Tau brightness maps display a higher 14 – 18 % feature coverage, comparable to that of Par 2244 and TWA 6. Drawing trends from these results is not trivial, as V830 Tau, V410 Tau and Par 2244 are young ($\lesssim 2\,\mathrm{Myr}$) while TAP 26 and TWA 6 are more evolved ($> 15\,\mathrm{Myr}$), and TWA 6 is of similar mass to TAP 26 and V830 Tau ($\sim 1\,\mathrm{M_\odot}$) whereas V410 Tau and Par 2244 are more massive (1.3 – $1.8\,\mathrm{M_\odot}$).

Concerning magnetic topologies (see figure 3.21), V830 Tau has a mainly poloidal, dipolar and axisymmetric topology, as expected from this fully convective star. TAP 26, on the other hand, was found to have a rather complex magnetic topology, where the poloidal dipole only constitutes 10 % of the magnetic energy whereas the toroidal component, contributing to 30 % of the total magnetic energy, is relatively high. The level of complexity in the field topology of TAP 26 is somewhat expected from a star that has a substantial radiative core.

The magnetic topology of V410 Tau however displays an atypical topology for a fully convective star, with a strong toroidal component (half of the magnetic energy) that keeps a constant orientation throughout the 8-year span of our data, and a non-axisymmetric poloidal field. The origin of this strong toroidal component, also observed on fully convective, $0.79 \pm 0.05\,\mathrm{M_\odot}$ LkCa 4, is unclear. Perhaps the high toroidal energy stems from a non-standard dynamo, or from remnants of subsurfacic radial shears dating back to the cTTS years, or even from a miraculous survival of the primordial toroidal energy generated after the second core collapse. For the latter hypothesis,

the early dissipation of the disc could be a lead to explore as to why such toroidal energy is not observed on cTTSs.

Completing the analysis of the MaTYSSE sample and analyzing more data, e.g. collected with SPIRou, is therefore necessary to clarify the magnetic panorama of wTTSs.

5.1.2 Intrinsic variability of surface brightness and magnetic topologies

Thanks to the span of our data sets, we were able to outline the presence of intrinsic variability of brightness distribution and magnetic topology at the surface of our three targets.

Made obvious by comparing the ability of ZDI to fit longer data sets versus shorter data sets, even with differential rotation modelling, this intrinsic variability was studied thanks to Gaussian processes. By fitting the RVs, the light curves, the Hα EW and the longitudinal field B_ℓ, we obtained variation time scales of $\sim$130 d for TAP 26 and $\sim$160 d for the RVs of V410 Tau, and $\geq$ 250 d for the V magnitude, Hα EW and B_ℓ for V410 Tau. These quantities are paramount to gauge the activity level of a star (e.g. the correlation of B_ℓ with stellar activity, Hébrard et al., 2016), and our study of V410 Tau offers a comparison between them on a 144-spectra 8-year-spanning high-resolution spectropolarimetric data set. The period derived from GPR on our V410 Tau raw RVs is shorter than the photometric period found by Stelzer et al. (2003) by 0.03 %, and is much closer to the period derived with GPR from B_ℓ than to the period derived from the Hα EW. It demonstrates that, for studying RV curves, B_ℓ is in this case a better activity proxy than Hα and that all activity indexes are not equal as far as what they can tell us about surface features affecting RV curves (see also Haywood et al., 2016). The decay time associated to RVs is much shorter than the differential rotation lap time and the decay times of the V magnitude, which suggests that RVs are more sensitive to small-scale short-lived features while the photometry is more sensitive to large-scale long-lasting features. The Hα EW and B_ℓ also exhibit long decay times, albeit with uncertainties too large to draw a definite conclusion.

A tentative new implementation of ZDI, where a map of the brightness variation rate is fitted alongside the brightness itself, was applied to a combined V410 Tau data set with mixed results: it significantly improves χ^2_r (from $\chi^2_\mathrm{r} = 2.5$ with classical ZDI to $\chi^2_\mathrm{r} = 1$ with new ZDI) and major trends in the evolution of the RV curve are well reproduced compared to classical ZDI models for each subset and to the GPR model, but residuals still display a significant rms of $\gtrsim 2\sigma$. In the future, self-consistent methods that combine the physical realism of ZDI and the flexibility of GPR will be developped and applied to more MaTYSSE data, as well as data from SPIRou (SpectroPolarimetre InfraRouge), the new infrared spectropolarimeter installed at CFHT.

5.1.3 Differential rotation and dynamos of wTTSs

Our results also brought new observational constraints on the differential rotation of young stars, with our three targets displaying an equator rotating faster than the poles, and TAP 26 having an almost solar level of differential rotation (0.0492 ± 0.0010 rad/d). The differential rotation of V410 Tau is on average much lower, at 0.0097 ± 0.0003 rad/d, i.e. 5 – 6 times weaker than that of the Sun, with values in individual epochs varying between 8.1 ± 1.8 mrad/d and 19.0 ± 4.3 mrad/d. Not many observational results have been obtained on the differential rotation of wTTSs yet; within MaTYSSE, the young V830 Tau displays a differential rotation of 17.2 ± 1.4 mrad/d, suggesting a trend that differential rotation increases with age, as the radiative core develops. This is consistent with what is observed for M dwarfs (Morin et al., 2010).

The combination of our differential rotation estimate and the 8-year-long span of our photometric V410 Tau data set allowed us to follow the latitudinal evolution of the main brightness features year after year, and to notice that they underwent a poleward migration from latitude 0 in 2008 to $\sim$50° in 2016. This is reminiscent of the Solar butterfly diagram, albeit reversed, and would suggest

that the dynamo wave, if cyclic, has a period of at least 8 yr and likely much longer (16 yr if our data covers only one half of a full cycle). This is accompanied by an almost-monotonous increase in the strength of the poloidal dipole from ∼200 to ∼500 G. This shows at least the existence of long-term variations on the surface of V410 Tau. Besides, for V410 Tau, the poloidal field almost doubles in strength throughout our observation run, but measures of $d\Omega$ on individual yearly data sets do not show an increase, which, if we are to assume a cyclic dynamo, would imply a phase shift between the magnetic field and the differential rotation. Photometric data over the past 60 yr show a complex evolution of the light curve of V410 Tau, and previous studies have showed cyclical variations of the light curve amplitude and extrema (Stelzer et al., 2003; Sokoloff et al., 2008; Oláh et al., 2009; Grankin & Artemenko, 2009; Savanov, 2012; Hambálek et al., 2019), but whether or not V410 Tau has a full-fledged cycle with polarity reversals like the Sun remains to be determined.

5.2 Angular momentum evolution of young stars & disc lifetimes

We observe that mildly accreting cTTSs with a strong dipolar/poloidal component in their magnetic fields tend to have rotation periods around 6 – 9 d (Donati et al., 2008a, 2010a, 2012). Taking this as a starting assumption, we computed the ages at which our wTTSs lost their coupling with their discs (see figure 3.2). In both cases, this loss would have been caused by the depletion of the inner disc. To do so, we used the stellar evolution models of Siess et al. (2000) to extract the moments of inertia, and, assuming that the wTTSs contracted at constant angular momentum after being decoupled from their disc, derived their radii at the time when they started spinning up. The stellar evolution models gave us the ages corresponding to those radii.

V410 Tau is already one of the youngest observed wTTSs, but its age at disc dissipation was estimated to ∼0.2 Myr, albeit with a relatively low precision, from our measurement of the stellar radius, and corroborated with the magnetic topologies we reconstructed from our spectra. It is a three-star system composed of an inner close binary A-B (mass ratio 0.2 ± 0.1, sky-projected eparation 16.8 ± 1.4 au) and a third component C further away (mass ratio $0.08^{+0.10}_{-0.08}$, sky-projected eparation 36 ± 3 au). V410 Tau was accounted for in the survey of Kraus et al. (2012) showing a correlation between the presence of a companion within 50 au and the early depletion of the accretion disc; our measurements of the age of V410 Tau, our guess of its age at disc dissipation and our guess at the separation between V410 Tau A-B (36 au) corroborate the trend found by that study, as well as give more precise parameters for that star.

Moreover, from the orbital separation of the hot Jupiter discovered within this work, TAP 26 was estimated to have lost its disc also at an age of less than 1 Myr.

The age estimates vary depending on which evolution model is chosen, but newer models (BHAC15, Baraffe et al. 2015, STAREVOL3.4, Amard et al. 2019) give our stars even younger ages (∼0.5, ∼13 and ∼1.5 Myr for V410 Tau, TAP 26 and V830 Tau resp.) than the models of Siess et al. (2000), which reinforces the evidence that these stars dissipated their discs in less than 1 Myr. This makes our three stars some of the wTTSs that lost their discs the earliest (Richert et al., 2018), and, as a result, they are among the fastest rotating wTTSs as they started spinning up early (Gallet & Bouvier, 2015).

5.3 Formation, migration, subsequent evolution of hot Jupiters

As of today, seven giant planets have been detected around wTTSs: V830 Tau b (Donati et al., 2016), K2-33 b(David et al., 2016), TAP 26 b and V1298 Tau b, c, d and e (David et al., 2019b), with a few other candidate close-by giant planets around young stars (e.g. CI Tau, Johns-Krull et al., 2016). V830 Tau b ($0.77 \pm 0.15\,M_{Jup}$, 4.93 ± 0.05 d) and TAP 26 b ($1.66 \pm 0.31\,M_{Jup}$, 10.79 ± 0.14 d)

were discovered through MaTYSSE, while K2-33 b and V1298 Tau b, c, d and e were detected via transits in the stellar light curve, and their masses are not yet well constrained. While not yet a statistically representative sample, we can outline important conclusions from these first results:

- it is possible to form hJs in time scales of as low as 2 Myr,
- both V830 Tau b and TAP 26 b have a quasi-circular orbit, which favors the planet-disc type II migration scenario over planet-planet scattering followed by tidal circularization,
- with two detections in a ∼30-star sample (not all of which having been studied as of today), one may wonder whether (i) the frequency of hJs is higher around young stars than around mature ones (≃1%, Wright et al., 2012), or (ii) our sample is biased towards planet-hosting stars. Concerning (i), hypotheses explaining the depletion of hJs as the star ages towards the MS include tidal and magnetic star-planet interactions that can end up ejecting the planet out of the system, or on the contrary precipitating it into the star (Strugarek et al., 2017). Concerning (ii), because planets are easier to detect around non-accreting TTSs as a result of their lower level of variability, observation samples like that of MaTYSSE are naturally driven towards young TTSs whose accretion discs vanished early, i.e. at a time when their large-scale fields were still strong and their magnetospheric gaps large, and thus for which hJs had more chances to survive type-II migration. A more definite conclusion must wait for a complete analysis of the full MaTYSSE sample.

No hJ was found around V410 Tau, and our results exclude the presence of a $> 1\,M_{Jup}$ planet within a 0.1 au radius of the star at a 3σ-level. The formation and/or the migration of giant exoplanets was perhaps prevented by the very early depletion of the disc, which, in turn, could potentially be related to the M dwarf companion. To tie in to the previous paragraph, there might exist an optimal age to dissipate the disc for forming hJs, i.e. not before planets have had the time to grow, but not after the field has weakened, causing the magnetospheric gap to shrink. Our age estimates would place this optimum somewhere in 0.3 – 1 Myr, but statistically significant conclusions must wait for the results of many more large surveys, including the SPIRou (Spectropolarimetre InfraRouge) Legacy Survey (SLS), where ∼60 wTTSs are to be monitored in the near-infrared wavelength domain.

5.4 Future perspectives

Concerning the stars studied in this thesis, it will be interesting to analyze further RV curves of TAP 26, in order to better constrain the orbital period of the planet and make it stand out from the aliases caused by the sampling of the observations analyzed so far. V410 Tau is a very interesting target for the study of dynamo because of the wealth of data and studies published about it; in particular, on top of the 60-year-long photometric monitoring mentioned above, several Doppler maps have been reconstructed. A study compiling all the Doppler maps, put in parallel with the light curve of V410 Tau, would perhaps enable to learn more on the secular magnetic activity of this young and massive wTTS.

In the near future, completing the analysis of the MaTYSSE sample will help getting a better general picture of the magnetic topologies of wTTSs, and better understand their dynamos. The ongoing aforementioned SLS will include the observation of ∼60 wTTSs by high-resolution spectropolarimeter SPIRou, in the near-infrared wavelength domain, where the Zeeman effect is larger and thus the magnetic field can be reconstructed with more precision. This will also be an important addition to the statistical study of wTTS dynamos. Moreover, new imaging techniques that can reconstruct the intrinsic variability of the stellar surfaces are under development, which will enable to finely model the evolution of wTTS activity on month-long / year-long time scales.

The study of young planetary systems will also benefit from the completion of the MaTYSSE analysis and the SLS. With the ∼60-strong sample of the SLS, we will be able to draw more reliable

statistics from our young-hJ-seeking campaigns. Moreover, magnetic activity manifests differently in the spectra, and a fortiori in the RV curves, depending on wavelength, whereas hJ signatures do not. Therefore, adding infrared spectropolarimetric observations of planet-hosting stars that have been observed by ESPaDOnS and/or NARVAL would enable to confirm the planetary signatures in the RVs and better constrain them.

Transiting young giant planets have been detected in the past few years from K2 light curves (K2-33 b, Mann et al. 2016; David et al. 2016 and V1298 Tau b, c, d and e, David et al. 2019b), and observing them with SPIRou would potentially enable to measure their obliquity, and observe their atmoshere. With the arrival of more space-based photometry data for the detection of exoplanets (from the currently operating telescope TESS, or from the upcoming CHEOPS, PLATO and ARIEL), we can expect more transiting young giant planets to be detected. Characterizing their orbits and atmospheres thanks to both photometry data and spectroscopic monitoring, with for example SPIRou or the upcoming nIRPS to be placed in Chile, will be a huge step forward in the study of the early evolution of giant planets.

Conclusion et perspectives futures

Cette thèse a visé à apporter des contraintes observationnelles aux scénarios théoriques de formation et de migration des Jupiters chauds (hJs), en recherchant les hJs autour des étoiles T Tauri à raies faibles (wTTSs) et en caractérisant leurs propriétés orbitales. Afin de pouvoir détecter les signatures potentielles des hJs dans les vitesses radiales (RVs) de ces étoiles actives, une compréhension précise de leur activité est nécessaire afin de filtrer la perturbation en RV introduite par l'activité stellaire qui contribue aux variations de RV à un niveau typique de $1\,\mathrm{km\,s^{-1}}$. Nos observations contribuent également à contraindre les théories des dynamos stellaires, ainsi que les théories de la formation des étoiles / des planètes. Il est crucial de contraindre en parallèle les théories de la formation de hJ et de la formation stellaire, car les interactions étoile-planète jouent un rôle majeur dans l'évolution des deux corps et de l'ensemble du système.

Activité et champs magnétiques des wTTSs

Brillance et champs magnétiques à la surface des WTTSs

Nos résultats permettent de voir et de comparer les cartes de brillance et les topologies magnétiques de trois wTTSs de masses et d'âges différents. Les cartes de brillance de TAP 26, V410 Tau et V830 Tau montrent toutes une calotte polaire froide, comme les autres étoiles MaTYSSE LkCa 4 (Donati et al., 2014), Par 1379 (Hill et al., 2017) et V1095 Sco (Nicholson et al., 2018). Cependant, contrairement aux cartes peu complexes de LkCa 4, Par 1379 et V1095 Sco, nos étoiles présentent une distribution relativement étalée des taches et des plages à leur surface, comme les étoiles MaTYSSE Par 2244 (Hill et al., 2017) et TWA 6 (Hill et al., 2019). Tandis que TAP 26 et V830 Tau ont des cartes de luminosité avec une couverture en taches et plages de 10 – 12 %, les cartes de brillance de V410 Tau montrent une couverture plus large, 14 – 18 %, comparable à celles de Par 2244 et TWA 6. Trouver des tendances dans ces résultats n'est pas trivial, car V830 Tau, V410 Tau et Par 2244 sont jeunes ($\lesssim 2\,\mathrm{Myr}$) tandis que TAP 26 et TWA 6 sont plus évoluées ($> 15\,\mathrm{Myr}$), et TWA 6 est de masse similaire à TAP 26 et V830 Tau ($\sim 1\,\mathrm{M_\odot}$) alors que V410 Tau et Par 2244 sont plus massives (1.3 – $1.8\,\mathrm{M_\odot}$).

En ce qui concerne les topologies magnétiques (voir figure 3.21), V830 Tau a une topologie principalement poloïdale, dipolaire et axisymétrique, comme attendu pour cette étoile entièrement convective. TAP 26, d'autre part, révèle une topologie magnétique plutôt complexe, où le dipôle poloïdal ne constitue que 10 % de l'énergie magnétique alors que la composante toroïdale, contribuant à 30 % de l'énergie magnétique totale, est relativement élevée. Le niveau de complexité de la topologie du champ de TAP 26 n'est pas inattendu pour une étoile avec un noyau radiatif bien développé.

La topologie magnétique de V410 Tau présente cependant une topologie atypique pour une étoile entièrement convective, avec une forte composante toroïdale (50 % de l'énergie magnétique) qui maintient une orientation constante pendant les 8 années que couvrent nos données, ainsi qu'un champ poloïdal non axisymétrique. L'origine de cette forte composante toroïdale, également

observée pour la wTTS entièrement convective LkCa 4, de masse $0.79 \pm 0.05\,\mathrm{M}_\odot$, n'est pas claire. Peut-être cette forte énergie toroïdale provient-elle d'une dynamo non standard, ou des restes d'un cisaillement radial subsurfacique remontant à la phase cTTS, ou même d'une survie miraculeuse de l'énergie toroïdale primordiale produite après le deuxième effondrement du cœur pré-stellaire. Pour cette dernière hypothèse, la dissipation précoce du disque pourrait être une piste à explorer pour expliquer pourquoi une telle énergie toroïdale n'est pas observée sur les cTTSs.

Il est donc nécessaire de compléter l'analyse de l'échantillon MaTYSSE et d'analyser d'autres données, par exemple celles recueillies avec SPIRou, pour clarifier le panorama magnétique des wTTSs.

Variabilité intrinsèque de la brillance surfacique et des topologies magnétiques

Grâce à l'étendue de nos jeux de données, nous avons pu mettre en évidence la présence d'une variabilité intrinsèque de la distribution de brillance et de la topologie magnétique à la surface de nos trois cibles.

Mise en évidence en comparant la capacité de ZDI à ajuster des jeux de données plus longs par rapport à des jeux de données plus courts, même avec la modélisation de la rotation différentielle, cette variabilité intrinsèque a été étudiée grâce aux processus gaussiens. En ajustant les RVs, les courbes de lumière, la largeur équivalente (EW) de Hα et le champ longitudinal B_ℓ, nous avons obtenu des échelles de temps de variation de $\sim$130 d pour TAP 26, de $\sim$160 d pour les RVs de V410 Tau, et ≥ 250 d pour la magnitude V, la EW de Hα et le B_ℓ de V410 Tau. Ces quantités sont primordiales pour mesurer le niveau d'activité d'une étoile (pour la corrélation de B_ℓ avec l'activité stellaire, voir par exemple Hébrard et al., 2016), et notre étude de V410 Tau offre une comparaison entre elles sur un jeu de données spectropolarimétriques haute résolution de 144 spectres sur 8 ans. La période dérivée de la régression par processus gaussiens (GPR) sur nos RVs brutes est plus courte que la période photométrique trouvée par Stelzer et al. (2003) de 0.03 %, et est beaucoup plus proche de la période dérivée avec GPR de B_ℓ que de la période dérivée de la EW de Hα. Ceci montre que, pour l'étude des courbes RV, B_ℓ est dans ce cas un meilleur indicateur d'activité que Hα et que tous les indices d'activité ne sont pas égaux dans la mesure où ils peuvent nous renseigner sur les caractéristiques de surface affectant les courbes RV (voir aussi Haywood et al., 2016). Le temps caractéristique de variation intrinsèque associé aux RVs est beaucoup plus court que le temps caractéristique de rotation différentielle et que le temps caractéristique de variation intrinsèque de la magnitude V, ce qui suggère que les RVs sont plus sensibles aux taches de courte vie et de petite taille alors que la photométrie est plus sensible aux taches de longue vie et de grande taille. La EW de Hα et B_ℓ présentent également des temps caractéristiques longs, bien qu'avec des incertitudes trop grandes pour en tirer une conclusion définitive. Nous avons noté que le temps caractéristique de rotation différentielle de TAP 26 est proche de son échelle de temps de variabilité intrinsèque, alors qu'il est beaucoup plus long ($\sim$600 d) pour V410 Tau, au moins comparé à l'échelle de temps de variation des RVs.

Une nouvelle implémentation provisoire de ZDI, où une carte du taux de variation de la brillance est ajustée parallèlement à la brillance elle-même, a été appliquée à un jeu de données étendu de V410 Tau, avec des résultats mitigés : elle améliore considérablement χ^2_r (de $\chi^2_\mathrm{r} = 2.5$ avec ZDI classique à $\chi^2_\mathrm{r} = 1$ avec le nouveau ZDI) et les grandes tendances dans l'évolution de la courbe RV sont bien reproduites par rapport aux modèles ZDI classique pour chaque sous-ensemble et au modèle GPR, mais les résidus affichent toujours une valeur efficace significative de $\gtrsim 2\sigma$. Dans le futur, des méthodes cohérentes combinant le réalisme physique de ZDI et la flexibilité du GPR seront développées et appliquées à d'autres données MaTYSSE, ainsi qu'aux données de SPIRou (SpectroPolarimetre InfraRouge), le nouveau spectropolarimètre infrarouge installé au CFHT.

Rotation différentielle et dynamos des wTTSs

Nos résultats ont également apporté de nouvelles contraintes observationnelles sur la rotation différentielle des étoiles jeunes, nos trois cibles présentant un équateur tournant plus vite que les pôles, et TAP 26 ayant un niveau de rotation différentielle presque solaire (0.0492 ± 0.0010 rad/d). La rotation différentielle de V410 Tau est en moyenne beaucoup plus faible, de 0.0097 ± 0.0003 rad/d, c'est-à-dire 5 – 6 fois plus faible que celle du Soleil, les valeurs aux époques individuelles variant entre 8.1 ± 1.8 mrad/d et 19.0 ± 4.3 mrad/d. Peu de résultats observationnels ont été obtenus sur la rotation différentielle des wTTSs ; au sein de MaTYSSE, la jeune V830 Tau affiche une rotation différentielle de 17.2 ± 1.4 mrad/d, suggérant une tendance selon laquelle la rotation différentielle augmente avec l'âge, à mesure que le noyau radiatif se développe. Ceci est cohérent avec ce qui est observé pour les naines M (Morin et al., 2010).

La combinaison de notre estimation de la rotation différentielle et de la durée de 8 ans de notre jeu de données photométriques sur V410 Tau nous a permis de suivre l'évolution latitudinale des principales taches et plages année après année, et de constater qu'elles ont subi une migration vers les pôles depuis la latitude 0 en 2008 vers $\sim 50°$ en 2016. Cela rappelle le diagramme papillon solaire, quoique inversé, et suggère que la dynamo, si elle est cyclique, a une période d'au moins 8 yr et probablement beaucoup plus (16 yr si nos données couvrent seulement une moitié de cycle complet). Ceci s'accompagne d'une augmentation presque monotone de la force du dipôle poloïdal de ~ 200 à ~ 500 G. Cela montre au moins l'existence de variations à long terme sur la surface de V410 Tau. En outre, pour V410 Tau, le champ poloïdal double presque en intensité tout au long de notre observation, mais les mesures de $d\Omega$ sur des jeux de données annuels individuels ne montrent pas d'augmentation, ce qui, si nous supposons une dynamo cyclique, implique un déphasage entre le champ magnétique et la rotation différentielle. Les données photométriques des 60 dernières années montrent une évolution complexe de la courbe de lumière de V410 Tau, et des études antérieures ont montré des variations cycliques de l'amplitude et des extrema de la courbe de lumière (Stelzer et al., 2003; Sokoloff et al., 2008; Oláh et al., 2009; Grankin & Artemenko, 2009; Savanov, 2012; Hambálek et al., 2019), mais il reste à déterminer si V410 Tau a ou non un cycle complet avec inversion de polarité comme pour le Soleil.

Évolution du moment angulaire et durée de vie des disques pour les étoiles jeunes

Nous observons que les cTTSs à accrétion modérée ayant une forte composante dipolaire/poloïdale dans leurs champs magnétiques ont tendance à avoir des périodes de rotation autour de 6 – 9 d (Donati et al., 2008a, 2010a, 2012). En partant de cette hypothèse, nous avons calculé l'âge auquel nos wTTSs ont perdu leur couplage avec leurs disques (voir figure 3.2). Dans les deux cas, cette perte aurait été causée par l'épuisement du disque interne. Pour ce faire, nous avons utilisé les modèles d'évolution stellaire de Siess et al. (2000) pour extraire les moments d'inertie, et, en supposant que les wTTSs se sont contractées à moment angulaire constant après avoir été découplées de leur disque, nous avons dérivé leurs rayons au moment où leur rotation a commencé à accélérer. Les modèles d'évolution stellaire nous ont donné les âges correspondant à ces rayons.

V410 Tau est déjà l'une des plus jeunes wTTSs observées, mais son âge de dissipation du disque a été estimé à ~ 0.2 Myr, avec une précision relativement faible, d'après notre mesure du rayon stellaire, et corroboré par les topologies magnétiques que nous avons reconstruites à partir de nos spectres. Il s'agit d'un système à trois étoiles composé d'une binaire A-B centrale (rapport massique 0.2 ± 0.1, séparation projetée sur le ciel 16.8 ± 1.4 au) et d'une troisième composante C plus lointaine (rapport massique $0.08^{+0.10}_{-0.08}$, séparation projetée sur le ciel 36 ± 3 au). V410 Tau a été prise en compte dans l'étude de Kraus et al. (2012) montrant une corrélation entre la présence

d'un compagnon à moins de 50 au et l'épuisement précoce du disque d'accrétion ; nos mesures de l'âge de V410 Tau, notre estimation de son âge à la dissipation du disque et notre estimation de la séparation entre V410 Tau A-B (36 au) confirment la tendance trouvée par cette étude, et donnent des paramètres plus précis pour cet astre.

De plus, d'après la séparation orbitale du Jupiter chaud découvert dans le cadre de ce travail, on estime que TAP 26 a également perdu son disque à un âge inférieur à 1 Myr.

Les estimations de l'âge varient selon le modèle d'évolution choisi, mais les modèles plus récents (BHAC15, Baraffe et al. 2015, STAREVOL3.4, Amard et al. 2019) donnent des âges encore plus jeunes ($\sim$0.5, $\sim$13 et $\sim$1.5 Myr pour V410 Tau, TAP 26 et V830 Tau resp.) que les modèles de Siess et al. (2000), ce qui renforce la conviction que ces étoiles ont dissipé leurs disques en moins de 1 Myr. Cela place nos trois étoiles parmi les wTTSs qui ont perdu leurs disques à l'âge le plus précoce (Richert et al., 2018), et, par conséquent, elles sont parmi les wTTSs qui tournent le plus vite car leur rotation a commencé à accélérer tôt (Gallet & Bouvier, 2015).

Formation, migration, évolution ultérieure des Jupiter chauds

À ce jour, sept planètes géantes ont été détectées autour de wTTSs : V830 Tau b (Donati et al., 2016), K2-33 b(David et al., 2016), TAP 26 b et V1298 Tau b, c, d et e (David et al., 2019a), avec quelques autres planètes géantes chaudes candidates autour d'étoiles jeunes (par exemple CI Tau, Johns-Krull et al., 2016). V830 Tau b ($0.77 \pm 0.15\,M_{Jup}$, 4.93 ± 0.05 d) et TAP 26 b ($1.66 \pm 0.31\,M_{Jup}$, 10.79 ± 0.14 d) ont été découverts dans le cadre de MaTYSSE, tandis que K2-33 b et V1298 Tau b, c, d et e ont été détectés via leurs transits dans les courbes de lumière de leurs étoiles, et leurs masses ne sont pas encore bien contraintes. Bien qu'il ne s'agisse pas encore d'un échantillon statistiquement représentatif, nous pouvons tirer des conclusions importantes de ces premiers résultats :

- il est possible de former des hJs dans des échelles de temps aussi faibles que 2 Myr,
- V830 Tau b et TAP 26 b ont tous deux une orbite quasi-circulaire, ce qui favorise le scénario de migration planète-disque de type II plutôt que les interactions planète-planète suivies de la circularisation par effet de marées,
- avec deux détections dans un échantillon de $\sim$30 étoiles (dont les données n'ont pas toutes été analysées à ce jour), nous pouvons nous demander si (i) la fréquence des hJs est plus élevée autour des étoiles jeunes que des étoiles matures ($\simeq$1%, Wright et al., 2012), ou (ii) notre échantillon est biaisé vers des étoiles hôtes de hJs. Concernant (i), les hypothèses expliquant l'appauvrissement en hJs au fur et à mesure que l'étoile vieillit vers la séquence principale incluent les interactions de marée et magnétiques entre étoile et planètes, qui peuvent finir par éjecter la planète du système, ou au contraire la précipiter dans l'étoile (Strugarek et al., 2017). En ce qui concerne (ii), puisque les planètes sont plus faciles à détecter autour des TTS non accrétantes en raison de leur variabilité plus faible, les échantillons d'observation comme celui de MaTYSSE sont naturellement biaisés vers de jeunes TTS dont les disques d'accrétion ont disparu tôt, c'est-à-dire à un moment où leurs champs à grande échelle étaient encore forts et leurs cavités magnétosphériques importantes, et où les hJs avaient donc plus de chances de survivre à une migration de type-II. Une conclusion plus précise doit attendre une analyse complète de l'échantillon MaTYSSE.

Aucun hJ n'a été trouvé autour de V410 Tau, et nos résultats excluent la présence d'une planète $> 1\,M_{Jup}$ dans un rayon de 0.1 au autour de l'étoile, à un niveau de 3σ. La formation et/ou la migration d'exoplanètes géantes a peut-être été empêchée par l'épuisement très précoce du disque, qui, à son tour, pourrait être lié à la présence du compagnon de type naine M. Pour faire le lien avec le paragraphe précédent, il pourrait exister un âge optimal pour dissiper le disque afin de former des hJs, c'est-à-dire pas avant que les planètes aient eu le temps de grandir, mais pas après que le

champ se soit affaibli, ce qui causerait la réduction de la cavité magnétosphérique. Nos estimations de l'âge placeraient cet optimum quelque part dans la plage 0.3 – 1 Myr, mais des conclusions statistiquement significatives devront attendre les résultats de nombreuses autres études, y compris la SPIRou (Spectropolarimetre InfraRouge) Legacy Survey (SLS), qui prévoit l'observation de ∼60 wTTS dans le domaine de longueurs d'onde du proche infrarouge.

Perspectives d'avenir

Concernant les étoiles étudiées dans cette thèse, il sera intéressant d'analyser d'autres courbes de RV de TAP 26, afin de mieux contraindre la période orbitale de la planète et de la différencier des alias causés par l'échantillonnage des observations analysées jusqu'ici. V410 Tau est une cible très intéressante pour l'étude de la dynamo en raison de la richesse des données et des études publiées au sujet de cette étoile ; en particulier, en plus des observations photométriques sur 60 ans mentionnées ci-dessus, plusieurs cartes Doppler ont été reconstruites. Une étude compilant toutes les cartes Doppler, mises en parallèle avec la courbe de lumière de V410 Tau, permettrait peut-être d'en savoir plus sur l'activité magnétique séculaire de cette wTTS jeune et massive.

Dans un avenir proche, la complétion de l'analyse de l'échantillon MaTYSSE permettra d'obtenir une meilleure vision d'ensemble des topologies magnétiques des wTTSs et de mieux comprendre leurs dynamos. Le SLS mentionné ci-dessus inclura l'observation de ∼60 wTTSs par le spectropolarimètre à haute résolution SPIRou, dans le domaine de longueurs d'onde du proche infrarouge, où l'effet Zeeman est plus grand et donc le champ magnétique peut être reconstruit avec plus de précision. Ce sera également un ajout important à l'étude statistique des dynamos des wTTSs. De plus, de nouvelles techniques d'imagerie permettant de reconstituer la variabilité intrinsèque des surfaces stellaires sont en cours de développement, ce qui permettra de modéliser finement l'évolution de l'activité des wTTSs sur des échelles de temps de l'ordre du mois / de l'année.

L'étude des jeunes systèmes planétaires bénéficiera également de la complétion de l'analyse MaTYSSE et du SLS. Grâce à l'échantillon de ∼60 étoiles du SLS, nous serons en mesure de tirer des statistiques plus fiables de nos campagnes de recherche de jeunes hJs. De plus, l'activité magnétique se manifeste différemment dans les spectres, et a fortiori dans les courbes de RV, selon la longueur d'onde, alors que les signatures hJs ne varient pas. Par conséquent, l'ajout d'observations spectropolarimétriques infrarouges d'étoiles hôtes de planètes qui ont été observées par ESPaDOnS et/ou NARVAL permettrait de confirmer les signatures planétaires dans les RVs et de mieux les contraindre.

Des jeunes planètes géantes en transit ont été détectées ces dernières années à partir des courbes de lumière K2 (K2-33 b, Mann et al. 2016; David et al. 2016 et V1298 Tau b, c, d et e, David et al. 2019b), et leur observation avec SPIRou permettrait potentiellement de mesurer leur obliquité, et d'observer leur atmosphère. Avec l'arrivée d'un plus grand nombre de données photométriques spatiales pour la détection d'exoplanètes (provenant du télescope TESS actuellement en service ou des prochains CHEOPS, PLATO et ARIEL), on peut s'attendre à ce que davantage de jeunes planètes géantes en transit soient découvertes. La caractérisation de leurs orbites et de leurs atmosphères grâce aux données photométriques et aux observations spectroscopiques, avec par exemple SPIRou ou nIRPS qui sera placé au Chili, sera un grand pas en avant dans l'étude de l'évolution précoce des planètes géantes.

Bibliography

Adams, F. C., Lada, C. J., & Shu, F. H. 1987, ApJ, 312, 788

Affer, L., Micela, G., Favata, F., Flaccomio, E., & Bouvier, J. 2013, MNRAS, 430, 1433

Agnew, M. T., Maddison, S. T., & Horner, J. 2018, MNRAS, 477, 3646

Aigrain, S., Pont, F., & Zucker, S. 2012, MNRAS, 419, 3147

ALMA Partnership, Brogan, C. L., Pérez, L. M., et al. 2015, ApJ, 808, L3

Amard, L., Palacios, A., Charbonnel, C., et al. 2019, arXiv e-prints, arXiv:1905.08516

André, P. 2002, in EAS Publications Series, ed. J. Bouvier & J.-P. Zahn, Vol. 3, 1–38

André, P. 2015, Spectral Classification of Embedded Stars, Gargaud M. et al. (eds) Encyclopedia of Astrobiology (Springer, Berlin, Heidelberg), 2308

André, P., Di Francesco, J., Ward-Thompson, D., et al. 2014, in Protostars and Planets VI, ed. H. Beuther, R. S. Klessen, C. P. Dullemond, & T. Henning, 27

Andre, P., Ward-Thompson, D., & Barsony, M. 2000, in Protostars and Planets IV, ed. V. Mannings, A. P. Boss, & S. S. Russell, 59

Andrews, S. M., Rosenfeld, K. A., Kraus, A. L., & Wilner, D. J. 2013, ApJ, 771, 129

Armitage, P. J. 2018, A Brief Overview of Planet Formation, Handbook of Exoplanets, ISBN 978-3-319-55332-0. (Springer International Publishing AG, part of Springer Nature), 135

Bachiller, R. 1996, ARA&A, 34, 111

Baraffe, I., Homeier, D., Allard, F., & Chabrier, G. 2015, A&A, 577, A42

Barbato, D., Sozzetti, A., Desidera, S., et al. 2018, A&A, 615, A175

Baruteau, C., Bai, X., Mordasini, C., & Mollière, P. 2016, Space Sci. Rev., 205, 77

Baruteau, C., Barraza, M., Pérez, S., et al. 2019, MNRAS, 486, 304

Baruteau, C., Crida, A., Paardekooper, S.-J., et al. 2014, Protostars and Planets VI, 667

Batygin, K., Bodenheimer, P. H., & Laughlin, G. P. 2016, ApJ, 829, 114

Benz, A. O. 2017, Living Reviews in Solar Physics, 14, 2

Bessolaz, N., Zanni, C., Ferreira, J., Keppens, R., & Bouvier, J. 2008, A&A, 478, 155

Blinova, A. A., Romanova, M. M., & Lovelace, R. V. E. 2016, MNRAS, 459, 2354

Bobylev, V. V. 2014, Astrophysics, 57, 583

Bodenheimer, P. H. 2011, Principles of Star Formation (Springer-Verlag Berlin Heidelberg)

Bolmont, E. & Mathis, S. 2016, Celestial Mechanics and Dynamical Astronomy, 126, 275

Bontemps, S., Andre, P., Terebey, S., & Cabrit, S. 1996, A&A, 311, 858

Boss, A. P. 2009, ApJ, 697, 1940

Boss, A. P., Butler, R. P., Hubbard, W. B., et al. 2007, Transactions of the International Astronomical Union, Series A, 26A, 183

Bouvier, J. 2007, in IAU Symposium, Vol. 243, IAU Symposium, ed. J. Bouvier & I. Appenzeller, 231–240

Bouvier, J., Alencar, S. H. P., Boutelier, T., et al. 2007, A&A, 463, 1017

Bouvier, J. & Bertout, C. 1989, A&A, 211, 99

Bouvier, J., Bertout, C., & Bouchet, P. 1988, A&AS, 75, 1

Bouvier, J., Matt, S. P., Mohanty, S., et al. 2014, in Protostars and Planets VI, ed. H. Beuther, R. S. Klessen, C. P. Dullemond, & T. Henning, 433
Bouvier, J., Wichmann, R., Grankin, K., et al. 1997, A&A, 318, 495
Bouy, H. & Alves, J. 2015, A&A, 584, A26
Bradshaw, S. J. & Hartigan, P. 2014, ApJ, 795, 79
Brogi, M., Snellen, I. A. G., de Kok, R. J., et al. 2012, Nature, 486, 502
Brown, S. F., Donati, J.-F., Rees, D. E., & Semel, M. 1991, A&A, 250, 463
Brun, A. S. & Browning, M. K. 2017, Living Reviews in Solar Physics, 14, 4
Carroll, T. A., Strassmeier, K. G., Rice, J. B., & Künstler, A. 2012, A&A, 548, A95
Chandrasekhar, S. 1961, Hydrodynamic and hydromagnetic stability (Oxford: Clarendon)
Charbonneau, P. 2013, Solar and Stellar Dynamos, Saas-Fee Advanced Course
Chene, A.-N., Padzer, J., Barrick, G., et al. 2014, in Society of Photo-Optical Instrumentation Engineers (SPIE) Conference Series, Vol. 9151, Proc. SPIE, 915147
Chib, S. & Jeliazkov, I. 2001, Journal of the American Statistical Association, 96, 270
Cieza, L. A., Olofsson, J., Harvey, P. M., et al. 2013, ApJ, 762, 100
Claret, A. 2000, A&A, 363, 1081
Coleman, G. A. L., Papaloizou, J. C. B., & Nelson, R. P. 2017, MNRAS, 470, 3206
Collier Cameron, A. & Li, J. 1994, MNRAS, 269, 1099
Collier Cameron, A. & Robinson, R. D. 1989, MNRAS, 236, 57
Crockett, C. J., Mahmud, N. I., Prato, L., et al. 2012, ApJ, 761, 164
Crutcher, R. M. 2012, ARA&A, 50, 29
David, T. J., Cody, A. M., Hedges, C. L., et al. 2019a, AJ, 158, 79
David, T. J., Hillenbrand, L. A., Petigura, E. A., et al. 2016, Nature, 534, 658
David, T. J., Petigura, E. A., Luger, R., et al. 2019b, ApJ, 885, L12
Davies, C. L., Gregory, S. G., & Greaves, J. S. 2014, MNRAS, 444, 1157
Dawson, R. I. & Johnson, J. A. 2018, ARA&A, 56, 175
de Zeeuw, P. T., Hoogerwerf, R., de Bruijne, J. H. J., Brown, A. G. A., & Blaauw, A. 1999, AJ, 117, 354
Donati, J., Skelly, M. B., Bouvier, J., et al. 2010a, MNRAS, 409, 1347
Donati, J., Skelly, M. B., Bouvier, J., et al. 2010b, MNRAS, 402, 1426
Donati, J.-F. 2001, in Lecture Notes in Physics, Berlin Springer Verlag, Vol. 573, Astrotomography, Indirect Imaging Methods in Observational Astronomy, ed. H. M. J. Boffin, D. Steeghs, & J. Cuypers, 207–+
Donati, J.-F. 2003, in Astronomical Society of the Pacific Conference Series, Vol. 307, Astronomical Society of the Pacific Conference Series, ed. J. Trujillo-Bueno & J. Sanchez Almeida, 41–+
Donati, J.-F. & Brown, S. F. 1997, A&A, 326, 1135
Donati, J.-F., Collier Cameron, A., & Petit, P. 2003, MNRAS, 345, 1187
Donati, J.-F., Gregory, S. G., Alencar, S. H. P., et al. 2012, MNRAS, 425, 2948
Donati, J.-F., Gregory, S. G., Alencar, S. H. P., et al. 2013, MNRAS, 436, 881
Donati, J.-F., Hébrard, E., Hussain, G., et al. 2014, MNRAS, 444, 3220
Donati, J.-F., Hébrard, E., Hussain, G. A. J., et al. 2015, MNRAS, 453, 3706
Donati, J.-F., Howarth, I. D., Jardine, M. M., et al. 2006, MNRAS, 370, 629
Donati, J.-F., Jardine, M. M., Gregory, S. G., et al. 2008a, MNRAS, 386, 1234
Donati, J.-F., Mengel, M., Carter, B. D., et al. 2000, MNRAS, 316, 699
Donati, J.-F., Moutou, C., Farès, R., et al. 2008b, MNRAS, 385, 1179
Donati, J. F., Moutou, C., Malo, L., et al. 2016, Nature, 534, 662
Donati, J.-F., Semel, M., Carter, B. D., Rees, D. E., & Collier Cameron, A. 1997, MNRAS, 291, 658
Donati, J. F., Semel, M., & Praderie, F. 1989, A&A, 225, 467

Donati, J.-F., Yu, L., Moutou, C., et al. 2017, MNRAS, 465, 3343
Dong, R., Liu, S.-y., Eisner, J., et al. 2018, ApJ, 860, 124
Duchêne, G. & Kraus, A. 2013, ARA&A, 51, 269
Evans, Neal J., I., Dunham, M. M., Jørgensen, J. K., et al. 2009, ApJS, 181, 321
Fabrycky, D. C. & Winn, J. N. 2009, ApJ, 696, 1230
Feigelson, E. D., Jackson, J. M., Mathieu, R. D., Myers, P. C., & Walter, F. M. 1987, AJ, 94, 1251
Gaia Collaboration, Brown, A. G. A., Vallenari, A., et al. 2018, A&A, 616, A1
Gallet, F. & Bouvier, J. 2015, A&A, 577, A98
Galli, P. A. B., Loinard, L., Ortiz-Léon, G. N., et al. 2018, ApJ, 859, 33
Ghez, A. M., Weinberger, A. J., Neugebauer, G., Matthews, K., & McCarthy, Jr., D. W. 1995, AJ, 110, 753
Ghez, A. M., White, R. J., & Simon, M. 1997, ApJ, 490, 353
Ghosh, P. & Lamb, F. K. 1979, ApJ, 234, 296
Gilliland, R. L., Brown, T. M., Christensen-Dalsgaard, J., et al. 2010, PASP, 122, 131
Goodwin, S. P., Kroupa, P., Goodman, A., & Burkert, A. 2007, in Protostars and Planets V, ed. B. Reipurth, D. Jewitt, & K. Keil, 133
Grankin, K. N. 1998, Astronomy Letters, 24, 497
Grankin, K. N. 2013, Astronomy Letters, 39, 251
Grankin, K. N. & Artemenko, S. A. 2009, Information Bulletin on Variable Stars, 5907, 1
Grankin, K. N., Bouvier, J., Herbst, W., & Melnikov, S. Y. 2008, A&A, 479, 827
Gregory, S. G., Donati, J.-F., Morin, J., et al. 2012, ApJ, 755, 97
Gully-Santiago, M. A., Herczeg, G. J., Czekala, I., et al. 2017, ApJ, 836, 200
Hambálek, Ä., VaÅko, M., Paunzen, E., & Smalley, B. 2019, MNRAS, 483, 1642
Han, E., Wang, S. X., Wright, J. T., et al. 2014, PASP, 126, 827
Haywood, R. D. 2015, PhD thesis, University of St Andrews
Haywood, R. D., Collier Cameron, A., Queloz, D., et al. 2014, MNRAS, 443, 2517
Haywood, R. D., Collier Cameron, A., Unruh, Y. C., et al. 2016, MNRAS, 457, 3637
Hébrard, É. M., Donati, J.-F., Delfosse, X., et al. 2016, MNRAS, 461, 1465
Hennebelle, P. & Ciardi, A. 2009, A&A, 506, L29
Herbst, W. 1989, AJ, 98, 2268
Herczeg, G. J. & Hillenbrand, L. A. 2014, ApJ, 786, 97
Hill, C. A., Carmona, A., Donati, J.-F., et al. 2017, MNRAS, 472, 1716
Hill, C. A., Folsom, C. P., Donati, J. F., et al. 2019, MNRAS, 484, 5810
Holman, M. J., Fabrycky, D. C., Ragozzine, D., et al. 2010, Science, 330, 51
Huerta, M., Johns-Krull, C. M., Prato, L., Hartigan, P., & Jaffe, D. T. 2008, ApJ, 678, 472
Hussain, G. A. J., Jardine, M., & Collier Cameron, A. 2001, MNRAS, 322, 681
Ingleby, L., Calvet, N., Herczeg, G., & Briceño, C. 2012, ApJ, 752, L20
Johns-Krull, C. M. 2007, ApJ, 664, 975
Johns-Krull, C. M., McLane, J. N., Prato, L., et al. 2016, ApJ, 826, 206
Johns-Krull, C. M., Valenti, J. A., & Koresko, C. 1999, ApJ, 516, 900
Kennedy, G. M. & Kenyon, S. J. 2008, ApJ, 673, 502
Kenyon, S. J. & Hartmann, L. 1987, ApJ, 323, 714
Kenyon, S. J. & Hartmann, L. 1995, ApJS, 101, 117
Kounkel, M., Hartmann, L., Loinard, L., et al. 2017, ApJ, 834, 142
Kraus, A. L., Ireland, M. J., Hillenbrand, L. A., & Martinache, F. 2012, ApJ, 745, 19
Kraus, A. L., Ireland, M. J., Huber, D., Mann, A. W., & Dupuy, T. J. 2016, AJ, 152, 8
Kraus, A. L., Ireland, M. J., Martinache, F., & Hillenbrand, L. A. 2011, ApJ, 731, 8
Kurucz, R. 1993, CDROM # 13 (ATLAS9 atmospheric models) and # 18 (ATLAS9 and SYNTHE routines, spectral line database) (Smithsonian Astrophysical Observatory, Washington D.C.)

Lada, E. A. 1992, ApJ, 393, L25
Landi degl'Innocenti, E. & Landolfi, M. 2004, Polarisation in spectral lines (Dordrecht/Boston/London: Kluwer Academic Publishers)
Lanza, A. F. 2006, MNRAS, 369, 1773
Lin, D. N. C., Bodenheimer, P., & Richardson, D. C. 1996, Nature, 380, 606
Lucy, L. B. & Sweeney, M. A. 1971, AJ, 76, 544
Luhman, K. L., Allen, P. R., Espaillat, C., Hartmann, L., & Calvet, N. 2010, ApJS, 186, 111
Machida, M. N. & Basu, S. 2019, ApJ, 876, 149
Machida, M. N. & Matsumoto, T. 2011, MNRAS, 413, 2767
Madhusudhan, N. 2019, ARA&A, 57, 617
Maeder, A. 2009, Physics, Formation and Evolution of Rotating Stars (Springer)
Mahmud, N. I., Crockett, C. J., Johns-Krull, C. M., et al. 2011, ApJ, 736, 123
Mann, A. W., Newton, E. R., Rizzuto, A. C., et al. 2016, AJ, 152, 61
Masunaga, H. & Inutsuka, S.-i. 2000, ApJ, 531, 350
Maury, A. J., André, P., Hennebelle, P., et al. 2010, A&A, 512, A40
Maury, A. J., André, P., Testi, L., et al. 2019, A&A, 621, A76
Mayor, M. & Queloz, D. 1995, Nature, 378, 355
Meunier, N., Desort, M., & Lagrange, A.-M. 2010, A&A, 512, A39
Meunier, N., Mignon, L., & Lagrange, A. M. 2017, A&A, 607, A124
Mordasini, C. 2018, Planetary Population Synthesis, Handbook of Exoplanets, ISBN 978-3-319-55332-0. (Springer International Publishing AG, part of Springer Nature), 143
Morin, J., Donati, J., Petit, P., et al. 2010, MNRAS, 407, 2269
Moutou, C., Donati, J.-F., Savalle, R., et al. 2007, A&A, 473, 651
Narain, U. & Ulmschneider, P. 1996, Space Sci. Rev., 75, 453
Nguyen, D. C., Brandeker, A., van Kerkwijk, M. H., & Jayawardhana, R. 2012, ApJ, 745, 119
Nicholson, B. A., Hussain, G. A. J., Donati, J. F., et al. 2018, MNRAS, 480, 1754
Nomura, H., Tsukagoshi, T., Kawabe, R., et al. 2016, ApJ, 819, L7
Offner, S. S. R., Clark, P. C., Hennebelle, P., et al. 2014, in Protostars and Planets VI, ed. H. Beuther, R. S. Klessen, C. P. Dullemond, & T. Henning, 53
Oláh, K., Kolláth, Z., Granzer, T., et al. 2009, A&A, 501, 703
Ortiz-León, G. N., Loinard, L., Kounkel, M. A., et al. 2017, ApJ, 834, 141
Parker, E. N. 1955, ApJ, 122, 293
Pecaut, M. J. & Mamajek, E. E. 2013, ApJS, 208, 9
Pecaut, M. J. & Mamajek, E. E. 2016, MNRAS, 461, 794
Perrot, C. A. & Grenier, I. A. 2003, A&A, 404, 519
Perryman, M. 2011, The Exoplanet Handbook (Cambridge University Press)
Perryman, M. 2018, The Exoplanet Handbook (Cambridge University Press)
Petit, P., Donati, J.-F., Hébrard, E., et al. 2015, A&A, 584, A84
Pollacco, D. L., Skillen, I., Collier Cameron, A., et al. 2006, PASP, 118, 1407
Pollack, J. B., Hubickyj, O., Bodenheimer, P., et al. 1996, Icarus, 124, 62
Preibisch, T., Kim, Y.-C., Favata, F., et al. 2005, ApJS, 160, 401
Press, W. H., Teukolsky, S. A., Vetterling, W. T., & Flannery, B. P. 1992, Numerical recipes in FORTRAN. The art of scientific computing (Press Syndicate of the University of Cambridge)
Press, W. H., Teukolsky, S. A., Vetterling, W. T., & Flannery, B. P. 2007, Numerical recipes. The art of scientific computing. Third Edition (Cambridge University Press)
Rasmussen, C. E. & Williams, C. K. I. 2006, Gaussian Processes for Machine Learning (The MIT Press)
Raymond, S. N., Izidoro, A., & Morbidelli, A. 2018, arXiv e-prints, arXiv:1812.01033
Rebull, L. M., Wolff, S. C., & Strom, S. E. 2004, AJ, 127, 1029

Rice, J. B., Strassmeier, K. G., & Kopf, M. 2011, ApJ, 728, 69
Richert, A. J. W., Getman, K. V., Feigelson, E. D., et al. 2018, MNRAS, 477, 5191
Romanova, M. M., Ustyugova, G. V., Koldoba, A. V., & Lovelace, R. V. E. 2004, ApJ, 616, L151
Rydgren, A. E. & Vrba, F. J. 1983, ApJ, 267, 191
Savanov, I. S. 2012, Astronomy Reports, 56, 722
Schneider, J. 2018, Definition of Exoplanets and Brown Dwarfs, Handbook of Exoplanets, ISBN 978-3-319-55332-0. (Springer International Publishing AG, part of Springer Nature), 119
Schneider, J., Dedieu, C., Le Sidaner, P., Savalle, R., & Zolotukhin, I. 2011, A&A, 532, A79
Semel, M. 1989, A&A, 225, 456
Semel, M., Donati, J.-F., & Rees, D. E. 1993, A&A, 278, 231
Siess, L., Dufour, E., & Forestini, M. 2000, A&A, 358, 593
Skelly, M. B., Donati, J.-F., Bouvier, J., et al. 2010, MNRAS, 403, 159
Skilling, J. & Bryan, R. K. 1984, MNRAS, 211, 111
Skumanich, A. 1972, ApJ, 171, 565
Sokoloff, D. D., Nefedov, S. N., Ermash, A. A., & Lamzin, S. A. 2008, Astronomy Letters, 34, 761
Southworth, J. 2011, MNRAS, 417, 2166
Stelzer, B., Fernández, M., Costa, V. M., et al. 2003, A&A, 411, 517
Stelzer, B., Flaccomio, E., Briggs, K., et al. 2007, A&A, 468, 463
Strassmeier, K. G. 2009, A&ARv, 17, 251
Strugarek, A., Bolmont, E., Mathis, S., et al. 2017, ApJ, 847, L16
Valenti, J. A. & Fischer, D. A. 2005, ApJS, 159, 141
van Eyken, J. C., Ciardi, D. R., von Braun, K., et al. 2012, ApJ, 755, 42
Vaytet, N., Commerçon, B., Masson, J., González, M., & Chabrier, G. 2018, A&A, 615, A5
Vogt, S. S. & Penrod, G. D. 1983a, PASP, 95, 565
Vogt, S. S. & Penrod, G. D. 1983b, in Astrophysics and Space Science Library, Vol. 102, IAU Colloq. 71: Activity in Red-Dwarf Stars, ed. P. B. Byrne & M. Rodono, 379–385
Vogt, S. S., Penrod, G. D., & Hatzes, A. P. 1987, ApJ, 321, 496
Vrba, F. J., Herbst, W., & Booth, J. F. 1988, AJ, 96, 1032
Welty, A. D. & Ramsey, L. W. 1995, AJ, 110, 336
Wenger, M., Ochsenbein, F., Egret, D., et al. 2000, A&AS, 143, 9
White, R. J., Greene, T. P., Doppmann, G. W., Covey, K. R., & Hillenbrand, L. A. 2007, in Protostars and Planets V, ed. B. Reipurth, D. Jewitt, & K. Keil, 117
Williams, J. P. & Best, W. M. J. 2014, ApJ, 788, 59
Williams, J. P. & Cieza, L. A. 2011, ARA&A, 49, 67
Wilson, R. W., Jefferts, K. B., & Penzias, A. A. 1970, ApJ, 161, L43
Winn, J. N. & Fabrycky, D. C. 2015, ARA&A, 53, 409
Wright, J. T., Marcy, G. W., Howard, A. W., et al. 2012, ApJ, 753, 160
Wurster, J., Bate, M. R., & Price, D. J. 2018, MNRAS, 480, 4434
Xiao, H. Y., Covey, K. R., Rebull, L., et al. 2012, ApJS, 202, 7
Yadav, R. K., Christensen, U. R., Morin, J., et al. 2015, ApJ, 813, L31
Youdin, A. N. & Goodman, J. 2005, ApJ, 620, 459
Yu, L., Donati, J. F., Grankin, K., et al. 2019, MNRAS, 489, 5556
Yu, L., Donati, J.-F., Hébrard, E. M., et al. 2017, MNRAS, 467, 1342
Zanni, C. & Ferreira, J. 2013, A&A, 550, A99

List of Figures

List of Tables

A | Complements

A.1 Zeeman effect and polarimetry

We write the electric component of a monochromatic wave propagating in vacuum along direction z at angular frequency ω as:

$$\vec{\boldsymbol{E}} = \mathrm{Re}\left[\begin{pmatrix} E_{0,x}\mathrm{e}^{i(kz-\omega t+\phi_x)} \\ E_{0,y}\mathrm{e}^{i(kz-\omega t+\phi_y)} \\ 0 \end{pmatrix}\right] = \mathrm{Re}\left[\begin{pmatrix} E_{0,x}\mathrm{e}^{i\phi_x} \\ E_{0,y}\mathrm{e}^{i\phi_y} \\ 0 \end{pmatrix}\mathrm{e}^{i(kz-\omega t)}\right].$$

The vector defined in the (x, y) plane as $(E_{0,x}\mathrm{e}^{i\phi_x}, E_{0,y}\mathrm{e}^{i\phi_y})$ is called the Jones vector. We define:

$$\begin{aligned} E_{\leftrightarrow} &= E_{0,x}\exp^{i\phi_x} \\ E_{\updownarrow} &= E_{0,y}\exp^{i\phi_y} \\ E_{45^\circ} &= (E_{\leftrightarrow} + E_{\updownarrow})/\sqrt{2} \\ E_{-45^\circ} &= (E_{\leftrightarrow} - E_{\updownarrow})/\sqrt{2} \\ E_{\circlearrowleft} &= (E_{\leftrightarrow} - iE_{\updownarrow})/\sqrt{2} \\ E_{\circlearrowright} &= (E_{\leftrightarrow} + iE_{\updownarrow})/\sqrt{2} \end{aligned}$$

Noting $I_{\leftrightarrow} = |E_{\leftrightarrow}|^2, I_{\updownarrow} = |E_{\updownarrow}|^2, I_{45^\circ} = |E_{45^\circ}|^2, I_{-45^\circ} = |E_{-45^\circ}|^2, I_{\circlearrowleft} = |E_{\circlearrowleft}|^2, I_{\circlearrowright} = |E_{\circlearrowright}|^2$, the Stokes parameters I, Q, U and V are defined and represented schematically in figure A.1.

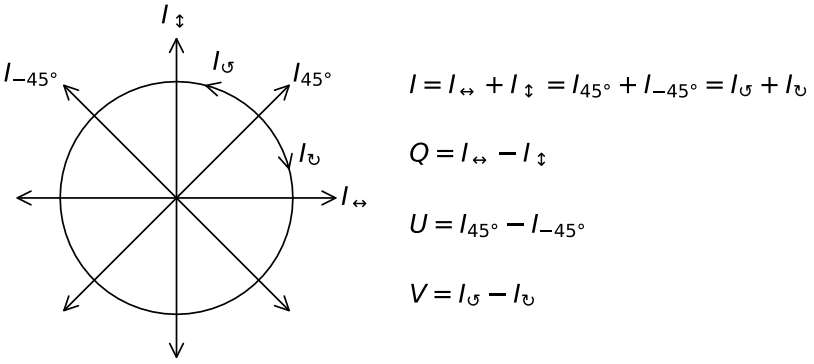

Figure A.1 – Stokes parameters and polarization. This convention considers that the observer is facing the source and $V > 0$ when the light wave propagates in a clockwise fashion as perceived by the observer.

The Zeeman effect The light associated to π and $\sigma_{b,r}$ transitions is polarized: for π, it vibrates along the same direction as $\vec{B}$ and for $\sigma_{b,r}$ the it vibrates circularly in the plane perpendicular to $\vec{B}$. If $\vec{B}$ points towards the observer, the polarization of the light associated with σ_b/σ_r transitions is positive/negative respectively. Thus, if $\vec{B}$ is aligned with the line of sight, π transitions are perceived as unpolarized and σ transtitions as circularly polarized, while, if $\vec{B}$ is perpendicular to the line of sight, π and σ transitions are perceived as linearly polarized.

Thus, if $\vec{B}$ is points towards the observer, then for a particular absorption line, the σ_b transitions will add a blueshifted absorption profile to $I_{\circlearrowleft}$ and the σ_r transitions a redshifted absorption profile to $I_{\circlearrowright}$, resulting in a net Stokes V profile as illustrated on figure A.2.

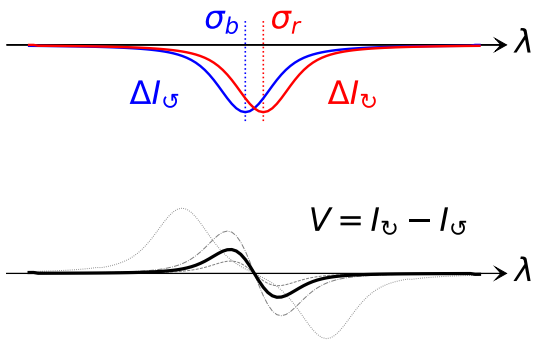

Figure A.2 – Stokes V line profile (black) in the presence of a magnetic field. Gray curves show how the Stokes V profiles would look under different intensities of magnetic field.

To produce unpolarized (Stokes I) and circularly polarized (Stokes V) spectra, ESPaDOnS and NARVAL use the double-beam method described in Donati et al. (1997) where the incident light beam is split into two beams that go through different optic paths, one from which $I_{\circlearrowleft}$ is measured and the other from which $I_{\circlearrowright}$ is measured. This is why there are two channels within each order in figure 2.1: they are the two beams after being reunited on the detector. To remove all spurious polarisation signatures at first order, each polarisation exposure sequence is a combination of 4 individual subexposures taken in different polarimeter configurations:

$$I = \sum_{1}^{4} I_{\circlearrowleft 1} + I_{\circlearrowright 1} + I_{\circlearrowleft 2} + I_{\circlearrowright 2} + I_{\circlearrowleft 3} + I_{\circlearrowright 3} + I_{\circlearrowleft 4} + I_{\circlearrowright 4},$$

$$V = I\frac{R-1}{R+1} \text{ where } R^4 = \frac{I_{\circlearrowleft 1}/I_{\circlearrowright 1}}{I_{\circlearrowleft 2}/I_{\circlearrowright 2}} \frac{I_{\circlearrowleft 4}/I_{\circlearrowright 4}}{I_{\circlearrowleft 3}/I_{\circlearrowright 3}}.$$

ESPaDOnS and NARVAL can also produce Q and U spectra following the same principle.

A.2 Least-Squares Deconvolution

Each spectral line of the observed spectra is affected by the characteristics of the corresponding chemical element and atomic transition, as well as by the distribution of RV, brightness and magnetic field at the surface of the star. Some particular lines trace particular phenomena, but for a large number of lines (Fe I lines for example, which are very numerous in wTTSs optical spectra), only the depth and Landé factor differ and the lines are otherwise affected the same way by the distribution of RV, brightness and magnetic field. A way to gather the information on those distributions within a compact form of data is thus to build an average line profile, which is representative of the way all those spectral lines were distorted in order to add up information from all spectral lines and boost the resulting S/N of both Stokes I and V LSD profiles.

The technique used in this study is called Least-Squares Deconvolution (LSD, see Donati et al., 1997). As its name spells it, it deconvolves the spectrum by a spectral mask and selects the kernel that yields the lowest χ^2_r fit. The weight of each line in the mask is proportional to the product of its wavelength, depth and Landé factor, so that the convolution between the final LSD profile and the mask should fit the shape of the observed spectrum at the locations of the used spectral lines. This process takes into account the way the Doppler effect varies with source wavelength, and removes the linear dependency of the Doppler broadening with the wavelength, which results in a LSD profile whose x-axis is directly the RV (see figure A.3).

The spectral masks, or line lists, employed in his thesis for LSD are computed from an ATLAS9 LTE model atmosphere (Kurucz, 1993) featuring adapted values of $T_{\rm eff}$ and $\log g$. Only moderate to strong atomic spectral lines are included in these lists (see e.g. Donati et al., 2010a, for more details). Altogether, about 7,800 spectral features (with about 40% from Fe I) are used.

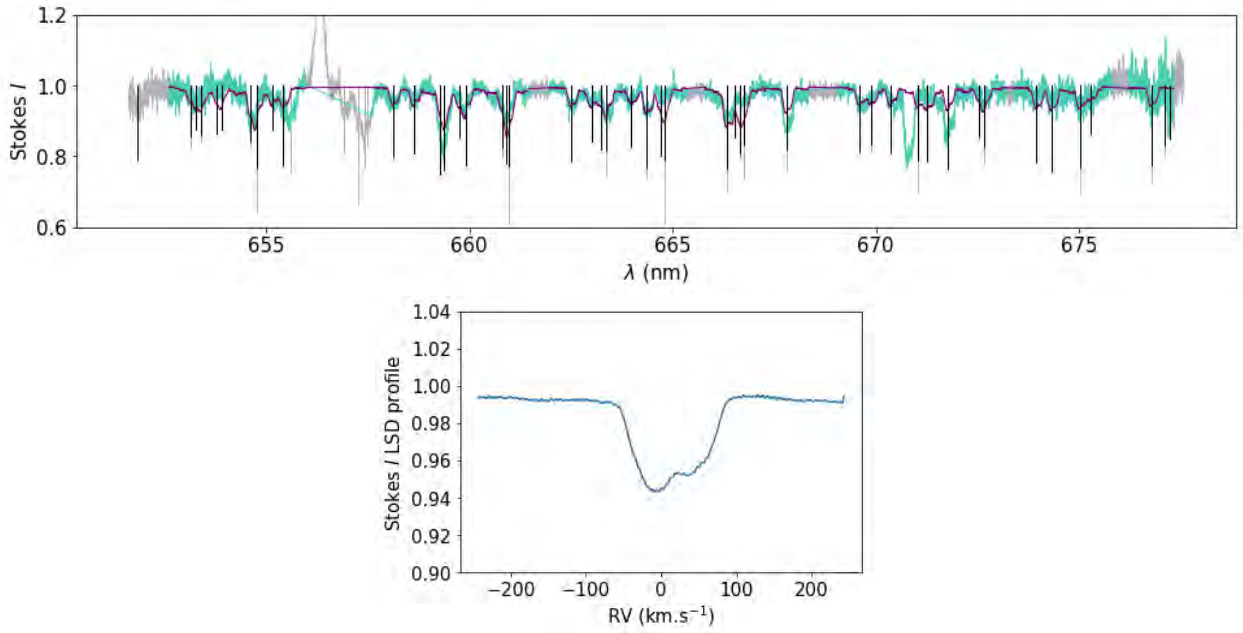

Figure A.3 – *Top*: order 27 of Stokes I observation of TAP 26 on 2017 Jan 20, with the spectrum in gray, the extracted part to be used for deconvolution in cyan, the complete list of atomic lines in gray, the lines selected for the deconvolution (the spectral mask) in black, and the model spectrum (i.e. the convolution of the LSD profile by the spectral mask) in purple. The length of the gray lines are proportional to their depth times their Landé factor times their wavelength, whereas the length of the black lines are proportional to their weight in the deconvolution. We note that the Hα line at $\lambda = 656.3$ nm was ignored for the deconvolution, and that the Lithium line at $\lambda = 670.7$ nm was not included in the spectral mask. We show only one spectral order, but LSD is applied to the whole spectrum at once. *Bottom*: LSD profile for this observation.

A.3 Zeeman-Doppler Imaging: stellar tomography

We apply a technique called Zeeman-Doppler Imaging (ZDI) to time series of LSD Stokes I and Stokes V profiles in order to reconstruct brightness and magnetic surface maps of the observed wTTSs. The details of ZDI were first described in papers Semel (1989), Donati et al. (1989), Semel et al. (1993), Brown et al. (1991) and Donati & Brown (1997), and successive improvements are described in Donati (2001), Donati et al. (2014). We provide here a simplified explanation adapted to the use we made of it.

ZDI takes inspiration from medical tomography, which consists of constraining a 3D distribution using series of 2D projections as seen from various angles. In our context, ZDI inverts simultaneous time series of 1D Stokes I and V LSD profiles into 2D brightness and magnetic field maps of the stellar surface. That is to say, ZDI looks for a solution $\mathcal{I}$ to the problem

$$\mathcal{D} = f(\mathcal{I}) + \epsilon,$$

where $\mathcal{D}$ represents the time series of Stokes I and Stokes V observations, f represents the ZDI direct process, $\mathcal{I}$ represents the brightness and magnetic maps and ϵ is noise.

The following section describes the model $\mathcal{I}$ and the direct process f, and the one after it explains the inversion process.

A.3.1 Model

The ZDI model $\mathcal{I}$ consists of a cell-covered truncated sphere, representing the part of a stellar surface which can be visible from Earth (see figure 2.5): with $\boldsymbol{i}$ the user-provided **inclination**, i.e. the angle between the rotation axis and the line of sight, the sphere is truncated at latitude $-i$. That surface is covered with a user-provided number of cells $\boldsymbol{n_{\mathrm{cell}}}$, organized in latitude rings. The number of latitude rings, the width of each ring and the number of cells per ring are computed so as to make the projected area of the cells facing the observer as homogeneous as possible. Each cell has a local brightness value as well as a local magnetic field expressed as the sum of its radial, meridional and azimuthal components.

We note that, while the brightness value can vary freely from cell to cell, the global magnetic field of the star is expressed as the sum of its poloidal and toroidal components, which in turn are expressed as spherical harmonics expansions, up to a user-provided maximum order $\boldsymbol{\ell_{\mathrm{max}}}$, and the projections of the field onto spherical coordinates are computed from there, as detailed in Donati et al. 2006 (section 5.1). This means that $\mathcal{I}$ is a vector of $n_{\mathrm{cell}} + 3\ \ell_{\mathrm{max}}(\ell_{\mathrm{max}} + 2)$ coefficients.

From these brightness and magnetic maps, ZDI computes synthetic Stokes I and Stokes V profiles of a model spectral line, of given wavelength λ_0, Landé factor g, width and depth, by adding the contributions of all visible cells. To compute the contribution of each cell to an observation, ZDI takes as input the **timestamp** of the observation, expressed in units of rotation cycles, the **differential rotation parameters**, the rotation-induced Doppler broadening, written $\boldsymbol{v \sin i}$ (where v is the equatorial rotation velocity), and the line-of-sight-projected proper motion of the star (or bulk radial velocity), $\boldsymbol{v_{\mathrm{rad}}}$. Here, we used a two-parameter sine-squared model for the differential rotation (Donati et al., 2000):

$$\Omega(\theta) = \Omega_{\mathrm{eq}} - (\sin\theta)^2 d\Omega, \tag{A.1}$$

where Ω is the rotation rate, θ is the latitude, Ω_{eq} is the rotation rate of the equator and $d\Omega$ is the difference between equatorial and polar rotation rates. In this work, the timestamps given to ZDI were expressed in rotational cycles (see for example ephemeris 3.1), so the differential rotation parameters were $(\boldsymbol{\beta}, \boldsymbol{\gamma})$ rather than $(\boldsymbol{\Omega_{\mathrm{eq}}}, \boldsymbol{d\Omega})$, where $\beta = 1 - \Omega_{\mathrm{eq}}/\Omega_0$ and $\gamma = d\Omega/\Omega_0$, with Ω_0 the reference rotation rate used to compute the rotational cycles.

ZDI first computes the position of each cell depending on the timestamp and the differential rotation (arranging the cells into latitude rings greatly simplifies this step), then the sky-projected area, limb darkening factor and local RV of each cell. For the limb darkening, we used the linear law (for more information on limb darkening, see for example Claret, 2000):

$$I = I_0(1 - \epsilon(1 - \mu)), \tag{A.2}$$

where μ is the cosine of the limb angle (between the line of sight and the normal to the surface, with $\mu = 1$ at the center of the visible disc), and ϵ was set at 0.75 for the stars studied in this thesis. In our ZDI version, the RV of each cell is computed from $v \sin i$ and v_{rad} as:

$$\mathrm{RV}(\theta, \phi) = v \sin i \sin\phi \cos\theta + v_{\mathrm{rad}}, \tag{A.3}$$

where ϕ is the azimuth of the cell ($\phi = 0$ corresponds to the meridian facing the observer). Thus ZDI takes into account only the stellar proper motion and solid-body rotation into the computation of the local RV, and not the differential rotation, stellar pulsations, convection or any other effects.

This means that when projected onto the sky plane, the iso-RVs appear parallel to the rotation axis (see figure 2.5).

The contribution of each cell is its local line profile, weighted by its brightness value, sky-projected area and limb darkening factor, and Doppler-shifted according to its RV. The local Stokes I and Stokes V profiles are computed following Unno-Rachkovsky's analytical solution to the polarised radiative transfer equations in a Milne-Eddington model atmosphere (Landi degl'Innocenti & Landolfi, 2004), from pre-defined global line properties (wavelength, Landé factor, depth, width) and from the local magnetic field. All the individual contributions are thus summed into integrated Stokes I and Stokes V profiles, which are then normalized so as to bring the continuum in the Stokes I profiles to 1.

Unno-Rachkovsky's analytical solution to the polarised radiative transfer equations in a Milne-Eddington model atmosphere is (normalized solution):

$$
\begin{aligned}
I &= \frac{\beta\mu(\eta_I+1)}{\Delta(\beta\mu+1)}\Big((\eta_I+1)^2+\rho_Q^2+\rho_U^2+\rho_V^2\Big)+\frac{1}{\beta\mu+1}\\
Q &= -\frac{\beta\mu}{\Delta(\beta\mu+1)}\Big((\eta_I+1)^2\eta_Q+(\eta_Q\rho_Q+\eta_U\rho_U+\eta_V\rho_V)\rho_Q-(\eta_I+1)(\eta_U\rho_V-\eta_V\rho_U)\Big)\\
U &= -\frac{\beta\mu}{\Delta(\beta\mu+1)}((\eta_I+1)^2\eta_U+(\eta_Q\rho_Q+\eta_U\rho_U+\eta_V\rho_V)\rho_U-(\eta_I+1)(\eta_V\rho_Q-\eta_Q\rho_V))\\
V &= -\frac{\beta\mu}{\Delta(\beta\mu+1)}((\eta_I+1)^2\eta_V+(\eta_Q\rho_Q+\eta_U\rho_U+\eta_V\rho_V)\rho_V)
\end{aligned}
$$

where

$$
\begin{aligned}
\eta_I &= \frac{\eta}{2}\left(h_\pi(\sin\gamma)^2+\frac{h_{\sigma,\mathrm{red}}+h_{\sigma,\mathrm{blue}}}{2}\Big((\cos\gamma)^2+1\Big)\right)\\
\eta_Q &= \frac{\eta}{2}\left(h_\pi-\frac{h_{\sigma,\mathrm{red}}+h_{\sigma,\mathrm{blue}}}{2}\right)(\sin\gamma)^2\cos 2\chi\\
\eta_U &= \frac{\eta}{2}\left(h_\pi-\frac{h_{\sigma,\mathrm{red}}+h_{\sigma,\mathrm{blue}}}{2}\right)(\sin\gamma)^2\sin 2\chi\\
\eta_V &= \frac{\eta}{2}(h_{\sigma,\mathrm{red}}-h_{\sigma,\mathrm{blue}})\cos\gamma\\
\rho_Q &= \eta\left(f_\pi-\frac{f_{\sigma,\mathrm{red}}+f_{\sigma,\mathrm{blue}}}{2}\right)(\sin\gamma)^2\cos 2\chi\\
\rho_U &= \eta\left(f_\pi-\frac{f_{\sigma,\mathrm{red}}+f_{\sigma,\mathrm{blue}}}{2}\right)(\sin\gamma)^2\sin 2\chi\\
\rho_V &= \eta(f_{\sigma,\mathrm{red}}-f_{\sigma,\mathrm{blue}})\cos\gamma\\
\Delta &= (\eta_I+1)^2\Big((\eta_I+1)^2-\eta_Q^2-\eta_U^2-\eta_V^2+(\rho_Q^2+\rho_U^2+\rho_V^2)\Big)-(\eta_Q\rho_Q+\eta_U\rho_U+\eta_V\rho_V)^2
\end{aligned}
$$

where β is the Milne-Eddington parameter (slope of the Planck function with respect to t_c, the continuum optical depth measured along the vertical), μ is the cosine of the limb angle, η is the ratio between line and continuum absorption coefficients, and γ and χ are respectively the inclination and azimuth angles of the magnetic field. h_π, $h_{\sigma,\mathrm{red}}$ and $h_{\sigma,\mathrm{blue}}$ are Voigt functions and f_π, $f_{\sigma,\mathrm{red}}$ and $f_{\sigma,\mathrm{blue}}$ are Faraday-Voigt functions, of damping constant 0.95 for the stars studied in this thesis; the shift in reduced wavelength is $4.67\times10^{-12}\times\frac{\lambda_0^2 gB}{\Delta\lambda}$ (with $\Delta\lambda$ equal to 40×10^{-4} nm for the stars studied in this thesis).

In short, ZDI:

- assumes a chemically homogeneous photosphere,
- considers small-scale RV dispersion to be the same everywhere on the photosphere (same local profile before application of the Zeeman effect),

◦ considers macro-RV dispersion being driven uniquely by stellar solid-body rotation (iso-RVs are parallel to the sky-projected rotation axis).

This choice is justified for the study of wTTSs because their $v \sin i$ is usually of the order of several tens of $\mathrm{km\,s^{-1}}$, making the stellar rotation a largely dominant factor in the dispersion of RV within the visible disc.

To sum things up,

f depends on:	$\mathcal{I}$ has:
- the number n_{cell} of cells covering the visible surface, - the timestamps of the spectropolarimetric observations, - the maximum spherical harmonics order $\ell_{\max}$, - the characteristics of the intrinsic line profile, - the inclination i of the rotation axis with respect to the line of sight, - $\beta = 1 - \Omega_{\mathrm{eq}}/\Omega_0$, - $\gamma = d\Omega/\Omega_0$, - the line-of-sight-projected equatorial rotation velocity $v \sin i$, - the line-of-sight-projected stellar proper motion v_{rad}.	- n_{cell} free parameters for the brightness - 3 $\ell_{\max}(\ell_{\max}+2)$ free parameters for the magnetic field.

A.3.2 Inversion algorithm

To invert Stokes I and Stokes V profiles into brightness and magnetic maps, ZDI follows a maximum entropy image reconstruction algorithm heavily inspired from Skilling & Bryan (1984). This algorithm relies on two quantities respectively called the reduced chi-square and the entropy.

$$\chi^2_{\mathrm{r}} = \frac{1}{N_{\mathrm{obs}}} \sum_{k=1}^{N_{\mathrm{obs}}} \frac{(F_k - D_k)^2}{\sigma_k^2} \tag{A.4}$$

is the reduced chi-square and is used to compare a series of observations $(D_k)_k$, with error bars $(\sigma_k)_k$, to a model $(F_k)_k$. If $\chi^2_{\mathrm{r}} = 1$, it is said the model fits the observations down to the noise level. In our case, F represents the ZDI synthetic profiles $f(\mathcal{I})$, D represents the observed profiles $\mathcal{D}$ and N_{obs} is the total number of points in $\mathcal{D}$.

$$S = \sum_{j=1}^{n_{\mathrm{tot}}} w_j S_j \tag{A.5}$$

is the information entropy of a model where w_j and S_j are respectively the weight and the entropy of the j-th model parameter. Here n_{tot} is the number of model parameters ($n_{\mathrm{cell}} + 3\ \ell_{\max}(\ell_{\max}+2)$). For the brightness cells, $S_j = -Q_j(\log(Q_j/A) - 1)$ is the Shannon entropy and the weights w_j are proportional to the cell area and to a user-provided ratio wcb between brightness entropy and magnetic entropy. For the magnetic field coefficients, $S_j = \sqrt{\alpha_j^2 + B^2} - B - \alpha_j \log\left(\frac{\sqrt{\alpha_j^2+B^2}+\alpha_j}{B}\right)$ and the weights are $w_j = 3\ell$ for the $2\ell_{\max}(\ell_{\max}+2)$ poloidal field coefficients, and $w_j = \ell$ for the $\ell_{\max}(\ell_{\max}+2)$ toroidal field coefficients (see also Brown et al., 1991; Hussain et al., 2001, section 2.1). According to Shannon's information theory, the level of information within a model decreases as its entropy increases.

Reduced chi-square and entropy can be defined slightly differently in other data analysis works, so we warn the reader not to immediately assume these exact expressions when encountering these quantities elsewhere.

For a high enough given $\chi^2_{\mathrm{r,aim}}$, there are often many solutions that can fit a time-series of Stokes I and Stokes V observations down to $\chi^2_{\mathrm{r}} = \chi^2_{\mathrm{r,aim}}$. Among all of them, ZDI looks for the one that maximizes S (for proof of unicity, see Skilling & Bryan, 1984). That model thus bears an amount of information as low as possible while still fitting the data, which makes it the most reliable. To find that model, ZDI uses a conjugate gradient algorithm to iteratively decrease χ^2_{r} towards $\chi^2_{\mathrm{r,aim}}$ while increasing S. At each step, ZDI:

- synthesizes Stokes I and Stokes V profiles for all observation dates from the current model,
- computes χ^2_{r}, S and their gradients,
- modifies the brightness and magnetic maps accordingly.

The algorithm is initialized with a user-provided default brightness and an initial magnetic field strength (shared among all the spherical harmonics modes), and converges when $\chi^2_{\mathrm{r,aim}}$ is reached and the gradients of χ^2_{r} and S are parallel.

A.4 Velocimetry method for the detection of hJs around wTTSs

This section gives the equation of RVs for a star around which a planet orbits on an elliptical orbit (see figure A.4), as a function of the planet mass and orbital parameters.

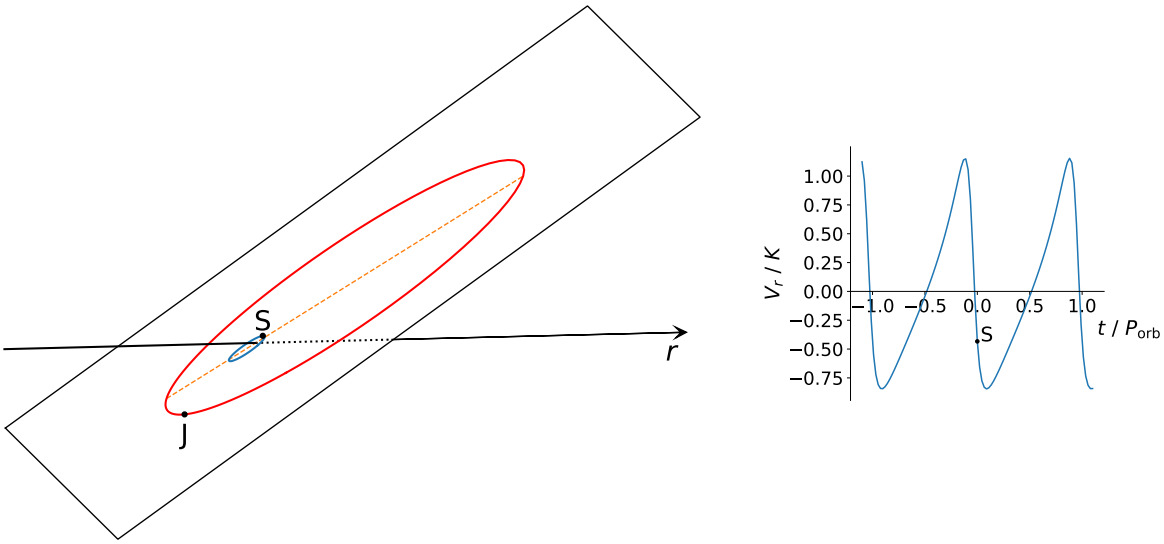

Figure A.4 – *Left:* orbits of a star S and of its hJ J around an assumedly immobile barycenter, in blue and red respectively. The r-axis represents the line of sight. The apsides line is plotted as an orange dashed line. *Right:* RV curve of the star S as a function of time t. K is the semi-amplitude of the RV modulations while P_{orb} is the orbital period.

To obtain the exact equation of V_r, the RV of the star, as a function of time t, we define notations as illustrated in figure A.5: the line of sight is called the r-axis, the acute angle between the r-axis and the normal to the orbit plane is called i, and (x, y) is an orthonormal coordinate

system of the orbit plane where the x-axis is perpendicular to the r-axis and is used as the reference for the polar coordinates system in the orbit plane.

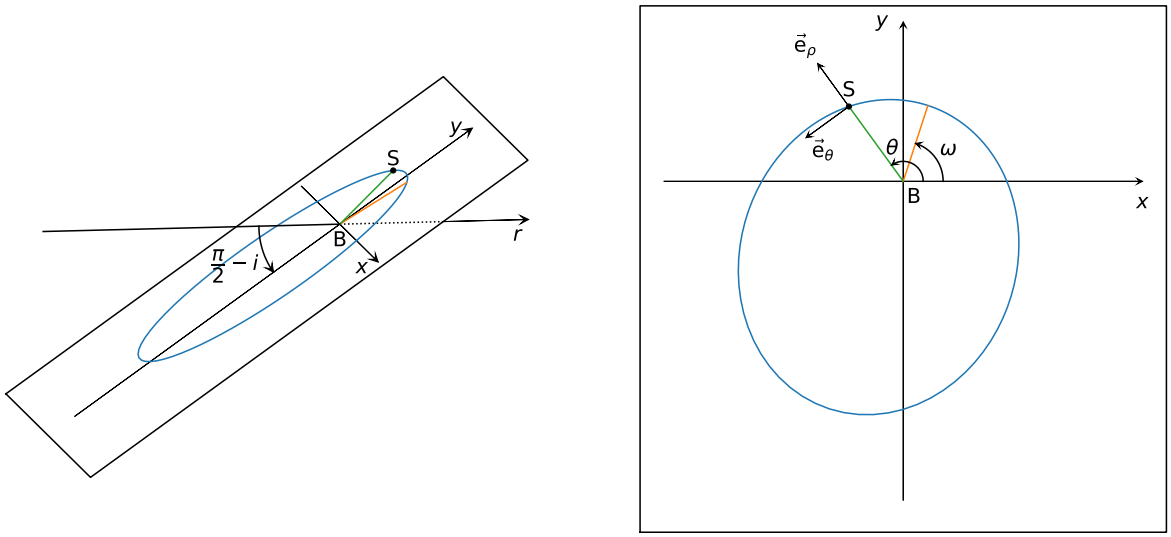

Figure A.5 – Orbit of a star S around an assumedly immobile barycenter B. *Left:* the r-axis represents the line of sight. The x-axis is the intersection between the sky plane and the orbit plane; it is perpendicular to the r-axis. (x, y) is an orthonormal coordinate system of the orbit plane. *Right:* polar coordinates in the orbit plane: ω is the argument of the periapsis, $(\vec{e}_\rho, \vec{e}_\theta)$ is the polar orthonormal base associated with the position of S.

We can derive from the laws of motion (see for example Perryman, 2011) that the orbit of the star verifies, in polar coordinates in the orbital plane:

$$\rho = \frac{p}{1 + e\cos(\theta - \omega)} \quad \text{where} \quad p = a(1 - e^2), \tag{A.6}$$

$$\rho^2\dot{\theta} = C \quad \text{where} \quad \dot{\theta} \equiv \frac{\partial\theta}{\partial t} \quad \text{and} \quad C \equiv \frac{2\pi a^2\sqrt{1-e^2}}{P_{\rm orb}}, \tag{A.7}$$

$$P_{\rm orb} = \frac{2\pi(M_\star + M_{\rm J})}{\sqrt{\mathcal{G}}}\left(\frac{a}{M_{\rm J}}\right)^{3/2} \simeq \frac{2\pi M_\star}{\sqrt{\mathcal{G}}}\left(\frac{a}{M_{\rm J}}\right)^{3/2} \quad \text{for } M_J \ll M_\star \tag{A.8}$$

with a the semi-major axis of the elliptic orbit of the star, $e \in [0; 1[$ its eccentricity, ω the argument of its periapsis, $P_{\rm orb}$ the orbital period, $\mathcal{G}$ the gravitational constant, and $M_\star$ and $M_{\rm J}$ the masses of the star and of the hJ respectively.

At time t, the position of the star S with respect to barycenter B is:

$$\overrightarrow{BS}(t) = \rho(t)\ \vec{e}_\rho(t),$$

therefore, with $\overrightarrow{V}_{\rm B}$ the constant velocity of B, the velocity of the star is:

$$\begin{aligned}
\overrightarrow{V}_\star &= \dot\rho\ \vec{e}_\rho + \rho\ \dot{\vec{e}}_\rho + \overrightarrow{V}_{\rm B} \\
\overrightarrow{V}_\star &= \frac{pe\dot\theta\sin(\theta-\omega)}{\big(1+e\cos(\theta-\omega)\big)^2}\ \vec{e}_\rho + \rho\dot\theta\ \vec{e}_\theta + \overrightarrow{V}_{\rm B} \qquad \text{(using A.6)} \\
\overrightarrow{V}_\star &= \frac{peC\sin(\theta-\omega)}{\rho^2\big(1+e\cos(\theta-\omega)\big)^2}\ \vec{e}_\rho + \frac{C}{\rho}\ \vec{e}_\theta + \overrightarrow{V}_{\rm B} \qquad \text{(using A.7)} \\
\overrightarrow{V}_\star &= \frac{eC\sin(\theta-\omega)}{p}\ \vec{e}_\rho + \frac{C\big(1+e\cos(\theta-\omega)\big)}{p}\ \vec{e}_\theta + \overrightarrow{V}_{\rm B} \qquad \text{(using A.6).}
\end{aligned}$$

To project on the line of sight and obtain $V_r = \overrightarrow{V}_\star \cdot \vec{e}_r$, we use:

$$\begin{aligned}
\vec{e}_\rho \cdot \vec{e}_r &= (\cos\theta\ \vec{e}_x + \sin\theta\ \vec{e}_y)\cdot\vec{e}_r = \sin\theta(\vec{e}_y\cdot\vec{e}_r) = \sin\theta\sin i \\
\vec{e}_\theta \cdot \vec{e}_r &= (-\sin\theta\ \vec{e}_x + \cos\theta\ \vec{e}_y)\cdot\vec{e}_r = \cos\theta(\vec{e}_y\cdot\vec{e}_r) = \cos\theta\sin i.
\end{aligned}$$

Finally:

$$\begin{aligned}
V_r &= \frac{eC\sin(\theta-\omega)}{p}\sin\theta\sin i + \frac{C\big(1+e\cos(\theta-\omega)\big)}{p}\cos\theta\sin i + V_{r,\rm B} \\
&= \frac{C\sin i}{p}\Big(e\big(\sin(\theta-\omega)\sin\theta + \cos(\theta-\omega)\cos\theta\big) + \cos\theta\Big) + V_{r,\rm B} \\
&= \frac{C\sin i}{p}\big(e\cos(\omega) + \cos\theta\big) + V_{r,\rm B} \\
&= \frac{2\pi a^2\sqrt{1-e^2}}{P_{\rm orb}}\frac{\sin i}{a(1-e^2)}\big(e\cos(\omega)+\cos\theta\big) + V_{r,\rm B} \\
V_r &= K\big(e\cos(\omega)+\cos\theta\big) + V_{r,\rm B} \quad \text{with } K \equiv \frac{2\pi a\sin i}{P_{\rm orb}\sqrt{1-e^2}}.
\end{aligned} \tag{A.9}$$

The dependency of θ with time is given by:

$$\theta(t) = \begin{cases} \omega + 2\tan^{-1}\left(\sqrt{\dfrac{1+e}{1-e}}\tan\left(\dfrac{E(t)}{2}\right)\right) & \text{for } E \neq \pi[2\pi], \\ \omega+\pi & \text{otherwise} \end{cases}$$

where $E(t)$ is the solution of

$$E - e\sin E = 2\pi(t/P_{\rm orb} - \phi),$$

with ϕ depending on the choice for the origin of time. E is called the eccentric anomaly.

Fitting such a curve into RV data points therefore requires to optimize the 6 parameters K, $P_{\rm orb}$, e, ω, ϕ and $V_{r,\rm B}$. For a circular orbit, $e = 0$ and we can set ω arbitrarily, so, choosing $\omega = 0$:

$$V_r = K\cos\left(2\pi\left(\frac{t}{P_{\rm orb}} - \phi\right)\right) + V_{r,\rm B},$$

which leaves 4 parameters to optimize: K, $P_{\rm orb}$, ϕ and $V_{r,\rm B}$.

For a Jupiter-size planet around a solar-size star, $M_J/M_\star \simeq 10^{-3}$ so we consider that $M_J \ll M_\star$

and derive information on a, on M_J and on the semi-major axis of the planet a_J as follows:

$$\begin{aligned} a\sin i &= \frac{K P_{\rm orb}\sqrt{1-e^2}}{2\pi} \\ M_J \sin i &\simeq a\sin i \left(\frac{2\pi M_\star}{P_{\rm orb}\sqrt{\mathcal{G}}}\right)^{2/3} \qquad \text{(using A.8)} \\ M_J \sin i &\simeq K\sqrt{1-e^2}\left(\frac{P_{\rm orb} M_\star^2}{2\pi\mathcal{G}}\right)^{1/3} \\ a_J = \frac{aM_\star}{M_J} &\simeq \left(\frac{P_{\rm orb}\sqrt{\mathcal{G}M_\star}}{2\pi}\right)^{2/3}. \end{aligned}$$

We note that, with V_r alone, it is not possible to derive M_J and i individually.

A.5 Numerical tools for analyzing pseudo-periodic signals

A.5.1 Lomb-Scargle periodogram

In order to look for dominant frequencies in signals that are unevenly sampled, such as astronomical observations, we use a tool called Lomb-Scargle periodograms. The content of this section is heavily inspired from chapter 13 of Press et al. (1992). For a set of times $(t_i)_{i=1,\dots,N}$ and corresponding observations $(h_i)_i$, the Lomb normalized periodogram gives the spectral power of angular frequency $\omega \equiv 2\pi f$:

$$P_N(\omega) \equiv \frac{1}{2\sigma^2}\left\{ \frac{\left[\sum_j \left(h_j - \bar{h}\right)\cos\omega(t_j-\tau)\right]^2}{\sum_j \cos^2\omega(t_j-\tau)} + \frac{\left[\sum_j \left(h_j - \bar{h}\right)\sin\omega(t_j-\tau)\right]^2}{\sum_j \sin^2\omega(t_j-\tau)} \right\} \tag{A.10}$$

where:

$$\begin{aligned} \bar{h} &\equiv \frac{1}{N}\sum_1^N h_i \\ \sigma^2 &\equiv \frac{1}{N-1}\sum_1^N (h_i-\bar{h})^2 \\ \tan(2\omega\tau) &= \frac{\sum_j \sin 2\omega t_j}{\sum_j \cos 2\omega t_j}. \end{aligned}$$

τ is defined so that shifting all t_i by any constant leaves P_N unchanged: P_N is independent from the choice of the origin of time. Furthermore, for any angular frequency ω, equation A.10 is equivalent to the spectral power one would obtain when fitting $A\cos\omega t + B\sin\omega t$ into $(h_i)_i$ with a least-squares approach.

The advantage of Lomb-Scargle periodograms is the ability to easily estimate the significance of a peak in the periodogram: if $(h_i)_i$ is a white noise realization, then, for a given angular frequency ω, the probability that its spectral power is larger than a given $z > 0$ is e^{-z}. Therefore, if the spectral power of M independent frequencies is computed, the probability that none of them is larger than z is $(1-e^{-z})^M$. As a consequence, if a peak of value z is observed in a periodogram, the probability for it to be a false alarm is:

$$\mathcal{P}(>z) = 1-(1-e^{-z})^M.$$

With a given range of sampled frequencies, the number of independent frequencies M remains to be determined. For small false-alarm probabilities $\mathcal{P}(> z) \ll 1$, we have $\mathcal{P}(> z) \simeq Me^{-z}$, so an error of $x\%$ on M induces an error of $\sim x\%$ on the levels of false-alarm. We usually look for levels spaced by factors of ~ 3, so the accuracy on the estimation of M does not need to be very high. In general, noting $T \equiv t_{\max} - t_{\min}$, for a dense sampling of the range $[0, f_{\max}]$ with $f_{\max} > f_c \equiv N/(2T)$, the following is a good enough estimate of M:

$$M \simeq N \frac{f_{\max}}{f_c}.$$

An example is displayed in figure A.6.

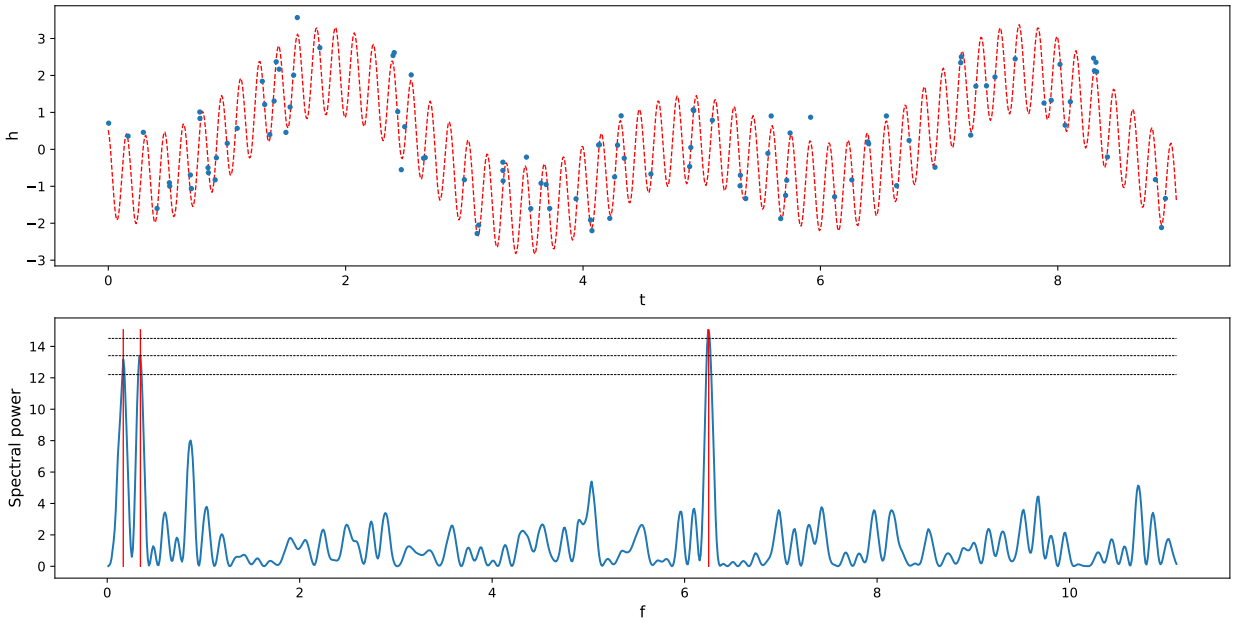

Figure A.6 – Example of a noised signal (top) and its Lomb-Scargle periodogram (bottom). *Top:* the theoretical signal, represented as a red dashed curve, is the sum of three sine curves whose frequencies are indicated by the red vertical lines in the bottom plot. The observed signal is a sample of $N = 100$ points in a time span $T = 9$ (arbitrary units), where a white noise of standard deviation 0.3 (arbitrary units) was added. *Bottom:* Lomb-Scargle periodogram for 1000 different frequencies evenly sampled between 0.01 and $f_{\max} = 2f_c \simeq 11.11$. The false-alarm probability levels of 0.1%, 0.03% and 0.01% are represented as horizontal black dashed lines (from bottom to top respectively).

A.5.2 Gaussian process regression

In the case of wTTSs, measurements such as the light curve are quasi-periodic on time spans of a few days, with the effect of stellar rotation dominating over other effects of shorter or longer time scales. However, when an observation run lengthens, the signal progressively loses its periodicity as the surface of the star evolves due to differential rotation, appearances and disappearances of spots, etc... Lomb-Scargle periodograms thus become less reliable and a new method is needed which can model these changes on longer time scales. Gaussian process regression (GPR, Rasmussen & Williams, 2006; Aigrain et al., 2012; Haywood et al., 2014; Donati et al., 2017) offers a welcome flexibility here. Let us explain it step by step.

Gaussian process By definition, a Gaussian process (GP) is a collection (finite or infinite) of random variables, any finite subset of which have a joint Gaussian distribution. A GP is characterized by its **mean** m and **covariance function** k and noted $\mathcal{GP}(m,k)$. Here the random variables will be predictions of a certain quantity evolving with time, for example the light curve $L(t)$. Modelling $L(t)$ by a GP of mean and covariance function $(\tilde{L}(t), k_L(t,t'))$ means that, for any times $t_1, t_2, ..., t_N$, the corresponding $L(t_1), L(t_2), ..., L(t_N)$ are correlated Gaussian random variables of joint probability distribution $\mathcal{N}(\tilde{\mathbf{L}}, K)$, where $\tilde{\mathbf{L}} = (\tilde{L}(t_1), \tilde{L}(t_2), ..., \tilde{L}(t_N))$ and K is the matrix defined by $K_{i,j} = k_L(t_i, t_j)$.

Inputs of GPR Let $f(t)$ be a scalar quantity that we want to model with GPR, on which we have measurements at times $(t_i)_{i=1,...,N}$, that we note $(y_i)_i$, with error bars $(\sigma_i)_i$. The inputs of GPR include the data points $(t_i, y_i, \sigma_i)_i$ of course, but also a prior distribution $\mathcal{GP}(m,k)$, which can be assimilated to a blind guess on f when no data is acquired yet. Once measurements start to be acquired, the probability distribution of f becomes conditioned by them as dictated by k. The resulting GP after accounting for all the measurements is called the posterior distribution of f.

Example: pseudo-periodic covariance function For example in our case, if we want to model our data with a pseudo-periodic function, we can set $k(t, t+P_{\text{rot}})$ to be relatively high. Thus, at an arbitrarily chosen t, while the prior distribution for $f(t)$ is $f(t) \sim \mathcal{N}(m(t), k(t,t))$, a measurement $(y(t+P_{\text{rot}}), \sigma(t+P_{\text{rot}}))$ will change the distribution of $f(t)$ by making it "closer to" $\mathcal{N}(y(t+P_{\text{rot}}), \sigma(t+P_{\text{rot}}))$. Figure 2.7 illustrates how the successive measurements condition the probability distribution on each $f(t)$, for a prior of the form:

$$\begin{aligned} m(t) &= 0 \\ k(t,t') &= \theta_1^2 \ \exp\left(-\frac{(t-t')^2}{\theta_3^2} - \frac{\sin^2\left(\frac{\pi(t-t')}{\theta_2}\right)}{\theta_4^2} \right). \end{aligned}$$

This covariance function is called a **pseudo-periodic covariance function** and its parameters, called **hyperparameters**, are the amplitude $\theta_1 > 0$, the cycle $\theta_2 > 0$, the decay time $\theta_3 > \theta_2$ and the smoothing parameter $\theta_4 \in [0;1[$. On figure 2.7, as is common with GPR, the GP is represented by its mean curve $\tilde{f}(t)$ and a shaded area of semi-amplitude $s(t)$, which indicate that, for any t, the posterior probability distribution of $f(t)$ is: $f(t)|\text{data} \sim \mathcal{N}(\tilde{f}(t), s(t)^2)$. This representation alone does not indicate how $f(t), f(t')$ are correlated for any $t \neq t'$.

Mathematical expression The exact mathematics are as follows (rigorous demonstrations are given in section 2.2 of Rasmussen & Williams, 2006, we simply paste the formulae here). We note:

- $\mathbf{t} = (t_1, t_2, ..., t_N)$ the vector of times at which data was taken,
- $\mathbf{y} = (y_1, y_2, ..., y_N)$ the vector of corresponding measurements,
- $\sigma_1, \sigma_2, ..., \sigma_N$ their respective error bars,
- $\mathbf{t}^* = (t_1^*, t_2^*, ..., t_M^*)$ the vector of times at which we wish to predict f using GPR,
- $\mathbf{f}^*$ the corresponding random variable,
- $\mathcal{GP}(m(t), k(t,t'))$ the prior,
- $\mathbf{m} = (m(t_1), m(t_2), ..., m(t_N))$ and $\mathbf{m}^* = (m(t_1^*), m(t_2^*), ..., m(t_M^*))$,
- $K(\mathbf{t}, \mathbf{t}^*)$ the $N \times M$ matrix whose element at i-th row, j-th column is $k(t_i, t_j^*)$, and we can define $K(\mathbf{t}, \mathbf{t})$, $K(\mathbf{t}^*, \mathbf{t})$ and $K(\mathbf{t}^*, \mathbf{t}^*)$ in an analogous manner.

GPR gives the posterior distribution:

$$\begin{aligned}\mathbf{f}^*|\mathbf{t},\mathbf{y},\mathbf{t}^* &\sim \mathcal{N}\Big(\tilde{\mathbf{f}}^*, \mathrm{cov}(\mathbf{f}^*)\Big), \\ \tilde{\mathbf{f}}^* &= \mathbf{m}^* + K(\mathbf{t}^*,\mathbf{t})\Big(K(\mathbf{t},\mathbf{t}) + \mathrm{diag}(\sigma_1^2,\sigma_2^2,...,\sigma_N^2)\Big)^{-1}(\mathbf{y}-\mathbf{m}) \\ \mathrm{cov}(\mathbf{f}^*) &= K(\mathbf{t}^*,\mathbf{t}^*) - K(\mathbf{t}^*,\mathbf{t})\Big(K(\mathbf{t},\mathbf{t}) + \mathrm{diag}(\sigma_1^2,\sigma_2^2,...,\sigma_N^2)\Big)^{-1}K(\mathbf{t},\mathbf{t}^*).\end{aligned} \tag{A.11}$$

Marginal likelihood of the covariance function In practice, the problem we face is that m, k are not exactly known: we can assume a parametrized form for them (for example equation 2.2), but without knowing the hyperparameters. As a matter of fact, the hyperparameters are generally the quantities we are really interested in. For a given prior $\mathcal{GP}(m,k)$, we introduce the **marginal likelihood**, defined formally as:

$$p(\mathbf{y}|\mathbf{t},(m,k)) = \int p(\mathbf{y}|\mathbf{f},\mathbf{t})p(\mathbf{f}|\mathbf{t},(m,k))\mathrm{d}\mathbf{f},$$

where $\mathbf{y}$ and $\mathbf{t}$ are the same as above. In the integrand, $\mathbf{f}$ represents a random realization of the prior distribution $\mathcal{GP}(m,k)$, so the quantity in the integrand is the probability that the actual quantity is $\mathbf{f}$ and that the measured data is $\mathbf{y}$. So the marginal likelihood is the probability of measuring $\mathbf{y}$ at times $\mathbf{t}$, integrated over all realizations of the prior $\mathcal{GP}(m,k)$. Intuitively, the more representative the prior distribution is of the data, the higher the marginal likelihood should be. In general we use the marginal likelihood in logarithmic form, which is expressed as a function of $\mathbf{t}$ and $\mathbf{y}$ as:

$$\log\mathcal{L}(m,k) = -\frac{1}{2}\Big(N\log(2\pi) + \log(\det C) + (\mathbf{y}-\mathbf{m})^T C^{-1}(\mathbf{y}-\mathbf{m})\Big),$$

where $C = K(\mathbf{t},\mathbf{t}) + \mathrm{diag}(\sigma_1^2,\sigma_2^2,...,\sigma_N^2)$. The term $\log(\det C)$ can be seen as a penalization term over the "complexity" of k, while the term $(\mathbf{y}-\mathbf{m})^T C^{-1}(\mathbf{y}-\mathbf{m})$ controls the quality of the fit. The prior of maximal marginal likelihood will thus be, roughly speaking, the simplest one among those that allow to fit the data well enough.

MCMC for the choice of the covariance function In the framework of this thesis, the covariance of the prior will always be pseudo-periodic (equation 2.2) and the mean will be, depending on the case, either zero or a keplerian curve with 3 or 5 parameters (see section 2.4.1). Our problem is thus to optimize the values of the hyperparameters $\boldsymbol{\theta} = (\theta_1,\theta_2,...,\theta_n)$. Theoretically, we should use Bayes' rule which gives us the probability for $\boldsymbol{\theta}$ given the measurements $\mathbf{y}(\mathbf{t})$:

$$p(\boldsymbol{\theta}|\mathbf{t},\mathbf{y}) = \frac{p(\mathbf{y}|\mathbf{t},\boldsymbol{\theta})p(\boldsymbol{\theta})}{p(\mathbf{y}|\mathbf{t})}.$$

$p(\mathbf{y}|\mathbf{t},\boldsymbol{\theta})$ is the marginal likelihood as defined in equation 2.3, $p(\boldsymbol{\theta})$ is the hyper-prior distribution, corresponding to a priori information we have on $\boldsymbol{\theta}$, and

$$p(\mathbf{y}|\mathbf{t}) = \int p(\mathbf{y}|\mathbf{t},\boldsymbol{\theta})p(\boldsymbol{\theta})\mathrm{d}\boldsymbol{\theta} \tag{A.12}$$

is a normalization constant. This time, there is no particular reason for the hyper-prior to follow a Gaussian probability distribution so we cannot simplify these expressions easily. Furthermore, the integral in equation A.12 is often difficult to evaluate in practice. As a result, we optimize $\boldsymbol{\theta}$ by maximizing the marginal likelihood $p(\mathbf{y}|\mathbf{t},\boldsymbol{\theta})$ instead. Despite having an analytical expression for the likelihood (equation 2.3), it is in general very time-consuming to invert it in order to obtain

the optimum. Therefore, we sample the hyperparameter space using a Markov Chain Monte-Carlo (MCMC) algorithm, which is a way to randomly sample the hyper-parameter space and compute the likelihood at each sampled point, by favoring regions of higher likelihood. A more rigorous explanation is provided for example at section 15.8 of Press et al. (2007) or in Haywood (2015). This exploration algorithm returns the posterior probability distribution in the hyper-parameter space, from prior distributions of the hyperparameters. For the pseudo-periodic covariance functions, the hyperparameters have the prior distributions as described in table A.1 within this thesis.

Table A.1 – Priors for our GPR-MCMC runs. For the modified Jeffreys prior, σ is the knee value, for the Gaussian prior m_2 is the mean and σ_2 is the standard deviation, and for the Jeffreys and the uniform priors a and b are the lower and upper boundaries.

Hyperparameter	Prior
θ_1	Modified Jeffreys (σ)
θ_2 ($P_{\rm rot}$)	Gaussian (m_2, σ_2^2)
θ_3 ($P_{\rm rot}$)	Jeffreys (a_3, b_3)
θ_4	Uniform (a_4, b_4)

B | Publications

B.1 As first author

B.1.1 MNRAS publication: Yu et al. 2017

Monthly Notices of the ROYAL ASTRONOMICAL SOCIETY

MNRAS **467,** 1342–1359 (2017) doi:10.1093/mnras/stx009
Advance Access publication 2017 January 7

A hot Jupiter around the very active weak-line T Tauri star TAP 26

L. Yu,[1,2]★ J.-F. Donati,[1,2] E. M. Hébrard,[3] C. Moutou,[4] L. Malo,[5] K. Grankin,[6] G. Hussain,[7,1] A. Collier Cameron,[8] A. A. Vidotto,[9] C. Baruteau,[1,2] S. H. P. Alencar,[10] J. Bouvier,[11,12] P. Petit,[1,2] M. Takami,[13] G. J. Herczeg,[14] S. G. Gregory,[8] M. Jardine,[8] J. Morin,[15] F. Ménard[11,12] and the MaTYSSE collaboration

[1]*Université de Toulouse, UPS-OMP, IRAP, 14 avenue E. Belin, Toulouse F-31400, France*
[2]*CNRS, IRAP / UMR 5277, 14 avenue E. Belin, Toulouse, F-31400, France*
[3]*Department of Physics and Astronomy, York University, Toronto, ON L3T 3R1, Canada*
[4]*CFHT Corporation, 65-1238 Mamalahoa Hwy, Kamuela, HI 96743, USA*
[5]*Département de physique, Université de Montréal, C. P. 6128, Succursale Centre-Ville, Montréal, QC H3C 3J7, Canada*
[6]*Crimean Astrophysical Observatory, Nauchny, Crimea 298409, Ukraine*
[7]*ESO, Karl-Schwarzschild-Str 2, D-85748 Garching, Germany*
[8]*SUPA, School of Physics and Astronomy, University of St Andrews, St Andrews, Scotland KY16 9SS, UK*
[9]*School of Physics, Trinity College Dublin, the University of Dublin, Dublin-2, Ireland*
[10] *Departamento de Fisica – ICEx – UFMG, Av. Antônio Carlos, 6627, 30270-901 Belo Horizonte, MG, Brazil*
[11]*Université Grenoble Alpes, IPAG, BP 53, F-38041 Grenoble Cédex 09, France*
[12]*CNRS, IPAG/UMR 5274, BP 53, F-38041 Grenoble Cédex 09, France*
[13]*Institute of Astronomy and Astrophysics, Academia Sinica, PO Box 23-141, 106 Taipei, Taiwan*
[14]*Kavli Institute for Astronomy and Astrophysics, Peking University, Yi He Yuan Lu 5, Haidian Qu, Beijing 100871, China*
[15]*LUPM, Université de Montpellier, CNRS, place E. Bataillon, F-34095 Montpellier, France*

Accepted 2017 January 3. Received 2016 December 19; in original form 2016 October 13

ABSTRACT

We report the results of an extended spectropolarimetric and photometric monitoring of the weak-line T Tauri star TAP 26, carried out within the Magnetic Topologies of Young Stars and the Survival of close-in massive Exoplanets (MaTYSSE) programme with the Echelle SpectroPolarimetric Device for the Observation of Stars (ESPaDOnS) spectropolarimeter at the 3.6-m Canada–France–Hawaii Telescope. Applying Zeeman–Doppler Imaging (ZDI) to our observations, concentrating in 2015 November and 2016 January and spanning 72 d in total, 16 d in 2015 November and 13 d in 2016 January, we reconstruct surface brightness and magnetic field maps for both epochs and demonstrate that both distributions exhibit temporal evolution not explained by differential rotation alone. We report the detection of a hot Jupiter (hJ) around TAP 26 using three different methods, two using ZDI and one Gaussian-process regression (GPR), with a false-alarm probability smaller than 6×10^{-4}. However, as a result of the aliasing related to the observing window, the orbital period cannot be uniquely determined; the orbital period with highest likelihood is 10.79 ± 0.14 d followed by 8.99 ± 0.09 d. Assuming the most likely period, and that the planet orbits in the stellar equatorial plane, we obtain that the planet has a minimum mass $M\sin i$ of 1.66 ± 0.31 M_{Jup} and orbits at 0.0968 ± 0.0032 au from its host star. This new detection suggests that disc type II migration is efficient at generating newborn hJs, and that hJs may be more frequent around young T Tauri stars than around mature stars (or that the MaTYSSE sample is biased towards hJ-hosting stars).

Key words: magnetic fields – techniques: polarimetric – planets and satellites: formation – stars: imaging – stars: individual: TAP 26 – stars: rotation.

1 INTRODUCTION

Studying young forming stars stands as our best chance to progress in our understanding of the formation and early evolution of planetary systems. For instance, detecting hot Jupiters (hJs) around

★ E-mail: louise.yu@irap.omp.eu

© 2017 The Authors
Published by Oxford University Press on behalf of the Royal Astronomical Society

Downloaded from https://academic.oup.com/mnras/article-abstract/467/2/1342/2869846 by Université Paul Sabatier - Toulouse 3 user on 16 December 2019

young stars (1–10 Myr) and determining their orbital properties can enable us to clarify how they form and migrate, and to better characterize the physical processes (e.g. planet–disc interaction, planet–planet scattering, Baruteau et al. 2014, in situ formation, Batygin, Bodenheimer & Laughlin 2016) responsible for generating such planets.

However, young stars are enormously active, rendering planet signatures in their spectra and/or light curves extremely difficult to detect in practice. Until very recently, most planets found so far around stars younger than 20 Myr were distant planets detected with imaging techniques (e.g. β Pic b, Lagrange et al. 2010, and LkCa 15, Sallum et al. 2015). Early claims of hJs orbiting around T Tauri stars (e.g. TW Hya, Setiawan et al. 2008) finally proved to be activity signatures mistakenly interpreted as radial velocity (RV) signals from close-in giant planets (Huélamo et al. 2008).

Following the recent discovery of newborn close-in giant planets (David et al. 2016; Donati et al. 2016; Mann et al. 2016) or planet candidates (van Eyken et al. 2012; Johns-Krull et al. 2016) around forming stars, time is ripe for a systematic exploration of hJs around T Tauri stars, and in particular the so-called weak-line T Tauri stars (wTTSs), whose accretion disc has just dissipated. This is one of the main goals of the Magnetic Topologies of Young Stars and the Survival of close-in massive Exoplanets (MaTYSSE) large-programme allocated on the 3.6-m Canada–France–Hawaii Telescope (CFHT), thanks to which the youngest hJ discovered so far was detected (Donati et al. 2016, 2017) and within which this study places.

In this paper, we present results for another wTTS, the young pre-main sequence (PMS) solar-mass star, TAP 26, (Feigelson et al. 1987; Grankin et al. 2008; Grankin 2013), located in the Taurus star-forming region. TAP 26 was observed in late 2015 and early 2016 with both the Echelle SpectroPolarimetric Device for the Observation of Stars (ESPaDOnS) spectropolarimeter and the 1.25-m telescope at the Crimean Astrophysical Observatory (CrAO). After documenting our observations (Section 2), we derive the stellar parameters of TAP 26 (Section 3), before reconstructing the surface magnetic and brightness maps by applying Zeeman–Doppler Imaging (ZDI) to our data (Section 4). We finally detail in Section 5 our detection of a planet RV signal in its spectrum, using three different methods. The first two methods are based on ZDI following previous studies (Donati et al. 2015, 2017; Petit et al. 2015), and the third one exploits Gaussian-process regression (GPR, Haywood et al. 2014; Rajpaul et al. 2015, see Section 5).

2 OBSERVATIONS

TAP 26 was observed in 2015 November and 2016 January using the high-resolution spectropolarimeter ESPaDOnS at the 3.6-m CFHT at Mauna Kea (Hawaii). ESPaDOnS collects stellar spectra spanning the entire optical domain (from 370 to 1000 nm) at a resolving power of 65 000 (i.e. resolved velocity element of 4.6 km s^{-1}) over the full wavelength range (Donati 2003). A total of 29 unpolarized (Stokes *I*) and circularly polarized (Stokes *V*) spectra were collected over a time span of 72 d, 16 spectra over 16 nights in 2015 November and 13 spectra over 13 nights in 2016 January. The rate was of one spectrum per night, except at the beginning of the 2015 November session where a three-day gap following the first observation was compensated by pairs of observations on November 25, November 29 and December 01. However, given the 0.71 d rotation period of TAP 26, phase coverage is not optimal and the 2015 November data set presents gaps of 0.15–0.25 rotation cycle (see Table 1).

Each polarization exposure sequence consists of four individual subexposures taken in different polarimeter configurations to allow the removal of all spurious polarization signatures at first order. All raw frames are processed with the nominal reduction package LIBRE ESPRIT as described in the previous papers of the series (e.g. Donati et al. 2010, 2011, 2014), yielding a typical rms RV precision of 20–30 m s^{-1} (Moutou et al. 2007; Donati et al. 2008). The peak signal-to-noise ratios (S/N, per 2.6 km s^{-1} velocity bin) achieved on the collected spectra range between 100 and 150 (median 140), depending mostly on weather/seeing conditions. The full journal of observations is presented in Table 1.

Rotational cycles (noted E in the following equation) are computed from Barycentric Julian Dates (BJDs) according to the ephemeris:

$$\mathrm{BJD(d)} = 2457344.8 + P_{\rm rot}E \quad (1)$$

in which the photometrically determined rotation period $P_{\rm rot}$ (equal to 0.7135 d, Grankin 2013) is taken from the literature and the initial Julian date (2457344.8 d) is chosen arbitrarily.

Least-squares deconvolution (LSD; Donati et al. 1997) was applied to all spectra. The line list we employed for LSD is computed from an ATLAS9 local thermodynamic equilibrium model atmosphere (Kurucz 1993) featuring $T_{\rm eff}$ = 4500 K and $\log g$= 4.5, the most appropriate model for TAP 26 (see Section 3). Only moderate to strong atomic spectral lines are included in this list (see e.g. Donati et al. 2010, for more details). Altogether, about 7800 spectral features (with about 40 per cent from Fe I) are used in this process. The Stokes *I* and Stokes *V* LSD profiles can be seen in Section 4. Significant distortions are visible in all Stokes *I* LSD profiles, indicating the presence of brightness inhomogeneities covering a large fraction of the surface of TAP 26 at the time of our observations. The noise level in Stokes I LSD profiles is measured from continuum intervals (see Table 1), and includes not only the noise from photon statistics, but also the (often dominant) noise introduced by LSD.

Among the 29 profiles we used, 11 were contaminated by solar light reflected off the Moon (5 in 2015 November, the Moon being at 9.°5 from TAP 26 and at 99 per cent illumination on 2015 November 26, and 6 in 2016 January, the Moon being at 12° from TAP 26 and at 85 per cent illumination on 2016 January 19); we applied a two-step process involving tomographic imaging, described in Donati et al. (2017), to filter out this contamination from our Stokes *I* LSD profiles.

Regarding the Stokes *V* profiles, Zeeman signatures are detected in all observations, featuring amplitudes of typically 0.1 per cent. Expressed in units of the unpolarized continuum level $I_{\rm c}$, the average noise levels of the Stokes *V* LSD signatures (dominated here by photon statistics) range from 2.3×10^{-4} to 3.9×10^{-4} per 1.8 km s^{-1} velocity bin – with a median value of 2.8×10^{-4}.

The emission core of the Ca II infrared triplet lines exhibit an average equivalent width of $\simeq$10 km s^{-1}, corresponding to the amount expected from chromospheric emission for such a wTTS. The He I D_3 line is relatively faint (average equivalent width of $\simeq$5 km s^{-1}), demonstrating that accretion is no longer taking place at its surface, in agreement with previous studies (Donati et al. 2014, 2015). The Hα line is also relatively weak by wTTS standards (Kenyon & Hartmann 1995), with an average equivalent width of 40 km s^{-1}, and is modulated with a period of 0.7132 $\pm$ 0.0002 d (see Appendix B).

Contemporaneous $VR_{\rm J}$ photometric observations were also collected from the CrAO 1.25-m telescope between 2015 August and 2016 March. They indicate a brightness modulation with a period of 0.7138 $\pm$ 0.0001 d of full amplitude 0.116 mag in *V* (see Table 2). By analogy with other wTTSs, these photometric variations can be safely attributed to the presence of brightness features at the surface

Downloaded from https://academic.oup.com/mnras/article-abstract/467/2/1342/2869846 by Université Paul Sabatier - Toulouse 3 user on 16 December 2019

Table 1. Journal of ESPaDOnS observations of TAP 26 collected in 2015 November (first 16 lines) and 2016 January (last 13 lines). Each observation consists of a sequence of four subexposures, each lasting 695 s. Columns 1–4, respectively, list (i) the UT date of the observation, (ii) the corresponding UT time (at mid-exposure), (iii) the BJD in excess of 2457300, and (iv) the peak signal to noise ratio (per 2.6 km s^{-1} velocity bin) of each observation. Column 5 lists the root-mean-square (rms) noise level (relative to the unpolarized continuum level I_c and per 1.8 km s^{-1} velocity bin) in the circular polarization profiles produced by LSD and column 6 lists the signal-to-noise ratio in the unpolarized profiles produced by LSD, measured from the noise level in intervals of continuum of the LSD profiles. Column 7 indicates the rotational cycle associated with each exposure (using the ephemeris given by equation 1). Column 8 lists the raw RVs computed from the unpolarized spectra, column 9 the filtered RVs (see Section 5.1) and column 10 the 1σ error bar on both RV_{raw} and RV_{filt}. Columns 11–13 list values for activity proxies mentioned in Appendix B: the line-of-sight-projected magnetic field averaged over the visible stellar hemisphere (also called longitudinal field) and the equivalent width of the Hα emission (counted from above the continuum level, expressed in km s^{-1}, and with a typical 1σ error bar of 3.0 km s^{-1}).

Date	UT (h:m:s)	BJD (2457300+)	S/N	σ_{LSD} (10^{-4})	S/N_I	Cycle	RV_{raw} (km s^{-1})	RV_{filt} (km s^{-1})	σ_{RV} (km s^{-1})	B_ℓ (G)	σ_{B_ℓ} (G)	$EW_{H\alpha}$ (km s^{-1})
Nov 18	09:36:28	44.90594	140	3.3	1867	0.148	1.049	0.141	0.075	99	45	39.3
Nov 22	12:11:18	49.01352	140	3.3	1835	5.905	− 1.115	0.026	0.076	−72	47	37.6
Nov 23	11:20:34	49.97830	140	3.1	1862	7.258	0.677	− 0.120	0.075	−20	46	36.2
Nov 24	11:20:25	50.97819	140	3.0	1890	8.659	0.915	− 0.020	0.074	−143	45	43.1
Nov 25	07:41:04	51.82588	140	3.3	1804	9.847	− 0.017	− 0.149	0.078	−182	47	44.0
Nov 25	13:49:53	52.08201	140	3.2	1861	10.206	1.204	− 0.077	0.075	−28	46	29.3
Nov 26	10:09:09	52.92871	150	3.0	1922	11.393	− 0.791	− 0.176	0.073	71	44	26.9
Nov 27	11:36:33	53.98941	120	3.9	1866	12.879	− 0.590	− 0.087	0.075	−44	46	52.7
Nov 28	11:25:28	54.98171	110	4.0	1849	14.270	0.491	− 0.019	0.076	−59	46	37.4
Nov 29	08:19:32	55.85260	140	3.1	1894	15.491	0.224	− 0.016	0.074	26	45	38.7
Nov 29	11:15:55	55.97508	140	3.3	1870	15.662	1.007	0.052	0.075	−129	46	42.1
Nov 30	07:30:58	56.81887	150	3.2	1863	16.845	0.508	0.184	0.075	−199	46	44.7
Dec 01	08:19:49	57.85279	140	3.2	1879	18.294	0.273	0.187	0.075	−107	45	47.2
Dec 01	11:18:25	57.97681	130	3.4	1909	18.468	0.158	0.084	0.074	40	45	44.1
Dec 02	07:48:41	58.83116	150	3.1	1887	19.665	1.068	0.097	0.074	−164	45	45.9
Dec 03	09:55:37	59.91929	150	3.0	1899	21.190	1.147	0.082	0.074	51	45	30.4
Jan 17	09:19:04	104.89186	130	3.5	1759	84.221	0.200	− 0.070	0.080	−45	49	34.0
Jan 18	05:01:52	105.71318	140	3.2	1816	85.372	− 0.500	− 0.144	0.077	−15	47	24.5
Jan 19	05:02:31	106.71356	140	3.4	1772	87.774	0.594	− 0.140	0.079	−36	48	57.9
Jan 20	07:55:33	107.83363	100	4.8	1708	88.344	− 0.478	− 0.078	0.082	−48	50	26.6
Jan 21	05:04:22	108.71467	140	3.4	1792	89.579	0.613	− 0.067	0.078	71	48	37.6
Jan 22	05:04:03	109.71438	120	4.1	1738	90.980	− 0.937	0.068	0.081	−201	49	44.0
Jan 23	06:06:31	110.75767	140	3.3	1802	92.442	0.376	0.190	0.078	1	47	38.9
Jan 24	05:05:28	111.71519	140	3.2	1780	93.784	0.944	0.102	0.079	−127	48	46.4
Jan 25	06:30:41	112.77428	140	3.3	1805	95.269	− 0.014	0.169	0.078	27	47	37.0
Jan 26	06:03:54	113.75560	140	3.5	1767	96.644	0.778	0.100	0.079	−51	48	44.9
Jan 27	06:58:50	114.79365	140	3.4	1774	98.099	− 1.185	− 0.011	0.079	−2	48	39.7
Jan 28	06:59:12	115.79383	140	3.4	1737	99.501	0.548	− 0.019	0.081	70	49	41.8
Jan 29	06:05:30	116.75644	130	3.5	1758	100.850	0.958	0.062	0.080	−71	49	41.7

of TAP 26 modulated by rotation. The small difference with the value found in Grankin (2013) suggests the presence of differential rotation in TAP 26 (see Section 4).

3 EVOLUTIONARY STATUS OF TAP 26

TAP 26 is a well-studied single wTTSs, close enough to T Tau, both spatially and in terms of velocity, to assume a distance of 147 ± 3 pc (Loinard et al. 2007; Torres et al. 2009), with an error bar similar to that found on other regions of Taurus like L1495.

Applying the automatic spectral classification tool especially developed in the context of Magnetic Protostars and Planets (MaPP) and MaTYSSE, following that of Valenti & Fischer (2005) and discussed in Donati et al. (2012), we find that the photospheric temperature and logarithmic gravity of TAP 26 are, respectively, equal to $T_{\rm eff}$= 4620 ± 50 K and $\log g = 4.5 \pm 0.2$ (with g in cgs units). This is warmer than the temperature quoted in the literature (4340 K, Grankin 2013), which is derived from photometry and thus expected to be significantly less accurate than ours, derived from high-resolution spectroscopic data, enabling to find the actual temperature without the disturbance of circumstellar and interstellar reddening.

Long-term photometric monitoring of TAP 26 indicates that its maximum V magnitude is equal to 12.16 (Grankin et al. 2008). Following Donati et al. (2014, 2015), we assume a spot coverage[1] of ≃25 per cent at maximum brightness, typical for active stars (and caused by, e.g. the presence of high-latitude cool spots and/or of small spots evenly spread over the whole stellar surface), we derive an unspotted V magnitude of 11.86 ± 0.20. From the difference between the $B - V$ index expected at the temperature of TAP 26 (equal to 0.99 ± 0.02, Pecaut & Mamajek 2013) and the averaged value measured for TAP 26 (equal to 1.13 ± 0.05, see Kenyon & Hartmann 1995; Grankin et al. 2008), and given the very weak impact of star-spot on $B - V$ (Grankin et al. 2008), we derive that the

[1] Spot coverage: integral of the difference between local brightness and photosphere brightness over the surface of the star, in units of photosphere brightness.

Downloaded from https://academic.oup.com/mnras/article-abstract/467/2/1342/2869846 by Université Paul Sabatier - Toulouse 3 user on 16 December 2019

Table 2. Journal of contemporaneous CrAO multicolour photometric observations of TAP 26 collected in late 2015 and early 2016, respectively, listing the UT date and Heliocentric Julian Date (HJD) of the observation, the measured V magnitude (1σ error bar of 0.016 mag) and $V - R_J$ Johnson photometric colours, and the corresponding rotational phase (using again the ephemeris given by equation 1). The table is divided into three periods spanning 1.5–2.5 months each, the second one covering the 2015 Nov set of spectropolarimetric observations and the third one overlapping the 2016 Jan set of spectropolarimetric observations.

Date	HJD (2457200+)	V (mag)	$V - R_J$	Cycle (−120+)
Aug 25	60.569	12.291	–	1.946
Aug 30	65.592	12.269	0.986	8.987
Aug 31	66.583	12.261	1.010	10.375
Sep 09	75.557	12.297	1.016	22.953
Sep 11	77.562	12.331	1.022	25.763
Sep 16	82.564	12.329	1.004	32.774
Sep 18	84.594	12.259	1.004	35.619
Sep 19	85.530	12.300	1.007	36.930
Sep 22	88.529	12.260	1.003	41.134
Sep 23	89.505	12.245	1.014	42.501
Sep 24	90.517	12.282	0.988	43.920
Sep 25	91.550	12.246	0.988	45.369
Sep 26	92.524	12.320	1.001	46.733
Sep 28	94.550	12.238	0.968	49.573
Oct 03	99.588	12.283	1.030	56.633
Oct 04	100.513	12.276	0.983	57.930
Oct 09	105.545	12.280	1.016	64.982
Oct 15	111.600	12.232	0.967	73.469
Oct 16	112.605	12.292	0.976	74.877
Oct 17	113.595	12.269	1.000	76.265
Oct 19	115.597	12.261	0.984	79.070
Oct 20	116.584	12.233	0.963	80.454
Oct 25	121.564	12.263	1.014	87.434
Oct 27	123.507	12.247	0.994	90.157
Oct 30	126.442	12.280	1.024	94.270
Nov 03	130.564	12.220	1.012	100.048
Nov 13	140.585	12.229	0.989	114.092
Dec 16	173.373	12.245	1.003	160.046
Dec 17	174.306	12.238	0.979	161.354
Jan 03	191.364	12.215	0.976	185.262
Jan 17	205.347	12.306	0.983	204.860
Jan 24	212.316	12.245	1.009	214.626
Jan 30	218.296	12.297	1.019	223.008
Feb 10	229.258	12.217	0.975	238.371
Feb 22	241.262	12.245	0.982	255.195
Mar 05	253.253	12.293	0.987	272.002
Mar 08	256.285	12.238	0.992	276.251
Mar 15	263.268	12.299	1.002	286.038

amount of visual extinction A_V that our target suffers is equal to 0.43 ± 0.15 (within 1.5σ of the value of Herczeg & Hillenbrand 2014, despite the very different methods used to estimate this parameter). Using the visual bolometric correction expected for the adequate photospheric temperature (equal to −0.55 ± 0.05, see Pecaut & Mamajek 2013) and the distance estimate assumed previously (147 ± 3 pc), corresponding to a distance modulus of 5.84 ± 0.04, we finally obtain a bolometric magnitude of 5.04 ± 0.26, or equivalently a logarithmic luminosity relative to the Sun of −0.12 ± 0.10. Coupling with the photospheric temperature obtained previously, we find a radius of 1.36 ± 0.17 $R_\odot$ for our target star.

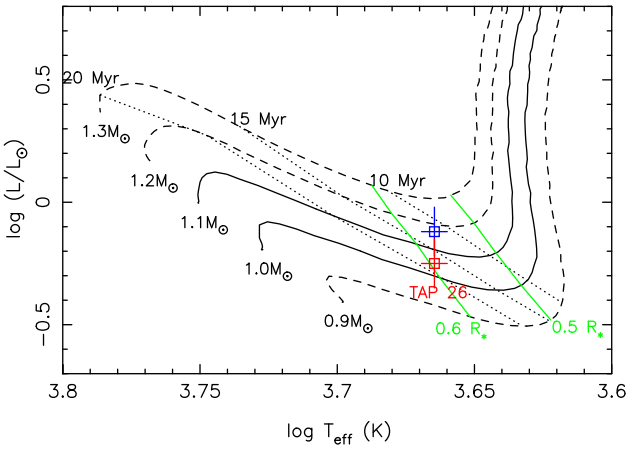

Figure 1. Observed location of TAP 26 in the HR diagram. The red and blue open squares (with 1σ error bars) depict the location of TAP 26 using two different ways of estimating the inclination angle of the rotation axis – with the red one showing our best estimate used throughout the paper. The PMS evolutionary tracks for 0.9, 1.0, 1.1, 1.2 and 1.3 $M_\odot$, and corresponding isochrones for 10, 15 and 20 Myr (Siess, Dufour & Forestini 2000) assume solar metallicity and include convective overshooting. The green lines depict where models predict PMS stars' radiative core reaches a radius of 0.5 $R_\star$ and 0.6 $R_\star$.

The rotation period of TAP 26 is well determined from long-term multicolour photometric monitoring, with an average value over the full data set equal to 0.7135 d (Grankin 2013). Coupling this rotation period along with our measurements of the line-of-sight-projected equatorial rotation velocity $v\sin i$ of TAP 26 (equal to 68.2 ± 0.5 km s^{-1}, see Section 4), we can infer that $R_\star \sin i = 0.96 \pm 0.05$ $R_\odot$, where $R_\star$ and i denote the radius of the star and the inclination of its rotation axis to the line of sight. Comparing with the radius derived from the luminosity and photometric temperature, we derive that $i = 45 \pm 8°$.

Using ZDI, we actually infer from our data that $i = 55 \pm 10°$ (see Section 4). The 1σ difference with the previous estimate can be simply interpreted as an overestimate in spottedness at maximum brightness. Assuming now a spottedness of 12 per cent at maximum brightness (instead of 25 per cent) reconciles both approaches and yields a logarithmic luminosity of −0.25 ± 0.10 and thus a radius of 1.17 ± 0.17 $R_\odot$, in good agreement with other studies (1.18 $R_\odot$ in Herczeg & Hillenbrand 2014).

Using the evolutionary models of Siess et al. (2000, assuming solar metallicity and including convective overshooting), we obtain that TAP 26 is a ≃17 Myr star (in good agreement with the estimate of Grankin 2013) and that its mass is $M_\star = 1.04 \pm 0.10$ $M_\odot$ (see Fig. 1). The average equivalent width of the 670.7 nm Li line is equal to 0.045 nm, in good agreement with that measured for solar-mass PMS stars in the 10–15 Myr Sco-Cen association at the corresponding temperature (Pecaut & Mamajek 2016), which further confirms our age estimate and thus the evolutionary status of TAP 26.

Referring to Donati et al. (2015, 2017), TAP 26 closely resembles an evolved version of the 2 Myr star V830 Tau that would have contracted and spun up by 4× towards the zero-age main sequence, with the rotation period and radius of V830 Tau being, respectively, 2.741 d and 2.0 ± 0.2 $R_\odot$. The increase in rotation rate matches quite well the predicted decrease in the moment of inertia between both epochs according to evolutionary models of Siess et al. (2000). Given the prominent role of the disc in braking the rotation of the

Downloaded from https://academic.oup.com/mnras/article-abstract/467/2/1342/2869846 by Universitie Paul Sabatier - Toulouse 3 user on 16 December 2019

Table 3. Parameters for TAP 26, inferred from the photometric and spectroscopic measurements and the ZDI analysis (see Section 4). Respectively: distance to Earth d, mass $M_\star$, radius $R_\star$, effective temperature $T_{\rm eff}$, decimal logarithm of surface gravity $\log g$, logarithmic luminosity $\log(L_\star/L_\odot)$, age, rotation period $P_{\rm rot}$, inclination of the rotation axis to the line of sight i, line-of-sight-projected equatorial rotation velocity $v\sin i$, equatorial rotation rate $\Omega_{\rm eq}$, difference $d\Omega$ between equatorial and polar rotation rates and mean RV in the barycentric rest frame $v_{\rm rad}$ (which was derived from our spectropolarimetric runs, see Section 4). T09 and G13 in the references, respectively, stand for Torres et al. (2009) and Grankin (2013).

Parameter	Value	Reference
d (pc)	147±3	T09
$M_\star$ ($M_\odot$)	1.04±0.10	
$R_\star$ ($R_\odot$)	1.17±0.17	
$T_{\rm eff}$ (K)	4,620±50	
$\log g$	4.5	
$\log(L_\star/L_\odot)$	−0.25 ±0.10	
Age (Myr)	≃17	
$P_{\rm rot}$ (d)	0.7135	G13
i (°)	55±10	
$v\sin i$ (km s^{-1})	68.2±0.5	
$\Omega_{\rm eq}$ (rad d^{-1})	8.8199±0.0003	
$d\Omega$ (rad d^{-1})	0.0492±0.0010	
$v_{\rm rad}$ (km s^{-1})	16.25 ± 0.20	

star and thus decreasing its angular momentum (Davies, Gregory & Greaves 2014; Gallet & Bouvier 2015), this also suggests that TAP 26 dissipated its accretion disc very early, typically as early as, or earlier than V830 Tau. We also note that our target is located past the theoretical threshold at which stars start to be more than half radiative in radius, suggesting that the magnetic field of TAP 26 already started to evolve into a complex topology (Gregory et al. 2012).

The stellar parameters inferred and used in this study are summarized in Table 3.

4 TOMOGRAPHIC IMAGING

In order to model the activity jitter of TAP 26 (see Section 5), we applied ZDI (Semel 1989; Brown et al. 1991; Donati & Brown 1997) to our data. ZDI takes inspiration from medical tomography, which consists of constraining a 3D distribution using series of 2D projections as seen from various angles (Vogt, Penrod & Hatzes 1987). In our context, ZDI inverts simultaneous time series of 1D Stokes I and V LSD profiles into 2D brightness and magnetic field maps of the stellar surface (see Donati et al. 2014). The magnetic field is decomposed into its poloidal and toroidal components, both expressed as spherical harmonics expansions (Donati et al. 2006).

Synthetic LSD profiles are derived from brightness and magnetic maps by summing up the spectral contribution of all cells, taking into account the Doppler broadening caused by the rotation of the star, the Zeeman effect induced by magnetic fields and the continuum centre-to-limb darkening. Local Stokes I and V profiles are computed using Unno–Rachkovsky's analytical solution to the polarized radiative transfer equations in a Milne–Eddington model atmosphere (Landi degl'Innocenti & Landolfi 2004). The local profile used in this study has a central wavelength, a Doppler width and a Landé factor of typical values 670 nm, 1.8 km s^{-1} and 1.2, respectively, and an equivalent width of 4.6 km s^{-1} corresponding to the LSD profiles of TAP 26. Technically, ZDI applies a conjugate gradient technique to iteratively reconstruct the brightness and magnetic surface maps with minimal information content (i.e. maximum Shannon entropy) that matches our observed LSD profiles at a given reduced chi-square ($\chi^2_{\rm r}$, defined as χ^2 divided by the number of data points[2]) level. Concerning the brightness, we note that, unlike in Donati & Collier Cameron (1997) where we fit a spot filling factor with pre-set spot parameters, here we fit the local brightness b_k of cell k, relative to the quiet photosphere ($0 < b_k < 1$ for dark spots and $b_k > 1$ for bright plages), as described in Donati et al. (2014).

ZDI can also take into account and model latitudinal differential rotation, shearing the brightness distribution and magnetic topology at the surface of the star, and assuming a solar-like surface rotation rate, $\Omega(\theta)$, varying with latitude, θ, as

$$\Omega(\theta) = \Omega_{\rm eq} - d\Omega(\sin\theta)^2, \quad (2)$$

where $\Omega_{\rm eq}$ is the equatorial rotation rate and $d\Omega$ is the difference between the equatorial and the polar rotation rates.

For a given set of parameters, ZDI looks for the map with minimal information content that matches the LSD profiles at $\chi^2_{\rm r}= 1$. As a by-product, we obtain the optimal stellar parameters for which the reconstructed images contain minimal information: $i = 55 \pm 10°$, $v\sin i = 68.2 \pm 0.5$ km s^{-1} and $v_{\rm rad}= 16.25 \pm 0.20$ km s^{-1} (the RV the star would have if unspotted and planet-free). Regarding differential rotation, we obtain $\Omega_{\rm eq}= 8.8199 \pm 0.0003$ rad d^{-1} and $d\Omega= 0.0492 \pm 0.0010$ rad d^{-1}, as outlined in more detail in Section 4.2.

4.1 Brightness and magnetic imaging

Given the long time span between our two data sets (about 60 d, see Table 1), we start by reconstructing separate brightness and magnetic maps for each epoch (2015 November and 2016 January), before investigating the temporal variability between both in more detail.

The Stokes I and V LSD profiles, which are displayed in Fig. 2, were used simultaneously to reconstruct both surface brightness and magnetic field maps. The synthetic LSD profiles presented in the figure match the observed ones at $\chi^2_{\rm r} = 1$, or, equivalently, at a χ^2 equal to 1484 for the 2015 November data set and 1157 for the 2016 January data set, and for both sets of Stokes I and V LSD profiles. The iterative reconstruction starts from unspotted magnetic maps corresponding to $\chi^2_{\rm r} = 13$ (2015 November) and 9 (2016 January), showing that the iterative algorithm of ZDI successfully manages to reproduce the data at noise level. In the particular case of Stokes I profiles, whose noise includes a significant level of systematics (see Section 2), we find that smaller error bars make ZDI unable to fit the data down to $\chi^2_{\rm r}= 1$; on the opposite, greater error bars result in a fit to the Stokes I profiles for which the raw radial velocities are not properly reproduced (see Section 5). This gives us confidence that the S/N values derived for the Stokes I LSD profiles (see Table 1) are accurate and reliable within 10 per cent.

The reconstructed brightness maps for 2015 November and 2016 January are shown in Fig. 3, at an epoch corresponding to rotation

[2] This follows the usual convention in regularized tomographic imaging techniques, where the number of model parameters is much smaller than the number of fitted data points and not taken into account in the expression of $\chi^2_{\rm r}$ (Donati et al. 2017).

Downloaded from https://academic.oup.com/mnras/article-abstract/467/2/1342/2869846 by Universitïe Paul Sabatier - Toulouse 3 user on 16 December 2019

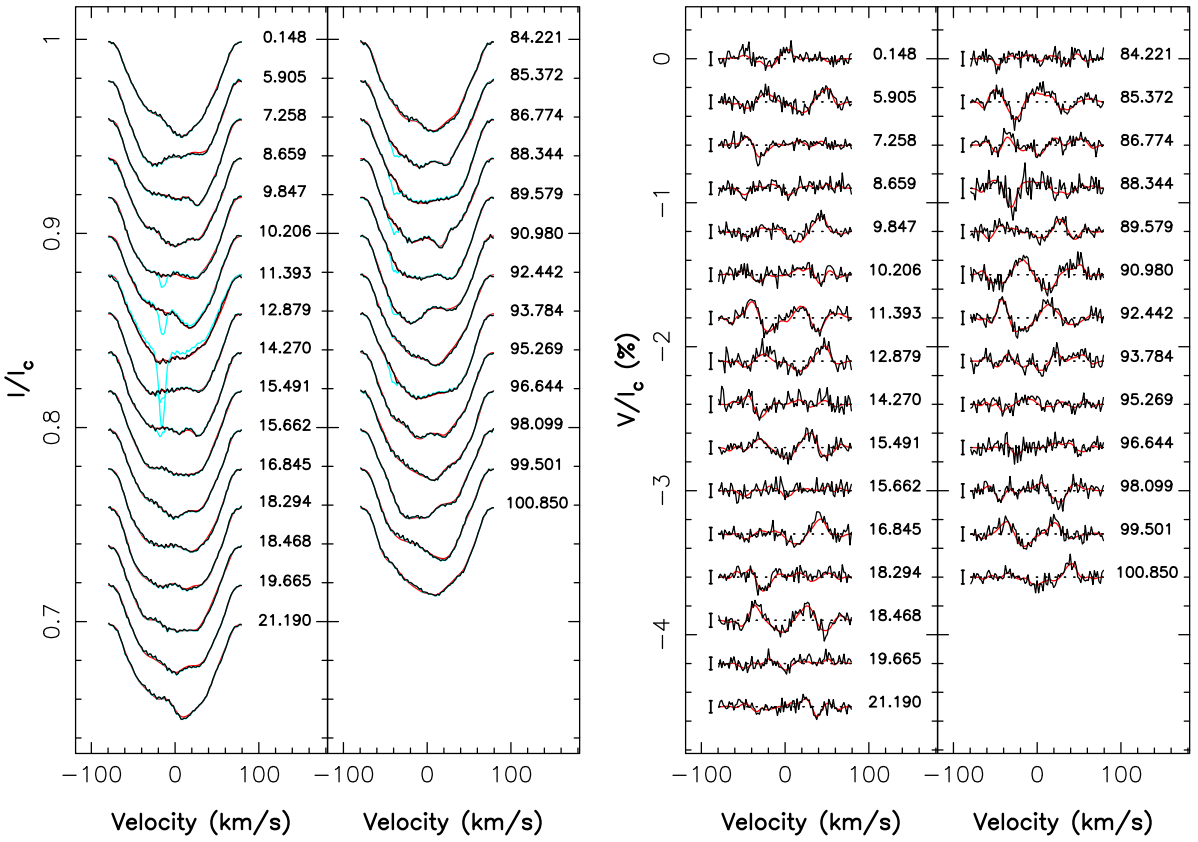

Figure 2. Maximum entropy fit (thin red lines) to the observed (thick black lines) Stokes *I* (left) and *V* (right) LSD profiles. The 2015 November data set is represented in the first and third panels and the 2016 January data set in the second and fourth panels. The Stokes *I* LSD profiles before the removal of lunar pollution are coloured in cyan, and 3σ error bars are displayed for the Stokes *V* profiles. The rotational cycles are written beside their corresponding profiles, in concordance with Table 1.

cycle 10.0 (in the ephemeris of equation 1) for 2015 November, and 92.0 for 2016 January (see Table 1); the colour scale codes the logarithmic relative brightness compared to that of the photosphere. The surface spot coverage we derive is similar at both epochs, reaching 10 per cent in the 2015 November map (5 per cent/5 per cent of cool spots/hot plages, respectively) and 12 per cent in the 2016 January map (7 per cent/5 per cent of cool spots/hot plages, respectively). Both reconstructed maps share some similarities, such as a large cool polar cap resembling that reconstructed on other rapidly rotating wTTSs (e.g. Skelly et al. 2010; Donati et al. 2014), plus a number of smaller features located at lower latitudes (in particular the two equatorial spots located at phases 0.22 and 0.92 in 2015 November, 0.27 and 0.97 in 2016 January) interleaved with bright plages. We stress that ZDI is only sensitive to the medium and large brightness features and misses small spots evenly distributed over the whole stellar surface, implying that the spottedness we recover for TAP26 is likely an underestimate. We observe a number of differences between both images potentially attributable to differential rotation and/or intrinsic variability (see Section 4.2); however, the limited phase coverage at both epochs makes the direct comparison of individual surface features between maps ambiguous and hazardous. We caution that the smallest scale structures may reflect to some extent the limited phase coverage and be subject to phase ghosting (e.g. Stout-Batalha & Vogt 1999).

Using the brightness maps reconstructed with ZDI, we can predict photometric light curves at both epochs, which are found to compare well with our contemporaneous CrAO observations (see Fig. 4). Note the small but significant temporal evolution of the light curve that we predict between both epochs; this variability is however not obvious from the observed photometric data given their limited sampling and comparatively large error bars (rms 16 mmag).

The reconstructed magnetic topology is shown in Fig. 5. The large-scale field reconstructed for TAP 26 features an rms magnetic flux of 330 and 430 G in 2015 November and 2016 January, respectively. The field is found to be mainly poloidal (70 per cent of the reconstructed magnetic energy), though with a significant toroidal component (30 per cent of the reconstructed magnetic energy). It is also largely axisymmetric (50 per cent and 80 per cent of the poloidal and the toroidal field energy, respectively).

The dipolar component of the large-scale field has a strength of 120 ± 10 G at both epochs, corresponding to about 10 per cent of the reconstructed poloidal field energy, and is tilted at $40 \pm 5^\circ$ to the line of sight, i.e. mid-way to the equator, towards phase 0.73 ± 0.03 and 0.85 ± 0.03 in 2015 November and 2016 January, respectively. The increase in the phase towards which the dipole is tilted suggests that intermediate to high latitudes (at which the dipole poles are anchored) are rotating more slowly than average by 0.19 per cent, i.e. with a period of $\simeq$0.7148 d; this is confirmed by the fact that the line-of-sight-projected (longitudinal) magnetic field B_ℓ (proportional to the first moment of the Stokes *V* profiles, e.g. Donati et al. 1997, and most sensitive to the low-order components of the large-scale field) exhibits a recurrence time-scale of $1.0014 \pm 0.003\ P_{\rm rot}$ (see Appendix B), i.e. slightly longer than $P_{\rm rot}$ by a similar amount. Higher order terms in the spherical harmonics expansion describing the field (in particular the quadrupolar and octupolar modes) get stronger between 2015 November and 2016

Downloaded from https://academic.oup.com/mnras/article-abstract/467/2/1342/2869846 by Universitïe Paul Sabatier - Toulouse 3 user on 16 December 2019

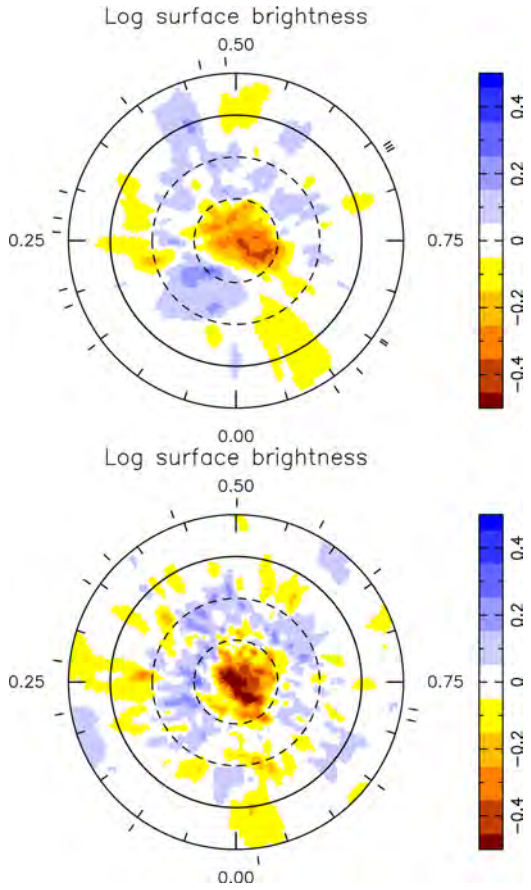

Figure 3. Flattened polar view of the surface-brightness maps for the 2015 November data set (top panel) and 2016 January data set (bottom panel). The equator and the 60°, 30° and −30° latitude parallels are depicted as solid and dashed black lines, respectively. The colour scale indicates the logarithm of the relative brightness, with brown/blue areas representing cool spots/bright plages. Finally, the outer ticks mark the phases of observation.

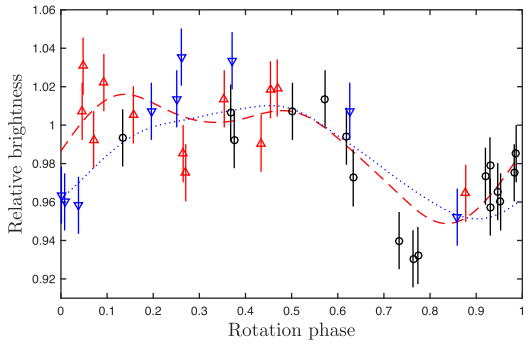

Figure 4. Photometry curves of the relative brightness as function of the rotation phase. The light curves synthesized from the reconstructed brightness maps for 2015 November and 2016 January are represented by a dashed red line and a dotted blue line, respectively. The CrAO measurements are represented as dots with 1σ error bars, with the observations from 2015 August–October in black circles, the observations from 2015 October–December in red upward-pointing triangles and the observations from 2015 December to 2016 March in blue downward-pointing triangles.

December, with total magnetic energies increasing from 85 per cent to 93 per cent of the poloidal field.

Finally, we show a large-scale extrapolation of the magnetic field (under the assumption of a potential field) in Fig. 6. Similarly to the brightness maps, the magnetic maps seem to point to a variation of the surface topology between late 2015 and early 2016, which is not explained by differential rotation alone, though the limited phase coverage calls for caution when comparing features between those maps.

The magnetic maps suggest that the magnetic topology at the rotation pole underwent a $\simeq$0.1 phase shift between both dates.

4.2 Intrinsic variability and differential rotation

When applying ZDI to the whole data set, i.e. modelling all Stokes *I* and *V* profiles with only one brightness map and one magnetic topology (see Appendix A), we obtain a minimum χ^2_r value of 1.4, even when taking into account differential rotation (starting from an initial value χ^2_r= 20). This indicates that intrinsic variability occurred during the 45 d gap (or 63 rotation cycles) separating both data sets.

Despite this variability, we attempted to retrieve differential rotation from the whole data set. The search for differential rotation parameters is done by minimizing the value of χ^2_r at a fixed amount of information, in this present case using the Stokes *I* profiles and brightness map reconstruction only. From the curvature of the χ^2_r paraboloid around the minimum, one can infer error bars on differential rotation parameters (Donati, Collier Cameron & Petit 2003). The spot coverage is fixed at 13 per cent (chosen to be slightly higher than the values found in each reconstruction) and the values we found are Ω_{eq}= 8.8199 ± 0.0003 rad d^{-1} and dΩ = 0.0492 ± 0.0010 rad d^{-1}, with a minimum χ^2_r of 1.4116. A map of $\Delta\chi^2$ is shown in Fig. 7, which presents a very clear paraboloid around the minimum we found, even if, due to our phase coverage, these precise values ask for further confirmation with the help of future data. This value of dΩ is close to the solar differential rotation (0.055 rad d^{-1}). The case with no differential rotation yields χ^2_r = 2.6907. Normalizing $\Delta\chi^2$ by the minimum χ^2 achieved over the map (to scale up error bars as a way to account for the contribution from the reported intrinsic variability) still yields a value in excess of 3300 and a negligible false alarm probability (FAP), unambiguously demonstrating that the star is not rotating as a solid body.

The differential rotation parameters we obtain imply a lap time of 128 ± 3 d, with rotation periods of 0.712 39 ± 0.000 03 d and 0.716 38 ± 0.000 08 d for the equator and pole, respectively, in good agreement with the range of rotation periods derived from photometry (ranging from 0.7135 to 0.7138, Grankin 2013). The 0.7132 d period found for the equivalent width of the Hα line and the 0.7145 d period found for the longitudinal magnetic field B_ℓ (see Appendix B) are also consistent. We note that the rotation periods found with photometry, the longitudinal magnetic field and Hα line correspond to latitudes ranging from 30° to 50°, indicating that an important amount of activity is concentrated at these mid-latitudes, with the dipole pole located in the upper part of this range, in good agreement with the ZDI reconstruction (see Section 4.1).

5 MODELLING THE PLANET SIGNAL

We describe below three different techniques aimed at characterizing the RV curve of TAP 26. The first two are those used in Donati

Downloaded from https://academic.oup.com/mnras/article-abstract/467/2/1342/2869846 by Universitïe Paul Sabatier - Toulouse 3 user on 16 December 2019

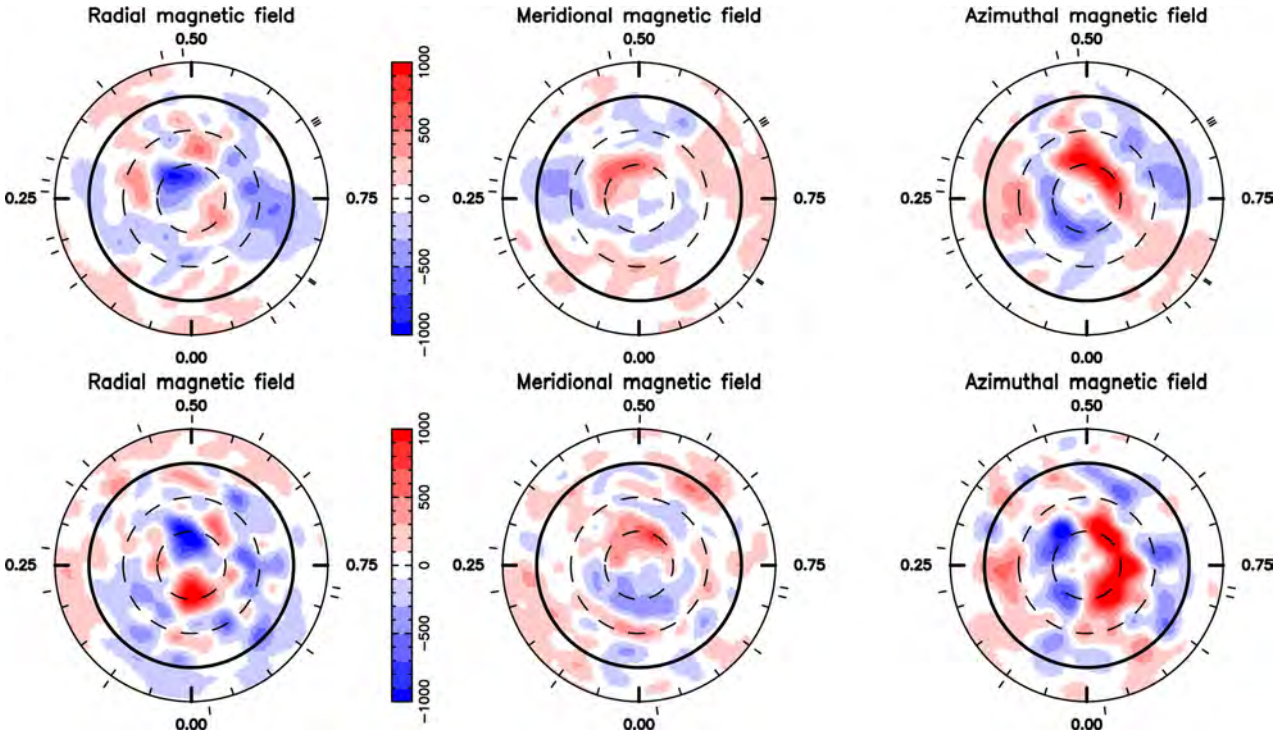

Figure 5. From left to right: radial, meridional and azimuthal component of the surface magnetic field (labelled in G), reconstructed with ZDI from the 2015 November data set (top panels) and the 2016 January data set (bottom panels).

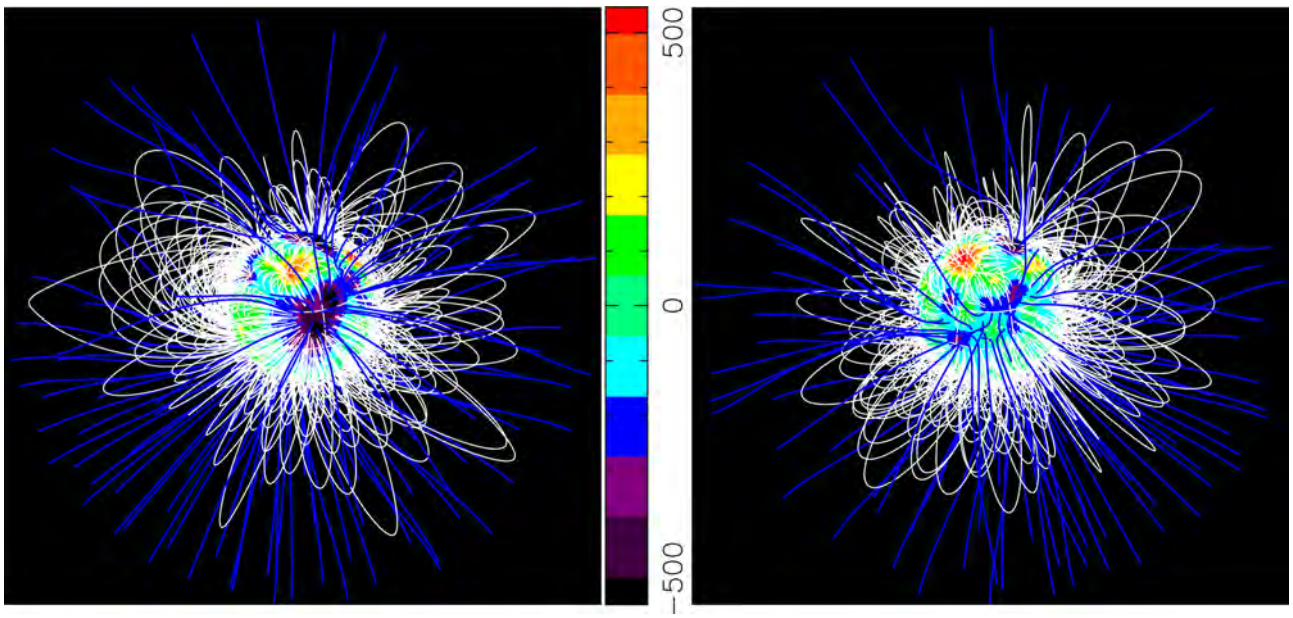

Figure 6. Potential field extrapolations of the reconstructed magnetic topology as seen by an Earth-based observer, in 2015 November (left) and in 2016 January (right) both at phase 0.8. Open and closed field lines are shown in blue and white, respectively, whereas colours at the stellar surface depict the local value of the radial field (in G, as shown in the left-hand panels of Fig. 5). The source surface at which the field becomes radial is set to 4 $R_\star$, slightly larger than the corotation radius of about 3 $R_\star$ (at which the Keplerian period equals the stellar rotation period) and beyond which field lines are expected to quickly open under centrifugal forces.

et al. (2017): filtering out the activity modelled with the help of ZDI, and the simultaneous fit of the planet parameters and the stellar activity. The third method follows the approach of Haywood et al. (2014) and Rajpaul et al. (2015) and uses GPR to model the activity directly from the raw RVs. The results obtained from these three methods are outlined and discussed in the following sections.

5.1 Jitter activity filtering

The first technique consists of using the previously reconstructed maps to predict the pollution to the RV curve caused by activity (called activity jitter in the following) and subtract it from the raw RVs. From the observed Stokes *I* LSD profiles, we compute, at both

Downloaded from https://academic.oup.com/mnras/article-abstract/467/2/1342/2869846 by Universitïe Paul Sabatier - Toulouse 3 user on 16 December 2019

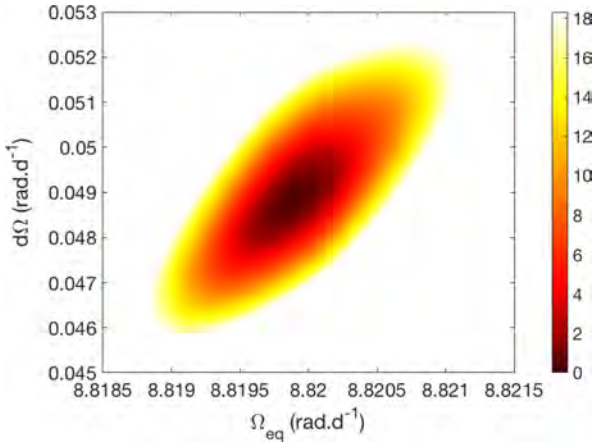

Figure 7. Map of $\Delta\chi^2$ as a function of Ω_{eq} and dΩ, derived from the modelling of our Stokes *I* LSD profiles of TAP 26 at constant information content. A well-defined paraboloid is observed with the outer colour contour corresponding to the 99.99 per cent confidence level area (i.e. a χ^2 increase of 18.4 for the 2581 Stokes *I* data points). The minimum value of χ_r^2 is 1.4116. The minimum χ_r^2 achieved is above unity due to intrinsic variability affecting the LSD profiles but not being taken into account within ZDI. The derived differential rotation parameters are $\Omega_{eq} = 8.8199 \pm 0.0003$ rad d^{-1} and d$\Omega = 0.0492 \pm 0.0010$ rad d^{-1}.

epochs, the raw RVs RV_{raw} (and error bars, see Table 1), as the first-order moment of the continuum-subtracted corresponding profiles (Donati et al. 2017). Likewise, the synthesized Stokes *I* LSD profiles derived from the brightness maps yield the synthesized activity jitter of the star (RV signal caused by the brightness distribution and stellar rotation). By subtracting the activity jitter from the raw RVs, we obtain filtered RVs RV_{filt} (see Table 1). We observe that the jitter has a mean semi-amplitude of 1.81 km s^{-1} in 2015 November and 1.21 km s^{-1} in 2016 January, whereas the filtered RV curve features a signal with a semi-amplitude of $\simeq$0.15 km s^{-1} (Fig. 8), i.e. 8 to 12 times smaller than the activity signal we filtered out. We note the very significant evolution in the activity curve between 2015 November and 2016 January, demonstrating that the brightness distribution has evolved at the surface of TAP 26, through differential rotation and intrinsic variability (see Section 4).

With an rms dispersion of 109 m s^{-1}, the filtered RVs clearly show the presence of a signal. Looking for a planet signature, we want to fit a sine curve (of semi-amplitude *K*, period P_{orb}, phase of inferior conjunction ϕ and offset RV_0) to these filtered RVs, which corresponds to a circular orbit (see Fig. 9). The phase of inferior conjunction, i.e. corresponding to the epoch at which the planet is closest to us, is defined relatively to the reference date $BJD_{c0} = 2457352.6485$ (rotation cycle 11.0, approximately at the centre of the 2015 November observation run), such that the inferior conjunction occurs at $BJD_c = BJD_{c0} + (\phi - 1)P_{orb}$. Due to the gap between both observing runs, several sine fits with different frequencies match the RV_{filt} as local minima of χ_r^2. The four best fits are shown in Fig. 9 and their characteristics are given in Table 4, with the value of the log likelihood as computed from the $\Delta\chi^2$ over these 29 RV data points. The residual RVs, derived from subtracting the best sine fit to the filtered RVs (shown in Fig. 9), feature an rms value of 51 m s^{-1}.

Plotting Lomb–Scargle periodograms for the raw RVs, filtered RVs and residual RVs further demonstrates the presence of a periodic signal in the filtered RVs (Fig. 10). The above-mentioned dominant periods are seen as peaks in the periodogram; periodograms of partial data (only the 2015 November data set, only the 2016 January data set, odd points and even points) are also shown, yielding peaks at the same frequencies albeit with a lower power. We highlight the fact that the highest peaks in the raw RVs correspond to the activity jitter and are located at $P_{rot}/2$ and its aliases, whereas little power concentrates at P_{rot} itself. A zoom-in of the filtered RV periodogram is also shown in Fig. 10 (bottom panel). The FAP is 0.06 per cent for the highest peak ($P_{orb} = 13.41$ d $= 18.80\ P_{rot}$), and no significant period stands out in the residual RVs after filtering out both the activity jitter and the planet signal corresponding to the highest peak. We carried out simulations to ensure that the detected peaks are not generated by the filtering process, see details in Appendix C. Study of other activity proxies shows that the detected orbital periods are not present in the activity signal either (Appendix B).

By fitting the filtered RVs with a Keplerian orbit rather than a circular orbit, we obtain an eccentricity of 0.16 ± 0.15, indicating that there is no evidence for an eccentric orbit (following the precepts of Lucy & Sweeney 1971). We can thus conclude that the orbit of TAP 26 b is likely close to circular, or no more than moderately eccentric.

5.2 Deriving the planetary parameters from the LSD profiles

A second technique, following the method of Petit et al. (2015), consists of taking into account the presence of a planet into the

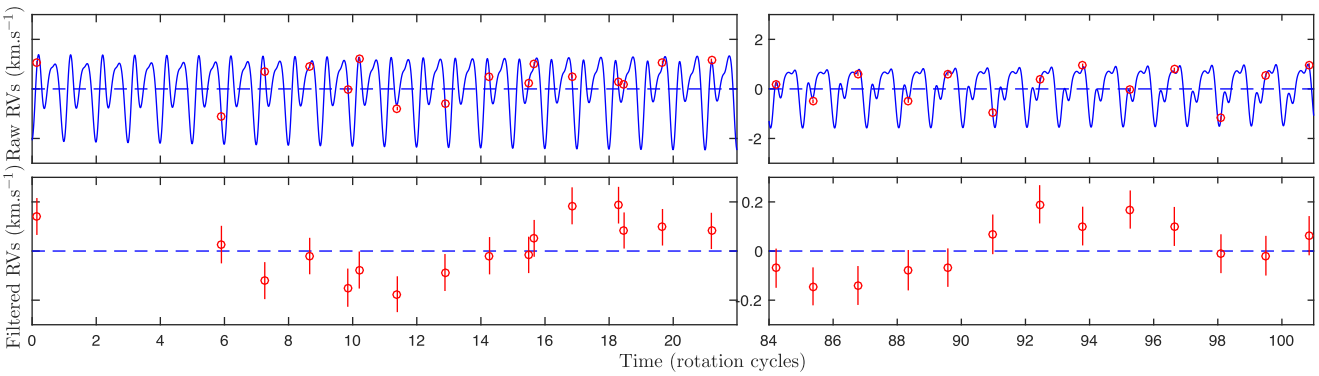

Figure 8. Top panels: RV (in the stellar rest frame) of TAP 26 as a function of rotation phase, as measured from our observations (open circles) and predicted by the tomographic maps (blue line). The synthesized raw RV curves exhibit only low-level temporal evolution resulting from differential rotation. Bottom panels: filtered RVs derived by subtracting the modelled activity jitter from the raw RVs, with a 10× zoom-in on the vertical axis.

Downloaded from https://academic.oup.com/mnras/article-abstract/467/2/1342/2869846 by Universitïe Paul Sabatier - Toulouse 3 user on 16 December 2019

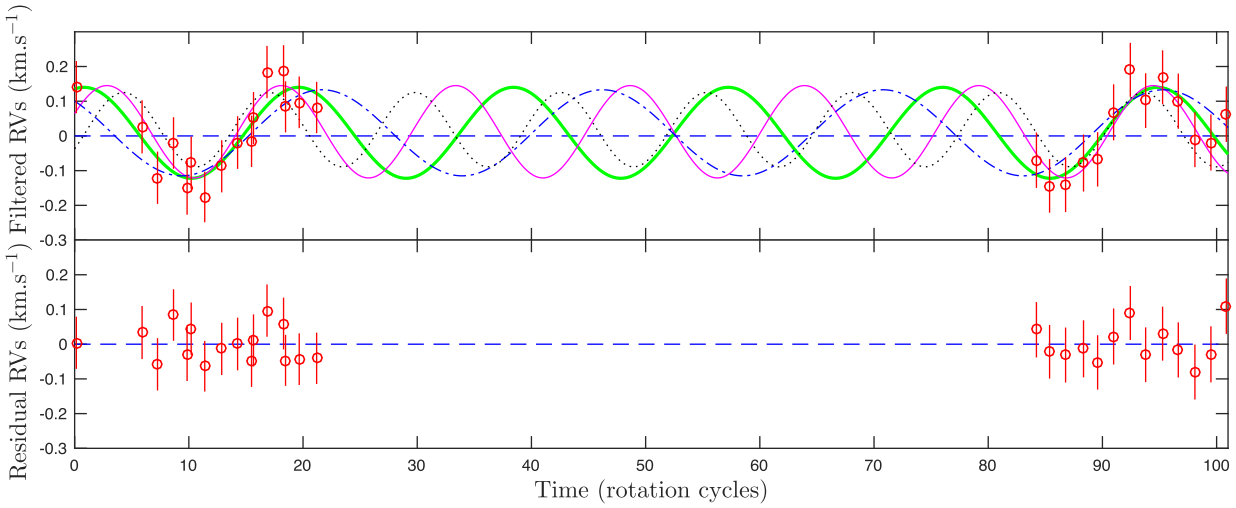

Figure 9. Top: filtered RVs of TAP 26 and four sine curves representing the best fits. The thick green curve represents the case $P_{\rm orb}/P_{\rm rot} = 18.80$, the thin magenta one $P_{\rm orb}/P_{\rm rot} = 15.27$, the dash–dotted blue one $P_{\rm orb}/P_{\rm rot} = 24.56$ and the dotted black one $P_{\rm orb}/P_{\rm rot} = 12.76$. Bottom: residual RVs resulting from the subtraction of the best fit (green curve) from the filtered RVs. The residual RVs feature an rms value of 51 m s^{-1}.

Table 4. Characteristics of the four best sine curve fits to the filtered RVs, and the case without planet. Respectively: semi-amplitude K, orbital period $P_{\rm orb}$ in units of $P_{\rm rot}$, orbital period $P_{\rm orb}$ in days, phase of inferior conjunction ϕ relative to cycle 11.0 (see ephemeris in equation 1), BJD of inferior conjunction, RV offset RV$_0$, corresponding $\chi^2_{\rm r}$, difference in χ^2 with the best fit ($\Delta\chi^2$, summed on the 29 data points) and natural logarithm (log$_e$) of the likelihood $\mathcal{L}_{r1}$ relative to the best fit. ϕ relates to the epoch of inferior conjunction BJD$_{\rm c}$ through BJD$_{\rm c}$=2457352.6485+$\phi P_{\rm orb}$, the reference date being chosen so as to minimize the variation of ϕ between the four cases.

K (km s^{-1})	$P_{\rm orb}$ ($P_{\rm rot}$)	$P_{\rm orb}$ (d)	ϕ	BJD$_{\rm c}$ (2457340+)	RV$_0$ (km s^{-1})	$\chi^2_{\rm r}$	$\Delta\chi^2$	log $\mathcal{L}_{r1}$	Style in Fig. 9
0.131±0.020	18.80±0.23	13.41±0.16	0.709±0.026	8.75±0.35	0.009±0.014	0.445	0	0.00	Thick green
0.133±0.021	15.27±0.14	10.90±0.10	0.715±0.024	9.54±0.26	0.012±0.014	0.542	2.80	−0.53	Full magenta
0.124±0.020	24.56±0.41	17.52±0.30	0.684±0.028	7.11±0.50	0.009±0.016	0.673	6.61	−1.85	Dash-dotted blue
0.107±0.021	12.76±0.14	9.11±0.10	0.724±0.031	10.14±0.28	0.018±0.015	1.079	18.38	−6.87	Dotted black
0					0.013±0.014	2.025	45.82	−19.73	Dashed blue

ZDI model. Rather than fitting the measured Stokes I LSD profiles with a synthetic activity jitter directly, we first apply a translation in velocity to each of them, to remove the reflex motion caused by a planet of given parameters, and then apply ZDI to the corrected data set. Practically speaking, we repeat the experiment for a range of values for the orbital parameters (K, $P_{\rm orb}$, ϕ) at the vicinity of the minima previously identified in Section 5.1 and look for the set of values that yields the best result. The same way as for differential rotation, we derive the error bars on all parameters from the curvature of the 3D $\chi^2_{\rm r}$ paraboloid around the minimum.

In the present case, since we have two data sets separated by a 45 d gap and we know that intrinsic variability occurred (see Sections 4 and 5.1), a modification to the method described above was implemented: after correcting the global data set from the reflex motion, ZDI is applied separately on each data set, reconstructing two different brightness maps (one for late 2015 and one for early 2016) in order to obtain a more precise reconstruction. The quantity used to measure the likelihood of each set of parameters is therefore a global $\chi^2_{\rm r}$, computed as a weighted average of both individual $\chi^2_{\rm r}$, with respective weights proportional to the number of data points in each set (1424 for 2015 November and 1157 for 2016 January).

As in the previous section, several minima are found, which are listed in Table 5. We also computed the relative likelihood of each case compared to the best one from the corresponding difference in $\chi^2_{\rm r}$. We note that the case with no planet yields $\chi^2_{\rm r} = 0.98631$, which leads to a relative probability lower than 10^{-9} compared to the case with a 10.91 d period planet.

Fig. 11 displays a $\Delta\chi^2$ map around the local minimum $P_{\rm orb}/P_{\rm rot}$= 15.29, at $\phi = 0.67$, showing the 99.99 per cent confidence area.

5.3 Gaussian-process regression (GPR)

The third method we used works directly with the raw RVs and aims at modelling the activity jitter and its temporal evolution with GPR, assuming it obeys an a priori covariance function (Haywood et al. 2014; Rajpaul et al. 2015). Similarly to the previous method, we fit both the orbit model and the jitter model simultaneously. For a planet with given parameters, we first remove the planet reflex motion from the RVs, then we fit the corrected RVs with a Gaussian process (GP) of pseudo-periodic covariance function:

$$c(t,t') = \theta_1^2 \exp\left[-\frac{(t-t')^2}{\theta_3^2} - \frac{\sin^2\left(\frac{\pi(t-t')}{\theta_2}\right)}{\theta_4^2}\right], \quad (3)$$

where t and t' are two dates, θ_1 is the amplitude (in km s^{-1}) of the GP, θ_2 the recurrence time-scale (in units of $P_{\rm rot}$), θ_3 the decay time-scale (i.e. the typical spot lifetime in the present case, in units of $P_{\rm rot}$) and θ_4 a smoothing parameter (within [0,1]) setting the amount of high-frequency structures that we allow the fit to include. From a given set of orbital parameters (K, $P_{\rm orb}$, ϕ) and of covariance function parameters (θ_1 to θ_4, called hyperparameters), we can

Downloaded from https://academic.oup.com/mnras/article-abstract/467/2/1342/2869846 by Universitie Paul Sabatier - Toulouse 3 user on 16 December 2019

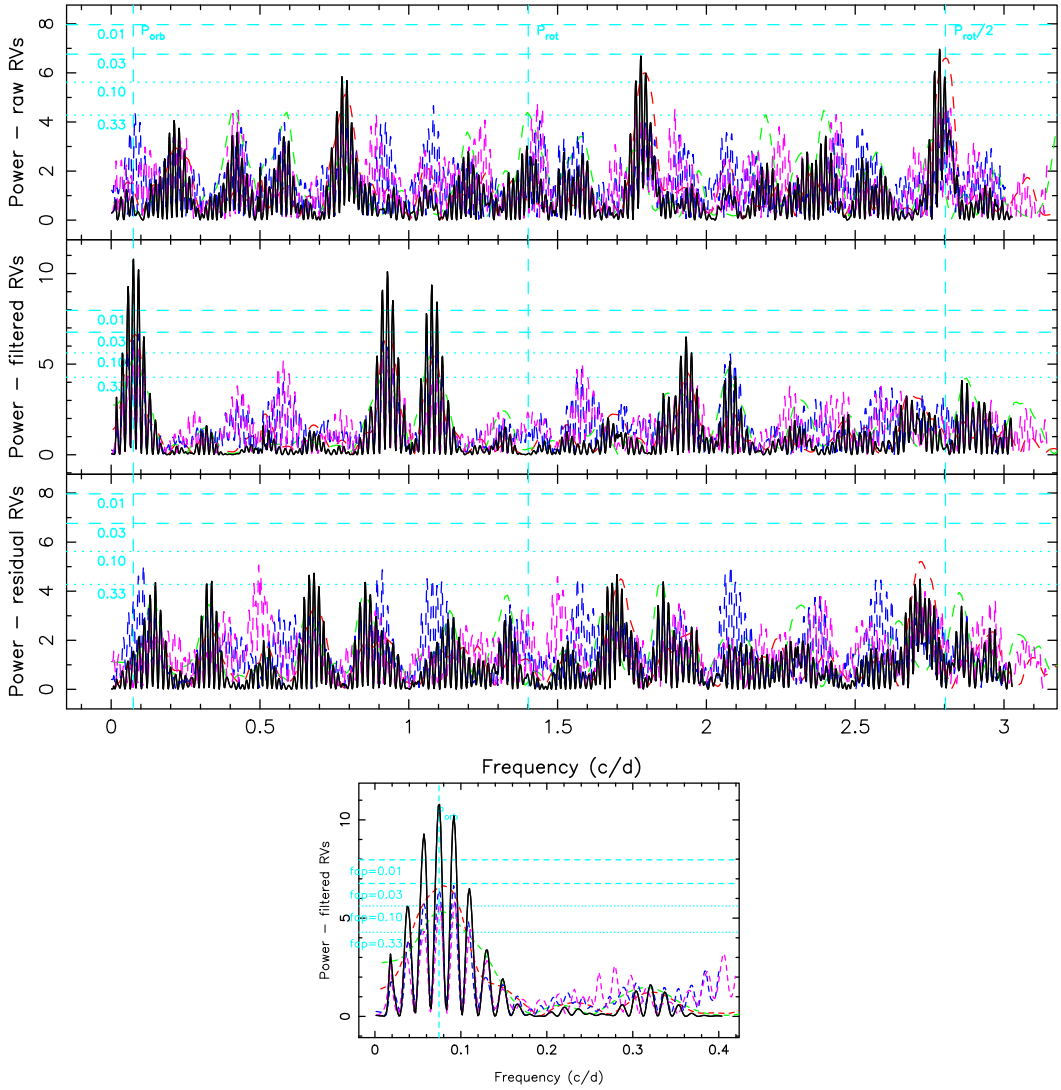

Figure 10. Top: periodograms of the raw (top), filtered (middle) and residual (bottom) RV curves over the whole data set (black line). The red line represents the 2015 November data set, the green line the 2016 January data set, the blue line the odd data points and the magenta line the even data points. FAP levels of 0.33 and 0.10 are displayed as horizontal dotted cyan lines, FAP levels of 0.03 and 0.01 are displayed as horizontal dashed cyan lines. The rotation frequency (1.402 cycles d^{-1}) is marked by a vertical cyan dashed line, as well as its first harmonic (2.803 cycles d^{-1}) and the orbital frequency that has the smallest FAP (0.06 per cent at 0.075 cycles d^{-1}, corresponding to P_{orb}=13.41 d). Aliases of the highest peaks, related to the observation window, appear as lower peaks separated by one cycle per day. Bottom: zoom-in the periodogram of filtered RVs.

Table 5. Optimal orbital parameters derived with the method described in Section 5.2, respectively: semi-amplitude K, orbital period P_{orb} in units of P_{rot}, orbital period P_{orb} in days, phase of inferior conjunction ϕ relative to cycle 11.0, BJD of inferior conjunction, χ^2_r, $\Delta\chi^2$ summed on 2581 data points, and natural logarithm of the likelihood $\mathcal{L}_{r2}$ relative to the best fit. The case where no planet is taken into account in the model is given for comparison.

K (km s^{-1})	P_{orb} (P_{rot})	P_{orb} (d)	ϕ	BJD_c (2457340+)	χ^2_r	$\Delta\chi^2$	$\log\mathcal{L}_{r2}$
0.154±0.022	15.29±0.15	10.91±0.11	0.671±0.035	9.06±0.38	0.968 24	0.00	0.00
0.144±0.023	18.78±0.25	13.40±0.18	0.685±0.041	8.43±0.55	0.969 79	4.00	−1.34
0.148±0.025	12.83±0.12	9.16±0.09	0.677±0.038	9.69±0.35	0.971 80	9.17	−3.61
0					0.986 31	46.62	−21.60

derive the GP that best fits the corrected RVs (noted y below) as well as the log likelihood $\log\mathcal{L}$ of the corresponding set of parameters from

$$2\log\mathcal{L} = -n\log(2\pi) - \log|C+\Sigma| - y^T(C+\Sigma)^{-1}y, \quad (4)$$

where n is the number of data points (29 in our case), C is the covariance matrix of all the observing epochs and Σ is the diagonal variance matrix of the raw RVs.

Coupled with a Markov Chain Monte Carlo (MCMC) simulation to explore the parameter domain, this method generates samples

Downloaded from https://academic.oup.com/mnras/article-abstract/467/2/1342/2869846 by Universitïe Paul Sabatier - Toulouse 3 user on 16 December 2019

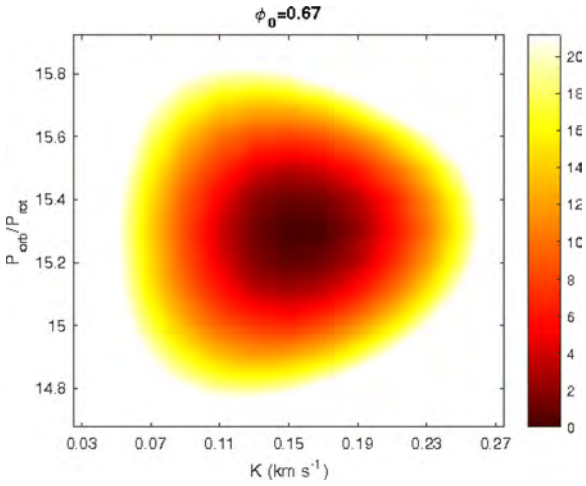

Figure 11. $\Delta\chi^2$ map as a function of K and $P_{\rm orb}/P_{\rm rot}$, derived with ZDI from corrected Stokes I LSD profiles at constant information content. Here the phase is fixed at 0.67, i.e. the value of ϕ at which the 3D paraboloid is minimum. The outer colour delimits the 99.99 per cent confidence level area (corresponding to a χ^2 increase of 21.10 for 2581 data points in our Stokes I LSD profiles). The minimum value of $\chi^2_{\rm r}$ is 0.968 24.

from the posterior probability distributions for the hyperparameters of the noise model and the orbital parameters. From these we can determine the maximum-likelihood values of these parameters and their uncertainty ranges. After an initial run where all the parameters are free to vary, we fix θ_4 and θ_3 to their respective best values (0.50 ± 0.09 and 180 ± 60 $P_{\rm rot} = 128 \pm 43$ d) before carrying out the main MCMC run to find the best estimates of the five remaining parameters. We note that the best value found for the decay time is exactly equal to the differential rotation lap time within error bars, and to twice the total span of our data. This decay time corresponds to both the differential rotation lap time and the star-spot coherence time, since these are the most influent phenomena on the periodicity of the activity jitter. Such a star-spot coherence time is consistent with previous studies (Lanza 2006; Grankin et al. 2008; Bradshaw & Hartigan 2014).

As shown in Fig. 12, this method successfully recovers the different minima previously found with the first two techniques, with little correlation between the various parameters thus minimum bias in the derived values. Applying the method of Chib & Jeliazkov (2001) to the MCMC posterior samples, we obtain that the marginal likelihood of the case $P_{\rm orb} = 12.61\ P_{\rm rot}$ is larger than that of the case $P_{\rm orb} = 15.12\ P_{\rm rot}$ by a Bayes factor of only 1.28, which implies that there is as yet no clear evidence in favour of either of them. The third most likely case, $P_{\rm orb} = 18.74\ P_{\rm rot}$, has a marginal likelihood which is inferior to the first one by a Bayes' factor of >8, and the case with no planet has a marginal likelihood which is smaller than that of the first case by a Bayes factor of 2×10^5. The three most likely sets of parameters are summarized in Table 6.

Trying to fit a non-circular Keplerian orbit to our data, i.e. adding the periapsis argument and the eccentricity e to the parameters in our MCMC run, we obtain $e = 0.05 \pm 0.18$, with a marginal likelihood slightly smaller than that of the case of a circular orbit. This further supports that the planet eccentricity is low if non-zero.

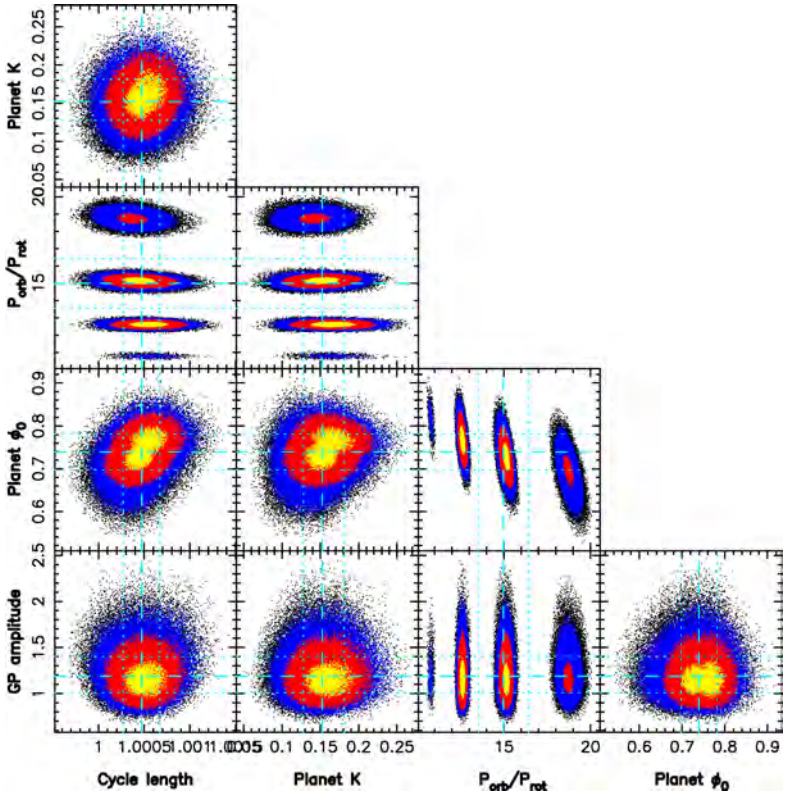

Figure 12. Phase plots of our 5-parameter MCMC run with yellow, red and blue points marking, respectively, the 1σ, 2σ and 3σ confidence regions. The optimal values found for each parameters are: $\theta_1 = 1.19 \pm 0.21$ km s^{-1}, $\theta_2 = 1.0005 \pm 0.0002$ $P_{\rm rot}$, $K = 0.152 \pm 0.029$ km s^{-1}. Several optima are detected for $P_{\rm orb}$: 12.61 ± 0.13 $P_{\rm rot}$, 15.12 ± 0.20 $P_{\rm rot}$ and 18.74 ± 0.34 $P_{\rm rot}$, ordered by decreasing likelihood. The corresponding phases ϕ are 0.766 ± 0.030, 0.728 ± 0.033 and 0.694 ± 0.042, respectively.

Downloaded from https://academic.oup.com/mnras/article-abstract/467/2/1342/2869846 by Universitie Paul Sabatier - Toulouse 3 user on 16 December 2019

Table 6. Sets of orbital parameters that allow us to fit the corrected RV curve best, using a GP with a covariance function given in equation (4), derived from the MCMC run. Respectively: reflex motion RV semi-amplitude K, orbital period $P_{\rm orb}$ in units of $P_{\rm rot}$, orbital period $P_{\rm orb}$ in days, phase of inferior conjunction ϕ relative to rotation cycle 11.00 (ephemeris defined in equation 1), BJD of inferior conjunction, natural logarithm of the marginal likelihood $\mathcal{L}$ and natural logarithm of the relative marginal likelihood $\mathcal{L}_{r3}$ as compared to the best case. The case where no planet is taken into account in the model is given for comparison.

K (km s^{-1})	$P_{\rm orb}$ ($P_{\rm rot}$)	$P_{\rm orb}$ (d)	ϕ	BJD$_{\rm c}$ (2457340+)	log $\mathcal{L}$	log $\mathcal{L}_{r3}$
0.163 ±0.028	12.61 ±0.13	8.99 ±0.09	0.766 ±0.030	10.54 ±0.27	−3.48	0.00
0.149 ±0.026	15.12 ±0.20	10.79 ±0.14	0.728 ±0.033	9.71 ±0.36	−3.73	−0.25
0.139 ±0.026	18.74 ±0.34	13.37 ±0.24	0.694 ±0.042	8.56 ±0.57	−5.60	−2.12
0					−15.80	−12.52

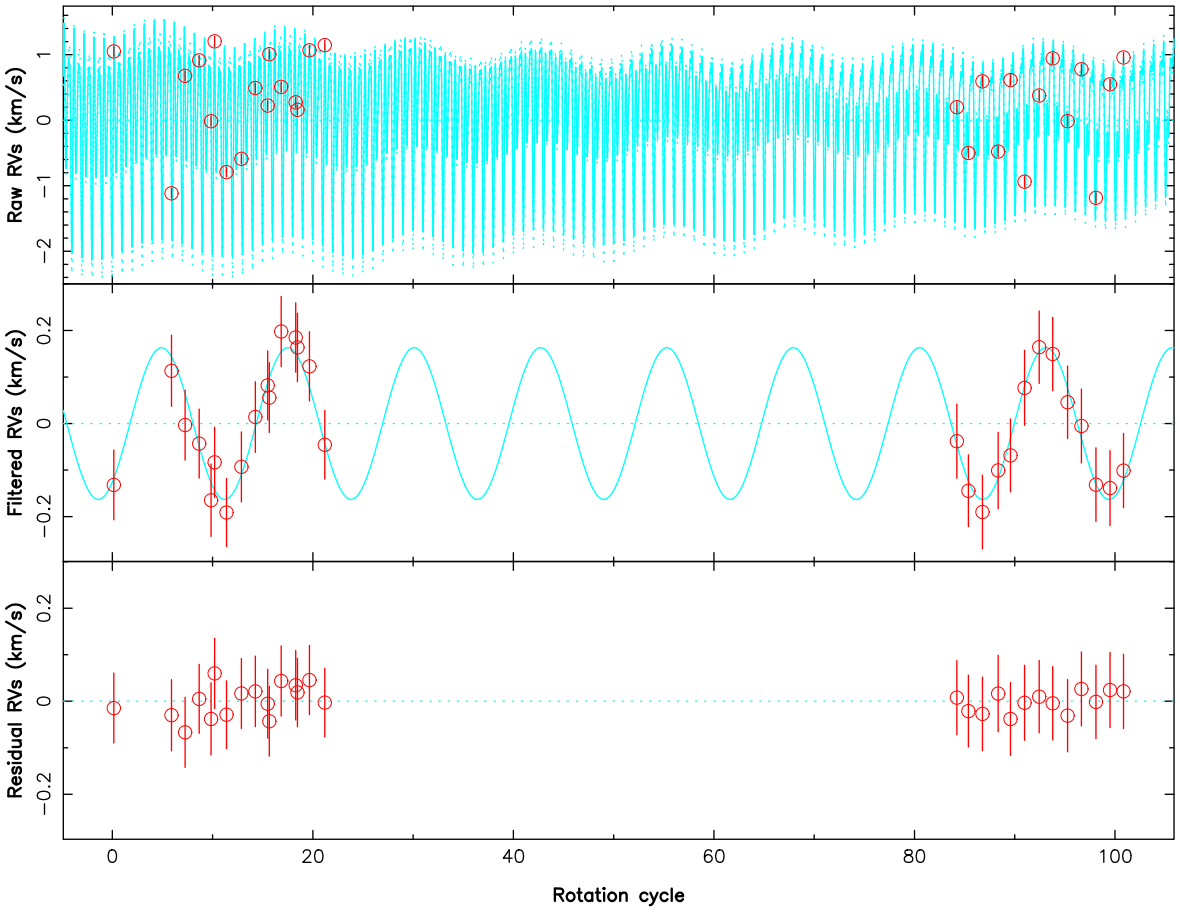

Figure 13. RV curves for a GPR fit of the activity jitter, with parameters $K = 0.163$ km s^{-1}, $P_{\rm orb}$= 12.61 $P_{\rm rot}$, $\phi = 0.766$, $\theta_1 = 1.19$ km s^{-1}, $\theta_2 = 1.0005$ $P_{\rm rot}$, $\theta_3 = 180$ $P_{\rm rot}$, $\theta_4 = 0.50$ $P_{\rm rot}$. Top panel: raw RVs and their error bars are shown in red, the solid cyan curve is the sum of the activity jitter predicted by GPR and the planet signal, and the dashed cyan lines show the 68.3 per cent confidence intervals about the prediction around this model. Middle panel: filtered RVs and their error bars, resulting from the subtraction of the GP-fitted activity jitter from the raw RVs (in red), and the sine curve corresponding to the assumed planet signal (in cyan). Bottom panel: residual RVs resulting from the subtraction of the planet signal from the filtered RVs, and their error bars. The residual RVs feature an rms value of 29 m s^{-1}, i.e. the GP fits the RVs down to $\chi^2_{\rm r} = 0.151$.

The best fit with our third method is shown in Fig. 13, where we see the raw RVs and the modelled RV curve predicted with this method, i.e. the sum of the GPR-fitted activity jitter and of the planet signal. Zooming in shows that this curve presents similarities with the RV jitter curve derived by ZDI (Fig. 8), indicating that, although working only with the RV data points, GPR successfully retrieves a convincing model for the activity. We also note the ability of the GP to model the activity jitter not only during our

Downloaded from https://academic.oup.com/mnras/article-abstract/467/2/1342/2869846 by Universitie Paul Sabatier - Toulouse 3 user on 16 December 2019

Table 7. Results yielded by the methods ZDI no. 1 (Section 5.1), ZDI no. 2 (Section 5.2) and GPR (Section 5.3), for the two periods $\simeq$15 $P_{\rm rot}$ and $\simeq$13 $P_{\rm rot}$. From top to bottom: reflex motion semi-amplitude K, phase of inferior conjunction ϕ relative to cycle 11.0, orbital period $P_{\rm orb}$ in units of $P_{\rm rot}$, orbital period $P_{\rm orb}$ in days, semimajor axis a, $M\sin i$ in units of Jovian mass, BJD of inferior conjunction $\mathrm{BJD_c}$, natural logarithm of relative likelihood as compared to the best case $\mathcal{L}_r$, GP amplitude θ_1 and GP recurrence time-scale θ_2. Results are displayed in bold font when the period is found with the highest likelihood using the corresponding method.

	ZDI no. 1	ZDI no. 2	GPR
K (km s^{-1})	0.133±0.021	**0.154±0.022**	0.149±0.026
ϕ	0.715±0.024	**0.671±0.035**	0.728±0.033
$P_{\rm orb}$ ($P_{\rm rot}$)	15.27±0.14	**15.29±0.15**	15.12±0.20
$P_{\rm orb}$ (d)	10.90±0.10	**10.91±0.11**	10.79±0.14
a (au)	0.0974±0.0032	**0.0975±0.0032**	0.0968±0.0032
$M\sin i$ ($\mathrm{M_{Jup}}$)	1.49±0.25	**1.73±0.27**	1.66±0.31
$\mathrm{BJD_c}$ (2457340+)	9.54±0.26	**9.06±0.38**	9.71±0.36
$\log \mathcal{L}_r$	−0.53	**0.00**	−0.25
θ_1 (km s^{-1})			1.19±0.21
θ_2 ($P_{\rm rot}$)			1.0004±0.0002
K (km s^{-1})	0.107±0.021	0.148±0.025	**0.163±0.028**
ϕ	0.724±0.031	0.677±0.038	**0.766±0.030**
$P_{\rm orb}$ ($P_{\rm rot}$)	12.76±0.14	12.83±0.12	**12.61±0.13**
$P_{\rm orb}$ (d)	9.11±0.10	9.16±0.09	**8.99±0.09**
a (au)	0.0864±0.0028	0.0868±0.0028	**0.0858±0.0028**
$M\sin i$ ($\mathrm{M_{Jup}}$)	1.13±0.23	1.56±0.28	**1.71±0.31**
$\mathrm{BJD_c}$ (2457340+)	10.14±0.28	9.69±0.35	**10.54±0.27**
$\log \mathcal{L}_r$	−6.87	−3.61	**0.00**
θ_1 (km s^{-1})			**1.19±0.21**
θ_2 ($P_{\rm rot}$)			**1.0005±0.0002**

observing runs, but also during the 45 d gap between them, emphasizing the variability of the RV signal with time. The residual RVs in the case presented here have an rms value of 29 m s^{-1} (close to the instrument RV precision 20–30 m s^{-1}) whereas the residual RVs derived with the first method yield an rms value of 51 m s^{-1}. Though the rms value is 2.5 times smaller than the error bar, GPR only fits two parameters, which illustrates its flexibility without decreasing its reliability, since the results are consistent with those found using independent methods (Sections 5.1 and 5.2). This demonstrates that GPR does a better job at modelling the activity jitter and its temporal evolution than the two previous methods, in agreement with the conclusions of Donati et al. (2016) in the case of the wTTS V830 Tau. As a result, we consider the optimal planet parameters derived with GPR as the most reliable ones, and therefore conclude that the orbital periods of 10.8 and 9.0 d are more or less equally likely.

Table 7 summarizes the likelihood of the different periods found with each method.

6 SUMMARY AND DISCUSSION

This paper reports the results of an extended spectropolarimetric run on the wTTS TAP 26, carried out within the framework of the international MaTYSSE Large Programme, using the echelle spectropolarimeter ESPaDOnS at CFHT, spanning 72 d from 2015 November 18 to 2015 December 03 then from 2016 January 17 to 29, and complemented by contemporaneous photometric observations from the 1.25-m telescope at CrAO.

Applying ZDI to our two data sets, we derived the surface brightness and magnetic maps of TAP 26, revealing the presence of cool spots and warm plages totalling up to 12 per cent of the stellar surface (we however caution that this is a lower limit given the insensitivity of ZDI to small spots evenly spread over the stellar surface). The large-scale field of TAP 26 is found to be mainly poloidal and axisymmetric, with a 120 G dipole component tilted at 40° from the rotation axis. The 2015 November and 2016 January maps are mostly similar, but none the less feature some differences that indicate temporal evolution of the surface brightness and the magnetic field, demonstrated by the inability of ZDI to model the whole data set at noise level, on a time-scale comparable to that spanning our sample (72 d). ZDI also enabled us to detect the differential rotation pattern at the surface of TAP 26, with $\mathrm{d}\Omega = 0.0492 \pm 0.0010$ rad d^{-1}, a value close to that of the Sun, implying a time for the equator to lap the pole by one rotation equal to 128 ± 3 d.

We then applied three different methods to search for a planetary signature in the observed spectra. The first method studies the radial velocities filtered out from the activity jitter predicted by ZDI. Our second method looks for the planet parameters that enable the best fit to the corrected LSD profiles, in a way similar to that used to estimate surface differential rotation. The third method uses GPR to fit the activity jitter in the raw RVs, and like the second method, searches for the orbital parameters that enable GPR to fit the raw RVs corrected from the reflex motion best. We find that GPR succeeds best at modelling the intrinsic variability occurring at the surface of TAP 26, and is able to fit raw RVs at an rms precision of 29 m s^{-1}, i.e. close to the instrumental precision of ESPaDOnS (20–30 m s^{-1}, Moutou et al. 2007; Donati et al. 2008) and 30 per cent better than with our first method (yielding an rms precision of 51 m s^{-1}). A similarly low rms was reached by GPR in the study of wTTS V830 Tau (35–37 m s^{-1}, Donati et al. 2017).

All three methods demonstrate the clear presence of a planet signature in the data, although the gap between both data sets generates aliasing problems, causing multiple nearby peaks to stand out in the periodogram. Of the dominant periods, the 10.8 d one emerges strongly for all three methods. It is the most likely with the second method, and equally likely as other periods when using

Downloaded from https://academic.oup.com/mnras/article-abstract/467/2/1342/2869846 by Université Paul Sabatier - Toulouse 3 user on 16 December 2019

the first and third methods (13.4 and 9.0 d, respectively). Although the 9.0 d orbital period ranks low (and in particular lower than the 13.4 d period) with our first and second methods, we none the less consider it as the second most likely given its first rank with GPR; the most probable explanation for this apparent discrepancy lies in the higher ability of GPR at modelling intrinsic variability of the activity jitter plaguing the RV curve. Allowing ZDI to model temporal evolution of spot distributions and magnetic topologies should bring all methods on an equal footing; this upgrade is planned for a forthcoming study.

Assuming the 10.79±0.14 d period is the true orbital period, and using the values yielded by GPR for K and ϕ, we find a circular orbit of semimajor axis $a = 0.0968 \pm 0.0032$ au $= 17.8 \pm 2.7\ R_\star$, epoch of inferior conjunction $\mathrm{BJD_c} = 2457349.71 \pm 0.36$ and $M\sin i = 1.66 \pm 0.31\ \mathrm{M_{Jup}}$. If the orbital plane is aligned with the equatorial plane of TAP 26, with an assumed inclination of 55°, we obtain a mass $M = 2.03 \pm 0.46\ \mathrm{M_{Jup}}$ for TAP 26 b. The 8.99 ± 0.09 d period leads to $a = 0.086 \pm 0.003$ au, $\mathrm{BJD_c} = 2457350.54 \pm 0.27$ and $M\sin i = 1.71 \pm 0.31\ \mathrm{M_{Jup}}$.

With an age of ≃17 Myr, TAP 26 is already an aging T Tauri star and on the verge of becoming a post T Tauri star, as demonstrated by its complex geometry and weaker dipole field component (consistent with TAP 26 having a mostly radiative interior). Akin to V830 Tau b (Donati et al. 2017), the hJ in a nearly circular orbit that we have discovered in the young system TAP 26 is better explained by type II disc migration than by planet–planet scattering coupled to tidal circularization. When compared to V830 Tau, a 2 Myr wTTS of similar mass (Donati et al. 2015, 2016, 2017), appears as an evolved version, rotating 4× faster than its younger sister, likely as a direct consequence of its 4× smaller moment of inertia (according to the evolutionary models of Siess et al. 2000).

Regarding the hJs we detected around TAP 26 and V830 Tau and despite their differences (in mass in particular), it would be tempting to claim that, like its host star, TAP 26 b is an evolved version of V830 Tau b. This would actually imply that TAP 26 b migrated outwards under tidal forces from a distance of ≃0.057 au (where V830 Tau b is located) to its current orbital distance of 0.094 au, as a result of the spin period of TAP 26 being ≃ 15 × shorter than the orbital period of TAP 26 b. This option seems however unlikely given the latest predictions of tidal interactions between a young T Tauri star and its close-in hJ (Bolmont & Mathis 2016), indicating that tidal forces can only have a significant impact on an hJ within 0.06 au of a solar-mass host star (for a typical TTS with a radius of ≃2 $\mathrm{R_\odot}$). The most likely explanation we see is thus that TAP 26 b:

(i) ended up its type-II migration in the accretion disc at the current orbital distance, when TAP 26 was still young, fully convective and hosting a large-scale dipole field of a few kG similar to that of AA Tau (Donati et al. 2010), i.e. strong enough to disrupt the disc up to a distance of 0.09 au;

(ii) was left over once the disc has dissipated at an age significantly smaller than 2 Myr, i.e. before the large-scale field had time to evolve into a weaker and more complex topology, and the inner accretion disc to creep in as a result of the decreasing large-scale field and the subsequent chaotic accretion (e.g. Blinova, Romanova & Lovelace 2016).

Admittedly, this scenario requires favourable conditions to operate; in particular, it needs the accretion disc to vanish in less than 2 Myr, which happens to occur in no more than 10 per cent of single T Tauri stars in Taurus (Kraus et al. 2012). In fact, since both TAP 26 and V830 Tau have the same angular momentum content, it is quite likely that TAP 26 indeed dissipated its disc very early (see Section 3). Quantitatively speaking, assuming (i) that the hJ we detected tracks the location of the inner disc when the disc dissipated, (ii) that the spin period at this time was locked on the Keplerian period of the inner disc (equal to the orbital period of the detected hJ) and (iii) that stellar angular momentum was conserved since then, we derive that the disc must have dissipated when TAP 26 was about three times larger in radius, at an age of less than 1 Myr (according to Siess et al. 2000). Generating a magnetospheric cavity of the adequate size (0.085–0.097 au depending on the orbital period) would have required TAP 26 to host at this time a large-scale dipole field of 0.3–1.0 kG for mass accretion rates in the range 10^{-9}–$10^{-8}\ \mathrm{M_\odot\ yr^{-1}}$, compatible with the large-scale fields found in cTTSs of similar masses (e.g. GQ Lup, Donati et al. 2012).

Along with other recent reports of close-in giant planets (or planet candidates) detected (or claimed) around young stars (van Eyken et al. 2012; David et al. 2016; Donati et al. 2016, 2017; Johns-Krull et al. 2016; Mann et al. 2016), our result may suggest a surprisingly high frequency of hJs around young solar-type stars, with respect to that around more evolved stars (≃1 per cent, Wright et al. 2012). However, this may actually reflect no more than a selection bias in the observation samples (as for their mature equivalents in the early times of velocimetric planet detections). Planets are obviously much easier to detect around non-accreting TTSs as a result of their lower level of intrinsic variability; observation samples (like that of MaTYSSE) are thus naturally driven towards young TTSs whose accretion discs vanished early, i.e. at a time when their large-scale fields were still strong and their magnetospheric gaps large, and thus for which hJs had more chances to survive type-II migration. A more definite conclusion must wait for a complete analysis of the full MaTYSSE sample.

More observations of TAP 26, featuring in particular a more regular temporal sampling, are currently being planned to better determine the characteristics of the newborn hJ we detected. Furthermore, analysing thoroughly the full MaTYSSE data set to pin down the frequency of newborn hJs within the sample observed so far will bring a clearer view on how the formation and migration of young giant planets is occurring. Ultimately, only a full-scale planet survey of young TTSs such as that to be carried out with SpectroPolarimètre InfraRouge, the new generation spectropolarimeter currently being built for CFHT and scheduled for first light in 2018, will be able to bring a consistent picture of how young close-in planets form and migrate, how their population relates to that of mature hJs, and more generally how young hJs impact the formation and early architecture of planetary systems like our Solar system.

ACKNOWLEDGEMENTS

This paper is based on observations obtained at the Canada–France–Hawaii Telescope (CFHT), operated by the National Research Council of Canada, the Institut National des Sciences de l'Univers of the Centre National de la Recherche Scientifique (INSU/CNRS) of France and the University of Hawaii. We thank the CFHT QSO team for the great work and effort at collecting the high-quality MaTYSSE data presented in this paper. MaTYSSE is an international collaborative research programme involving experts from more than 10 different countries (France, Canada, Brazil, Taiwan, UK, Russia, Chile, USA, Ireland, Switzerland, Portugal, China and Italy). We also warmly thank the IDEX initiative at Université Fédérale Toulouse Midi-Pyrénées (UFTMiP) for funding the STEPS collaboration program between IRAP/OMP and ESO. We acknowledge funding from the LabEx OSUG@2020 that allowed

Downloaded from https://academic.oup.com/mnras/article-abstract/467/2/1342/2869846 by Universitïe Paul Sabatier - Toulouse 3 user on 16 December 2019

purchasing the ProLine PL230 CCD imaging system installed on the 1.25-m telescope at CrAO. SGG acknowledges support from the Science and Technology Facilities Council (STFC) via an Ernest Rutherford Fellowship [ST/J003255/1]. SHPA acknowledges financial support from CNPq, CAPES and Fapemig. We would also like to acknowledge the Centre de Données Astronomiques de Strasbourg for the SIMBAD data base.

REFERENCES

Baruteau C. et al., 2014, in Beuther H., Klessen R. S., Dullemond C. P., Henning T., eds, Protostars and Planets VI. Univ. Arizona Press, Tucson, AZ, p. 667
Batygin K., Bodenheimer P. H., Laughlin G. P., 2016, ApJ, 829, 114
Blinova A. A., Romanova M. M., Lovelace R. V. E., 2016, MNRAS, 459, 2354
Bolmont E., Mathis S., 2016, Celest. Mech. Dyn. Astron., 126, 275
Bradshaw S. J., Hartigan P., 2014, ApJ, 795, 79
Brown S. F., Donati J.-F., Rees D. E., Semel M., 1991, A&A, 250, 463
Chib S., Jeliazkov I., 2001, J. Am. Stat. Assoc., 96, 270
David T. J. et al., 2016, Nature, 534, 658
Davies C. L., Gregory S. G., Greaves J. S., 2014, MNRAS, 444, 1157
Donati J.-F., 2003, in Trujillo-Bueno J., Sanchez Almeida J., eds, ASP Conf. Ser. Vol. 307, Solar Polarization. Astron. Soc. Pac., San Francisco, p. 41
Donati J.-F., Brown S. F., 1997, A&A, 326, 1135
Donati J.-F., Collier Cameron A., 1997, MNRAS, 291, 1
Donati J.-F., Semel M., Carter B. D., Rees D. E., Collier Cameron A., 1997, MNRAS, 291, 658
Donati J.-F., Collier Cameron A., Petit P., 2003, MNRAS, 345, 1187
Donati J.-F. et al., 2006, MNRAS, 370, 629
Donati J.-F. et al., 2008, MNRAS, 385, 1179
Donati J.-F. et al., 2010, MNRAS, 409, 1347
Donati J.-F. et al., 2011, MNRAS, 412, 2454
Donati J.-F. et al., 2012, MNRAS, 425, 2948
Donati J.-F. et al., 2014, MNRAS, 444, 3220
Donati J.-F. et al., 2015, MNRAS, 453, 3706
Donati J.-F. et al., 2016, Nature, 534, 662
Donati J.-F. et al., 2017, MNRAS, 465, 3343
Feigelson E. D., Jackson J. M., Mathieu R. D., Myers P. C., Walter F. M., 1987, AJ, 94, 1251
Gallet F., Bouvier J., 2015, A&A, 577, A98
Grankin K. N., 2013, Astron. Lett., 39, 251
Grankin K. N., Bouvier J., Herbst W., Melnikov S. Y., 2008, A&A, 479, 827
Gregory S. G., Donati J.-F., Morin J., Hussain G. A. J., Mayne N. J., Hillenbrand L. A., Jardine M., 2012, ApJ, 755, 97
Haywood R. D. et al., 2014, MNRAS, 443, 2517
Herczeg G. J., Hillenbrand L. A., 2014, ApJ, 786, 97
Huélamo N. et al., 2008, A&A, 489, L9
Johns-Krull C. M. et al., 2016, ApJ, 826, 206
Kenyon S. J., Hartmann L., 1995, ApJS, 101, 117
Kraus A. L., Ireland M. J., Hillenbrand L. A., Martinache F., 2012, ApJ, 745, 19
Kurucz R., 1993, ATLAS9 atmospheric models CD-ROM No. 13 and ATLAS9 and SYNTHE routines, spectral line database CD-ROM No. 18. Smithsonian Astrophysical Observatory, Washington D.C.
Lagrange A.-M. et al., 2010, Science, 329, 57
Landi degl'Innocenti E., Landolfi M., 2004, Polarisation in spectral lines. Kluwer, Dordrecht
Lanza A. F., 2006, MNRAS, 369, 1773
Loinard L., Torres R. M., Mioduszewski A. J., Rodríguez L. F., González-Lópezlira R. A., Lachaume R., Vázquez V., González E., 2007, ApJ, 671, 546
Lucy L. B., Sweeney M. A., 1971, AJ, 76, 544
Mann A. W. et al., 2016, AJ, 152, 61
Moutou C. et al., 2007, A&A, 473, 651
Pecaut M. J., Mamajek E. E., 2013, ApJS, 208, 9
Pecaut M. J., Mamajek E. E., 2016, MNRAS, 461, 794
Petit P. et al., 2015, A&A, 584, A84
Rajpaul V., Aigrain S., Osborne M. A., Reece S., Roberts S., 2015, MNRAS, 452, 2269
Sallum S. et al., 2015, Nature, 527, 342
Semel M., 1989, A&A, 225, 456
Setiawan J., Henning T., Launhardt R., Müller A., Weise P., Kürster M., 2008, Nature, 451, 38
Siess L., Dufour E., Forestini M., 2000, A&A, 358, 593
Skelly M. B., Donati J.-F., Bouvier J., Grankin K. N., Unruh Y. C., Artemenko S. A., Petrov P., 2010, MNRAS, 403, 159
Stout-Batalha N. M., Vogt S. S., 1999, ApJS, 123, 251
Torres R. M., Loinard L., Mioduszewski A. J., Rodríguez L. F., 2009, ApJ, 698, 242
van Eyken J. C. et al., 2012, ApJ, 755, 42
Valenti J. A., Fischer D. A., 2005, ApJS, 159, 141
Vogt S. S., Penrod G. D., Hatzes A. P., 1987, ApJ, 321, 496
Wright J. T., Marcy G. W., Howard A. W., Johnson J. A., Morton T. D., Fischer D. A., 2012, ApJ, 753, 160

SUPPORTING INFORMATION

Supplementary data are available at *MNRAS* online.

diffs_2_3.pdf
tap26_2016_sub3_online.pdf

Please note: Oxford University Press is not responsible for the content or functionality of any supporting materials supplied by the authors. Any queries (other than missing material) should be directed to the corresponding author for the article.

Downloaded from https://academic.oup.com/mnras/article-abstract/467/2/1342/2869846 by Universitie Paul Sabatier - Toulouse 3 user on 16 December 2019

APPENDIX A: ADDITIONAL FIGURES

Images of brightness and magnetic field on the surface of TAP 26, as derived with ZDI using our 29 spectra, are shown in Fig. A1.

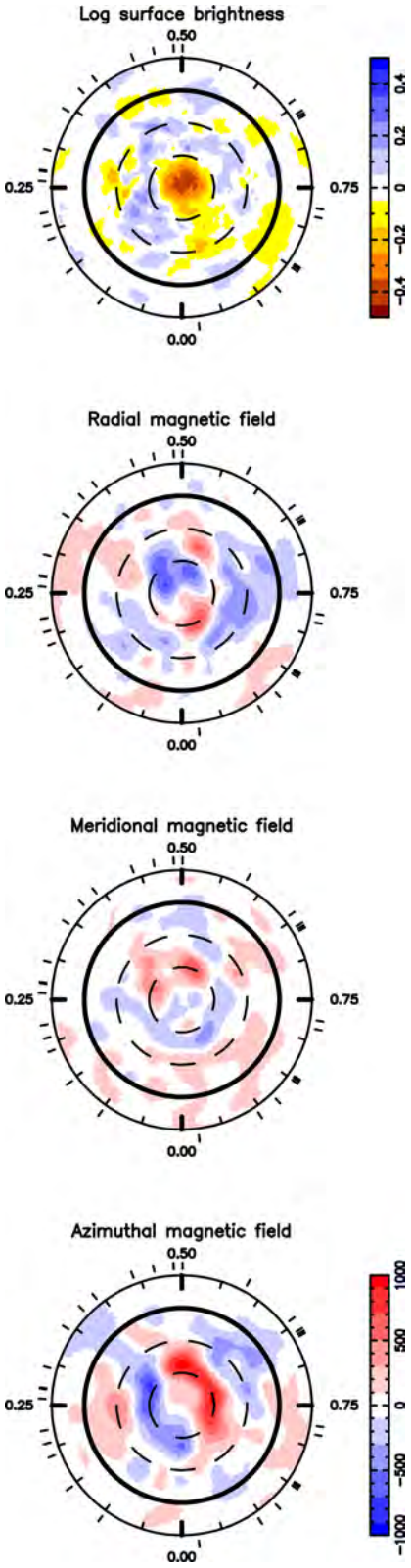

Figure A1. Brightness and magnetic components surface maps when fitting the 2015 November and 2016 January data sets altogether, at rotation cycle 51.

APPENDIX B: ACTIVITY PROXIES

In order to investigate whether the detected periodic RV signal may relate to activity, we plotted periodograms of the longitudinal magnetic field B_ℓ and of the Hα emission equivalent width (Figs B1 and B2, respectively). Peak frequencies for these proxies are located at periods of 0.7145 ± 0.0002 d and 0.7132 ± 0.0001 d, respectively, as well as their aliases. Given the surface differential rotation parameters measured for TAP 26 (see Section 4.2), the values of their respective periods indicate that the longitudinal field traces an average latitude of 46° whereas the bulk of Hα emission comes from a lower average latitude of 27° (see equation 2). As opposed to the raw RVs, the rotation period $P_{\rm rot}$ has a higher power than its first harmonic $P_{\rm rot}/2$ (Fig. 10). No signal is detected at the planet periods found in Section 5.

Plotting phase-folded curves of the longitudinal magnetic field and the Hα emission equivalent width (where the x-axis indicates the rotation phase as defined in equation 1), in Figs B3 and B4, we observe a decrease in the longitudinal magnetic field around phase 0.77 in 2015 November and phase 0.97 in 2016 January, which correspond approximately to the phases where the dipole pole points towards the Earth (0.73 ± 0.03 and 0.85 ± 0.03, respectively), causing B_ℓ to have strong negative values and showing the importance of the dipole in the value of B_ℓ. Similarly, the increase in emission equivalent width of the Hα line between phases 0.6 and 0.9 illustrates the correlation between the lower harmonics of the magnetic field of TAP 26 and this activity proxy.

Downloaded from https://academic.oup.com/mnras/article-abstract/467/2/1342/2869846 by Universitïe Paul Sabatier - Toulouse 3 user on 16 December 2019

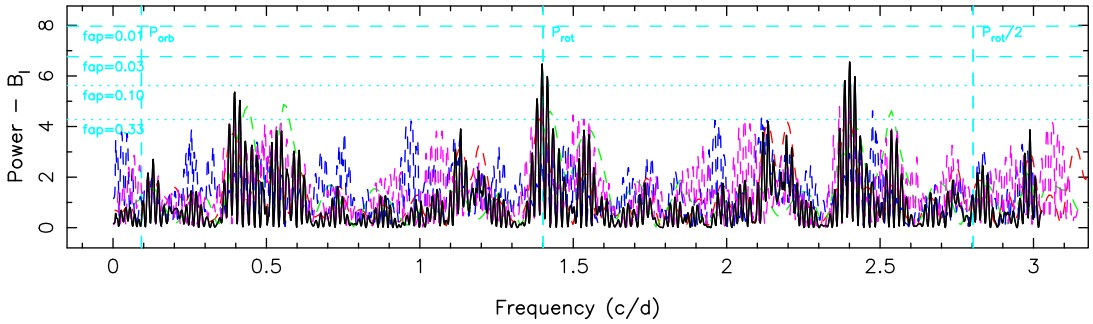

Figure B1. Periodogram of the longitudinal magnetic field. The rotation period at 0.7135 d is represented by a dashed vertical cyan line, as well as its first harmonic and the orbital period at 10.92 d.

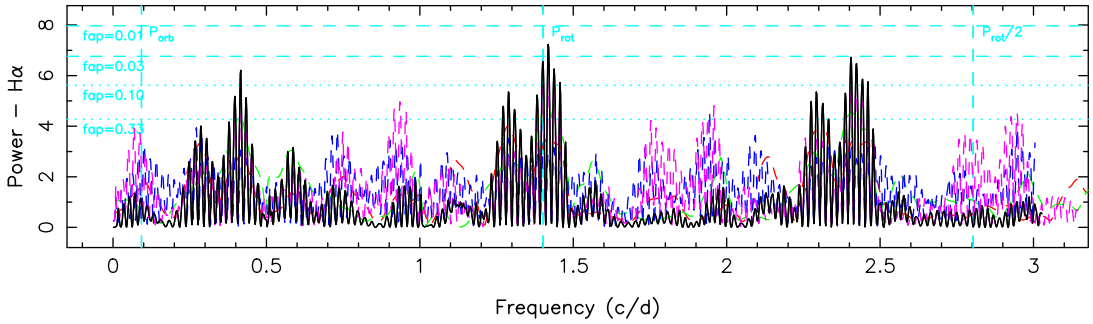

Figure B2. Periodogram of the Hα line equivalent width. The rotation period at 0.7135 d is represented by a dashed vertical cyan line, as well as its first harmonic and the orbital period at 10.92 d.

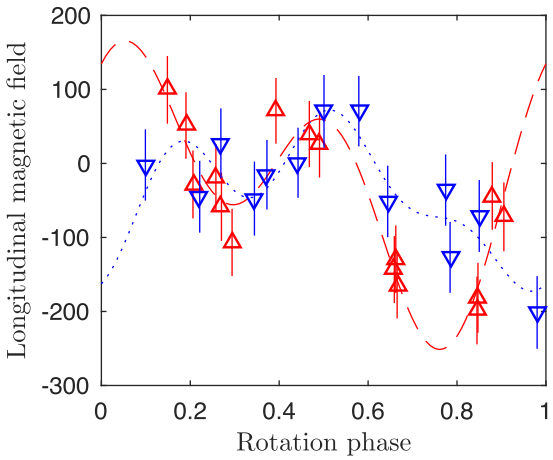

Figure B3. Folded curve of the longitudinal magnetic field against the rotation phase. 2015 November (red upward-pointing triangles) data are fitted with the sum of a sine curve and one harmonic (red dashed line) and 2016 January (blue downward-pointing triangles) data are fitted with the sum of a sine curve and two harmonics (blue dotted line).

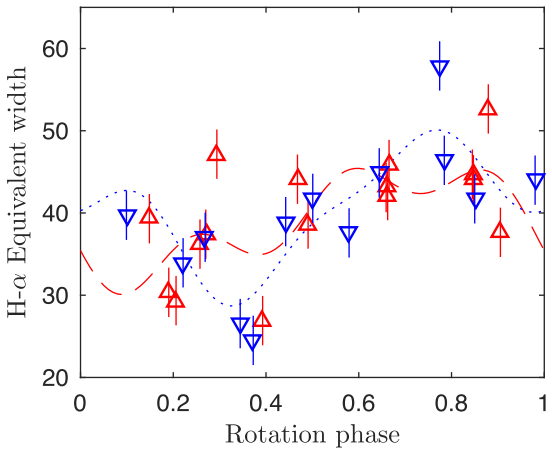

Figure B4. Folded curve of the equivalent width of Hα against the rotation phase. 2015 November (red upward-pointing triangles) and 2016 January (blue downward-pointing triangles) data are fitted with the sum of a sine curve and two harmonics (red dashed line and blue dotted line, respectively).

This paper has been typeset from a TEX/LATEX file prepared by the author.

Downloaded from https://academic.oup.com/mnras/article-abstract/467/2/1342/2869846 by Universitie Paul Sabatier - Toulouse 3 user on 16 December 2019

APPENDIX C: SIMULATIONS

In order to check that the detected planetary signal does not come from the filtering process, we conducted simulations to test our three methods on two different data sets: one where the presence of a planet was input in the simulation (scenario #1), and one without any planet (scenario #2). Stokes *I* and *V* LSD profiles were generated from the brightness and magnetic maps found in Sec. 4, at the same dates of observation as the real data, with a comparable noise level. The added planet signature had the properties of the best fit found with the second method (Sec. 5.2): K=0.154 km s^{-1}, $P_{\rm orb}/P_{\rm rot}$=15.29, ϕ=0.671. Applying ZDI to these data sets, we reconstructed brightness and magnetic maps as in Sec. 4. For both simulations, the maps we found look similar to the ones reconstructed from the real data, with an information loss amounting to 4% for the spottedness and ≃80 G for the rms magnetic flux, but the main features, such as the polar spot, are recovered. Fig. C1 shows the brightness maps for simulation #1, at both epochs.

As in Sec. 5.1, synthetic RV curves are shown in Fig. C2, C3 for simulations #1 and #2 respectively. While a signal is detected in the filtered RVs of simulation #1 (rms 107 m s^{-1}), no significant signal is detected in the filtered RVs in simulation #2 (rms 58 m s^{-1}). Table C1 summarises the characteristics of the best fit to the filtered RVs for both scenarii, in comparison with a (K=0 km s^{-1}, RV$_0$=0 km s^{-1}) curve. The periodograms of the filtered RV curves, displayed in Fig. C4 and Fig. C5, further confirm this, with simulation #2 yielding no significant signal at the frequencies found with our three methods in Sec. 5.

We note that changing the noise pattern can make the FAP of the filtered RVs highest peak vary between 4% and 26% for simulation #2 (no planet). It can also change the relative power of the different orbital periods in the filtered RVs for simulation #1: most of the time the ≃10.8 d period is recovered as the highest peak with a FAP<0.5%, but the ≃9.0 d period reaches a smaller $\chi^2_{\rm r}$ in one case out of five. This sheds light on why the different methods do not always favour the same orbital periods in our analysis.

The second method also recovers the different orbital periods from simulation #1, the ≃10.8 d one being the most likely, with a $\Delta\chi^2$ of 7.37 compared to the ≃13.4 d period and 7.67 compared to the ≃9.0 d period. Fig. C6 shows the $\chi^2_{\rm r}$ map around the minimum $P_{\rm orb}$≃10.8 d for ϕ=0.67 (value at the 3-D local minimum), with the white colour bounding the 99.99% confidence region. We chose not to apply this method on simulation #2 (without planet) because it runs computations for orbital parameters close to the local minima found with the first method, and no such significant minima were found for simulation #2.

GPR also successfully recovers the input planet period in simulation #1, as shown in Fig. C7 on which the raw RVs, the planet signal and the residual RVs at $P_{\rm orb}$=15.31$P_{\rm rot}$

Scenario #1	Scenario #2
K=0.122±0.020 km s^{-1}	K=0.036±0.021 km s^{-1}
$P_{\rm orb}/P_{\rm rot}$=15.35±0.16	
ϕ=0.647±0.026	
RV$_0$=0.018±0.014 km s^{-1}	
$\chi^2_{\rm r}$=0.540	$\chi^2_{\rm r}$=0.436
K=0 km s^{-1}	K=0 km s^{-1}
$\chi^2_{\rm r}$=1.893	$\chi^2_{\rm r}$=0.529
$\Delta\chi^2$=39.2	$\Delta\chi^2$=2.7
$\Delta(\log \mathcal{L}_r)$=-16.57	$\Delta(\log \mathcal{L}_r)$=-0.49

Table C1. Results found with the 1st method on both simulation datasets. The first column shows the results on the scenario with a planet and the second column shows the results on the scenario without planet. For each, a comparison is made between the best sine fit to the filtered RVs and a fit by a constant value, with the reflex motion semi-amplitude K, the orbital period $P_{\rm orb}$ in units of $P_{\rm rot}$, the phase of inferior conjunction ϕ relative to cycle 11.0, the mean RV RV$_0$ and $\chi^2_{\rm r}$. Differences in χ^2 (summed on 29 data points) and in logarithmic ($\log_e$) likelihood are given in the last row.

Scenario #1
K=0.155±0.022 km s^{-1}
$P_{\rm orb}/P_{\rm rot}$=15.32±0.14
ϕ=0.662±0.036
$\chi^2_{\rm r}$=0.95226
K=0 km s^{-1}
$\chi^2_{\rm r}$=0.97529
$\Delta\chi^2$=30.0
$\Delta(\log \mathcal{L}_r)$=-10

Table C2. Characteristics of the best fit found with the 2nd method on simulation #1 (top row), compared to a fit with a no-planet model (i.e. K=0 km s^{-1}, middle row). Differences in χ^2 (summed on 2581 data points) and in logarithmic ($\log_e$) likelihood are given in the last row.

Scenario #1	Scenario #2
K=0.138±0.027 km s^{-1}	K=0.060±0.052 km s^{-1}
$P_{\rm orb}/P_{\rm rot}$=15.31±0.21	
ϕ=0.646±0.038	
θ_1=1.14±0.21 km s^{-1}	
θ_2=1.0002±0.0002 $P_{\rm rot}$	
log $\mathcal{L}_r$=-6.20	log $\mathcal{L}_r$=-5.99
K=0 km s^{-1}	K=0 km s^{-1}
log $\mathcal{L}_r$=-21.42	log $\mathcal{L}_r$=-5.48
Δ(log $\mathcal{L}_r$)=-15.22	Δ(log $\mathcal{L}_r$)=-0.51

Table C3. Characteristics of the best fit (first row) found with the 3rd method on simulation #1 (left) and #2 (right), compared to a fit with a no-planet model (i.e. K=0 km s^{-1}, middle row). Differences in logarithmic (log$_e$) likelihood are given in the last row.

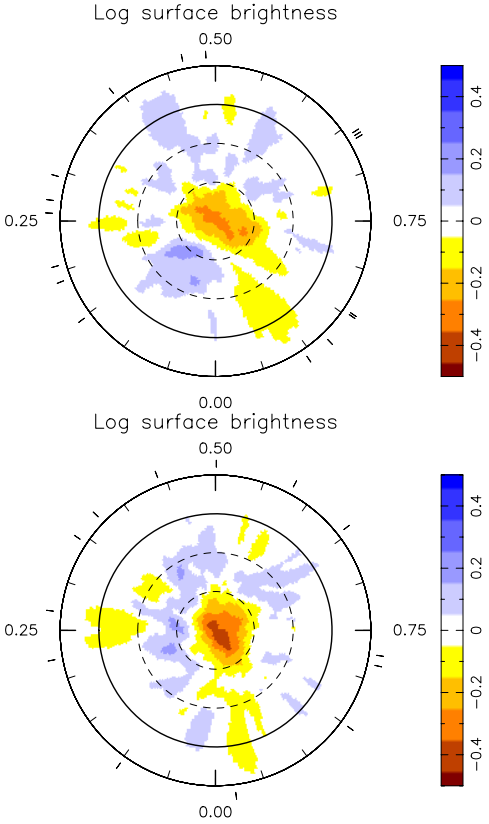

Figure C1. Brightness maps reconstructed from the simulation #1 data, for the 2015 Nov data subset (top) and the 2016 Jan data subset (bottom). Both maps feature a spot coverage of ≃8%.

are seen. The results of the MCMC runs are shown in the phase plots of Fig. C8 and C9, demonstrating that no orbital period stands out in simulation #2, i.e., in the activity jitter synthesised from the reconstructed brightness maps, whereas several orbital periods are detected in simulation #1, ≃10.8 d and ≃9.0 d being respectively the most likely and the second most likely, with a Bayes factor of only 1.25 between them. The comparison with a MCMC run where no planet is subtracted is shown in table C3 for both scenarii, demonstrating that, for scenario #1, taking a planet into account in the model results in a significant increase in the likelihood of the best fit, whereas it is not the case for scenario #2.

We conclude that all three methods enable us to recover the planet signal (scenario #1), and that the detected periods in the observational filtered RVs are not artifacts of the numerical process (scenario #2). Furthermore, for our particular observation window, the noise pattern can change the relative likelihood of the different detected peaks, as can the choice of the method to use.

This paper has been typeset from a TEX/LATEX file prepared by the author.

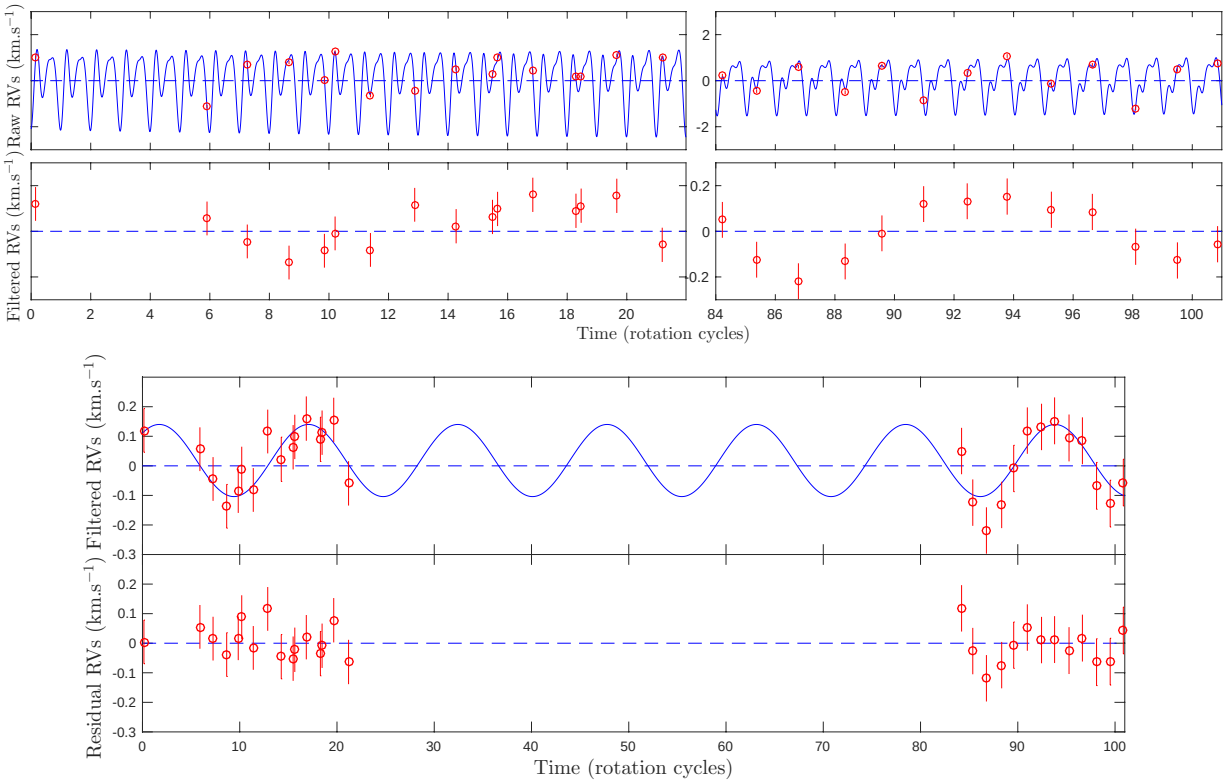

Figure C2. Simulation #1: raw, filtered and residual RV curves as derived with the method described in 5.1. The residual RVs feature a rms value of 59 m s^{-1}.

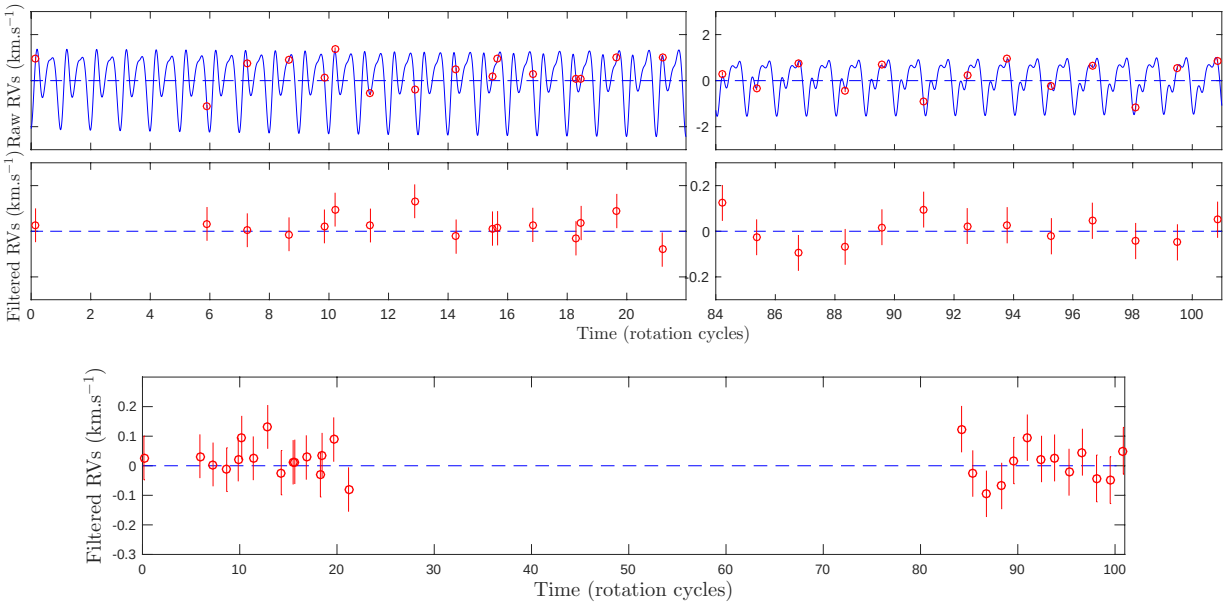

Figure C3. Simulation #2: raw and filtered RV curves as derived with the method described in 5.1. The filtered RVs feature a rms value of 58 m s^{-1}.

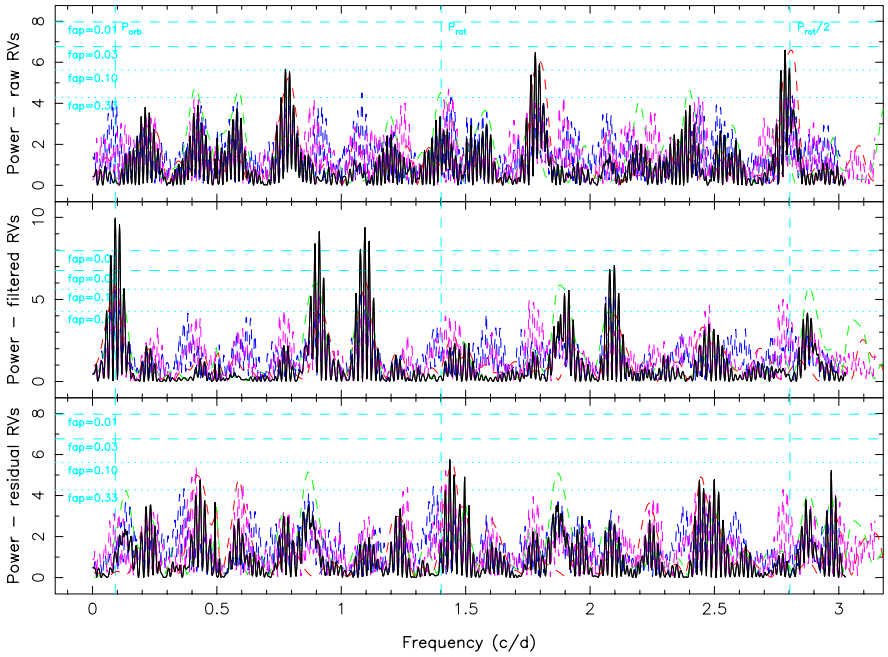

Figure C4. Simulation #1: periodograms of the raw (top), filtered (middle) and residual (bottom) RVs.

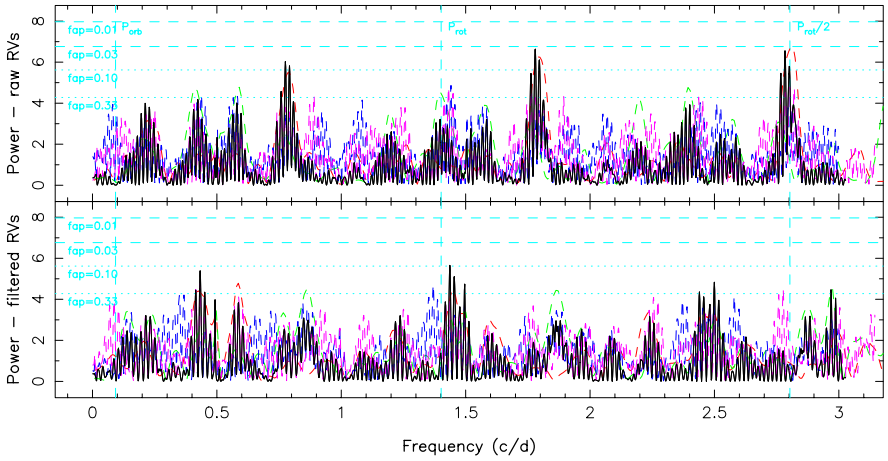

Figure C5. Simulation #2: periodograms of the raw (top) and filtered (bottom) RVs.

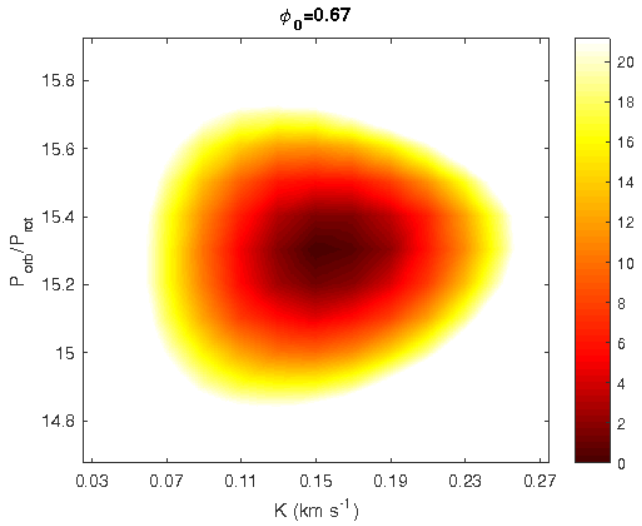

Figure C6. Simulation #1: $\Delta\chi^2$ map at ϕ=0.67 as derived with the method described in 5.2, centered around the minimum $P_{\rm orb}$=15.3 $P_{\rm rot}$. Parameters values are found to be K=0.155±0.022 km s^{-1}, $P_{\rm orb}$=15.32±0.14 $P_{\rm rot}$. The minimum value of $\chi^2_{\rm r}$ is 0.95226

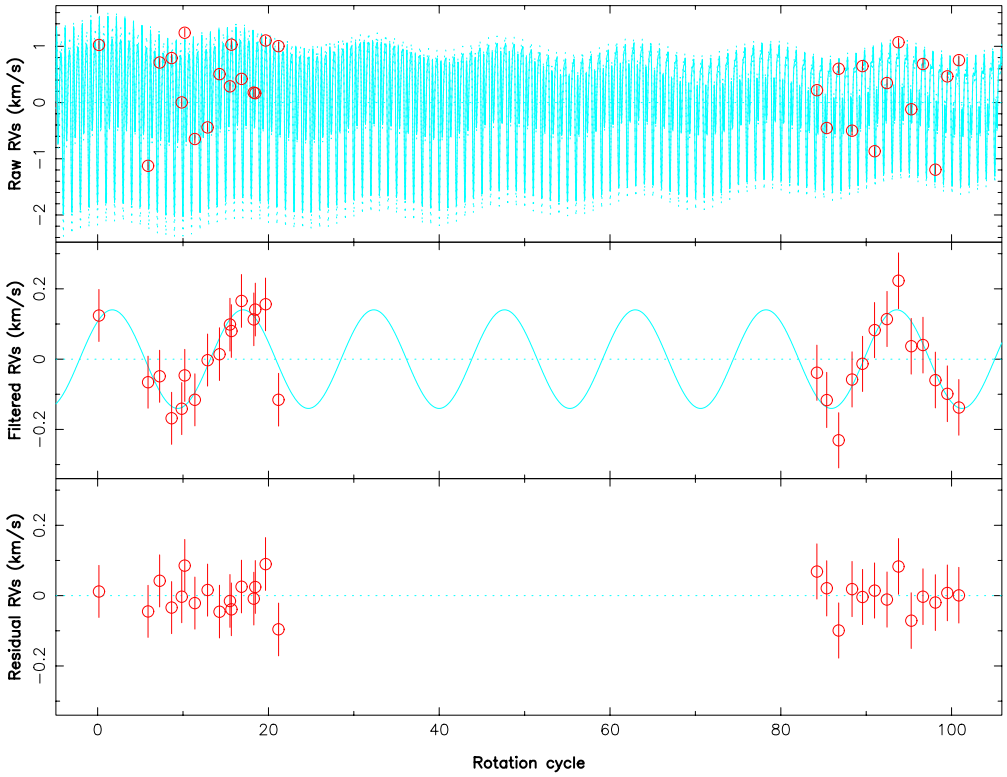

Figure C7. Example of GPR for simulation #1. Top: raw RVs (red dots) and GP fit+planet (cyan), middle: curves as derived with the method described in 5.3, for the local minimum $P_{\rm orb}$=15.31±0.21 $P_{\rm rot}$, K=0.138±0.027, ϕ=0.646±0.038,. The rms of the residual RVs amounts to 47 m s^{-1}.

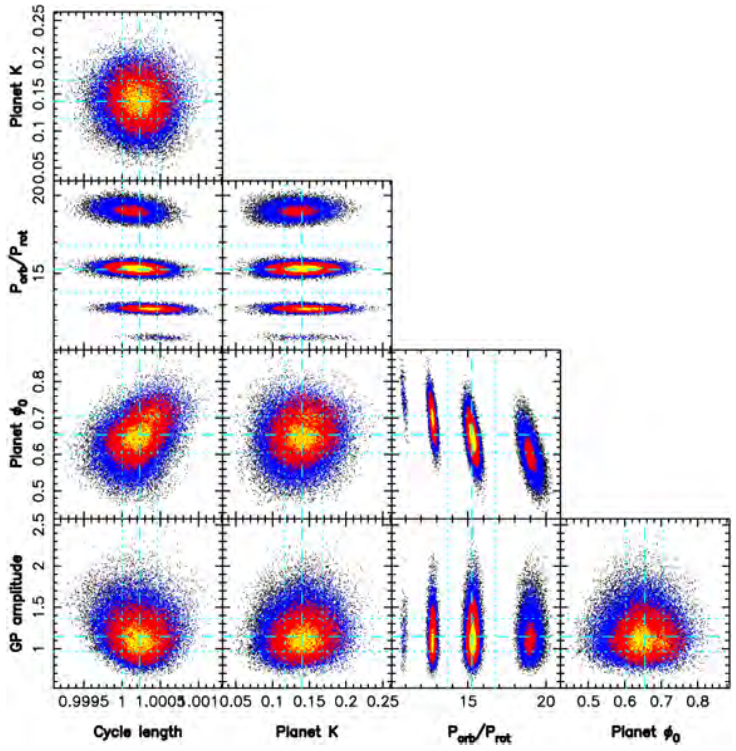

Figure C8. Simulation #1: phase plots of the MCMC run as described in 5.3. We find θ_1=1.15±0.19 km s^{-1}, θ_2=1.0002±0.0002 $P_{\rm rot}$, K=0.140±0.026 km s^{-1}, and the dominant orbital periods $P_{\rm orb}$=15.31±0.21 $P_{\rm rot}$ and $P_{\rm orb}$=12.74±0.13 $P_{\rm rot}$, with the corresponding phases being ϕ=0.646±0.038 and ϕ=0.699±0.036 respectively.

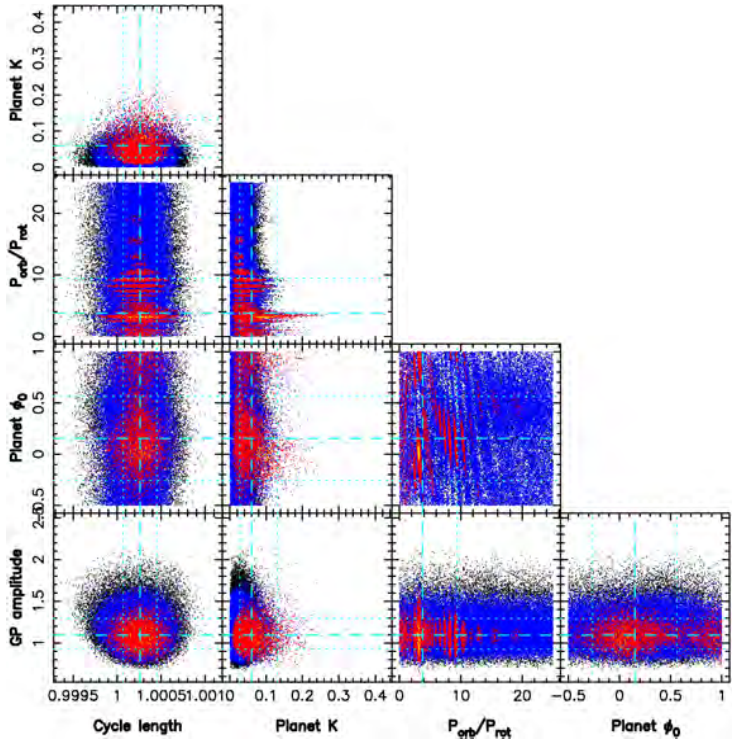

Figure C9. Simulation #2: phase plots of the MCMC run as described in 5.3. We find θ_1=1.09±0.19 km s^{-1}, θ_2=1.0003±0.0002 $P_{\rm rot}$ and K=0.060±0.053 km s^{-1}.

B.1.2 MNRAS publication: Yu et al. 2019

Monthly Notices
of the
ROYAL ASTRONOMICAL SOCIETY

MNRAS **489,** 5556–5572 (2019)
Advance Access publication 2019 September 5

doi:10.1093/mnras/stz2481

Magnetic field, activity, and companions of V410 Tau

L. Yu,[1]★ J.-F. Donati,[1] K. Grankin,[2] A. Collier Cameron,[3] C. Moutou,[4] G. Hussain,[1,5] C. Baruteau,[1] L. Jouve[1] and the MaTYSSE collaboration

[1]*Univ. de Toulouse, CNRS, IRAP, 14 Avenue E. Belin, F-31400 Toulouse, France*
[2]*Crimean Astrophysical Observatory, 298409 Nauchny, Crimea*
[3]*SUPA, School of Physics & Astronomy, University of St Andrews, St Andrews, Scotland KY16 9SS, UK*
[4]*CFHT Corporation, 65-1238 Mamalahoa Hwy, Kamuela, HI 96743, USA*
[5]*ESO, Karl-Schwarzschild-Str 2, D-85748 Garching, Germany*

Accepted 2019 September 3. Received 2019 August 28; in original form 2019 July 11

ABSTRACT

We report the analysis, conducted as part of the MaTYSSE programme, of a spectropolarimetric monitoring of the ∼0.8 Myr, ∼1.4 $M_\odot$ disc-less weak-line T Tauri star V410 Tau with the ESPaDOnS instrument at the Canada–France–Hawaii Telescope and NARVAL at the Télescope Bernard Lyot, between 2008 and 2016. With Zeeman-Doppler Imaging, we reconstruct the surface brightness and magnetic field of V410 Tau, and show that the star is heavily spotted and possesses a ∼550 G relatively toroidal magnetic field. We find that V410 Tau features a weak level of surface differential rotation between the equator and pole ∼5 times weaker than the solar differential rotation. The spectropolarimetric data exhibit intrinsic variability, beyond differential rotation, which points towards a dynamo-generated field rather than a fossil field. Long-term variations in the photometric data suggest that spots appear at increasing latitudes over the span of our data set, implying that, if V410 Tau has a magnetic cycle, it would have a period of more than 8 yr. Having derived raw radial velocities (RVs) from our spectra, we filter out the stellar activity jitter, modelled either from our Doppler maps or using Gaussian process regression. Thus filtered, our RVs exclude the presence of a hot Jupiter-mass companion below ∼0.1 au, which is suggestive that hot Jupiter formation may be inhibited by the early depletion of the circumstellar disc, which for V410 Tau may have been caused by the close (few tens of au) M dwarf stellar companion.

Key words: magnetic fields – techniques: polarimetric – stars: imaging – stars: individual: V410 Tau – stars: rotation.

1 INTRODUCTION

Investigating the birth and youth of low-mass stars ($<3\,M_\odot$) and of their planetary systems heavily contributes to unveiling the origin and history of the Sun and of its planets, in particular the life-hosting Earth. We know that stars and their planets form from the collapse of parsec-sized molecular clouds which progressively flatten into massive accretion discs, until finally settling as pre-main-sequence (PMS) stars surrounded by protoplanetary discs. T Tauri stars (TTSs) are PMS stars that have emerged from their dust cocoons and are gravitationally contracting towards the main sequence (MS); typically aged 1–15 Myr, they are classical TTSs (cTTSs) when they are still surrounded by a massive accretion disc (where planets are potentially forming), and weak-line TTSs (wTTSs) when their accretion has stopped and their inner disc has dissipated. Large-scale magnetic fields are known to play a crucial role in the early life of low-mass stars, as they can open a magnetospheric gap at the centre of the disc, funnel accreting disc material on to the star, induce stellar winds and prominences, and thus impact the angular momentum evolution of TTSs (Donati & Landstreet 2009). Observing and understanding the magnetic topologies of TTSs is therefore a necessary endeavour to complete our understanding of stellar and planetary formation (e.g. Bouvier et al. 2007).

Since the first detection of a magnetic field around a cTTS nearly 20 yr ago (Johns-Krull, Valenti & Koresko 1999), the large-scale topologies of a dozen cTTSs were mapped (e.g. Donati et al. 2007; Hussain et al. 2009; Donati et al. 2010a, 2013) thanks to the MaPP (Magnetic Protostars and Planets) Large Observing Programme allocated on the 3.6 m Canada–France–Hawaii Telescope (CFHT) with the ESPaDOnS (Echelle SpectroPolarimetric Device for the

★ E-mail: louise.yu@irap.omp.eu

© 2019 The Author(s)
Published by Oxford University Press on behalf of the Royal Astronomical Society

Downloaded from https://academic.oup.com/mnras/article-abstract/489/4/5556/5561492 by Université Paul Sabatier - Toulouse 3 user on 16 December 2019

Observation of Stars) high-resolution spectropolarimeter, using Zeeman-Doppler Imaging (ZDI), a tomography technique designed for imaging the brightness features and magnetic topologies at the surfaces of active stars (e.g. Donati & Brown 1997). This first exploration showed that the topologies of cTTSs are either quite simple or rather complex depending on whether the stars are fully convective or largely radiative, respectively (Gregory et al. 2012; Donati et al. 2013). Moreover, these fields are reported to vary with time (e.g. Donati et al. 2011, 2012, 2013) and resemble those of mature stars with similar internal structure (e.g. Morin et al. 2008), suggesting that they are produced through dynamo processes within the bulk of the convective zone.

The MaTYSSE (Magnetic Topologies of Young Stars and the Survival of close-in giant Exoplanets) Large Programme aims at mapping the large-scale magnetic topologies of ∼35 wTTSs, comparing them to those of cTTSs and MS stars, and probing the potential presence of massive close-in exoplanets (hot Jupiters/hJs) around its targets. It was allocated at CFHT over semesters 2013a to 2016b (510 h) with complementary observations from the ESPaDOnS twin NARVAL on the Télescope Bernard Lyot (TBL) at Pic du Midi in France and from the HARPS spectropolarimeter at the ESO Telescope at La Silla in Chile. Up to now, about a dozen wTTSs were studied with MaTYSSE for their magnetic topologies and activity, for example V410 Tau (Skelly et al. 2010), LkCa 4 (Donati et al. 2014), and V830 Tau (Donati et al. 2017). These studies showed that the fields of wTTSs are much more diverse than those of cTTSs, with for example V410 Tau and LkCa 4 displaying strong toroidal components despite being fully convective, as opposed to the results obtained on cTTSs (see discussion in Donati et al. 2014). MaTYSSE fostered the detection of two hJs around wTTSs, the 2 Myr-old V830 Tau b (Donati et al. 2016, 2017) and the 17 Myr-old TAP 26 b (Yu et al. 2017).

This new study focuses on V410 Tau, a very young (∼1 Myr in Skelly et al. 2010) disc-less wTTS (Luhman et al. 2010) with a well-constrained rotation period of 1.872 d (Stelzer et al. 2003). One of the most observed wTTSs, V410 Tau has been the target of both photometric and spectropolarimetric observation campaigns. High variability detected in its light curve (Bouvier & Bertout 1989; Grankin et al. 2008; Sokoloff et al. 2008) indicates a high level of activity, confirmed with Doppler maps (Skelly et al. 2010; Rice, Strassmeier & Kopf 2011; Carroll et al. 2012) showing that the photosphere features large polar and equatorial cool spots, responsible for these modulations. Magnetic maps made by Skelly et al. (2010) and Carroll et al. (2012) have shown a highly toroidal and non-axisymmetric large-scale field despite the mostly convective structure of V410 Tau.

We first describe our data, comprising new NARVAL data from MaTYSSE added to previous spectropolarimetric data taken with ESPaDOnS and NARVAL in 2008–2011, and contemporaneous photometric observations taken at the Crimean Astronomical Observatory (CrAO) and from the Super Wide Angle Search for Planets (SuperWASP) campaign (Section 2). We then derive the general properties of V410 Tau (Section 3), after which we pursue the investigation of both its photosphere and its magnetic field, using ZDI with a model including both bright plages and cool spots (Section 4). Then, we disentangle the activity jitter from the actual radial velocities (RVs) in the RV curve, using models from our ZDI maps and Gaussian process regression (GPR), in order to look for a potential planet signature (Section 5), before finally discussing our results and concluding (Section 6).

2 OBSERVATIONS

Our spectropolarimetric data set spans from 2008 October to 2016 January, totalling 144 high-resolution optical spectra, both unpolarized (Stokes *I*) and circularly polarized (Stokes *V*). It is composed of eight runs, most of which cover around 15 d, taken during four different seasons: 2008b–2009a, 2011a, 2013b, and 2015b–2016a. The full journal of observations is available in Table A1. The 2008b data set and four points in the 2009a data set were taken with the ESPaDOnS echelle spectropolarimeter at CFHT, while the rest were taken with the ESPaDOnS twin NARVAL installed at TBL.

The raw frames are processed with the nominal reduction package LIBRE ESPRIT as described in e.g. Donati et al. (1997, 2011), yielding a typical root-mean-square (rms) RV precision of 20–30 m s^{-1} (Moutou et al. 2007; Donati et al. 2008). The peak signal-to-noise ratios (S/N, per 2.6 km s^{-1} velocity bin) reached on the spectra range between 82 and 238 for the majority (three spectra have an S/N lower than 70 and were rejected for ZDI and the RV analysis), with a median of 140.

Time is counted in units of stellar rotation, using the same reference date and rotation period as in Skelly et al. (2010), namely BJD$_0$ = 2454832.58033 and $P_{\rm rot}$ = 1.871970 ± 0.000010 d (Stelzer et al. 2003), respectively:

$$c = ({\rm BJD} - {\rm BJD}_0)/P_{\rm rot}. \quad (1)$$

The stellar phase is defined as the decimal part of the cycle *c*.

The emission core of the Ca II infrared triplet (IRT) presents an average equivalent width (EW) of ≃13 km s^{-1} (0.37 Å). The He I D_3 line is relatively weak with an average EW of 13 km s^{-1} as well (0.25 Å), in agreement with the non-accreting status of V410 Tau. The H α line has an average EW of 14 km s^{-1} (0.33 Å) and an rms EW of 27 km s^{-1} and exhibits a periodicity of period 1.8720 ± 0.0009 d (see Appendix C, available online). From the He I D_3 line, we detected small flares on 2008 December 10 (rotational cycle −15+3.514, as per Table A1), on the night of 2013 December 8 to 2013 December 9 (rotational cycles 959+4.090 and 959+4.151), and on the night of 2016 January 20 (rotational cycles 1376+0.021 and 1376+0.040). One big flare, on 2008 December 15 (rotational cycle −15+6.181), was visible not only in He I D_3 (EW ≃ 30 km s^{-1}) but also in H α (EW ≃ 230 km s^{-1}) and the Ca II IRT (core emission EW ≃ 40 km s^{-1}). We removed the six flare-subjected observations from our data sets in order to proceed with the mapping of the photosphere and surface magnetic field, as well as the RV analysis.

Least-squares deconvolution (LSD; see Donati et al. 1997) was applied to all our spectra in order to add up information from all spectral lines and boost the resulting S/N of both Stokes *I* and *V* LSD profiles. The spectral mask we employed for LSD was computed from an ATLAS9 LTE model atmosphere (Kurucz 1993) featuring $T_{\rm eff}$ = 4500 K and log g = 3.5, and involves about 7800 spectral features (with about 40 per cent from Fe I, see e.g. Donati et al. 2010b, for more details). Stokes *I* and Stokes *V* LSD profiles shown in Section 4 display distortions that betray the stellar activity with a periodicity corresponding to the rotation of the star. Moonlight pollution, which affects 15 of our Stokes *I* LSD profiles, was filtered out using a two-step tomographic imaging process described in Donati et al. (2016). The S/N in the Stokes *I* LSD profiles, ranging from 1633 to 2930 (per 1.8 km s^{-1} velocity bin) with a median of 2410, is measured from continuum intervals, including not only the noise from photon statistics, but also the (often dominant) noise introduced by LSD (see Table A1). The S/N in Stokes *V* LSD

Downloaded from https://academic.oup.com/mnras/article-abstract/489/4/5556/5561492 by Universitïe Paul Sabatier - Toulouse 3 user on 16 December 2019

profiles, dominated by photon statistics, range from 1817 to 6970 with a median value of 3584.

Phase coverage is of varying quality depending on the observation epoch. The 2008b data set, with only six points, covers only half the surface of the star (phases −0.20 to 0.30). The 2009a data set, although the densest with 48 points in 16 d and including data from both instruments, lacks observations between phases 0.05 and 0.20. The 2011a data set presents a large gap between phases −0.05 and 0.15, and a smaller one between phases 0.65 and 0.80. The 2013b and 2015b data sets are well sampled, and the 2016a data set, with only nine points, lacks observations between phases 0.25 to 0.45 and −0.15 to 0.05.

Contemporaneous BVR_JI_J photometric measurements, documented in Table A2, were taken from the Crimean Astrophysical Observatory 1.25 and 0.60 m telescopes between 2008 August and 2017 March, counting 420 observations distributed over nine runs at a rate of one run per year, each run covering 3–7 months. In each run, the visible magnitude presents modulations of a period ∼1.87 d and amplitude varying from 0.04 to 0.24 mag (see Appendix B, available online). The visible magnitude reaches a global minimum of 10.563 during the 2014b run. We also used 2703 data points of visible magnitude from the Wide Angle Search for Planets (WASP; Pollacco et al. 2006) photometric campaign covering semesters 2010b–2011a. Plots of the photometric data contemporaneous to our spectropolarimetric runs (i.e. 2008b + 2009a, 2010b + 2011a, 2013b + 2014a, and 2015b + 2016a) are visible in Section 4.

3 EVOLUTIONARY STATUS OF V410 TAU

V410 Tau is a very well-observed three-star system located in the Taurus constellation at $d = 129.0 \pm 0.5$ pc from Earth (Galli et al. 2018, we chose this value over the *Gaia* result, 130.4 ± 0.9 pc, because it is both in agreement with it and more precise). V410 Tau B was estimated to have a mass 0.2 ± 0.1 times that of V410 Tau A, and V410 Tau C to have a mass $0.08^{+0.10}_{-0.08}$ times that of V410 Tau AB (Kraus et al. 2011). The sky-projected separation between V410 Tau A and V410 Tau B was measured at 0.13 ± 0.01 arcsec, i.e. 16.8 ± 1.4 au, and that between V410 Tau AB and V410 Tau C was measured at 0.28 ± 0.01 arcsec, i.e. 36 ± 3 au. Given that V410 Tau A is much brighter than V410 Tau B and V410 Tau C in the optical bandwidth (Ghez, White & Simon 1997), we consider that the spectra analysed in this study characterize the light of V410 Tau A predominantly. Applying the automatic spectral classification tool developed within the frame of the MaPP and MaTYSSE projects (Donati et al. 2012), we constrain the temperature and logarithmic gravity of V410 Tau A to, respectively, $T_{\rm eff} = 4500 \pm 100$ K and $\log g = 3.8 \pm 0.2$.

Its rotation period was previously estimated to $P_{\rm rot} = 1.871970 \pm 0.000010$ d (Stelzer et al. 2003), a value which we use throughout this paper to phase our data (see equation 1). Comparing both our contemporary measurements (Table A2) and those found in Grankin et al. (2008), we find that the minimum magnitude measured on V410 Tau is 10.52 ± 0.02, value that we use as a reference to compute the unspotted magnitude.

Our photometric measurements yield a mean $B - V$ index of 1.17 ± 0.02, and since the theoretical B-V at 4500 K is 1.04 ± 0.02 (Pecaut & Mamajek 2013; Table 6), the amount of visual extinction is $A_V = 3.1 \times (1.17 - 1.04) = 0.40 \pm 0.10$. The bolometric correction at $T_{\rm eff}$ being equal to −0.64 ± 0.05 (Pecaut & Mamajek 2013; Table 6), and the distance modulus to $-5 \times \log_{10}(d/10) = -5.55 \pm 0.01$, we find an absolute magnitude of 3.93 ± 0.11.

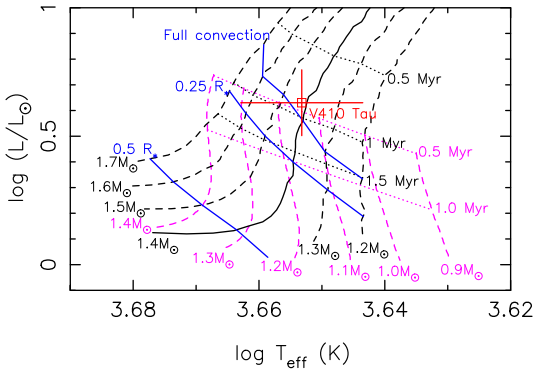

Figure 1. Position of V410 Tau (red) in the Hertzsprung–Russell diagram. The curves yielded by the Siess models (with solar metallicity and overshooting) are represented in black and those yielded by the Baraffe models are represented in magenta. In both cases, evolution tracks are displayed in dashed lines, except the Siess 1.4 $M_\odot$ track, the one we chose to model the evolution of V410 Tau, which is shown as a full line. Isochrones are displayed in dotted lines. The thresholds where the radiative core starts developing ('Full convection') and where it reaches 25 per cent of the stellar radius, according to the Siess models, are marked in blue.

The value of $v \sin i$[1] found from the spectra, 73.2 ± 0.2 km s^{-1} (see Section 4), indicates that the minimum radius of the star $R_\star \sin i$ is equal to 2.708 ± 0.007 $R_\odot$, which implies a maximum absolute unspotted magnitude of 3.67 ± 0.10 given the photospheric temperature. The discrepancy with the value found in the previous paragraph indicates the presence of dark spots on the photosphere even when the star is the brightest. If we assume a spot coverage at maximum brightness of ∼25 per cent, typical of active stars, (like it was done in Donati et al. 2014, 2015; Yu et al. 2017), then the unspotted absolute magnitude would be 3.61 ± 0.32, which corresponds to an inclination[2] of 77 ± 22°. However, the models best fitting our spectra have an inclination of 50 ± 10° (see Section 4), which would require the spot coverage at maximum brightness to actually be ∼50 per cent. Such a high permanent spot coverage is unusual but not unconceivable, since another wTTS, LkCa4, was observed to have as much as 80 per cent of its surface covered with spots (Gully-Santiago et al. 2017). Assuming a spot coverage at maximum brightness of 50 ± 15 per cent for V410 Tau, we derive an absolute unspotted magnitude of 3.17 ± 0.33, a logarithmic luminosity $\log(L_\star/L_\odot) = 0.63 \pm 0.13$, and a stellar radius $R_\star = \sqrt{L_\star/L_\odot} \times (T_\odot/T_\star)^2 = 3.4 \pm 0.5$ $R_\odot$. This value for the radius, combined with the $v \sin i$ derived from the spectra, yields an inclination of 53 ± 11°.

The position of V410 Tau on the Hertzsprung–Russell diagram is displayed in Fig. 1. According to Siess, Dufour & Forestini (2000) stellar evolution models for PMS stars, with solar metallicity and overshooting, V410 Tau is a 1.42 ± 0.15 $M_\odot$ star, aged 0.84 ± 0.20 Myr and fully convective. Baraffe models (Baraffe et al. 2015) disagree with the Siess models for stars as young as V410 Tau and yield an age of <0.5 Myr with a mass of 1.14 ± 0.10 $M_\odot$. However, for the sake of consistency with the other MaPP and MaTYSSE studies, we will consider the values yielded by the Siess models in this paper. Our values are in good agreement with Welty & Ramsey (1995) and Skelly et al. (2010), who had previously derived masses of ∼1.5 and 1.4 ± 0.2 $M_\odot$,

[1] Line-of-sight-projected equatorial rotation velocity.
[2] Angle between the stellar rotation axis and the line of sight.

Downloaded from https://academic.oup.com/mnras/article-abstract/489/4/5556/5561492 by Universitïe Paul Sabatier - Toulouse 3 user on 16 December 2019

Table 1. Physical parameters of wTTS V410 Tau. From top to bottom: distance from Earth, effective temperature, rotation period, luminosity, minimum stellar radius, stellar radius, line-of-sight-projected equatorial velocity, inclination, mass, and age.

Parameter	Value	Reference
d	129.0 ± 0.5 pc	Galli et al. (2018)
$T_{\rm eff}$	4500 ± 100 K	
$P_{\rm rot}$	1.87197 ± 0.00010 d	Stelzer et al. (2003)
$\log(L_\star/{\rm L}_\odot)$	0.63 ± 0.13	
$R_\star \sin i$	2.708 ± 0.007 $R_\odot$	
$R_\star$	3.4 ± 0.5 $R_\odot$	
$v \sin i$	73.2 ± 0.2 km s^{-1}	ZDI (Section 4)
i	50 ± 10°	ZDI (Section 4)
$M_\star$	1.42 ± 0.15 $M_\odot$	
Age	0.84 ± 0.20 Myr	

respectively, radii of ∼2.64 and ∼3.0 $R_\odot$, respectively, and ages of 1–2 and 1.2 ± 0.3 Myr, respectively. Moreover, Skelly et al. (2010) had deduced that V410 Tau could have a radiative core of radius between 0.0 $R_\star$ and 0.28 $R_\star$. Table 1 sums up the stellar parameters of V410 Tau found in this study.

4 STELLAR TOMOGRAPHY

To map the surface brightness and magnetic topology of V410 Tau, we use the tomographic technique ZDI (Donati & Brown 1997), which inverts simultaneous time series of Stokes *I* and Stokes *V* LSD profiles into brightness and magnetic field surface maps. At each observation date, Stokes *I* and Stokes *V* profiles are synthesized from model maps by integrating the spectral contribution of each map cell over the visible half of the stellar surface, Doppler shifted according to the local RV (i.e. line-of-sight-projected velocity) and weighted according to the local brightness, cell sky-projected area, and limb darkening. The main modifier of local RV at the surface of the star is, in ZDI, the assumed rotation profile at the stellar surface, e.g. the solid-body rotation of the star or a square-cosine-type latitudinal differential rotation. Local Stokes *I* and Stokes *V* line profiles are computed from the Unno–Rachkovsky analytical solution to the polarized radiative transfer equations in a Milne–Eddington model atmosphere (this is where the local magnetic field and the Zeeman effect intervene, see Landi degl'Innocenti & Landolfi 2004). To fit the LSD profiles of V410 Tau in this study, we chose a spectral line of mean wavelength, Doppler width, Landé factor, and EW of respective values 640 nm, 1.8, 1.2, and 3.8 km s^{-1}.

ZDI uses a conjugate gradient algorithm to iteratively reconstruct maps whose synthetic profiles can fit the LSD profiles down to a user-provided reduced chi-square ($\chi^2_{\rm r}$) level. To lift degeneracy among the multiple solutions compatible with the data at the given reduced chi square, ZDI looks for the maximal-entropy solution, considering that the minimized information from the resulting maps is the most reliable. While the brightness value can vary freely from cell to cell, the surface magnetic field is modelled as a combination of poloidal and toroidal fields, both represented as weighted sums of spherical harmonics and projected on to the spherical coordinate space (Donati et al. 2006, for the equations). In this study, the magnetic field was fitted with spherical harmonics of orders $l = 1$ to $l = 15$.

Because ZDI does not reconstruct intrinsic temporal variability except for differential rotation, there is a limit to the duration a fittable data set can span. At the same time, ZDI needs a good phase coverage from the data to build a complete map. For those reasons, ZDI was not applied to runs 2008 October and 2013 November; moreover, we reconstructed a different set of brightness and magnetic images for each of the runs on which ZDI was applied.

Using ZDI on our data yielded values for $v \sin i$ and i of 73.2 ± 0.5 and 50 ± 10° km s^{-1}, respectively. We also adjusted the systemic RV of V410 Tau with ZDI, and noticed a drift in the optimal value with time (see Table 2).

4.1 Brightness and magnetic imaging

Time series of Stokes *I* and Stokes *V* LSD profiles are shown in Fig. 2, both before and after removal of lunar pollution, as well as synthetic profiles generated from the reconstructed ZDI maps. The corresponding maps are shown in Fig. 3, with brightness maps in the first column and radial, meridional, and azimuthal components of the surface magnetic field in the second to fourth columns. Properties of these reconstructed maps are listed in Table 2. Since the 2008 December data set has a phase coverage of only half the star, the derived parameters characterizing the global field topology at this epoch are no more than weakly meaningful and were not used for the following analysis and discussion. Our data have been fitted down to $\chi^2_{\rm r} = 1$ with a feature coverage between 15 per cent and 18 per cent depending on the epochs, and a large-scale field strength of 0.5–0.6 kG. Since ZDI is only sensitive to mid- to large-scale surface features, and returns the maximum-entropy solution, this amount of spot coverage is not discrepant with the assumption made in Section 3; it further suggests that 30 per cent of the star is more or less evenly covered with small-scale dark features.

Table 2. Characteristics of the ZDI models for V410 Tau at each observation epoch. *Column 1*: observation epoch. *Column 2*: number of spectropolarimetric observations used for ZDI. *Column 3*: contribution of cool ('spots') and hot ('plages') areas on the brightness map. *Column 4*: average magnetic strength, defined as the square root of the average squared magnetic field over the surface of the star. *Columns 5–7*: normalized contribution of the poloidal field, part of the poloidal field that is dipolar, and part of the poloidal field that is symmetric. *Columns 8–9*: part of the toroidal field that is dipolar and part of the toroidal field that is symmetric. *Column 10*: dipole characteristics: field strength, tilt with respect to the rotation axis, and phase of the pole. *Column 11*: systemic RV of the star as measured with ZDI, the error bar on those values is 0.20 km s^{-1}. Error bars on the magnetic field ratios are typically of 0.1.

Date	$N_{\rm obs}$	Spot + plage coverage (per cent)	B (G)	$r_{\rm pol}$	$r_{\rm dip/pol}$	$r_{\rm sym/pol}$	$r_{\rm dip/tor}$	$r_{\rm sym/tor}$	Dipole strength (G), tilt, and phase	RV$_{\rm bulk}$ (km s^{-1})
2008 Dec	6	5.8 + 4.4	486	0.32	0.13	0.37	0.89	0.96	129, 23°, and 0.71	16.30
2009 Jan	48	9.6 + 7.1	556	0.55	0.26	0.09	0.54	0.79	165, 54°, and 0.54	16.30
2011 Jan	20	8.1 + 6.6	560	0.40	0.24	0.23	0.72	0.85	239, 44°, and 0.62	16.40
2013 Dec	25	11.0 + 7.5	568	0.49	0.23	0.34	0.66	0.81	254, 18°, and 0.56	16.50
2015 Dec	21	8.9 + 6.7	600	0.68	0.37	0.45	0.62	0.78	458, 30°, and 0.54	16.65
2016 Jan	9	7.9 + 6.5	480	0.77	0.38	0.30	0.68	0.87	400, 44°, and 0.51	16.65

Downloaded from https://academic.oup.com/mnras/article-abstract/489/4/5556/5561492 by Universitïe Paul Sabatier - Toulouse 3 user on 16 December 2019

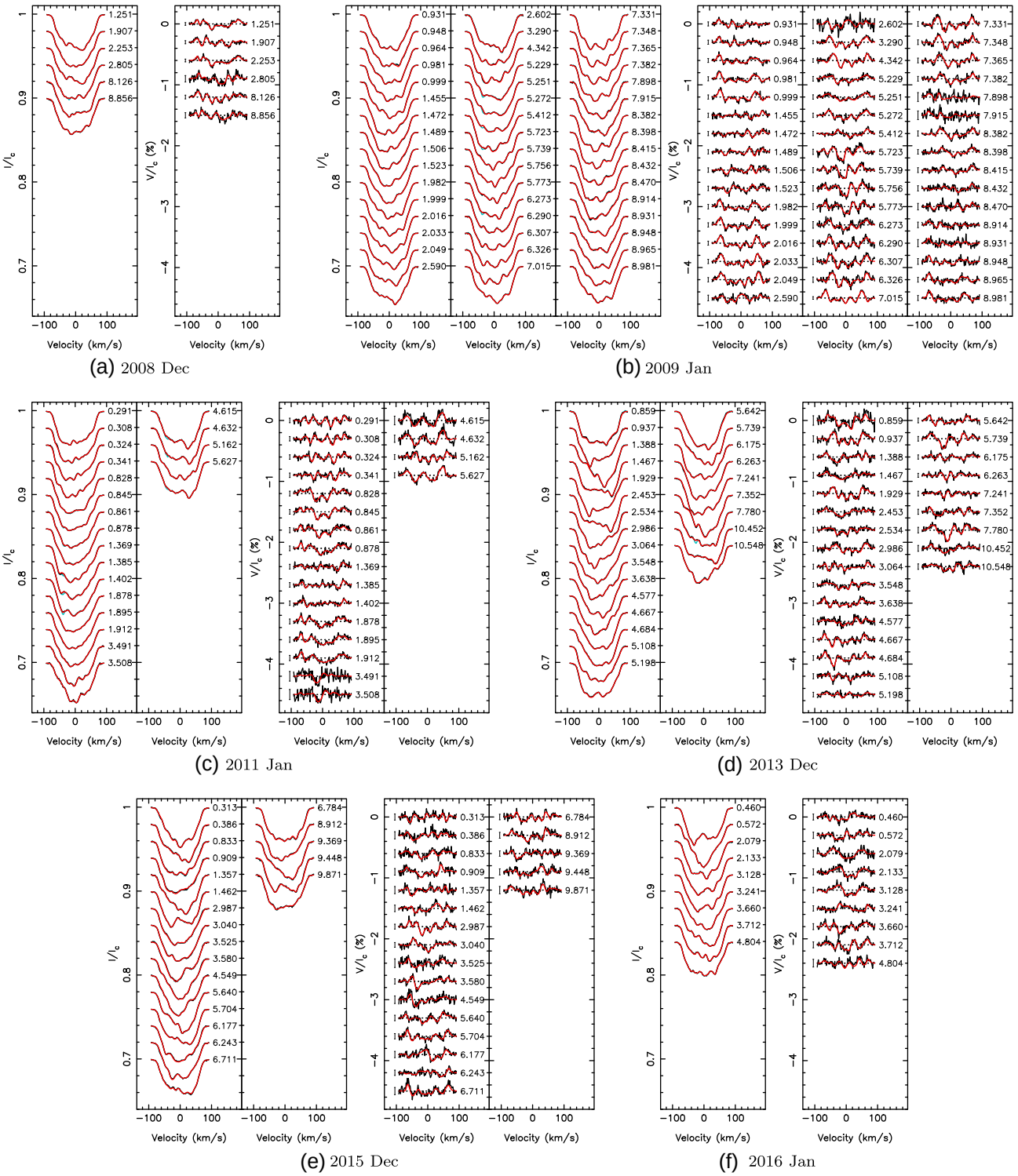

Figure 2. LSD profiles for observation epochs (a) 2008 Dec, (b) 2009 Jan, (c) 2011 Jan, (d) 2013 Dec, (e) 2015 Dec, and (f) 2016 Jan. On the right of each profile is written the corresponding rotation cycle as indicated in Table A1. The cyan, black, and red lines represent, respectively, the profiles before removal of Moon pollution, after removal of Moon pollution, and the fit obtained with Zeeman-Doppler Imaging. For each epoch, Stokes *I* profiles are on the left and Stokes *V* profiles on the right. 3σ-error bars are displayed beside each Stokes *V* profile.

Brightness maps display a complex structure with many relatively small-scale features, and a high contrast. At all epochs, a large concentration of dark spots is observed at the pole. In 2009 January, 2013 December, and 2015 December, the brightness map exhibits a strong equatorial spot, respectively at phases 0.27, 0.48, and 0.48. The presence of a strong polar spot is consistent with the maps published in Skelly et al. (2010), Rice et al. (2011), and Carroll et al. (2012) for data set 2009 Janunary. At that

Downloaded from https://academic.oup.com/mnras/article-abstract/489/4/5556/5561492 by Universitïe Paul Sabatier - Toulouse 3 user on 16 December 2019

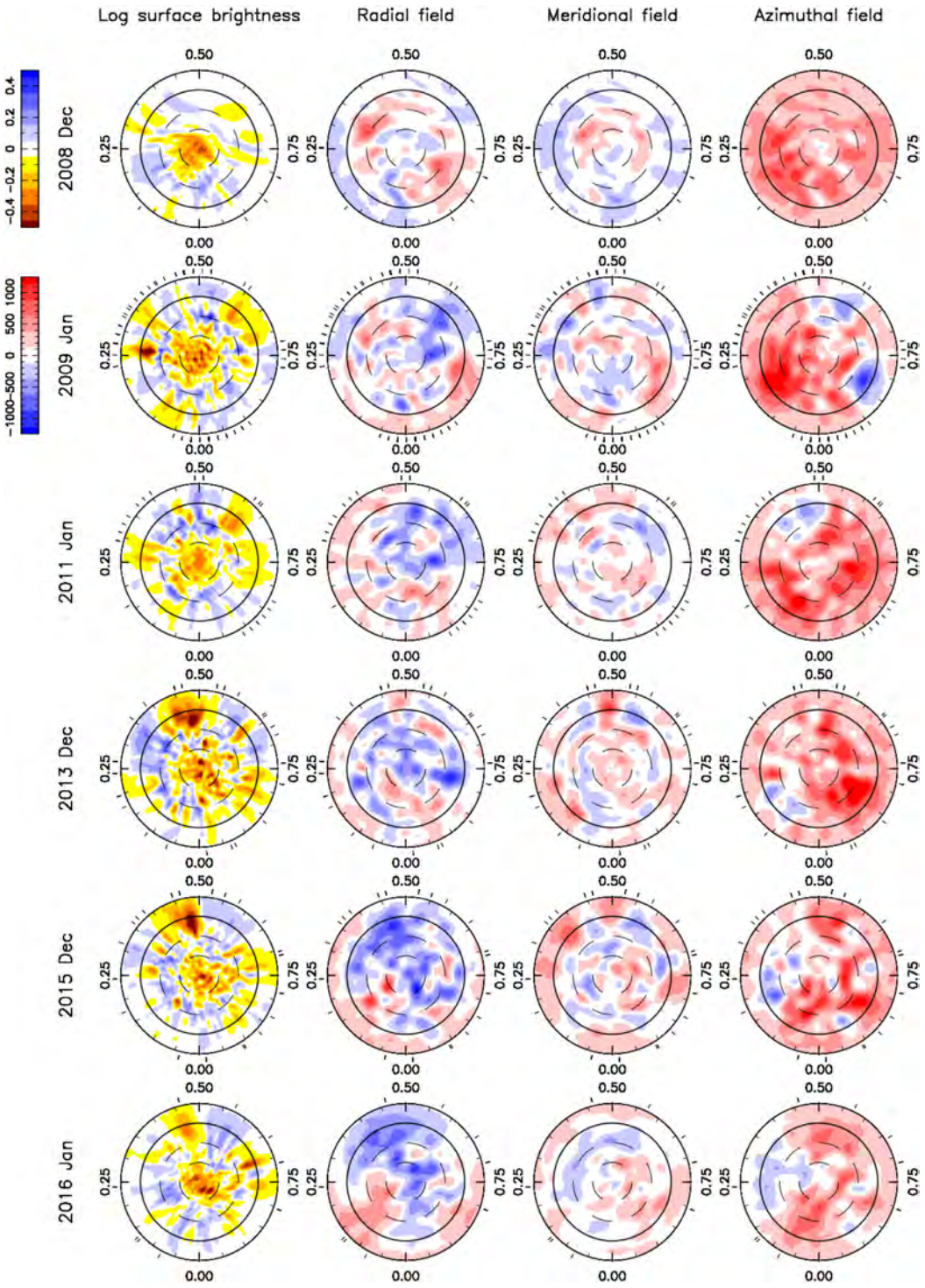

Figure 3. ZDI maps of the logarithmic relative surface brightness (first column), and the radial, meridional, and azimuthal magnetic field (second to fourth columns) of V410 Tau, reconstructed from data collected in 2008 Dec, 2009 Jan, 2011 Jan, 2013 Dec, 2015 Dec, and 2016 Jan (top to bottom rows). Each map is shown as a flattened polar view, with the equator being represented as a full line, and 60°, 30°, and −30° latitude parallels as dashed lines, and ticks around the star mark the spectropolarimetric observations. For the brightness maps, cool spots are coloured in brown and bright plages in blue. For the magnetic maps, red represents outwards and anticlockwise field on the radial and azimuthal field maps, respectively, and the direction of the visible pole on the meridional field maps.

particular epoch, the equatorial spot at phase 0.27, and another equatorial spot at phase 0.60, are also visible in both Skelly et al. (2010) and Rice et al. (2011, fig. 8), albeit less contrasted compared to other features than they are on our map. A remnant of the 2015 December equatorial spot is observed on the 2016 January map, where its intensity seems to have decreased, but this has to be taken with caution since ZDI maps are somewhat dependent on phase coverage. Dark spots and bright plages

Downloaded from https://academic.oup.com/mnras/article-abstract/489/4/5556/5561492 by Universitïe Paul Sabatier - Toulouse 3 user on 16 December 2019

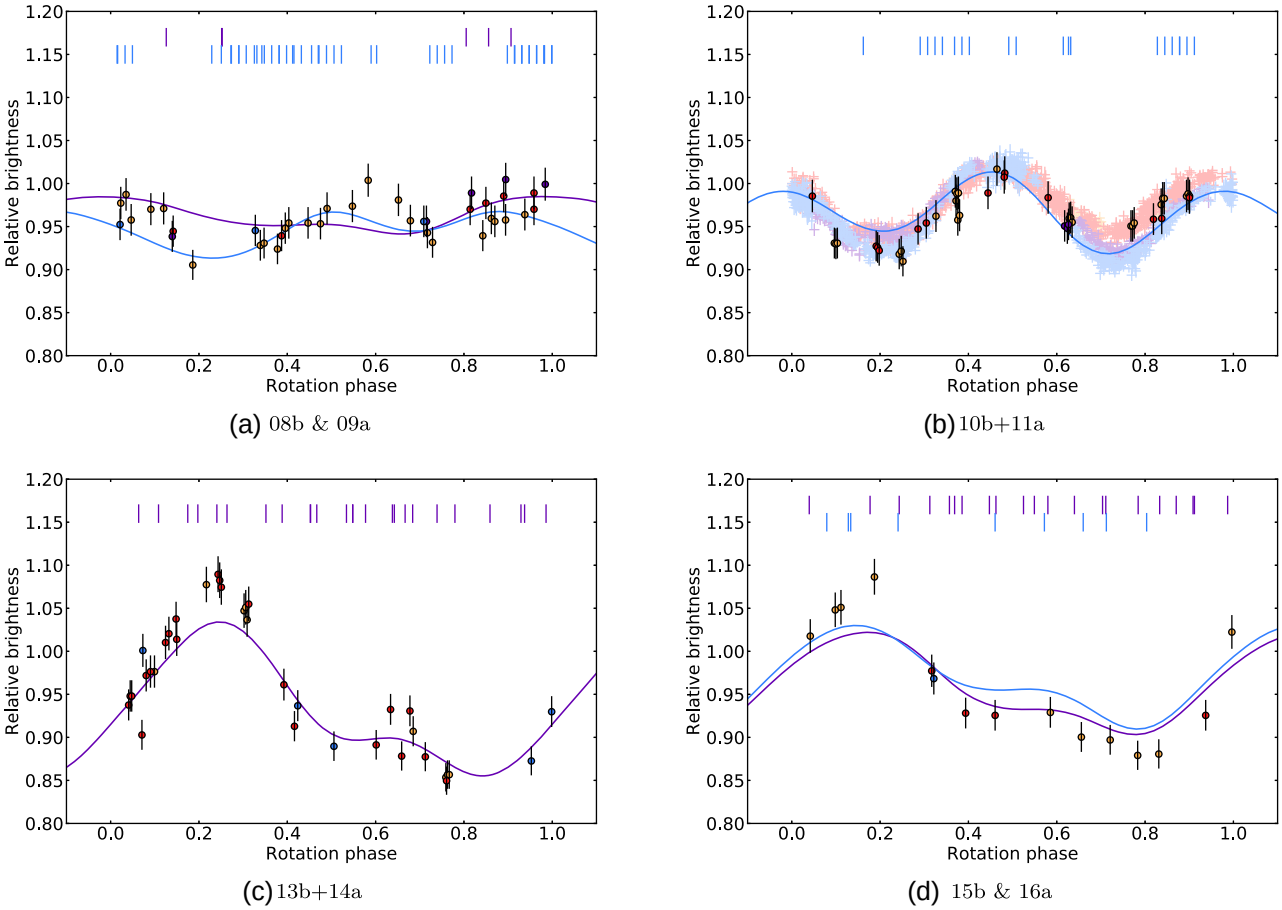

Figure 4. Phase-folded photometry data (dots with 1σ error bars) and ZDI models (lines) for observation epochs (a) 08b and 09a, (b) 10b+11a, (c) 13b + 14a, and (d) 15b and 16a. In the case of 08b and 09a and 15b and 16a, two ZDI curves are plotted for the two ZDI maps reconstructed within each epoch. Orange, red, purple, and blue colours each indicate a quarter of the total time span of the observations (photometric and spectropolarimetric together), in chronological order. Spectropolarimetric observations are marked by ticks above the light curves. In panel b, WASP data were added as desaturated crosses, with the size of the cross branches indicating their 1σ error bars.

contribute to the feature coverage at about 9 per cent/7 per cent, respectively.

Photometry curves from the ZDI brightness maps were synthesized and a comparison to contemporary CrAO data, and WASP data in the case of 2011 January, is shown in Fig. 4. Despite a slightly underestimated amplitude at phase 0.60 in 2008b–2009a, at phase 0.20 in 2011a, at phase 0.20 in 2013b, and at phases 0.20 and 0.80 in 2015b–2016a, ZDI manages to retrieve the measured photometric variations of V410 Tau rather satisfyingly. We notice a small temporal evolution of the light curve in the WASP data during season 2010b–2011a, where the regions around phases 0.20 and 0.70 globally darken by 0.02–0.03 mag ($\simeq 4\sigma$) over the 4 months that the data set spans.

The magnetic field maps also show a high complexity, with a poloidal component that has a weak dipolar contribution and that is rather non-axisymmetric, and a toroidal component contributing to ∼50 per cent of the overall magnetic energy in 2009, 2011, and 2013, and decreasing towards ≃30 per cent in 2015–2016, that is both strongly dipolar and highly axisymmetric. The dipole pole is tilted at various angles depending on the epoch, with a tilt as high as 54° in 2009 January, down to 18° in 2013 December. The phase of the pole is always around 0.50–0.60, and the intensity of the poloidal dipole increases over time, from 165 G in 2009 January to ≃ 400 G in 2015–2016. We note that the maximum emission of H α corresponds to the phase at which the dipole is tilted (Fig. C1). For visualization purposes, three-dimensional potential fields were extrapolated from the radial components of the magnetic maps, and displayed in Fig. 5, with phase 0.50 facing the reader.

We do not observe a particular correlation between our brightness and our magnetic maps, meaning the areas with strong magnetic field are not necessarily crowded with dark spots, according to the ZDI reconstruction.

4.2 Differential rotation

Without differential rotation, ZDI cannot fit an extended data set, such as 2008 December + 2009 January, 2013 November + 2013 December, or 2015 December + 2016 January (shortened in this subsection to 08b + 09a, 13b, and 15b + 16a, respectively), down to $\chi^2_r = 1$, it only manages to reach values of 1.66, 1.20, and 2.64, respectively. This implies that some level of variability exists and impacts the data on time-scales of a few months, which could come from the presence of differential rotation at the surface of V410 Tau. We model differential rotation with the following law:

$$\Omega(\theta) = \Omega_{\rm eq} - (\cos\theta)^2 {\rm d}\Omega,$$

Downloaded from https://academic.oup.com/mnras/article-abstract/489/4/5556/5561492 by Universitïe Paul Sabatier - Toulouse 3 user on 16 December 2019

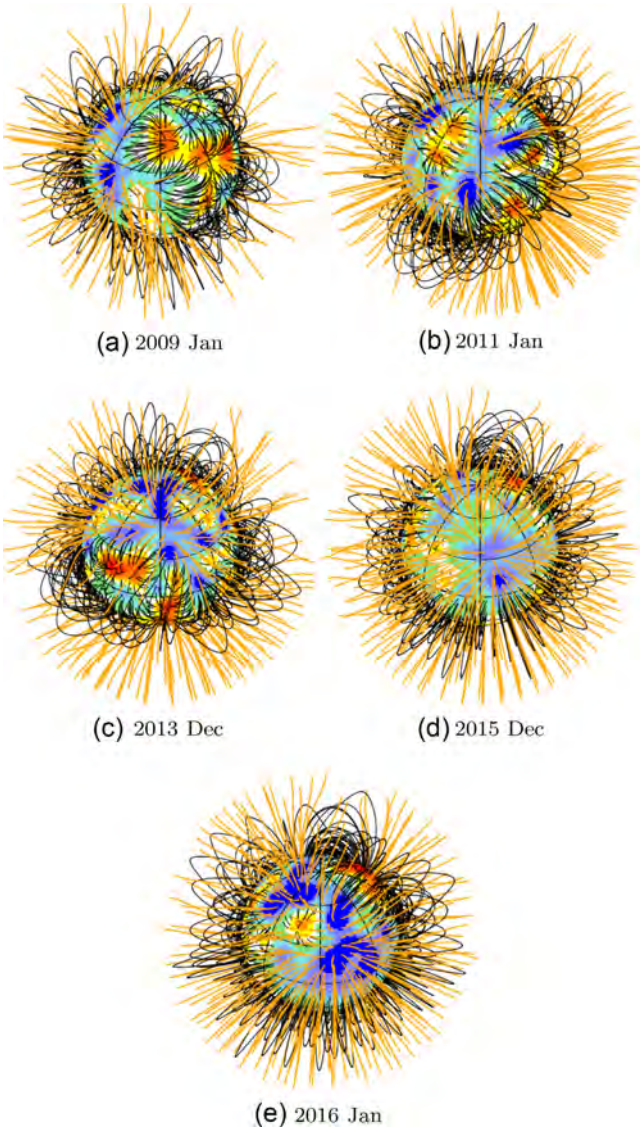

Figure 5. Potential field extrapolations of the ZDI-reconstructed surface radial field, as seen by an Earth-based observer, for observation epochs (a) 2009 Jan, (b) 2011 Jan, (c) 2013 Dec, (d) 2015 Dec, and (e) 2016 Jan at phase 0.50. Open/closed field lines are shown in orange/black, respectively, and colours on the stellar surface depict the local value of the radial field (in G, as shown in the left-hand panels of Fig. 3). The source surface at which field lines open is set to 2.1 $R_\star$, corresponding to the corotation radius and beyond which field lines are expected to quickly open under centrifugal forces given the high rotation rate of V410 Tau.

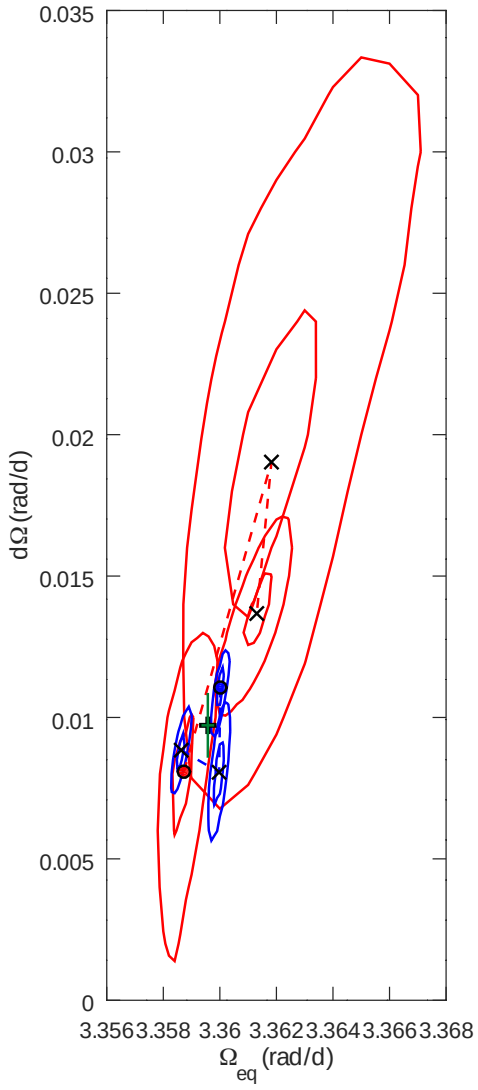

Figure 6. Evolution of the differential rotation of V410 Tau as measured from Stokes *I* (blue) and Stokes *V* (red) profiles. The points corresponding to observation epoch 2008b–2009a are marked with o symbols, then the dashed lines link the epochs in chronological order (2013b–2014a and 2015b–2016a are marked with x symbols). 68.3 per cent and 99.7 per cent contours of confidence are displayed for each observation epoch. The weighted average of the six measurements, chosen to produce the maps shown in Section 4, is represented as a black +, with overlayed error bars in green.

where θ is the colatitude, $\Omega_{\rm eq}$ the equatorial rotation rate, and dΩ the pole-to-equator rotation rate difference. We constrain $\Omega_{\rm eq}$ and dΩ by pre-setting the amount of information ZDI is allowed to reconstruct, and having ZDI minimize the $\chi^2_{\rm r}$ in these conditions.

We performed this analysis on the three aforementioned extended data sets, and on Stokes *I* and Stokes *V* time series separately, reconstructing only brightness or only magnetic field, respectively. From the resulting $\chi^2_{\rm r}$ maps over the $\{\Omega_{\rm eq}$,d$\Omega\}$ space, one can plot the contours of the 1σ (68.3 per cent) and 3σ (99.7 per cent) areas of confidence for each observation epoch. Fig. 6, which shows such contours, highlights clear minima surrounded by almost elliptic areas of confidence at each epoch, and shows that each 3σ-confidence area overlaps at least two other 3σ-confidence areas. Numerical results for each epoch are given in Table 3. We chose to use a unique set of parameters to reconstruct all images shown in Section 4: the weighted means of the six seasonal minima, $\Omega_{\rm eq} = 3.35957 \pm 0.00006$ rad d^{-1} and dΩ = 0.0097 ± 0.0003 rad d^{-1}.

Following the method described in Donati, Collier Cameron & Petit (2003), we computed, for each epoch, the colatitude at which the rotation rate is constant along the confidence ellipse major axis. This value corresponds to the colatitude where the barycentre of the brightness/magnetic features imposing a correlation between $\Omega_{\rm eq}$ and dΩ are located. For both Stokes *I* and Stokes *V*, we note a slight increase with time of the cosine of this colatitude (Table 3), i.e. an increase in the barycentric latitude of the dominant features of $5 \pm 2^\circ$ and $15 \pm 5^\circ$, respectively.

Downloaded from https://academic.oup.com/mnras/article-abstract/489/4/5556/5561492 by Universitïe Paul Sabatier - Toulouse 3 user on 16 December 2019

Table 3. Summary of differential rotation parameters obtained for V410 Tau on each season. All rotation rates are given in mrad d^{-1}. Column 2 gives the total number of data points used in the imaging process, then columns 3–7 correspond to Stokes *I* data while column 8–12 correspond to Stokes *V* data. Columns 3 and 8 list the derived equatorial rotation rate Ω_{eq}, with its 68 per cent (i.e. 1σ) confidence interval, columns 4 and 9 the difference in rotation rate $d\Omega$ between the equator and pole, with its 68 per cent confidence interval, columns 5 and 10 give the reduced chi square of the ZDI model compared to the data, columns 6 and 11 give the inverse slope of the ellipsoid in the Ω_{eq}–$d\Omega$ plane (also equal to $\cos^2\theta_s$, where θ_s denotes the colatitude of the gravity centre of the spot distribution, see Donati et al. 2000), and columns 7 and 12 give the rotation rate Ω_s at colatitude θ_s.

		Stokes *I* data / brightness reconstruction					Stokes *V* data / magnetic field reconstruction				
Epoch	n	Ω_{eq}	$d\Omega$	χ^2_r	$\cos^2\theta_s$	Ω_s	Ω_{eq}	$d\Omega$	χ^2_r	$\cos^2\theta_s$	Ω_s
08b + 09a	5562	3360.0 ± 0.1	11.1 ± 0.6	1.276	0.12 ± 0.03	3358.7 ± 0.4	3358.7 ± 0.3	8.1 ± 1.8	1.127	0.11 ± 0.03	3357.9 ± 0.5
13b	2781	3360.0 ± 0.1	8.1 ± 0.7	1.341	0.11 ± 0.03	3359.1 ± 0.3	3361.8 ± 1.3	19.0 ± 4.3	1.038	0.23 ± 0.03	3354.6 ± 2.1
15b + 16a	3090	3358.6 ± 0.1	8.8 ± 0.5	2.583	0.18 ± 0.03	3357.0 ± 0.4	3361.3 ± 0.4	13.7 ± 1.0	1.046	0.32 ± 0.03	3352.7 ± 0.8

These models exclude solid-body rotation at a level of 3.6σ to 22σ depending on the epoch. We note that, even with differential rotation, ZDI cannot fit the data of 08b + 09a and of 15b + 16a down to $\chi^2_r = 1$, no matter the amount of information allowed. This indicates that surface features are also altered by a significant level of intrinsic variability within the 2 month span of our data set. This issue is further discussed in section 5.3.

5 RADIAL VELOCITIES

Radial velocity values were derived as the first-order moment of the continuum-subtracted Stokes *I* LSD profiles, for all spectra except the three with low S/N and the six in which we identified flares (see Table A1). The raw RVs we obtain contain a contribution from the inhomogeneities on the photosphere, called activity jitter, which we aim to filter out in order to access the actual RV of the star, and look for a potential planet signature. The activity jitter is modelled with two different techniques, ZDI and GPR. Raw RVs and jitter models are plotted in Fig. 7 and listed in Table A1. For the 2015–2016 points, a new version of ZDI, with the logarithmic brightness of surface features allowed to linearly vary with time, was tested (section 5.3). The raw RVs present modulations whose amplitude vary between 4 and 8.5 km s^{-1}, with a global rms of 1.8 km s^{-1}. Like with the photometric data, the RV variations are the lowest in 2009 January and the strongest in 2013 December.

5.1 Activity jitter

The first method consists in deriving the activity jitter from the ZDI models (see Fig. 2), computed as the first-order moment of the continuum-subtracted synthetic Stokes *I* profiles. Indeed, when computing the raw RV from the observed Stokes *I* LSD profiles, this activity jitter is added on top of the radial motion of the star as a whole. We model the activity jitter separately for epochs 2009 January, 2011 January, 2013 December, 2015 December, and 2016 January (excluding 2008 December because of the poor phase coverage).

The second method uses GPR (Haywood et al. 2014; Donati et al. 2017), a numerical method focusing on the statistical properties of the model. In short, GPR extrapolates a continuous curve described by a given covariance function from some given data points. To describe the activity jitter here, we use a pseudo-periodic covariance function:

$$K(t,t') = \theta_1^2 \exp\left[-\frac{(t-t')^2}{\theta_3^2} - \frac{\sin^2\left(\frac{\pi(t-t')}{\theta_2}\right)}{\theta_4^2}\right], \quad (2)$$

where t and t' are the dates of the two RV points between which the covariance is computed, θ_1 is the amplitude of the GP, θ_2 the recurrence time-scale (expected to be close to P_{rot}), θ_3 the decay time-scale (i.e. the typical spot lifetime in the present case), and θ_4 a smoothing parameter (within [0, 1]) setting the amount of high-frequency structures that we allow the fit to include. The modelling process therefore consists in optimizing the four parameters θ_1, θ_2, θ_3, and θ_4, called hyperparameters. To do so, we use a Markov Chain Monte Carlo algorithm, and allocate to each point of the hyperparameter space a likelihood value, which takes into account both the quality of the fit and some penalizations on the hyperparameters (for example we penalize high amplitudes, low decay times, and low smoothings). The priors are listed in Table 4. The phase plot of the MCMC is displayed in Fig. 8 and the best fit is shown in Fig. 7, together with the ZDI fits. We note that, contrary to ZDI, GPR, being capable of describing intrinsic variability in a consistent way, is able to fit our whole 8 yr long data set with one model. We obtain $\theta_1 = 1.8^{+0.2}_{-0.2}$ km s^{-1}, $\theta_2 = 0.9991 \pm 0.0002\ P_{rot}$, $\theta_3 = 86^{+24}_{-19}\ P_{rot}$, and $\theta_4 = 0.35 \pm 0.03\ P_{rot}$.

The rms of the filtered RVs for each epoch and each method are summarized in Table 5. The RV curve filtered from the ZDI model presents a global rms of 0.167 km s^{-1}, i.e. $\sim 2 < \sigma_{RV} >$ (see Table A1). The epoch where the filtering is most efficient is 2009 January, although the rms of the filtered RVs is only at $1.5 < \sigma_{RV} >$, and it goes up to $3 < \sigma_{RV} >$ in 2011 January and 2013 December. On the other hand, the GPR model filters the RV out down to 0.076 km s^{-1} $= 0.94 < \sigma_{RV} >$.

5.2 Periodograms

Lomb–Scargle periodograms for both raw and filtered RVs, for both methods (Fig. 9 for each individual epoch, Fig. 10 for the whole data set), show that the stellar rotation period or its first harmonic are clearly present in 2009 January and 2011 January, but not well retrieved in 2013 December, 2015 December, and 2016 January. However the periodogram for the whole RV_{raw} data set presents neat peaks at P_{rot} and its first two harmonics. P_{rot} and its first harmonic are well filtered out by both modelling methods, and the second harmonic is well filtered out in the GP residuals. A weak signal remains at $P_{rot}/3$ in the ZDI residuals but looking at a phase-folded plot does not reveal any particularly obvious tendency, leading us to suspect that it mostly reflects the contribution of a few stray points. No other period stands out with a false-alarm probability lower than 5 per cent, which allows us to conclude that no planet signature is found in this data set with our filtering methods.

5.3 New ZDI: with short-time intrinsic evolution

Seeing that the filtered RVs when using GPR have an rms twice lower than when using ZDI (Table 5), we try to improve our ZDI filtering process by implementing a new feature: instead of only

Downloaded from https://academic.oup.com/mnras/article-abstract/489/4/5556/5561492 by Universitïe Paul Sabatier - Toulouse 3 user on 16 December 2019

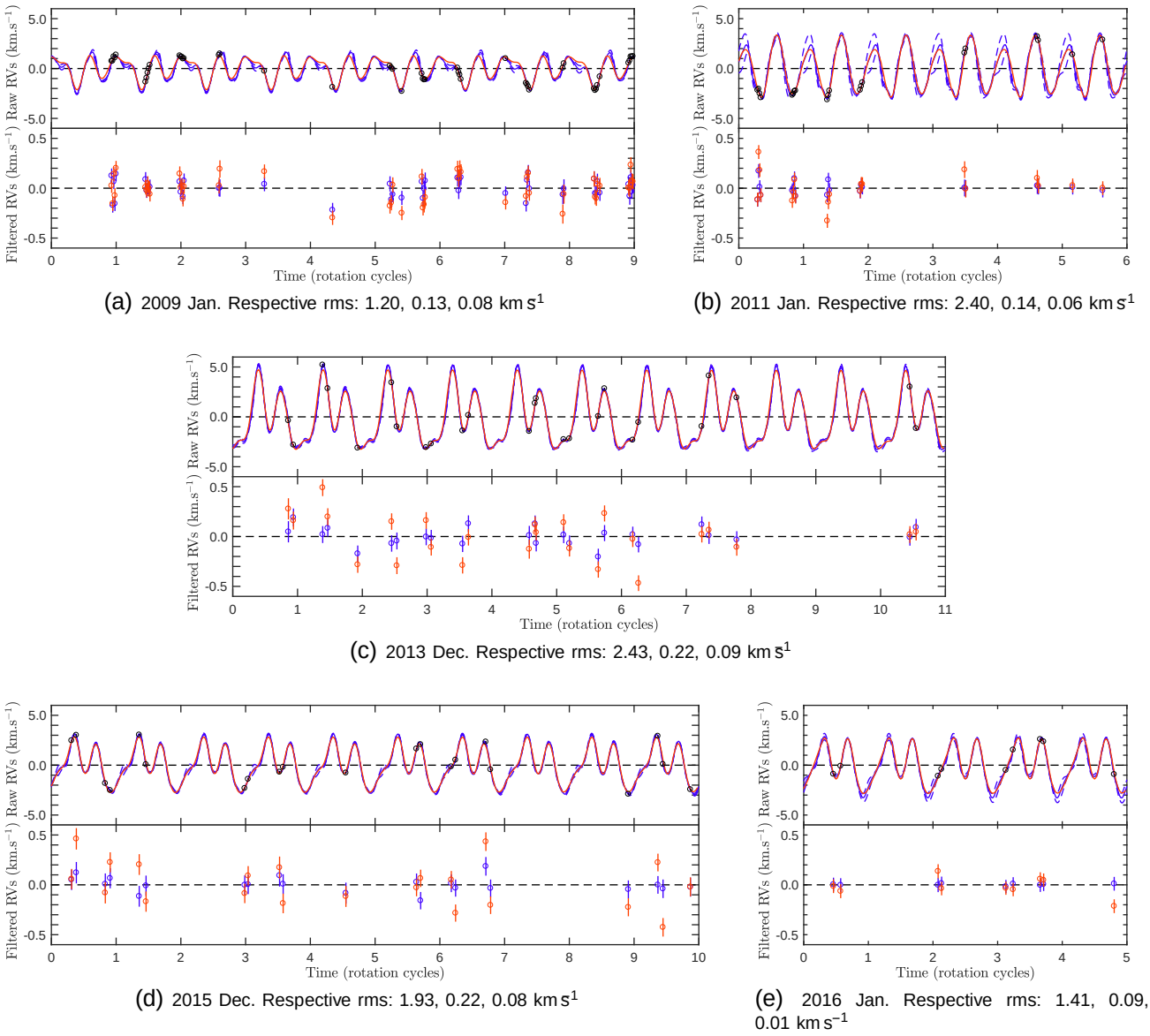

(a) 2009 Jan. Respective rms: 1.20, 0.13, 0.08 km s^{1}

(b) 2011 Jan. Respective rms: 2.40, 0.14, 0.06 km s^{1}

(c) 2013 Dec. Respective rms: 2.43, 0.22, 0.09 km s^{1}

(d) 2015 Dec. Respective rms: 1.93, 0.22, 0.08 km s^{1}

(e) 2016 Jan. Respective rms: 1.41, 0.09, 0.01 km s^{-1}

Figure 7. Raw and filtered RVs of V410 Tau for each observation epoch. On each figure, the top plot depicts the raw RVs (red dots), the ZDI reconstruction (red full line), and the GP fit (blue full line with 1σ area of confidence marked as blue dashed lines, see Section 5.1). The bottom plot depicts the RVs filtered from the ZDI-modelled activity (red dots) and the RVs filtered from the GP-modelled activity (blue dots). The subcaptions indicate the rms of the raw RVs, the ZDI-filtered RVs, and the GPR-filtered RVs, respectively. All rotational cycles are displayed as in Table A1.

Table 4. Priors for our GP–MCMC run on our raw RVs. For the modified Jeffreys prior, the knee value is given, for the Gaussian prior we give the mean and standard deviation, and for the Jeffreys and the uniform priors we give the lower and upper boundaries.

Hyperparameter	Prior
θ_1 (km s^{-1})	Modified Jeffreys ($\sigma_{\rm RV}$)
θ_2 ($P_{\rm rot}$)	Gaussian (1.0000, 0.1000)
θ_3 ($P_{\rm rot}$)	Jeffreys(0.1, 500.0)
θ_4	Uniform (0, 1)

having one brightness value in each cell, we give it a brightness value and an evolution parameter, so that ZDI brightness maps are allowed to evolve with time to better fit time series of LSD profiles with variability. Thus we reconstruct two maps for the brightness: the brightness at time 0 and the map of the evolution parameter. We choose, for now, a simple model where the logarithmic relative brightness of each cell k is allowed to evolve linearly with time:

$$\log Q_k(t) = \log Q_k(0) + m_k t, \quad (3)$$

where $Q_k(t)$ is the local surface brightness and m_k is the evolution parameter. Applying this new method to the 2015–2016 extended data set, we manage to fit the whole data set down to a $\chi^2_{\rm r}$ of 1 where classical ZDI, even with differential rotation, could not reach lower than $\chi^2_{\rm r} = 2.5$ (see Section 4.2). Maps associated with this reconstruction are shown in Fig. 11, and derived RVs are plotted in Figs 12 and 13, to be compared with RVs derived from classical ZDI maps. The rms of the filtered RVs here, 0.194 km s^{-1}, does not decrease compared to when using classical ZDI, which means our model is still too simple and cannot fully account for the observed

Downloaded from https://academic.oup.com/mnras/article-abstract/489/4/5556/5561492 by Universitie Paul Sabatier - Toulouse 3 user on 16 December 2019

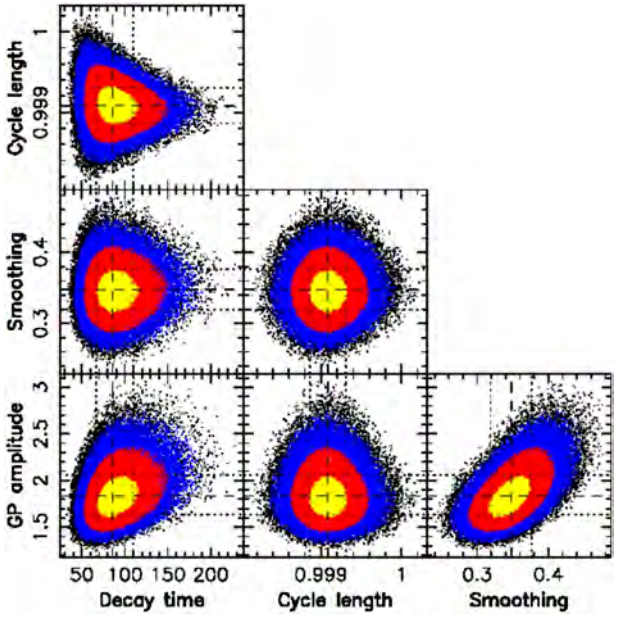

Figure 8. Phase plot of the MCMC–GPR run on the raw RVs, model without planet. The yellow, red, and blue colours indicate respectively the 1σ, 2σ, and 3σ areas of confidence, and the optimal values for the hyperparameters are marked with black dashed lines, with 1σ intervals marked with black dotted lines. GP amplitude (θ_1): $1.8^{+0.2}_{-0.2}$ km s^{-1}, Cycle length (θ_2): 0.9991 ± 0.0002 $P_{\rm rot}$, Decay time (θ_3): 86^{+24}_{-19} $P_{\rm rot}$, Smoothing (θ_4): 0.35 ± 0.03.

Table 5. Rms of RVs. All rms RVs are given in km s^{-1}.

Epoch	2009	2011	2013	2015	2016	All
Raw	1.200	2.392	2.429	1.932	1.411	1.8
ZDI filt.	0.131	0.141	0.215	0.222	0.094	0.167
GP filt.	0.084	0.064	0.087	0.075	0.009	0.076

variability. However, Fig. 13 shows that global trends in the temporal evolution of the RV curve are well reproduced by this new ZDI model, such as the jitter maximum moving from phase 0.37 to 0.32, or the local minimum at phase 0.54 in 2015 December moving to 0.50 in 2016 January.

6 SUMMARY AND DISCUSSION

This paper reports the analysis of an extended spectropolarimetric data set on the ∼0.8 Myr wTTS V410 Tau, taken with the instruments ESPaDOnS at CFHT and NARVAL at TBL, spanning 8 yr and split between six observation epochs (2008b, 2009a, 2011a, 2013b, 2015b, and 2016a), the last three of which were observed as part of the MaTYSSE observation programme. Contemporaneous photometric observations from the CrAO and from the WASP programme complemented the study. ESPaDOnS, NARVAL, and CrAO observations are documented in Appendix A (available online).

V410 Tau is composed of an inner close binary (V410 Tau A-B) around which orbits a third component (C Ghez et al. 1997), with V410 Tau A being much brighter than the other two in the optical domain, and thus the star that our data inform. The stellar parameters derived in this work are summed up in Table 1: at ∼0.8 Myr, V410 Tau is a 1.42 ± 0.15 $M_\odot$ and 3.4 ± 0.5 $R_\odot$ wTTS.

6.1 Activity and magnetic field of V410 Tau

Applying LSD then ZDI on our data set, we estimated the $v \sin i$ and inclination of V410 Tau at 73.2 ± 0.5 and $50 \pm 10^\circ$ km s^{-1}, respectively. Considering the well-determined rotation period of 1.871970 ± 0.000010 (Stelzer et al. 2003) and the minimal observed visible magnitude of 10.52 (Grankin et al. 2008), this implies a relatively high level (∼50 per cent) of spot coverage. We reconstructed brightness and magnetic surface maps at each observation epoch, constrained the differential rotation, and found a drift in the bulk radial velocity. Our ZDI brightness maps display a relatively highly spotted surface: the spot coverage reaches 6.5–11.5 per cent depending on the epoch (not counting 2008 December where only half the star was imaged) and the plage coverage is found around 7 per cent at all epochs. Since ZDI mostly recovers large non-axisymmetric features and misses small ones evenly distributed over the star, the spot and plage coverage is underestimated, which makes this result compatible with the spot coverage obtained from the aforementioned V magnitude measurements. We note that V410 Tau being heavily spotted makes it difficult to pinpoint its age. We fit a two-temperature model (photosphere at 4500 K and fixed-temperature spots with a varying filling factor) into our $B - V$ and V magnitude data, and found an optimal spot temperature of around 3750 K, which implies a contrast of ∼750 K between dark spots and the photosphere (see Fig. B7). This contrast is slightly lower than the one retrieved for the 2 Myr wTTS LkCa 4 in Gully-Santiago et al. (2017). V410 Tau always presents a high concentration of dark spots around the pole, and several big patches of dark spots on the equator.

V410 Tau has a relatively strong large-scale magnetic field, with an average surface intensity that is roughly constant over the years at 550 ± 50 G. Its radial field reaches local values beyond −1 and +1 kG in several epochs. The brightness and magnetic surface maps both present some variability from epoch to epoch (Fig. 3, Table 2), which points to a dynamo-generated magnetic field rather than a fossil one. The magnetic energy is, at all epochs, equally distributed between the poloidal and toroidal components of the field, with the poloidal component being rather non-dipolar and non-axisymmetric, whereas the toroidal component is mostly dipolar and axisymmetric. The poloidal dipole, tilted towards a phase that stays within 0.6 ± 0.1 during the whole survey, but at an angle varying between 20° and 55° depending on the epoch, sees its intensity increase almost monotonously from 165 to 458 G over 8 yr, and the dipolar contribution to the poloidal field also increases from ∼25 per cent to ∼40 per cent (see Table 2).

The toroidal component, which displays a constant orientation throughout our data set, is unusually strong compared to other fully convective rapidly rotating stars (e.g. V830 Tau is 90 per cent poloidal, see Donati et al. 2017). A similarly strong toroidal field was observed on one other MaTYSSE target, LkCa 4 (Donati et al. 2014). The origin of this strong toroidal field is still unclear: could it be maintained by an α^2 dynamo, like in the simulations of low-Rossby fully convective stars by Yadav et al. (2015)? The remnants of a subsurfacic radial shear between internal layers accelerating due to contraction, and disc-braked outer layers? Or would the even earlier toroidal energy, from right after the collapse of the second Larson core (as found in the simulations of Vaytet et al. 2018), somehow not have entirely subsided yet? Would the early dissipation of the disc, a common factor between LkCa 4 and V410 Tau, have something to do with this?

At ∼0.8 Myr, V410 Tau is one of the youngest observed wTTSs (Kraus et al. 2012; Fig. 3). Assuming that, when the disc was present,

Downloaded from https://academic.oup.com/mnras/article-abstract/489/4/5556/5561492 by Universitïe Paul Sabatier - Toulouse 3 user on 16 December 2019

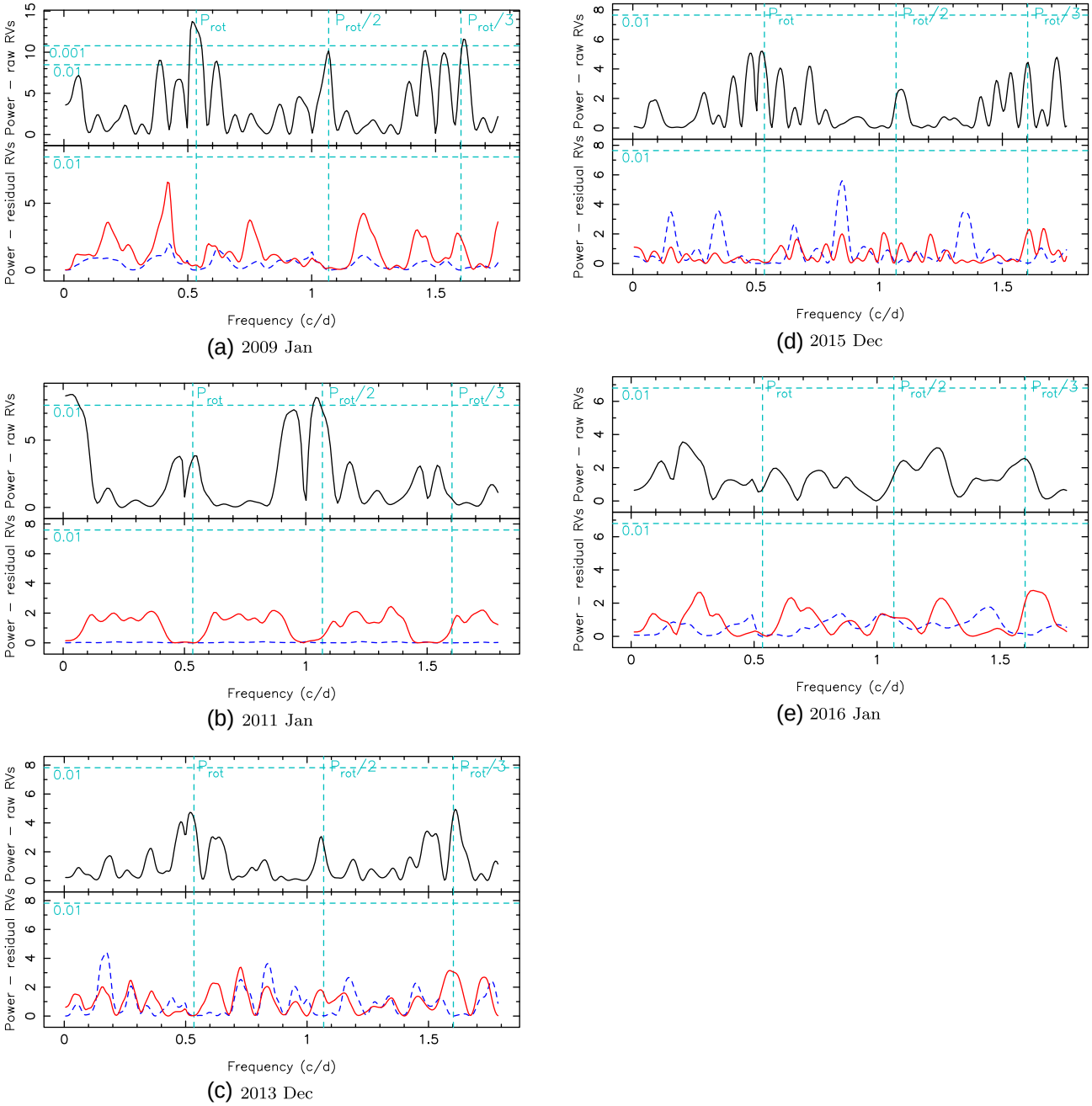

Figure 9. Periodograms of the raw RVs (top), of the ZDI-filtered RVs (bottom, red full line) and of the GP-filtered RVs (bottom, blue dashed line), for observation epochs (a) 2009 Jan, (b) 2011 Jan, (c) 2013 Dec, (d) 2015 Dec, and (e) 2016 Jan. False-alarm probability levels of 1 per cent and 0.1 per cent are represented as horizontal cyan dashed lines, and $P_{\rm rot}$ and its first two harmonics as vertical cyan dashed lines.

V410 Tau was magnetically locked to it at a rotation period of ∼8 d with a cavity of ∼0.085 au (similarly to cTTSs BP Tau, AA Tau, and GQ Lup, see Donati et al. 2008, 2010b, 2012, respectively), then V410 Tau should have had a radius of ∼7 $R_\odot$ when the disc dissipated, to match the angular momentum that we measure today (Bouvier 2007). According to the Siess models (Siess et al. 2000), this corresponds to an age of ∼0.2 Myr. With a radius of ∼7 $R_\odot$, V410 Tau would have needed a magnetic dipole barely above 100 G to maintain the assumed magnetospheric cavity, even with an accretion rate of $\sim 10^{-8}$ $M_\odot$ yr^{-1} just before disc dissipation. That value is compatible with the 200–400 G dipole we measure on the ∼3.5 $R_\odot$ star today. Kraus et al. (2012; Fig. 1) shows a correlation between the presence of a close companion and the early depletion of the accretion disc, which indicates that V410 Tau B, observed at a projected separation of 16.8 ± 1.4 au (Ghez et al. 1995), could have been responsible for the early depletion of the disc.

In our H α dynamic spectra, we observe a conspicuous absorption feature in the second part of the 2009 January run around phase 0.95 (Fig. C1), that could be the signature of a prominence (see e.g. Collier Cameron & Woods 1992). Fitting a sine curve in the absorption feature yields an amplitude of ∼2 $v \sin i$, corresponding to a prominence ∼2 $R_\star$ away from the centre of V410 Tau, confirm-

Downloaded from https://academic.oup.com/mnras/article-abstract/489/4/5556/5561492 by Universitïe Paul Sabatier - Toulouse 3 user on 16 December 2019

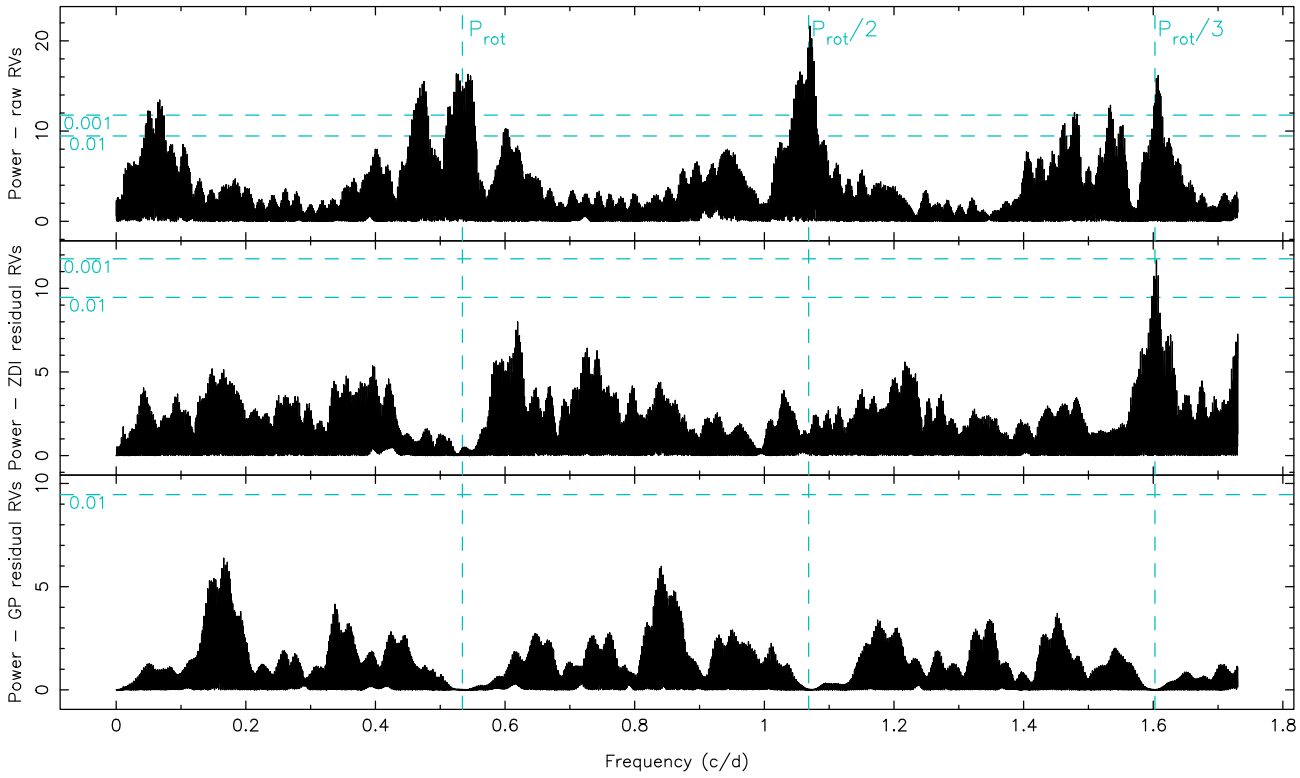

Figure 10. Periodograms of the raw RVs (top), of the RVs filtered from ZDI-modelled activity (middle) and of the RVs filtered from GP-modelled activity (bottom, blue dashed line), for observation epochs (a) 2009 Jan, (b) 2011 Jan, (c) 2013 Dec, (d) 2015 Dec, and (e) 2016 Jan. Periodograms of the whole data set raw RVs (top), RVs filtered from ZDI-modelled activity (middle) and RVs filtered from GP-modelled activity (bottom). False-alarm probability levels of 1 per cent and 0.1 per cent are represented as horizontal cyan dashed lines, and $P_{\rm rot}$ and its first two harmonics as vertical cyan dashed lines.

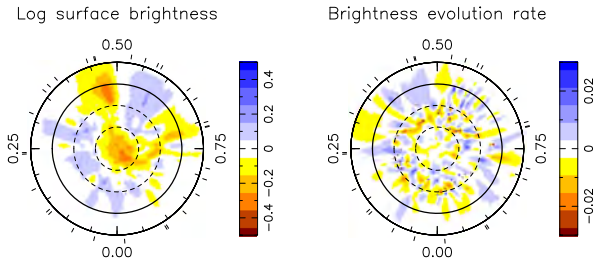

Figure 11. Brightness map and evolution rate reconstructed by ZDI on data set 2015 Dec–2016 Jan. Pole-on view with the equator being represented as a full line, and 60°, 30°, and −30° latitude parallels as dashed lines. Cool spots are coloured in brown and bright plages in blue, and ticks around the star mark the spectropolarimetric observations.

ing that the prominence is located close to the corotation radius. Plotting the 3D potential field extrapolation of the reconstructed surface radial field for 2009 January, at phases 0.95, 0.20, 0.45, and 0.70, we observe the presence of closed field lines reaching $\sim 2\,R_\star$ at phase 0.95 (Fig. 14), which may be able to support the observed prominence. We also observe similar absorption features in 2009 January around phase 0.8 and in 2011 January around phase 0.35, but they are less well covered by our observations. We however found corresponding field lines at the right phase for each (see Fig. 14 for 2009 January).

We also constrained the differential rotation of V410 Tau with ZDI: we obtained six values for the equatorial rotation rate $\Omega_{\rm eq}$ and for the pole-to-equator rotation rate difference $\mathrm{d}\Omega$, by using separately our Stokes I and Stokes V LSD profiles from each of the three data sets 2008b + 2009a, 2013b, and 2015b + 2016a. Overall mean values are $\Omega_{\rm eq} = 3.35957 \pm 0.00022$ rad d^{-1} and $\mathrm{d}\Omega = 0.0097 \pm 0.0011$ rad d^{-1}. The differential rotation of V410 Tau is thus relatively weak, with a pole-to-equator rotation rate difference 5.6 times smaller than that of the Sun, and a lap time of 648 ± 73 d. Compared to other wTTSs previously analysed within the MaTYSSE programme, the differential rotation of V410 Tau is similar to that of V830 Tau (Donati et al. 2017) but much smaller than that of TAP 26, which is almost of solar level, consistent with the fact that TAP 26 is no longer fully convective and has developed a radiative core (of size $0.6\,R_\star$, Yu et al. 2017).

6.2 Mid-term variability of V410 Tau

Even with differential rotation, it is impossible for our current version of ZDI to model data sets spanning a few months down to noise level, which shows that the surface of V410 Tau undergoes significant intrinsic variability, corroborating the hypothesis of a dynamo-generated field. The variations of the photosphere and of the surface magnetic field over the years might be the manifestation of a magnetic cycle, whose existence has been suggested by previous studies (Stelzer et al. 2003; Hambálek et al. 2019). No clear change in $\mathrm{d}\Omega$ is observed while the dipole grows in intensity (Table 3), which could indicate a time lag in the dynamo interaction between the magnetic field and the rotation profile.

The bulk RV of V410 Tau exhibits a drift throughout our 8 yr campaign, from 16.30 ± 0.05 km s^{-1} in 2008b–2009a to 16.65 ± 0.05 km s^{-1} in 2015b–2016a. One explanation could be a variation in the suppression of convective blueshift in regions of

Downloaded from https://academic.oup.com/mnras/article-abstract/489/4/5556/5561492 by Universitïe Paul Sabatier - Toulouse 3 user on 16 December 2019

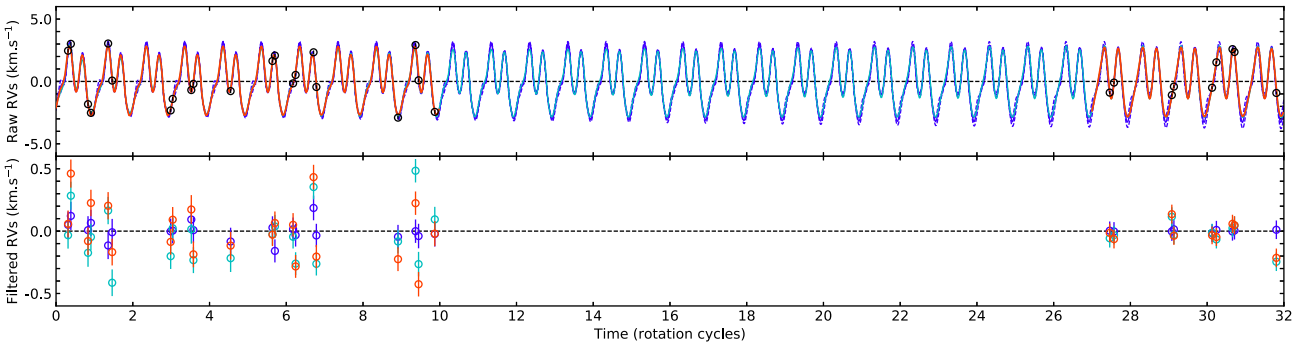

Figure 12. Comparison between the GP model, the new ZDI model, and the classical ZDI models for V410 Tau RVs in season 2015b–2016a. Rotation cycles are offset to concur with Table A1. Top: raw RVs (black dots) with 1σ error bars, GP model (purple full line), new ZDI model (cyan full line), and classical ZDI models for both observation epochs 2015 Dec and 2016 Jan (red full lines). Bottom: RVs filtered from the GP model (purple dots), from the new ZDI model (cyan dots), or from the classical ZDI models (red dots). The rms of the filtered RVs with GP, new ZDI, and classical ZDI are, respectively, 0.065, 0.194, and 0.193 km s^{-1}.

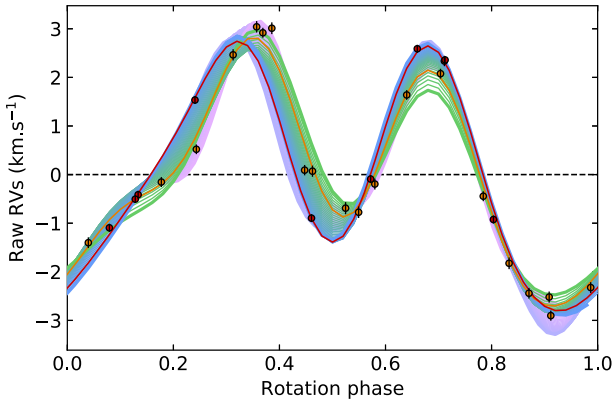

Figure 13. Raw RVs of V410 Tau in the 2015b–2016a season, between cycles 1349 and 1381 as referenced in Table A1, plotted against stellar rotation phase. The GPR and new ZDI models are represented by full lines coloured in gradients, from earliest to latest cycle, respectively, pink to purple and green to blue, while the classical ZDI models for 2015 Dec and 2016 Jan are plotted in orange and red, respectively. Observations are plotted as dots with 1σ error bars, orange for 2015 Dec and 2016 Jan.

strong magnetic field (Meunier, Desort & Lagrange 2010; Haywood et al. 2016), which could further support a secular evolution of the magnetic topology. It could also be a manifestation of the binary motion of V410 Tau A-B. The central binary of V410 Tau was observed twice, with a sky-projected separation of 16.8 ± 1.4 au in 1991 October and 9.5 ± 0.3 au in 1994 October (0.13 ± 0.01 arcsec and 0.074 ± 0.002 arcsec, respectively, in Ghez et al. 1995), and a mass ratio of 0.20 ± 0.10 (Kraus et al. 2011). Assuming a mass ratio of 0.2 and an edge-on circular orbit, we find that an orbit of the primary star of radius 6.0 au, i.e. binary separation 36.0 au and period 166 a, fits our bulk RVs and the sky-projected separations at a level of 2σ (see Fig. 15). No binary motion was detected in the 2013–2017 astrometry measurements of Galli et al. (2018), which is consistent with our model where the sky-projected velocity varies by only 0.13 mas a^{-1} over these 3.5 yr (roughly a 50th of the orbital period). More measurements would enable to estimate the eccentricity and potentially fit the sky-projected separations to a better level, as well as to decide whether the binary motion can explain the RV drift observed in this study.

The rotation period derived from our *V* magnitude measurements, in each observing season, also displays long-term variations. Placing the periods found from the photometric data on a period-latitude diagram representing the modelled differential rotation (Fig. B5), we observe that the latitudes corresponding to the successive periods tend to increase from 0 in 2008 to ∼50° in 2016. We note that this trend is observed with both the periods derived from sine fits to the photometric data and those derived from GPR (see Appendix B, available online). This implies that the largest features, i.e. those with the biggest impact on the photometric curve, underwent a poleward migration, reminiscent of the Solar butterfly diagram (albeit reversed). This would suggest that the dynamo wave, if cyclic, has a period of at least 8 a and likely much longer (16 a if our data covers only one half of a full cycle). Previous studies using different data have suggested the existence of an activity cycle on V410 Tau, with periods of 5.4 and 15 a, respectively (Stelzer et al. 2003; Hambálek et al. 2019). We further note that our differential rotation measurements confirm that the barycentre of surface features migrates to higher latitudes over time (see Fig. 6).

Applying GPR with MCMC parameter exploration to our H α EWs and longitudinal magnitude field measurements (B_ℓ, first-order moment of the Stokes *V* LSD profiles, Donati & Brown 1997), we also found rotation periods from which we derive mean barycentric latitudes of features constraining the modelling of each quantity (see Fig. 16). The period found from H α is equal within error bars to the one derived in Stelzer et al. (2003) from photometry, whereas the period found from B_ℓ seems tied to equatorial features. It is worth mentioning that we also find long decay times for these two activity proxies: 589^{+774}_{-335} and 604^{+553}_{-289} d, respectively, which suggests, with the caution needed with such high error bars, that the H α and B_ℓ modulations are particularly sensitive to large, long-lasting features. The phase plots are displayed in Appendix C (available online).

6.3 Radial velocity modulations

We modelled the activity RV jitter from line profiles synthesized from our ZDI maps, and filtered it out from the RV curve of V410 Tau. From an rms of 1.802 km s^{-1} in the raw RVs, we get residuals with an rms of 0.167 km s^{-1}. We also applied GPR to our raw RVs and found a jitter of periodicity 1.87029 ± 0.00037 d and decay time 160^{+45}_{-35} d, with residuals of rms 0.076 km s^{-1}. The period derived from the GPR on our raw RVs is shorter than the

Downloaded from https://academic.oup.com/mnras/article-abstract/489/4/5556/5561492 by Universitïe Paul Sabatier - Toulouse 3 user on 16 December 2019

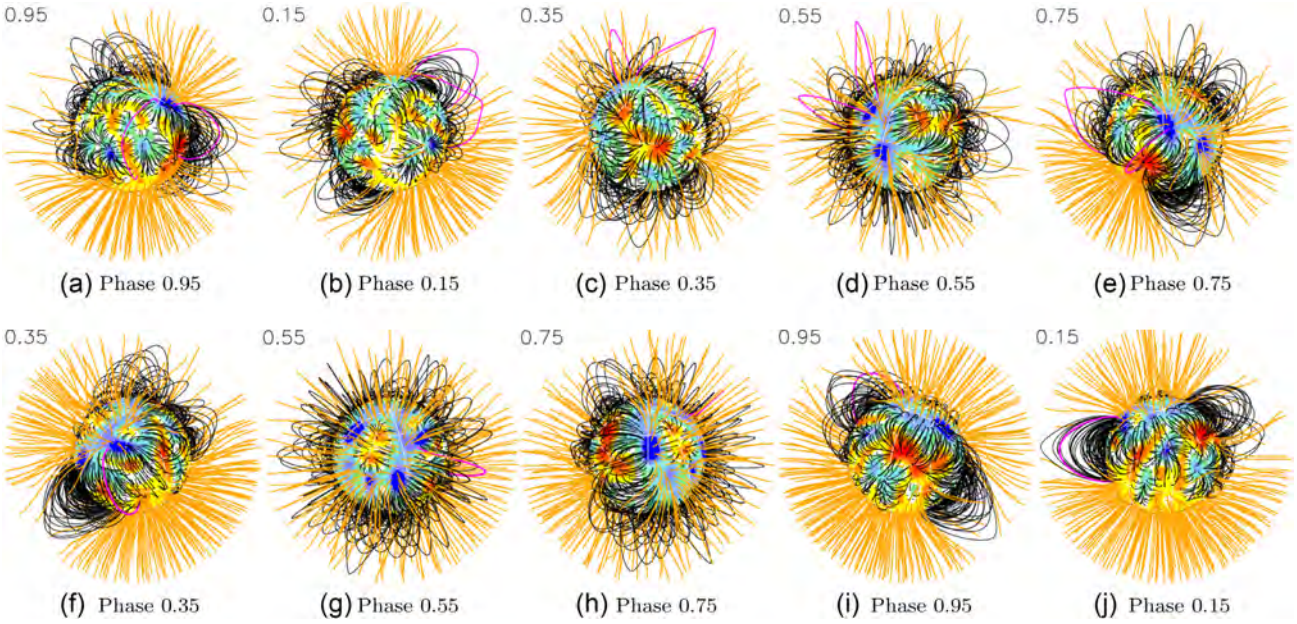

Figure 14. Potential field extrapolations of the ZDI-reconstructed surface radial field, as seen by an Earth-based observer, for observation epochs 2009 Jan (top) and 2011 Jan (bottom) at different phases. Open/closed field lines are shown in orange/black, respectively, and colours at the stellar surface depict the local value of the radial field (in G, as shown in the left-hand panels of Fig. 3). The source surface at which field lines open is set to 2.18 $R_\star$. The field lines that would carry the potential observed prominences (phases 0.95 and 0.8 in 2009, phase 0.35 in 2011) are coloured in magenta. Animated versions with the star rotating are available at http://userpages.irap.omp.eu/ lyu/jan09a.gif and http://userpages.irap.omp.eu/ lyu/jan11n.gif.

period we used to phase our data, and corresponds to a latitude of 5.5°. This period is much closer to the period derived with GPR from B_ℓ than to the period derived from Hα, showing that in this case, B_ℓ is a better activity proxy than Hα (for a more systematic study of the correlation of B_ℓ with stellar activity, see Hébrard et al. 2016). The decay time associated with RVs is much shorter than the differential rotation lap time and the decay times of the V magnitude, Hα, and B_ℓ (see Table 6), which suggests that RVs are more sensitive to small-scale short-lived features while the photometry, Hα, and B_ℓ are more sensitive to large-scale long-lasting features.

Through both processes, the residual RVs present no significant periodicity which would betray the presence of a potential planet. To estimate the planet mass detection threshold, GPR–MCMC was run on simulated data sets, composed of a base activity jitter (our GP model from Section 5), and a circular planet signature, plus a white noise of level 0.081 km s^{-1}. Various planet separations and masses were tested, and for each case, GPR–MCMC was run several times with different randomization seeds, to mitigate statistical bias. For every randomization seed, GPR–MCMC was run with a model including a planet and a model including no planet, and the difference of logarithmic marginal likelihood between them (hereafter $\Delta\mathcal{L}$) was computed. Finally, the detection threshold was set at $\Delta\mathcal{L} = 10$ and the minimum detectable mass at each separation was interpolated from the mass/$\Delta\mathcal{L}$ curve. Fig. 17 shows the planet mass detection threshold as a function of planet–star separation: we thus obtained a detectability threshold of $\sim$1 M_{Jup} for $a < 0.09$ au and $\sim$4.6 M_{Jup} for $a = 0.15$ au. The figure also shows the parameters of V830 Tau b and TAP 26 b, showing that we would likely have detected a planet like TAP 26 b but not one like V830 Tau b. Planets beyond $a = 0.15$ au are difficult to detect due to the temporal coverage of our data, that never exceeds 19 d at any given epoch. The early depletion of the disc may have prevented the formation and/or the migration of giant exoplanets. Kraus et al. (2016) outlines a correlation between the presence of a close companion and a lack of planets, in a sample of binary stars with mass ratios $q > 0.4$, which could support the hypothesis that V410 Tau B, although having a slightly lower mass ratio ($q = 0.2 \pm 0.1$, Kraus et al. 2011), played a role in the early disc dissipation, which in turn prevented the formation of a hot Jupiter.

In terms of methodology, GPR fits the data down to a significantly lower χ^2_r than ZDI because it is capable of accounting for most of the mid-term variability, contrarily to ZDI, which for now only integrates differential rotation and a simplistic description of intrinsic variability. Small structures evolve on time-scales of $\sim$few weeks, so we need to be able to model their temporal evolution in a more elaborate way to be able to match the capability of GPR to fit time-variable RV curves. Self-consistent methods that combine the physical faithfulness of ZDI and the flexibility of GPR will be developed in the near future and applied to more MaTYSSE data, as well as to data from the SPIRou (Spectropolarimetre InfraRouge) Legacy Survey (SLS). Finally, observing V410 Tau and other wTTSs with SPIRou will yield spectra in the near-infrared, where we expect a smaller jitter than in the optical bandwidth, and will offer an opportunity to benchmark our activity jitter filtering technique performances.

ACKNOWLEDGEMENTS

This paper is based on observations obtained at the Canada–France–Hawaii Telescope (CFHT), operated by the National Research Council of Canada, the Institut National des Sciences de l'Univers of the Centre National de la Recherche Scientifique (INSU/CNRS) of France and the University of Hawaii, and at the Télescope Bernard Lyot (TBL), operated by Observatoire Midi-Pyrénées and by INSU/CNRS. We thank the Queued Service Observations (QSO) teams of CFHT and TBL for their great work and efforts at collecting the high-quality MaTYSSE (Magnetic Topologies of Young Stars

Downloaded from https://academic.oup.com/mnras/article-abstract/489/4/5556/5561492 by Universitïe Paul Sabatier - Toulouse 3 user on 16 December 2019

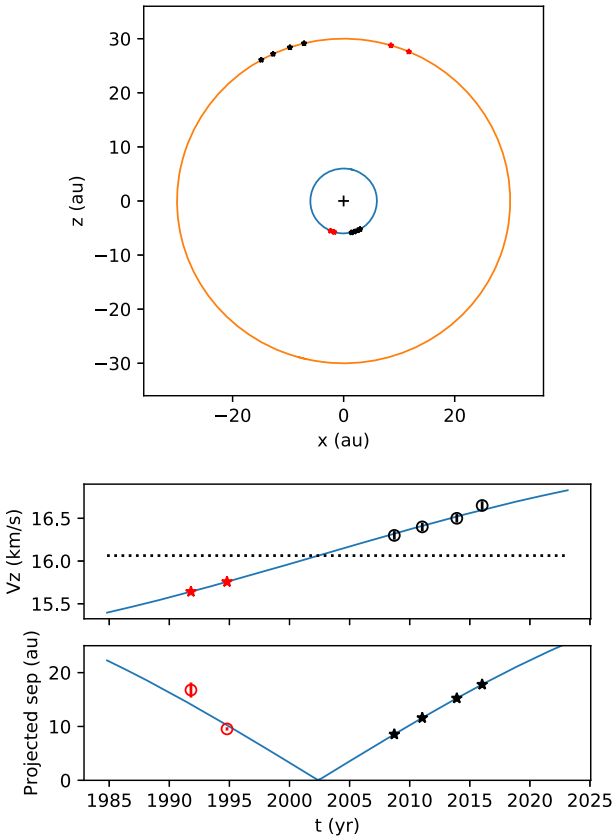

Figure 15. Circular model for the binary motion of V410 Tau A and V410 Tau B: edge-on orbit, separation 36.0 au, period 166 a and systemic radial velocity 16.06 km s^{-1}. *Top*: top view of the model orbit, with the z-axis parallel to the line of sight, where the positions of V410 Tau A and B according to the model are marked by red and black stars at the times of the separation measurements and of our spectropolarimetric seasons (2008b–2009a, 2011a, 2013b, and 2015b–2016a) respectively. *Middle*: RV_{bulk} of V410 Tau A with time, as measured by us in black dots with 1σ error bars and as derived from the model orbit in blue. The predicted RV_{bulk} at the times of the separation measurements are represented by red stars. *Bottom*: Sky-projected binary separation as a function of time, as measured by Ghez et al. (1995) in red dots with 1σ error bars, and as derived from the model orbit in blue. The predicted sky-projected separations at the dates of our observing seasons are marked in black stars.

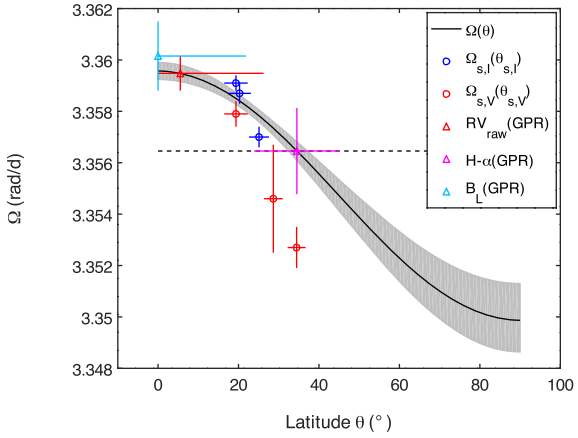

Figure 16. Differential rotation curve of V410 Tau (black full line) with 1σ uncertainty in grey, with $\Omega_{eq} = 3.35957 \pm 0.00006$ rad d^{-1} and $d\Omega = 0.0097 \pm 0.0003$ rad d^{-1}. The stellar rotation rate chosen to phase our data is represented as a dashed horizontal line. The rotation rates derived from the RVs (red), from the H α EWs (magenta), and from the longitudinal field measurements (cyan) are positioned on the differential rotation curve as triangles with 1σ error bars, thus yielding the barycentric latitude of the features determining the period. The dots represent couples $\{90 - \theta_s, \Omega_s\}$ derived in our epoch-wise differential rotation measurements, those coming from Stokes *I* / Stokes *V* data being plotted in blue / red, respectively.

Table 6. Various evolution time-scales.

Quantity	Time-scale (d)
RV decay time	160^{+45}_{-35}
V mag decay time	314^{+31}_{-29}
H α decay time	589^{+774}_{-335}
B_ℓ decay time	604^{+553}_{-289}
Differential rotation lap time	648 ± 73

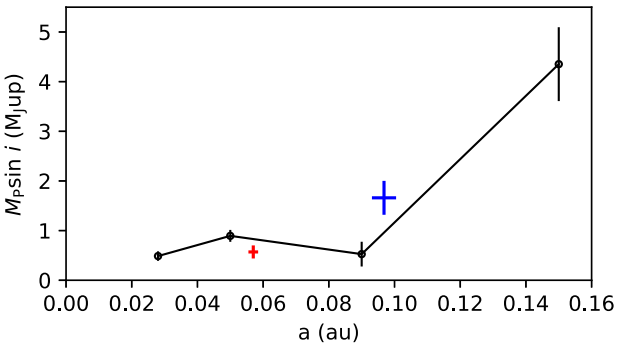

Figure 17. Detectability threshold in terms of $M\sin i$ for planets at various *a*, with the RV filtering technique involving GPR. V830 Tau b is plotted in red (parameters from Donati et al. 2017) and TAP 26 b in blue (parameters from Yu et al. 2017).

and the Survival of close-in massive Exoplanets) data presented here, without which this study would not have been possible. MaTYSSE is an international collaborative research programme involving experts from more than 10 different countries (France, Canada, Brazil, Taiwan, United Kingdom, Russia, Chile, United States of America, Ireland, Switzerland, Portugal, China, and Italy).

JFD also warmly thanks the Initiative d'Excellence (IDEX) at Université Fédérale Toulouse Midi-Pyrénées (UFTMiP) for funding the STEPS collaboration program between the Institut de Recherche en Astrophysique et Planétologie at the Observatoire Midi-Pyrénées (IRAP/OMP) and the European Southern Observatory (ESO). JFD acknowledges funding from the European Research Council (ERC) under the H2020 research & innovation programme (grant agreements 740651 New Worlds). We acknowledge funding from the Laboratoire d'Excellence (LabEx) OSUG@2020 (Observatoire des Sciences de l'Univers de Grenoble) that allowed purchasing the ProLine PL230 CCD imaging system installed on the 1.25 m telescope at the Crimean Astrophysical Observatory.

Finally, we warmly thank the referee for taking the time to review this research.

This research has made use of the SIMBAD data base, operated at CDS, Strasbourg, France, and of the Matplotlib python module (Hunter 2007).

Downloaded from https://academic.oup.com/mnras/article-abstract/489/4/5556/5561492 by Universitïe Paul Sabatier - Toulouse 3 user on 16 December 2019

REFERENCES

Baraffe I., Homeier D., Allard F., Chabrier G., 2015, A&A, 577, A42
Bouvier J., 2007, in Bouvier J., Appenzeller I., eds, Proc. IAU Symp. 243, Star-Disk Interaction in Young Stars. Kluwer, Dordrecht, p. 231
Bouvier J., Alencar S. H. P., Harries T. J., Johns-Krull C. M., Romanova M. M., 2007, in Reipurth B., Jewitt D., Keil K., eds, Protostars and Planets V. University of Arizona Press, Tucson, p. 479
Bouvier J., Bertout C., 1989, A&A, 211, 99
Carroll T. A., Strassmeier K. G., Rice J. B., Künstler A., 2012, A&A, 548, A95
Collier Cameron A., Woods J. A., 1992, MNRAS, 258, 360
Donati J.-F., Brown S. F., 1997, A&A, 326, 1135
Donati J.-F., Collier Cameron A., Petit P., 2003, MNRAS, 345, 1187
Donati J.-F., Landstreet J. D., 2009, ARA&A, 47, 333
Donati J.-F., Mengel M., Carter B. D., Marsden S., Collier Cameron A., Wichmann R., 2000, MNRAS, 316, 699
Donati J.-F., Semel M., Carter B. D., Rees D. E., Collier Cameron A., 1997, MNRAS, 291, 658
Donati J.-F. et al., 2006, MNRAS, 370, 629
Donati J.-F. et al., 2007, MNRAS, 380, 1297
Donati J.-F. et al., 2008, MNRAS, 386, 1234
Donati J.-F. et al., 2010a, MNRAS, 402, 1426
Donati J.-F. et al., 2010b, MNRAS, 409, 1347
Donati J.-F. et al., 2011, MNRAS, 412, 2454
Donati J.-F. et al., 2012, MNRAS, 425, 2948
Donati J.-F. et al., 2013, MNRAS, 436, 881
Donati J.-F. et al., 2014, MNRAS, 444, 3220
Donati J.-F. et al., 2015, MNRAS, 453, 3706
Donati J.-F. et al., 2017, MNRAS, 465, 3343
Donati J. F. et al., 2016, Nature, 534, 662
Galli P. A. B. et al., 2018, ApJ, 859, 33
Ghez A. M., Weinberger A. J., Neugebauer G., Matthews K., McCarthy D. W. Jr, 1995, AJ, 110, 753
Ghez A. M., White R. J., Simon M., 1997, ApJ, 490, 353
Grankin K. N., Bouvier J., Herbst W., Melnikov S. Y., 2008, A&A, 479, 827
Gregory S. G., Donati J.-F., Morin J., Hussain G. A. J., Mayne N. J., Hillenbrand L. A., Jardine M., 2012, ApJ, 755, 97
Gully-Santiago M. A. et al., 2017, ApJ, 836, 200
Hambálek Ä., VaÅko M., Paunzen E., Smalley B., 2019, MNRAS, 483, 1642
Haywood R. D. et al., 2014, MNRAS, 443, 2517
Haywood R. D. et al., 2016, MNRAS, 457, 3637
Hunter J. D., 2007, Computing in Science & Engineering, 9, 90
Hussain G. A. J. et al., 2009, MNRAS, 398, 189
Hébrard É. M., Donati J.-F., Delfosse X., Morin J., Moutou C., Boisse I., 2016, MNRAS, 461, 1465
Johns-Krull C. M., Valenti J. A., Koresko C., 1999, ApJ, 516, 900
Kraus A. L., Ireland M. J., Hillenbrand L. A., Martinache F., 2012, ApJ, 745, 19
Kraus A. L., Ireland M. J., Huber D., Mann A. W., Dupuy T. J., 2016, AJ, 152, 8
Kraus A. L., Ireland M. J., Martinache F., Hillenbrand L. A., 2011, ApJ, 731, 8
Kurucz R., 1993, CDROM # 13 (ATLAS9 atmospheric models) and # 18 (ATLAS9 and SYNTHE routines, spectral line database). Smithsonian Astrophysical Observatory, Washington DC
Landi degl'Innocenti E., Landolfi M., 2004, Polarisation in Spectral Lines. Kluwer Academic Publishers, Dordrecht
Luhman K. L., Allen P. R., Espaillat C., Hartmann L., Calvet N., 2010, ApJS, 186, 111
Meunier N., Desort M., Lagrange A.-M., 2010, A&A, 512, A39
Morin J. et al., 2008, MNRAS, 390, 567
Moutou C. et al., 2007, A&A, 473, 651
Pecaut M. J., Mamajek E. E., 2013, ApJS, 208, 9
Pollacco D. L. et al., 2006, PASP, 118, 1407
Rice J. B., Strassmeier K. G., Kopf M., 2011, ApJ, 728, 69
Siess L., Dufour E., Forestini M., 2000, A&A, 358, 593
Skelly M. B., Donati J.-F., Bouvier J., Grankin K. N., Unruh Y. C., Artemenko S. A., Petrov P., 2010, MNRAS, 403, 159
Sokoloff D. D., Nefedov S. N., Ermash A. A., Lamzin S. A., 2008, Astron. Lett., 34, 761
Stelzer B. et al., 2003, A&A, 411, 517
Vaytet N., Commerçon B., Masson J., González M., Chabrier G., 2018, A&A, 615, A5
Welty A. D., Ramsey L. W., 1995, AJ, 110, 336
Yadav R. K., Christensen U. R., Morin J., Gastine T., Reiners A., Poppenhaeger K., Wolk S. J., 2015, ApJ, 813, L31
Yu L. et al., 2017, MNRAS, 467, 1342

SUPPORTING INFORMATION

Supplementary data are available at *MNRAS* online.

Appendix A. Observations.
Appendix B. Photometry Analysis.
Appendix C. Activity Proxies.

Please note: Oxford University Press is not responsible for the content or functionality of any supporting materials supplied by the authors. Any queries (other than missing material) should be directed to the corresponding author for the article.

This paper has been typeset from a TEX/LATEX file prepared by the author.

Downloaded from https://academic.oup.com/mnras/article-abstract/489/4/5556/5561492 by Universitïe Paul Sabatier - Toulouse 3 user on 16 December 2019

APPENDIX A: OBSERVATIONS

This appendix informs all the observations, both spectropolarimetric (Table A1) and photometric (Table A2), that we used in this study, excluding the WASP data. The spectropolarimetric data are spread over 8 runs (2008 Oct, 2008 Dec, 2009 Jan, 2011 Jan, 2013 Nov, 2013 Dec, 2015 Dec and 2016 Jan) and the photometric data are spread over 9 seasons: 08b+09a (short for 2008b + 2009a; all the other seasons follow the same naming convention), 09b+10a, 10b, 11b+12a, 12b+13a, 13b+14a, 14b, 15b+16a and 16b+17a.

The instruments with which the spectropolarimetric data was taken, ESPaDOnS and NARVAL, are twin spectropolarimeters and cover a 370 to 1000 nm wavelength domain, with respective resolving powers of 65 000 (i.e. resolved velocity element of 4.6 $\mathrm{km\,s^{-1}}$) and 60 000 (resolved velocity element of 5.0 $\mathrm{km\,s^{-1}}$). Each polarization exposure sequence consists of four subexposures of 600 s each, taken in different polarimeter configurations to allow the removal of all spurious polarization signatures at first order (Donati et al. 1997), except three observations comprised of only two subexposures of 600 s (2008 Dec 05 at phase 0.827, 2009 Jan 05 at phase 0.602, and 2013 Nov 07 at phase 0.541), and three observations comprised of four subexposures of 800 s (2009 Jan 10 at phases 0.229, 0.251 and 0.272).

The telescopes used for photometry at CrAO are AZT-11, a 1.25 m telescope with a five-channel photometer-polarimeter, and T60Sim, a 0.60 m telescope with a four-channel photometer.

Table A1. Information on the V410 Tau spectropolarimetric data. The first three columns contain the time at which the observations were taken: Coordinated Universal Time in the 1st column, Barycentric Julian Date in the 2nd and corresponding rotational cycle of V410 Tau, c, in the 3rd, as is defined in equation 1. The 4th column indicates the instrument used for the observation (E: ESPaDOnS, N: NARVAL) and column 5 the spectrum S/N. Column 6 indicates rejected spectra or the presence of moon pollution ([a]: not used in ZDI, [b]: not used in GPR, [c]: not used for period retrieval from Hα EW). Columns 7 and 8 contain the S/N in the Stokes I and Stokes V LSD profiles respectively. Columns 9 to 12 show the raw RVs, the RVs filtered with ZDI, the RVs filtered with GPR and the 1σ RV error bar respectively, column 13 lists the equivalent width of the Hα line (with a typical error bar of 10 km s^{-1}) and column 14 informs the longitudinal projection of the magnetic field integrated over the visible surface (with a typical error bar of 50 G).

UTC 2008 Oct	BJD 2454700+	Cycle -42+	Instr.	S/N	Comment	S/N$_I$	S/N$_V$	RV$_{raw}$ (km s^{-1})	RV$_{filt/ZDI}$ (km s^{-1})	RV$_{filt/GP}$ (km s^{-1})	σ_{RV} (km s^{-1})	EW$_{H\alpha}$ (km s^{-1})	B$_{long}$ (G)
15 11:42:34	54.992	0.552	E	228	Isolated[a]	2313	6167	-0.119		-0.006	0.078	54.188	-156
16 11:09:41	55.969	1.075	E	107	Isolated[a]	2184	2743	1.681		0.004	0.084	-0.857	102
19 09:09:16	58.886	2.633	E	227	Isolated[a]	2346	6305	1.069		-0.001	0.077	42.548	-142
19 13:53:44	59.083	2.738	E	204	Isolated[a]	2295	5491	0.696		0.006	0.079	12.192	-167
2008 Dec	2454800+	-15+											
05 13:01:49	6.049	0.827	E	61	Bad S/N[a,b]							10.874	
06 08:06:19	6.843	1.251	E	238		2669	6759	0.792	0.016	-0.068	0.071	31.589	-50
07 13:32:32	8.070	1.907	E	209		2672	5784	-0.516	-0.043	-0.000	0.071	17.226	240
08 05:05:16	8.718	2.253	E	230		2634	6437	0.913	0.135	0.097	0.072	19.302	-59
09 05:54:32	9.752	2.805	E	110	Moon	2514	2847	-1.484	-0.129	-0.010	0.075	-1.567	-40
10 13:46:11	11.079	3.514	E	201	He I D_3 flare[a,b]							50.202	
15 13:36:10	16.072	6.181	E	212	Big flare[a,b,c]							231.256	
19 04:58:16	19.712	8.126	E	185		2619	4876	0.425	-0.234	-0.010	0.072	18.761	46
20 13:45:25	21.078	8.856	E	142		2537	3502	-1.188	-0.072	-0.009	0.074	5.692	150
2009 Jan	2454800+	0+											
02 19:38:17	34.323	0.931	N	167		2610	4531	0.742	0.025	0.125	0.073	-12.991	149
02 20:23:28	34.354	0.948	N	166		2570	4408	0.754	-0.155	-0.171	0.073	-9.125	177
02 21:08:39	34.386	0.964	N	166		2622	4566	1.192	0.141	0.064	0.072	-14.394	97
02 21:53:50	34.417	0.981	N	167		2601	4546	1.065	-0.074	-0.156	0.073	-18.321	126
02 22:41:08	34.450	0.999	N	159		2609	4438	1.369	0.201	0.143	0.073	-14.991	114
03 19:11:19	35.304	1.455	N	160		2551	4235	-1.347	0.010	0.088	0.074	29.299	-124
03 19:56:30	35.336	1.472	N	157		2586	4427	-0.955	-0.020	-0.024	0.073	30.601	-161
03 20:42:21	35.367	1.489	N	160		2565	4321	-0.430	0.047	0.009	0.074	32.998	-151
03 21:28:13	35.399	1.506	N	151		2524	4080	-0.018	0.000	-0.006	0.075	35.709	-216
03 22:13:25	35.431	1.523	N	148		2544	4053	0.346	-0.059	0.013	0.074	43.994	-158
04 18:52:52	36.291	1.982	N	149		2552	3997	1.289	0.145	0.065	0.074	-8.025	169
04 19:38:04	36.323	1.999	N	156		2608	4291	1.176	0.007	-0.039	0.073	-7.124	81
04 20:23:16	36.354	2.016	N	159		2610	4421	1.171	0.026	0.018	0.073	-2.797	114
04 21:08:28	36.385	2.033	N	158		2594	4337	0.973	-0.110	-0.086	0.073	1.774	117
04 21:53:40	36.417	2.049	N	158		2583	4235	1.014	0.016	0.074	0.073	6.863	18
05 22:10:16	37.428	2.590	N	127		2355	3240	1.332	0.026	-0.002	0.079	43.598	-141
05 22:44:08	37.452	2.602	N	86		2118	2064	1.480	0.193	0.002	0.087	42.265	-311
07 05:38:42	38.740	3.290	E	199		2681	5764	-0.259	0.167	0.040	0.071	31.322	-82
09 04:54:60	40.709	4.342	E	193		2650	5144	-1.874	-0.296	-0.219	0.072	39.064	-26
10 20:45:05	42.369	5.229	N	158	Moon	2453	3917	0.281	-0.178	0.043	0.076	7.610	-9
10 21:43:38	42.409	5.251	N	158	Moon	2495	4210	0.087	-0.147	-0.115	0.075	15.255	-79
10 22:42:09	42.450	5.272	N	165	Moon	2463	4271	-0.069	0.033	-0.063	0.076	23.200	-67
11 04:58:44	42.712	5.412	E	163	Moon	2686	4299	-2.287	-0.249	-0.097	0.071	19.993	-137
11 18:56:02	43.293	5.723	N	136		2391	3495	-0.506	0.115	0.064	0.078	14.943	-200
11 19:41:16	43.324	5.739	N	142		2467	3711	-1.032	-0.197	-0.102	0.076	8.644	-167
11 20:26:27	43.356	5.756	N	131		2360	3369	-1.132	-0.165	-0.006	0.079	7.370	-57
11 21:11:39	43.387	5.773	N	116	Moon	2214	2911	-1.109	-0.091	0.074	0.084	4.870	37
11 21:56:50	43.419	5.790	N	17	Bad S/N[a,b]							2.131	
12 19:41:03	44.324	6.274	N	117		2185	2788	0.062	0.191	0.104	0.084	27.575	-123
12 20:26:17	44.356	6.290	N	114		2212	2847	-0.360	0.097	-0.025	0.084	33.439	4
12 21:11:29	44.387	6.307	N	117		2253	2927	-0.630	0.196	0.092	0.082	37.490	-116
12 22:01:04	44.421	6.325	N	132		2415	3410	-1.081	0.162	0.108	0.078	41.752	-93
14 04:59:12	45.712	7.015	E	232		2723	6970	1.004	-0.143	-0.052	0.070	-37.801	69
14 19:12:20	46.304	7.331	N	144		2325	3772	-1.462	-0.081	-0.154	0.080	39.919	-93
14 19:57:30	46.335	7.348	N	146		2425	3848	-1.603	0.111	0.080	0.077	30.220	-111
14 20:42:42	46.367	7.365	N	147		2470	3862	-1.816	0.150	0.157	0.076	28.237	-93
14 21:27:54	46.398	7.381	N	147		2448	3821	-2.156	-0.050	-0.004	0.077	28.349	-82
15 20:41:08	47.366	7.898	N	90		1893	2066	0.045	-0.259	-0.065	0.096	11.370	278
15 21:26:20	47.397	7.915	N	92		1893	2089	0.499	-0.060	-0.006	0.096	7.425	218
16 18:24:01	48.270	8.382	N	137		2429	3520	-2.014	0.093	0.093	0.077	20.336	-58
16 19:09:13	48.302	8.398	N	150		2513	3951	-2.196	-0.088	-0.052	0.075	18.041	-97
16 19:54:26	48.333	8.415	N	145		2484	3779	-2.079	-0.102	-0.053	0.076	20.508	-99
16 20:39:38	48.365	8.432	N	133		2410	3442	-1.687	0.040	0.068	0.078	21.507	41
16 21:24:49	48.396	8.449	N	16	Bad S/N[a,b]							21.522	
16 22:23:00	48.436	8.470	N	113		2317	2783	-0.820	0.024	-0.047	0.080	22.599	-126
17 18:20:13	49.268	8.914	N	127		2374	3291	0.560	0.004	0.038	0.079	-2.751	153
17 19:05:25	49.299	8.931	N	103		2116	2484	0.778	-0.002	-0.079	0.087	-6.869	113
17 19:50:37	49.330	8.948	N	121		2394	3126	1.191	0.233	0.106	0.078	-10.239	157
17 20:35:49	49.362	8.965	N	140		2514	3740	1.158	0.075	-0.033	0.075	-15.775	106
17 21:21:01	49.393	8.981	N	137		2483	3616	1.222	0.066	0.030	0.076	-22.467	115

(a) Observations of the late 2008 and early 2009 runs.

Table A1. (Continued from previous page).

UTC 2011 Jan	BJD 2455500+	Cycle 397+	Instr.	S/N	Comment	S/N_I	S/N_V	RV_{raw} ($km\,s^{-1}$)	$RV_{filt/ZDI}$ ($km\,s^{-1}$)	$RV_{filt/GP}$ ($km\,s^{-1}$)	σ_{RV} ($km\,s^{-1}$)	$EW_{H\alpha}$ ($km\,s^{-1}$)	B_{long} (G)
14 19:01:45	76.297	0.291	N	145		2789	4035	-2.162	-0.114	-0.117	0.069	-15.778	-43
14 19:46:58	76.328	0.308	N	152		2757	4175	-2.052	0.363	0.172	0.070	-24.729	-147
14 20:32:12	76.360	0.324	N	155		2789	4172	-2.511	0.181	0.011	0.069	-28.375	-41
14 21:17:25	76.391	0.341	N	150		2765	4113	-2.923	-0.070	-0.071	0.069	-25.398	-103
15 19:09:27	77.302	0.828	N	138		2710	3877	-2.672	-0.127	-0.023	0.071	6.283	-30
15 19:54:41	77.334	0.845	N	144	Moon	2739	3915	-2.552	-0.043	-0.002	0.070	2.985	-24
15 20:39:55	77.365	0.861	N	133	Moon	2693	3584	-2.287	0.085	0.097	0.071	0.295	-61
15 21:25:07	77.396	0.878	N	143		2761	3909	-2.226	-0.084	-0.078	0.069	-3.177	-48
16 19:27:12	78.314	1.369	N	146	Moon	2710	3867	-3.130	-0.327	-0.069	0.071	0.040	-29
16 20:12:25	78.346	1.385	N	148	Moon	2735	4044	-2.706	-0.140	0.085	0.070	3.591	30
16 20:57:37	78.377	1.402	N	151	Moon	2802	4122	-2.236	-0.063	-0.018	0.069	10.411	-39
17 18:20:45	79.268	1.878	N	135		2706	3739	-2.165	-0.028	-0.033	0.071	-0.629	-33
17 19:05:56	79.299	1.895	N	130		2671	3441	-1.782	0.041	0.030	0.071	-1.757	-25
17 19:51:09	79.331	1.912	N	132		2698	3503	-1.406	0.039	0.009	0.071	-6.538	70
20 18:49:53	82.288	3.491	N	86		2194	1903	1.561	0.186	0.003	0.084	19.874	126
20 19:35:05	82.320	3.508	N	82		2173	1817	1.979	-0.008	-0.003	0.085	27.037	18
22 21:18:44	84.391	4.615	N	93	Moon	2249	2087	3.210	0.100	0.025	0.083	34.575	15
22 22:03:58	84.423	4.632	N	106	Moon	2484	2539	2.815	0.024	0.014	0.076	29.770	-70
23 21:53:42	85.415	5.162	N	147		2714	3773	1.397	0.027	0.008	0.070	6.158	-40
24 18:46:11	86.285	5.627	N	140	Moon	2779	3766	2.885	0.000	-0.023	0.069	37.130	-104

(b) Observations of the early 2011 run.

UTC 2013 Nov	BJD 2456600+	Cycle 946+	Instr.	S/N	Comment	S/N_I	S/N_V	RV_{raw} ($km\,s^{-1}$)	$RV_{filt/ZDI}$ ($km\,s^{-1}$)	$RV_{filt/GP}$ ($km\,s^{-1}$)	σ_{RV} ($km\,s^{-1}$)	$EW_{H\alpha}$ ($km\,s^{-1}$)	B_{long} (G)
07 22:44:14	4.453	0.528	N	118	Isolated[a]	1792	2855	-0.186		0.059	0.101	42.094	-87
07 23:18:58	4.477	0.541	N	88	Isolated[a]	1783	2191	-0.922		-0.033	0.102	48.184	-50
2013 Dec	2456600+	959+											
02 21:38:55	29.408	0.859	N	86		1700	1941	-0.374	0.277	0.048	0.106	-0.205	-279
03 01:09:58	29.554	0.937	N	123		2042	3010	-2.818	0.160	0.191	0.090	21.666	-60
03 21:25:55	30.399	1.388	N	134		2193	3409	5.209	0.490	0.020	0.085	27.245	-147
04 00:57:14	30.545	1.467	N	130		2161	3175	2.841	0.198	0.084	0.086	52.594	19
04 21:43:24	31.411	1.929	N	150		2282	3959	-3.122	-0.282	-0.172	0.082	24.550	-47
05 21:15:09	32.391	2.453	N	135		2261	3536	3.431	0.150	-0.070	0.082	53.441	-61
06 00:54:07	32.543	2.534	N	131		2192	3327	-0.989	-0.292	-0.044	0.085	56.121	-54
06 21:12:11	33.389	2.986	N	130		2211	3431	-3.067	0.161	-0.004	0.084	18.241	-76
07 00:41:21	33.534	3.063	N	147		2222	3798	-2.708	-0.107	-0.017	0.084	-9.025	-158
07 22:27:39	34.441	3.548	N	148		2285	3983	-1.396	-0.289	-0.074	0.082	49.419	42
08 02:30:09	34.610	3.638	N	148		2247	3876	0.152	-0.008	0.130	0.082	46.173	-81
08 22:49:21	35.456	4.090	N	165	He I D_3 flare[a,b]							21.045	
09 01:31:57	35.569	4.151	N	163	He I D_3 flare[a,b]							12.729	
09 20:41:53	36.368	4.577	N	112		1905	2698	-1.451	-0.126	0.011	0.096	49.343	21
10 00:43:24	36.536	4.667	N	148		2263	3888	1.360	0.118	0.129	0.082	32.864	-83
10 01:29:32	36.568	4.684	N	149		2278	3953	1.840	0.041	-0.068	0.082	28.874	-111
10 20:34:03	37.362	5.109	N	140		2243	3654	-2.267	0.140	0.016	0.083	-5.886	-72
11 00:34:03	37.529	5.197	N	151		2318	4015	-2.188	-0.120	-0.069	0.080	-31.885	104
11 20:33:11	38.362	5.642	N	147		2272	3909	0.047	-0.331	-0.204	0.082	55.426	-87
12 00:53:59	38.543	5.739	N	148		2317	3928	2.837	0.232	0.034	0.081	19.504	-101
12 20:28:06	39.358	6.175	N	160		2359	4379	-2.323	-0.026	0.020	0.079	-13.047	-6
13 00:27:29	39.525	6.263	N	169		2375	4647	-0.553	-0.468	-0.081	0.079	-5.297	-52
14 20:21:32	41.354	7.241	N	149		2268	3915	-0.962	0.022	0.119	0.082	-8.269	61
15 01:21:03	41.562	7.352	N	141		2230	3620	4.118	0.065	0.009	0.083	3.858	-62
15 20:34:39	42.363	7.780	N	132	Moon	2168	3299	1.919	-0.107	-0.032	0.085	-4.559	-103
20 20:38:45	47.365	10.452	N	126		2198	3078	3.010	0.020	-0.007	0.085	34.878	-100
21 00:57:56	47.545	10.548	N	136		2185	3356	-1.160	0.045	0.092	0.085	36.919	-54

(c) Observations of the late 2013 run.

UTC 2015 Dec	BJD 2457300+	Cycle 1349+	Instr.	S/N	Comment	S/N_I	S/N_V	RV_{raw} ($km\,s^{-1}$)	$RV_{filt/ZDI}$ ($km\,s^{-1}$)	$RV_{filt/GP}$ ($km\,s^{-1}$)	σ_{RV} ($km\,s^{-1}$)	$EW_{H\alpha}$ ($km\,s^{-1}$)	B_{long} (G)
01 22:44:05	58.453	0.313	N	121		1776	2974	2.464	0.058	0.050	0.102	-6.540	-60
02 02:00:59	58.590	0.386	N	109		1690	2561	3.011	0.461	0.122	0.107	1.045	-239
02 22:07:10	59.427	0.833	N	101		1699	2360	-1.825	-0.080	0.008	0.107	0.196	-262
03 01:30:49	59.569	0.909	N	114		1807	2794	-2.520	0.226	0.066	0.101	-5.859	-108
03 21:39:29	60.408	1.357	N	109		1743	2543	3.040	0.203	-0.115	0.104	-10.697	-112
04 02:23:31	60.605	1.462	N	119		1786	2804	0.070	-0.168	-0.009	0.102	19.800	-165
06 22:53:07	63.459	2.987	N	152		1875	3764	-2.324	-0.086	-0.002	0.097	9.991	-17
07 01:15:19	63.558	3.040	N	152		1886	3853	-1.401	0.091	0.004	0.097	-0.787	-68
07 23:02:53	64.466	3.525	N	94		1633	2122	-0.690	0.173	0.093	0.110	30.595	-70
08 01:31:49	64.569	3.580	N	142		1844	3566	-0.195	-0.186	0.008	0.099	34.071	-251
09 21:05:04	66.384	4.549	N	103		1713	2409	-0.775	-0.116	-0.083	0.105	37.568	-128
11 22:05:07	68.426	5.640	N	129		2147	3344	1.638	-0.028	0.028	0.086	71.742	-187
12 00:56:44	68.545	5.704	N	136		2124	3424	2.077	0.065	-0.159	0.087	28.515	-65
12 22:13:39	69.432	6.177	N	113		2077	2927	-0.153	0.050	0.015	0.089	-29.140	-58
13 01:11:33	69.555	6.243	N	135		2144	3458	0.521	-0.283	-0.032	0.086	-16.825	-23
13 22:12:08	70.431	6.711	N	106		1962	2553	2.337	0.433	0.186	0.093	9.573	-93
14 01:29:54	70.568	6.784	N	134		2095	3343	-0.445	-0.204	-0.035	0.088	9.052	-145
18 01:04:45	74.550	8.912	N	124		2036	3124	-2.902	-0.225	-0.046	0.090	13.281	-144
18 21:36:31	75.406	9.369	N	138		2087	3452	2.918	0.224	-0.000	0.089	-21.444	-171
19 01:09:10	75.553	9.447	N	124		1972	3016	0.091	-0.426	-0.039	0.093	17.394	-189
19 20:09:16	76.345	9.870	N	106		1918	2497	-2.441	-0.020	-0.023	0.095	21.741	-16
2016 Jan	2457400+	1376+							($km\,s^{-1}$)	($km\,s^{-1}$)	($km\,s^{-1}$)		
20 22:42:30	8.450	0.021	N	153	He I D_3 flare[a,b]							23.847	
20 23:35:42	8.487	0.040	N	154	He I D_3 flare[a,b]							13.077	
21 18:28:09	9.273	0.460	N	127		2817	3105	-0.896	-0.014	0.003	0.068	31.341	-154
21 23:28:57	9.482	0.572	N	121		2765	2956	-0.092	-0.064	-0.003	0.069	37.161	-280
24 19:12:18	12.303	2.079	N	105		2702	2587	-1.095	0.136	-0.002	0.071	-10.058	54
24 21:38:26	12.405	2.134	N	121		2831	3058	-0.414	-0.037	0.014	0.068	-23.494	45
26 18:19:49	14.267	3.128	N	135		2930	3444	-0.506	-0.034	-0.016	0.066	-31.556	0
26 23:23:18	14.478	3.241	N	140		2886	3485	1.534	-0.047	0.010	0.067	-39.330	-34
27 18:13:34	15.262	3.660	N	124		2853	3091	2.589	0.058	-0.003	0.068	28.597	-202
27 20:34:49	15.360	3.712	N	122		2898	3126	2.359	0.047	0.005	0.067	31.543	-94
29 21:36:35	17.403	4.803	N	100		2792	2378	-0.924	-0.214	0.011	0.069	41.991	-166

(d) Observations of the late 2015 and early 2016 runs.

Table A2. Information on the V410 Tau photometric data. For each table, the first and second columns indicate the time at which the observations were taken, in UTC and BJD format respectively. The third column contains the measured visible magnitude, then columns 4 to 6 list color indexes B-V, V-R_J and V-I_J provided in the Johnson UBVRI system, and column 7 indicates the name of the telescope used for the observation.

Date	HJD (2454000+)	V (mag)	B-V	V-R_J	V-I_J	Telescope	Date	HJD (2455000+)	V (mag)	B-V	V-R_J	V-I_J	Telescope
03-Aug-2008	682.5282	10.878	1.182	1.075	-	AZT-11	15-Aug-2009	59.5212	10.894	1.147	1.133	-	AZT-11
04-Aug-2008	683.5300	10.896	1.192	-	-	AZT-11	15-Aug-2009	59.5320	10.904	1.149	1.131	-	AZT-11
09-Aug-2008	688.5258	10.857	1.169	1.046	-	AZT-11	15-Aug-2009	59.5418	10.886	1.154	1.095	-	AZT-11
10-Aug-2008	689.5304	10.806	1.185	1.047	-	AZT-11	16-Aug-2009	60.5209	10.812	1.164	1.063	-	AZT-11
12-Aug-2008	691.5306	10.831	1.168	1.062	-	AZT-11	16-Aug-2009	60.5289	10.807	1.167	1.045	-	AZT-11
13-Aug-2008	692.5308	10.918	1.203	1.059	-	AZT-11	16-Aug-2009	60.5369	10.812	1.169	1.072	-	AZT-11
14-Aug-2008	693.5253	10.874	1.166	1.054	-	AZT-11	19-Aug-2009	63.5237	10.857	1.152	1.126	-	AZT-11
14-Aug-2008	693.5471	10.887	1.183	1.051	-	AZT-11	19-Aug-2009	63.5314	10.855	1.153	1.077	-	AZT-11
26-Aug-2008	705.5112	10.842	1.188	1.025	-	AZT-11	19-Aug-2009	63.5394	10.829	1.148	1.069	-	AZT-11
01-Sep-2008	711.5369	10.891	1.189	1.047	-	AZT-11	19-Aug-2009	63.5474	10.838	1.157	1.084	-	AZT-11
01-Sep-2008	711.5527	10.888	1.190	1.041	-	AZT-11	21-Aug-2009	65.5183	10.798	1.146	1.058	-	AZT-11
02-Sep-2008	712.5160	10.855	1.182	1.049	-	AZT-11	21-Aug-2009	65.5267	10.794	1.156	1.058	-	AZT-11
02-Sep-2008	712.5308	10.859	1.173	1.035	-	AZT-11	21-Aug-2009	65.5348	10.796	1.143	1.054	-	AZT-11
02-Sep-2008	712.5763	10.857	1.159	1.055	-	AZT-11	24-Aug-2009	68.4813	10.830	1.166	1.053	-	AZT-11
03-Sep-2008	713.5146	10.868	1.184	1.047	-	AZT-11	24-Aug-2009	68.4892	10.847	1.165	1.071	-	AZT-11
03-Sep-2008	713.5295	10.861	1.181	1.035	-	AZT-11	24-Aug-2009	68.4982	10.841	1.159	1.066	-	AZT-11
04-Sep-2008	714.5299	10.850	1.151	1.051	-	AZT-11	25-Aug-2009	69.5189	10.781	1.140	1.103	-	AZT-11
05-Sep-2008	715.4831	10.861	1.148	1.051	-	AZT-11	25-Aug-2009	69.5258	10.769	1.153	1.098	-	AZT-11
05-Sep-2008	715.5357	10.862	1.150	1.095	-	T60Sim	25-Aug-2009	69.5329	10.771	1.151	1.080	-	AZT-11
05-Sep-2008	715.5636	10.842	1.151	1.039	-	AZT-11	27-Aug-2009	71.5171	10.788	1.141	1.042	-	AZT-11
06-Sep-2008	716.5612	10.835	1.170	1.070	-	T60Sim	27-Aug-2009	71.5242	10.783	1.159	1.036	-	AZT-11
07-Sep-2008	717.5431	10.839	1.210	1.052	-	T60Sim	29-Aug-2009	73.5157	10.810	1.157	1.072	-	AZT-11
08-Sep-2008	718.4556	10.824	1.177	1.038	-	T60Sim	29-Aug-2009	73.5229	10.808	1.162	1.071	-	AZT-11
08-Sep-2008	718.5607	10.843	1.185	1.036	-	T60Sim	29-Aug-2009	73.5297	10.810	1.162	1.073	-	AZT-11
11-Sep-2008	721.5327	10.858	1.189	1.002	-	T60Sim	16-Sep-2009	91.4903	10.892	1.155	1.079	-	AZT-11
30-Sep-2008	740.5057	10.843	1.202	1.045	-	T60Sim	16-Sep-2009	91.4972	10.887	1.147	1.083	-	AZT-11
30-Sep-2008	740.5724	10.835	1.186	1.044	-	AZT-11	16-Sep-2009	91.5040	10.891	1.140	1.076	-	AZT-11
30-Sep-2008	740.6480	10.826	1.175	1.044	-	AZT-11	20-Sep-2009	95.4203	10.792	1.155	1.042	-	AZT-11
01-Oct-2008	741.5784	10.878	1.176	1.057	-	AZT-11	20-Sep-2009	95.4286	10.787	1.149	1.045	-	AZT-11
04-Oct-2008	744.5202	10.843	1.171	1.056	-	T60Sim	20-Sep-2009	95.4360	10.773	1.158	1.037	-	AZT-11
04-Oct-2008	744.5202	10.822	1.162	1.042	-	T60Sim	22-Sep-2009	97.5267	10.745	1.154	1.022	-	AZT-11
23-Oct-2008	763.5826	10.872	1.167	1.048	-	AZT-11	22-Sep-2009	97.5338	10.747	1.150	1.049	-	AZT-11
30-Oct-2008	770.4631	10.822	1.173	1.056	-	AZT-11	22-Sep-2009	97.5410	10.747	1.147	1.028	-	AZT-11
30-Oct-2008	770.6079	10.805	1.174	1.027	-	AZT-11	24-Sep-2009	99.5012	10.743	1.166	1.017	-	AZT-11
07-Nov-2008	778.5546	10.879	1.185	1.050	-	AZT-11	24-Sep-2009	99.5087	10.748	1.171	1.032	-	AZT-11
08-Nov-2008	779.6318	10.859	1.169	1.052	-	AZT-11	24-Sep-2009	99.5159	10.751	1.158	1.026	-	AZT-11
01-Dec-2008	802.5990	10.811	1.157	1.053	-	AZT-11	26-Sep-2009	101.5720	10.770	1.162	1.014	-	AZT-11
01-Jan-2009	833.1937	10.871	1.168	1.042	-	AZT-11	26-Sep-2009	101.5777	10.777	1.172	1.043	-	AZT-11
21-Jan-2009	853.2120	10.863	1.181	1.047	-	AZT-11	26-Sep-2009	101.5828	10.791	1.167	1.050	-	AZT-11
26-Jan-2009	858.2434	10.859	1.160	1.055	-	AZT-11	27-Sep-2009	102.4691	10.896	1.180	1.030	-	AZT-11
							28-Sep-2009	103.5756	10.774	1.181	1.042	-	AZT-11
							30-Sep-2009	105.4924	10.788	1.187	1.053	-	AZT-11
							30-Sep-2009	105.5064	10.792	1.176	1.042	-	AZT-11
							30-Sep-2009	105.5868	10.778	1.186	1.051	-	AZT-11
							30-Sep-2009	105.5923	10.777	1.190	1.016	-	AZT-11

(a) Photometric measurements of the set 08b+09a (left) and of the first half of the set 09b+10a (right).

Table A2. (Continued from previous page).

Date	HJD (2455000+)	V (mag)	B-V	V-R$_J$	V-I$_J$	Telescope	Date	HJD (2455000+)	V (mag)	B-V	V-R$_J$	V-I$_J$	Telescope
09-Oct-2009	114.4547	10.734	1.136	1.025	-	AZT-11	03-Sep-2010	443.5388	10.782	1.149	1.032	-	AZT-11
10-Oct-2009	115.3930	10.850	1.178	1.043	-	AZT-11	03-Sep-2010	443.5463	10.807	1.150	1.037	-	AZT-11
10-Oct-2009	115.4597	10.873	1.162	1.072	-	AZT-11	03-Sep-2010	443.5538	10.801	1.163	1.049	-	AZT-11
11-Oct-2009	116.4768	10.744	1.166	1.031	-	AZT-11	04-Sep-2010	444.5159	10.776	1.177	1.042	-	AZT-11
11-Oct-2009	116.5391	10.763	1.167	1.032	-	AZT-11	04-Sep-2010	444.5222	10.773	1.190	1.039	-	AZT-11
11-Oct-2009	116.6024	10.776	1.175	1.042	-	AZT-11	04-Sep-2010	444.5284	10.776	1.167	1.037	-	AZT-11
19-Oct-2009	124.5660	10.773	1.163	1.052	-	AZT-11	05-Sep-2010	445.5842	10.742	1.140	1.029	-	AZT-11
19-Oct-2009	124.5733	10.808	1.176	1.034	-	AZT-11	10-Sep-2010	450.5110	10.838	1.166	1.038	-	AZT-11
23-Oct-2009	128.3930	10.823	1.187	1.029	-	AZT-11	10-Sep-2010	450.5175	10.839	1.171	1.025	-	AZT-11
23-Oct-2009	128.4038	10.819	1.181	1.043	-	AZT-11	10-Sep-2010	450.5238	10.838	1.157	1.040	-	AZT-11
31-Oct-2009	136.4814	10.846	1.138	1.069	-	AZT-11	11-Sep-2010	451.5063	10.805	1.179	1.067	-	AZT-11
31-Oct-2009	136.4886	10.850	1.133	1.067	-	AZT-11	11-Sep-2010	451.5126	10.804	1.177	1.051	-	AZT-11
31-Oct-2009	136.4958	10.839	1.140	1.060	-	AZT-11	11-Sep-2010	451.5187	10.810	1.178	1.071	-	AZT-11
07-Nov-2009	143.5181	10.870	1.180	1.046	-	AZT-11	14-Sep-2010	454.5298	10.853	1.181	1.050	-	AZT-11
07-Nov-2009	143.6312	10.895	1.175	1.048	-	AZT-11	14-Sep-2010	454.5382	10.849	1.180	1.048	-	AZT-11
08-Nov-2009	144.3301	10.686	1.146	1.012	-	AZT-11	14-Sep-2010	454.5455	10.863	1.161	1.053	-	AZT-11
08-Nov-2009	144.3365	10.699	1.148	1.007	-	AZT-11	15-Sep-2010	455.5121	10.815	1.186	1.062	-	AZT-11
08-Nov-2009	144.5302	10.741	1.164	1.041	-	AZT-11	15-Sep-2010	455.5190	10.815	1.182	1.062	-	AZT-11
08-Nov-2009	144.5420	10.732	1.162	1.031	-	AZT-11	15-Sep-2010	455.5258	10.811	1.179	1.083	-	AZT-11
08-Nov-2009	144.6125	10.765	1.158	1.045	-	AZT-11	16-Sep-2010	456.5575	10.802	1.153	1.041	-	AZT-11
09-Nov-2009	145.3064	10.847	1.192	1.040	-	AZT-11	17-Sep-2010	457.5121	10.787	1.174	1.055	-	AZT-11
09-Nov-2009	145.5874	10.915	1.180	1.051	-	AZT-11	17-Sep-2010	457.5186	10.779	1.178	1.030	-	AZT-11
09-Nov-2009	145.6245	10.862	1.178	1.053	-	AZT-11	17-Sep-2010	457.5251	10.779	1.187	1.063	-	AZT-11
10-Nov-2009	146.5472	10.759	1.176	1.021	-	AZT-11	18-Sep-2010	458.5115	10.770	1.160	1.020	-	AZT-11
10-Nov-2009	146.5560	10.757	1.174	1.017	-	AZT-11	18-Sep-2010	458.5181	10.773	1.145	1.033	-	AZT-11
23-Nov-2009	159.4806	10.717	1.160	1.019	-	AZT-11	18-Sep-2010	458.5246	10.772	1.151	1.049	-	AZT-11
23-Nov-2009	159.4856	10.719	1.160	1.024	-	AZT-11	12-Oct-2010	482.5118	10.842	1.172	1.034	-	AZT-11
21-Dec-2009	187.2062	10.727	1.157	1.025	-	AZT-11	12-Oct-2010	482.5180	10.844	1.178	1.039	-	AZT-11
21-Dec-2009	187.2141	10.729	1.147	1.030	-	AZT-11	12-Oct-2010	482.5245	10.848	1.158	1.057	-	AZT-11
21-Dec-2009	187.2227	10.735	1.136	1.030	-	AZT-11	29-Oct-2010	499.5370	10.819	1.164	1.056	-	AZT-11
21-Dec-2009	187.3067	10.712	1.144	1.021	-	AZT-11	30-Oct-2010	500.5347	10.806	1.177	1.042	-	AZT-11
21-Dec-2009	187.3151	10.715	1.150	1.012	-	AZT-11	01-Nov-2010	502.5591	10.778	1.167	1.042	-	AZT-11
21-Dec-2009	187.3225	10.708	1.148	1.018	-	AZT-11	05-Nov-2010	506.5768	10.776	1.172	1.051	-	AZT-11
24-Dec-2009	190.2749	10.882	1.192	1.055	-	AZT-11	06-Nov-2010	507.5761	10.778	1.172	1.029	-	AZT-11
24-Dec-2009	190.2824	10.892	1.191	1.076	-	AZT-11	13-Nov-2010	514.5477	10.811	1.163	1.045	-	AZT-11
24-Dec-2009	190.3358	10.908	1.189	1.058	-	AZT-11	14-Nov-2010	515.5455	10.805	1.172	1.018	-	AZT-11
26-Jan-2010	223.2694	10.772	1.186	1.041	-	AZT-11	17-Nov-2010	518.5531	10.772	1.152	1.014	-	AZT-11
26-Jan-2010	223.2732	10.766	1.171	1.039	-	AZT-11	18-Nov-2010	520.4961	10.747	1.157	1.039	-	AZT-11
26-Jan-2010	223.2771	10.770	1.178	1.041	-	AZT-11	18-Nov-2010	520.4939	10.752	1.155	1.024	-	AZT-11
26-Jan-2010	223.2814	10.775	1.164	1.047	-	AZT-11	08-Dec-2010	539.4696	10.815	1.164	1.052	-	AZT-11
22-Feb-2010	250.2121	10.884	1.187	1.048	-	AZT-11	08-Dec-2010	539.4811	10.818	1.173	1.053	-	AZT-11
22-Feb-2010	250.2159	10.908	1.155	1.027	-	AZT-11	08-Dec-2010	539.4859	10.813	1.179	1.052	-	AZT-11
22-Feb-2010	250.2197	10.890	1.142	1.078	-	AZT-11							
22-Feb-2010	250.2236	10.913	1.169	1.064	-	AZT-11							

(b) Photometric measurements of the second half of the set 09b+10a (left) and of the set 10b (right).

Table A2. (Continued from previous page).

Date	HJD (2455000+)	V (mag)	B-V	V-R$_J$	V-I$_J$	Telescope	Date	HJD (2455000+)	V (mag)	B-V	V-R$_J$	V-I$_J$	Telescope
29-Jul-2011	772.5187	10.801	1.154	1.049	1.767	AZT-11	23-Sep-2011	828.5423	10.848	1.193	1.059	1.778	AZT-11
02-Aug-2011	776.5394	10.816	1.176	1.030	1.762	AZT-11	23-Sep-2011	828.5512	10.857	1.184	1.048	1.787	AZT-11
03-Aug-2011	777.5088	10.847	1.183	1.059	1.787	AZT-11	26-Sep-2011	831.5396	10.883	1.180	1.057	1.801	AZT-11
03-Aug-2011	777.5158	10.834	1.203	1.050	1.780	AZT-11	26-Sep-2011	831.5461	10.878	1.185	1.056	1.801	AZT-11
03-Aug-2011	777.5221	10.844	1.191	1.069	1.794	AZT-11	26-Sep-2011	831.5527	10.883	1.187	1.062	1.803	AZT-11
05-Aug-2011	779.5239	10.823	1.185	1.042	1.783	AZT-11	28-Sep-2011	833.5811	10.877	1.198	1.059	1.803	AZT-11
05-Aug-2011	779.5312	10.826	1.184	1.035	1.789	AZT-11	28-Sep-2011	833.5880	10.878	1.185	1.072	1.799	AZT-11
05-Aug-2011	779.5383	10.831	1.186	1.054	1.790	AZT-11	28-Sep-2011	833.5944	10.893	1.187	1.068	1.815	AZT-11
06-Aug-2011	780.5127	10.742	1.163	1.012	1.715	AZT-11	02-Oct-2011	837.5672	10.844	1.194	1.059	1.783	AZT-11
06-Aug-2011	780.5191	10.742	1.148	1.021	1.720	AZT-11	02-Oct-2011	837.5745	10.832	1.188	1.055	1.782	AZT-11
06-Aug-2011	780.5259	10.738	1.148	1.025	1.718	AZT-11	02-Oct-2011	837.5813	10.848	1.182	1.059	1.795	AZT-11
07-Aug-2011	781.5278	10.815	1.199	1.035	1.773	AZT-11	05-Oct-2011	840.5208	10.757	1.154	1.041	1.730	AZT-11
23-Aug-2011	797.5141	10.775	1.158	1.029	1.734	AZT-11	05-Oct-2011	840.5275	10.758	1.156	1.028	1.737	AZT-11
23-Aug-2011	797.5221	10.755	1.150	1.027	1.729	AZT-11	05-Oct-2011	840.5341	10.766	1.150	1.027	1.741	AZT-11
23-Aug-2011	797.5289	10.758	1.152	1.031	1.731	AZT-11	20-Oct-2011	855.6103	10.801	1.179	1.071	1.766	AZT-11
23-Aug-2011	797.5168	10.765	1.190	1.019	1.725	AZT-11	20-Oct-2011	855.6176	10.821	1.166	1.045	1.757	AZT-11
23-Aug-2011	797.5241	10.755	1.158	1.033	1.721	AZT-11	20-Oct-2011	855.6247	10.808	1.197	1.045	1.761	AZT-11
23-Aug-2011	797.5308	10.756	1.160	1.035	1.721	AZT-11	22-Oct-2011	857.5245	10.834	1.151	1.048	1.770	AZT-11
24-Aug-2011	798.5194	10.831	1.173	1.054	1.786	AZT-11	04-Nov-2011	870.6130	10.816	1.160	1.062	1.780	AZT-11
24-Aug-2011	798.5278	10.828	1.182	1.050	1.783	AZT-11	06-Nov-2011	872.6375	10.882	1.173	1.066	1.799	AZT-11
24-Aug-2011	798.5347	10.828	1.177	1.054	1.781	AZT-11	07-Nov-2011	873.5742	10.854	1.178	1.062	1.781	AZT-11
25-Aug-2011	799.5576	10.815	1.166	1.049	1.773	AZT-11	19-Nov-2011	885.5749	10.793	1.149	1.046	1.761	AZT-11
25-Aug-2011	799.5638	10.821	1.163	1.054	1.771	AZT-11	23-Nov-2011	889.6055	10.908	1.205	1.051	1.807	AZT-11
27-Aug-2011	801.5312	10.864	1.181	1.060	1.797	AZT-11	25-Nov-2011	891.5719	10.878	1.183	1.080	1.803	AZT-11
27-Aug-2011	801.5385	10.869	1.175	1.051	1.794	AZT-11	25-Nov-2011	891.5787	10.893	1.196	1.080	1.801	AZT-11
27-Aug-2011	801.5457	10.861	1.180	1.057	1.793	AZT-11	25-Nov-2011	891.5855	10.867	1.196	1.075	1.799	AZT-11
29-Aug-2011	803.5316	10.877	1.191	1.056	1.797	AZT-11	28-Nov-2011	894.5180	10.741	1.154	1.020	1.719	AZT-11
29-Aug-2011	803.5380	10.876	1.198	1.053	1.803	AZT-11	02-Dec-2011	898.2574	10.732	1.144	1.030	1.714	AZT-11
29-Aug-2011	803.5445	10.872	1.190	1.050	1.797	AZT-11	02-Dec-2011	898.3005	10.727	1.127	1.017	1.726	AZT-11
01-Sep-2011	806.4727	10.818	1.142	1.036	1.761	AZT-11	03-Dec-2011	899.5691	10.841	1.193	1.067	1.797	AZT-11
01-Sep-2011	806.4800	10.809	1.159	1.026	1.753	AZT-11	04-Dec-2011	900.5568	10.787	1.174	1.022	1.757	AZT-11
01-Sep-2011	806.4873	10.798	1.159	1.034	1.746	AZT-11	28-Dec-2011	924.5089	10.722	1.157	1.006	1.718	AZT-11
03-Sep-2011	808.5388	10.739	1.142	1.009	1.719	AZT-11	28-Dec-2011	924.5157	10.717	1.159	1.010	1.716	AZT-11
03-Sep-2011	808.5456	10.743	1.141	1.003	1.723	AZT-11	19-Jan-2012	946.2393	10.817	1.183	1.058	1.780	AZT-11
03-Sep-2011	808.5525	10.752	1.142	1.026	1.722	AZT-11	19-Jan-2012	946.2463	10.819	1.177	1.056	1.781	AZT-11
06-Sep-2011	811.5790	10.832	1.183	1.059	1.786	AZT-11	28-Jan-2012	955.2345	10.869	1.175	1.058	1.798	AZT-11
23-Sep-2011	828.5314	10.848	1.189	1.059	1.787	AZT-11							

(c) Photometric measurements of the set 11b+12a.

Table A2. (Continued from previous page).

Date	HJD (2456000+)	V (mag)	B-V	V-R_J	V-I_J	Telescope	Date	HJD (2456000+)	V (mag)	B-V	V-R_J	V-I_J	Telescope
13-Aug-2012	153.4989	10.801	1.166	1.036	1.762	AZT-11	16-Oct-2012	217.5183	10.802	1.190	1.048	1.789	AZT-11
13-Aug-2012	153.5059	10.836	1.195	1.078	1.768	AZT-11	17-Oct-2012	218.6062	10.732	1.164	1.021	1.735	AZT-11
13-Aug-2012	153.5129	10.820	1.187	1.063	1.762	AZT-11	17-Oct-2012	218.6137	10.740	1.156	1.020	1.742	AZT-11
18-Aug-2012	158.4723	10.635	1.121	1.013	1.674	AZT-11	17-Oct-2012	218.6220	10.752	1.155	1.037	1.745	AZT-11
18-Aug-2012	158.4829	10.695	1.139	1.028	1.720	AZT-11	20-Oct-2012	221.6156	10.860	1.193	1.062	1.803	AZT-11
18-Aug-2012	158.4913	10.670	1.121	1.022	1.705	AZT-11	21-Oct-2012	222.5558	10.799	1.181	1.049	1.774	AZT-11
18-Aug-2012	158.4988	10.642	1.125	1.008	1.692	AZT-11	21-Oct-2012	222.5627	10.807	1.165	1.038	1.782	AZT-11
21-Aug-2012	161.5144	10.829	1.189	1.072	1.790	AZT-11	21-Oct-2012	222.5702	10.791	1.184	1.050	1.774	AZT-11
21-Aug-2012	161.5214	10.832	1.197	1.061	1.799	AZT-11	23-Oct-2012	224.5439	10.804	1.188	1.060	1.781	AZT-11
21-Aug-2012	161.5306	10.824	1.177	1.056	1.802	AZT-11	23-Oct-2012	224.5509	10.809	1.183	1.042	1.777	AZT-11
22-Aug-2012	162.5606	10.768	1.171	1.012	1.751	AZT-11	23-Oct-2012	224.5577	10.817	1.186	1.050	1.780	AZT-11
22-Aug-2012	162.5672	10.778	1.167	1.041	1.756	AZT-11	25-Oct-2012	226.5496	10.793	1.177	1.040	1.766	AZT-11
23-Aug-2012	163.5296	10.780	1.164	1.035	1.765	AZT-11	25-Oct-2012	226.5576	10.788	1.177	1.034	1.764	AZT-11
23-Aug-2012	163.5560	10.815	1.193	1.064	1.774	AZT-11	25-Oct-2012	226.5645	10.800	1.176	1.047	1.775	AZT-11
24-Aug-2012	164.5151	10.790	1.162	1.042	1.765	AZT-11	26-Oct-2012	227.5960	10.756	1.165	1.035	1.751	AZT-11
24-Aug-2012	164.5221	10.789	1.168	1.033	1.764	AZT-11	09-Nov-2012	241.3498	10.818	1.176	1.052	1.776	AZT-11
24-Aug-2012	164.5288	10.794	1.169	1.047	1.769	AZT-11	09-Nov-2012	241.3572	10.784	1.176	1.034	1.776	AZT-11
25-Aug-2012	165.4764	10.816	1.173	1.043	1.776	AZT-11	11-Nov-2012	243.4725	10.782	1.159	1.045	1.759	AZT-11
25-Aug-2012	165.4836	10.801	1.175	1.046	1.767	AZT-11	11-Nov-2012	243.4829	10.780	1.168	1.052	1.757	AZT-11
25-Aug-2012	165.4907	10.808	1.165	1.053	1.776	AZT-11	11-Nov-2012	243.4986	10.783	1.164	1.050	1.759	AZT-11
26-Aug-2012	166.5257	10.809	1.178	1.042	1.777	AZT-11	12-Nov-2012	244.4816	10.730	1.168	1.027	1.746	AZT-11
26-Aug-2012	166.5327	10.809	1.173	1.040	1.778	AZT-11	12-Nov-2012	244.4910	10.732	1.167	1.024	1.746	AZT-11
26-Aug-2012	166.5402	10.812	1.190	1.047	1.774	AZT-11	12-Nov-2012	244.5133	10.734	1.161	1.040	1.744	AZT-11
31-Aug-2012	171.5560	10.716	1.154	1.017	1.737	AZT-11	17-Nov-2012	249.4379	10.843	1.200	1.067	1.792	AZT-11
31-Aug-2012	171.5628	10.719	1.155	1.015	1.739	AZT-11	17-Nov-2012	249.4459	10.847	1.193	1.059	1.798	AZT-11
31-Aug-2012	171.5692	10.716	1.169	1.039	1.739	AZT-11	17-Nov-2012	249.4524	10.849	1.195	1.069	1.797	AZT-11
11-Sep-2012	182.5588	10.775	1.167	1.043	1.761	AZT-11	08-Dec-2012	270.4771	10.813	1.176	1.047	1.778	AZT-11
11-Sep-2012	182.5663	10.791	1.161	1.042	1.772	AZT-11	08-Dec-2012	270.4845	10.808	1.173	1.052	1.778	AZT-11
13-Sep-2012	184.5151	10.771	1.168	1.047	1.760	AZT-11	08-Dec-2012	270.4924	10.796	1.165	1.057	1.778	AZT-11
13-Sep-2012	184.5232	10.748	1.160	1.031	1.753	AZT-11	31-Dec-2012	293.2226	10.681	1.150	1.025	1.726	AZT-11
13-Sep-2012	184.5295	10.758	1.162	1.041	1.763	AZT-11	31-Dec-2012	293.2294	10.681	1.162	1.020	1.716	AZT-11
17-Sep-2012	188.5117	10.712	1.147	1.005	1.750	AZT-11	01-Jan-2013	294.1756	10.799	1.183	1.036	1.759	AZT-11
17-Sep-2012	188.5201	10.702	1.162	1.012	1.727	AZT-11	01-Jan-2013	294.1848	10.809	1.175	1.050	1.773	AZT-11
17-Sep-2012	188.5269	10.721	1.145	1.009	1.739	AZT-11	01-Jan-2013	294.1998	10.804	1.176	1.039	1.765	AZT-11
23-Sep-2012	194.5221	10.809	1.177	1.042	1.782	AZT-11	14-Jan-2013	307.1871	10.784	1.166	1.040	1.752	AZT-11
23-Sep-2012	194.5300	10.810	1.180	1.034	1.783	AZT-11	14-Jan-2013	307.1984	10.786	1.161	1.032	1.751	AZT-11
23-Sep-2012	194.5375	10.809	1.161	1.039	1.785	AZT-11	14-Jan-2013	307.2176	10.782	1.162	1.038	1.754	AZT-11
25-Sep-2012	196.5659	10.807	1.187	1.044	1.776	AZT-11	19-Jan-2013	312.1867	10.727	1.144	1.031	1.737	AZT-11
25-Sep-2012	196.5764	10.810	1.180	1.062	1.781	AZT-11	19-Jan-2013	312.1936	10.728	1.150	1.032	1.732	AZT-11
25-Sep-2012	196.5840	10.813	1.177	1.062	1.783	AZT-11	19-Jan-2013	312.2004	10.728	1.150	1.022	1.736	AZT-11
26-Sep-2012	197.5275	10.726	1.110	1.016	1.729	AZT-11	05-Feb-2013	329.3020	10.843	1.178	1.055	1.784	AZT-11
26-Sep-2012	197.5354	10.767	1.119	1.047	1.761	AZT-11	09-Feb-2013	333.3268	10.792	1.151	1.051	1.771	AZT-11
26-Sep-2012	197.5426	10.767	1.152	1.034	1.761	AZT-11	09-Feb-2013	333.3352	10.774	1.155	1.050	1.773	AZT-11

(d) Photometric measurements of the set 12b+13a.

Table A2. (Continued from previous page).

Date	HJD (2456000+)	V (mag)	B-V	V-R$_J$	V-I$_J$	Telescope	Date	HJD (2456000+)	V (mag)	B-V	V-R$_J$	V-I$_J$	Telescope
15-Aug-2013	520.5078	10.786	1.155	1.041	1.785	AZT-11	24-Aug-2014	894.5694	10.773	1.172	1.077	1.766	AZT-11
16-Aug-2013	521.5032	10.599	1.139	0.994	1.688	AZT-11	26-Aug-2014	896.5491	10.737	1.157	1.036	1.748	AZT-11
18-Aug-2013	523.5349	10.630	1.122	1.015	1.706	AZT-11	27-Aug-2014	897.5327	10.586	1.138	0.994	1.701	AZT-11
18-Aug-2013	523.5419	10.626	1.118	1.005	1.703	AZT-11	29-Aug-2014	899.5342	10.563	1.137	0.918	1.687	AZT-11
18-Aug-2013	523.5478	10.641	1.130	1.027	1.716	AZT-11	30-Aug-2014	900.5322	10.783	1.171	1.060	1.763	AZT-11
01-Sep-2013	537.4939	10.852	1.183	1.068	1.803	AZT-11	31-Aug-2014	901.5369	10.589	1.145	0.990	1.691	AZT-11
01-Sep-2013	537.5010	10.848	1.200	1.045	1.798	AZT-11	01-Sep-2014	902.5422	10.847	1.192	1.067	1.793	AZT-11
01-Sep-2013	537.5084	10.848	1.172	1.069	1.793	AZT-11	02-Sep-2014	903.5363	10.646	1.150	1.030	1.715	AZT-11
11-Sep-2013	547.4908	10.706	1.162	1.028	1.736	AZT-11	04-Sep-2014	905.4926	10.661	1.145	1.044	1.731	AZT-11
09-Oct-2013	575.5352	10.711	1.164	1.026	1.737	AZT-11	05-Sep-2014	906.5293	10.816	1.200	1.067	1.757	AZT-11
09-Oct-2013	575.5534	10.706	1.160	1.021	1.739	AZT-11	16-Sep-2014	917.5786	10.865	1.217	1.094	1.801	AZT-11
11-Oct-2013	577.5338	10.640	1.169	1.002	1.709	AZT-11	20-Sep-2014	921.5653	10.786	1.181	1.074	1.782	AZT-11
13-Oct-2013	579.5838	10.587	1.146	0.990	1.682	AZT-11	20-Sep-2014	921.5653	10.804	1.188	1.069	1.779	AZT-11
13-Oct-2013	579.5907	10.594	1.141	1.003	1.689	AZT-11	25-Sep-2014	926.4602	10.764	1.156	1.056	1.768	AZT-11
13-Oct-2013	579.5976	10.602	1.143	1.005	1.694	AZT-11	01-Oct-2014	932.6078	10.893	1.192	1.099	1.821	AZT-11
25-Oct-2013	591.5467	10.756	-	1.020	1.751	AZT-11	05-Oct-2014	936.5958	10.767	1.191	1.075	1.755	AZT-11
25-Oct-2013	591.6288	10.758	-	1.028	1.744	AZT-11	15-Oct-2014	946.5919	10.637	1.165	1.021	1.707	AZT-11
26-Oct-2013	592.3649	10.791	1.168	1.009	1.730	AZT-11	19-Oct-2014	950.6129	10.676	1.161	1.053	1.764	AZT-11
27-Oct-2013	593.3578	10.805	1.166	1.067	1.788	AZT-11	26-Oct-2014	957.4846	10.607	1.153	-	1.700	AZT-11
27-Oct-2013	593.5660	10.822	1.182	1.062	1.796	AZT-11	28-Oct-2014	959.5475	10.620	1.151	0.989	1.715	AZT-11
29-Oct-2013	595.5280	10.857	1.196	1.070	1.812	AZT-11	02-Nov-2014	964.4461	10.894	1.192	1.089	1.819	AZT-11
30-Oct-2013	596.5614	10.622	1.137	1.000	1.694	AZT-11	05-Nov-2014	967.5922	10.778	1.176	-	1.776	AZT-11
01-Nov-2013	598.6273	10.779	1.163	1.000	1.726	AZT-11	05-Nov-2014	967.5959	10.792	1.150	-	1.793	AZT-11
08-Nov-2013	605.4124	10.750	1.165	1.056	1.758	AZT-11	13-Nov-2014	975.4212	10.777	1.189	1.071	1.768	AZT-11
08-Nov-2013	605.4189	10.738	1.162	1.022	1.750	AZT-11	14-Nov-2014	976.4189	10.626	1.146	1.017	1.714	AZT-11
08-Nov-2013	605.4253	10.738	1.167	1.028	1.750	AZT-11	13-Dec-2014	1005.4167	10.808	1.173	1.057	1.781	AZT-11
08-Nov-2013	605.5687	10.669	1.153	1.036	1.726	AZT-11	14-Dec-2014	1006.5163	10.694	1.183	1.041	1.750	AZT-11
09-Nov-2013	606.5695	10.821	1.178	1.055	1.790	AZT-11							
10-Nov-2013	607.4549	10.658	1.149	1.007	1.713	AZT-11							
23-Nov-2013	620.5919	10.665	1.176	1.027	1.721	AZT-11							
03-Dec-2013	630.4060	10.723	1.150	1.031	1.728	AZT-11							
04-Feb-2014	693.2297	10.828	1.186	1.058	1.775	AZT-11							
05-Feb-2014	694.2651	10.807	1.182	1.060	1.783	AZT-11							
18-Feb-2014	707.2155	10.751	1.172	1.006	1.747	AZT-11							
21-Mar-2014	738.2431	10.759	1.182	1.048	1.758	AZT-11							
23-Mar-2014	740.2544	10.679	1.164	1.045	1.731	AZT-11							

(e) Photometric measurements of the set 13b+14a (left) and of the set 14b (right).

Table A2. (Continued from previous page).

Date	HJD (2457000+)	V (mag)	B-V	V-R_J	V-I_J	Telescope	Date	HJD (2457000+)	V (mag)	B-V	V-R_J	V-I_J	Telescope
15-Aug-2015	250.5211	10.864	1.166	1.109	1.779	AZT-11	03-Sep-2016	635.4773	10.735	1.156	-	1.742	AZT-11
16-Aug-2015	251.5160	10.660	1.145	-	1.716	AZT-11	08-Sep-2016	640.5200	10.759	1.174	-	-	AZT-11
17-Aug-2015	252.5152	10.868	1.174	1.100	1.780	AZT-11	10-Sep-2016	642.5399	10.715	1.165	0.964	-	AZT-11
25-Aug-2015	260.5188	10.726	1.155	-	1.745	AZT-11	12-Sep-2016	644.5383	10.714	1.166	-	1.747	AZT-11
27-Aug-2015	262.5817	10.699	1.153	-	1.743	AZT-11	14-Sep-2016	646.5414	10.715	1.166	-	1.741	AZT-11
09-Sep-2015	275.5796	10.731	1.162	-	-	AZT-11	19-Nov-2016	712.5682	10.849	1.184	-	1.782	AZT-11
11-Sep-2015	277.5817	10.696	1.161	-	-	AZT-11	20-Jan-2017	774.2898	10.812	1.170	-	1.768	AZT-11
16-Sep-2015	282.5832	10.890	1.185	-	-	AZT-11	23-Jan-2017	777.1821	10.806	1.171	-	-	AZT-11
18-Sep-2015	284.5447	10.888	1.172	-	-	AZT-11	31-Jan-2017	785.2764	10.736	1.149	-	-	AZT-11
25-Sep-2015	291.5730	10.830	1.159	-	1.768	AZT-11	12-Feb-2017	797.2023	10.827	1.183	-	-	AZT-11
04-Oct-2015	300.4300	10.775	1.171	-	1.756	AZT-11	27-Feb-2017	812.3250	10.873	1.167	0.984	1.795	AZT-11
03-Nov-2015	330.5253	10.831	1.181	-	1.776	AZT-11	09-Mar-2017	822.3079	10.738	1.147	-	1.759	AZT-11
04-Nov-2015	331.5427	10.834	1.182	-	-	AZT-11							
05-Nov-2015	332.5222	10.834	1.174	-	-	AZT-11							
30-Jan-2016	418.3730	10.785	1.182	-	-	AZT-11							

(f) Photometric measurements of the set 15b+16a (left) and of the set 16b+17a (right).

APPENDIX B: PHOTOMETRY ANALYSIS

From our photometric data, we retrieved the stellar rotation period at each epoch and derived the photosphere contrast.

To retrieve the stellar rotation period, we applied two types of models to our V magnitude curves: a periodic fit involving the fundamental frequency and the first two harmonics to each of the 9 datasets individually (as well as a periodic fit involving the fundamental frequency and the first four harmonics to the whole data set), and GPR (see Section 5). Since the data sets 15b+16a and the 16b+17a are particularly small (15 and 13 points respectively) and consecutive, we grouped them together for the GPR.

The results of the sine fits are listed in Table B1, and plotted in Figures B1 and B2. All observation epochs yield a modulation period within 1σ of the value we use throughout this paper for the stellar rotation period. We note that the error bar recovered on the whole data set is underestimated since it was measured on the curvature of the $\chi^2_r(P_{rot})$ curve around the minimum, curve which presents many aliased local minima due to the observation sampling.

For the GPR, we made a first run on the global data set (phase plot in Fig. B3) and used its result to freeze the decay time for the modelling of the individual data sets, to avoid degeneracy. The retrieved hyperparameters are given in Table B2. The phase plots of the individual data sets are displayed in Figure B4. Again, a neat period around 1.87 is outlined for each data set. The periods found with GPR and with sine fits are generally consistent, but the error bar for the rotation period on the whole data set is more trustworthy when computed statistically from GPR-MCMC than from the local curvature of the sine fit aliased χ^2_r curve.

All derived rotation periods, from sine fits and GPR, are plotted against their corresponding latitude using the ZDI-retrieved differential rotation in Figure B5), and the thus-derived latitudes are plotted against time in Figure B6, showing a global increasing trend of that latitude, regardless of the period retreval method.

We computed B-V(V) models from the Kurucz models for colors of main sequence stars with log(g)=3.5, T_{eff}=4500 K and E(B-V)=0.10 mag (Kurucz 1993): we fit a two-temperature model with a photospheric temperature of 4500 K and different values for the spot temperature. Then, for each tested spot temperature, for all values of spot coverage from 0 too 100 %, we computed the resulting B and the resulting V using the following formulas, from which we derived the B-V. The resulting models are plotted in Figure B7. We find that a spot temperature of 3750 K fits our B-V measurements well, from which we deduce that the extension of our data imply a spot coverage on V410 Tau between 50 and 75%, in agreement with the assumption in Section 5.3.

$$V(r) = -2.5\log_{10}(r10^{-\frac{V_{spot}}{2.5}} + (1-r)10^{-\frac{V_{star}}{2.5}})$$
$$B(r) = -2.5\log_{10}(r10^{-\frac{B_{spot}}{2.5}} + (1-r)10^{-\frac{B_{star}}{2.5}})$$

APPENDIX C: ACTIVITY PROXIES

This section shows the line profiles of Hα, He I and Ca II, as well as some results on B_ℓ.

Table B1. Sinfit results on photometric data.

Data	Period (d)	Amplitude (mag)	Dispersion (mag)
08b+09a	1.8695 ± 0.0014	0.019 ± 0.005	0.015
09b+10a	1.8701 ± 0.0004	0.069 ± 0.004	0.020
10b	1.8718 ± 0.0013	0.016 ± 0.005	0.011
11b+12a	1.8704 ± 0.0006	0.045 ± 0.004	0.014
12b+13a	1.8724 ± 0.0005	0.051 ± 0.003	0.018
13b+14a	1.8713 ± 0.0004	0.114 ± 0.006	0.018
14b	1.8722 ± 0.0010	0.117 ± 0.006	0.021
15b+16a	1.8720 ± 0.0012	0.089 ± 0.007	0.014
16b+17a	1.8736 ± 0.0013	0.088 ± 0.013	0.006
All V mag	1.871254 ± 0.000030	0.0568 ± 0.0032	0.047

C1 Hα

Hα dynamic spectra are plotted in Figure C1, with the 2009 Jan data set being split in half to better see the absorption feature around phase 0.95. We also see two other absorption features in 2009 Jan around phase 0.80 and in 2011 Jan around phase 0.35, and we fit a sine curve in each to determine the potential altitude of a prominence or cloud that could be the origin of these absorption features. We find a sine semi-amplitude of ~2 $v \sin i$ for each of them.

Lomb-Scargle periodograms for individual epochs are plotted in Figure C2, and the periodogram for the whole data set is shown in Figure C3, showing a neat peak at the rotation period.

C2 He I D_3

The He I line profiles are shown in Fig. C5. We can clearly see the flares at the dates marked in Table A2.

C3 Ca II

The Ca II line profiles are shown in Fig. C6.

C4 B_ℓ

We derived longitudinal magnetic field values as first-order moments of our Stokes V LSD profiles, and applied a GPR-MCMC run on them. The phase plot is shown in Figure C7.

This paper has been typeset from a TEX/LATEX file prepared by the author.

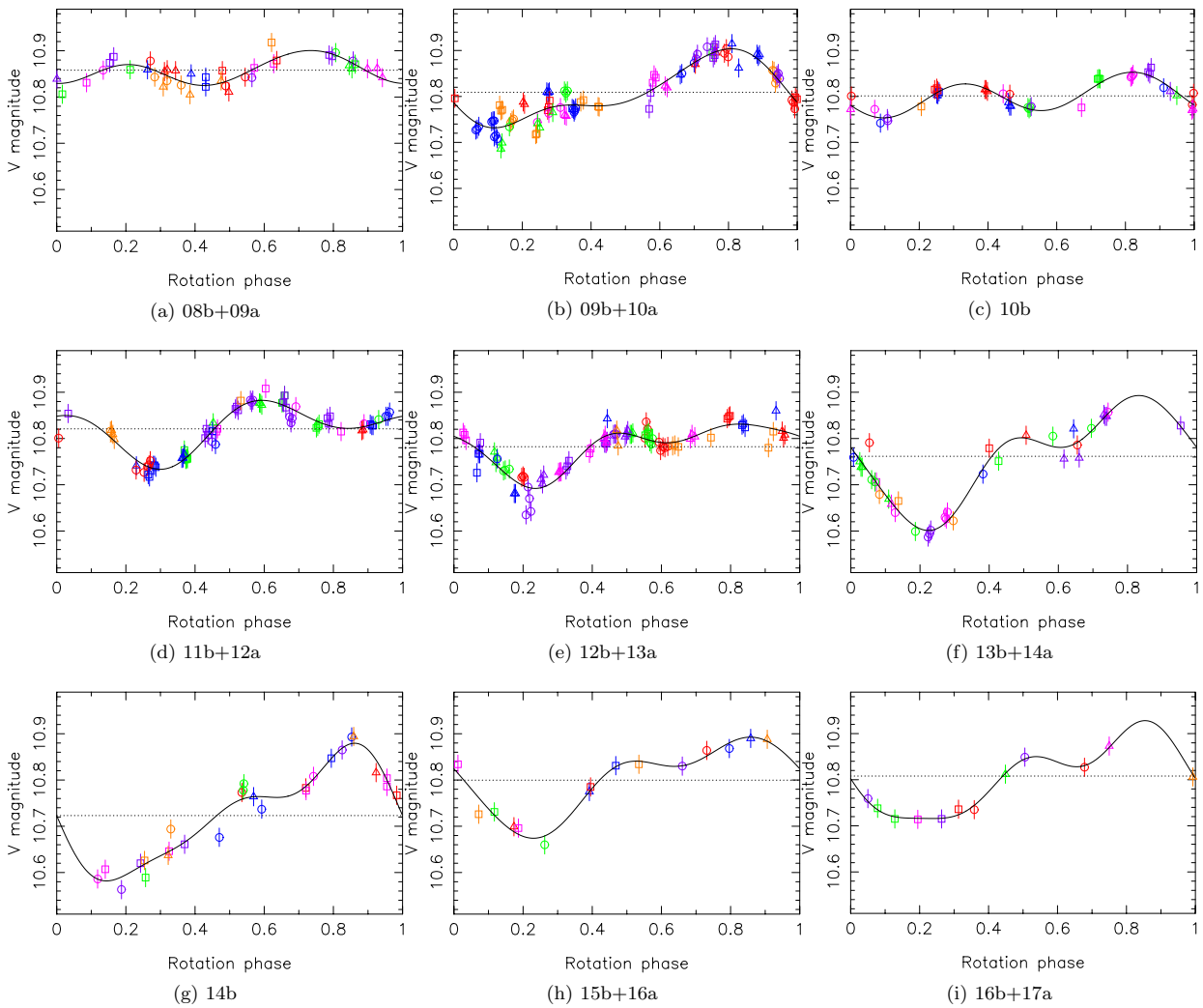

(a) 08b+09a (b) 09b+10a (c) 10b

(d) 11b+12a (e) 12b+13a (f) 13b+14a

(g) 14b (h) 15b+16a (i) 16b+17a

Figure B1. Fits of the V magnitude measurements at each epoch by a sine curve and two harmonics. Each data set was folded according to the corresponding period listed in Table B1. As a consequence, the rotation phase used in these plots does not correspond to the rotation phase in Table A1, but rather to the phase in the model sine curves.

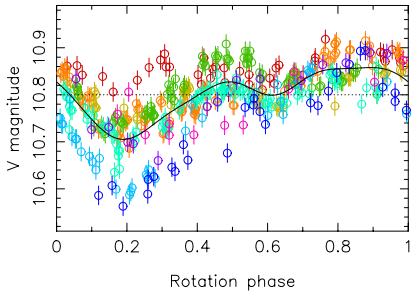

Figure B2. Fit of the V magnitude in the whole data set by a sine curve and four harmonics. The color-to-dataset correspondency is as follows: red=08b+09a, orange=09b+10a, yellow=10b, green=11b+12a, turquoise=12b+13a, cyan=13b+14a, blue=14b, purple=15b+16a, pink=16b+17a.

Table B2. Results of the GPR-MCMC runs on our V magnitude measurements.

Data set	GP Period (d) (best)	Decay time (d) (best)	Smoothing (d) (best)	Amplitude (mag) (best)
08b+09a	1.8693 ± 0.0014 (1.8694)	311.1333	0.7 ± 0.3 (0.5)	$0.03^{+0.02}_{-0.01}$ (0.02)
09b+10a	1.8714 ± 0.0008 (1.8715)	311.1333	1.2 ± 0.3 (1.2)	$0.12^{+0.05}_{-0.04}$ (0.11)
10b	1.8723 ± 0.0013 (1.8722)	311.1333	0.6 ± 0.2 (0.5)	$0.04^{+0.03}_{-0.02}$ (0.03)
11b+12a	1.8704 ± 0.0007 (1.8705)	311.1333	1.0 ± 0.3 (0.7)	$0.09^{+0.05}_{-0.03}$ (0.05)
12b+13a	1.8718 ± 0.0009 (1.8718)	311.1333	0.6 ± 0.2 (0.5)	$0.06^{+0.03}_{-0.02}$ (0.04)
13b+14a	1.8721 ± 0.0008 (1.8722)	311.1333	0.7 ± 0.2 (0.6)	$0.09^{+0.03}_{-0.02}$ (0.08)
14b	1.8735 ± 0.0012 (1.8732)	311.1333	0.6 ± 0.2 (0.5)	$0.11^{+0.04}_{-0.03}$ (0.09)
15b+16a +16b+17a	1.8727 ± 0.0010 (1.8729)	311.1333	0.9 ± 0.3 (0.7)	$0.08^{+0.03}_{-0.02}$ (0.06)
All V mag	1.8715 ± 0.0003 (1.8714)	314^{+31}_{-29} (311.1333)	0.74 ± 0.08 (0.73)	$0.071^{+0.009}_{-0.008}$ (0.070)

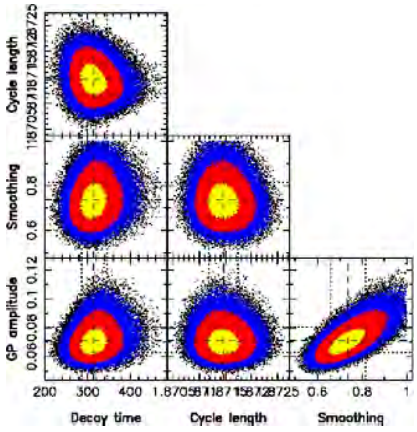

Figure B3. GPR-MCMC phase plot for the entire data set of V magnitudes. GP amplitude $\theta_1 = 0.0712^{+0.0093}_{-0.0082}$ mag, cycle length $\theta_2 = 1.8715 \pm 0.0003$ d, decay time $\theta_3 = 314^{+31}_{-29}$ d, smoothing parameter $\theta_4 = 0.74 \pm 0.08$ d.

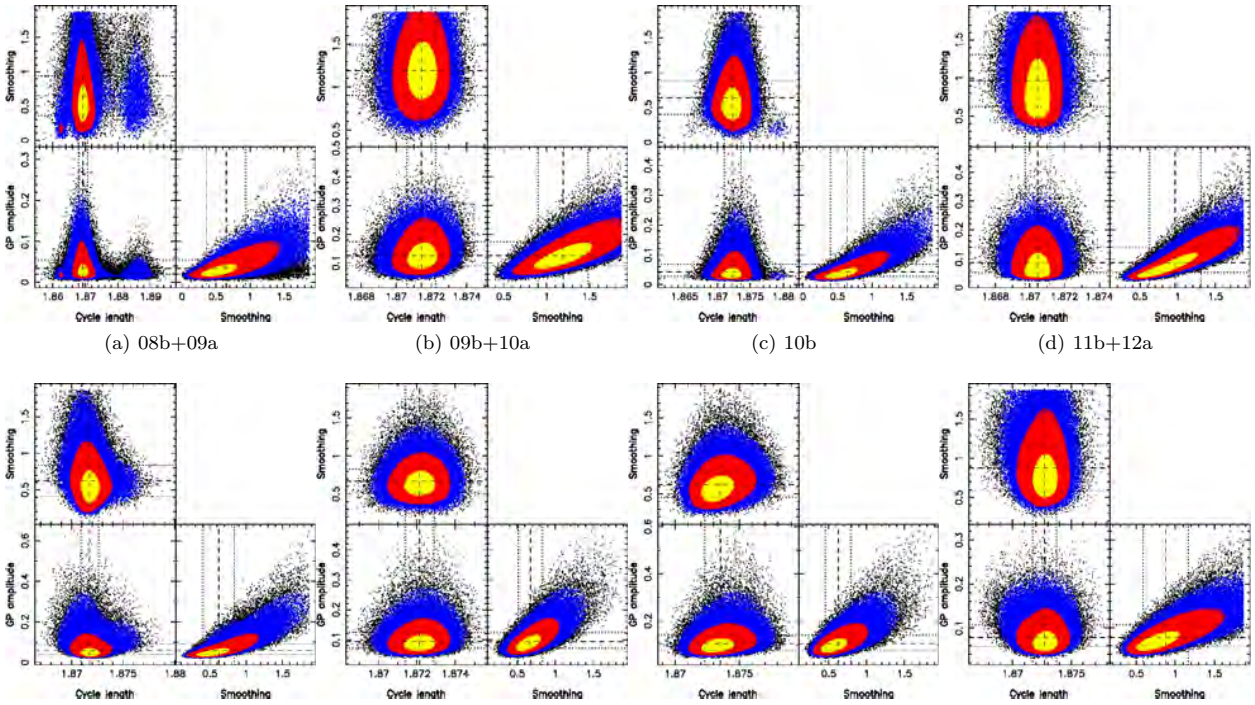

(a) 08b+09a (b) 09b+10a (c) 10b (d) 11b+12a

(e) 12b+13a (f) 13b+14a (g) 14b (h) 15b+16a+16b+17a

Figure B4. MCMC phase plots for GPR applied to each of our V magnitude data sets.

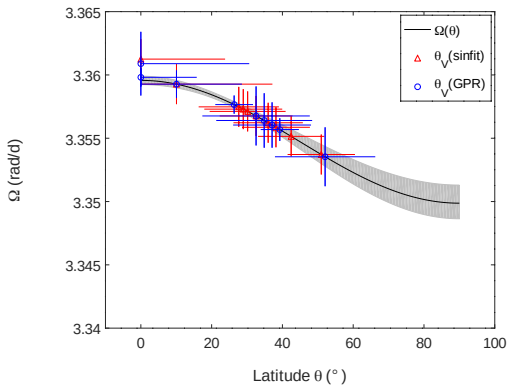

Figure B5. Differential rotation curve in blue, with parameters Ω_{eq} and $d\Omega$ as defined in the introduction of Section 4. Red: Hα rotation rates, green: B_ℓ rotation rates, circles: derived from 2013 Dec data set, triangles: derived from 2015 Dec data set, x symbols: derived from the whole data set (143 points for Hα and 135 for B_ℓ). Photometry rotation rates are displayed, those derived with sinfit (Table B1) in green and those derived with GPR (Table B2) in magenta.

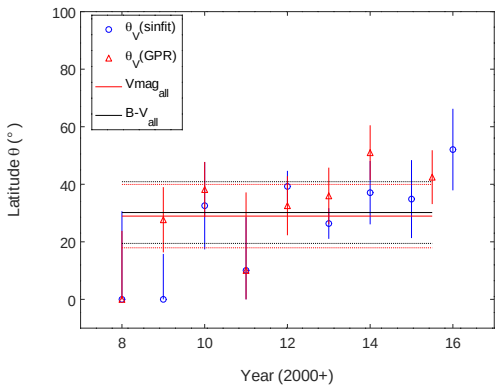

Figure B6. Colatitude found for the V magnitude, for each epoch and for the whole data set with sinfit (x-coordinate: 20) as well as for B-V with sinfit (x-coordinate: 21).

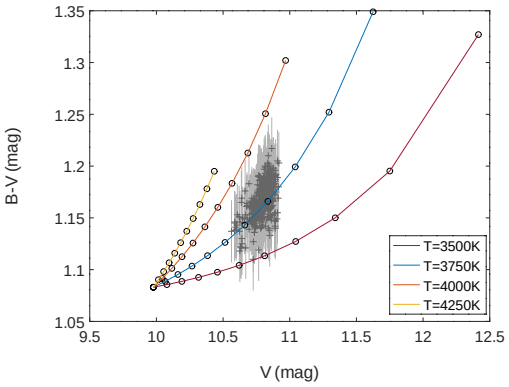

Figure B7. Fit of the B-V(V) curve with Kurucz models, with a photosphere temperature of 4500 K, $\log g$ of 3.5, E(B-V) of 0.10. Each full line corresponds to a particular value of the spot temperature, and dots mark the spot coverage with steps of 10% (the dot at V=10.0 and B-V=1.08 corresponding to a 0% spot coverage). The extension of our data correspond to a spot coverage constantly between 50% and 75%.

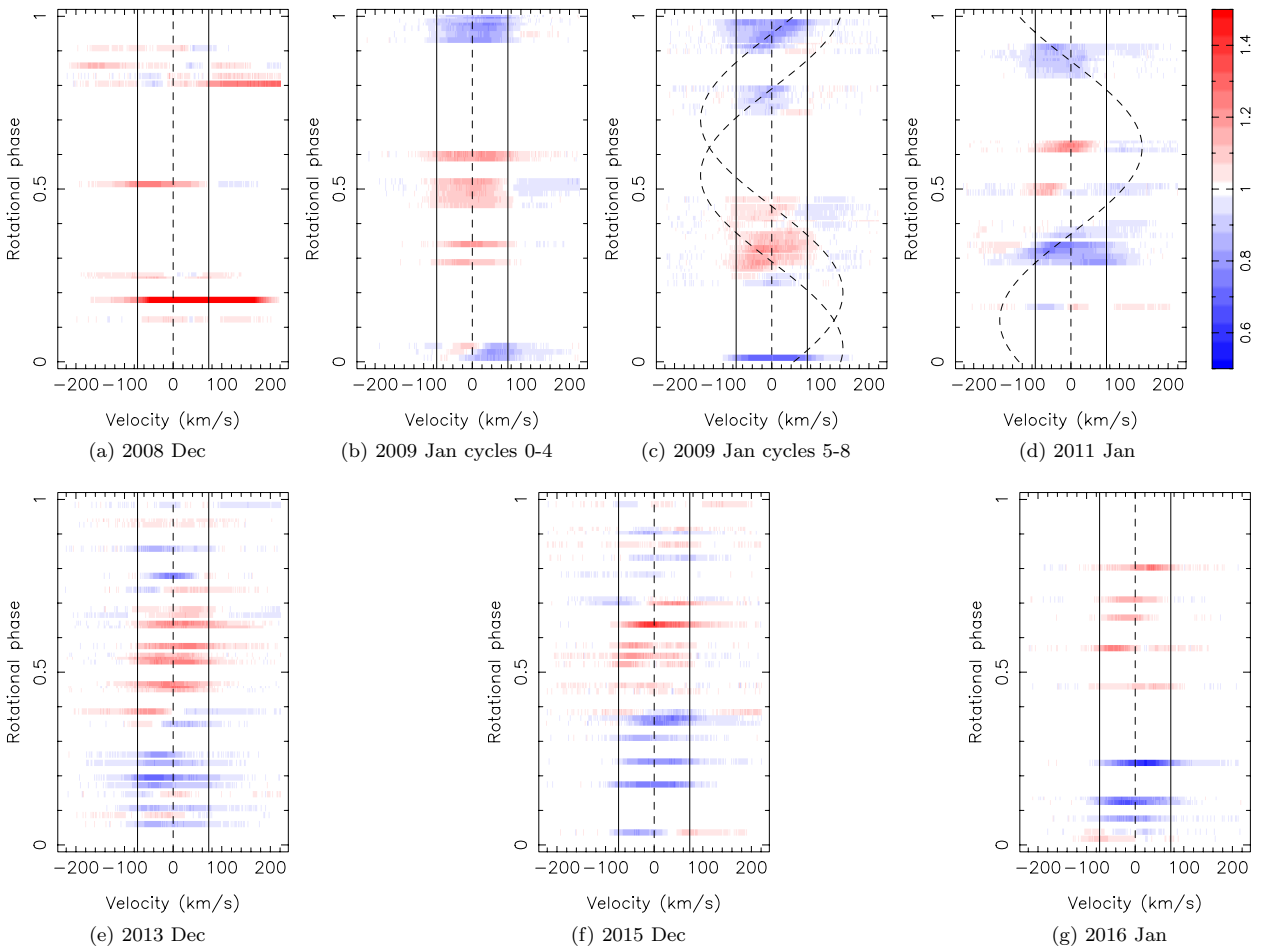

(a) 2008 Dec (b) 2009 Jan cycles 0-4 (c) 2009 Jan cycles 5-8 (d) 2011 Jan

(e) 2013 Dec (f) 2015 Dec (g) 2016 Jan

Figure C1. Hα dynamical spectra for epochs 2008 Dec (a), 2009 Jan (b,c), 2011 Jan (d), 2013 Dec (e), 2015 Dec (f) and 2016 Jan (g).

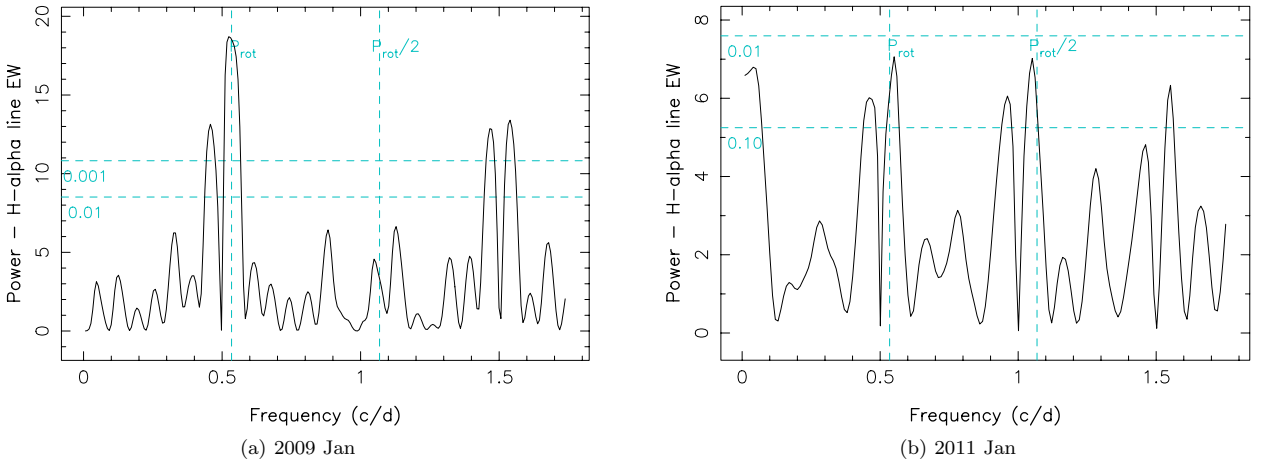

(a) 2009 Jan (b) 2011 Jan

Figure C2. Periodograms for the Hα line EW, for observation epochs 2009 Jan (a), 2011 Jan (b), 2013 Dec (c) and 2015 Dec (d). False-alarm probability levels of 1% and 0.1% are represented as horizontal cyan dashed lines, and $P_{\rm rot}$ and its first harmonic as vertical cyan dashed lines.

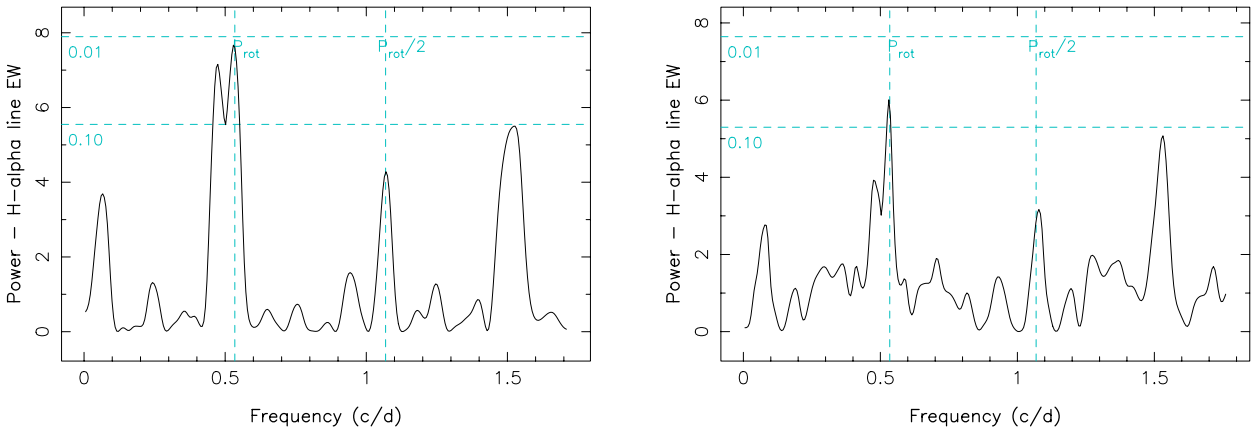

(c) 2013 Dec (d) 2015 Dec

Figure C2. (Continued from the previous page).

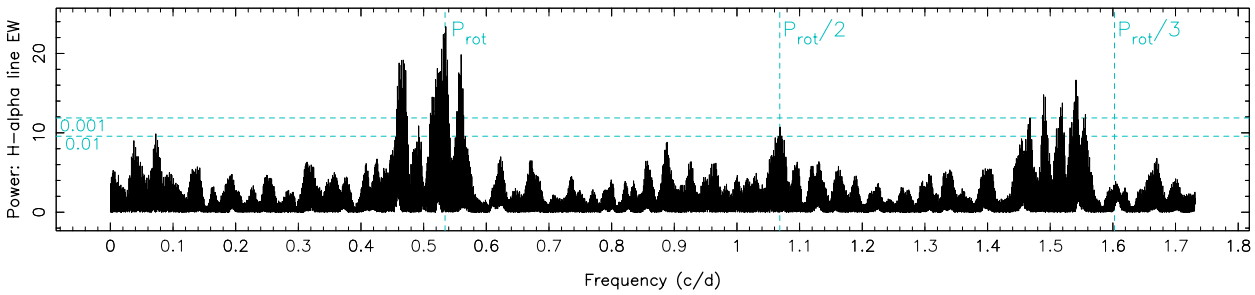

Figure C3. Periodogram of the equivalent width of the Hα line. The maximum power is found at 3.3636 rad/d, or 1.8680 d.

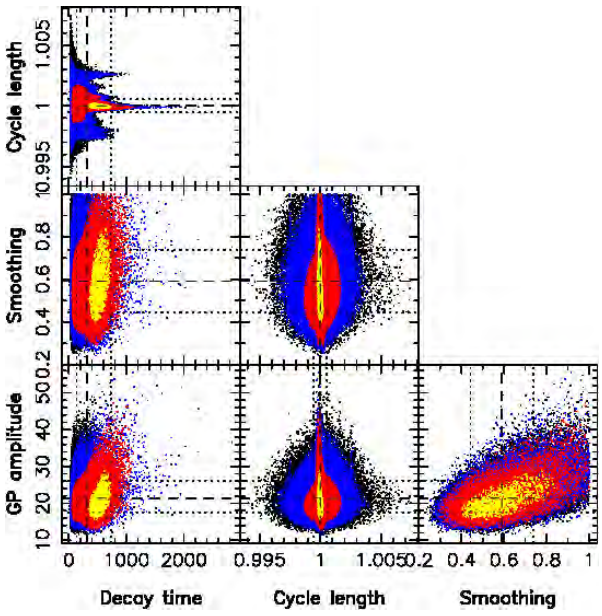

Figure C4. GPR-MCMC phase plot for our Hα equivalent width data. Amplitude $\theta_1 = 21.4^{+4.7}_{-3.9}$ km s^{-1}, decay time $\theta_3 = 315^{+414}_{-179}$ $P_{\rm rot}$, Cycle length $\theta_2 = 1.0000 \pm 0.0005$ $P_{\rm rot}$, Smoothing $\theta_4 = 0.59 \pm 0.15$ $P_{\rm rot}$.

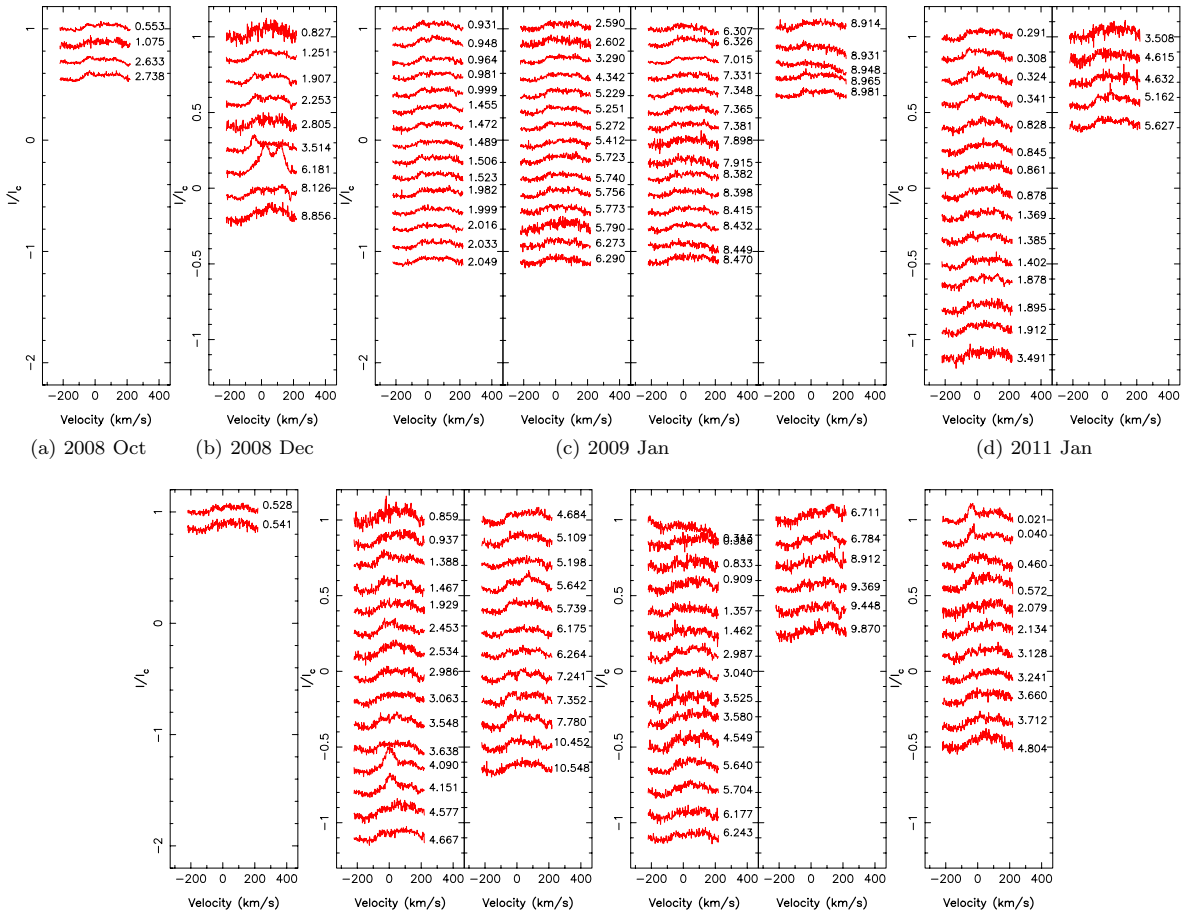

(a) 2008 Oct (b) 2008 Dec (c) 2009 Jan (d) 2011 Jan

(e) 2013 Nov (f) 2013 Dec (g) 2015 Dec (h) 2016 Jan

Figure C5. . He I D_3 Oct 2008 (ref cycle: -42), Dec 2008 (ref cycle: -15), Jan 2009 (ref cycle: 0), Jan 2011 (ref cycle: 397) Nov 2013 (ref cycle: 946), Dec 2013 (ref cycle: 959), Dec 2015 (ref cycle: 1349) and Jan 2016 (ref cycle: 1376)

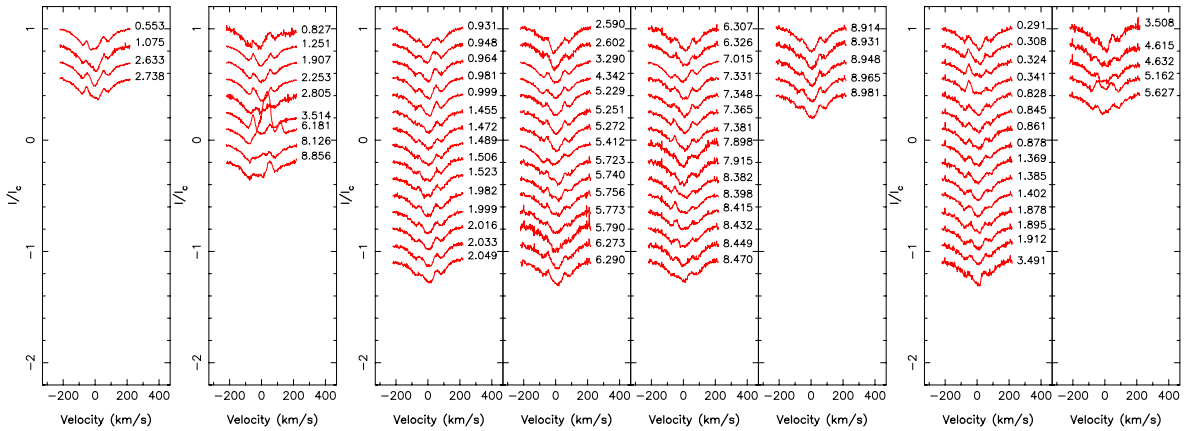

(a) 2008 Oct (b) 2008 Dec (c) 2009 Jan (d) 2011 Jan

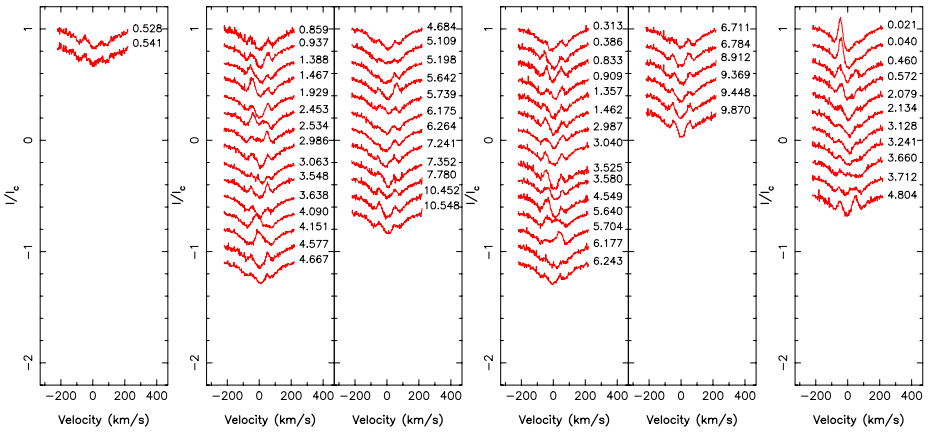

(e) 2013 Nov (f) 2013 Dec (g) 2015 Dec (h) 2016 Jan

Figure C6. Ca II D_3 Oct 2008 (ref cycle: -42), Dec 2008 (ref cycle: -15), Jan 2009 (ref cycle: 0), Jan 2011 (ref cycle: 397) Nov 2013 (ref cycle: 946), Dec 2013 (ref cycle: 959), Dec 2015 (ref cycle: 1349) and Jan 2016 (ref cycle: 1376)

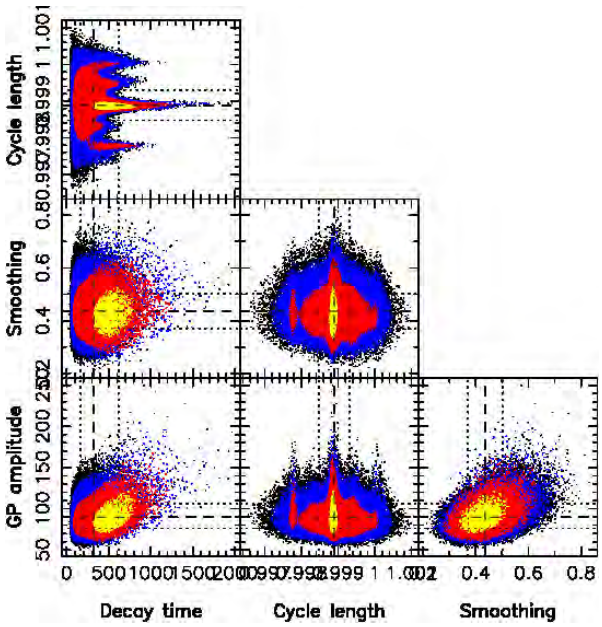

Figure C7. GPR-MCMC phase plot for B_ℓ. GP amplitude $\theta_1 = 90^{+16}_{-14}$ G, cycle length $\theta_2 = 0.9989 \pm 0.0004$ $P_{\rm rot}$, decay time $\theta_3 = 322^{+295}_{-154}$ $P_{\rm rot}$, smoothing $\theta_4 = 0.436 \pm 0.066$ $P_{\rm rot}$.

B.2 As secondary author

B.2.1 Nature publication: Donati et al. 2016

LETTER

doi:10.1038/nature18305

A hot Jupiter orbiting a 2-million-year-old solar-mass T Tauri star

J. F. Donati[1,2], C. Moutou[3], L. Malo[3], C. Baruteau[1,2], L. Yu[1,2], E. Hébrard[4], G. Hussain[5], S. Alencar[6], F. Ménard[7,8], J. Bouvier[7,8], P. Petit[1,2], M. Takami[9], R. Doyon[10] & A. Collier Cameron[11]

Hot Jupiters are giant Jupiter-like exoplanets that orbit their host stars 100 times more closely than Jupiter orbits the Sun. These planets presumably form in the outer part of the primordial disk from which both the central star and surrounding planets are born, then migrate inwards and yet avoid falling into their host star[1]. It is, however, unclear whether this occurs early in the lives of hot Jupiters, when they are still embedded within protoplanetary disks[2], or later, once multiple planets are formed and interact[3]. Although numerous hot Jupiters have been detected around mature Sun-like stars, their existence has not yet been firmly demonstrated for young stars[4–6], whose magnetic activity is so intense that it overshadows the radial velocity signal that close-in giant planets can induce. Here we report that the radial velocities of the young star V830 Tau exhibit a sine wave of period 4.93 days and semi-amplitude 75 metres per second, detected with a false-alarm probability of less than 0.03 per cent, after filtering out the magnetic activity plaguing the spectra. We find that this signal is unrelated to the 2.741-day rotation period of V830 Tau and we attribute it to the presence of a planet of mass 0.77 times that of Jupiter, orbiting at a distance of 0.057 astronomical units from the host star. Our result demonstrates that hot Jupiters can migrate inwards in less than two million years, probably as a result of planet–disk interactions[2].

Very few exoplanets have yet been discovered around young, forming Sun-like stars aged less than ten million years (Myr)[7,8]—called the T Tauri stars—either through the radial velocity variations or the photometric transits they induce in the light of their stars. Yet detections of young planets are key for our understanding of how planetary systems form and this is especially true of young hot Jupiters, which are thought to have a critical impact on the early architecture of these systems. The first claimed detection of a young hot Jupiter[4] orbiting a T Tauri star was quickly refuted; the reported periodic radial velocity fluctuations were finally attributed to activity[5] and to cool spots at the stellar surface[9]. The recent candidate detection of a transiting hot Jupiter around a T Tauri star[6] is still pending confirmation.

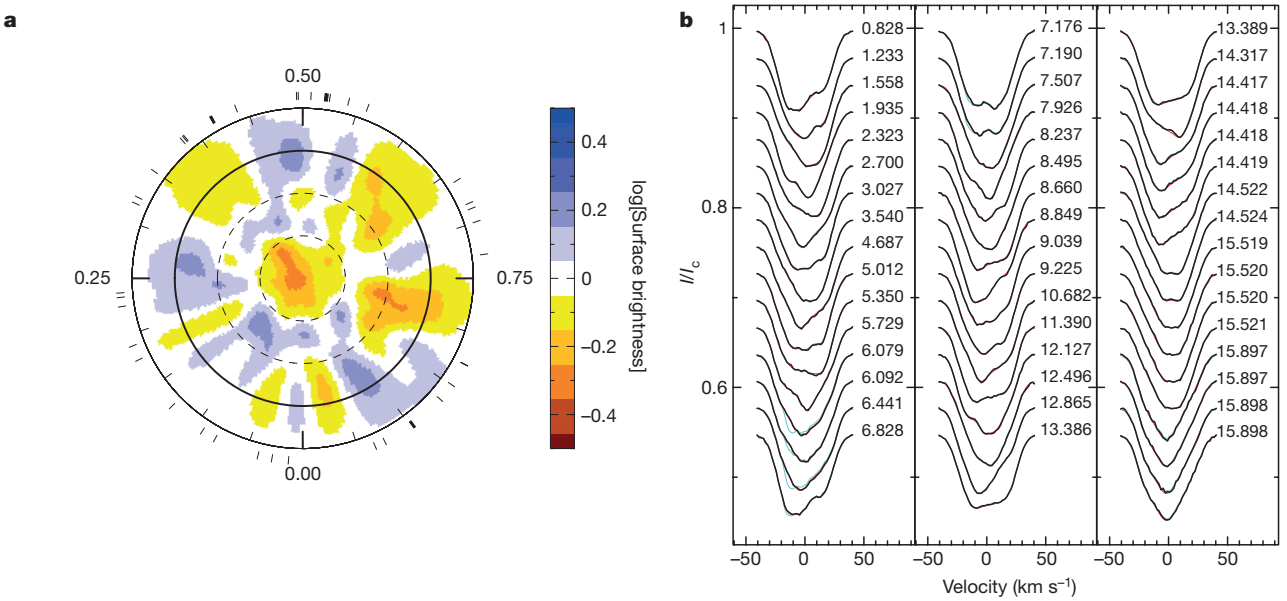

Figure 1 | Brightness map of V830 Tau and fit to the LSD profiles. **a**, Logarithmic brightness at the surface of V830 Tau as derived with Doppler imaging. Cool spots show as brown features and bright plages show as blue features. The rotation axis of the star is tilted at 55° to the line of sight, and the projected equatorial rotation velocity is equal to 30.5 km s^{-1} (ref. 12). The star is shown in a flattened polar view, with the pole in the centre and the equator depicted as a bold circle. Ticks outside the image mark the phases of observations. **b**, Observed (black line) and modelled (red) LSD profiles of V830 Tau throughout our November–December 2015 run. LSD profiles before their filtering from lunar contamination are also shown (cyan lines). Numbers on the right of each profile indicate the rotation cycle. Cycles 6.079 to 7.190 are the most affected, contamination being much smaller or negligible in all other observations. I/I_c, normalized intensity.

[1]Université de Toulouse, UPS-OMP, IRAP, 14 avenue Belin, F–31400 Toulouse, France. [2]Centre National de la Recherche Scientifique (CNRS), IRAP/UMR 5277, 14 avenue Belin, F-31400 Toulouse, France. [3]Canada–France–Hawaii Telescope (CFHT) Corporation, 65-1238 Mamalahoa Highway, Kamuela, Hawaii 96743, USA. [4]Department of Physics and Astronomy, York University, Toronto, Ontario L3T 3R1, Canada. [5]European Southern Observatory (ESO), Karl-Schwarzschild-Strasse 2, D-85748 Garching, Germany. [6]Departamento de Fisica, ICEx, UFMG, avenida Antonio Carlos, 6627, 30270-901 Belo Horizonte, MG, Brazil. [7]Université Grenoble Alpes, IPAG, BP 53, F–38041 Grenoble Cedex 09, France. [8]CNRS, IPAG/UMR 5274, BP 53, F–38041 Grenoble Cedex 09, France. [9]Institute of Astronomy and Astrophysics, Academia Sinica, PO Box 23-141, 106 Taipei, Taiwan. [10]Département de physique, Université de Montréal, CP 6128, Succursale Centre-Ville, Montréal, Quebec H3C 3J7, Canada. [11]SUPA, School of Physics and Astronomy, University of St Andrews, St Andrews, KY16 9SS, UK.

© 2016 Macmillan Publishers Limited. All rights reserved

T Tauri stars are known to harbour cool spots and bright features (plages) on their surfaces, generating radial velocity fluctuations with semi-amplitudes of several kilometres per second[10], that is, much larger than the perturbations expected from a putative planet, even for close-in massive hot Jupiters inducing typical radial velocity signals of ~0.1 km s^{-1}. Detecting hot Jupiters around T Tauri stars through velocimetry or photometry is thus quite challenging and requires efficient tools for filtering out the dominant jitter that activity induces in the spectra and light curves of young stars. We recently proposed a new method to achieve this goal[11], whose first applications to non-accreting (weak-line) T Tauri stars proved promising though inconclusive[12].

V830 Tau is a ~2-Myr-old solar-mass T Tauri star[12] contracting towards the main sequence and currently spinning once in 2.741 days[13], that is, ~10 times faster than the Sun. Evolutionary models[14] suggest that it is fully or largely convective. Unlike 80% of the T Tauri stars in the Taurus star-forming region[15], V830 Tau exhibits no significant infrared excess, implying that most of its inner accretion disk has already dissipated. This is consistent with its status as a non-accreting weak-line T Tauri star, and makes it an ideal place to look for the presence of hot Jupiters at an early stage of star and planet formation.

In late 2015, we collected 48 high-resolution spectra of V830 Tau (see Extended Data Table 1) as part of the MaTYSSE Large Program aimed at detecting hot Jupiters around weak-line T Tauri stars[11]. Applying least-squares deconvolution[16] (LSD) to our spectra, we derived accurate average line profiles and their temporal modulation over ~15 rotation cycles. Longitudinal magnetic fields were also derived from our circularly polarized data and the Zeeman signatures that fields generate in spectral lines[16]. Using tomographic techniques inspired from medical imaging, one can reconstruct distributions of spots and plages at the surfaces of rotating cool active stars from sets of densely sampled line profiles covering several rotation cycles. This method, called Doppler imaging[17], can also probe the photospheric shear associated with surface differential rotation through the amount of twisting it generates in brightness maps[18,19].

Our Doppler imaging code was previously applied to a small set of 15 LSD profiles of V830 Tau, from which the distribution of surface features and the differential rotation pattern were recovered[12]; it even

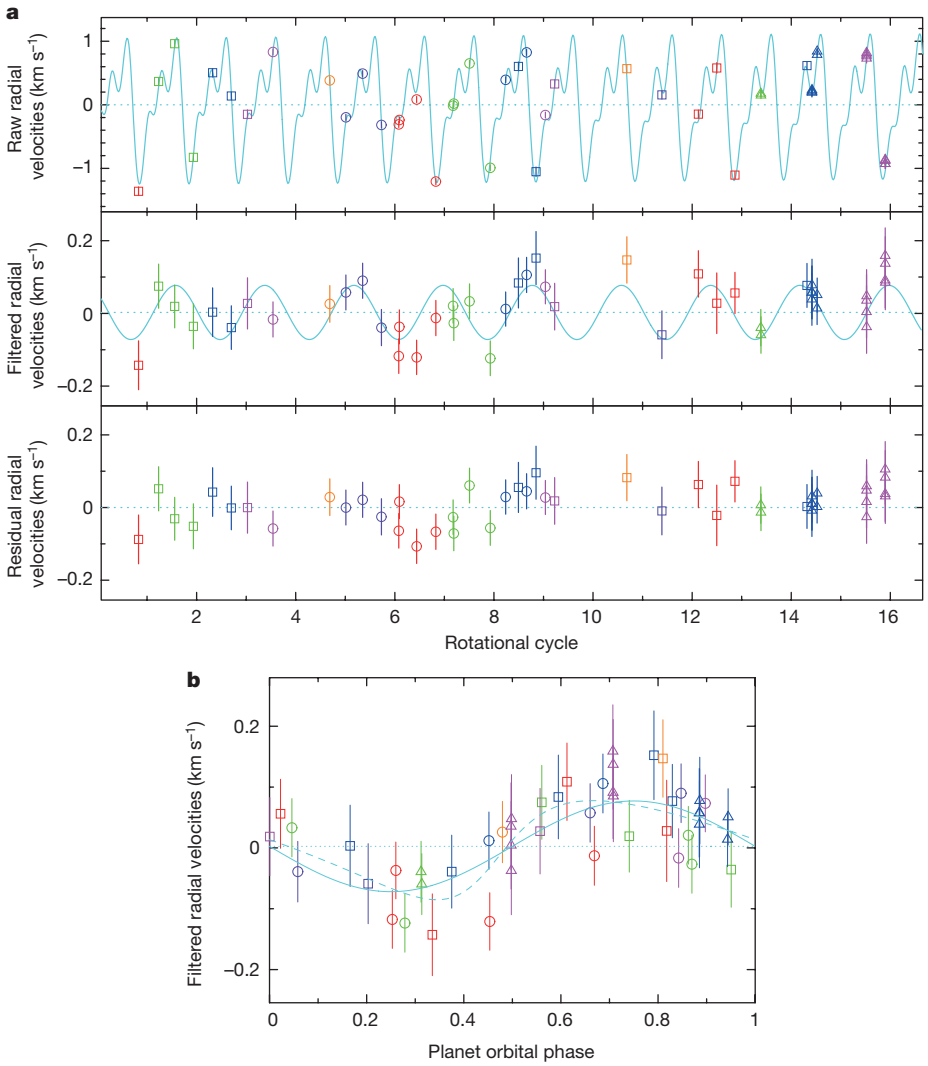

Figure 2 | Raw, filtered and residual radial velocities of V830 Tau. **a**, Top, raw radial velocities of V830 Tau (open symbols and 1σ error bars) and the model inferred with Doppler imaging (cyan line); the model slowly evolves with time as a result of differential rotation. Open circles, squares and triangles depict ESPaDOnS, NARVAL and ESPaDOnS/GRACES data. Middle, activity-filtered radial velocities and best sine fit to the data (cyan line). The period and semi-amplitude of the planet radial velocity signal are equal to 4.93 ± 0.05 days and 75 ± 11 m s^{-1} (1σ error bars). Bottom, residual radial velocities once the planet signal is removed and activity is filtered out, with a final root-mean-square dispersion of 48 m s^{-1}. Different colours code different rotation cycles. **b**, Activity-filtered radial velocities (with 1σ error bars) phase-folded on the planet orbital period of 4.93 days. Although the fit to the data is marginally better with an eccentric orbit (dashed line) than with a circular orbit (solid line), the significance of the derived eccentricity (0.30 ± 0.15) is too low to be reliable[23].

© 2016 Macmillan Publishers Limited. All rights reserved

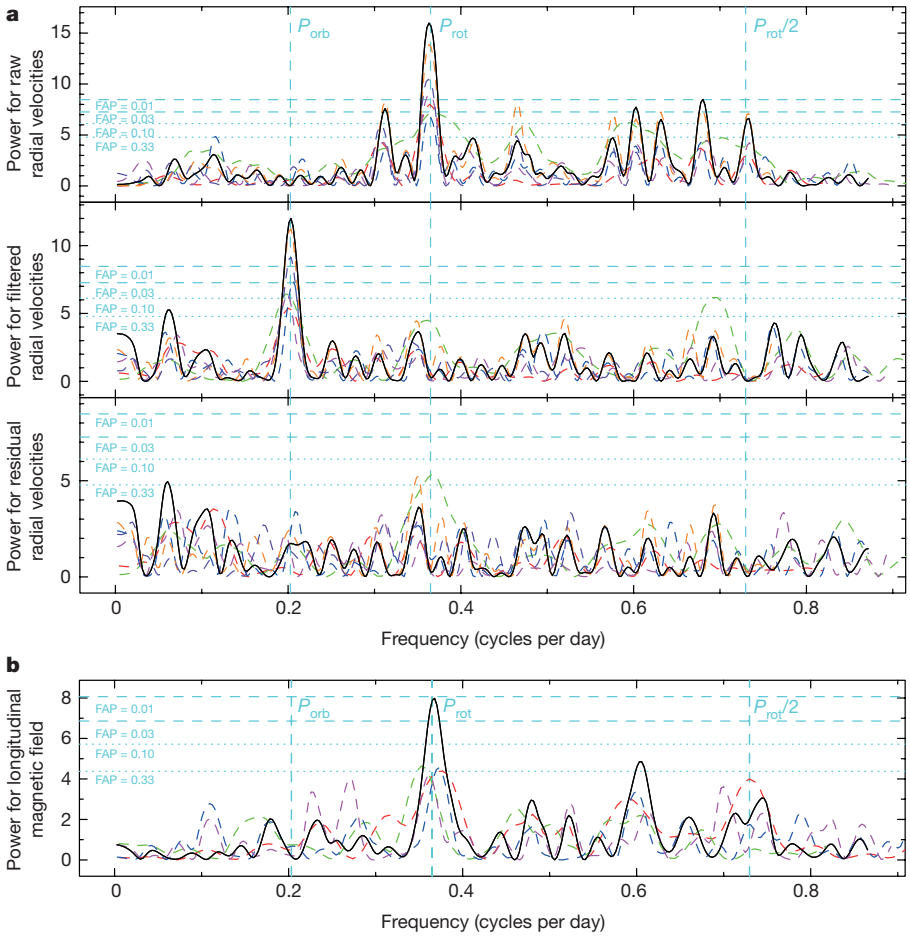

Figure 3 | Periodogram of the radial velocities and activity of V830 Tau. **a**, Periodograms of the raw (top), filtered (middle) and residual (bottom) radial velocities shown in Fig. 2a. The black line is for the full set, while the dashed red, green, blue and pink lines are for the first half, the second half, the even points and the odd points only; the purple dashed lines are the periodograms once the 15 radial velocity points affected by lunar contamination are removed and the orange dashed lines are the periodograms once the 6 radial velocity points strongly affected by lunar contamination are removed. (Similar results are obtained when analysing subsets of filtered radial velocities from a global Doppler imaging modelling, or when Doppler imaging filtering is applied to subsets of LSD profiles). The stellar rotation period (2.741 days), its first harmonic and the planet orbital period (4.93 days) are depicted with vertical dashed lines. The horizontal dotted and dashed lines trace the 33%, 10%, 3% and 1% false alarm probabilities (FAP). The planet signal in the filtered radial velocities is detected in the full set with a FAP $< 0.03\%$. **b**, Periodogram of the line-of-sight projected (longitudinal) magnetic field, a reliable activity proxy[22], featuring a clear peak at the stellar rotation period but no power at the planet orbital period.

suggested the potential presence of a hot Jupiter, though with a very low confidence level. The version of the Doppler imaging code used here implements a novel technique to filter out lunar contamination (which plagues spectra collected in non-photometric conditions), yielding good results when phase coverage is dense. Applying the code to our new set of 48 LSD profiles of V830 Tau yields the map and fit shown in Fig. 1. We again clearly detect differential rotation (see Extended Data Fig. 1) and confirm that it is ~3 times weaker than that of the Sun, reflecting that V830 Tau is largely or fully convective[20].

From the brightness image reconstructed with Doppler imaging, we derive the model radial velocity curve that V830 Tau should exhibit if all profile perturbations were attributable to surface features and differential rotation. By subtracting these modelled radial velocities from the observed ones (both computed as the first moment of the LSD profiles), we obtain the activity-filtered radial velocities of V830 Tau, whose amplitude is typically ~10 times lower than the raw radial velocities (see Fig. 2). A clear radial velocity signal, with a period of 4.93 ± 0.05 days and a semi-amplitude of 75 ± 11 m s^{-1}, is detected in the activity-filtered radial velocities at a confidence level $> 99.97\%$ (see Figs 2 and 3). Using a Bayesian approach[21], we find that the 4.93-day peak is at least 10^5 times more likely than any of the other features in the periodogram (see Extended Data Fig. 2a). The regular phase coverage of our data also allows us to check that the 4.93-day signal is present in smaller subsets (for example, first and second half, even and odd points) though, as expected, with a lower confidence level. Similarly, we checked that our detection holds when profiles affected by lunar contamination are excluded (see Fig. 3 and Extended Data Fig. 2a) and when differential rotation is neglected. Periodograms of the longitudinal fields and of the Hα emission, both reliable proxies for the activity jitter plaguing radial velocity curves[22], show no power at a period of 4.93 days (see Fig. 3b and Extended Data Fig. 2b), demonstrating that the signal we report is unrelated to activity.

We interpret this radial velocity signal as being caused by a giant planet of mass 0.77 ± 0.15 Jupiter masses in a circular orbit around V830 Tau at a distance of 0.057 ± 0.001 AU (see Extended Data Table 2). Although the filtered radial velocities are marginally better fitted for an eccentric orbit ($e = 0.30 \pm 0.15$, see Fig. 2), we still favour a circular orbit given the large error bar on the eccentricity[23]. Removing the planet signal from the original data and repeating the activity-filtering process yields residual radial velocities with a root-mean-square dispersion of 48 m s^{-1} (that is, consistent with the average noise level, see Extended Data Table 1) and no peak with a FAP <30% left in the periodogram. Using the alternative option of fitting both the brightness map and the planet parameters simultaneously[24] yields identical results

© 2016 Macmillan Publishers Limited. All rights reserved

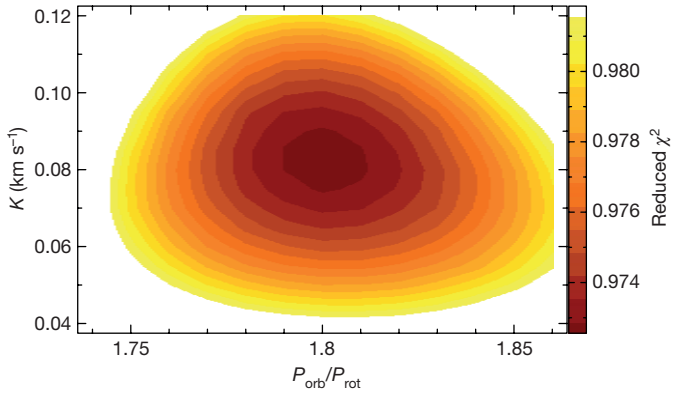

Figure 4 | Adjusting the planet parameters while modelling activity. Variations in the reduced χ^2 (shown as the colour scale) of the Doppler imaging fit to the LSD profiles for a given level of spottedness and assuming the presence of a planet in circular orbit, for a range of orbital periods P_{orb} and semi-amplitudes K of the radial velocity signature. (This is a two-dimensional cut from a three-dimensional map, with the phase of the radial velocity signal also included as a search parameter). The location of the minimum and local paraboloid curvature yield the optimal values of P_{orb} and K and their respective 1σ error bars[24], equal to 4.94 ± 0.05 days and 82 ± 10 m s^{-1}, in agreement with the results of our main filtering technique. The outer colour contour traces the projected 99.99% confidence interval, corresponding to a χ^2 increase of 21.1 for a three-parameter fit to the 2,208 data points of the LSD profiles. With respect to our best model incorporating a planet, a model with no planet corresponds to a χ^2 increase of 82, implying that the planet is detected with a FAP $< 10^{-15}$, much smaller than the FAP derived from the periodogram of the 48 radial velocity points (see Fig. 3) thanks to the larger number of data points in the fitted LSD profiles.

and demonstrates that our optimal model including a planet is orders of magnitude more likely than a model with no planet (see Fig. 4). Simulations in conditions identical to those of our observations yield results in close agreement with those of Figs 2 and 3 (see Extended Data Figs 3 and 4), further demonstrating that our filtering process induces no spurious peak and that the radial velocity signal we detect is unrelated to activity.

A careful re-analysis of our original data[12] demonstrates that, despite being affected by intrinsic variability from the host star, they nonetheless confirm the presence of the planet signal detected in our new data. In particular, applying our filtering analysis to the main subset of our original data (featuring dense enough coverage for our technique to perform reliably) yields filtered radial velocities agreeing well with those derived from the new data. Fitting both sets together further improves the confidence level at which the planet is detected (see Extended Data Fig. 2c).

The detection we report among the small sample of weak-line T Tauri stars (~10) already studied with MaTYSSE suggests that close-in giant planets are potentially more frequent around T Tauri stars than around mature low-mass stars, ~1% of which are known to host hot Jupiters[25,26]. Poisson statistics, however, indicate that there is still a ~10% chance that hot Jupiters are similarly frequent for both populations. A more quantitative conclusion will have to await a thorough analysis of all MaTYSSE data, complemented by the large T Tauri star survey to be carried out with SPIRou, the new near-infrared cryogenic spectropolarimeter and velocimeter to be installed at CFHT in 2017.

The broad consensus is that hot Jupiters form beyond a few astronomical units from their host stars and migrate inwards to their eventual close-in orbits. The delivery of hot Jupiters to these orbits may result from planet–disk interactions[2] (disk migration) or from dynamical interactions with a planetary[3] or a stellar companion, followed by orbital circularisation (high-eccentricity migration). These highly debated migration channels were proposed as tentative explanations for hot Jupiters with orbits either well aligned or misaligned with the spin axis of their host stars[27]. Our detection of a hot Jupiter on a ~5-day circular (or moderately eccentric) orbit around a 2-Myr-old star is most naturally explained by the mechanism of hot Jupiter delivery by disk migration, which produces hot Jupiters with nearly circular orbits, rather than by planet–planet scattering, which generates highly eccentric ($e > 0.9$) hot Jupiters whose circularization timescales are at least 100 to 1,000 times longer[28] than the age of V830 Tau given typical tidal dissipation factors in giant planets[29]. Our result thus yields strong support to the theory of giant planet migration in gaseous protoplanetary disks[2] and confirms that the architecture of planetary systems, on which hot Jupiters have a strong impact, is probably dynamic from the very early stages of planetary formation.

Global models of planet formation and evolution show that giant planets can reach a mass and an orbital period similar to those of V830 Tau b in 2–3 Myr, whether formation occurs through core accretion or disk gravitational instability. Large uncertainties in these models make it difficult to accurately predict the occurrence rate of hot Jupiters and thus to associate V830 Tau b with either formation scenario. The ~300 G dipole of the star's magnetic field[12] is strong enough to have disrupted the central 0.06 AU of the now-dissipated disk for accretion rates $< 2 \times 10^{-10} M_\odot$ yr^{-1}. For rates of $\sim 10^{-9} M_\odot$ yr^{-1}, more typical of those of the classical T Tauri stars that still feed from their disks, a > 700 G dipole field is required, which is again compatible with observations of classical T Tauri stars similar to V830 Tau[12,30]. This shows that the field of V830 Tau may well have stopped the planet within the magnetospheric gap[1] at the end of its disk migration, and saved it from falling into the star.

Online Content Methods, along with any additional Extended Data display items and Source Data, are available in the online version of the paper; references unique to these sections appear only in the online paper.

Received 26 February; accepted 28 April 2016.
Published online 20 June 2016.

1. Lin, D. N. C., Bodenheimer, P. & Richardson, D. C. Orbital migration of the planetary companion of 51 Pegasi to its present location. *Nature* **380,** 606–607 (1996).
2. Baruteau, C. *et al.* in *Protostars and Planets VI* (eds Beuther, H., Klessen, R., Dullemond, C. & Henning, T.) Vol. 914, 667–689 (Univ. Arizona Press, 2014).
3. Chatterjee, S., Ford, E. B., Matsumura, S. & Rasio, F. A. Dynamical outcomes of planet-planet scattering. *Astrophys. J.* **686,** 580–602 (2008).
4. Setiawan, J. *et al.* A young massive planet in a star–disk system. *Nature* **451,** 38–41 (2008).
5. Huélamo, N. *et al.* TW Hydrae: evidence of stellar spots instead of a hot Jupiter. *Astron. Astrophys.* **489,** L9–L13 (2008).
6. van Eyken, J. C. *et al.* The PTF Orion project: a possible planet transiting a T-Tauri star. *Astrophys. J.* **755,** 42–55 (2012).
7. Kraus, A. L. & Ireland, M. J. LkCa 15: a young exoplanet caught at formation? *Astrophys. J.* **745,** 5–16 (2012).
8. Sallum, S. *et al.* Accreting protoplanets in the LkCa 15 transition disk. *Nature* **527,** 342–344 (2015).
9. Donati, J.-F. *et al.* The large-scale magnetic field and poleward mass accretion of the classical T Tauri star TW Hya. *Mon. Not. R. Astron. Soc.* **417,** 472–487 (2011).
10. Mahmud, N. I. *et al.* Starspot-induced optical and infrared radial velocity variability in T Tauri star Hubble I 4. *Astrophys. J.* **736,** 123–131 (2011).
11. Donati, J.-F. *et al.* Modeling the magnetic activity and filtering radial velocity curves of young Suns: the weak-line T Tauri star LkCa 4. *Mon. Not. R. Astron. Soc.* **444,** 3220–3229 (2014).
12. Donati, J.-F. *et al.* Magnetic activity and hot Jupiters of young Suns: the weak-line T Tauri stars V819 Tau and V830 Tau. *Mon. Not. R. Astron. Soc.* **453,** 3707–3720 (2015).
13. Grankin, K. N., Bouvier, J., Herbst, W. & Melnikov, S. Y. Results of the ROTOR-program. II. The long-term photometric variability of weak-line T Tauri stars. *Astron. Astrophys.* **479,** 827–843 (2008).
14. Siess, L., Dufour, E. & Forestini, M. An internet server for pre-main sequence tracks of low- and intermediate-mass stars. *Astron. Astrophys.* **358,** 593–599 (2000).
15. Kraus, A. L., Ireland, M. J., Hillenbrand, L. A. & Martinache, F. The role of multiplicity in disk evolution and planet formation. *Astrophys. J.* **745,** 19–29 (2012).
16. Donati, J.-F., Semel, M., Carter, B. D., Rees, D. E. & Collier Cameron, A. Spectropolarimetric observations of active stars. *Mon. Not. R. Astron. Soc.* **291,** 658–682 (1997).
17. Vogt, S. S., Penrod, G. D. & Hatzes, A. P. Doppler images of rotating stars using maximum entropy image reconstruction. *Astrophys. J.* **321,** 496–515 (1987).
18. Donati, J.-F. & Collier Cameron, A. Differential rotation and magnetic polarity patterns on AB Doradus. *Mon. Not. R. Astron. Soc.* **291,** 1–19 (1997).

© 2016 Macmillan Publishers Limited. All rights reserved

19. Donati, J.-F., Collier Cameron, A. & Petit, P. Temporal fluctuations in the differential rotation of cool active stars. *Mon. Not. R. Astron. Soc.* **345,** 1187–1199 (2003).
20. Morin, J. *et al.* The stable magnetic field of the fully convective star V374 Peg. *Mon. Not. R. Astron. Soc.* **384,** 77–86 (2008).
21. Mortier, A., Faria, J. P., Correia, C. M., Santerne, A. & Santos, N. C. BGLS: A Bayesian formalism for the generalised Lomb-Scargle periodogram. *Astron. Astrophys.* **573,** 101–106 (2015).
22. Haywood, R. D. *et al.* The Sun as a planet-host star: proxies from SDO images for HARPS radial-velocity variations. *Mon. Not. R. Astron. Soc.* **457,** 3637–3651 (2016).
23. Lucy, L. B. & Sweeney, M. A. Spectroscopic binaries with circular orbits. *Astron. J.* **76,** 544–556 (1971).
24. Petit, P. *et al.* A maximum entropy approach to detect close-in giant planets around active stars. *Astron. Astrophys.* **584,** 84–91 (2015).
25. Mayor, M. *et al.* The HARPS search for southern extra-solar planets. Occurrence, mass distribution and orbital properties of super-Earths and Neptune-mass planets. Preprint at http://arxiv.org/abs/1109.2497 (2011).
26. Wright, J. T. *et al.* The frequency of hot Jupiters orbiting nearby solar-type stars. *Astrophys. J.* **753,** 160–164 (2012).
27. Winn, J. N. & Fabrycky, D. C. The occurrence and architecture of exoplanetary systems. *Annu. Rev. Astron. Astrophys.* **53,** 409–447 (2015).
28. Ogilvie, G. I. Tidal dissipation in stars and giant planets. *Annu. Rev. Astron. Astrophys.* **52,** 171–210 (2014).
29. Goldreich, P. & Soter, S. *Q* in the Solar System. *Icarus* **5,** 375–389 (1966).
30. Donati, J.-F. *et al.* Magnetometry of the cTTS GQ Lup: non-stationary dynamos and spin evolution of young Suns. *Mon. Not. R. Astron. Soc.* **425,** 2948–2963 (2012).

Acknowledgements This paper is based on observations obtained at the CFHT Corporation (operated by the National Research Council of Canada, the Institut National des Sciences de l'Univers of the Centre National de la Recherche Scientifique (INSU/CNRS) of France and the University of Hawaii), at the Télescope Bernard Lyot (TBL) (operated by the Observatoire Midi-Pyrénées and by INSU/CNRS), and at the Gemini Observatory (operated by the Association of Universities for Research in Astronomy under a cooperative agreement with the National Science Foundation (NSF) on behalf of the Gemini partnership: the NSF of the United States, the National Research Council of Canada, CONICyT of Chile, the Ministerio de Ciencia, Tecnología e Innovación Productiva of Argentina, and the Ministério da Ciência, Tecnologia e Inovação of Brazil). We thank the Queue Service Observing teams of CFHT, TBL and the Gemini Observatory, without whom this study would not have been possible. We also thank the IDEX initiative of Université Fédérale Toulouse Midi-Pyrénées for awarding a 'Chaire d'Attractivité' to G.H., in the framework of which this work was done. S.A. acknowledges financial support from Conselho Nacional de Desenvolvimento Científico e Tecnológico (CNPq), Coordenação de Aperfeiçoamento de Pessoal de Nível Superior (CAPES) and Fundação de Amparo a Pesquisa do Estado de Minas Gerais (Fapemig).

Author Contributions This work merged data collected with two different instruments and three different telescopes. J.F.D. led the data processing, analysis and manuscript preparation. C.M., L.M., L.Y. and E.H. participated in the data collection and data analysis. C.B. contributed to the theoretical implications of the results. All authors, including G.H., S.A., M.T., F.M., J.B., P.P., R.D. and A.C.C., were involved in elaborating the observing proposals, in discussing the results at various stages of the analysis, and in providing contributions to older versions of the manuscript.

Author Information Reprints and permissions information is available at www.nature.com/reprints. The authors declare no competing financial interests. Readers are welcome to comment on the online version of the paper. Correspondence and requests for materials should be addressed to J.F.D. (jean-francois.donati@irap.omp.eu).

© 2016 Macmillan Publishers Limited. All rights reserved

METHODS

Spectropolarimetry with ESPaDOnS/NARVAL and the MaTYSSE programme. ESPaDOnS[31] and NARVAL are twin spectropolarimeters installed at the Cassegrain focus of the 3.6-m CFHT on top of Maunakea (Hawaii), and of the 2-m Bernard Lyot Telescope on top of Pic du Midi (France), respectively. Both include a fibre-fed bench-mounted high-resolution spectrograph, yielding full coverage of the 370–1,000 nm wavelength range in a single exposure at a spectral resolving power of 65,000. ESPaDOnS can also be fed from the 8-m Gemini-N Telescope next to CFHT, through a 300-m fibre link called GRACES[32], yielding spectra with either similar resolving power (in star-only mode) or half of it (in star + sky mode). In this run, we secured 16 spectra with ESPaDOnS from 2015 November 17 to December 02 in fair-weather conditions, 16 spectra with NARVAL from 2015 November 10 to December 17 in moderate to good weather, and 16 spectra with ESPaDOnS/GRACES on four different nights towards the end of the run (with 2 spectra in star-only mode and 14 spectra in star + sky mode). The full journal of observations is given in Extended Data Table 1. ESPaDOnS and NARVAL observations were secured in spectropolarimetric mode (circular polarization) in the framework of the MaTYSSE (MAgnetic Topologies of Young Stars and the Survival of close-in giant Exoplanets)[11] Large Programme, whereas ESPaDOnS/GRACES observations were collected in Director Discretionary Time in spectroscopic mode (no polarimetric unit on Gemini-N). All spectra were derived from raw frames with the reference pipeline implementing optimal extraction and radial velocity correction from telluric lines[16], yielding a typical root-mean-square radial velocity precision of 30 m s^{-1} (ref. 33).

Deriving mean line profiles with LSD. LSD[16] is a multiline technique similar to cross-correlation, used to derive line profiles with enhanced signal-to-noise ratio *S*/*N* from thousands of spectral lines simultaneously. For this study, the line list we used for LSD is derived from spectrum synthesis through model atmospheres computed assuming local thermodynamic equilibrium[34], for atmospheric parameters relevant for V830 Tau[12] (effective temperature of 4,250 K, logarithmic gravity of 4.0 and solar metallicity). Resulting *S*/*N* in LSD profiles are in the range 950–1,540 (see the journal of observations in Extended Data Table 1), corresponding to average multiplex gains in *S*/*N* of ∼10. LSD was also applied to circularly polarized spectra to retrieve average Zeeman signatures and longitudinal field estimates[16].

Doppler imaging of stellar surfaces and the modelling of differential rotation. Doppler imaging is a tomographic technique inspired from medical imaging, with which distributions of brightness features and magnetic fields at the surfaces of rotating stars can be reconstructed from time series of high-resolution spectropolarimetric observations. Doppler imaging is based on the fact that, thanks to the Doppler effect, line profiles of rotating stars can be interpreted as one-dimensional images of stellar surfaces, resolved in the Doppler direction but otherwise blurred. By coupling many such one-dimensional images recorded at different rotation phases, one can reliably reconstruct the parent surface distribution that gives rise to the observed line profiles and rotational modulation. First introduced in the late 1980s[17], Doppler imaging has been extensively used to investigate, with unprecedented accuracy, surface features and magnetic fields in cool stars other than the Sun[35,36]. Technically speaking, Doppler imaging follows the principles of maximum-entropy image reconstruction, and iteratively looks for the image with lowest information content that fits the data at a given χ^2 level. For more details on the imaging process, our previous MaTYSSE studies[11,12] give a detailed account of all modelling steps. In this Letter, we carried out Doppler imaging modelling using either unpolarized (Stokes I) spectra only, or both unpolarized and circularly polarized (Stokes V) spectra simultaneously, with identical results regarding filtering performances and the extraction of radial velocity signals.

By looking at how surface maps get twisted as a function of time, Doppler imaging can also estimate the amount of latitudinal differential rotation shearing stellar photospheres[18,19]. In this study we assume a typical solar-like differential rotation law in which the surface rotation rate varies with latitude θ as $\sin^2\theta$, and depends on two main parameters, the rotation rate at the equator Ω_{eq} and the difference in rotation rate between the equator and the pole, $d\Omega$. Both parameters are derived by looking for the pair that minimizes the χ^2 of the fit to the data (at constant information content in the reconstructed image, see Extended Data Fig. 1), whereas the corresponding error bars are computed from the curvature of the χ^2 paraboloid at its minimum[19]. Although helpful to achieve a more accurate description of the activity jitter and a cleaner filtering of raw radial velocity curves (at periods P_{rot} and $P_{rot}/2$ in particular), differential rotation as weak as that of V830 Tau has little impact on the filtered radial velocities; similar conclusions regarding the planet signal are obtained when assuming that V830 Tau is rotating as a solid body. A similar Doppler-imaging-based technique can be used to diagnose the presence of hot Jupiters around active stars[24], with the planet parameters replacing those describing differential rotation. This alternate method yields identical results to those presented here for our data set (see Fig. 4).

Filtering LSD profiles from lunar contamination. Spectra recorded in non-photometric conditions near full-moon epochs are often contaminated by solar light reflected off the moon and diffused by clouds. To filter out this pollution, whose location and width is well known at any given epoch but whose strength we want to determine, we implement a dual-step Doppler imaging process. The first step consists in applying Doppler imaging to the set of original LSD profiles, with scaled-up error bars for all pixels potentially affected by lunar contamination; the strength of the lunar contamination is then measured with a Gaussian fit to the residuals, and subtracted from the polluted LSD profiles. In the second step, conventional Doppler imaging is applied to the set of filtered LSD profiles with original error bars. This dual-step process is found to be very efficient when applied to densely sampled data sets like the one presented here, in which profiles at similar phases but different rotation cycles provide a strong constraint on the strength of lunar pollution. In our data, 6 LSD profiles suffer from a strong pollution (rotation cycles 6.0 to 7.6, see Fig. 1), whereas 9 others are affected at a much weaker level.

If we exclude the 6 strongly moon-polluted profiles (or all 15 moon-polluted profiles) from our data set, the radial velocity signal from V830 Tau b is still clearly detected, though with a lower confidence rate of 99.9% (or 99%), reflecting the poorer temporal coverage and the degraded window function (see Fig. 3a and Extended Data Fig. 2a). This check shows that our decontamination process is successful at restoring the original profile distortions and at retaining the radial velocity content, provided the data set is dense enough.

Revisiting the original data set from 2014 December and 2015 January. A careful re-analysis of our original data (consisting of two subsets shifted in time by 17 days[12], see Extended Data Table 3) indicates that variability occurred at the surface of the star between the two subsets. Whereas Doppler imaging succeeds at adjusting the main subset (9 evenly spaced points secured in 2015 January) down to the noise level, as for our new data, fitting both subsets together requires us to lower *S*/*N* values in the 2014 December subset by ∼15% in order to reach unit reduced χ^2. This is definite evidence that intrinsic variability (beyond pure differential rotation) occurred at the surface of V830 Tau between both subsets, with profile 6 of the 2014 December subset being the most affected. This variability reflects a modification in the brightness map, subtle enough to affect Doppler imaging no more than moderately, yet large enough to substantially affect filtered radial velocities, which are quite sensitive even to small features in the brightness map. It illustrates how tricky activity filtering can get when dealing with intrinsic variability, and how critical dense and even phase coverage is to diagnose it efficiently.

As a result of this variability, our filtering analysis can only be applied to the individual subsets of our original data, and in fact to no more than the 2015 January subset, the other being far too sparse and uneven for the technique to perform reliably. We find that the filtered radial velocities from the main subset (see Extended Data Table 3) agree with those of our new data; fitting them together improves the confidence level at which the planet is detected, but not the accuracy on the orbital period (see Extended Data Fig. 2c).

Enabling us to shortcut the computation of filtered radial velocities, the Doppler-imaging-based method of adjusting the planet parameters simultaneously with the distribution of surface features[24] offers an alternative way to confirm that the radial velocity signal from the detected planet is present in our original data. (This method however still suffers from the inability of Doppler imaging to describe intrinsic variability beyond differential rotation). Freezing the planet orbital period to the value found in our new analysis (4.93 days) and applying this technique to the full set of our original data with only profile 6 removed, we find a semi-amplitude of 67 ± 18 m s^{-1} for the planet radial velocity signature, which agrees well with the measurement derived from our main study. We also confirm that our original data are better explained by a model including a planet in a 4.93-day orbit than by one with no planet, with a false-alarm probability of ∼0.01% (corresponding to a χ^2 increase of 19 for the 644 data points of the fitted LSD profiles).

Code availability. The Doppler imaging code used for this study is as yet undocumented and has thus not been released in the public domain.

31. Donati, J.-F. ESPaDOnS: An Echelle SpectroPolarimetric Device for the Observation of Stars at CFHT. *ASP Conf. Proc.* **307,** 41–50 (2003).
32. Chené, A. N. *et al.* GRACES: Gemini remote access to CFHT ESPaDOnS spectrograph through the longest astronomical fiber ever made: experimental phase completed. *Proc. SPIE* **9151,** 47–62 (2014).
33. Moutou, C. *et al.* Spectropolarimetric observations of the transiting planetary system of the K dwarf HD 189733. *Astron. Astrophys.* **473,** 651–660 (2007).
34. Kurucz, R. ATLAS9 atmospheric models, ATLAS9 and SYNTHE routines, spectral line database. CDROM 13 and 18, http://kurucz.harvard.edu/cdroms.html (1993).
35. Collier Cameron, A. Spot mapping in cool stars. *Lecture Notes Phys.* **573,** 183–206 (2001).
36. Morin, J. Magnetic fields from low-mass stars to brown dwarfs. EAS Publ. Ser. 57, 165–191 (2012).

© 2016 Macmillan Publishers Limited. All rights reserved

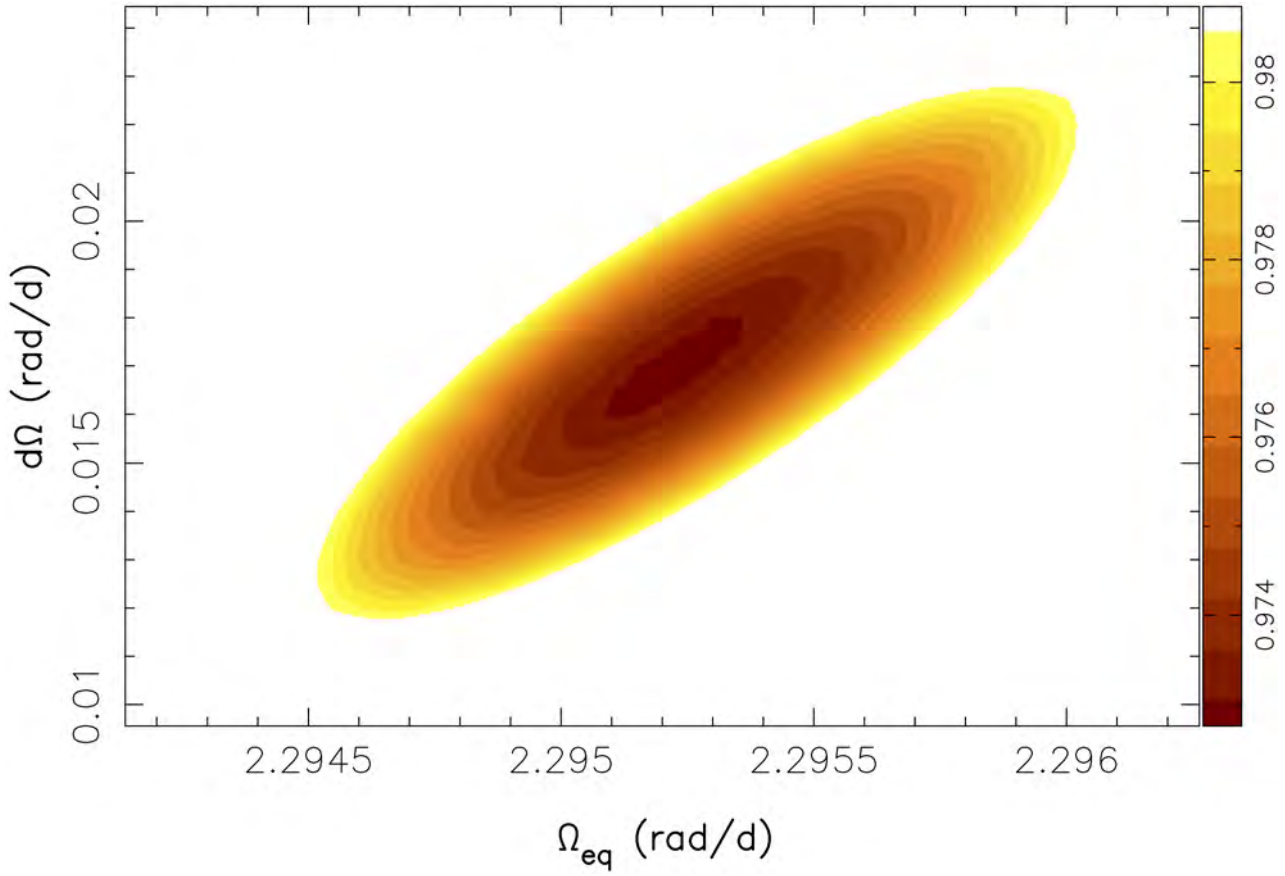

Extended Data Figure 1 | Estimating the surface differential rotation parameter. Variations of the reduced χ^2 as a function of the surface differential rotation parameters Ω_{eq} and $d\Omega$, denoting respectively the rotation rate at the equator and the difference in rotation rate between the equator and the pole (and assuming a solar-like sine-square differential rotation law). The location of the minimum and the local paraboloid curvature yield the optimal parameters and their respective 1σ error bars[19], equal to 2.29525 ± 0.00020 and 0.0172 ± 0.0014 radians per day. The outer colour contour traces the 99.99% confidence interval (corresponding to a χ^2 increase of 18.4 for a two-parameter optimization problem).

© 2016 Macmillan Publishers Limited. All rights reserved

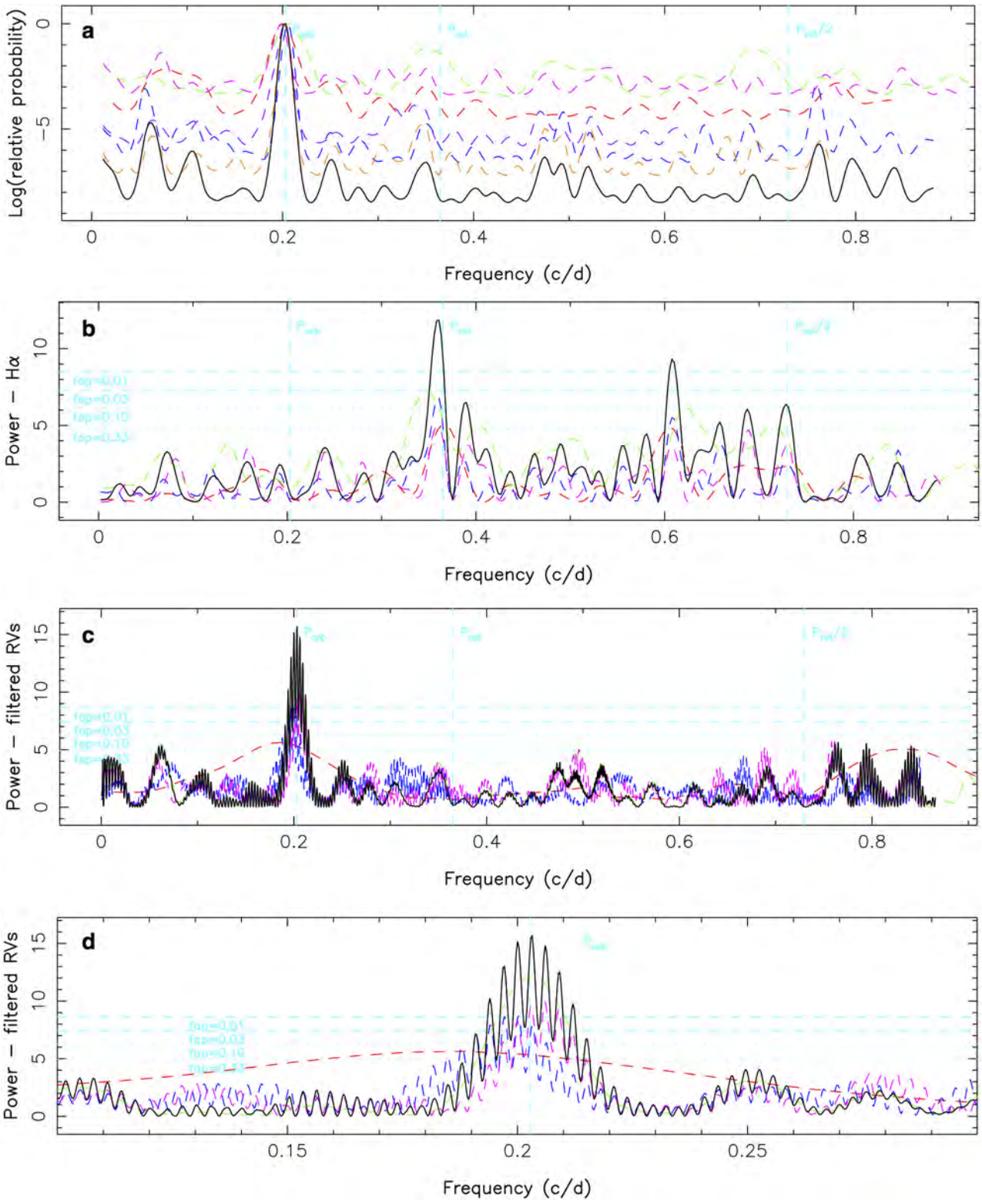

Extended Data Figure 2 | Complementary periodograms. a, Same as Fig. 3a (middle plot) using the BGLS approach[21], showing that the 4.93-day peak we detect is at least 10^5 times more likely than any other features. **b**, Same as Fig. 3b for Hα emission, another activity proxy, featuring a clear peak at the stellar rotation period but no power at the planet orbital period. **c**, Same as Fig. 3a (middle plot) for our new data combined with the 2015 January subsample of our original data[12]. The planet is now detected with a higher confidence level (FAP $< 10^{-5}$) but the accuracy of the orbital period is not much improved (with multiple nearby peaks of similar strength). The red and green dashed lines are for the original and new data respectively. **d**, Same as **c**, zooming on the orbital frequency. The orbital period corresponding to the strongest peak is equal to 4.924 ± 0.004 days (1σ error bar).

© 2016 Macmillan Publishers Limited. All rights reserved

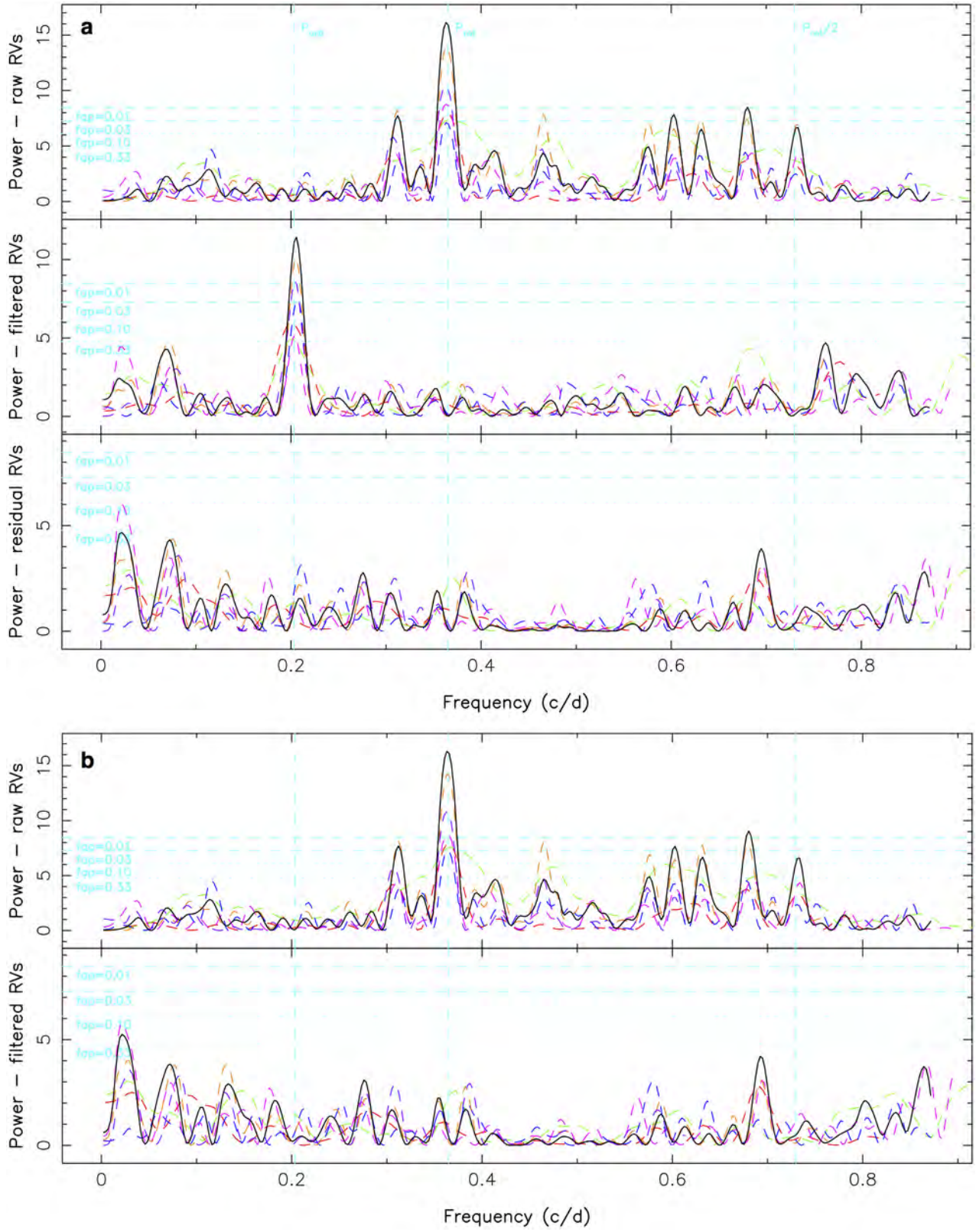

Extended Data Figure 3 | Periodograms of simulated data. a, Same as Fig. 3, for simulated data computed using the brightness map, differential rotation and planet parameters inferred from the real data, and assuming the same coverage and similar *S*/*N* (equal for all LSD profiles). As for our observations, the planet signal is detected at a confidence level >99.9% in the filtered radial velocities despite being invisible in the raw radial velocities, and the planet parameters are well recovered. The periodogram of the raw radial velocities is very similar to that of Fig. 3, featuring the main peaks (at P_{rot} and $P_{rot}/2$) and their aliases; residual radial velocities mostly reflect the noise in the data. **b**, Same as the upper two panels of **a** but with no planet included in the simulation. No signal with a confidence level >90% is recovered in the filtered radial velocities, demonstrating that the filtering process is not generating spurious radial velocity signals, in particular at a period of 4.93 days.

© 2016 Macmillan Publishers Limited. All rights reserved

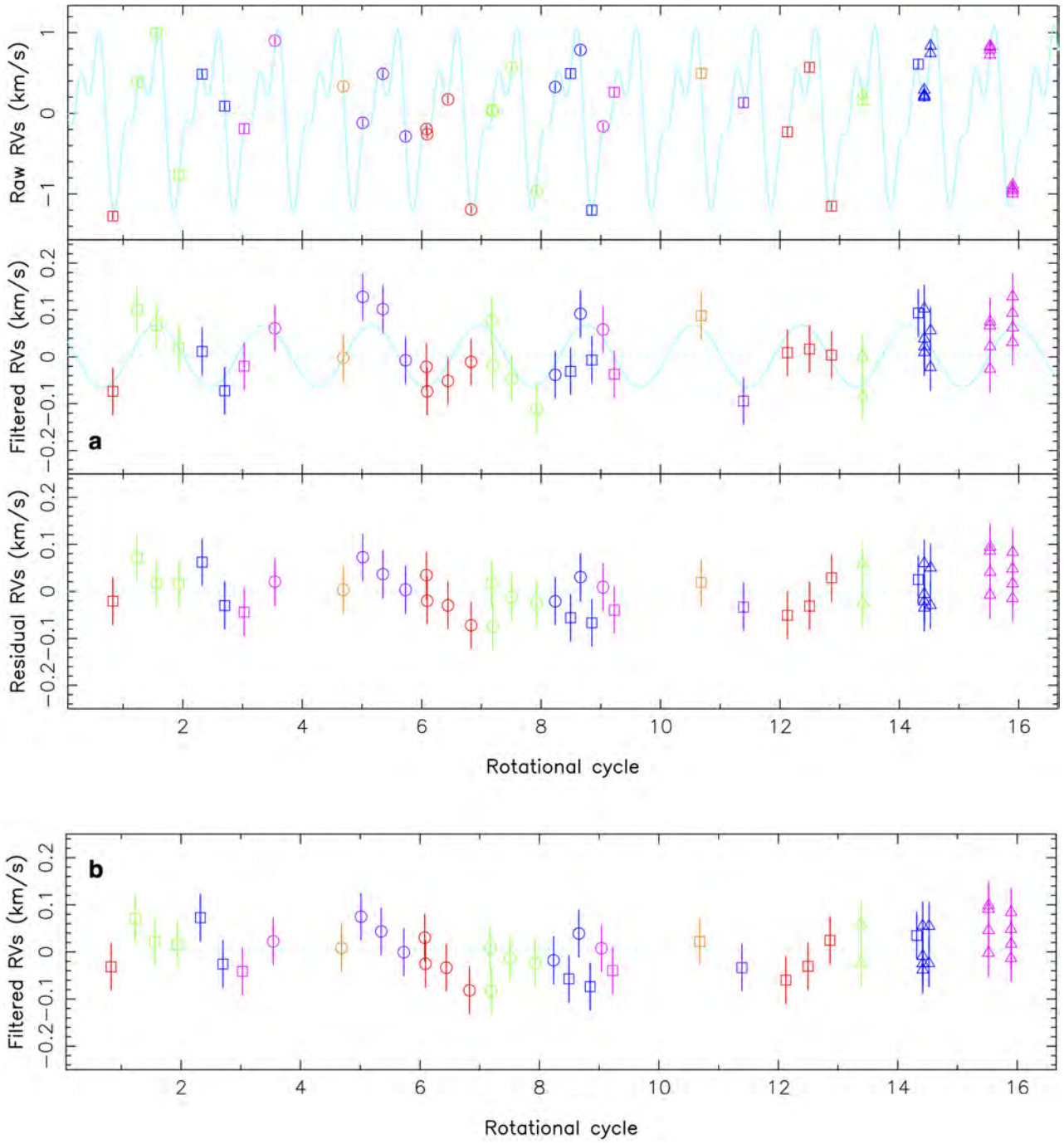

Extended Data Figure 4 | Radial velocity curves of simulated data. **a**, Same as Fig. 2a for the simulated data described in Extended Data Fig. 3a (using the same brightness map, differential rotation and planet parameters as those of V830 Tau b). The simulated radial velocities (periodograms shown in Extended Data Fig. 3a) share obvious similarities with the observed ones, and the planet signal is safely recovered (root-mean-square dispersion of residual radial velocities equal to 45 m s^{-1}). **b**, Same as the middle panel of **a** but with no planet included. As for the periodogram (see Extended Data Fig. 3b, bottom panel), no signal is detected, further illustrating that activity induces no spurious planet signature. As for Fig. 2, simulated radial velocity measurements are depicted in all panels with their 1σ error bars.

© 2016 Macmillan Publishers Limited. All rights reserved

Extended Data Table 1 | Journal of observations

UT date (2015)	instrument	BJD (2457300+)	R (K)	t_{exp} (s)	S/N	S/N_{LSD}	rot cycle r (118+)	orb cycle o (5-)	raw RV (km/s)	filt RV (km/s)	RV err (km/s)
Nov 11	NARVAL	37.5066	65	4800	90	1149	0.828	0.332	-1.362	-0.150	0.067
Nov 12	NARVAL	38.6187	65	4800	100	1251	1.233	0.557	0.365	0.074	0.061
Nov 13	NARVAL	39.5077	65	4800	103	1278	1.558	0.738	0.960	0.022	0.059
Nov 14	NARVAL	40.5427	65	4800	95	1233	1.935	0.948	-0.828	-0.035	0.062
Nov 15	NARVAL	41.6051	65	4800	89	1152	2.323	1.163	0.504	0.005	0.067
Nov 16	NARVAL	42.6375	65	4800	105	1257	2.700	1.373	0.137	-0.036	0.060
Nov 17	NARVAL	43.5347	65	4800	84	1113	3.027	1.555	-0.151	0.031	0.070
Nov 18	ESPaDOnS	44.9422	65	2780	162	1420	3.540	1.840	0.830	-0.016	0.048
Nov 21	ESPaDOnS	48.0862	65	2780	168	1380	4.687	2.478	0.382	0.031	0.050
Nov 22	ESPaDOnS	48.9770	65	2780	170	1428	5.012	2.658	-0.199	0.060	0.048
Nov 23	ESPaDOnS	49.9011	65	2780	169	1428	5.350	2.846	0.489	0.087	0.048
Nov 24	ESPaDOnS	50.9411	65	2780	158	1396	5.729	3.057	-0.317	-0.041	0.050
Nov 25	ESPaDOnS	51.9015	65	2780	154	1482	6.079	3.252	-0.312	-0.120	0.048
Nov 25	ESPaDOnS	51.9372	65	2780	164	1480	6.092	3.259	-0.243	-0.040	0.047
Nov 26	ESPaDOnS	52.8917	65	2780	164	1539	6.441	3.452	0.089	-0.126	0.047
Nov 27	ESPaDOnS	53.9535	65	2780	160	1439	6.828	3.668	-1.207	-0.016	0.049
Nov 28	ESPaDOnS	54.9089	65	2780	144	1458	7.177	3.862	-0.014	0.018	0.047
Nov 28	ESPaDOnS	54.9449	65	2780	131	1453	7.190	3.869	0.020	-0.028	0.048
Nov 29	ESPaDOnS	55.8153	65	2780	166	1434	7.507	4.045	0.648	0.029	0.048
Nov 30	ESPaDOnS	56.9632	65	2780	175	1436	7.926	4.278	-0.992	-0.123	0.048
Dec 01	ESPaDOnS	57.8164	65	2780	167	1447	8.237	4.451	0.393	0.014	0.047
Dec 02	NARVAL	58.5216	65	4800	89	1131	8.495	4.594	0.602	0.078	0.069
Dec 02	ESPaDOnS	58.9744	65	2780	168	1428	8.660	4.686	0.823	0.113	0.049
Dec 02	NARVAL	59.4928	65	4800	82	1089	8.849	4.791	-1.054	0.148	0.073
Dec 03	ESPaDOnS	60.0148	65	2780	176	1458	9.039	4.897	-0.163	0.073	0.047
Dec 04	NARVAL	60.5247	65	4800	90	1191	9.225	5.001	0.328	0.019	0.064
Dec 07	NARVAL	64.5183	65	4800	108	1221	10.682	5.811	0.568	0.151	0.064
Dec 09	NARVAL	66.4571	65	4800	89	1161	11.390	6.204	0.155	-0.068	0.066
Dec 11	NARVAL	68.4771	65	4800	88	1218	12.127	6.614	-0.148	0.103	0.064
Dec 12	NARVAL	69.4897	65	4800	69	978	12.496	6.819	0.578	0.024	0.083
Dec 13	NARVAL	70.5011	65	4800	104	1335	12.865	7.024	-1.107	0.055	0.057
Dec 15	ESPaDOnS / GRACES	71.9290	35	540	218	1385	13.386	7.314	0.178	-0.048	0.068
Dec 15	ESPaDOnS / GRACES	71.9359	35	540	214	1388	13.389	7.315	0.148	-0.068	0.068
Dec 17	NARVAL	74.4815	65	4800	90	1257	14.317	7.832	0.617	0.080	0.060
Dec 18	ESPaDOnS / GRACES	74.7548	35	85	72	974	14.417	7.887	0.222	0.058	0.073
Dec 18	ESPaDOnS / GRACES	74.7565	35	85	73	992	14.418	7.888	0.203	0.039	0.072
Dec 18	ESPaDOnS / GRACES	74.7581	35	85	78	990	14.418	7.888	0.222	0.057	0.072
Dec 18	ESPaDOnS / GRACES	74.7597	35	85	77	996	14.419	7.888	0.242	0.078	0.071
Dec 18	ESPaDOnS / GRACES	75.0425	65	360	123	1396	14.522	7.946	0.788	0.016	0.045
Dec 18	ESPaDOnS / GRACES	75.0474	65	360	107	1369	14.524	7.947	0.840	0.053	0.046
Dec 21	ESPaDOnS / GRACES	77.7761	35	85	75	990	15.519	8.500	0.792	0.037	0.072
Dec 21	ESPaDOnS / GRACES	77.7777	35	85	74	986	15.520	8.500	0.766	0.006	0.072
Dec 21	ESPaDOnS / GRACES	77.7793	35	85	74	982	15.520	8.501	0.729	-0.035	0.073
Dec 21	ESPaDOnS / GRACES	77.7810	35	85	74	976	15.521	8.501	0.819	0.050	0.073
Dec 22	ESPaDOnS / GRACES	78.8110	35	85	58	946	15.897	8.710	-0.864	0.161	0.076
Dec 22	ESPaDOnS / GRACES	78.8126	35	85	64	956	15.897	8.710	-0.928	0.093	0.076
Dec 22	ESPaDOnS / GRACES	78.8143	35	85	61	964	15.898	8.711	-0.880	0.139	0.074
Dec 22	ESPaDOnS / GRACES	78.8159	35	85	62	958	15.899	8.711	-0.929	0.087	0.075

Rotation and orbital cycles r and o are respectively given by the ephemeris BJD = 2,457,011.8 + 2.741r and 2,457,360.52 + 4.93o. For each observation, R, S/N and S/N_{LSD} list the resolving power, the S/N in the raw spectrum and the S/N in the LSD profile, whereas the last three columns list the raw and filtered radial velocities (RV) and the corresponding 1σ error bars (reflecting both the photon noise and the instrumental radial velocity precision). The first and fifth column respectively list the observing dates in universal time (UT) and the corresponding exposure time t_{exp}.

© 2016 Macmillan Publishers Limited. All rights reserved

Extended Data Table 2 | Main parameters of the planet and of the host star

orbital period (d)	K (m/s)	BJD of transit	orbital distance (au)	m_{planet} sin i ($M_{\oplus}$)	m_{planet} ($M_{\oplus}$)
4.93±0.05	75±11	2457360.52±0.10	0.057±0.001	0.63±0.11	0.77±0.15

M_{star} ($M_{\odot}$)	R_{star} ($R_{\odot}$)	age (Myr)	T_{eff} (K)	log($L/L_{\odot}$)	P_{rot} (d)	v sin i (km/s)	i (°)	distance (pc)
1.00±0.05	2.0±0.2	~2	4250±50	0.08±0.10	2.741	30.5±0.5	55±10	131±3

Top, main parameters (with 1σ error bars) of V830 Tau b assuming a circular orbit. Bottom, main parameters (with 1σ error bars) of the host star V830 Tau[12], with T_{eff} denoting the effective temperature of the photosphere.

© 2016 Macmillan Publishers Limited. All rights reserved

Extended Data Table 3 | Journal of observations for the original data

UT date (2014-2015)	instrument	BJD (2457000+)	R (K)	t_{exp} (s)	S/N	S/N_{LSD}	rot cycle r	raw RV (km/s)	filt RV (km/s)	RV err (km/s)
Dec 20	ESPaDOnS	11.8899	65	2800	170	1501	0.033	0.721		0.049
Dec 21	ESPaDOnS	12.8622	65	2800	170	1504	0.388	0.197		0.050
Dec 22	ESPaDOnS	13.9010	65	2800	180	1520	0.767	-0.513		0.049
Dec 28	ESPaDOnS	20.0190	65	2800	140	1498	2.999	0.446		0.049
Dec 29	ESPaDOnS	20.8759	65	2800	160	1478	3.311	-0.137		0.050
Dec 30	ESPaDOnS	21.8154	65	2800	160	1478	3.654	0.240		0.050
Jan 07	ESPaDOnS	29.8629	65	2800	170	1498	6.590	-0.044	0.031	0.049
Jan 08	ESPaDOnS	30.8217	65	2800	180	1490	6.940	-0.206	-0.031	0.049
Jan 09	ESPaDOnS	31.8181	65	2800	170	1523	7.303	-0.151	-0.062	0.051
Jan 10	ESPaDOnS	32.8186	65	2800	150	1476	7.668	0.044	-0.011	0.050
Jan 11	ESPaDOnS	33.8669	65	2800	180	1495	8.051	1.085	0.076	0.050
Jan 12	ESPaDOnS	34.7215	65	2800	170	1473	8.362	0.246	0.073	0.050
Jan 13	ESPaDOnS	35.7150	65	2800	160	1501	8.725	-0.264	-0.001	0.050
Jan 14	ESPaDOnS	36.7141	65	2800	170	1501	9.089	0.929	-0.067	0.050
Jan 15	ESPaDOnS	37.8043	65	2800	170	1470	9.487	-0.202	-0.052	0.050

Same as Extended Data Table 1 for the 2014 December and 2015 January data[12]. Our filtering technique is found to be reliable only for data sets with dense and regular phase coverage, hence the absence of filtered radial velocities for the 2014 December subset of 2×3 points, which does not satisfy this requirement. Filtered radial velocities from 2015 January 07–15 agree well with those derived from our new data (see Extended Data Table 1).

© 2016 Macmillan Publishers Limited. All rights reserved

B.2.2 MNRAS publication: Donati et al. 2017

Monthly Notices of the ROYAL ASTRONOMICAL SOCIETY

MNRAS **465,** 3343–3360 (2017) doi:10.1093/mnras/stw2904
Advance Access publication 2016 November 10

The hot Jupiter of the magnetically active weak-line T Tauri star V830 Tau

J.-F. Donati,[1,2]★ L. Yu,[1,2] C. Moutou,[3] A. C. Cameron,[4] L. Malo,[3,5] K. Grankin,[6] E. Hébrard,[7] G. A. J. Hussain,[1,8] A. A. Vidotto,[9] S. H. P. Alencar,[10] R. D. Haywood,[11] J. Bouvier,[12,13] P. Petit,[1,2] M. Takami,[14] G. J. Herczeg,[15] S. G. Gregory,[4] M. M. Jardine,[4] J. Morin[16] and the MaTYSSE collaboration

[1]*Université de Toulouse, UPS-OMP, IRAP, 14 Avenue E. Belin, Toulouse F-31400, France*
[2]*CNRS, IRAP/UMR 5277, Toulouse, 14 Avenue E. Belin, Toulouse F-31400, France*
[3]*CFHT Corporation, 65-1238 Mamalahoa Hwy, Kamuela, HI 96743, USA*
[4]*SUPA, School of Physics and Astronomy, Univ. of St Andrews, St Andrews, Scotland KY16 9SS, UK*
[5]*Département de physique, Université de Montréal, C.P. 6128, Succursale Centre-Ville, Montréal, QC H3C 3J7, Canada*
[6]*Crimean Astrophysical Observatory, Nauchny 298409, Crimea*
[7]*Department of Physics and Astronomy, York University, Toronto, ON L3T 3R1, Canada*
[8]*ESO, Karl-Schwarzschild-Str. 2, D-85748 Garching, Germany*
[9]*School of Physics, Trinity College Dublin, the University of Dublin, College Green, Dublin 2, Ireland*
[10]*Departamento de Fìsica – ICEx – UFMG, Av. Antônio Carlos, 6627, 30270-901 Belo Horizonte, MG, Brazil*
[11]*Harvard–Smithsonian Center for Astrophysics, 60 Garden Street, Cambridge, MA 02138, USA*
[12]*Université Grenoble Alpes, IPAG, BP 53, F-38041 Grenoble Cédex 09, France*
[13]*CNRS, IPAG / UMR 5274, BP 53, F-38041 Grenoble Cédex 09, France*
[14]*Institute of Astronomy and Astrophysics, Academia Sinica, PO Box 23-141, 106 Taipei, Taiwan*
[15]*Kavli Institute for Astronomy and Astrophysics, Peking University, Yi He Yuan Lu 5, Haidian Qu, Beijing 100871, China*
[16]*LUPM, Université de Montpellier, CNRS, place E. Bataillon, F-34095 Montpellier, France*

Accepted 2016 November 7. Received 2016 November 7; in original form 2016 September 16

ABSTRACT

We report results of an extended spectropolarimetric and photometric monitoring of the weak-line T Tauri star V830 Tau and its recently detected newborn close-in giant planet. Our observations, carried out within the MaTYSSE (Magnetic Topologies of Young Stars and the Survival of close-in giant Exoplanets) programme, were spread over 91 d, and involved the ESPaDOnS and Narval spectropolarimeters linked to the 3.6-m Canada–France–Hawaii, the 2-m Bernard Lyot, and the 8-m Gemini-North Telescopes. Using Zeeman-Doppler Imaging, we characterize the surface brightness distributions, magnetic topologies, and surface differential rotation of V830 Tau at the time of our observations, and demonstrate that both distributions evolve with time beyond what is expected from differential rotation. We also report that near the end of our observations, V830 Tau triggered one major flare and two weaker precursors, showing up as enhanced redshifted emission in multiple spectral activity proxies. With three different filtering techniques, we model the radial velocity (RV) activity jitter (of semi-amplitude 1.2 km s^{-1}) that V830 Tau generates, successfully retrieve the 68 ± 11 m s^{-1} RV planet signal hiding behind the jitter, further confirm the existence of V830 Tau b, and better characterize its orbital parameters. We find that the method based on Gaussian-process regression performs best thanks to its higher ability at modelling not only the activity jitter, but also its temporal evolution over the course of our observations, and succeeds at reproducing our RV data down to an rms precision of 35 m s^{-1}. Our result provides new observational constraints on scenarios of star/planet formation and demonstrates the scientific potential of large-scale searches for close-in giant planets around T Tauri stars.

Key words: techniques: polarimetric – stars: formation – stars: imaging – stars: individual: V830 Tau – stars: magnetic field – planetary systems.

★ E-mail: jean-francois.donati@irap.omp.eu

© 2016 The Authors
Published by Oxford University Press on behalf of the Royal Astronomical Society

1 INTRODUCTION

Magnetic fields are thought to play a key role in the formation of stars and their planets (e.g. André, Basu & Inutsuka 2009; Baruteau et al. 2014), and for their subsequent evolution into maturity. For instance, large-scale fields of low-mass pre-main-sequence (PMS) stars, the so-called T Tauri stars (TTSs), are known to control and even trigger physical processes such as accretion, outflows, and angular momentum transport, through which they mostly dictate the rotational evolution of TTSs (e.g. Bouvier et al. 2007; Frank et al. 2014). Large-scale fields of TTSs may also help newborn close-in giant planets to avoid falling into their host stars and survive the fast migration that accretion discs efficiently trigger, thanks to the magnetospheric gaps that they carve at the disc centre (e.g. Lin, Bodenheimer & Richardson 1996; Romanova & Lovelace 2006). The recent discoveries (or candidate detections) of newborn close-in giant planets around TTSs (van Eyken et al. 2012; David et al. 2016; Donati et al. 2016; Johns-Krull et al. 2016; Mann et al. 2016) render the study of the latter topic particularly attractive and timely.

Although first detected long ago (e.g. Johns-Krull, Valenti & Koresko 1999; Johns-Krull 2007), magnetic fields of TTSs are not yet fully characterized, neither for those still surrounded by their accretion discs (the classical T Tauri stars/cTTSs) nor for those whose discs have dissipated already (the weak-line T Tauri stars/wTTSs). Only recently were the field topologies of a dozen cTTSs unveiled (e.g. Donati et al. 2007, 2010, 2013; Hussain et al. 2009) thanks to the MaPP (Magnetic Protostars and Planets) Large Observing Programme on the 3.6 m Canada–France–Hawaii Telescope (CFHT) with the ESPaDOnS high-resolution spectropolarimeter (550 h of clear time over semester 2008b to 2012b). This first exploration revealed for instance that large-scale fields of cTTSs can be either relatively simple or quite complex depending on whether the host star is largely convective or mostly radiative (Gregory et al. 2012; Donati et al. 2013); it also showed that these fields vary with time (e.g. Donati et al. 2011, 2012, 2013) and mimic the fields of mature stars with similar internal structures (Morin et al. 2008), suggesting a dynamo origin.

The ongoing MaTYSSE (Magnetic Topologies of Young Stars and the Survival of close-in giant Exoplanets) Large Programme, allocated at CFHT over semesters 2013a–2016b (510 h) with complementary observations with the Narval spectropolarimeter on the 2-m Télescope Bernard Lyot (TBL) at Pic du Midi in France (450 h, allocated) and with the HARPS spectropolarimeter at the 3.6-m ESO Telescope at La Silla in Chile (135 h, allocated), is carrying out the same kind of magnetic exploration on a few tens of wTTSs (Donati et al. 2014, 2015, hereafter D14, D15). MaTYSSE also aims at probing the potential presence of newborn close-in giant exoplanets (hot Jupiters/hJs) at an early stage of star/planet formation; it recently succeeded at detecting the youngest such body orbiting only 0.057 au (or 6.1 stellar radii) away from the 2 Myr wTTS V830 Tau (Donati et al. 2016, hereafter D16), strongly suggesting that disc migration is a viable and likely efficient mechanism for generating hJs.

In this new paper, we revisit the latest MaTYSSE data set collected on V830 Tau, including extended observations from early 2016 that follow the late 2015 ones from which V830 Tau b was detected, as well as contemporaneous photometry secured at the Crimean Astrophysical Observatory (CrAO). After briefly documenting these additional data (Section 2), we apply Zeeman-Doppler Imaging (ZDI) to both subsets to accurately model the surface features and large-scale magnetic fields generating the observed activity (Section 3). This modelling is then used to predict the activity jitter[1] and retrieve the planet signature using two complementary methods, yielding results in agreement with a third completely independent technique based on Gaussian-process regression (e.g. Haywood et al. 2014; Rajpaul et al. 2015) and with those of D16 (Section 4). We finally summarize our results and stress how MaTYSSE-like explorations can unlock current limitations in our understanding of how giant planets and planetary systems form (Section 5).

2 SPECTROPOLARIMETRIC AND PHOTOMETRIC OBSERVATIONS OF V830 TAU

Following our intensive campaign in late 2015 (D16), V830 Tau was re-observed from 2016 Jan 14 to Feb 10, using again ESPaDOnS at the CFHT, its clone Narval at the TBL, and ESPaDOnS coupled to Gemini-North through the GRACES fibre link (Chene et al. 2014). ESPaDOnS and Narval collect spectra covering 370–1000 nm at a resolving power of 65 000 (Donati 2003). A total of 15, 6, and 6 spectra were, respectively, collected with ESPaDOnS, Narval, and ESPaDOnS/GRACES, at a daily rate from Jan 14 to 30 and more sparsely afterwards. ESPaDOnS and NARVAL were used in spectropolarimetric modes, with all collected spectra consisting of a sequence of four individual subexposures (of duration 690 and 1200 s each for ESPaDOnS and Narval, respectively) recorded in different polarimeter configurations to allow the removal of all spurious polarization signatures at first order. ESPaDOnS/GRACES spectra were collected in spectroscopic 'star only' mode, with a resolution similar to that of all other spectra, and consist of single 300 s observations. All raw frames are processed with the reference pipeline LIBRE ESPRIT implementing optimal extraction and radial velocity (RV) correction from telluric lines, yielding a typical rms RV precision of 20–30 m s^{-1} (Moutou et al. 2007; Donati et al. 2008). Least-squares deconvolution (LSD; Donati et al. 1997) was applied to all spectra, using the same line list as in our previous studies (D15, D16). The full journal of observations is presented in Table 1.

Rotational and orbital cycles of V830 Tau (denoted r and o in the following equations) are computed from Barycentric Julian Dates (BJDs) according to the ephemerides:

$$\mathrm{BJD(d)} = 2\,457\,011.80 + 2.741r \quad (1)$$

$$\mathrm{BJD(d)} = 2\,457\,360.52 + 4.93o \quad (2)$$

in which the photometrically determined rotation periods $P_{\rm rot}$ and the orbital period $P_{\rm orb}$ of the hJ are set to 2.741 d and 4.93 d, respectively (Grankin 2013, hereafter G13; D16). Although the initial Julian date of the first ephemeris is chosen arbitrarily, that of the second one coincides with the inferior conjunction (with the hJ in front).

As in our late-2015 data (D16), a few spectra (eight altogether, corresponding to cycles 1.347, 2.090, 2.692, 2.820, 3.068, 3.185, 3.914, and 4.135) were weakly affected by moonlight in the far blue wing of the spectral lines, due to the proximity of the moon (passing within Taurus in Dec and Jan) and/or to non-photometric conditions. To filter this contamination from our Stokes I LSD profiles, we applied the dual-step method described in D16, specifically designed for this purpose and shown to be quite efficient at restoring

[1] Throughout the paper, we call 'activity jitter' or 'jitter' the RV signal that activity generates, and not an 'independent, identically distributed Gaussian noise' as in, e.g. Aigrain et al. (2012).

Table 1. Journal of ESPaDOnS observations of V830 Tau collected in from 2016 Jan 14 to Feb 10. ESPaDOnS and Narval spectropolarimetric observations consist of sequences of four subexposures (each lasting 690 s and 1200 s, respectively) whereas ESPaDOnS/GRACES exposures correspond to single (unpolarized) observations lasting 300 s each. Columns 1–5, respectively, list (i) the UT date of the observation, (ii) the instrument used, (iii) the corresponding UT time (at mid-exposure), (iv) the Barycentric Julian Date (BJD), and (v) the peak signal-to-noise ratio S/N (per 2.6 km s^{-1} velocity bin) of each observation. Columns 6 and 7, respectively, list the S/N in Stokes *I* LSD profiles (per 1.8 km s^{-1} velocity bin), and the rms noise level (relative to the unpolarized continuum level I_c) in Stokes *V* LSD profiles (whenever relevant). Columns 8 and 9 indicate the rotational *r* and orbital *o* cycles associated with each exposure (using the ephemerides given by equation 2). Columns 10–12, respectively, give the raw and ZDI-filtered RVs v_{raw} and v_{fil}, as well as the corresponding 1σ error bars σ_{RV}. No v_{fil} estimates are available for Jan 30 and Feb 10 spectra, affected by strong flares. The observation log of our late 2015 data can be found in D16 (Extended Data Table 1).

Date (2016)	Instrument	UT (hh:mm:ss)	BJD (2457400+)	S/N	S/N$_{LSD}$	σ_{LSD} (0.01 per cent)	*r* (142+)	*o* (8+)	v_{raw} (km s^{-1})	v_{fil} (km s^{-1})	σ_{RV} (km s^{-1})
Jan 14	ESPaDOnS	08:19:57	1.85135	150	1460	3.3	0.303	0.384	0.254	−0.017	0.049
Jan 15	ESPaDOnS	08:16:30	2.84889	150	1400	3.3	0.667	0.586	0.789	0.020	0.051
Jan 16	ESPaDOnS	08:34:49	3.86153	160	1480	2.9	1.036	0.791	−0.287	0.005	0.048
Jan 17	ESPaDOnS	05:02:34	4.71408	170	1470	2.9	1.347	0.964	−0.008	0.000	0.049
Jan 18	ESPaDOnS	07:32:40	5.81823	160	1420	3.1	1.750	1.188	−0.380	−0.016	0.050
Jan 19	ESPaDOnS	05:55:30	6.75069	170	1470	2.9	2.090	1.377	−0.123	−0.092	0.049
Jan 20	Narval	21:30:38	8.39998	90	1130	5.1	2.692	1.712	0.546	0.089	0.063
Jan 21	ESPaDOnS	05:55:40	8.75065	150	1440	3.3	2.820	1.783	−1.013	0.034	0.050
Jan 21	Narval	22:16:00	9.43141	100	1240	4.6	3.068	1.921	−0.099	0.035	0.058
Jan 22	ESPaDOnS	05:56:39	9.75126	140	1450	3.5	3.185	1.986	0.386	−0.006	0.049
Jan 23	ESPaDOnS	07:00:55	10.79581	160	1450	3.0	3.566	2.198	1.170	0.015	0.050
Jan 24	ESPaDOnS	05:57:09	11.75144	170	1450	3.0	3.914	2.392	−1.258	−0.069	0.049
Jan 24	Narval	20:25:57	12.35475	70	970	6.5	4.135	2.514	0.180	0.025	0.074
Jan 25	ESPaDOnS	07:23:59	12.81166	150	1470	3.4	4.301	2.607	0.284	−0.011	0.049
Jan 26	ESPaDOnS	06:59:05	13.79429	150	1420	3.5	4.660	2.806	0.840	−0.011	0.051
Jan 26	Narval	19:34:05	14.31857	90	1130	5.4	4.851	2.912	−1.160	0.039	0.064
Jan 27	ESPaDOnS	06:05:23	14.75691	170	1470	2.9	5.011	3.001	−0.482	0.009	0.049
Jan 28	ESPaDOnS	06:05:42	15.75705	160	1440	3.1	5.376	3.204	−0.176	−0.031	0.050
Jan 29	ESPaDOnS	06:58:43	16.79378	150	1410	3.3	5.754	3.415	−0.444	−0.036	0.051
Jan 29	Narval	20:01:53	17.33762	80	1210	5.6	5.952	3.525	−0.956	0.011	0.059
Jan 30	Narval	20:15:57	18.34730	80	1190	6.1	6.321	3.730	0.000		0.060
Feb 04	GRACES	07:12:12	22.80262	140	1560		7.946	4.633	−1.017	−0.005	0.046
Feb 04	GRACES	07:18:12	22.80678	150	1560		7.948	4.634	−0.978	0.023	0.046
Feb 09	GRACES	07:16:45	27.80532	150	1470		9.771	5.648	−0.621	−0.019	0.049
Feb 09	GRACES	07:22:39	27.80941	150	1470		9.773	5.649	−0.628	−0.010	0.049
Feb 10	GRACES	05:21:11	28.72497	160	1600		10.107	5.835	−0.653		0.045
Feb 10	GRACES	05:27:05	28.72907	160	1590		10.108	5.836	−0.647		0.045

the original RVs down to noise level (50 m s^{-1} rms in our case, see Table 1).

Contemporaneous BVR$_J$I$_J$ photometric observations were also collected from the CrAO 1.25 m telescope (see Table 2), showing that V830 Tau exhibited significantly larger brightness fluctuations than a year before (D15), with a full amplitude of 0.28 mag and a period of 2.7424 ± 0.0014 d (compatible within error bars with the average periods of Grankin 2013, used to phase our spectroscopic data, see equation 2).

We note that V830 Tau features emission in various spectral activity proxies, as expected from its youth and fast rotation. More specifically, Balmer lines and, in particular Hα, are in emission, as well as the central core of the Ca II infrared triplet (IRT) lines, with typical equivalent widths of 85 and 16 km s^{-1} for Hα and the Ca II IRT emission core, respectively. The He I D_3 line is most of the time quite shallow, with an average equivalent width of 5 km s^{-1}.

In 2016 however, we detected several flares of V830 Tau, showing up as enhanced redshifted emission in all activity proxies including He I, a reliable proxy whose high excitation potential makes it possible to separate flares from phases of enhanced chromospheric activity (e.g. Montes et al. 1997). The most intense flare occurred on Feb 10 during our last pair of observations (cycles 10.107, and 10.108), when Hα, Ca II IRT, and He I emission reach equivalent widths of 280, 32, and 25 km s^{-1} and feature large redshifts of 15–35 km s^{-1} (with respect to the stellar rest frame, shifted from the Barycentric rest frame by $\simeq$17 km s^{-1}) and asymmetric profiles (with a conspicuous red tail for Hα, see Fig. 1, and He I). We note that one of our photometric measurements was secured just after this large flare (at rotation cycle 152.283, or 10.283 in the reference frame of Table 1). At this time, the star was observed to be 54 mmag (i.e. 2.7σ) brighter than four rotation cycles earlier at almost the same phase (cycle 148.289, see Table 2). This shows that even the largest flare of our run was barely detectable in the light curve, to the point that it is not even clear which of the two photometric measurements at this phase deviates most from the bulk of our data points (see Section 3).

A weaker flare was detected 10.3 d earlier on Jan 30 (cycle 6.321), with activity proxies exhibiting similar albeit less drastic characteristics, e.g. He I emission with an equivalent width of 11 km s^{-1} and a redshift of $\simeq$20 km s^{-1} (with respect to the stellar rest frame, or $\simeq$10 km s^{-1} with respect to the average velocity of the He I line). A third flare was recorded on Jan 26 (cycle 4.851), mostly in Hα (with an equivalent width reaching 122 km s^{-1}), but short enough to be seen only with Narval, but neither a few hours before (cycle 4.660) nor later (cycle 5.011) with ESPaDOnS; this flare has only mild He I characteristics, however, with an equivalent width only slightly above average and no significant redshift (with respect to the average line velocity).

Table 2. Journal of contemporaneous CrAO multicolour photometric observations of V830 Tau collected from 2015 Oct 30 to 2016 Mar 15, respectively, listing the Heliocentric Julian Date (HJD) of the observation, the measured V magnitude, $B-V$, $V-R_J$, and $V-I_J$ Johnson photometric colours, and the corresponding rotational cycle (using again the ephemerides of equation 2). The middle line separates observations collected in 2015 and 2016. The typical 1σ error bar on V is 20 mmag.

HJD (2457300+)	V (mag)	$B-V$ (mag)	$V-R_J$ (mag)	$V-I_J$ (mag)	r (114+)
26.4574	12.410		1.339	2.182	0.797
28.5085	12.378			2.242	1.545
30.6098	12.322	1.375	1.325	2.151	2.311
31.5960	12.474	1.413	1.341	2.231	2.671
32.5964	12.267	1.349		2.143	3.036
40.5358	12.307		1.340	2.165	5.933
44.4530	12.321		1.321	2.146	7.362
47.5027	12.342		1.307	2.162	8.475
47.5524	12.367		1.335	2.180	8.493
73.3208	12.317		1.319	2.161	17.894
73.5082	12.261		1.305	2.130	17.962
74.2657	12.268		1.310	2.128	18.238
91.3173	12.281		1.307	2.122	24.459
101.2599	12.199		1.282	2.094	28.087
105.2842	12.356		1.319	2.155	29.555
112.2820	12.244		1.284	2.113	32.108
118.2602	12.306		1.339	2.160	34.289
127.2569	12.362		1.325	2.165	37.571
129.2079	12.252		1.296	2.105	38.283
141.2201	12.413		1.343	2.204	42.665
142.2211	12.210		1.301	2.106	43.031
153.2096	12.219		1.297	2.106	47.040
156.2255	12.196		1.288	2.094	48.140
158.2696	12.329		1.332	2.148	48.886
163.2378	12.425		1.322	2.217	50.698

The three Stokes I spectra corresponding to the two first flares turned out to yield discrepant RV estimates (with excess blueshifts of order 0.3 km s^{-1}), most likely as a result of flaring, and were removed from the subsequent modelling (see Sections 3 and 4). The Stokes V spectrum associated with the second flare compares well with those collected at similar phases but previous cycles (0.303, 4.301), suggesting that it was largely unaffected by the flare and thus used for magnetic imaging (see Section 3). The Stokes I (and V) spectra corresponding to the third, milder, flare, yielding an RV estimate consistent with those from the two unperturbed ESPaDOnS spectra bracketing the flare, were also kept in the sample.

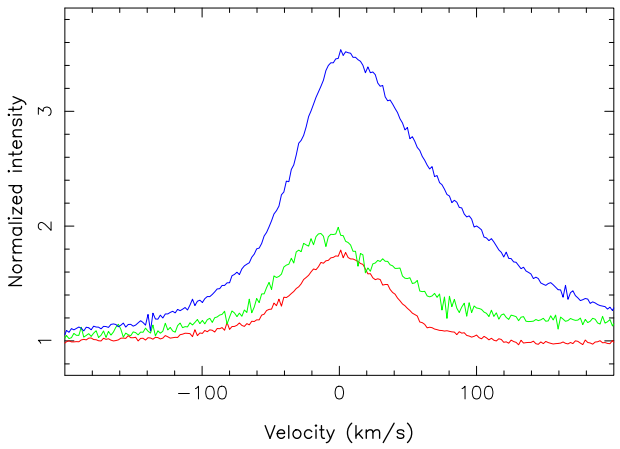

Figure 1. Hα profiles of V830 Tau on 2016 Jan 17 (cycle 1.347, red line), Feb 10 (cycle 10.107, blue), and Jan. 30 (cycle 6.321, green). A red component/tail is clearly present in the latter two profiles (recorded during a flare) while absent in the first one (more typical of V830 Tau).

3 TOMOGRAPHIC MODELLING OF SURFACE FEATURES, MAGNETIC FIELDS, AND ACTIVITY

We applied ZDI to both our late-2015 and early-2016 sets of phase-resolved Stokes I and V LSD profiles, keeping them separate from each other in a first step. ZDI is a tomographic technique inspired from medical imaging, with which distributions of brightness features and magnetic fields at the surfaces of rotating stars can be reconstructed from time series of high-resolution spectropolarimetric observations (Brown et al. 1991; Donati & Brown 1997; Donati 2001; Donati et al. 2006). Technically speaking, ZDI follows the principles of maximum-entropy image reconstruction, and iteratively looks for the image with lowest information content that fits the data at a given χ^2 level. By working out the amount of latitudinal shearing that surface maps are subject to as a function of time, ZDI can also infer an estimate of differential rotation at photospheric level (Donati & Collier Cameron 1997; Donati, Collier Cameron & Petit 2003).

For this study, we used the latest implementation of ZDI, where the large-scale field is decomposed into its poloidal and toroidal components, both expressed as spherical harmonics expansions (Donati et al. 2006), and where the brightness distribution incorporates both cool spots and warm plages[2] (D14, D15, D16). The local Stokes I and V profiles are computed using Unno–Rachkovsky's analytical solution to the polarized radiative transfer equations in a Milne–Eddington model atmosphere, taking into account the local brightness and magnetic field; these local profiles are then integrated over the visible hemisphere to derive the synthetic profiles of the rotating star, to be compared with our observations. This computation scheme provides a reliable description of how line profiles are distorted in the presence of magnetic fields (including magneto-optical effects, e.g. Landi degl'Innocenti & Landolfi 2004).

In this new paper, we assume for V830 Tau the same parameters as in our previous studies in particular an inclination of the rotation axis to the line-of-sight i equal to $55^\circ \pm 10^\circ$ and a line-of-sight-projected equatorial rotation velocity $v\sin i$ equal to 30.5 ± 0.5 km s^{-1} (D15, D16).[3] We recall that the inclination angle i is derived both from the measured stellar parameters (see section 3 of D15) and by minimizing the information content of reconstructed images, with a typical error bar of order 10°. We further assume that the (weak) surface differential rotation of V830 Tau is as derived by D16 from our late 2015 data alone, before revisiting the subject using the

[2] In this paper, the term 'plage' refers to a photospheric region brighter than the quiet photosphere, and not to a bright region at chromospheric level (as in solar physics).

[3] The distance assumed for V830 Tau in D15 and D16, i.e. 131 ± 3 pc, is likely underestimated, since V830 Tau is located in L1529 rather than L1495, and thus close to DG Tau for which the adopted distance is 150 ± 5 pc (Rodríguez et al. 2012, hereafter R12). Given that this difference in distance is comparable flux-wise to the uncertainty on the unspotted magnitude of V830 Tau, we still assume for V830 Tau the same stellar parameters as in D15 and D16 (see Table 3). Assuming instead that V830 Tau is 30 per cent brighter would mostly imply that it is younger, with an age of $\simeq$1.5 Myr (using the evolutionary models of Siess, Dufour & Forestini 2000 as in D15).

Table 3. Summary of the main parameters of V830 Tau, with references as mentioned whenever appropriate (G13 and R12 stand for Grankin 2013 and Rodríguez et al. 2012).

Parameter	Value	Reference
$M_\star$ ($M_\odot$)	1.00 ± 0.05	D15
$R_\star$ ($R_\odot$)	2.0 ± 0.2	D15
Age (Myr)	$\simeq$2.2	D15
$P_{\rm rot}$ (d)	2.741	G13
BJD_0	2 457 011.80	D15
$\Omega_{\rm eq}$ (rad d^{-1})	$2.295\,25 \pm 0.000\,20$	D16
$d\Omega$ (rad d^{-1})	0.0172 ± 0.0014	D16
i (°)	55 ± 10	D15
$v \sin i$ (km s^{-1})	30.5 ± 0.5	D15
distance (pc)	150 ± 5	R12
$T_{\rm eff}$(K)	4250 ± 50	D15

whole data set in Section 3.2. The parameters of V830 Tau used in our study are summarized in Table 3.

3.1 Brightness and magnetic imaging

In Fig. 2, we show our sets of Stokes *I* and *V* LSD profiles of V830 Tau from early 2016, along with the fit to the data. A similar plot is provided in Appendix A for our late-2015 data set (see Fig. A1, repeating fig. 1 of D16 for Stokes *I* profiles, and including Stokes *V* profiles not previously shown in D16). The fit we obtain in both cases corresponds to a χ^2 equal to the number of data points, i.e. to a unit $\chi^2_{\rm r}$ level (where $\chi^2_{\rm r}$ is simply taken here as χ^2 divided by the number of data points,[4] respectively, equal to 1104 and 2208 for the early-2016 and late-2015 Stokes *I* data sets, and to 966 and 1472 for the corresponding Stokes *V* data sets). The initial $\chi^2_{\rm r}$ values, corresponding to input maps with null fields and no brightness features, are equal to 27 and 19 for the early-2016 and late-2015 data sets, respectively, clearly demonstrating the overall success of ZDI at modelling the observed modulation of both Stokes *I* and *V* LSD profiles.

The reconstructed brightness maps of V830 Tau at both epochs are shown in Fig. 3. The two maps share obvious similarities and exhibit similar spottedness levels, i.e. $\simeq$13 per cent of the stellar surface[5] (7 per cent and 6 per cent for cool and warm features, respectively). In particular, most cool spots and warm plages present in either maps are recovered at both epochs. One can also notice differential rotation shearing the brightness distribution between late 2015 and early 2016 (a time gap corresponding to 49 d or 18 rotation cycles), with equatorial and polar features being both shifted by a few per cent of a rotation cycle to smaller and larger phases, respectively[6] (implying a fast equator and a slow pole, in good quantitative agreement with D16). Some intrinsic temporal evolution beyond differential rotation may be visible in our images as well, with, e.g. the appearance of a warm equatorial plage at phase 0.08 in early 2016 that was not visible (or not as strong) in late 2015; however, even though phase coverage is fairly good in our case at both epochs, quantifying spot evolution by visually comparing images derived from differently sampled data sets is notoriously ambiguous and misleading. We come back to this point in Section 3.2.

We stress that the derived brightness images predict light curves that are in good agreement with our observations (see Fig. 4), even though these images were produced from our sets of LSD profiles only. Note the small temporal evolution in the predicted light curves between both epochs, that our photometric observations cannot confirm due to their limited sampling and precision. This further demonstrates that LSD profiles contain enough information to accurately predict the surface distribution of brightness features, and in particular those responsible of the RV activity jitter (see Section 4); on the opposite, it is quite obvious that photometric information is way too limited (even when better sampled and more precise) to infer complex spot distributions such as those we reconstruct for V830 Tau. It implies that jitter-filtering techniques based solely on photometry (e.g. Aigrain et al. 2012) are likely to yield poorer results, especially for moderate to fast rotators whose optical RV curves are much more sensitive than photometry to small features in surface brightness distributions.

The large-scale magnetic topologies we retrieve for V830 Tau at both epochs (see Fig. 5) are again very similar, with rms surface magnetic fluxes of 350 G, and resemble that found previously for this star (D15). As for the brightness maps, the main magnetic regions that we recover are visible at both epochs. More specifically, the field is found to be 90 per cent poloidal, featuring a 340 G dipole field tilted at $22^\circ \pm 5^\circ$ to the rotation axis towards phase 0.79 $\pm$ 0.03 (in late 2015) and 0.88 $\pm$ 0.03 (in early 2016), and that gathers 60 per cent of the poloidal field energy. Weaker quadrupolar and octupolar components (of strength 100–150 G) and smaller scale features are also present on V830 Tau, giving the field close to the stellar surface a more complex appearance than that of the dominating dipole. With an rms flux of $\simeq$110 G, the toroidal field is weak and of rather complex topology. The extrapolated large-scale magnetic topology (in the assumption of a potential field) is shown in Fig. 6 at both epochs.

As for the brightness maps, the magnetic images show evidence of a global differential rotation shear similar to that reported by D15, with equatorial regions (e.g. the strong negative azimuthal feature at phase 0.17) moving to slightly earlier phases from late 2015 to early 2016, and higher latitude regions (e.g. the positive radial field region at phase 0.05 and latitude 60°) moving to later phases at the same time. The increase in the phase towards which the dipole is tilted (0.79 and 0.88 in late 2015 and early 2016, respectively) comes as additional evidence that high latitudes (at which the dipole poles are anchored) are rotating more slowly than average, by typically 1 part in 200; this is further confirmed by the fact that the line-of-sight projected (longitudinal) magnetic fields (proportional to the first moment of the Stokes *V* profiles, e.g. Donati et al. 1997, and most sensitive to the low-order components of the large-scale field) exhibit a recurrence time-scale of 1.004 $\pm$ 0.003 $P_{\rm rot}$, i.e. slightly longer than $P_{\rm rot}$ by a similar amount.

We also report that the phase of maximum Hα emission of V830 Tau coincides, in both late 2015 and early 2016, with that of the high-latitude regions at which the dipole field is anchored; this is

[4] This is the usual convention in regularized tomographic imaging techniques where the number of model parameters, reflecting the (ill-defined) number of resolution elements in the reconstructed image, is much smaller than the number of fitted data points and not taken into account in the expression of $\chi^2_{\rm r}$.

[5] We stress that ZDI is only sensitive to large brightness features, and not to small ones evenly distributed at the surface of the star; for this reason, the value we quote here for the spot coverage of V830 Tau is likely to be a lower limit, in agreement with photometric monitoring suggesting a typical spot coverage in the range 30–50 per cent for V830 Tau (Grankin et al. 2008).

[6] For instance, the equatorial plage at phase 0.46 in early 2016 is found at phase 0.48 in late 2015, while the cool polar cap is rotated by $\simeq$0.1 cycle in the other direction. Note that the latest map is shown first in Fig. 3 and following plots.

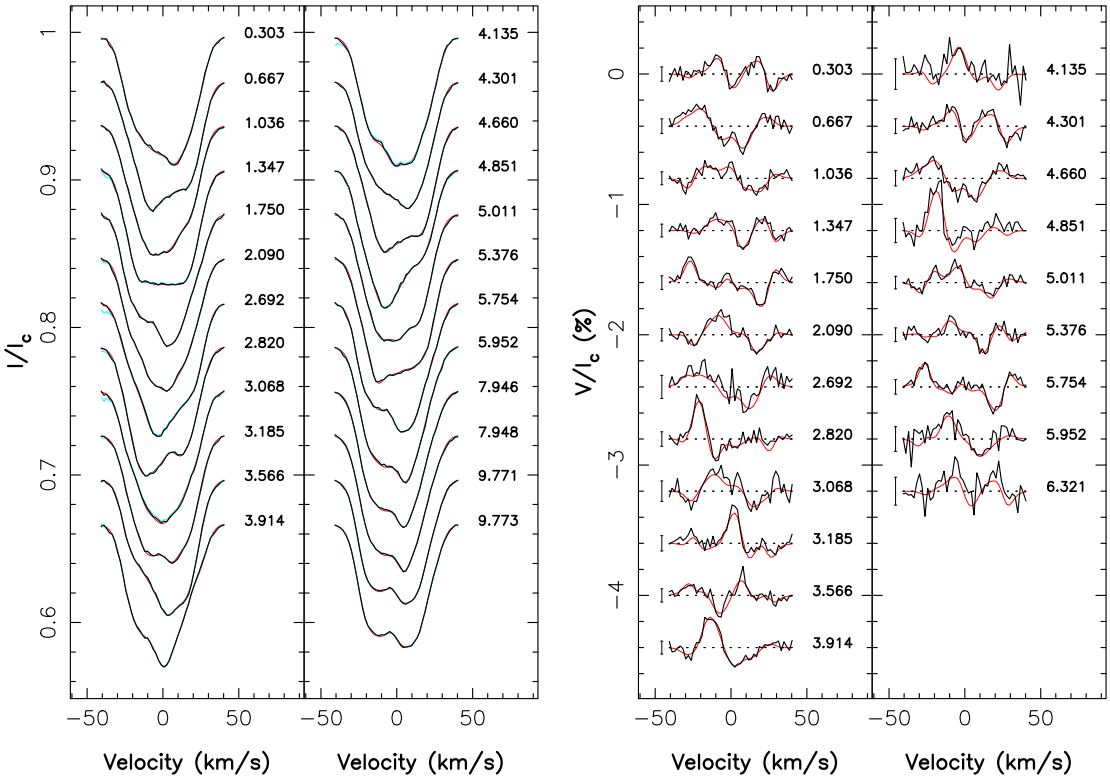

Figure 2. Maximum-entropy fit (thin red line) to the observed (thick black line) Stokes *I* (left-hand panel) and Stokes *V* (right-hand panel) LSD photospheric profiles of V830 Tau in early 2016. (The red and black lines almost perfectly overlap for Stokes *I* LSD profiles.) Stokes *I* LSD profiles prior to their filtering from lunar contamination (in the far blue wing) are also shown (cyan line). Rotational cycles and 3σ error bars (for Stokes *V* profiles) are also shown next to each profile.

obvious from the dynamic spectra of the Hα residuals that we provide as an additional figure in the appendix (see Fig. A2). A logical by-product is that Hα emission of V830 Tau, like its longitudinal field, is modulated by a period slightly longer than $P_{\rm rot}$, and equal to $1.004 \pm 0.002\ P_{\rm rot}$. From the solar analogy, one would have expected chromospheric emission to be minimum when open field lines point towards the observer, i.e. at phase 0.8–0.9 (see Fig. 6); this is however not what we observe, suggesting that the Hα emission we detect comes from regions close to (but not coinciding with) the strongest radial field regions that we reconstruct at high latitudes (see Fig. 5).

We also note apparent temporal evolution of the magnetic topology, with, e.g. the positive radial field region close to the equator at phase 0.33 growing much stronger between late 2015 and early 2016, though we caution again that a simple visual image comparison of individual features can be misleading.

3.2 Intrinsic variability and surface differential rotation

The most reliable way to assess whether intrinsic variability occurred at the surface of V830 Tau between late 2015 and early 2016 is to attempt modelling both data sets simultaneously with a unique brightness and magnetic topology, and see whether one can fit the full set to the same $\chi^2_{\rm r}$ level as that achieved for the individual sets (i.e. 1.0, see Section 3). We find that this is not possible, with a minimum achievable $\chi^2_{\rm r}$ of 1.62 and 1.18 for Stokes *I* and Stokes *V* data, respectively (starting from initial $\chi^2_{\rm r}$ of 35 and 5); this confirms our previous suspicion that intrinsic variability occurred at the surface of V830 Tau throughout the 91 d (33 rotation cycles) of our observing campaign, and in particular over the 49 d shift between our two data sets. The global fit to the full data set we obtain nonetheless captures most of the observed line profile fluctuations, indicating that the intrinsic variability at work at the surface of V830 Tau remained moderate and local without altering the brightness and magnetic surface distributions too drastically; this further confirms our visual impression that images from both epochs shared obvious similarities.

Despite this intrinsic variability, we attempted to estimate differential rotation from our full data set. As in previous papers, we achieve this by assuming that the rotation rate at the surface of V830 Tau $\Omega(\theta)$ varies with latitude θ as $\sin^2\theta$ and depends on two main parameters, the rotation rate at the equator $\Omega_{\rm eq}$ and the difference in rotation rate dΩ between the equator and the pole (so that $\Omega(\theta) = \Omega_{\rm eq} - {\rm d}\Omega\sin^2\theta$). Both parameters are derived by looking for the pair that minimizes the $\chi^2_{\rm r}$ of the fit to the data (at constant information content in the reconstructed image), whereas the corresponding error bars are computed from the curvature of the $\Delta\chi^2$ paraboloid at its minimum (Donati et al. 2003). ($\Delta\chi^2$ is defined as the χ^2 increase with respect to the minimum χ^2 in the map.) Results are shown in Fig. 7. The differential rotation we derive from our complete data set is slightly smaller (though still compatible at a $\simeq 3\sigma$ level) than that inferred from the late-2015 Stokes *I* LSD profiles only (D16). Despite the fact that this weakening is observed in both Stokes *I* and *V* data, we think that this small change likely results from intrinsic variability at the surface of V830 Tau.[7]

[7] For this reason, the differential rotation parameters of D16 were used as reference throughout this paper, their impact on most results being however quite small given how weakly the photosphere of V830 Tau is sheared.

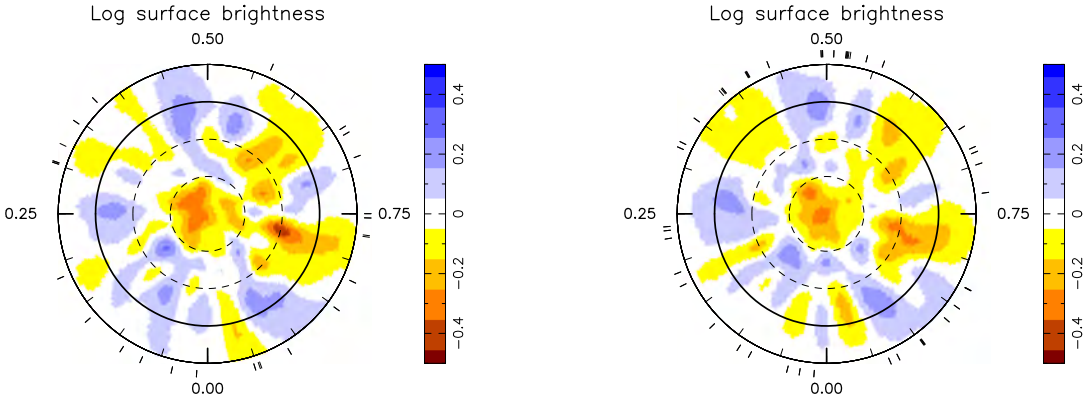

Figure 3. Maps of the logarithmic brightness (relative to the quiet photosphere), at the surface of V830 Tau in early 2016 (left) and late 2015 (right). Cool spots/bright plages show up as brown/blue features. The star is shown in flattened polar projection down to latitudes of −30°, with the equator depicted as a bold circle and parallels as dashed circles. Radial ticks around each plot indicate phases of observations.

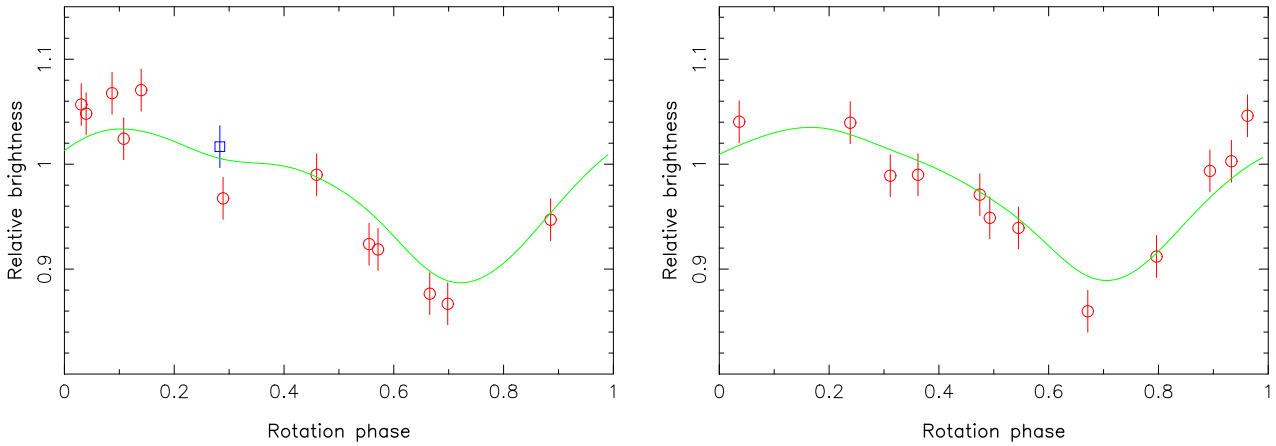

Figure 4. Brightness variations of V830 Tau in early 2016 (left) and late 2015 (right) as predicted from the tomographic modelling of our spectropolarimetric data (see Fig. 3, green line), compared with contemporaneous photometric observations in the *V* band (open symbols and 1σ error bars of 20 mmag) at the 1.25-m CrAO telescope (see Table 2). The photometric measurement collected immediately after the large flare detected in our early 2016 spectroscopy data (see Section 2) is shown as an open blue square in the left-hand panel.

Further evidence that high latitudes of V830 Tau are rotating more slowly than average (in agreement with the differential rotation pattern we recover) comes from the drift to later phases of the polar regions at which the large-scale dipole field component is anchored and where Hα emission is strongest.

4 FILTERING THE ACTIVITY JITTER AND MODELLING THE PLANET SIGNAL

We describe below the results of the independent techniques aimed at characterizing the RV signature of V830 Tau b from our data. The first two methods are those already outlined in D16 and used to detect V830 Tau b from the late-2015 data alone, that we now apply to both late-2015 and early-2016 data sets, with some modifications to account for the intrinsic variability between the two epochs (see Section 3.2). The third one follows the approach of Haywood et al. (2014) and Rajpaul et al. (2015), and uses Gaussian-process regression (GPR) to model activity directly from the raw RVs. The results obtained with each technique are described and compared in the following sections.

4.1 Modelling the planet signal from filtered RVs (ZDI no. 1)

The first technique consists in using the ZDI brightness images of Fig. 3 to predict the RV curves expected for V830 Tau at each epoch, and compare them with observed raw RVs. Modelled and raw RVs are both computed as the first-order moment of Stokes *I* LSD profiles (i.e. $\int(1 - I(v))v\mathrm{d}v / \int(1 - I(v))\mathrm{d}v$ where v is the RV across the line profile) while error bars on raw RVs are derived from those propagated from the observed spectra to the Stokes *I* LSD profiles (and checked for consistency through simulated data sets as in D16); activity-filtered RVs are then derived by simply subtracting the modelled RVs from the observed ones (D16, see Table 1). Even though the intrinsic variability observed at the surface of V830 Tau is only moderate (see Section 3.2), using a specific ZDI map for each data subset (i.e. late 2015 and early 2016) is essential to obtain precise filtered RVs; using a single image for both subsets and ignoring the temporal evolution of the surface brightness distribution between the two epochs (beyond that caused by differential rotation) significantly degrades the quality of the modelling and therefore the precision of the filtered RVs.

The results we obtain are shown in Fig. 8 for the raw, filtered, and residual RVs, and in Fig. 9 for the corresponding periodograms. The planet RV signal is very clearly detected in the filtered RVs,

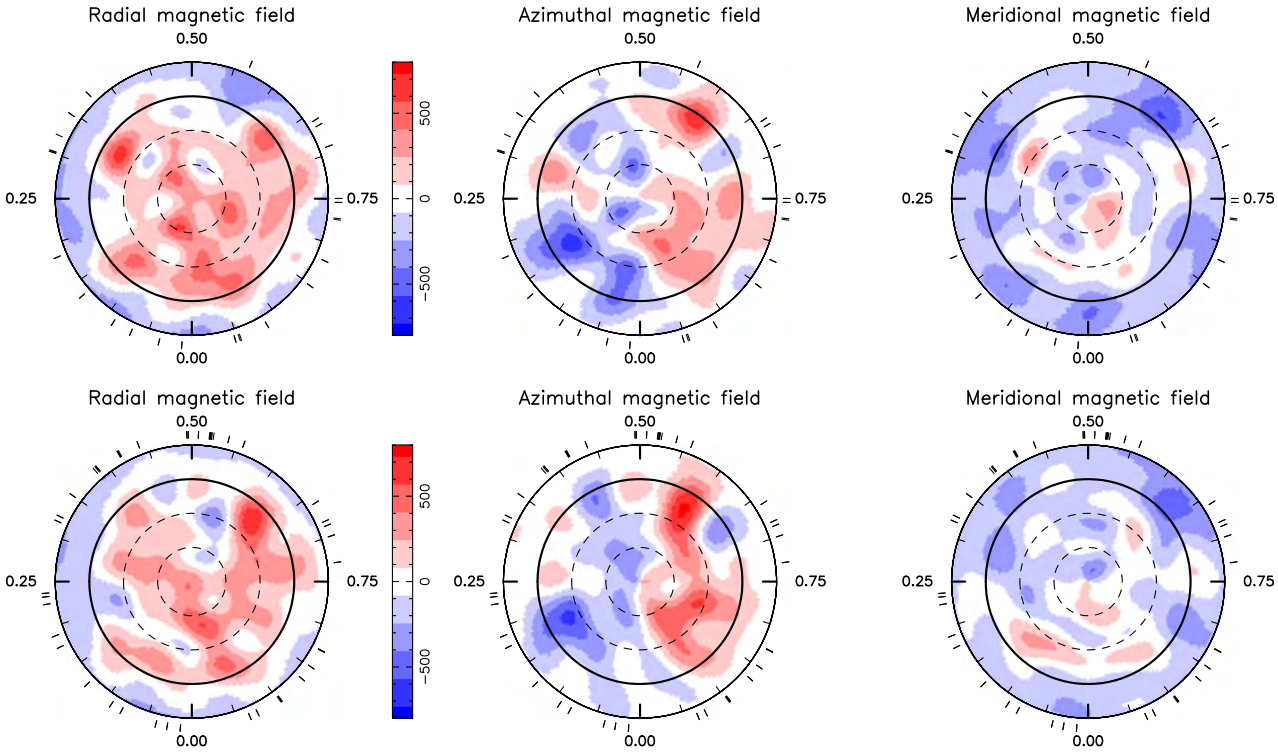

Figure 5. Maps of the radial (left), azimuthal (middle), and meridional (right) components of the magnetic field ***B*** at the surface of V830 Tau in early 2016 (top) and late 2015 (bottom). Magnetic fluxes in the colour lookup table are expressed in G. The star is shown in flattened polar projection as in Fig. 3.

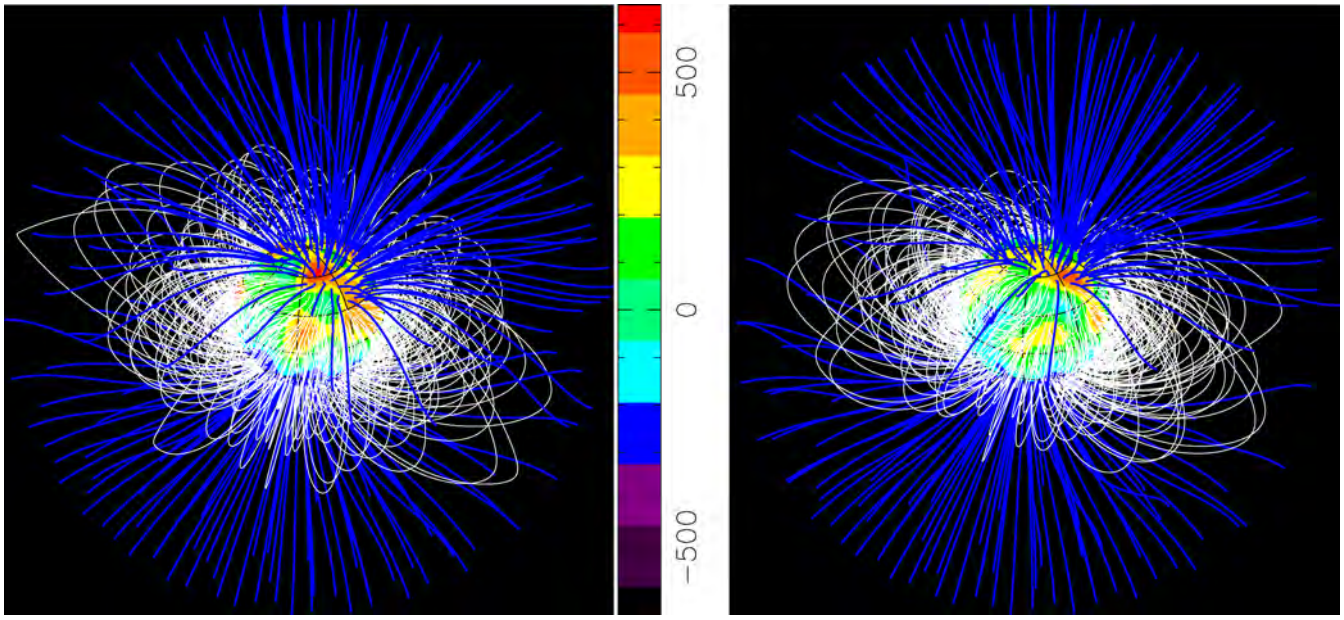

Figure 6. Potential extrapolations of the magnetic field reconstructed for V830 Tau in early 2016 (left) and late 2015 (right), as seen by an Earth-based observer at phase 0.10. Open and closed field lines are shown in blue and white, respectively, whereas colours at the stellar surface depict the local values (in G) of the radial field (see left-hand panels of Fig. 5). The source surface at which the field becomes radial is set at a distance of 4 $R_\star$, close to the corotation radius of V830 Tau (at which the Keplerian orbital period equals the stellar rotation period and beyond which field lines tend to open under the effect of centrifugal forces, Jardine 2004) but smaller than the Alfvén radius expected for a TTS-like V830 Tau ($>6\ R_\star$, see Vidotto & Donati 2016). Note how the high-latitude open-field regions slightly lag behind rotation between both epochs as a result of differential rotation.

with a false-alarm probability (FAP) lower than 10^{-5}. The χ^2 decrease that we obtain with our fit to the filtered RVs (with respect to a case with no planet) is about 36 (for 72 RV points and 4 degrees of freedom), suggesting a similarly low FAP value of $<10^{-6}$. The corresponding curve features a semi-amplitude equal to $K = 60 \pm 10$ m s^{-1} and an orbital period of $P_{\rm orb} = 4.97 \pm 0.03$ d, in agreement with the estimates of D16 ($K = 75 \pm 12$ m s^{-1} and $P_{\rm orb} = 4.93 \pm 0.05$ d). Fitting a Keplerian orbit through

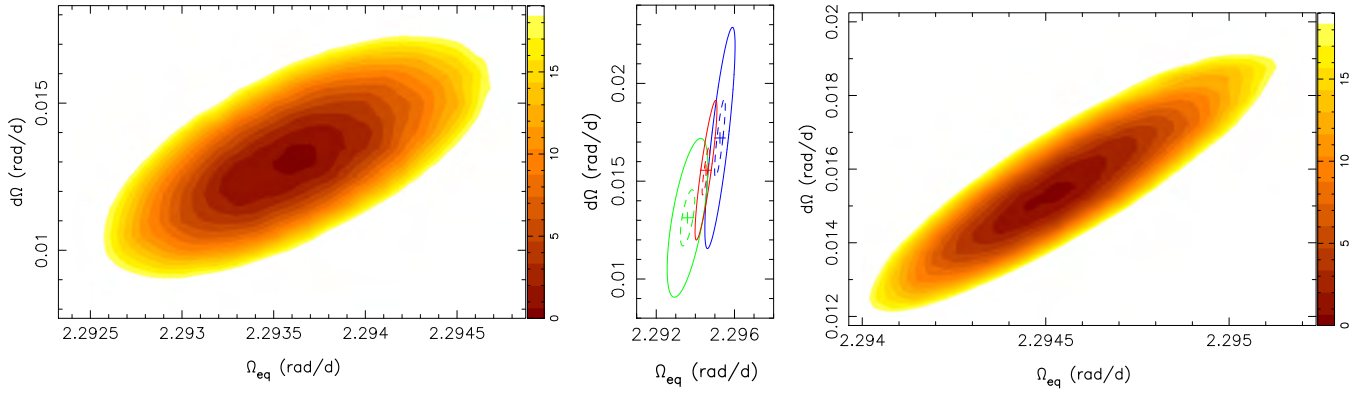

Figure 7. Variations of $\Delta\chi^2$ as a function of the differential rotation parameters $\Omega_{\rm eq}$ and dΩ, derived from modelling our full set of Stokes *I* (right) and *V* (left) LSD profiles of V830 Tau at a constant information content. A well-defined paraboloid is observed in both cases, with the outer colour contour tracing the 99.99 per cent confidence interval (corresponding to a $\Delta\chi^2$ of 18.4 for the 2438 Stokes *V* and 3312 Stokes *I* data points). In both cases, the minimum $\chi^2_{\rm r}$ achieved (equal to 1.62 and 1.18 for Stokes *I* and Stokes *V* data, respectively) is significantly larger than 1; this value is used to normalize χ^2 before computing $\Delta\chi^2$ so as to account for intrinsic variability (affecting the brightness distribution and magnetic field of V830 Tau over the course of our 91-d run, see Section 3.2) when estimating errors bars on differential rotation parameters. The values we obtain for these parameters are equal to $\Omega_{\rm eq} = 2.294\,55 \pm 0.000\,14$ rad d^{-1} and d$\Omega = 0.0156 \pm 0.0009$ rad d^{-1} for the Stokes *I* data, and $\Omega_{\rm eq} = 2.293\,60 \pm 0.000\,25$ rad d^{-1} and d$\Omega = 0.0131 \pm 0.0010$ rad d^{-1} for the Stokes *V* data. The middle plot emphasizes how the confidence intervals from both measurements compare with each other, and with that derived from the late-2015 Stokes *I* LSD profiles only (D16). The 68.3 per cent and 99.99 per cent confidence intervals (dashed and full lines) are shown in green, red, and blue for the full Stokes *V*, the full Stokes *I*, and the late-2015 Stokes *I* data sets, respectively.

the data marginally improves the fit, but the derived eccentricity (0.21 ± 0.15) is not measured with enough precision to be reliable (Lucy & Sweeney 1971); it confirms at least that V830 Tau b is close to circular or only weakly eccentric. The residual RVs show an rms dispersion of 44 m s^{-1}, fully compatible with the errors of our RV estimates (see Table 1) that mostly reflect the photon noise in our LSD profiles (and to a lesser extent the intrinsic RV precision of ESPaDOnS, equal to 20–30 m s^{-1}, Moutou et al. 2007; Donati et al. 2008). Residual RVs in the first part of the run (late 2015) exhibit a larger-than-average dispersion (of 50 m s^{-1} rms, i.e. close to the value of 48 m s^{-1} found by D16 from modelling the late 2015 data only) that mostly reflects the limits in our assumption of a constant brightness distribution at the surface of the star (sheared by differential rotation) on a relatively long data set (15 rotation cycles) and to a small extent potential residual pollution by the moon between rotational cycles 6.0 and 7.2 (see Fig. A1).

Lomb–Scargle periodograms of the longitudinal fields and the Hα emission fluxes of V830 Tau (see Fig. 9, middle and bottom panels) both show that activity concentrates mostly at the rotation period (with a recurrence period slightly longer than $P_{\rm rot}$, see Section 3) and first harmonic, but not in a significant way at the planet orbital period. This further confirms that the RV signal from V830 Tau b cannot be attributed to activity.

4.2 Deriving planet parameters from LSD Stokes *I* profiles (ZDI no. 2)

The second method, proposed by Petit et al. (2015) and inspired from our differential rotation measurement technique, directly works with Stokes *I* LSD profiles, and consists in finding out the planet characteristics and brightness distribution that best explain the observed profile modulation. More specifically, we assume the presence of a close-in planet in a circular orbit with given parameters (K, $P_{\rm orb}$ and phase of inferior conjunction), correct our LSD profiles from the reflex motion induced by the planet, reconstruct with ZDI the brightness image associated with the corrected LSD profiles at a given information content (i.e. image spottedness), and iteratively derive which planet parameters allow the best fit to the data. This technique was found to yield results in agreement with those our first direct method gave when previously applied to our V830 Tau data (D15, D16).

The method was slightly modified to handle two different subsets of data at the same time, following Yu et al. (2016). The main difference is that, for each set of planet parameters, we now reconstruct two different brightness images (one for each subset) with ZDI, both at constant information content; we then compute a global $\chi^2_{\rm r}$ for this dual image reconstruction as a weighted mean of the $\chi^2_{\rm r}$s associated with the two ZDI images (with weights equal to the number of data points in the subsets). This allows us in particular to handle different brightness distributions for different epochs, without which data cannot be optimally fitted as a result of the intrinsic variability that the spot configuration is subject to (see Section 3.2).

The planet parameters we derive with this second technique are equal to $K = 62 \pm 9$ m s^{-1} and $P_{\rm orb} = 4.97 \pm 0.03$ d, very similar to those obtained with our first method and again in agreement with those of D16. The corresponding χ^2 map (projected on to the K versus $P_{\rm orb}$ plane that passes through the global minimum), shown in Fig. 10, features a clear minimum. With respect to our best model incorporating a planet, a model with no planet corresponds to a $\Delta\chi^2$ of 75, indicating that the planet is detected with an FAP level $<10^{-15}$; the much lower FAP directly reflects the larger $\Delta\chi^2$ obtained with this method, reflecting that line profiles of rapid rotators contain more (or less-noisy) information than their first moments (the raw and filtered RVs).

4.3 Deriving planet parameters from raw RVs using GPR

The third method we applied to our data works directly from raw RVs and uses GPR to model the activity jitter as well as its temporal evolution, given its covariance function (e.g. Haywood et al. 2014; Rajpaul et al. 2015). Assuming again the presence of a close-in planet of given characteristics, we correct the raw RVs from the reflex motion induced by the planet and fit the corrected RVs with a Gaussian process (GP) based on a pseudo-periodic covariance

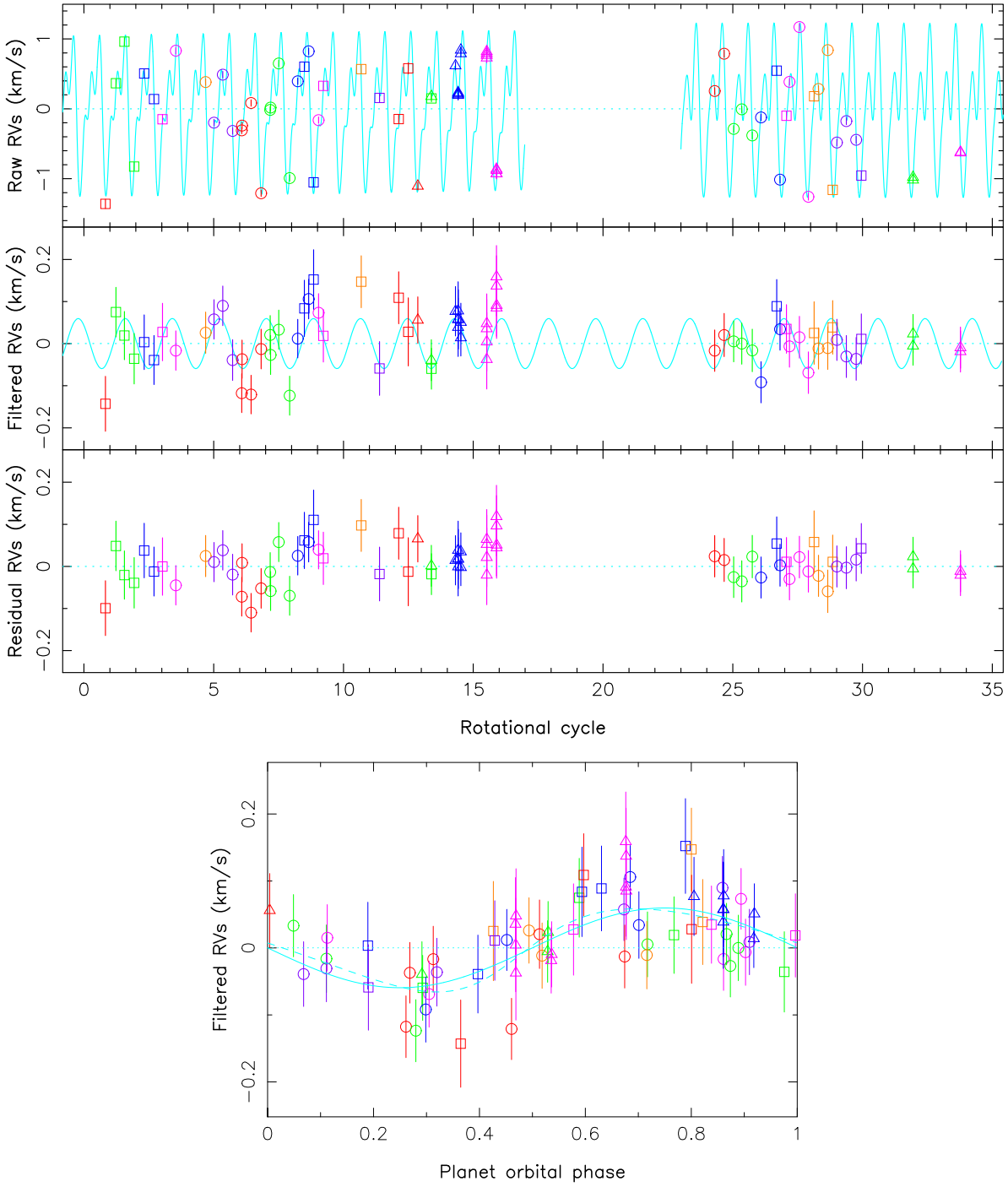

Figure 8. Top panel: raw (top), filtered (middle), and residual (bottom) RVs of V830 Tau (open symbols and 1σ error bars, with circles, squares, and triangles depicting ESPaDOnS, NARVAL, and ESPaDOnS/GRACES data, and colours coding rotation cycles). The raw RVs exhibit a semi-amplitude of 1.2 km s^{-1} and an rms dispersion of 0.65 km s^{-1} throughout the whole run. Rotation cycles of the 2016 data are shifted by +24 in this plot with respect to their values in Table 1 and Fig. 2. The RV jitter predicted by ZDI at both epochs, as well as the best sine fit to the filtered RVs, are added in the top and middle plots (cyan lines). Note how the jitter model changes between late 2015 and early 2016, and how both of them slowly evolve with time as a result of differential rotation. The rms dispersion of the residual RVs is 44 m s^{-1}, in agreement with our measurement errors (see Table 1). Bottom panel: activity-filtered RVs phase-folded on the planet orbital period. The fit to the data is only marginally better with an eccentric orbit (dashed line) than with a circular one (solid line).

function $c(t, t')$ at epochs t and t' of the form:

$$c(t,t') = \theta_1^2 \exp\left(-\frac{(t-t')^2}{\theta_3^2} - \frac{\sin^2\left(\frac{\pi(t-t')}{\theta_2}\right)}{\theta_4^2}\right), \qquad (3)$$

where θ_1 is the amplitude of the GP (in km s^{-1}), θ_2 the recurrence time-scale (i.e. close to 1 here, in units of $P_{\rm rot}$), θ_3 the decay time-scale (i.e. the typical spot lifetime here, in units of $P_{\rm rot}$), and θ_4 a smoothing parameter (within [0,1]) setting the amount of high-frequency structure that we allow the fit to include. For a given set

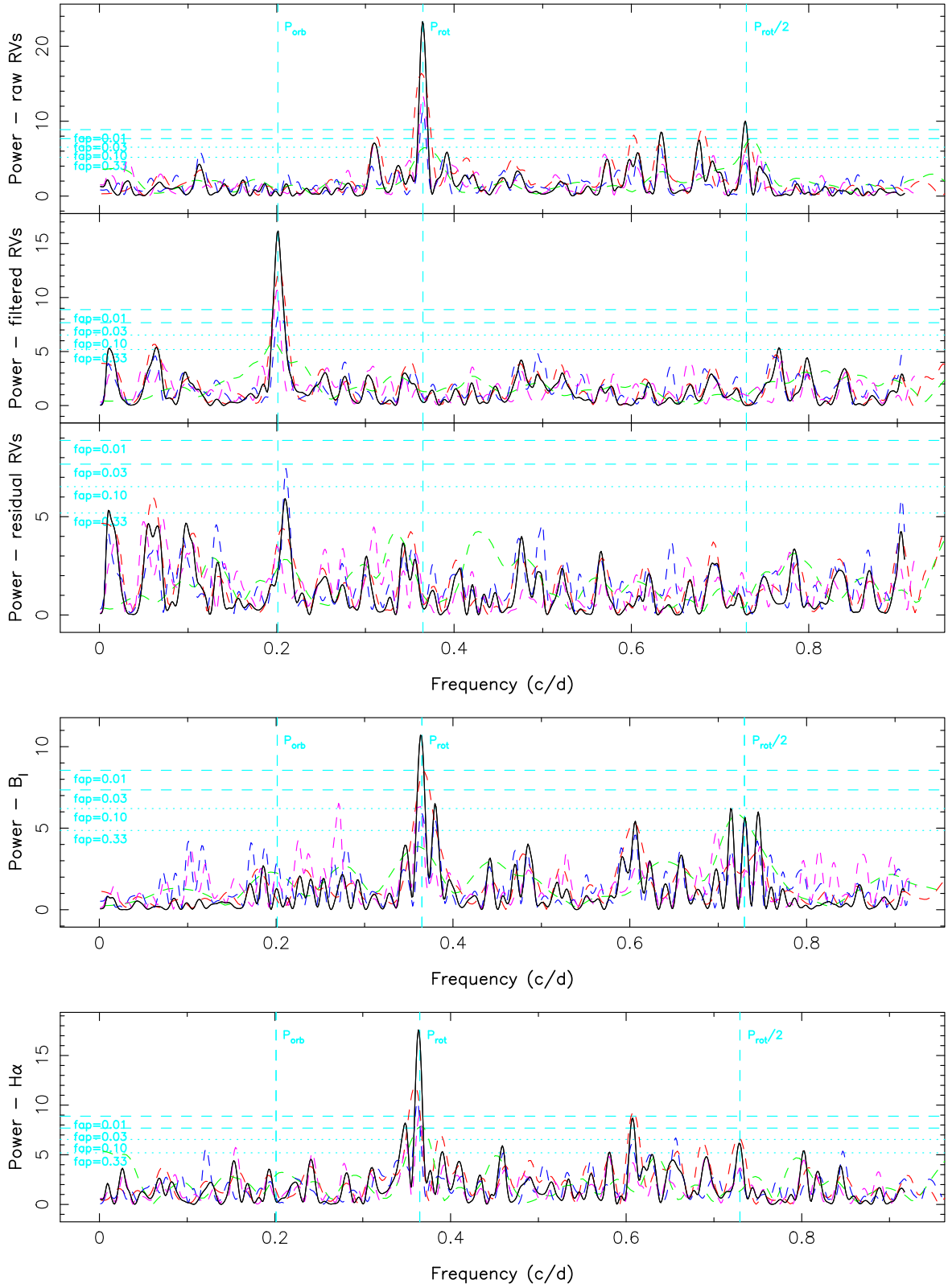

Figure 9. Top panel: Lomb–Scargle periodograms of the raw (top), filtered (middle), and residual RVs (bottom) shown in Fig. 8. The black line is for the full set, while the dashed red, green, blue, and pink lines are for the late-2015, the early-2016, the even, and the odd points only. The stellar rotation period, its first harmonic, and the planet orbital period are depicted with vertical dashed lines. The horizontal dotted and dashed lines trace the 33 per cent, 10 per cent, 3 per cent, and 1 per cent FAP levels. The planet signal in the filtered RVs is detected in the full set with an FAP level $<10^{-5}$. Middle panel: periodogram of the longitudinal magnetic field, a reliable activity proxy (Haywood et al. 2016), featuring a clear peak at the stellar rotation period but no power at the planet orbital period. Bottom panel: same as middle panel for the Hα emission.

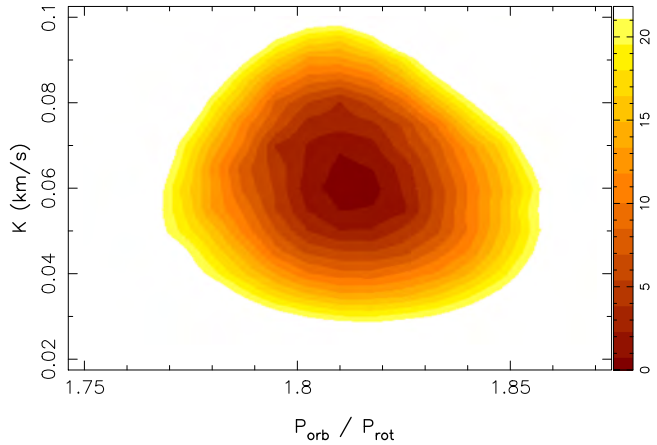

Figure 10. Variations of $\Delta\chi^2$ of the ZDI fits to the late-2015 and early-2016 LSD profiles of V830 Tau (for a fixed spottedness level at both epochs), after removing the reflex motion of a close-in a planet and for a range of orbital periods $P_{\rm orb}$ (actually the ratio of the orbital to rotation period $P_{\rm orb}/P_{\rm rot}$) and semi-amplitudes K of the planet RV signature. This is a 2D cut from a 3D map, with the phase of the RV signal also included as a search parameter. A clear minimum is obtained in the $\Delta\chi^2$ landscape, whose projection in a K versus $P_{\rm orb}/P_{\rm rot}$ plane passing through the minimum is shown here. The outer colour contour traces the projected 99.99 per cent confidence interval, corresponding to a $\Delta\chi^2$ of 21.1 for a three-parameter fit to the 3312 data points of the LSD profiles.

of planet parameters and of the four GP hyper parameters θ_1–θ_4, we can compute the GP that best fits the corrected raw RVs (denoted y) and estimate the log likelihood $\log\mathcal{L}$ of the corresponding parameter set from:

$$2\log\mathcal{L} = -n\log(2\pi) - \log|C+\Sigma| - y^T(C+\Sigma)^{-1}y, \qquad (4)$$

where C is the covariance matrix for all observing epochs, Σ the diagonal variance matrix of the raw RVs, and n the number of data points. Coupling this with a Markov Chain Monte Carlo (MCMC) simulation to explore the parameter domain, we can determine the optimal set of planet and GP hyper parameters that maximizes likelihood, as well as the relative probability of this optimal model with respect to one with no planet (and only the GP modelling activity).

We start by carrying out an initial MCMC run with input priors, whose results (the posterior distributions) are used to infer refined priors and proposal distributions capable of ensuring both an efficient mixing and convergence of the chain as well as a thorough exploration of the domain of interest (through a standard Metropolis–Hastings jumping scheme); these refined priors are found to be weakly dependent on the input priors, already suggesting that our data contain enough information to reliably characterize the GP and planet parameters. The main MCMC run uses our refined priors, listed in Table 4 for the various parameters; we usually carry out two successive main runs, a first one with all four GP hyper parameters and three planet parameters free to vary, then a second one with both θ_3 and θ_4 fixed to their best values, and the remaining five parameters left free to vary. The goal of this sequential approach is to incorporate as much prior information about the stellar activity as possible into our model (hence the stronger refined priors) so that the GP yields a robust estimation of the uncertainties on the final parameters (particularly the planet mass) given these priors (see Haywood et al. 2014; Lopez-Morales et al. 2016 for a similar approach).

Table 4. Priors used in our MCMC simulation for the planet and GP hyper parameters. We mention the mean and standard deviation used for the refined Gaussian priors (plus the standard deviation assumed for our initial MCMC run), the minimum and maximum values allowed for the uniform and Jeffreys priors, as well as the knee value for the modified Jeffreys priors [following Haywood et al. (2014), with $\sigma_{\rm RV}$ noting the S/N^2-weighted average RV error of our measurements, equal to 53 m s^{-1}, see Table 1]. The planet phase ϕ_0 relates to the epoch of inferior conjunction BJD$_{\rm t}$ through BJD$_{\rm t} = \phi_0 P_{\rm orb} + t_0$ where $t_0 = 2457\,359.9069$ d (corresponding to rotation cycle 127.0) is the reference zero time we used for our observations.

Parameter	Prior
$P_{\rm orb}/P_{\rm rot}$	Gaussian (1.80, 0.012, initial 0.10)
K (km s^{-1})	Modified Jeffreys ($\sigma_{\rm RV}$)
ϕ_0	Gaussian (0.13, 0.04, initial 0.10)
GP amplitude θ_1 (km s^{-1})	Modified Jeffreys ($\sigma_{\rm RV}$)
Recurrence period θ_2 ($P_{\rm rot}$)	Gaussian (1.0, 0.001, initial 0.010)
Spot lifetime θ_3 ($P_{\rm rot}$)	Jeffreys (0.1, 500.0)
Smoothing parameter θ_4	Uniform (0, 1)

We find that θ_3, the hyper parameter describing spot lifetime, gives the best result for a value of $\theta_3 = 44 \pm 11 P_{\rm rot} = 120 \pm 30$ d, only slightly longer than the full duration of our observing run (91 d). This further confirms the importance of taking into account the temporal evolution of brightness maps in activity filtering studies, even in the case of wTTSs like V830 Tau whose spot distributions are known to be fairly stable on long time-scales; whereas this is true for the largest surface features, this is no longer the case for the smaller ones whose effect on RV curves is significant. Similarly, we get that $\theta_4 = 0.6 \pm 0.1$ yields the most likely fit to the data; this reflects the lack of fine structure in the RV curves, as expected from the fact that RVs are the first-order moment of Stokes I LSD profiles that acts as a low-pass filter on surface brightness distributions. With the final MCMC run, we obtain that the recurrence time-scale θ_2 is equal to $\theta_2 = 0.9986 \pm 0.0007 P_{\rm rot}$, i.e. only very slightly shorter than the average rotation period $P_{\rm rot}$ on which our data were phased (see equation 2); we note that this period matches well the equatorial rotation period of V830 Tau (see Table 3 and Section 3.2), suggesting that RVs are primarily affected by equatorial features at the stellar surface. For the GP amplitude θ_1, we find that $\theta_1 = 0.878 \pm 0.135$ km s^{-1}, $\simeq$30 per cent larger than the rms dispersion of our raw RVs (equal to 0.65 km s^{-1} prior to any activity filtering, or removal of planetary-induced reflex motions).

For the planet parameters, we find that $K = 68 \pm 11$ m s^{-1} and $P_{\rm orb} = 4.93 \pm 0.03$ d, whereas the most accurate epoch of inferior conjunction (assuming a circular orbit) is found to be BJD$_{\rm t}$ = 2 457 360.51 $\pm$ 0.14. The corresponding fit to the data, shown in Fig. 11, demonstrates that the GP is doing a very nice job at modelling not only the activity, but also its evolution with time. Comparing with the results of our first method (see Fig. 8), we can see that both the GP and ZDI predict similar RV curves. However, thanks to its higher flexibility, the GP does a better job at matching the data, not only for our second data set where temporal variability is higher (given the faster evolution of the predicted RV curve, see Fig. 11) and where the planet signal is clearly better recovered, but also for our first data set where the slower spot evolution is enhanced by the longer time span (of 15 rotation cycles). As a result, the rms dispersion of the RV residuals has further decreased to 37 m s^{-1}, 16 per cent smaller than with our first method, including in the first part of our run (late 2015) where the fit to the data is now tighter (rms dispersion of RV residuals of 40 m s^{-1} instead of 50 m s^{-1}, and close to that of the full run). Given this, we consider

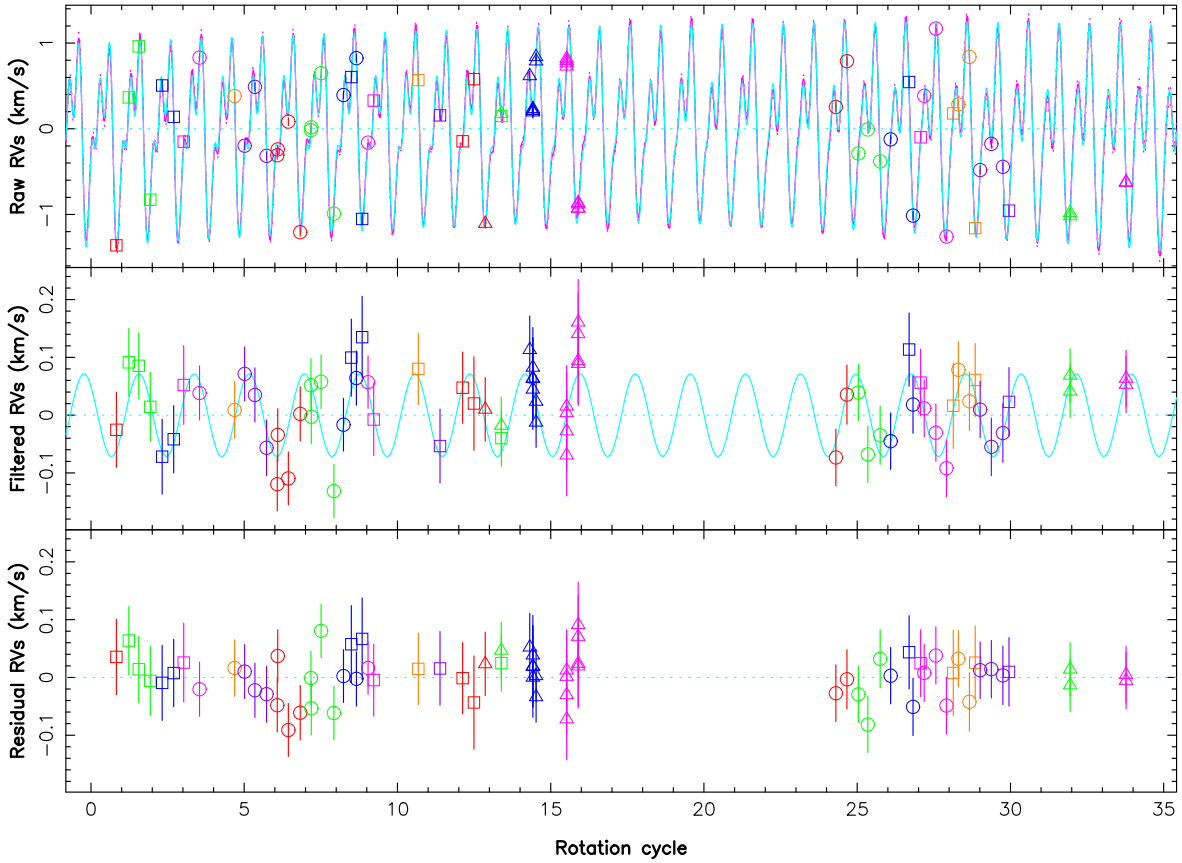

Figure 11. Same as Fig. 8 but now using a planet+GP fit to the data (pink line), where the GP is modelling the activity jitter (cyan line) while the planet and GP parameters are determined using an MCMC simulation. Note how the GP succeeds at modelling the activity and its temporal evolution throughout the whole observing window, and not just for the two separate subsets. The rms dispersion of the residual RVs is 37 m s^{-1}.

that the planet parameters derived with this third method, and in particular K and $P_{\rm orb}$, are likely more accurate than the estimates obtained with the two previous techniques; they also agree better with the initial estimates of D16 inferred from the late 2015 data only. The phase plots of our final five-parameter MCMC run are provided in Appendix A (see Fig. A3, left-hand panel), showing little correlation between the various parameters and thus minimum bias in the derived values.

When applying this technique to the full series of raw RVs collected to date on V830 Tau, including our original set secured in late 2014 and early 2015 (D15, D16), we further enhance the precision on the derived parameters, in particular on the orbital period that we can now pin down to $P_{\rm orb} = 4.927 \pm 0.008$ d. The derived semi-amplitude of the RV curve is the same as in the previous fit ($K = 68 \pm 11$ m s^{-1}) whereas the epoch of inferior conjunction (assuming a circular orbit) is only slightly improved (BJD$_{\rm t}$ = 2 457 360.522 $\pm$ 0.124). The phase plots of this MCMC run are also provided in Appendix A (see Fig. A3, right-hand panel).

Applying the method of Chib & Jeliazkov (2001) to the MCMC posterior samples, we obtain that the marginal likelihood of the model including the planet is higher than that of a model with no planet by a Bayes' factor of 10^8 (10^9 when also including our raw RVs from late 2014 and early 2015), providing a strong and independent confirmation that V830 Tau hosts a close-in giant planet in a 4.93 d orbit. Assuming now a planet on an elliptical orbit (and using $\sqrt{e}\cos\omega$ and $\sqrt{e}\sin\omega$ as search parameters where e and ω, respectively, denote the eccentricity and argument of periapsis of the orbit, Ford 2006) yields a low eccentricity of 0.16 ± 0.20; the marginal likelihood of this latter model is however larger than that of the circular planet model by a Bayes' factor of <3, implying that there is no evidence yet that the planet is eccentric. We provide the MCMC phase plots of the eccentric orbit model in Fig. A4.

The planet parameters derived with all three methods are summarized in Table 5, with those derived in D16 (from our late 2015 data only) listed as well for an easy comparison.

5 SUMMARY AND DISCUSSION

This paper reports the results of an extended spectropolarimetric run on the wTTS V830 Tau, carried out in the framework of the international MaTYSSE Large Programme, using ESPaDOnS on the CFHT, Narval on the TBL, and GRACES/ESPaDOnS on Gemini-North, spanning from 2015 Nov 11 to Dec 22, then from 2016 Jan 14 to Feb 10, and complemented by contemporaneous photometric observations from the 1.25-m telescope at CrAO. This new study is an in-depth follow-up of a previous one, based only on the first part of this data set and focused on the detection of the young close-in hJ orbiting V830 Tau in 4.93 d (D16), and of an older one that suspected the presence of V830 Tau b, but from too sparse a data set to firmly demonstrate the existence of the planet (D15).

Applying ZDI to our two new data subsets, we derived the surface brightness and magnetic maps of V830 Tau. Cool spots and warm plages are again present on V830 Tau, totalling 13 per cent of the overall stellar surface for those to which ZDI is sensitive. The

Table 5. Summary of our results using the three filtering techniques described in Section 4; columns 2–4 are for the two ZDI-based and GPR methods described in Sections 4.1–4.3 and applied to our new data from late 2015 to early 2016, whereas column 5 is for GPR applied to the entire data set (including that of D15). Column 6 recalls the results derived in D16 from the late 2015 data only as a comparison. The first table section lists the derived planet parameters (with M_p denoting the planet mass), the second one mentions the inferred GP hyper parameters in the GPR case, and the last one recalls the achieved χ^2_r (to the filtered RVs for ZDI no. 1, to the Stokes *I* profiles for ZDI no. 2, and to the raw RVs for GPR), and the rms dispersion of the RV residuals (whenever relevant).

Parameter	ZDI no. 1	ZDI no. 2	GPR	GPR (all data)	D16
P_{orb} (d)	4.97 ± 0.03	4.97 ± 0.03	4.93 ± 0.03	4.927 ± 0.008	4.93 ± 0.05
K (m s^{-1})	60 ± 10	62 ± 9	68 ± 11	68 ± 11	75 ± 12
ϕ_0	0.128 ± 0.025	0.142 ± 0.024	0.122 ± 0.028	0.125 ± 0.025	0.123 ± 0.025
BJD$_t$ (2457300+)	60.54 ± 0.13	60.61 ± 0.12	60.51 ± 0.14	60.523 ± 0.124	60.52 ± 0.13
$M_p \sin i$ (M_{Jup})	0.50 ± 0.09	0.52 ± 0.09	0.57 ± 0.10	0.57 ± 0.10	0.63 ± 0.10
M_p (M_{Jup}) assuming $i = 55°$	0.61 ± 0.11	0.63 ± 0.11	0.70 ± 0.12	0.70 ± 0.12	0.77 ± 0.12
a (au)				0.057 ± 0.001	
$a/R_\star$				6.1 ± 0.6	
GP amplitude θ_1 (km s^{-1})			0.878 ± 0.135	0.842 ± 0.105	
Recurrence period θ_2 (P_{rot})			0.9986 ± 0.0007	0.9985 ± 0.0006	
Spot lifetime θ_3 (d)			120 ± 30		
Smoothing parameter θ_4			0.6 ± 0.1		
χ^2_r	0.68	1.0	0.48	0.42	0.75
rms RV residuals (m s^{-1})	44		37	35	48

brightness maps from late 2015 and early 2016 are similar, except for differential rotation slightly shearing the photosphere of V830 Tau and for small local changes in the spot distribution, reflecting their temporal evolution on a time-scale of only a few weeks. The magnetic maps of V830 Tau are also quite similar at both epochs and to that reconstructed from our previous data set (D15), featuring a mainly poloidal field whose dominant component is a 340 G dipole tilted at 22° from the rotation axis. As for the brightness distribution, the magnetic field is also sheared by a weak surface differential rotation, and is evolving with time over the duration of our observing run.

We detected several flares of V830 Tau during the second part of our run, where one major event and a weaker precursor were strong enough to impact RVs at a level of about 0.3 km s^{-1}. In addition to generate intense emission in the usual spectral activity proxies including the Hα, Ca II IRT, and He I D_3 lines, these flares triggered large redshifts of the emission component, especially for the He I D_3 line whose redshift reaches up to 35 km s^{-1} with respect to the stellar rest frame, and 25 km s^{-1} with respect to the average line position in a quiet state. By analogy with the Sun and young active stars (e.g. Collier Cameron & Robinson 1989a,b), we propose that the flares we detect on V830 Tau relate to coronal mass ejections and reflect the presence of massive prominences in the magnetosphere of V830 Tau, likely confined by magnetic fields in the equatorial belt of closed-field loops encircling the star (see Fig. 6), and whose stability is perturbed by the photospheric shear stressing the field or by the hot Jupiter itself in the case of large magnetic loops extending as far as the giant planet orbit (at 6.1 $R_\star$). High-cadence spectral monitoring in various activity proxies is required to investigate such flares in more detail, work out the fate of associated prominences once no longer magnetically confined, and diagnose the main triggering mechanism behind them.

We applied three different methods to our full data set to further confirm the existence of its hJ, and better characterize its orbital parameters. The first two methods, using ZDI to model and predict the RV activity jitter, are those with which V830 Tau b was originally detected, in a slightly modified version allowing them to handle two different ZDI images (corresponding to the late-2015 and early-2016 subsets) at the same time and account for the potential evolution of brightness distributions between the two epochs. Our third technique is fully independent from the two others and directly works from raw RVs, using GPR to model the RV activity jitter and MCMC to infer the optimal planet, and GP parameters and error bars in a Bayesian formalism, following Haywood et al. (2014). All three methods unambiguously confirm the existence of V830 Tau b and yield consistent results for the planet parameters when applied to our new data; in particular, all are able to reliably recover the RV planet signal (of semi-amplitude 68 ± 11 m s^{-1}) hiding behind the activity jitter (of semi-amplitude 1.2 km s^{-1} and rms dispersion 0.65 km s^{-1}) that the brightness distribution of V830 Tau is inducing. The third method is found to perform best, thanks to its higher flexibility and better performances at modelling the temporal evolution of the RV activity jitter. Applying this third method to all raw RVs collected to date on V830 Tau (including those of D15) allows us to significantly improve the precision on the planet orbital period. We also confirm that the planet orbit is more or less circular, with no evidence for a non-zero eccentricity at a 1σ precision of 0.15–0.20. Further work is needed to enable ZDI reconstructing time-variable features and make it as efficient as GPR for filtering activity from RV curves of young active stars.

Spectropolarimetry is found to be essential for retrieving the large-scale topology of the magnetic field that fuels all activity phenomena, but not critical for modelling and filtering the activity jitter at optical wavelengths, largely dominated by the impact of surface brightness features; however, spectropolarimetry is expected to become crucial at nIR wavelengths where brightness features contribute less jitter and Zeeman distortions are much larger than in the optical (e.g. Reiners et al. 2013; Hébrard et al. 2014).

Along with the latest reports of similar detections (or candidate detections) of young close-in giants around TTSs (e.g. van Eyken et al. 2012; David et al. 2016; Johns-Krull et al. 2016; Mann et al. 2016; Yu et al. 2016), our result suggests that newborn hJs may be frequent, possibly more so than their mature equivalents around Sun-like stars (Wright et al. 2012). The orbital fate of young hJs like V830 Tau b under tidal forces and strong winds as the host star progresses on its evolutionary track, contracts and spins up to the

main sequence, and at the same time loses angular momentum to its magnetic wind and planet, is still unclear (e.g. Vidotto et al. 2010; Bolmont & Mathis 2016). One can expect V830 Tau b, whose orbital period is currently longer than the stellar spin period, to be spiralling outwards, at least until V830 Tau is old enough to rotate more slowly than its close-in giant; investigating whether tidal forces will still be strong enough by then to successfully drag V830 Tau b back and kick it into its host star in the next few hundred Myr, may tell whether and how frequent newborn close-in giants can be reconciled with the observed sparse population of mature hJs.

Alternatively, the MaTYSSE sample may be somehow biased towards wTTSs hosting hJs (e.g. Yu et al. 2016). In particular, our sample is likely biased towards wTTSs whose discs have dissipated early, i.e. at a time where the star, still fully convective, hosted a magnetic field strong enough to carve a large magnetospheric gap (Gregory et al. 2012; Donati et al. 2013) and trigger stable accretion (Blinova, Romanova & Lovelace 2016). This may come as favourable conditions for hJs to survive type-II migration, when compared to more evolved cTTSs featuring weaker fields, smaller magnetospheric gaps, and chaotic accretion.

Last but not least, we stress that V830 Tau is the first known non-solar planet host that exhibits radio emission (Bower et al. 2016), which opens very exciting perspectives for in-depth studies of star–planet interactions, and possibly even of exoplanetary magnetic fields (Vidotto et al. 2010; Vidotto & Donati 2016).

Applying the complementary detection techniques outlined in this paper to extended spectropolarimetric data sets such as those gathered within MaTYSSE, or forthcoming ones to be collected with SPIRou, the nIR spectropolarimeter/high-precision velocimeter currently in construction for CFHT (first light planned in 2017), should turn out extremely fruitful and enlightening for our understanding of star/planet formation, about which little observational constraints yet exist.

ACKNOWLEDGEMENTS

This paper is based on observations obtained at the CFHT (operated by the National Research Council of Canada/CNRC, the Institut National des Sciences de l'Univers/INSU of the Centre National de la Recherche Scientifique/CNRS of France and the University of Hawaii), at the TBL (operated by Observatoire Midi-Pyrénées and by INSU/CNRS), and at the Gemini Observatory (operated by the Association of Universities for Research in Astronomy, Inc., under a cooperative agreement with the National Science Foundation/NSF of the United States of America on behalf of the Gemini partnership: the NSF, the CNRC, CONICYT of Chile, Ministerio de Ciencia, Tecnología e Innovación Productiva of Argentina, and Ministério da Ciência, Tecnologia e Inovação of Brazil). This research also uses data obtained through the Telescope Access Program (TAP), which has been funded by the National Astronomical Observatories of China, the Chinese Academy of Sciences (the Strategic Priority Research Program 'The Emergence of Cosmological Structures' grant no. XDB09000000), and the Special Fund for Astronomy from the Ministry of Finance.

We thank the QSO teams of CFHT, TBL, and Gemini for their great work and efforts at collecting the high-quality MaTYSSE data presented here, without which this study would not have been possible. MaTYSSE is an international collaborative research programme involving experts from more than 10 different countries.

We also warmly thank the IDEX initiative at Université Fédérale Toulouse Midi-Pyrénées (UFTMiP) for funding the STEPS collaboration programme between IRAP/OMP and ESO and for allocating a 'Chaire d'Attractivité' to GAJH allowing her regularly visiting Toulouse to work on MaTYSSE data. We acknowledge funding from the LabEx OSUG@2020 that allowed purchasing the ProLine PL230 CCD imaging system installed on the 1.25-m telescope at CrAO. SGG acknowledges support from the Science & Technology Facilities Council (STFC) via an Ernest Rutherford Fellowship [ST/J003255/1]. SHPA acknowledges financial support from CNPq, CAPES, and Fapemig.

We finally thank the referee, Teruyuki Hirano, for his valuable comments that helped us improve the paper.

REFERENCES

Aigrain S., Pont F., Zucker S., 2012, MNRAS, 419, 3147
André P., Basu S., Inutsuka S., 2009, in Chabrier G., ed., Structure Formation in Astrophysics. Cambridge Univ. Press, Cambridge, p. 254
Baruteau C. et al., 2014, in Beuther H., Klessen R. S., Dullemond C. P., Henning T., eds, Protostars and Planets VI. Univ. Arizona Press, Tucson, p. 667
Blinova A. A., Romanova M. M., Lovelace R. V. E., 2016, MNRAS, 459, 2354
Bolmont E., Mathis S., 2016, Celest. Mech. Dyn. Astron, 126, 275
Bouvier J., Alencar S. H. P., Harries T. J., Johns-Krull C. M., Romanova M. M., 2007, in Reipurth B., Jewitt D., Keil K., eds, Protostars and Planets V. Univ. Arizona Press, Tucson, p. 479
Bower G. C., Loinard L., Dzib S., Galli P. A. B., Ortiz-León G. N., Moutou C., Donati J.-F., 2016, ApJ, 830, 107
Brown S. F., Donati J.-F., Rees D. E., Semel M., 1991, A&A, 250, 463
Chene A.-N. et al., 2014, Proc. SPIE Vol. 9151, Advances in Optical and Mechanical Technologies for Telescopes and Instrumentation. SPIE, Bellingham, p. 915147
Chib S., Jeliazkov I., 2001, J. Am. Stat. Assoc., 96, 270
Collier Cameron A., Robinson R. D., 1989a, MNRAS, 236, 57
Collier Cameron A., Robinson R. D., 1989b, MNRAS, 238, 657
David T. J. et al., 2016, Nature, 534, 658
Donati J. et al., 2010, MNRAS, 409, 1347
Donati J. et al., 2011, MNRAS, 412, 2454
Donati J. F. et al., 2016, Nature, 534, 662 (D16)
Donati J.-F., 2001, in Boffin H. M. J., Steeghs D., Cuypers J., eds, Lecture Notes in Physics, Vol. 573, Astrotomography, Indirect Imaging Methods in Observational Astronomy. Springer, Berlin, p. 207
Donati J.-F., 2003, in Trujillo-Bueno J., Sanchez Almeida J., eds, ASP Conf. Ser. Vol. 307, ESPaDOnS: An Echelle SpectroPolarimetric Device for the Observation of Stars at CFHT. Astron. Soc. Pac., San Francisco, p. 41
Donati J.-F., Brown S. F., 1997, A&A, 326, 1135
Donati J.-F., Collier Cameron A., 1997, MNRAS, 291, 1
Donati J.-F., Semel M., Carter B. D., Rees D. E., Collier Cameron A., 1997, MNRAS, 291, 658
Donati J.-F., Collier Cameron A., Petit P., 2003, MNRAS, 345, 1187
Donati J.-F. et al., 2006, MNRAS, 370, 629
Donati J.-F. et al., 2007, MNRAS, 380, 1297
Donati J.-F. et al., 2008, MNRAS, 385, 1179
Donati J.-F. et al., 2012, MNRAS, 425, 2948
Donati J.-F. et al., 2013, MNRAS, 436, 881
Donati J.-F. et al., 2014, MNRAS, 444, 3220 (D14)
Donati J.-F. et al., 2015, MNRAS, 453, 3706 (D15)
Ford E. B., 2006, ApJ, 642, 505
Frank A. et al., 2014, in Beuther H., Klessen R. S., Dullemond C. P., Henning T., eds, Protostars and Planets VI. Univ. Arizona Press, Tucson, p. 451
Grankin K. N., 2013, Astron. Lett., 39, 251 (G13)
Grankin K. N., Bouvier J., Herbst W., Melnikov S. Y., 2008, A&A, 479, 827
Gregory S. G., Donati J.-F., Morin J., Hussain G. A. J., Mayne N. J., Hillenbrand L. A., Jardine M., 2012, ApJ, 755, 97
Haywood R. D. et al., 2014, MNRAS, 443, 2517
Haywood R. D. et al., 2016, MNRAS, 457, 3637

Hébrard É. M., Donati J.-F., Delfosse X., Morin J., Boisse I., Moutou C., Hébrard G., 2014, MNRAS, 443, 2599
Hussain G. A. J. et al., 2009, MNRAS, 398, 189
Jardine M., 2004, A&A, 414, L5
Johns-Krull C. M., 2007, ApJ, 664, 975
Johns-Krull C. M., Valenti J. A., Koresko C., 1999, ApJ, 516, 900
Johns-Krull C. M. et al., 2016, ApJ, 826, 206
Landi degl'Innocenti E., Landolfi M., 2004, Polarisation in Spectral Lines. Kluwer, Dordrecht
Lin D. N. C., Bodenheimer P., Richardson D. C., 1996, Nature, 380, 606
Lopez-Morales M. et al., 2016, preprint (arXiv:1609.07617)
Lucy L. B., Sweeney M. A., 1971, AJ, 76, 544
Mann A. W. et al., 2016, AJ, 152, 61
Montes D., Fernandez-Figueroa M. J., de Castro E., Sanz-Forcada J., 1997, A&AS, 125
Morin J. et al., 2008, MNRAS, 390, 567
Moutou C. et al., 2007, A&A, 473, 651
Petit P. et al., 2015, A&A, 584, A84
Rajpaul V., Aigrain S., Osborne M. A., Reece S., Roberts S., 2015, MNRAS, 452, 2269
Reiners A., Shulyak D., Anglada-Escudé G., Jeffers S. V., Morin J., Zechmeister M., Kochukhov O., Piskunov N., 2013, A&A, 552, A103
Rodríguez L. F., González R. F., Raga A. C., Cantó J., Riera A., Loinard L., Dzib S. A., Zapata L. A., 2012, A&A, 537, A123 (R12)
Romanova M. M., Lovelace R. V. E., 2006, ApJ, 645, L73
Siess L., Dufour E., Forestini M., 2000, A&A, 358, 593
van Eyken J. C. et al., 2012, ApJ, 755, 42
Vidotto A. A., Donati J.-F., 2016, A&A, in press
Vidotto A. A., Opher M., Jatenco-Pereira V., Gombosi T. I., 2010, ApJ, 720, 1262
Wright J. T., Marcy G. W., Howard A. W., Johnson J. A., Morton T. D., Fischer D. A., 2012, ApJ, 753, 160
Yu L. et al. 2016, MNRAS, in press

APPENDIX A: ADDITIONAL FIGURES

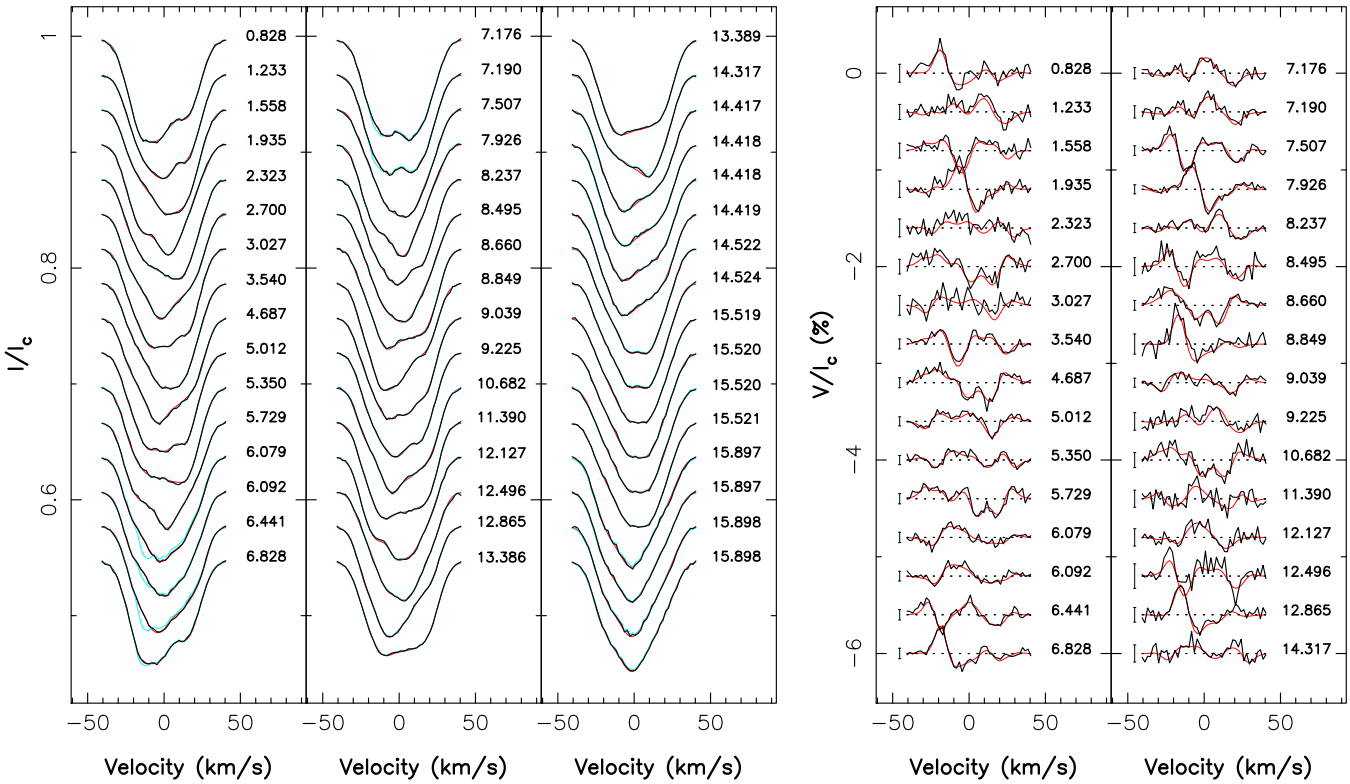

Figure A1. Same as Fig. 2 for our late 2015 observations.

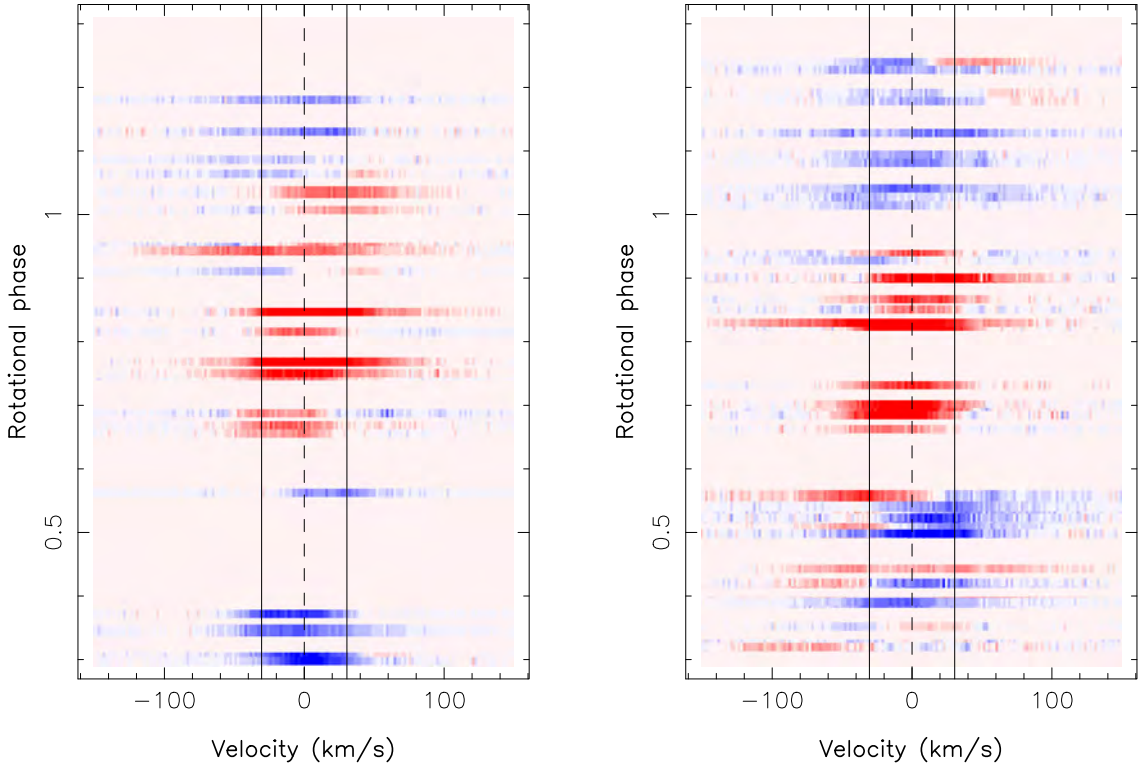

Figure A2. Dynamic spectra of Hα residual of V830 Tau in late 2016 (left) and early 2015 (right), with residuals computed with respect to the S/N^2-weighted mean over the whole observing run (after the removal of a few flaring spectra, see Section 2). Note how the phase of maximum Hα emission increases from 0.8 to 0.9 from late 2015 to early 2016. Red/blue means positive/negative residuals, with amplitudes ranging from –0.3 to 0.3 (in units of the continuum level), whereas the dashed and full vertical lines depict the line centre (in the stellar rest frame) and the stellar rotational broadening $v \sin i$.

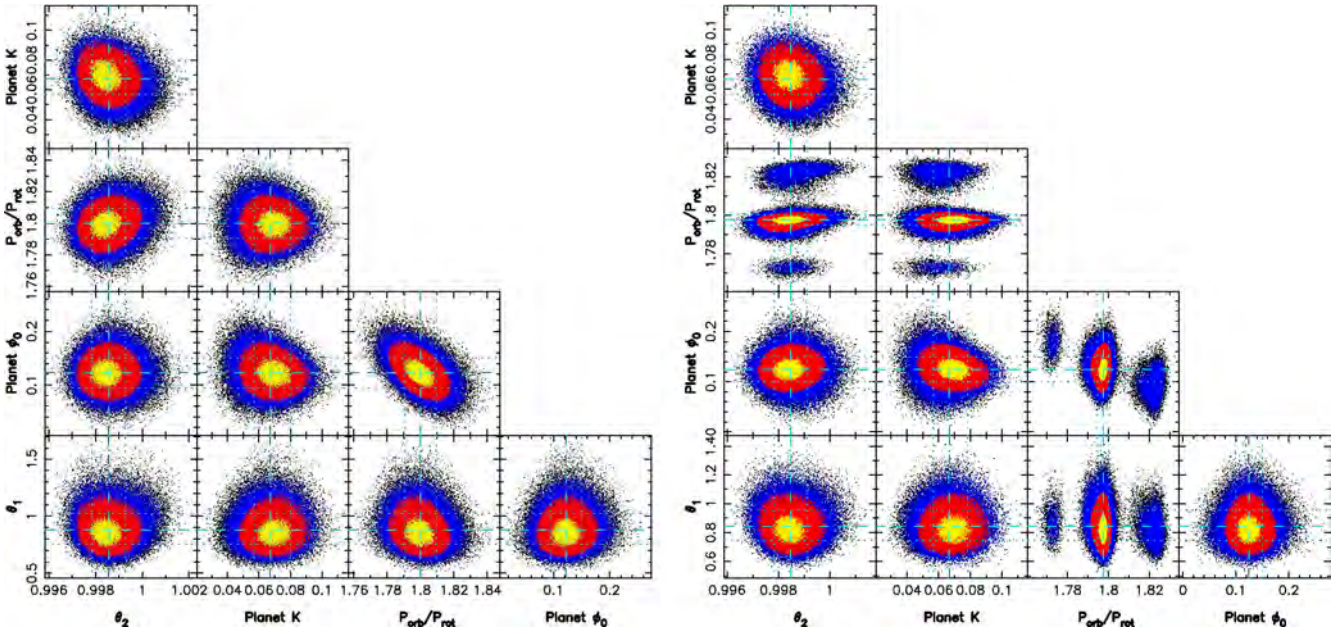

Figure A3. Phase plots of our final five-parameter MCMC run using both the late 2015 and early 2016 data (left) and all raw RVs collected to date on V830 Tau (right), with yellow, red, and blue points marking the 1σ, 2σ, and 3σ confidence regions, respectively. The optimal parameter we derive from the left-hand panel are, respectively, equal to $\theta_1 = 0.878 \pm 0.135$ km s^{-1}, $\theta_2 = 0.9986 \pm 0.0007 P_{\rm rot}$, $K = 68 \pm 11$ m s^{-1}, $P_{\rm orb}/P_{\rm rot} = 1.80 \pm 0.01$ (i.e. $P_{\rm orb} = 4.93 \pm 0.03$ d), and $\phi_0 = 0.122 \pm 0.028$ (i.e. BJD$_{\rm t} = 2\,457\,360.51 \pm 0.14$ d). Fitting all raw RVs allows us to significantly improve the precision on the rotation period ($P_{\rm orb}/P_{\rm rot} = 1.7976 \pm 0.0027 \pm 0.01$, i.e. $P_{\rm orb} = 4.927 \pm 0.008$ d) and to slightly refine the epoch of inferior conjunction ($\phi_0 = 0.125 \pm 0.025$, i.e. BJD$_{\rm t} = 2\,457\,360.523 \pm 0.124$ d). Note the little correlation between the various parameters.

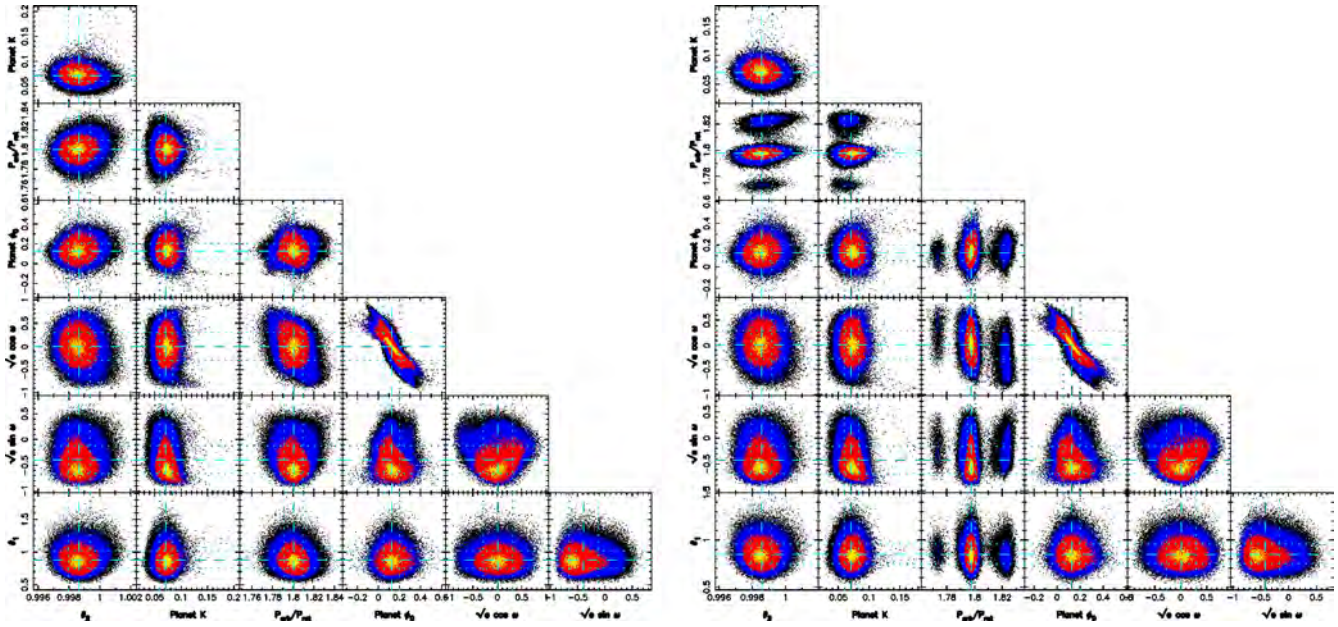

Figure A4. Same as Fig. A3 when fitting an eccentric orbit using parameter $\sqrt{e}\cos\omega$ and $\sqrt{e}\sin\omega$ as search parameters where e and ω, respectively, denote the eccentricity and argument of periapsis of the orbit; the marginal likelihood of the best eccentric orbit model is not significantly larger than that of the best circular orbit model, implying that there is no evidence that the planet is eccentric.

This paper has been typeset from a TEX/LATEX file prepared by the author.